ADVANCED SEISMIC RISK ASSESSMENT OF CALIFORNIA BOX-GIRDER BRIDGES USING EMERGING MODELING TECHNIQUES AND INNOVATIVE RISK MODELS

A Dissertation
Presented to
The Academic Faculty

By

Qiu Zheng

In Partial Fulfillment
of the Requirements for the Degree
Doctor of Philosophy in the
School of Civil and Environmental Engineering
Georgia Institute of Technology

Georgia Institute of Technology
December 2021

ADVANCED SEISMIC RISK ASSESSMENT OF CALIFORNIA BOX-GIRDER BRIDGES USING EMERGING MODELING TECHNIQUES AND INNOVATIVE RISK MODELS

Thesis committee:

Dr. Reginald DesRoches, Advisor
Department of Civil and Environmental Engineering
Rice University

Dr. Chuang-Sheng Walter Yang, Co-advisor
School of Civil and Environment Engineering
Georgia Institute of Technology

Dr. Yang Wang
School of Civil and Environment Engineering
Georgia Institute of Technology

Dr. Rafi L. Muhanna
School of Civil and Environment Engineering
Georgia Institute of Technology

Dr. David Goldsman
School of Industrial and Systems Engineering
Georgia Institute of Technology

Date approved: November 23, 2021

Dedication To

My Grandmother

ACKNOWLEDGMENTS

I want to express my sincere appreciation for everyone who helped me through these years pursuing my Ph.D. degree.

First and foremost, I am deeply grateful for all the supports from my primary advisor, Professor Reginald DesRoches. He has offered the support, help, trust, and encouragement that armed me on my way here. There is no way to convey my gratitude and respect for Professor DesRoches. The circumstance in the afternoon when he accepted me into his group was always unforgettable. When he said 'Yes' to my application, I could feel that the path to my dream was lightened up by him. I have been taken great care of since the first day I began working with him.

Warmest gratitude is also extended to my co-advisor, Dr. Chuang-Sheng Walter Yang. He trained me step-by-step with doing finite element simulations, conducting analytical analysis, preparing for academic presentations, writing papers, and ultimately to this dissertation. He spent most of his time in these years to guide me from a knowing-nothing-undergraduate student to a mature researcher who can deal with any challenges in the future. In addition, he also offered kind care in my daily life at Georgia Tech. I want to say a sincere 'thank you' for his instruction and kindness.

My sincere thanks go to the members of my doctoral committee: Professor Yang Wang, Professor Rafi L. Muhanna, and Professor David Goldsman. They generously invested time and support throughout the development of this study, and their valuable comments helped improve my work.

I gratefully acknowledge the support I have received from the California Department of Transportation while pursuing my doctoral studies. Particularly, I would like to thank Cliff Roblee for the substantial editorial input to my draft manuscript including significant original content for Chapter-4 on emerging capacity models. As a project manager, he has devoted all his enthusiasm to this project and provided detailed inventory data. His genius insight always found the path to overcoming difficulties. I truly benefited from his professional support and sound advice. I would also like to thank Sharon Yen from Caltrans for her suggestions on bridge designs. Both Cliff and Sharon helped a lot with this study.

I also want to thank Dr. Yazhou Xie from McGill University for sharing his knowledge, good ideas, and active interest in this research. His work regarding the backfill model and foundations is essential to the developed fragility models presented in this work. I also wish to acknowledge Professor Shashi Kunnath from UC Davis. He offered professional insights in compiling the column dataset and column modeling. In particular, the work on non-local column modeling by him and his team guided the column simulations in this study.

Last but not least, I would like to express my deep gratitude to my family. I want to thank my parents for their unconditional support and love throughout my life. I am grateful to them and my grandmother for all their sacrifice in raising me. I thank my little sister, an angel in my life, for offering me lots of happiness. I am also thankful to my girlfriend, Mingshu, who has been my best companion and friend since the day we met. She has celebrated each of my accomplishments and supported me whenever I needed it.

DISCLAIMER

The current study is supported by the California Department of Transportation (Caltrans), USA, through Project P266, Task 1780: Production Development of Generation-2 Fragility (g2F) Models for California Bridges.

The contents of this report reflect the views of the author, who is responsible for the facts and accuracy of the data presented herein. The contents do not necessarily reflect the official views or policies of the State of California or the Federal Highway Administration. This publication does not constitute a standard, specification, or regulation.

The bridge-component capacity models presented herein, while the best available at the time of publication of this dissertation, are considered preliminary as they have not been fully vetted by Caltrans. Therefore, the fragility models presented for select bridge classes in this dissertation, while broadly representative of expected risk levels and trends, should not be considered as the final authoritative versions of the g2F models intended for application. Authoritative versions of all g2F products will be solely published by Caltrans as finalized.

TABLE OF CONTENTS

LIST OF TABLES

LIST OF FIGURES

LIST OF SYMBOLS AND ABBREVIATION

CCLS	Component Capacity Limit State
CDS	Component Damage State
CDST	Component Damage State Threshold
EDP	Engineering Demand Parameter
FAR+	Filtered Adaptive Regression - Logistic Incorporation of Omitted Data
HS-R	High State - Redundancy
IDA	Incremental Dynamic Analysis
IM	Intensity Measurement
LHS	Latin Hypercube Sampling
M-MARS	Modified Multivariate Adaptive Regression Spline
M-PARS	Multiphase Performance Assessment of structural Response to Seismic Excitations
MARS	Multivariate Adaptive Regression Spline
MSA	Multiple-Stripe Analysis
NLTHA	Nonlinear Time History Analysis
OpenSees	Open System for Earthquake Engineering Simulation
PSDM	Probabilistic Seismic Demand Model
RBS	Representative Bridge System

SUMMARY

Seismic fragility models depict the structural failure probability under earthquakes and play an essential role in planning mitigation strategies for, and prioritizing emergency response after, a natural hazard. This dissertation concentrates on developing a new generation of seismic fragility models for select concrete box-girder bridges in California in terms of advanced numerical bridge models, comprehensive bridge component capacity models, and robust seismic risk analysis methodologies. The dissertation first introduces emerging modeling techniques that can improve the fidelity of numerical models. Most importantly, an abutment backwall fracture model is proposed to eliminate an enormous error due to excessive lateral supports from abutment foundations in conventional abutment models. In the aspect of capacity models, seven damage states for columns are established based on a newly developed column dataset with 198 laboratory tests. Next, appropriate geometrical and material uncertainties are identified and applied in the finite element bridge models. Furthermore, to ensure that the 352 virtual bridge realizations meet the design criteria in California, three sampling techniques are proposed to correlate different uncertainties. After acquiring seismic response demands of bridge components, several methods of establishing a probabilistic seismic demand model (PSDM), relating structural seismic demand and ground motion intensity measurement, are examined. A new method called modified multiple adaptive regression splines (M-MARS) is proposed to construct the PSDM. Following is the development of four-level fragility models, from low-level component fragilities to high-level system fragilities. Ultimately, conclusions are made based on the research findings and comparisons of results through a developed bridge grouping method.

CHAPTER 1

INTRODUCTION

1.1 Problem Description

Highway bridges play a crucial role in the transportation systems, yet past earthquakes have demonstrated their vulnerability (Caltrans, 1994; Jibson and Harp, 2011). Earthquake damage to highway bridges could cause significant disruption to the transportation network, delay emergency response, and finally lead to casualties and economic losses to communities. Therefore, understanding the seismic behavior of highway bridges is valuable for pre-earthquake planning and post-earthquake responses.

Fragility analysis provides an approach for characterizing the seismic behavior of highway bridges. A seismic fragility curve quantitatively depicts the vulnerability of bridges with a conditional probabilistic measurement, which describes the probability that the demand of a structural component or structural system exceeds a given capacity limit state when subjected to a range of potential seismic events with a specified measure of intensity (such as pseudo-spectral acceleration at 1.0 second, S_{a1}).

It is well recognized that California is a state exposed to high seismic risk by historical earthquakes. To mitigate potential impacts, the California Department of Transportation (Caltrans) has deployed the ShakeCast platform (Lin and Wald, 2008), developed by the United States Geological Survey (USGS), to estimate earthquake damage to highway bridges in California. The ShakeCast platform combines capabilities of ShakeMap – a map showing the severity of a ground-shaking broadcast in nearly real-time after an earthquake – with pre-established fragility models for each bridge in California inventory to provide post-earthquake situational awareness of damage to the transportation network and valuable guidance for prioritizing emergency response and inspection. It is also used as a planning tool to examine and mitigate the impacts of scenario earthquakes.

The operation of the ShakeCast platform posts the need for proper fragility models of various bridge systems. The currently deployed fragility models in the ShakeCast platform are HAZUS-based models developed in the 1990s (FEMA, 2003). By necessity, these early models are too broad and simplified to achieve the full potential for Caltrans application in terms of the following aspects. (1) The estimation of bridge seismic performance is based on simplified two-dimensional analysis and compared to a limited set of damage observations. (2) The bridge taxonomy is based on the limited data fields available in the National Bridge Inventory (NBI) and considers only limited bridge parameters. (3) The damage definitions were broadly classified as four bridge-system-level states, from minor to complete, that can neither adequately account for Caltrans' post-earthquake inspection and repair strategies nor be readily tied to bridge downtime and repair cost estimates. (4) This early framework is not well aligned with Caltrans seismic design philosophy or the California bridge inventory.

1.2 Research Objectives and Scope

This research seeks to add to the existing body of knowledge of bridge seismic fragility analysis. The intention is to improve upon the HAZUS fragility models for the ShakeCast application. Specifically, it broadly outlines procedures being adopted for the development of 'Generation-2 Fragility (g2F)' models and illustrates the methodology for a select set of modern box-girder concrete bridge classes. To achieve this goal, this study centers on improving modeling fidelity in terms of demand model and bridge uncertainty sampling, refining damage state definitions, advancing the regression methodologies for highly nonlinear seismic demand data, and establishing multiple-stage fragility models.

This dissertation summarizes research advances in the following areas:

• Applied emerging numerical modeling techniques to capture the seismic response of bridge columns with different failure modes, including calibration of the numerical models against laboratory tests;

• Developed an improved abutment modeling scheme and incorporated new backwall-connection models to account for backwall fracture mechanism;

• Compiled a literature-based dataset summarizing the performance of 198 laboratory column tests, including systematic characterization of specimen detailing, testing parameters, and damage states as a function of load-displacement response. These column designs were further grouped for different design eras and failure modes to support the development of a family of capacity models;

• Developed an extensive analytically based column performance data set using the validated column models for the same design era, and failure mode groupings noted above. These analytical results are used to extend the literature-based experimental findings, specifically for: 1) California bridge-column designs, 2) high damage state performance, and 3) consideration of the effects of bent configuration and boundary conditions;

• Facilitated Caltrans development of a new system of column capacity limit states involving eight states (including 'no observable damage') for each of the design eras and failure modes noted above. These models are based on combined findings from the experimental and analytical data sets noted above;

• Facilitated Caltrans development of comparable eight-state capacity models for other bridge components including abutment backwalls and shear keys and column keys;

• Developed and implemented several sampling constraints for generating realistic virtual bridge realizations for demand analysis which reflect both bridge design policies and observed California bridge inventory trends;

• Generated and completed three-dimension nonlinear finite-element analyses for models of several Caltrans bridge classes, including capture of the seismic response of individual bridge components;

• Adapted advanced statistical regression techniques to model probabilistic seismic demand models (PSDMs) for highly nonlinear seismic demand data;

• Generated internally-consistent sets of fragility curves for components, component groups, bridge regions, and the overall bridge system. This included defining unique bridge-system fragility curves conditioned on different component subgroups;

Although this study is primarily centered on modern box-girder bridges with ductile seismic design details, it also considers some numerical modeling techniques and capacity models applicable to bridges with pre-ductile design detailing.

1.3 Dissertation Outline

The remaining content of the dissertation is organized into the following chapters:

• **Chapter 2** is an overview of existing literature regarding bridge seismic fragility models, including the current state of practice and research studies on demand modeling of bridge system(s), damage state system, development of probabilistic seismic demand models (PSDM), as well as the development of bridge fragility.

• **Chapter 3** presents the demand modeling methodologies for multiple components/objects in the bridge system. Specifically, modeling procedures for columns with flexural or shear failure modes and several abutment components are discussed. Simulation results are compared against the experimental tests.

• **Chapter 4** details the development of column capacity models. After first describing the work in compiling the literature-based experimental dataset, the column bent redundancy effect is identified and included in the column capacity model. In addition, this chapter briefly discusses capacity models for other bridge components.

• **Chapter 5** focuses on sampling procedures for bridge component details and mixtures needed to create virtual bridge realizations which reflect authentic bridge design in California. Of particular note, this chapter identifies realistic design constraints on random sampling procedures – such as the specification of column-foundation designs to be compatible with column-hinge capacities – and ultimately proposes a modified sampling procedure to account for such constraints.

- **Chapter 6** outlines the statistical framework adopted for the development of fragility models starting from a Probabilistic Seismic Demand Model (PSDM) coupled with a Component Capacity Limit State (CCLS) model. This chapter outlines alternative regression methods and adopts a hybrid strategy that is well suited to the handling of highly nonlinear seismic demand data. This chapter also describes roll-up procedures adopted for the development of component-group or system-level fragility models from the base component models and outlines an innovative method to group bridges based on system-level models.

- **Chapter 7** summarizes the research and draws conclusions. Anticipated impacts of the work and suggestions for future research are offered in this chapter as well.

CHAPTER 2
LITERATURE REVIEW

Since 2008, the California Department of Transportation (Caltrans) has used the ShakeCast (Lin and Wald, 2008) alerting system to provide early situational awareness to emergency managers. ShakeCast uses a combination of ground-shaking maps – created in nearly real-time by the United States Geological Survey (USGS), coupled with pre-calculated bridge fragility models – to estimate the bridge damage rapidly. This research outlines methods applicable to the development of fragility models for concrete bridge types representing roughly 75% of California's bridge inventory and demonstrates these methods for a subset of concrete bridge classes. This chapter first reviews the general framework for fragility modeling, then provides a more detailed look at existing practices for the modeling and capacity definitions of two critical bridge components, columns, and abutments. Subsequent chapters detail advances in modeling these components better to support overall bridge seismic risk evaluation for California bridges.

2.1 Framework of Seismic Fragility Analysis

A seismic fragility model is specified under a seismic ground motion intensity. As represented in Equation 2.1, a fragility model depicts the probability of a structure reaching a damage state (DS) given an hazard intensity parameter, or Intensity Measurement (IM).

$$Fragility = P(DS|IM). \tag{2.1}$$

Expert opinion, empirical, and analytical analysis are three widely-used methods to develop fragility curves. Expert opinion fragility curves are built using an estimation of its percentiles provided by experts, which is highly subjective and primarily relies on the seismic experience of experts (ATC, 1985). Empirical models are developed based on the damage level of past hazard events, offering an expected value to a database of structure damage observations. Limitations of the empirical method include the scarcity of detailed damage data along with the limited magnitude range and geographic regions where damaging earthquake motions have been recorded (Basöz et al., 1999a; Basöz and Kiremidjian, 1999b; Yamazaki et al., 1999; Shinozuka et al., 2000a).

Due to the limitations of the expert opinion and the empirical methods, analytical fragility analysis is frequently adopted. Analytical fragility analysis is conducted with numerical simulations accounting for uncertainties embedded in design parameters, such as bridge geometry, materials properties, and ground motions. The fragility model in this method represents the probability of conditional demand ($D|IM$) exceeding capacity (C) corresponding to a specific damage state:

$$Fragility = P(D \geq C|IM). \tag{2.2}$$

If the capacity is expressed as a cumulative probability function $F_C(\cdot)$ and a structural demand given an intensity measurement is assumed to have a probability density function $f_{D|IM}(\cdot)$, the above probability in can be written in a convolutional form:

$$P(D \geq C|IM) = \int_{-\infty}^{\infty} F_C(x) f_{D|IM}(x) dx \tag{2.3}$$

Based on different methods of acquiring seismic demand values, analytical fragility analysis is further categorized as elastic spectral method (Hwang et al., 2000), nonlinear static analysis (or capacity spectrum method) (Dutta and Mander, 1998), and Nonlinear Time History Analysis (NLTHA). Compared to the other two, NLTHA has been identified as a more reliable method (Shinozuka et al., 2000b) in terms of prediction the structural seismic demands.

The conditional probability distribution of seismic demand in Equation 2.2 is established by Probabilistic Seismic Demand Model (PSDM) through analysis of bridge classes subjected to different ground motion intensities. Based on the way of selecting ground motions, multiple methods for establishing PSDM using NLTHA were proposed. Formulated by Vamvatsikos and Cornell (2002), Incremental Dynamic Analysis (IDA) is a method that involves scaling each ground motion in a suite until it causes structure-collapse. The scaling approach raises concerns about unrealistic ground motion frequencies that might not be representative of the seismic hazard of the site. Multiple-Stripe Analysis (MSA) is then proposed in the work by Jalayer (2003), and further discussed by Baker (2015), to overcome the scaling issue in IDA. Unlike IDA that only one suite of ground motion is scaling to all IM, MSA scales unique suite of ground motions for each targeting IM. While many researchers used this method to study structural fragility, this method requires a sufficient number of ground motions in a suite to get a reliable estimation of failure probability. Moreover, both of IDA and MSA predict failure probability at some specific IM, and cannot directly establish a continuous fragility model.

Therefore, this research uses the cloud approach to establish PSDM due to its relatively high accuracy and cost-efficiency compared to the other methods. Cloud approach conducts NLTHA in a suite of ground motions which possesses nearly continuous IM, and then generates the conditional demand probability distribution by regression analysis. By means of regression, the continuity of the data is taken into account, thus minimizing the effect of possible outliers.

Figure 2.1 demonstrates the basic procedure for developing fragility models and implementation of these models into the ShakeCast platform. The first step is establishing a proper ground motion suite for California earthquakes. The list of ground motions used in this project was assembled by Caltrans using the NGA-2 database (see Appendix B). Next, three-dimensional non-linear finite-element models for different Representative Bridge System (RBS) are built within the research-grade finite element simulation

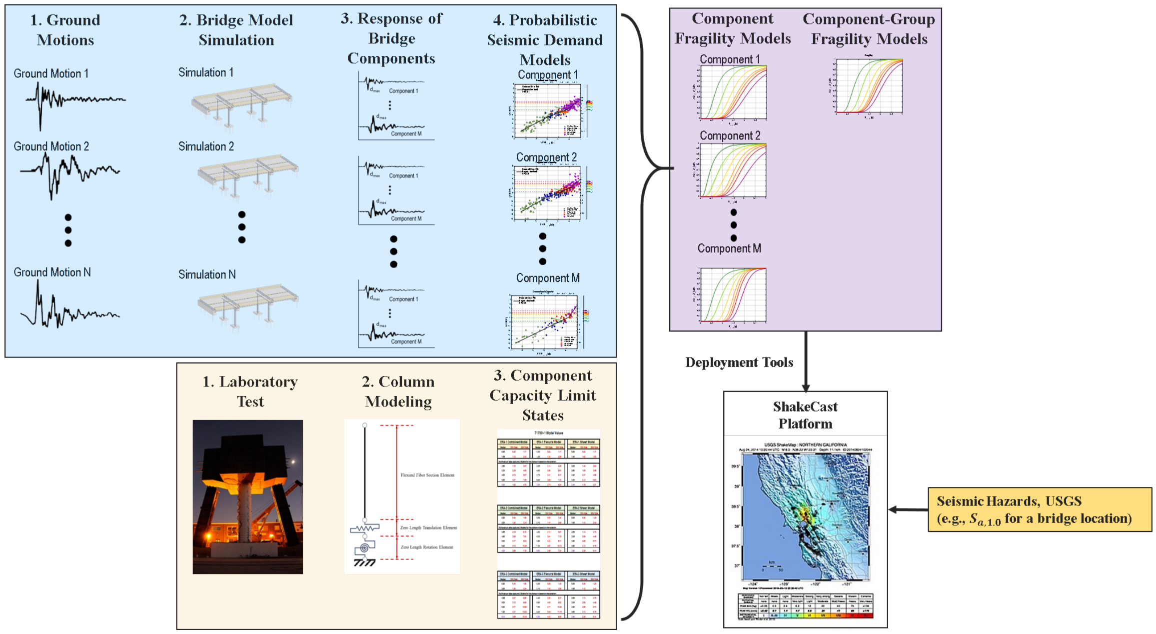

Figure 2.1: Procedure for developing fragility models using the cloud method.

platform Open System for Earthquake Engineering Simulation (OpenSees) (McKenna et al., 2000). NLTHA are carried out to obtain the maximum/average responses of multiple pre-determined Engineering Demand Parameter (EDP).

Component capacity models establish the relationship between component damage and one or more EDP's. To develop such models, experimental results related to bridge component capacities are collected and organized to create limit state thresholds for all bridge components and corresponding damage definitions. Specifically, this research compiles a dataset for laboratory column test specimens based on an extensive literature review. The dataset summarizes specimen details and damage state values. To complement the limited data for the high damage states, calibrated finite element models are established to analyze the column till collapse, accounting for the effect of column bent. The capacity models are ultimately developed considering different failure modes and column bent effect.

A combination of PSDM and capacity models generates fragility models for different components. A roll-up procedure is then applied to develop component-group and system fragility models.

In application, these fragility models will be assigned to each bridge in California within the ShakeCast platform. Combined with the site-specific ground-motion hazard determined by the USGS, the seismic damage risk for highway bridges can be estimated for either individual events or on a uniform hazard basis.

2.2 Seismic Analysis of Bridge Components

The establishment of a demand model is critical, and the most computationally complex step in fragility modeling. Among all the bridge components, the internal supports and abutments are pivotal in the demand model due to their high nonlinearity and seismic vulnerability.

2.2.1 Column Modeling

In modern ductile design, bridge design policies have evolved to ensure the columns are flexural critical in most cases. But back to early design eras, bridge columns were usually lightly confined and thus tended to have a shear failure or flexural-shear failure during earthquake loading. As depicted in Figure 2.2, a column is defined as flexural critical if the shear force is always smaller than its shear capacity, whereas the other two types of columns would touch the shear capacity line during the increase of shear force. The difference between flexural-shear and shear critical columns is that a flexural-shear column triggers shear failure after its yield displacement (Ghannoum and Moehle, 2012).

Various models for shear capacity and modeling of shear columns are introduced in the literature (Umehara, 1983; Priestley et al., 1994, 1996; Sezen, 2002; Elwood, 2002; Giannini et al., 2008; Ghannoum and Moehle, 2012; Jeon et al., 2015) and design codes (Elwood et al., 2007; Caltrans, 2015*d*, 2018; AASHTO, 2010; ACI, 2014). The easiest approach to consider a shear behavior is using the *Section Aggregator* in OpenSees to couple a shear behavior into a typical fiber section (Giannini et al., 2008). However, in

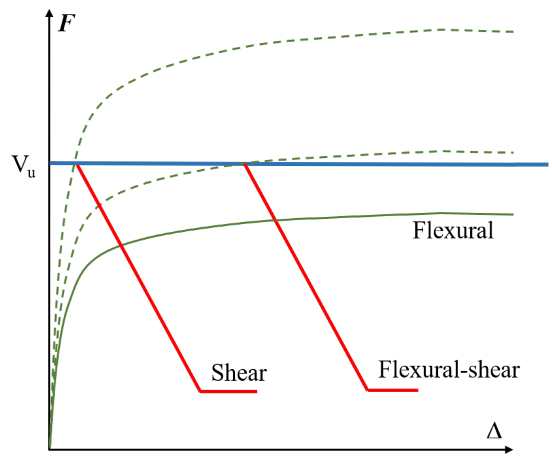

Figure 2.2: Definition of flexural, flexural-shear, and shear columns.

this method, the shear behavior is only considered at the sectional level, and it is difficult to develop the relationship between shear stress and shear deformation. Other approaches focused on developing a relationship of shear force and shear displacement. Shear failure can be captured using a “zero-length” spring (or a shear spring). There are a few methods available to define a trigger condition of shear failure. Elwood (2002) proposed a shear spring with a shear limit curve. Shear degradation is triggered when the demand value reaches the shear capacity limit curve V_u, as shown in Figure 2.2, which was defined to happen at a drift ratio of 1%. In addition, the axial limit curve can also be implemented to consider the axial failure after the shear failure occurs using a shear-friction model so that users can model the column from the initial state to the collapsed state. Ghannoum and Moehle (2012) proposed a trigger condition relevant to a rotation angle in the plastic hinge length.

Among these methods, defining a zero-length shear spring is the most straightforward and thus has been widely used. The most important step for defining a shear spring is to find the shear capacity for a column. There are many existing shear capacity models, but most are used in building columns. Due to different ranges of axial load ratios between building columns and bridge columns, three shear capacity models applicable to bridge columns are introduced in the following.

Model proposed by Priestley et al. (1994)

Priestley proposed a shear capacity model based on experimental tests of bridge piers. He proposed a model with three terms, concrete V_c, steel V_s, and axial load V_P. Priestley pointed out the concrete shear capacity decreases as displacement ductility increases while the steel term remains the same. Priestley indicated the compression angle as demonstrated in Figure 2.3(a) was relative to the shear capacity, which also shows that the axial load term is inversely proportioned to the compression depth of concrete c.

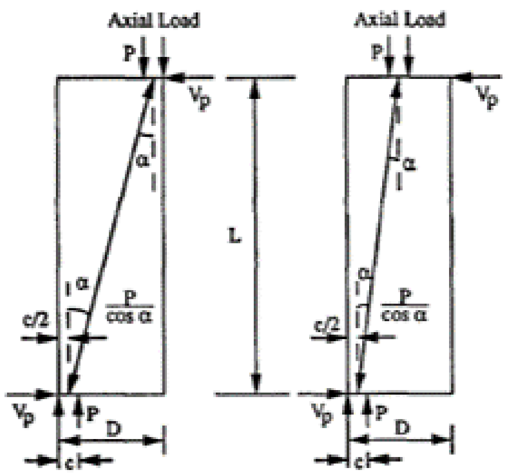

(a)

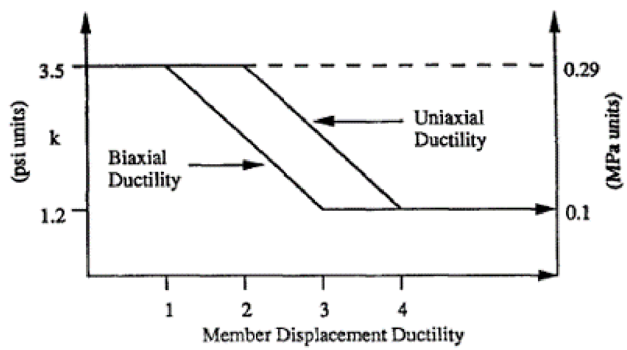

(b)

Figure 2.3: Shear capacity model proposed by Priestley et al. (1994): (a) demonstration of axial load term; and (b) amplification factor.

As the displacement ductility increases, the compression depth of concrete c will decrease. Therefore, the axial load component increases as displacement increases. Moreover, increasing column displacement could result in a larger shear capacity when a large axial load situation exists. The model is finally represented in Equation 2.4, where k is an amplification factor determined by Figure 2.3(b) and accounts for concrete material softening; f'_{co} is the compression strength of concrete; A_g is the gross area of the cross-sections; k_s is a multiplier for steel transverse reinforcement area. As suggested by Priestley et al. (1994), for circular section, k_s = 1.571; for rectangular section, k_s is the number of total transverse reinforcement number in a layer. A_h, f_{yh}, and s are the area, yield strength, and spacing of transverse reinforcement, respectively; D_c is the depth of core concrete. In the calculation of steel term, $\cot 30°$ accounts for the assumption that the shear crack is about 30 degrees. In the term for axial load P, M/VD is the component shear span.

$$V = V_c + V_s + V_P \tag{2.4a}$$

$$V_c = k\sqrt{f'_{co}\mathrm{psi}} \cdot 0.8A_g \tag{2.4b}$$

$$V_s = k_s \frac{A_h f_{yh} D_c}{s} \cot 30° \tag{2.4c}$$

$$V_P = \frac{D - c}{\frac{2M}{V}} P \tag{2.4d}$$

This model considers a shear crack angle in the transverse reinforcement term. Additionally, the ductility modification term is separated into two parts, which indicates that the shear span ratio may affect the member ductility. However, the determination of c is not an easy practice in the calculation.

*Model used in Caltrans (2015*d*)*

Two terms named the concrete V_c and the steel V_s are considered in the Caltrans' shear capacity model. The axial load effect is accounted in the concrete term with a multiplier no larger than 1.5. The steel term is approximately equal to the model proposed by Priestley et al. (1994).

$$V = V_c + V_s \tag{2.5a}$$

$$V_c = v_c A_e \leq 4\sqrt{f'_{co}\text{psi}} \cdot 0.8A_g \tag{2.5b}$$

$$V_s = k_s \frac{A_h f_{yh} D_c}{s} \leq 4\sqrt{f'_{co}\text{psi}} \cdot 0.8A_g \tag{2.5c}$$

$$v_c = f_1 f_2 \sqrt{f'_{co}\text{psi}} \tag{2.5d}$$

$$f_2 = 1 + \frac{P}{2000A_g} < 1.5 \tag{2.5e}$$

For f_1, if calculate the shear capacity inside the plastic hinge region:

$$0.3 \leq f_1 = (\rho_{sv} f_h)/0.15 + 3.67 - \mu \leq 3.0 \tag{2.5f}$$

$$\rho_{sv} f_h \leq 0.35 \tag{2.5g}$$

If it is outside the plastic hinge region:

$$f_1 = 3.0 \tag{2.5h}$$

Material softening effects are considered in Equation 2.5d, where μ is the column displacement ductility. However, as a model used for design, this model is more conservative than other models.

Model proposed by Sezen (2002)

This model is adopted in ASCE specifications (Elwood et al., 2007) and other researchers' works by the reason of its relatively high accuracy and easy implementation. Shear capacity from steel is the same as the equations in Caltrans' model, while concrete component additionally considers the shear span, axial load, and material properties.

$$V = k(V_c + V_s) \tag{2.6a}$$

$$V_c = \lambda \left(\frac{6\sqrt{f'_{co}\text{psi}}}{\frac{M}{VD}} \sqrt{1 + \frac{P}{6\sqrt{f'_{co}\text{psi}}A_g}} \right) \cdot 0.8A_g \tag{2.6b}$$

$$V_s = k_s \frac{A_h f_{yh} D_c}{s} \tag{2.6c}$$

In Equation 2.6, λ equals to 0.75 and 1.0 for light- and normal-weight aggregate concrete respectively. Shear capacity degrades as displacement ductility increases, following the coefficient k, which accounts for material softening, and possible geometry nonlinearity.

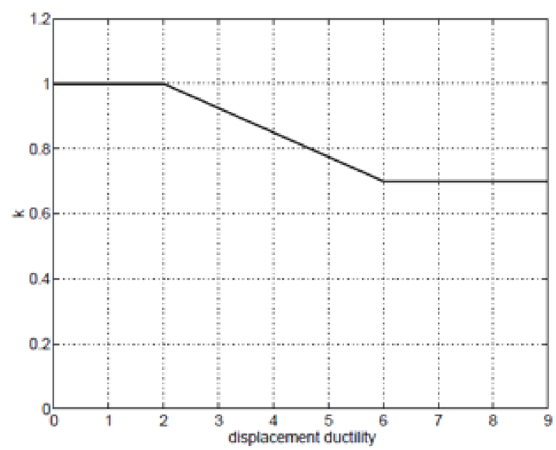

Figure 2.4: Definition of coefficient k in the shear capacity model proposed by Sezen (2002).

2.2.2 Abutment Modeling

There are two general types of abutments in California bridge inventory, seat abutment and diaphragm abutment (Figure 2.5). The inclusion of bearings denotes seat abutments, while an integral connection of the deck with the abutment wall is a defining deature of diaphragm abutments.

Figure 2.6 and Table 2.1 summarize seat abutment type findings from an inventory

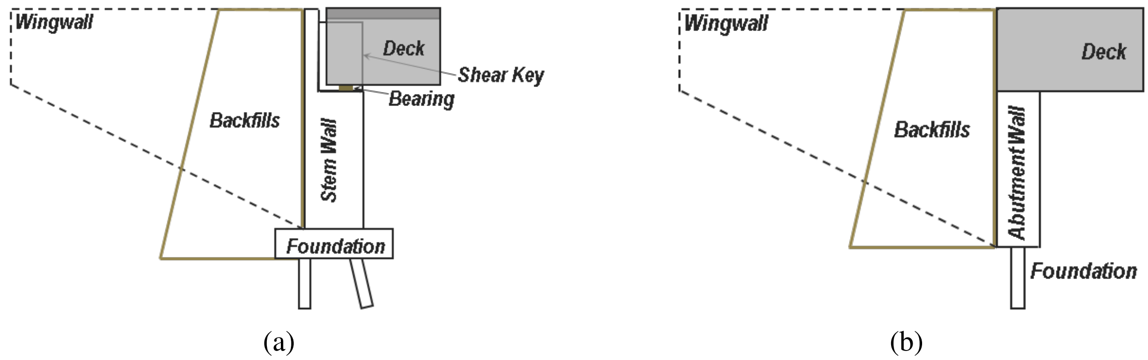

Figure 2.5: Examples of abutment in California bridges: (a) seat abutment, and (b) diaphragm abutment.

analysis of a sample of California box-girder bridges within three design eras. Abutment choice has evolved from prevailingly diaphragm-type abutments in earlier design eras to seat-type abutments in over 98% of bridges designed since the 1990's. As detailed in Table 2.1, seat-abutment types B and C with the use of haunches on the backwall and/or deck are limited mainly to bridges designed prior to the early 1970's. Modern bridge designs in California use either a stem wall or cantilever wall with a straight backwall and no haunch on the deck resulting a relatively small gap between the deck and straight backwall having mean value of approximately 2.1 inch.

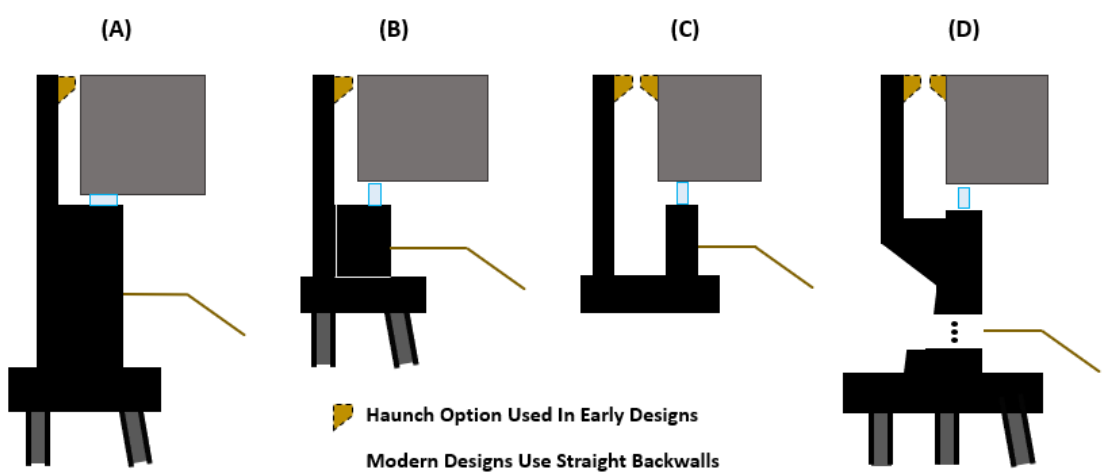

Figure 2.6: Conceptual illustration of alternative seat-abutment designs used in California box-girder bridges: A) stem wall support, B) pedestal support, C) free wall support and D) cantilever. (Roblee, 2020*e*)

Table 2.1: Seat-type abutment usage from inventory analysis of Caltrans box-girder bridge class (Roblee, 2020*e*)

Year Bridge Built	Bridges w/ Seat-Type Abutments	Proportion of Seat-Type Abutments by Design Type									
		Straight Backwall & Deck					Haunch on Backwall and/or Deck				
		Total	A	B	C	D	Total	A	B	C	D
>1991	98%	100%	82%	0%	0%	18%	0%	0%	0%	0%	0%
1973-1991	53%	94%	71%	0%	0%	23%	6%	5%	0%	0%	1%
<1973	30%	35%	6%	16%	0%	13%	65%	11%	22%	8%	24%

Previous studies regarding abutment modeling focused on the constitutive behavior of abutment components, such as backfills, bearings, and shear keys; and on capturing the overall abutment response.

For the backfill modeling, early Caltrans guidelines (Caltrans, 1990) had adopted an approximate bilinear form and specified a unit-width stiffness value of 20.0 kips/in/ft and truncation pressure value of 55.0 psi for modeling the passive resistance of abutment backfills. However, the bilinear form does not fully account for the real nonlinear behavior of backfills. Experimental studies (Caltrans, 1990; Maroney et al., 1993) showed that the ultimate soil pressure occurred at displacements from 6 to 10% of the backwall height. Subsequent studies (Nielson, 2005; Jeon et al., 2015b) used multi-linear models for modeling backfills, where the initial stiffness and ultimate deformation of sandy and clayey backfills were assumed to be within 20.0 kips/in/ft to 50.0 kips/in/ft, and 6 to 10% of the backwall height, respectively. Further experimental and theoretical studies also led to the use of hyperbolic curves to model backfills (Duncan and Mokwa, 2001; Shamsabadi et al., 2007; Wilson and Elgamal, 2006; Shamsabadi and Yan, 2008), some of which were applied in preliminary bridge-fragility feasibility analyses (Ramanathan, 2012). Current Caltrans guidelines (Caltrans, 2019) retain the approximate bilinear form, but now specify a unit-width stiffness value of 50.0 kips/in/ft and truncation pressure value of 35.0 psi, along with wall-height scaling rules, for modeling the passive resistance of abutment backfills meeting current material standards.

Other abutment components can be modeled at various degrees of sophistication. On the simpler end, seismic responses of backfills and foundation piles or footings have been combined into a single simplified trilinear hysteresis model – with only the foundation capacity acting in the active direction and the combination of foundation capacity and backfill considered in the passive direction (Gehl et al., 2014). For bearings, various models (e.g., for steel and elastomeric bearings) were proposed in Nielson (2005) due to their distinctive constitutive behaviors revealed by experiments. Constitutive behaviors for three different types of shear keys have been studied experimentally and analytically (Megally et al., 2001, 2003), where the types are internal shear keys, external non-isolated shear keys, and external isolated shear keys. The role of shear keys in bridges crossing fault-rupture zones has been examined (Goel and Chopra, 2008), and the effects of abutment-embankment interaction have also been investigated (Zhang and Makris, 2002; Inel, 2002; Kotsoglou and Pantazopoulou, 2007; Taskari and Sextos, 2015). Other studies have examined the vertical responses of abutment systems (Kavianijopari, 2011; Liang et al., 2016). The vertical stiffness of an abutment was assumed to be contributed by the bearings, embankments, and stem wall.

The aforementioned abutment components have been examined and applied in numerical analyses. Figure 2.7 illustrates a conventional modeling scheme (Nielson, 2005; Mangalathu, 2017; Mangalathu et al., 2016) which considers bearings, the gap and impact between the abutment and deck, foundations, and backfills in the longitudinal direction; and bearings, shear keys, and foundations in the transverse direction. The backwall and the stem wall are connected rigidly and are represented with only one node. A spring with a bilinear behavior is usually used to represent elastomeric bearings. Model verification and detailed modeling techniques of other types of bearings can be found in a relevant study (Nielson, 2005). The gap and impact spring is used to capture the gap between the backwall and the deck, as well as energy dissipation during the impact process (Muthukumar and DesRoches, 2006; Muthukumar, 2003). A multi-linear model is used to capture the seismic responses of piles in the abutment foundations (Xie et al., 2021). Different types of shear keys can be simulated by three backbone curves (Megally et al., 2001, 2003). The backfill is typically modeled using nonlinear springs with a hyperbolic backbone (Shamsabadi et al., 2007; Shamsabadi and Yan, 2008; Xie et al., 2019) where the passive resistance of the backfill depends on the mobilized soil height. Conventional model responses for two backfill-height options will be examined and compared to those for a new proposed model in later chapters. These options are taken as either the height of the backwall only, or the total height of the abutment wall (backwall plus stem wall), which serve to bracket and provide context for the responses of the proposed model.

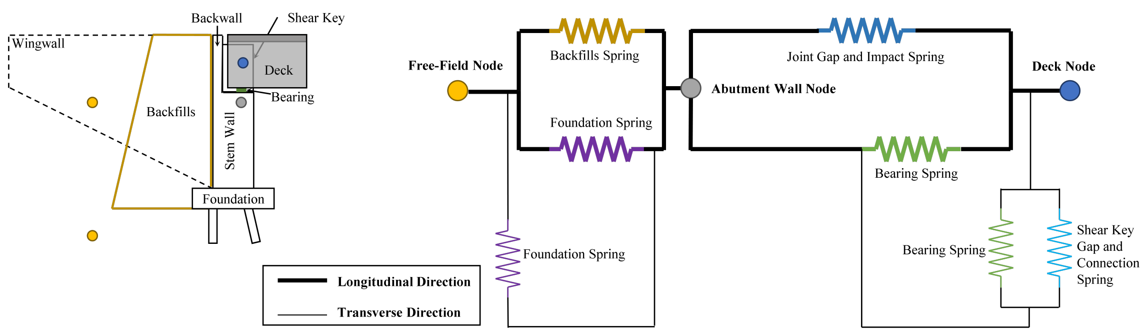

Figure 2.7: Conventional abutment modeling schemes

Crucial damage mechanisms associated with abutment backwalls (Figure 2.8) were observed in past earthquakes. To be specific, an abutment backwall in modern bridges is designed to be a sacrificial component, which is intended to fail prior to the foundations supporting the bridge and backwall (Caltrans, 2019). This design philosophy limits demand on abutment foundations so as to avoid time-consuming foundation excavation and repair, thus ensuring rapid post-earthquake repair actions and reduction of both direct repair costs and downtime-induced indirect losses (Caltrans, 2017).

In a bridge with seat abutment, the bridge decks are supported by abutments through bearings and restrained longitudinally by backwalls once the joint gaps are closed. The backwall is a key component that significantly affects the interaction between backfills and abutments, and the dynamic interplay of various bridge components changes dramatically before and after the backwall fracture. In particular, abutment foundations are completely engaged in the lateral support system before the backwall failure, whereas only the backfill

(a)

(b)

Figure 2.8: Examples of backwall damage (Jibson and Harp, 2011): (a) punching of the Tubul bridge deck into the backwall of the north abutment, and (b) damage at the base of the north abutment backwall of the El Bar bridge.

behind the backwall provides the primary lateral resistance once the backwall fails. As a result, lateral responses of columns and bearings will be underestimated if the backwall failure is not considered. Stefanidou et al. (2017) investigated soil-structure interaction and seismic fragility assessment of bridges with backwalls using a numerical backwall model that considered the flexural failure mechanism – the formation of a plastic hinge at the backwall bottom. Taskari and Sextos (2015) considered an additional lower bound case in the force transformer mechanism prior to and after backwall failure (i.e., backwall completely breaks off).

Three drawbacks are inherent to the conventional abutment modeling scheme. First, it does not account for a backwall fracture mechanism that is expected to significantly impact the seismic performance of adjacent components, including abutment foundations, bent columns, and deck displacements. Second, as a consequence of neglecting backwall fracture, the entire backfill height is inaccurately assumed to contribute to passive resistance. In fact, before backwall fracture, the full height of backfill behind the abutment wall provides lateral support to the bridge system. However, after fracture, only the soil behind the backwall contributes to lateral support of the deck. Therefore, it is imperative to separate the backfill behind the abutment wall into two parts to model their behaviors at different stages of loading appropriately. Finally, bearing deformation in the longitudinal passive-direction is limited to the size of the deck-abutment joint gap since the backwall restrains further movement in that direction.

To this end, a holistic modeling scheme that can capture the shear failure mechanism of abutment straight backwalls is required to more accurately simulate the seismic performance of modern highway bridges with abutment straight backwalls.

2.3 Column Capacity Limit State Models

In addition to the establishment of probabilistic demand models, the development of compatible capacity models (or CCLS) is essential to the definition of fragility models.

Since the column is the most critical component in the bridge system, this section focuses on the existing practice of defining CCLS for columns. Table 2.2 provides a summary of several recent column capacity models and Table 2.3 summarizes the values for column capacity damage states for a couple of existing studies.

Table 2.2: Comparison of capacity model descriptions in existing works

	Year Bridge Built	**DS2 (Slight/Minor)**	**DS3 (Moderate)**	**DS4 (Extensive)**	**DS5 (Complete)**
FEMA (1999)	All	Minor cracking & spalling at hinges, Column minor spalling (Requires no more than cosmetic repair)	Moderate (shear cracks) cracking & spalling of column (Structurally sound)	Column degrading without collapse - shear failure (Structurally unsafe)	Column collapse (May lead to imminent deck collapse)
Pan et al. (2007)	All	Initiation of yielding	Formation of plastic hinge	Reach of maximum moment	Crushing of concrete when concrete strain equals -0.005
Ramanathan (2012); and Dukes (2013)	<1973	Cracking	Minor cover spalling anywhere along the column height	Large shear cracks; major spalling; exposed core; confinement yielding	Loss of confinement; longitudinal bar buckling or rupture; core crushing
	1973 to 1991	Cracking	Minor cover spalling anywhere along the column height	Major spalling; exposed core; confinement yielding	Loss of confinement; longitudinal bar buckling or rupture; core crushing; large residual drift
	>1991	Cracking	Minor cover spalling concentrated at the top and bottom of the column	Major spalling; exposed core; confinement yielding	Loss of confinement; longitudinal bar buckling or rupture; core crushing

Hwang et al. (2001) used a model based on HAZUS (FEMA, 1999), in terms of displacement ductility, with thresholds of 1.00, 1.20, 1.76, and 4.76 corresponding to the first yielding of longitudinal reinforcement, column yielding, concrete strain reaching -0.002, and maximum displacement ductility defined by Buckle and Friedland (1995), respectively. Their damage states ranged from no damage to the complete state and were calculated based on material properties. For the first three states, the section curvature values were obtained and then converted to displacement ductility values using an assumed plastic hinge length. As suggested by FEMA (1999), the total dispersion (capacity and demand) was taken as 0.4 for fragility curves expressed in terms of SA; and 0.5 for those expressed in terms of PGA.

Choi and Jeon (2003) and Choi et al. (2004) defined column capacity limit states with curvature ductility thresholds of 1.00, 2.00, 4.00, and 7.00, corresponding to five damage states similar to the research by Hwang et al. (2001). The capacity model developed using experimental tests of non-seismically designed columns. Also, lap-splice columns were considered in these researches. Engineering judgment was needed when the damage state thresholds for different experimental tests values were defined.

Similarly, Nielson (2005) used a column capacity model with median curvature ductility values of 1.00, 1.58, 3.22, and 6.84 as thresholds of the damage states described as minor spalling, moderate cracking (shear cracks) and spalling, degradation without collapse, and collapse, respectively. These values were converted from the displacement ductility model from Hwang et al. (2001).

Pan et al. (2007) assumed that shear failure would not happen in bridge columns and defined five damage states with curvature ductility as the EDP. These critical limit states were related to the column integrity, the initiation of yielding, formation of the plastic hinge, reaching the peak moment, and crushing of concrete when the strain of concrete equal to about 0.005. The damage state values in this research were obtained based on ten numerical simulations of bridge columns, considering variation in material strength and dead loads.

Ramanathan (2012) and Dukes (2013) used curvature ductility in their research. Four damage states were defined based on expert opinions from Caltrans design engineers and maintenance personnel combined with consideration of limited experimental test data of components. A set of Caltrans-specific damage states were proposed in their research. However, follow-up work (DesRoches et al., 2012) found the column capacity values extremely conservative and called for additional research to better define column capacity models. A clear contribution of this capacity limit state system was the consideration of column capacity varied from different design eras.

Mangalathu (2017) extended the column capacity limit states by considering experimental test data for a total of 48 columns. Based on these tests, new column capacity limit states were proposed using the same four damage state definitions as Ramanathan (2012). However, these models combined different failure modes such as flexural, shear, and lap-splice, so they did not differentiate between failure modes now recognized to have very different capacity model values.

Several existing studies focused on post-1990 ductile designed columns (Kim and Shinozuka, 2004; Banerjee and Shinozuka, 2007; Mackie et al., 2007; Kwon and Elnashai, 2010) are also summarized in Table 2.3.

The following chapter will detail how this research investigation addressed these issues by clearly separating column failure modes, extending the experimental dataset, and enhancing the experimental findings with analytical simulations of column performance for each failure mode.

2.4 Closure

This chapter first reviewed the various fragility modeling techniques, concluding that the cloud method is the most efficient when used with analytic fragility analysis. In addition, this section outlined key process steps needed to establish a fragility model using NLTHA.

Table 2.3: Comparison of capacity model values in existing works

	Engineering Demand Parameter	Year Bridge Built	DS2 (Slight/Minor)	DS3 (Moderate)	DS4 (Extensive)	DS5 (Complete)
Hwang et al. (2001)	Displacement ductility	All	1	1.2	1.76	4.76
Choi and Jeon (2003)	Curvature ductility	All	1	2	4	7
Kim and Shinozuka (2004) (Bridge-I)	Displacement ductility	>1991	1.3	2.6	4.3	8.3
Kim and Shinozuka (2004) (Bridge-II)	Displacement ductility	>1991	1.4	2.8	4.6	9.2
Nielson (2005)	Curvature ductility	All	1	1.58	3.22	6.84
Banerjee and Shinozuka (2007)	Rotational ductility	>1991	1.58	3.33	6.24	9.16
citetaddcap2007b	Displacement ductility	>1991	0.23	1.64	6.09	6.72
Kwon and Elnashai (2010)	Column top displacement	>1991	-	2.86	4.88	19.69
Ramanathan (2012) and Dukes (2013)	Curvature ductility	<1973	0.8	0.9	1	1.2
		1973 to 1991	1	2	3.5	5
		>1991	1	4	8	12
Mangalathu (2017)	Curvature ductility	<1973	0.8	2.3	5.2	8.8
		1973 to 1991	1	5	8	11
		>1991	1	5	11	17.5

This chapter also outlined several important limitations of prior bridge-fragility modeling now being addressed by this research, including the needs for: 1) consistent and calibrated modeling of flexure, shear, and mixed flexure-shear column failure modes, 2) accurate modeling of the abutment backwall fracture mechanism and its associated impacts on overall bridge response, and 3) improved column capacity models, with clear separation of failure modes and design eras, which consider a broader set of experimental results and are supplemented by analytical simulations to account for a wider range of damage states. Each of these recognized limitations is addressed in the following chapters.

CHAPTER 3

ADVANCED FINITE ELEMENT MODELING OF BRIDGE COMPONENTS

Previous researchers have devoted considerable attention to accurate and effective modeling of the seismic behavior of various bridge components, including the deck, columns, and abutment. These efforts include modeling the structure in a realistic scheme, capturing a proper failure mode, and simplifying the model to improve computational efficiency. This chapter discusses the modeling techniques for developing a three-dimensional nonlinear bridge model within finite element modeling platform OpenSees (McKenna et al., 2000). The improvement of modeling fidelity through these proposed techniques is illustrated using a two-span bridge (see Appendix A).

3.1 Superstructure

It is recommended by Nielson (2005) to model the deck elements in OpenSees using elastic elements since the superstructure elements typically remain elastic during an earthquake. Two alternative strategies for modeling the superstructure were proposed by Priestley et al. (1996) as shown in Figure 3.1, grillage and spine, both of which model the superstructure with stick elements. The spine model is a further simplification of the grillage model.

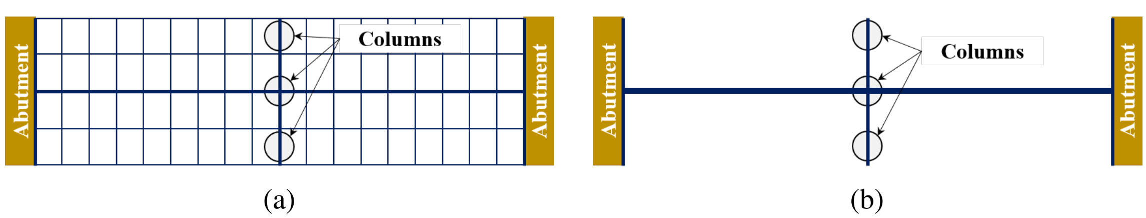

Figure 3.1: Modeling scheme for bridge superstructure: (a) grillage, and (b) spine.

While saving some computational time, the spine model has a significant drawback. The axial load is concentrated at the bridge centerline, and thus the force transfer to the substructure is influenced by the transverse beam stiffness. The undesirable impacts become most notable in bents having a central column and include: 1) The center column has a higher axial load than the others, and 2) external columns have an initial transverse displacement at the base upon gravity loading. The central column's high axial load incorrectly estimates column strength degradation due to concrete crushing, notable P-Delta effect, or shear failure. The initial transverse displacement amplifies the transverse demand under a small ground motion intensity range, influences the regression model, and ultimately overestimates the failure probability by about 0.1 to 0.2 g in terms of median S_{a1} of the column fragility models. The added modeling sophistication increases computational time, but not significantly. Hence, this research has elected to use the grillage scheme to model the superstructure. A simple comparison illustrates this effect in the following subsection 3.5.2.

3.2 Internal Support Bents

California bridges have different internal support types, with the most common being single column bent (isSB) and multi-column bents (isMB). Pier walls and shaft bents are also common but are not considered herein.

3.2.1 Bents

As shown in Figure 3.2, the column bent is modeled using a combination of fiber-section column elements and rigid links for connection to the superstructure. Column foundation elements, including both lateral and rotational springs are discussed in subsection 3.2.6 and Figure 3.19. Separate lateral element models represent piles, spread footings, and the soil loads applied to the sides of the pile cap or footing. The rotational element considers rotation failure associated with either excessive axial pile displacement (i.e., geotechnical failure) or foundation-to-column connection details (i.e., structural failure).

Columns in single-column bents are located at the bottom of the center cell, while in multi-column bents, they are evenly spaced as a function of column and cell number. Note

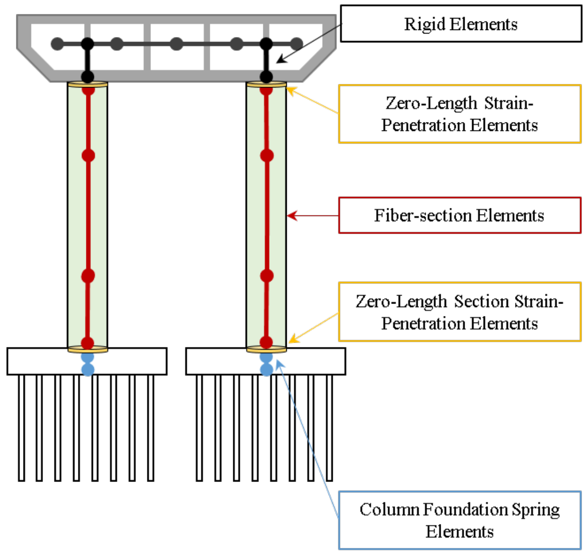

Figure 3.2: Typical modeling scheme for a bridge bent.

that all bridge models are constrained to have an odd number of cells. In this research, the distance is assumed to follow a relationship in Table 3.1. For example, a bent with five cells and two columns, the column spacing is 3.0 times the cell spacing, as illustrated in Figure 3.2.

Table 3.1: Column spacing (times of cell spacing) with respect to the number of box-girder cells and bent columns

		Column Number		
		2	3	4
Cells	3	2.0	-	-
	5	3.0	1.5	1.0
	7	4.0	2.5	2.0
	9	5.0	3.0	2.0
	11	-	4.0	3.0
	13	-	-	4.0

3.2.2 Flexural Columns

Columns are one of the most vulnerable components in a bridge system during earthquakes. As presented in Figure 3.2, a column is simulated with force-based elements along with zero-length section elements to account for strain-penetration effects at the two ends of the column (Zhao and Sritharan, 2007). Cross-sections in the force-based element and the zero-length section element are fiber-based. Fiber cross-sections benefit from allowing the specification of unique material properties for different locations across the cross-section. Specifically, the concrete is simulated using different constitutive models in cover (unconfined concrete) and core (confined concrete). Reinforcement is modeled with hysteretic material accounting for reinforcement rupture and buckling.

Concrete

This research uses the *Concrete02* material (Yassin, 1994) in OpenSees for modeling of concrete. Compared to other materials available in OpenSees, *Concrete02* is the most stable and computationally-efficient. Although *Concrete02* material applies the Kent-and-Park concrete model (Kent and Park, 1971) having a linear descending branch, this research adopts the Mander's concrete model to achieve a better accuracy.

As suggested by Mander et al. (1988), the basic formula of the concrete constitutive model is given by Equation 3.1 and Figure 3.3.

$$f_c = \frac{f'_{cc} x r}{r - 1 + x^r}, \tag{3.1}$$

where f'_{cc} is the compressive strength of confined concrete (defined later).

$$x = \frac{\varepsilon_c}{\varepsilon_{cc}} \tag{3.2}$$

defines the ductility of the concrete strain, where ε_c is the compressive concrete strain normalized by ε_{cc}, the strain at peak stress (defined later).

$$r = \frac{E_c}{E_c - E_{sec}}, \tag{3.3}$$

is the parameter to define the relationship of the secant stiffness $E_{sec} = f'_{co}/\varepsilon_{co}$ and tangent stiffness $E_c = 57000\sqrt{f'_{co}\text{psi}}$. Using the *Concrete02* material inherently implies

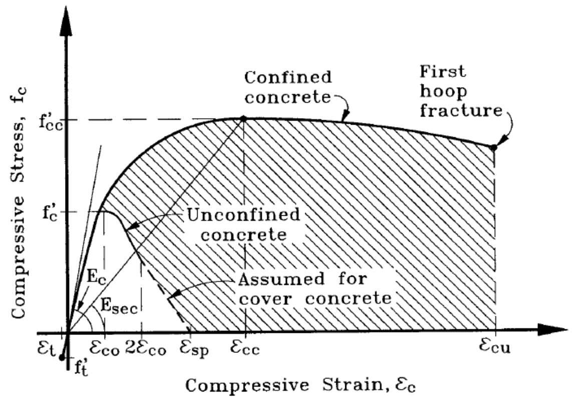

Figure 3.3: Stress-strain model for concrete in compression (Mander et al., 1988).

the constant value of $r = 2$ as a result of the assumption that the strain at peak strength is defined by $\varepsilon_{co} = 2f'_{co}/E_c$. Denote $y = f_c/f'_{cc}$, Equation 3.1 simplifies into the following form:

$$y = \frac{2x}{1+x^2}. \tag{3.4}$$

For confined concrete, the compressive strength is related to the effective lateral confining stress in the two directions of the section:

$$f'_{lx} = k_e \rho_x f_{yh}, \tag{3.5a}$$

$$f'_{ly} = k_e \rho_y f_{yh}, \tag{3.5b}$$

where ρ_x and ρ_y is the transverse reinforcement ratio; f_{yh} is the transverse reinforcement strength; and k_e is a confinement effectiveness coefficient defined by Equation 3.6:

$$k_e = \begin{cases} \dfrac{\left(1 - \dfrac{s'}{2d_s}\right)^2}{1 - \rho_{cc}}, & \text{for circular hoops confinement;} \\[2em] \dfrac{1 - \dfrac{s'}{2d_s}}{1 - \rho_{cc}}, & \text{for circular spirals confinement;} \\[2em] \dfrac{\left(1 - \displaystyle\sum_{i=1}^{n} \dfrac{(w_i')^2}{6b_c d_c}\right)\left(1 - \dfrac{s'}{2b_c}\right)\left(1 - \dfrac{s'}{2d_c}\right)}{1 - \rho_{cc}}, & \text{for rectangular hoops.} \end{cases} \tag{3.6}$$

where s' is clear spacing of transverse reinforcements; d_s, b_c, and d_c are the dimensions of the confined concrete; w_i is the clear distance of two adjacent longitudinal reinforcement in rectangular sections; ρ_{cc} is the longitudinal reinforcement ratio of core concrete.

The effective lateral confining stresses then induce the confined concrete strength given by Chang and Mander (1994):

$$f'_{cc} = f'_{co}\left[1.0 + A\overline{x}\left(0.1 + \frac{0.9}{1 + B\overline{x}}\right)\right], \tag{3.7a}$$

$$f'_{max} = \max\,(f'_{lx}, f'_{ly}), \tag{3.7b}$$

$$f'_{min} = \min\,(f'_{lx}, f'_{ly}), \tag{3.7c}$$

$$\overline{x} = \frac{f'_{lx} + f'_{ly}}{2f'_{co}}, \tag{3.7d}$$

$$q = \frac{f'_{min}}{f'_{max}}, \tag{3.7e}$$

$$A = 6.8886 - (0.6069 + 17.275q)e^{-4.989q}, \tag{3.7f}$$

$$B = \frac{4.5}{\frac{5}{A}(0.9849 - 0.6306e^{-3.8939q}) - 0.1} - 5.0. \tag{3.7g}$$

Figure 3.4 illustrates the enhancement of confined concrete strength f'_{cc}/f'_{co} with relationship to different parameters. Confinement strength ratio $\overline{x}$ is the ratio of lateral confining stress to the unconfined concrete strength. $\overline{x}$ represents unconfined concrete, as the plot indicates $f'_{cc}/f'_{co} = 1$. As the confinement strength ratio increases, the enhancement increases in a hyperbolic shape. The other parameter q indicates the unbalance confinement in the two directions of the section. Unbalance confinement decreases the enhancement of confined concrete, especially for the range of $q < 0.5$. In real situations, the unbalanced ratios for wide sections are commonly larger than 0.5, which causes a slight difference compared to a balanced confined section (regular section).

As suggested by Priestley et al. (1996), the strain corresponding to peak stress for confined concrete is given by Equation 3.8a; and the ultimate strain is given by Equation 3.8b, where ε_{su} is the transverse reinforcement strain at maximum tensile

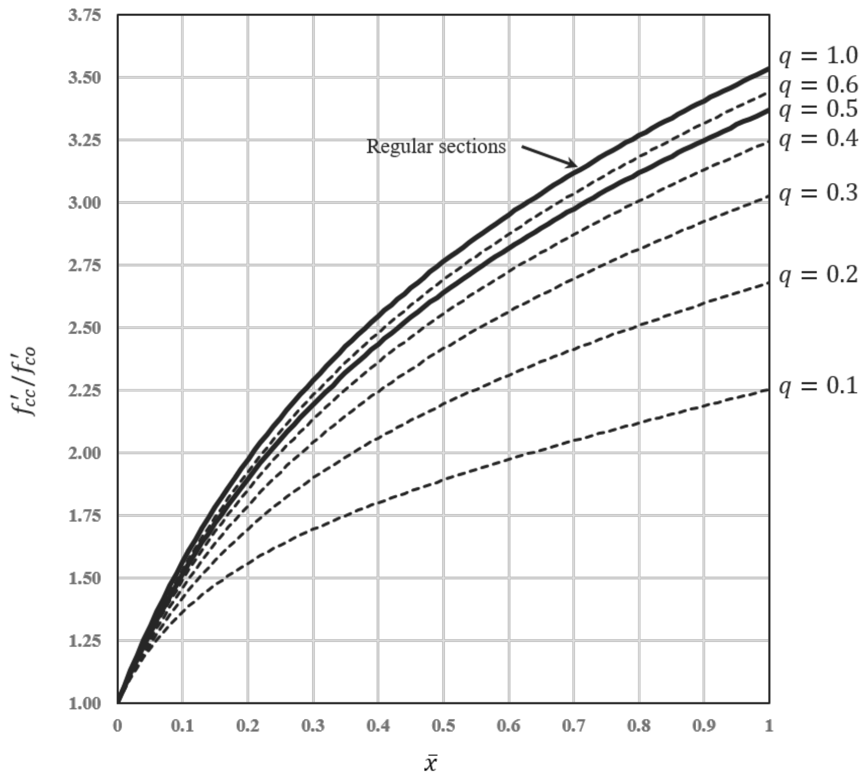

Figure 3.4: Compression strength enhancement of confined sections.

strength (defined later).

$$\varepsilon_{cc} = \varepsilon_{co}\left[1 + 5\left(\frac{f'_{cc}}{f'_{co}} - 1\right)\right], \tag{3.8a}$$

$$\varepsilon_{cu} = \varepsilon_{sp} + \frac{1.4\rho_s f_{yh}\varepsilon_{su}}{f'_{cc}}. \tag{3.8b}$$

Note that unconfined concrete is a special case when there is zero confining stress ($\overline{x} = 0$) and thus Equation 3.1 to Equation 3.8 are all applicable to unconfined concrete.

Determination of the end of the linear degrading portion (residual strength) of the *Concrete02* material is an important part of defining the concrete material. In this research, stress is assumed to be linear degrading after $2\varepsilon_{co}$ and degrading to zero strength at the spalling strain ε_{sp} for unconfined concrete (Mander et al., 1988). Based on Equation 3.4, $2\varepsilon_{co}$ corresponds to $0.8f'_{co}$ and therefore results in a spalling strain $\varepsilon_{sp} = 6\varepsilon_{co}$ for unconfined concrete with zero residual strength. Confined concrete is assumed to have 20% capacity remaining and then interpolate the corresponding residual strain using ε_{cu}.

Reinforcement

Hysteretic material is selected to model the reinforcement behavior because it has good stability, the capability to define a buckling branch, and compatibility with other possible failure modes such as a lap-splice column (subsection 3.2.4). The material accounts for strain hardening and reinforcement fracture on the tension side, while on the compression side, the material reflects the buckling effect.

Tension parameters includes stress-strain values for yielding (ε_y, f_y), ultimate strength (ε_{su}, f_u), and fracture strain ε_f.

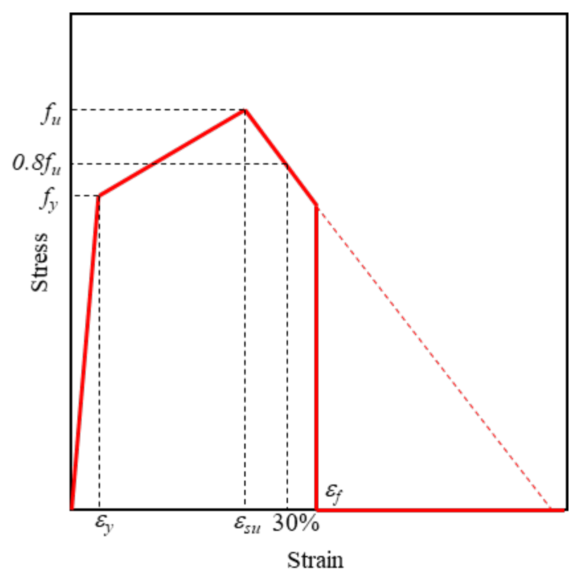

Figure 3.5: Stress-strain model for steel in tension.

While it is straightforward to define the yield point with yielding strength and initial stiffness $E_s = 29\,000\,\text{ksi}$, the ultimate strength point is defined differently in various studies. Priestley et al. (1996) suggested that $f_u = 1.5f_y$ for most reinforcement types and indicated the ratio would decrease as the strength increases. Bozorgzadeh et al. (2006) use a normal distribution which has 1.55 mean and ranges between 1.40 and 1.70 to define the ratio f_u/f_y. In this research, data in Paik et al. (2017) is analyzed, and a linear relationship is proposed to define the ultimate strength as:

$$\frac{f_u}{f_y} = -0.011 f_y + 2.067 \tag{3.9}$$

Substituting the typical reinforcements strength in California bridges, 50.0 ksi to 78.0 ksi,

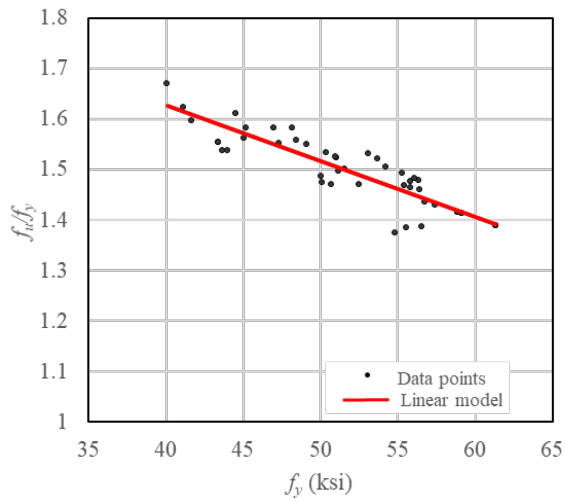

Figure 3.6: Linear model to estimate the steel ultimate strength.

the ratio derived from the model is 1.20 to 1.52, which is comparable to values used in other existing research. Strain ε_{su} corresponding to the ultimate strength is determined by Equation 3.10 (Caltrans, 2019). Reinforcement sizes used in California bridge columns are typically #11 or #14, and thus $\varepsilon_{su} = 0.060$ is used in most of cases.

$$\varepsilon_{su} = \begin{cases} 0.090, & \text{for \#10 bars or smaller;} \\ 0.060, & \text{for \#11 bars or larger.} \end{cases} \tag{3.10}$$

In order to determine the necking/degrading branch, it is assumed that the descending line is passing through 30% tensile strain when the strength degrades to 80% of the ultimate strength. This determines a linear descending model for the steel. Fracture strain is then imposed to the *Hysteretic* material using the *MinMax* material in OpenSees, which models a sudden drops at the specified strain ε_f. An exponential relationship is developed based on coupon test data in various studies (Priestley et al., 1996; Paik et al., 2017; Schoettler et al., 2012; Bao et al., 2017):

$$\frac{\varepsilon_f}{\varepsilon_y} = 2850 \exp\left(-0.05 f_y\right) \tag{3.11}$$

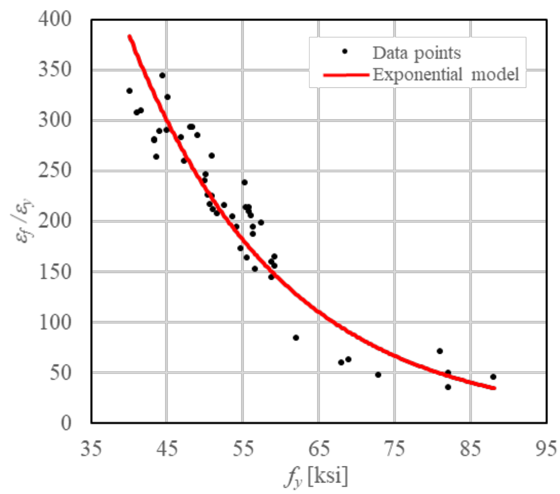

Figure 3.7: Exponential model to estimate the steel fracture strain.

Based on this relationship, typical steel strength results in a fracture strain with a range of 20% to 35%. This model also has a negative relationship with the steel yield strength, which coincides with the idea that high-strength steel tends to be brittle.

The compression side of the steel considers buckling behavior, where the model proposed by Zong et al. (2014) is adopted. Except for the yield point defined by $(-\varepsilon_y, -f_y)$, the other two points for buckling (ε_b, f_b) and residual (ε_r, f_r) are described here to define the backbone shape.

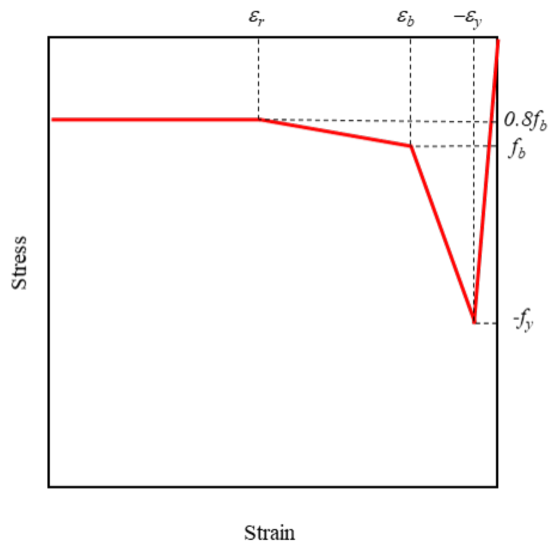

Figure 3.8: Stress-strain model for steel in compression.

The buckling point is defined in Equation 3.12:

$$\varepsilon_b = -C_s L_1 \varepsilon_y, \tag{3.12a}$$

$$f_b = -C_s \left[\frac{\alpha}{100}(L_1 + 1) - 1\right] f_y \leq -0.1 f_y. \tag{3.12b}$$

where $L_1 = 800M^{-2.5} + 2.5$, $\alpha = 3.0 - 0.2M^2$, and material strength parameter $M = s/d_b\sqrt{f_y/61\,\mathrm{ksi}}$.

The stiffness reduction coefficient C_s that varies with relative stiffness k/k_0 and material strength parameter M is estimated by:

$$C_s = \begin{cases} \left[1 - (1 - k/k_0)^2\right]^{1/(4.5 - 0.25M)}, & \text{for } 0 < k/k_0 < 1; \\ 1.0, & \text{for } k/k_0 \geq 1. \end{cases} \tag{3.13}$$

Critical stiffness $k_0 = 0.5\pi^4 E_s I_b / s^3$ is a property parameter for the longitudinal reinforcement with moment of inertia I_b and center-to-center transverse reinforcement spacing s (un-support length). The equivalent stiffness of transverse reinforcement confinement k is calculated by $k = F_y/\Delta_y$. Δ_y and F_y are the solution of the following equations, which result in a buckling distance with force equilibrium between buckling force and confinement force:

$$\Delta_y = R - \frac{R}{\cos\theta}, \tag{3.14a}$$

$$\varepsilon_y = \frac{(\tan(\theta) - \theta)R}{\pi R}, \tag{3.14b}$$

$$F_y = 2\varepsilon_y E_s A_h \sin\theta, . \tag{3.14c}$$

where R is the radius of column core, and A_h is the area of transverse reinforcement section.

Lastly, the residual strength f_r is simply defined as $80\% f_b$, and the residual strain is calculated by the following:

$$\frac{\varepsilon_r}{\varepsilon_b} = \min\left(L_1 - 30, 1.5L_1\right) + L_1 \tag{3.15}$$

The pinching parameters used in this research are $p_x = 0.35$ and $p_y = 0.95$, and the damage parameters are approximated as $d_1 = 0.02 - 0.008\rho_{sv}\rho_{sl} \geq 0.007$ and $d_2 = 0.02$.

Strain Penetration

Strain penetration occurs at the joint area of columns in the bridge. The connections of the column bottom with foundations and the column top with the bridge deck are the two locations to consider strain penetration effects. In these locations, bar-slip decreases the stiffness of the component. As such, the *Bond_SP01* material is used in a zero-length section at the end of the column. The most critical modeling parameter to determine is the amplification factor SF, which simplifies the bar-slip deformation in the embedded longitudinal reinforcements into a zero-length section.

As suggested by Lehman and Moehle (2000), the development length for the tensile embedded reinforcement to develop the yield strength is:

$$l_{sy} = \frac{f_y d_b}{48\sqrt{f'_{co}\text{psi}}}; \tag{3.16}$$

and the bar-slip at the joint is:

$$u_{sy} = 0.5\varepsilon_y l_{sy}. \tag{3.17}$$

Then the amplification factor is determined by the following:

$$SF = \frac{u_{sy}}{\varepsilon_y}. \tag{3.18}$$

In the above equations Equation 3.16 to Equation 3.18, d_b and f_y are the diameter and yield strength of the longitudinal reinforcements. When amplifying the steel strain with a factor of SF, the concrete material should also be amplified with the same multiplier in order to keep the section integrity and numerical stability (Jeon et al., 2015).

Mesh-Dependent Strain Localization

Modeling of a structural member with a fiber-based model, with the consideration of axial load-bending moment interaction, gives relatively higher accuracy than achieved with a hinge-type model (Powell and Chen, 1986). However, in the presence of softening constitutive model, two problems stand out in the fiber-based model simulation. First, the global post-peak displacement-loading response is highly sensitive to the discretization of structure members. In order words, changing either the length of the first member (hinge region) in a displacement-based formulation (DBE), or the distance of the first two integration points (IPs) in a force-based formulation (FBE), significantly impact the strength-degradation branch in the simulation. Second, the local strain-stress response concentrates at the first member (or between the first two integration points), which generates unexpected high strain at the first element and, in turn, governs the global responses' degradation.

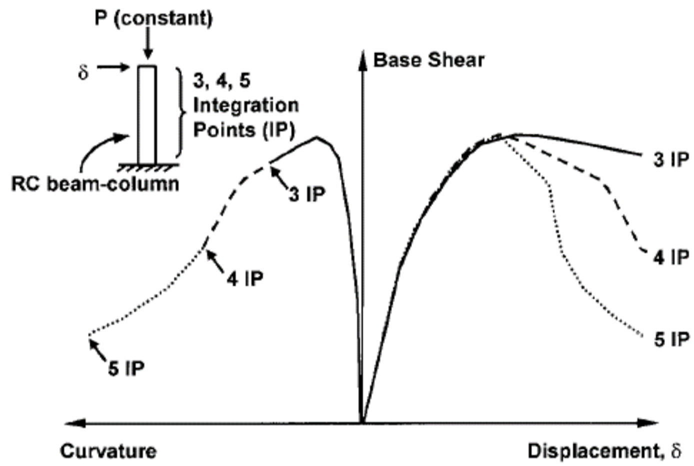

Figure 3.9: Localization issue in force-based formulation (Coleman and Spacone, 2001).

In order to address the localization issue, this research adopts a modeling technique similar to the plastic hinge integration method proposed by Scott and Fenves (2006). As shown in Figure 3.2, the column is modeled using a fixed length of force-based element at the hinge region with two Gauss-Lobatto integration points located at the element ends. The length of the hinge element is estimated based on the formula proposed by Paulay and Priestley (1992):

$$l_p = 0.08L + 0.15 f_y d_b \tag{3.19}$$

In this manner, the local plastic deformation is fixed in a reasonable range.

Validation is conducted by comparing the modeling results against the laboratory tests in Appendix C. It is noticed that most of the laboratory tests stop with 80% capacity remaining and thus cannot be used to study the localization problem. Instead of comparing the experiment results, the simulation result using this proposed method is compared with a simulation using the non-local method. Non-local is an emerging modeling technique that is objective to member discretization (Kenawy et al., 2018). Although not easy to apply to large bridge models, results for a single column model are compared herein using the column configuration in Appendix A. Figure 3.10 illustrates

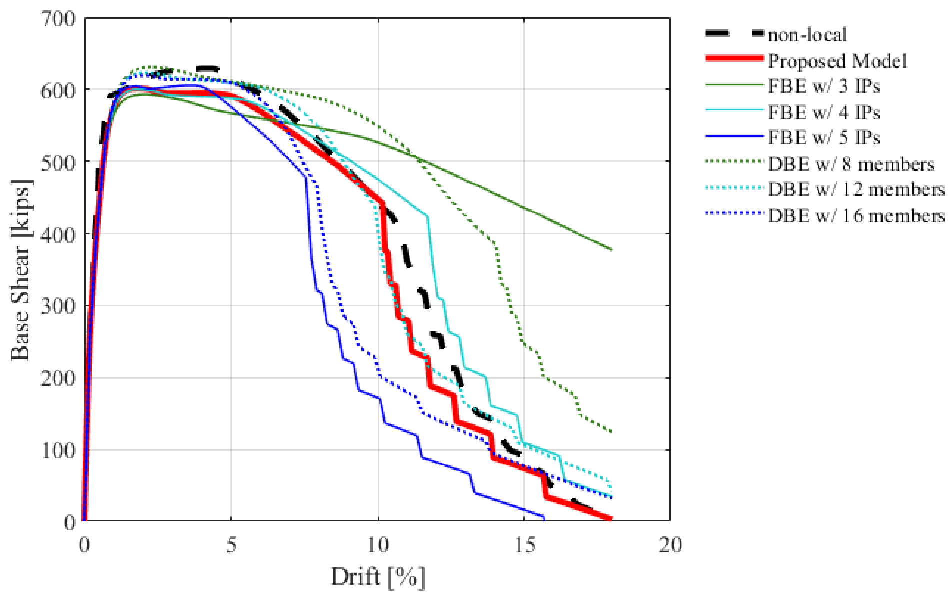

Figure 3.10: Comparison of the adopted modeling scheme with other modeling methods.

that the adopted modeling scheme generates results that are comparable with the non-local method (Kenawy et al., 2020), whereas other traditional methods with FBE (or DBE) produce results that are dependent on the number of integration points (or elements).

3.2.3 Reduced Sections

California bridges supported on multi-column bents often use a ”pinned” or reduced section, connection to the foundation element. Figure 3.11(a) provides an example connection illustrating that pin bases are constructed with smaller section sizes and fewer longitudinal reinforcements. It can also be seen from the figure that a construction joint disconnects the column and foundation, but a smaller ”column key” section with reduced reinforcements extends into the foundation. In order to capture its behavior, this project uses a zero-length strain-penetration section to model the pin section.

Figure 3.11(b) compares the adopted model to the typical simplified pin-base model (ideal pin with zero moment capacity) and shows the adopted model shows almost twice of base shear and initial stiffness for this reduced section detail.

Although the proposed model improves upon the model with an ideal pin in estimating

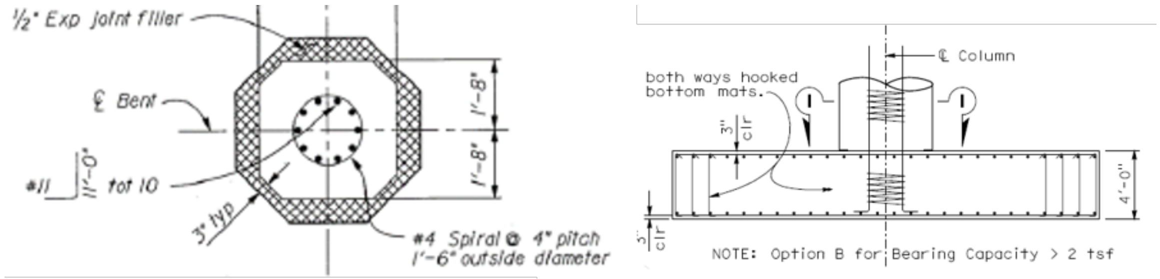

(a)

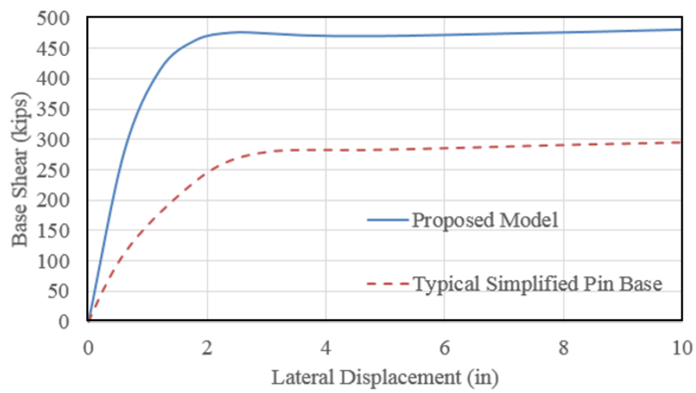

(b)

Figure 3.11: (a) Reinforcement detailing of a typical pin base in California bridge; and (b) pushover response comparing two modeling techniques for configuration in Appendix A.

the moment capacity, the expansion joint-filler is not considered here and thus leads to underestimation of the moment capacity. Validation in Appendix C shows approximately 15% underestimation for the tests with free-top. However, because the column top for box-girder bridges is almost always fixed to the bridge deck, such an underestimation is expected to have a negligible effect on estimating bridge performance.

3.2.4 Lap-splice Columns

It is estimated (Roblee, 2017*a*) that nearly 80% of pre-ductile California bridge columns have 'starter bar' details or a lap-spliced connection of longitudinal reinforcement at the column base. Previous studies Hwang et al. (2001); Zhang et al. (2004); Kim and Shinozuka (2004); Barkhordary et al. (2009) showed that lap-splice columns quickly lose their capacity once reinforcement in the lap-splice region starts to dislocate. Therefore, lap-splice columns often behave very brittlely and substantially impact bridge seismic performance.

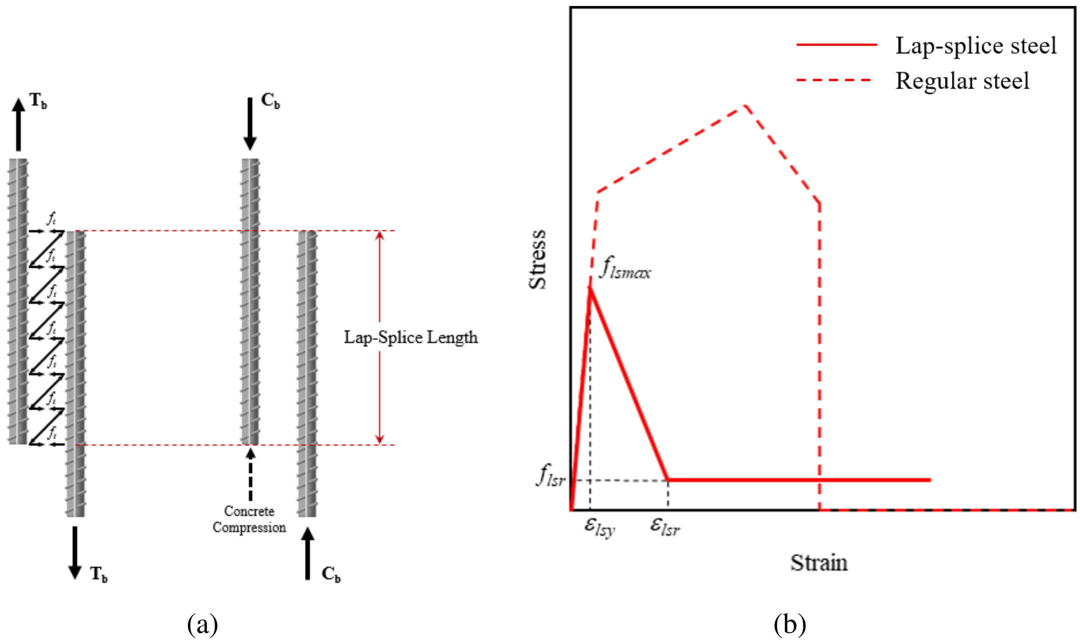

Figure 3.12: (a) Lap-splice reinforcement behavior in tension (Priestley et al., 1996) and compression; and (b) material model in tension side.

The mechanism of lap-splice reinforcement is represented in Figure 3.12. As suggested by Priestley et al. (1996) and Barkhordary et al. (2009), lap-splice stress on the compression side is assumed to behave the same as regular reinforcement since lap-splice reinforcement is supported by concrete. However, dislocation of lap-splice reinforcement in the tension side results in the lap-splice failure stress f_{lsmax}. It is the forces to overcome the tension of concrete blocks surrounding the reinforcement:

$$T_b = A_b f_{lsmax} = f_t p l_p \leq A_b f_y \tag{3.20}$$

in which A_b is the area of lapped reinforcements, f_t is the tensile strength of concrete that can be estimated with $7.5\sqrt{f'_{co}\text{psi}}$ (Chang and Mander, 1994), l_p is lap-splice length, and f_y is yield strength of reinforcement. It can be seen from this equation that lengthening the lap-splice length is an effective way to prevent lap-splice failure. If the developed strength in the lapped reinforcement can attain the steel yield strength, the member will not fail at the lap-splice and the steel follows the original constitutive model in Figure 3.5.

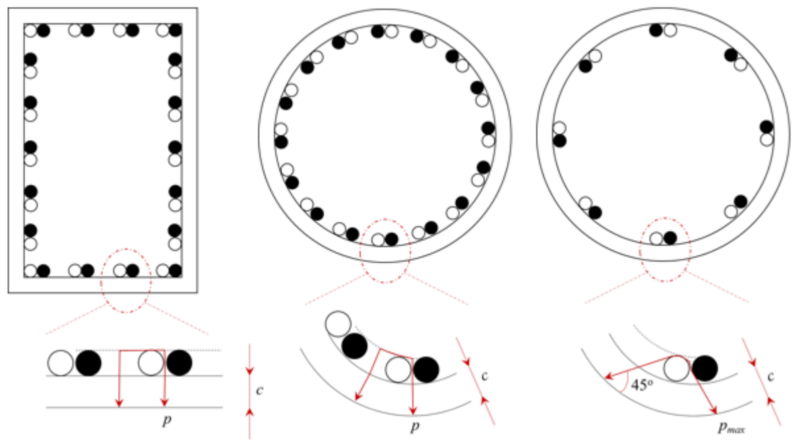

Figure 3.13: Perimeter of concrete block during lap-splice failure (Priestley et al., 1996): white and black circles represent the two lapped reinforcements.

The perimeter of concrete blocks surrounding the reinforcement p is illustrated in Figure 3.13. For cases with small spacing between longitudinal reinforcements (s_a), the surrounding concrete block considered to dislocate is calculated by adding up half of the average spacing between the reinforcements ($s_a/2$), twice the clear cover c and reinforcement diameter d_b ($2(c + d_b)$). If the spacing between longitudinal reinforcement (s_a) is large enough, the cross-section of the dislocating concrete block becomes a 45-degree triangle. Therefore, the perimeter of the concrete block surrounding reinforcement is given by Priestley et al. (1996):

$$p = \frac{s_a}{2} + 2(c + d_b) \leq 2\sqrt{2}(c + d_b) \tag{3.21}$$

After the complete spalling of cover concrete, the lap-splice strength degrades to the residual stress f_{lsr}. Residual stress describes the friction forces between reinforcement and core concrete with compression in their surface provided by transverse reinforcement in the lap-splice region.

$$A_b f_{lsr} = \mu A_h f_{yh} \frac{l_p}{s} \leq A_b f_{lsmax} \tag{3.22}$$

where μ takes 1.4 as suggested by Barkhordary et al. (2009). When the calculated residual strength is larger than f_{lsmax}, the softening branch in Figure 3.12(b) becomes flat. From this point of view, decreasing the spacing of transverse reinforcement in the lap-splice region is another strategy to prevent brittle behavior in lap-splice columns.

Lap-splice strain is determined by adding up elastic deformation and lap-splice deformation (Barkhordary et al., 2009).

$$\varepsilon = \varepsilon_e + \varepsilon_{ls} \tag{3.23a}$$

$$\varepsilon_e = f_{lsmax}/E_s \tag{3.23b}$$

$$\varepsilon_{ls} = u/l_{ss}. \tag{3.23c}$$

Lap-splice displacement u corresponding to maximum stress f_{lsmax} is suggested as 0.04 inches, while a typical lug-spacing of about 0.4 inches is used to compute the residual stress f_{lsr}. Fictitious length l_{ss} is used to measure the length of lap-splice deformation, which is estimated to be equal to the section depth as suggested by Barkhordary et al. (2009).

3.2.5 Shear/Flexural-Shear Columns

As outlined in subsection 2.2.1, multiple modeling techniques can be used to model a shear or flexural-shear column. In this research, a zero-length shear spring is used, and the capacity model proposed by Sezen (2002) is adapted herein.

Examination of three experimental tests reveals the limitations of the Sezen (2002) model. Load-deflection responses for three tests by Ang (1985) are shown in Figure 3.14 with their corresponding design parameters summarized in Table 3.2. The table notes that Unit-6 and Unit-1 are generally identical except for the shear span ratio, and Unit-15 and Unit-1 have identical designs except for their longitudinal reinforcement ratio.

Table 3.2: Parameters for three specimen in tests by Ang (1985)

Specimen § parameter	D in	M/VD –	α_P %	f_y ksi	f_h ksi	f'_{co} ksi	d_b in	s in	A_h in^2	ρ_{sl} %	ρ_{sv} %	V_n kips
Unit-6	15.75	1.5	0.0	63.24	47.57	4.37	0.63	2.36	0.044	3.20	0.509	87.67
Unit-1	15.75	2.0	0.0	63.24	47.57	5.44	0.63	2.36	0.044	3.20	0.509	71.94
Unit-15	15.75	2.0	0.0	63.24	47.28	5.05	0.63	2.36	0.044	1.92	0.509	51.70

§ D = diameter of specimen; M/VD = shear span ratio; α_P = axial load ratio; f_y = longitudinal reinforcement yield strength; f_h = transverse reinforcement yield strength; f'_{co} = concrete strength; d_b = diameter of longitudinal reinforcement; s = spacing of transverse reinforcement; A_h = area of transverse reinforcement; ρ_{sl} = longitudinal reinforcement ratio; ρ_{sv} = transverse reinforcement ratio; and V_n = experimental shear strength.

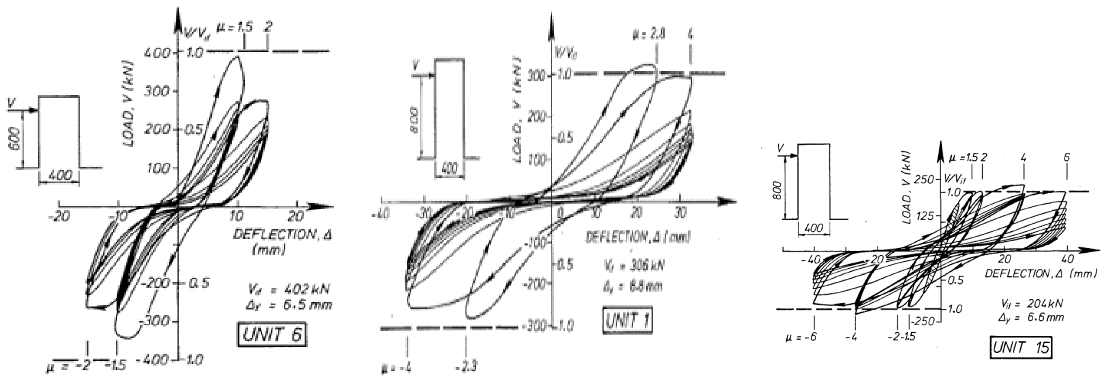

(a) (b) (c)

Figure 3.14: Experimental results (Ang, 1985): (a) Unit-6; (b) Unit-1; and (c) Unit-15.

Modification-1: Degradation Factor

Compared to Unit-1, Unit-6 has a smaller shear span ratio equaling 1.5, and the response is more brittle after the peak shear capacity. Similar behaviors are observed in other cases like Figure 3.15.

Consequently, the proposed model modifies the amplification factor k considering the geometry and reinforcement configuration effects on the column ductility. With calibration to the experiment test result, the column is classified as a 'normal' case if the shear span ratio M/VD is larger than 2.0 and the transverse reinforcement ratio ρ_{sv} is larger than 0.20%. In the figure, 'Highly brittle' cases are columns either with shear span ratios smaller than 1.75 or transverse reinforcement ratios smaller than 0.15%. The test result for Unit-20 in Figure 3.15(a) leads to the selection of 1.75 as the lower bound for shear span ratio. Lastly, linear interpolation is assumed for columns located between the two bounds.

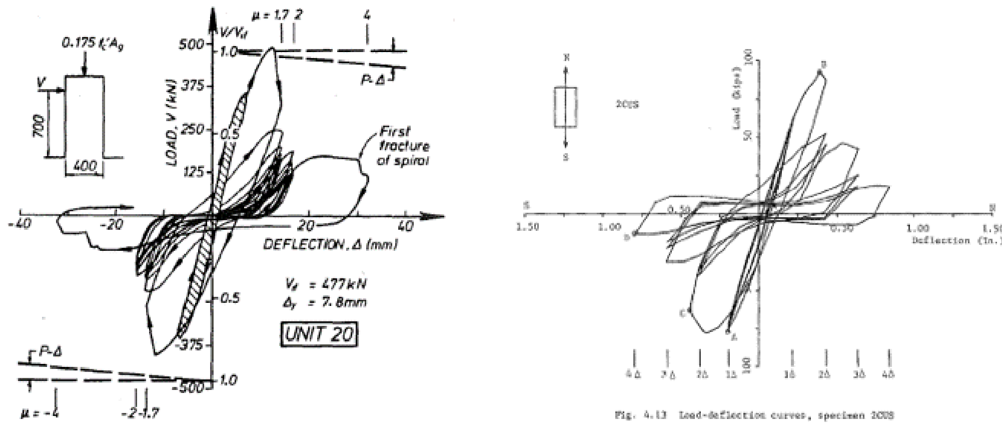

(a) (b)

Figure 3.15: Experimental results with highly brittle performance: (a) Unit-20 (Ang, 1985) with $M/VD = 1.75$ and $\rho_{sv} = 0.38\%$; and (b) 2CUS (Umehara, 1983) with $M/VD = 1.13$ and $\rho_{sv} = 0.36\%$.

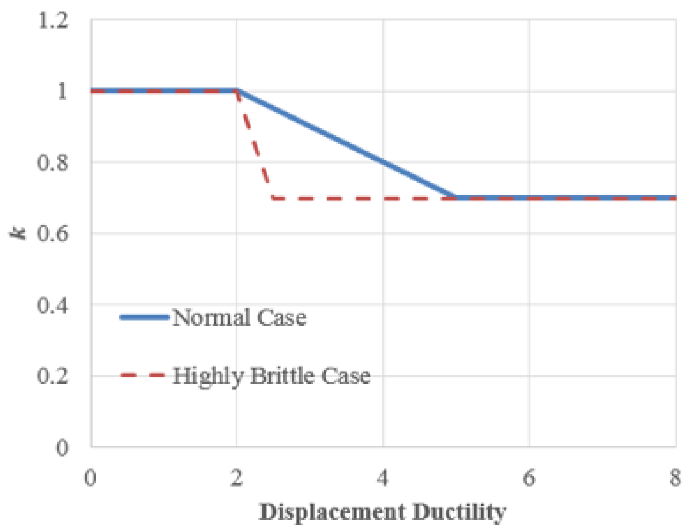

Figure 3.16: Modified amplification factor k in the proposed shear capacity model.

Broadly, this model implies that the shear capacity degrades as displacement ductility increases. This model relates the rate of degradation to a function of the geometry (M/VD) and confinement condition (ρ_{sv}).

Modification-2: Longitudinal Reinforcement Term

Comparison of Unit-1 and Unit-15 also suggest that the shear capacity may be affected by the longitudinal reinforcement ratio. Unit-1 has a larger longitudinal reinforcement ratio and a higher shear capacity than Unit-15. A similar observation occurs in specimen R-5 in tests conducted by Sun et al. (1993). This column has a 5% longitudinal reinforcement ratio and results in a flexural failure with longitudinal reinforcement buckling with minor diagonal cracking, even with a relatively small transverse reinforcement ratio (0.18%). This phenomenon can be explained by considering the additional confinement provided by longitudinal reinforcements. Therefore, an additional term is added to the shear capacity to account for the possible additional confinement effect from longitudinal reinforcement per Equation 3.24d, in which k_{sl} is the participation coefficient of longitudinal reinforcement and the corresponding bending depth, which is suggested to use 0.075. However, if the transverse reinforcement ratio is too small, the flexural capacity provided by longitudinal reinforcement may not develop before the shear failure happens. Therefore, a threshold of 0.175% transverse reinforcement ratio is adopted to apply this term. The threshold is taken as the mean value of column transverse reinforcement ratio in pre-ductile (era-1) column designs (era-1).

Modification-3: Transverse Reinforcement Term

In the model proposed by Priestley et al. (1994), the transverse reinforcement term considers a cracking angle. This term depicts the number of transverse reinforcements across the shear cracks. The model takes the cracking angle as 30 degrees. In another shear capacity model (Kato and Ohnishi, 2002), the cracking angle was taken as 45 degrees. Therefore, a mean value of these two (37 degrees) is used in the proposed model.

Modification-4: Shear Span Ratio

In the model proposed by Sezen (2002), the shear span ratio was limited to the range of 2.0 to 4.0. After modeling and comparing with the experimental results, the shear span ratio for a valid model is extended to 1.5. When the shear span ratio is smaller than 1.5, it is taken as 1.5 for the following calculation.

The final model is summarized as below.

$$V = k(V_c + V_{sv} + V_{sl}) \tag{3.24a}$$

$$V_c = \lambda \left(\frac{6\sqrt{f'_{co}\text{psi}}}{\frac{M}{VD}} \sqrt{1 + \frac{P}{6\sqrt{f'_{co}\text{psi}}A_g}} \right) \cdot 0.8A_g \tag{3.24b}$$

$$V_{sv} = k_{sv}\frac{A_h f_{yh} D_c}{s} \cot 37° \tag{3.24c}$$

$$V_{sl} = \begin{cases} 0 & , \rho_{sv} < 0.175\% \\ k_{sl}\dfrac{f_y \rho_s l A_g}{\frac{M}{VD}} & , \text{otherwise.} \end{cases} \tag{3.24d}$$

Modeling of Degradation of Monotonic to Collapse State

After establishing the nominal shear capacity of the column, the shear spring response must control degradation to the residual capacity following a specified degradation stiffness. The residual capacity is often specified as 20% of the nominal shear capacity. However, from the limited yet informative monotonic pushover results, the degradation may be better characterized using a bi-linear relationship. The highly brittle cases ($M/VD < 1.75$ or $\rho_{sv} < 0.175\%$) has a steeper first degradation branch and a flatter second branch (Figure 3.17(a)), while the normal cases exhibit the opposite sequence (Figure 3.17(b)). Based on these experiment results, a new degradation model is developed to construct a shear spring for modeling shear failure.

Before shear failure occurs, the specimen follows typical flexural behavior, and the shear spring deforms elastically with stiffness calculated by Equation 3.25 where G_c is the

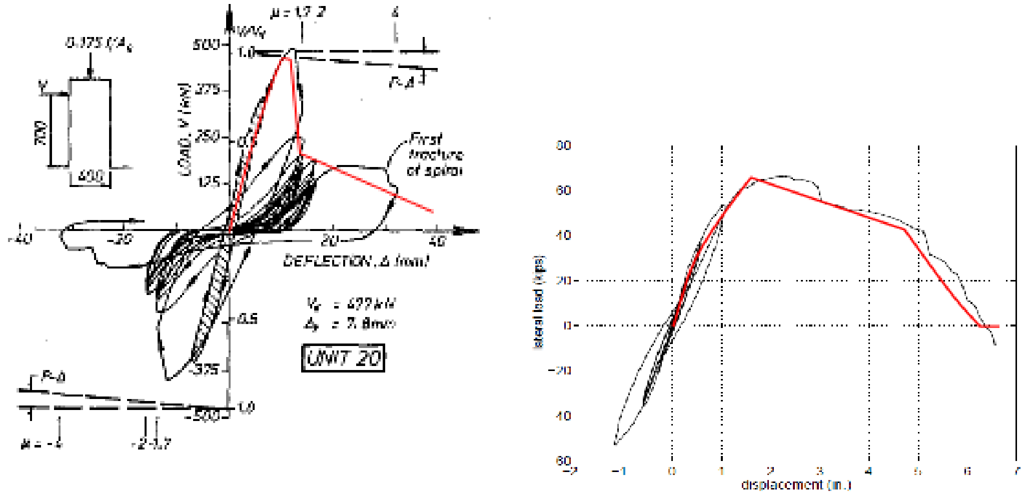

(a) (b)

Figure 3.17: Approximated bi-linear degradation of shear columns: (a) Unit-20 in highly brittle case (Ang, 1985) with $M/VD = 1.75$; and (b) specimen-4 in normal case (Sezen, 2002).

concrete shear modulus.

$$K_{elastic} = \frac{G_c A_g}{\frac{M}{V}} \tag{3.25}$$

After triggering the shear failure, the shear capacity degrades following the degradation stiffness given by the shear capacity model, i.e.:

$$\begin{cases} K_{d1} = -0.6\dfrac{V_n}{d_y}, & \text{for highly brittle case} \\ K_{d2} = -0.1\dfrac{V_n}{d_y}, & \text{for normal case} \end{cases} \tag{3.26}$$

in which d_y = yield displacement of the column specimen, and linear interpolation is applied to those cases between the above two situations.

The second leg of the degradation line is assumed to apply from about 65% capacity remaining through zero capacity (or entirely collapsed). Equation 3.27 is adopted to calculate the ultimate displacement at collapse, illustrated by the red dashed extension in the shear-spring model shown in Figure 3.18. The ultimate displacement assumes half of the capacity degrades following K_{d1} and the other half degrades following K_{d2}.

$$\Delta_C = e_1 + \frac{0.5V_n}{K_{d1}} + \frac{0.5V_n}{K_{d2}} \tag{3.27}$$

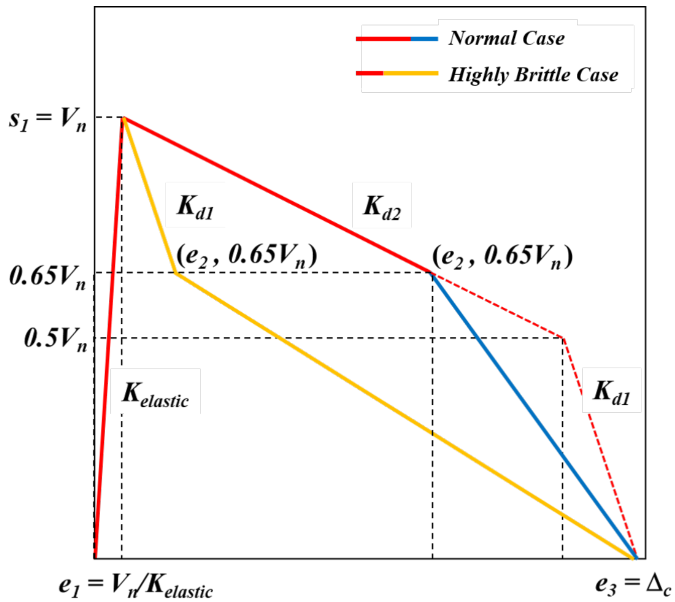

Figure 3.18: Illustration of shear spring definition.

Appendix C provides comparisons of responses using the proposed analytical methodology with experimental test results for an extensive and diverse set of column designs having a range of failure modes. Overall, these results show that the new modified methodology captures critical response characteristics for a broader range of column designs and at a higher degree of fidelity than could be achieved using the unmodified method.

3.2.6 Column Foundation

As illustrated in Figure 3.19, column foundations are modeled as a combination of lateral translational springs and rotational springs in each of two directions. The lateral springs include ones to capture the foundation-base response, associated with pile lateral resistance or spread-footing frictional resistance, and soil springs capturing soil load on the side faces

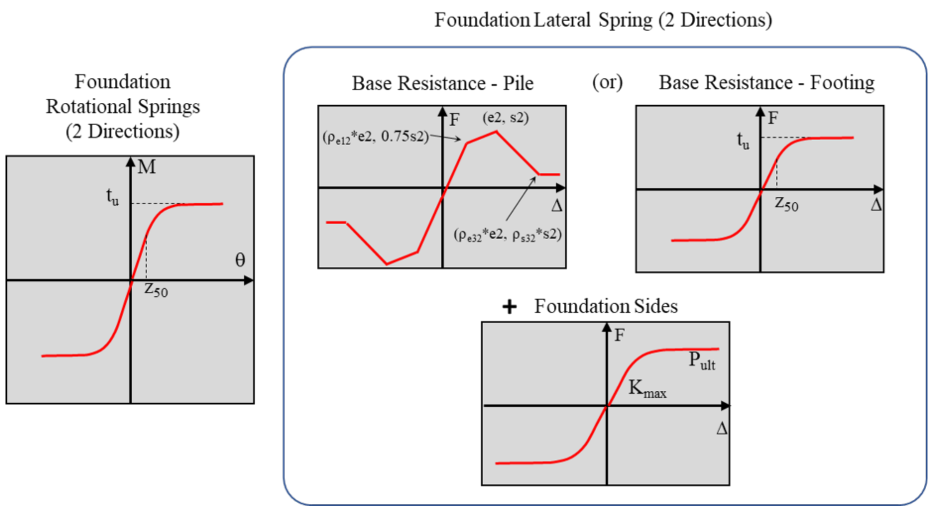

Figure 3.19: Response models for column foundations.

of either the pile cap or spread footing. The response model for foundation-base springs is the same as those used in the abutment foundation and will be discussed next. The soil springs capture the resistance applied by the soil to the side faces of a pile cap or footing and are therefore symmetric. More detail is provided in the next section.

The rotational spring assigned to the column foundation considers the lesser of two potential rotational failure mechanisms: 1) 'geotechnical' failure associated with excessive axial displacement of piles at the foundation perimeter, and 2) 'structural' failure associated with excessive rotation of poor column-foundation connection details. The *TzSimple1* material in OpenSees is used to model the column foundation rotation. Compared to past studies which used elastic rotational springs, this enhanced strategy allows for characterization of alternative foundation failure mechanisms for poorly-designed foundations where column hinge capacity exceeds either the structural or geotechnical capacity of the foundation.

3.3 Abutment

As previously noted in Table 2.1 and Figure 2.6, abutment choice in California has evolved from primarily diaphragm-type abutments used in earlier design eras to seat-type abutments used in over 98% of bridges designed since the 1990's. Modern bridge designs use either a stem wall or cantilever wall with a straight backwall and no haunch on the deck. Therefore, under considerable seismic loading, the superstructure end diaphragm pushes against the straight backwall, resulting in shear fracture near the base of the backwall. Moreover, the use of haunches on the backwall and/or deck is generally limited to early bridge designs from before the early 1970's. This section will focus primarily on modeling the type A abutment without a haunch as it is widely used in modern bridge designs. Other types of abutment types will also be discussed based on this study.

3.3.1 General Scheme

A new abutment modeling scheme shown in Figure 3.20(a) has been developed to address the aforementioned modeling issues with the conventional modeling scheme in Figure 2.7. A more rigorous and robust spring system is considered in the longitudinal direction by separating the abutment wall into two segments – the backwall and the stem wall. The lateral behavior of the backwall is simulated using a backwall connection spring that connects the backwall node and the stem wall node (i.e., the seat node). In this way, the backfill can be consequently separated into two portions, namely backfill-A and backfill-B, if the backwall connection fractures. Specifically, the backfill-A spring represents the backfill behind the backwall and connects the backwall node to the free-field node. The backfill-B spring connects the abutment stem wall/seat node to the free field node, capturing the passive resistance of the remaining backfill (i.e., the backfill behind the stem wall). Therefore, impact forces between the deck and backwall will transfer into backfill-B and the abutment foundation before the failure of the backwall connection. However, after complete fractures of the backwall, only a limited amount of lateral force from the deck can be transferred to the abutment foundations through the bearings, and most of the force is taken by backfill-A. In the transverse direction, a soil spring is added to the model to approximate soil resistance acting on the side of the stem wall and wing wall.

The geometric interactions of various abutment and soil components are well represented using the new spring system, where each spring captures the appropriate response of each distinct component. In this manner, the temporal change in the dynamic interplay among these components can be reliably quantified, particularly before and after the backwall fracture when subjected to strong earthquakes. The shape of the backbone curves for each constitutive nonlinear spring is provided in Figure 3.20(b) and will be discussed in the following sections.

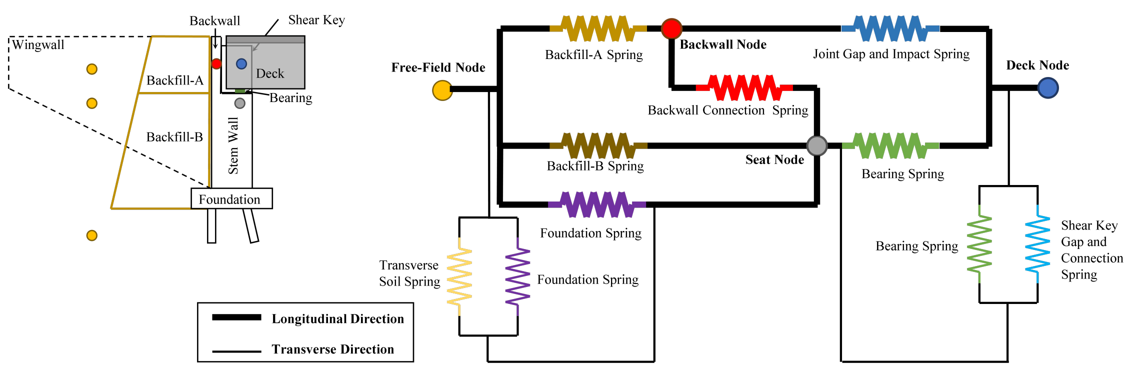

(a)

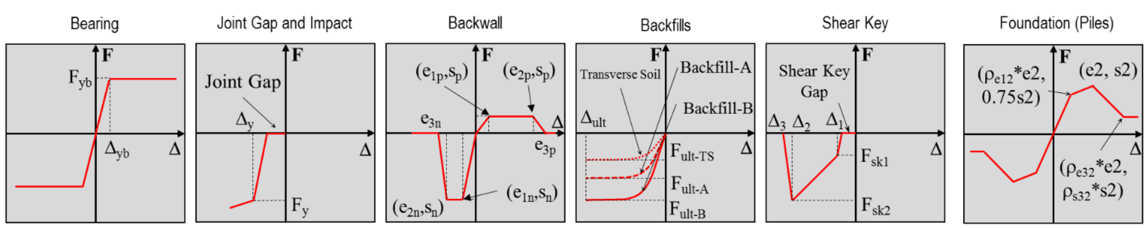

(b)

Figure 3.20: (a) Adopted abutment model incorporating the backwall fracture mechanism (Zheng et al., 2021), and (b) backbone responses of bridge component nonlinear springs within the abutment modeling scheme.

3.3.2 Shear Key

Megally et al. (2001) summarized the behavior of three types of shear keys named external isolated shear key, external non-isolated shear key, and internal shear key. As illustrated in Figure 3.21, the component response of external keys (both non-isolated and isolated) can

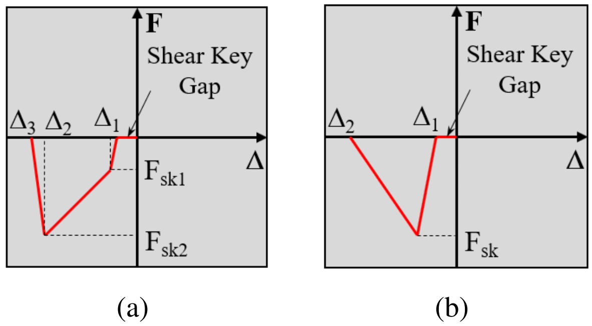

Figure 3.21: Generic response models for abutment shear keys: (a) external; and (b) internal.

be generically represented with three segments, whereas only two segments are needed to capture the response of internal keys. In this research, the OpenSees modeling of all shear keys uses *Hysteretic* material in series with a gap spring.

As an emerging type of shear key, the external isolated key fuses at a lower capacity level than the non-isolated key as a means to protect the lower portion of the abutment, i.e., abutment foundations. Although it is not considered in the probabilistic simulations due to its limited usage in existing bridges, the isolated shear key is used in the bride shown in Appendix A and therefore is used in the deterministic simulation of the following section.

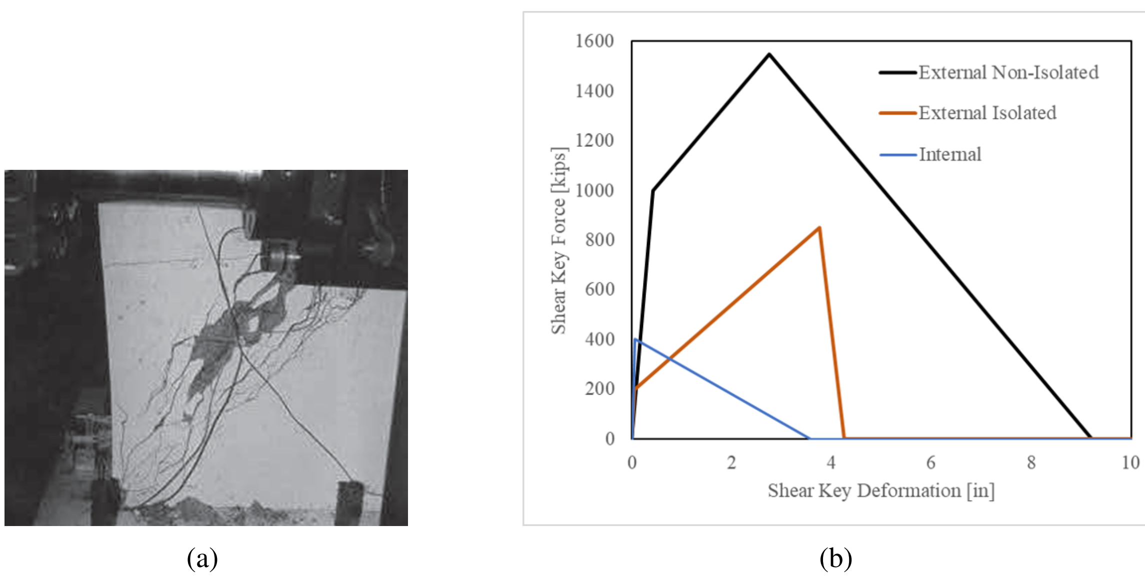

Figure 3.22: (a) Example of shear key diagonal crackings during tests (Megally et al., 2001), and (b) simplified response models for three types of shear keys.

The most prevalent abutment shear key in California box-girder bridges is the external non-isolated shear key. The response of a typical non-isolated shear key is modeled as three phases until failure following the simplification by Goel and Chopra (2008). Initial observed damage is the onset of concrete cracking, indicating the yielding of the shear key. As the extending cracks cut across more and more reinforcements in the abutment wall, the shear key capacity climbs to the peak. Strength softening initiates when the reinforcement cannot resist the widening of concrete cracks. In this stage, concrete spalling is seen at the toe of the wall. An external non-isolated key fails through a combination of mechanisms, including fracture of reinforcements, concrete crushing at the toe, and large opening of the inclined cracks.

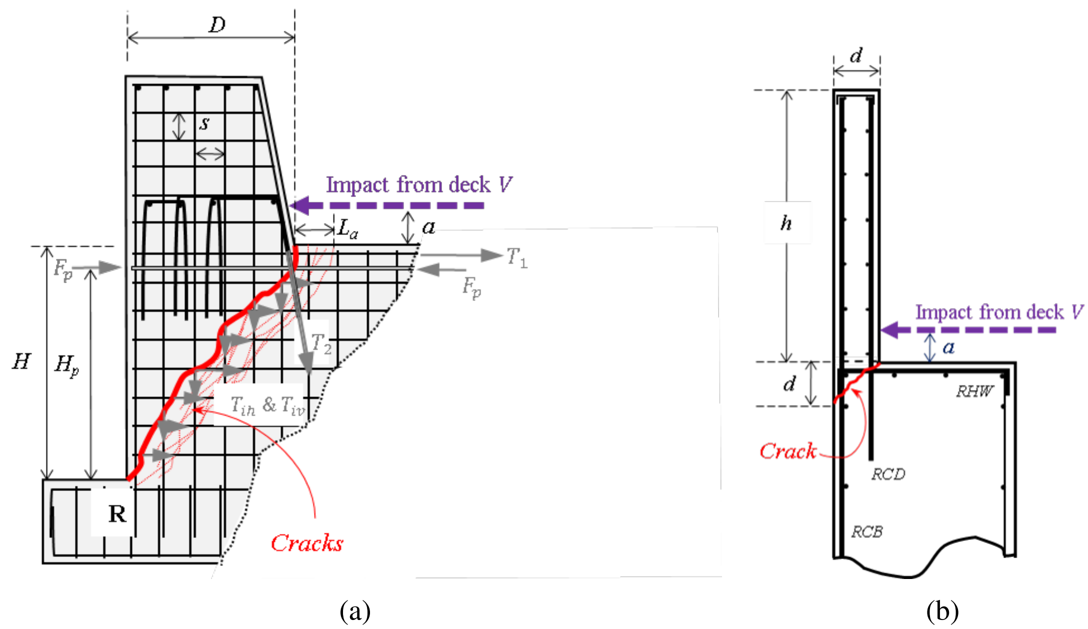

Figure 3.23: Illustration of the failure mechanisms: (a) the non-isolated shear key (out-of-plane breadth noted as b); and (b) backwall passive fracture (out-of-plane width noted as w).

The capacity V_{key} for the external non-isolated shear key consists of a concrete term V_c and a steel term V_s. The associated variables in Equation 3.28 are schematically illustrated in Figure 3.23(a). Through experimental verification (Megally et al., 2001, 2003), the concrete term was directly adopted from the ACI 318-14 (ACI, 2014), in which b denotes the out-of-plane breadth. The steel term can be derived by considering the moment equilibrium of the left portion of the cracked shear key relative to the base of the diagonal shear cracks in the stem wall (i.e., point R in Figure 3.23(a)). Specifically, the term of F_pH_p denotes the moment induced by the pretension force F_p multiplied by the lever arm of H_p. Similarly, T_1H and T_2D denote the moments contributed by the major horizontal reinforcement and the first row of steel bars crossing the shear key interface, respectively. The last two terms denote the moments contributed by the distributed reinforcement, where n_h and n_v are the numbers of side faces for horizontal and vertical side reinforcement, respectively.

$$V_{key} = V_c + V_s \tag{3.28a}$$

$$V_c = 2.4bH\sqrt{f'_{co}\mathrm{psi}} \tag{3.28b}$$

$$V_s = \frac{1}{H+a}\left(F_pH_p + T_1H + T_2D + \frac{n_hT_{ih}H^2}{2s} + \frac{n_vT_{iv}D^2}{2s}\right) \tag{3.28c}$$

It was then proposed in Megally et al. (2001) that the force and deformation for the shear key response model in Figure 3.21(a) can be calculated as the following, in which b in Equation 3.29g is the out-of-plane breadth. Note that Δ_1, Δ_2 and Δ_3 here does not include the initial shear key gap.

$$\Delta_1 = \sqrt{2}\varepsilon_y(L_d + L_a)\frac{h+d}{\sqrt{h^2+d^2}} \tag{3.29a}$$

$$\Delta_2 = \sqrt{2}\varepsilon_y(L_d + L_a)\frac{h+d}{s} \tag{3.29b}$$

$$\Delta_3 = \sqrt{2}\cdot 0.007 \cdot (L_d + L_a)\frac{h+d}{s} \tag{3.29c}$$

$$F_{sk1} = V_s + \frac{\Delta_1}{\Delta_2}V_c \tag{3.29d}$$

$$F_{sk2} = V_{key} \tag{3.29e}$$

$$L_d = \frac{d_b f_y}{25\sqrt{f'_{co}\mathrm{psi}}} \tag{3.29f}$$

$$L_a \approx b \tag{3.29g}$$

Although internal shear keys are uncommon in modern ductile (era-3) abutment designs, they appear in about 30% of early-ductile (era-2) bridges and are often used in combination with external non-isolated shear keys. Such a combination increases the transverse resistance and hence might cause damage to the abutment foundation. It was suggested by Megally et al. (2001) that the softening brunch of the internal shear key typically extends approximately 3.5 in after the peak and the strength approximately takes the minimal of three terms as shown in Equation 3.30, where f'_{co} is concrete strength and A_c is the area of the shear key-abutment interface.

$$V_N = \min\left(11.3\sqrt{f'_{co}}, 800\mathrm{psi}, 0.2f'_{co}\right)A_c \tag{3.30}$$

Validation of the finite element simulation versus experimental tests (Megally et al., 2001) is demonstrated in Figure 3.24.

Based on the inventory results, it is assumed that no shear key elements exist in pre-ductile designed (era-1) bridges. Instead, the constrained transverse response of rocker bearings provides lateral restraint for era-1 bridges.

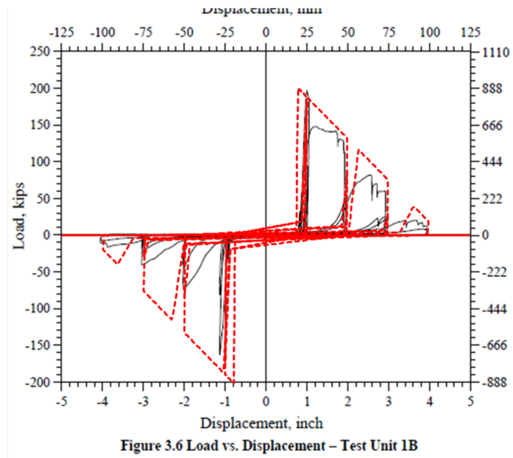

Figure 3.24: Validation of the OpenSees model (red lines) against experimental tests by Megally et al. (2001).

3.3.3 Backwall Fracture

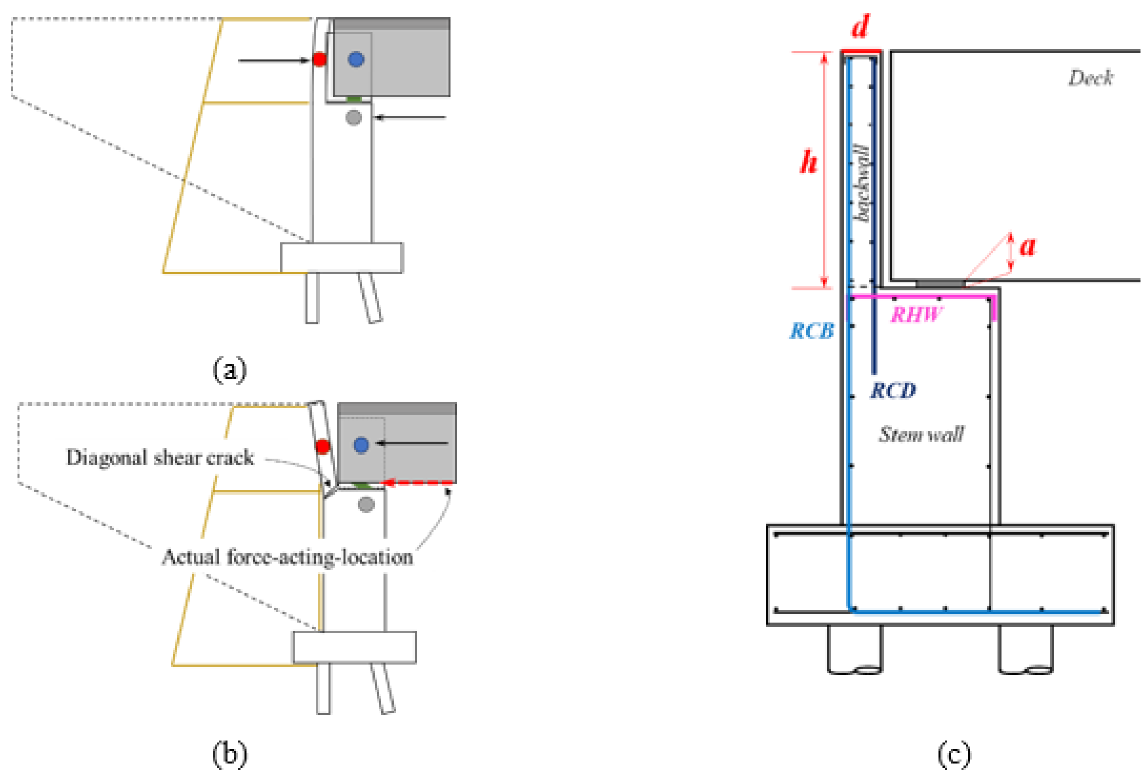

Figure 3.25: (a) Active bending, (b) passive fracture, and (c) a typical seat abutment design

This section describes the development of the backwall connection model that considers two different failure modes in the two longitudinal loading directions. In the active direction (Figure 3.25(a)), the backwall undergoes flexural bending when there is an active displacement of the stem wall (seat node) relative to the free-field, and backwall nodes: (1) the seat node moves toward the free-field and backfill-A causes bending of the backwall; or (2) the backwall node itself moves along the active direction under earthquakes because of its lumped inertia mass. This backwall response in the active direction is referred to as active bending. In the passive direction (Figure 3.25(b)), the backwall response is dominated by shear failure when the deck impacts the base of the backwall. Such shear failure in the passive direction is termed the passive fracture.

Figure 3.26(a) shows the complete parameterized backwall-connection response model for straight backwall systems that exhibits both passive fracture and active bending, while Figure 3.26(b) shows the bending response is used in both loading directions for haunched backwalls where the deck load in the passive direction is applied near the top of the backwall. Note that for straight-backwall systems, the passive fracture failure mechanism is considered essential for capturing designed sacrificial backwall behavior. In contrast, the active bending mechanism is not expected to cause backwall connection failure but is included in model development to have a numerically complete response model for loading in both longitudinal directions.

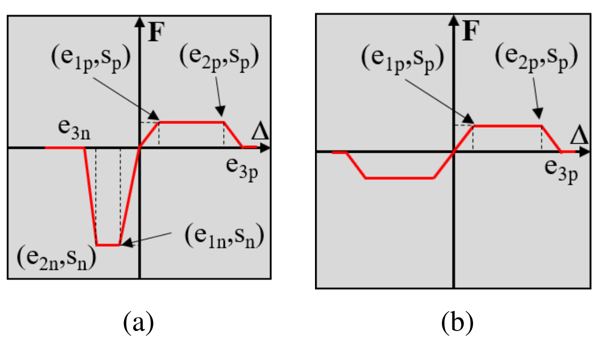

Figure 3.26: Generic abutment-backwall connection response models: (a) straight type exhibiting passive fracture and active bending; and (b) haunched type showing bending response in both loading directions.

Figure 3.25(c) shows a typical straight-backwall abutment design, where its geometry and reinforcement details are summarized in Table 3.3. These dimensional models were created from a sample of 75 straight backwall of abutment designs for California box-girder bridges (Roblee, 2018g). The bridges in the sample were randomly selected by bridge number and broadly reflected geometric variability representative of modern (post-1970's) abutment designs used throughout the state. Based on a statistical analysis of the sample plans, the backwall depth is assumed to be constant, and the remaining parameters are considered lognormally distributed. In particular, distributions for three parameters characterizing steel reinforcement are obtained, including the horizontal reinforcement on the top of the stem wall (RHW), the vertical reinforcement close to the backfill (RCB), and the vertical reinforcement close to the deck (RCD). The statistical distributions of these parameters listed in Table 3.3 form the basis to develop the probabilistic response model for the backwall connection spring.

Table 3.3: Distributions of geometric parameters and reinforcing details for abutment backwall

Parameter	**Unit**	**Distribution**				
		Type§	$\mu^\dagger$	$\sigma^\dagger$	LB⊕	UB⊕
Backwall depth d	in	C	12	-	-	-
Backwall height h	ft	LN	6	0.24	4.5	7
Bearing thickness a	in	LN	3	0.3	1.5	5.5
RCB area per wall width, A_{RCB}	in^2/ft	LN	0.35	0.6	0.15	1.6
RCD area per wall width, A_{RCD}	in2/ft	LN	0.2	0.4	0.15	0.6
RHW area per wall width, A_{RHW}	in2/ft	LN	0.4	0.6	0.15	1.6

§ C = constant, LN = lognormal, N = normal, B = binomial, and U = uniform.
† μ denotes the mean and median for normal distribution and lognormal distribution, respectively; σ denotes standard deviation and dispersion (logarithmic standard deviation) for normal distribution and lognormal distribution, respectively.
⊕ LB = lower bound, UB = upper bound.

Active Bending

Static pushover analyses were conducted in OpenSees on 320 backwall samples with a unit width (1 foot) to generate probabilistic backbone curves in active bending. Latin Hypercube Sampling (LHS) is used to generate the 320 numerical backwall samples from the statistical distributions shown in Table 3.3. Note that the 320 number is considered sufficiently large to obtain accurate results from LHS sampling and capture a representative range of responses. The pushover force is applied at the mass center for each analysis, namely mid-height on the backwall.

Figure 3.25(a) represents the simplification procedure used to characterize each active-direction pushover response as a trilinear backbone model. Each backbone response exhibits three phases: the initial linear elastic phase, the post-yielding plateau phase, and the strength degradation phase. The simplification process involved first identifying the fracture point with two controlling parameters: the displacement where the reinforcement fractures e_{2p} (unit: in) and the corresponding capacity s_p (unit: kips per ft). A horizontal line was then drawn back from the fracture point to the initial response to define the yield displacement e_{1p} (unit: in), which determines the initial stiffness. Finally, a residual strength was assumed to be a conservatively low value of 5% of s_p.

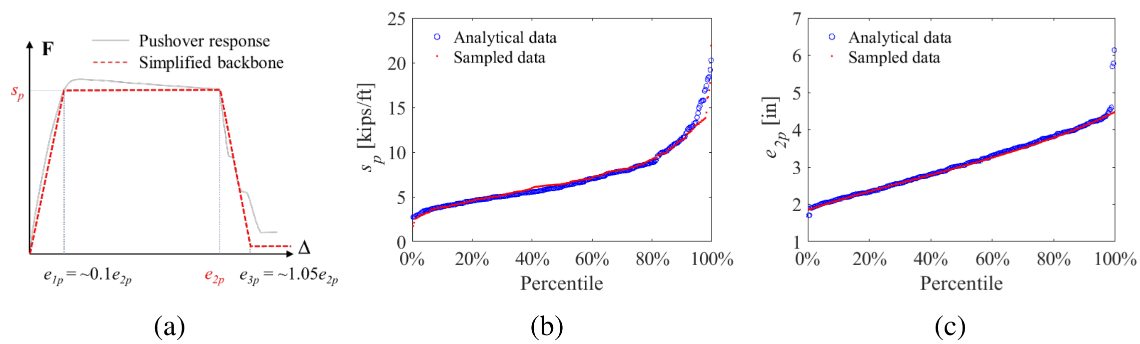

Figure 3.27: Backwall active bending model: (a) backbone curve modified from each pushover response, comparison of distributions between analytical results and samples from the generic model for (b) sp , and (c) $e2p$.

For application in the probabilistic analyses, it is convenient to express the backbone shape with two controlling parameters, accounting for variable backwall heights. A generic model was proposed in Equation 3.31. From basic mechanics for a cantilever beam, Equation 3.31a relates the lateral resistance of a cantilever beam s_p to be the base moment capacity, M, divided by the backwall height h. Equation 3.31b provides the distribution parameters for M determined from 320 backwall realizations. The other controlling parameter e_{2p} is approximately proportional to h^2, as given by Equation 3.31c, because the contribution of the yield displacement to the total displacement is implicit and the plastic hinge length is a proportion of the backwall height h. The value for the proportion parameter k in Equation 3.31c is estimated as $0.1\,\text{in/ft}^2$. The yield displacement is assumed to be $0.1e_{2p}$ for simplicity.

Fixed ratio models in terms of e_{2p} were found to reasonably characterize the backbone displacement values e_{1p} and e_{3p}. Figure 3.25(b) and (c) compare the distributions between the analytical results (from pushover responses) and the sampled results (from the proposed generic model) for the remaining two controlling parameters. A two-sample Kolmogorov-Smirnov test (Kolmogorov, 1933; Smirnov et al., 1948) is applied to the data to test whether the two datasets come from the same distribution. The p-values for testing s_p and e_{2p} are 0.546 and 0.997, respectively, much higher than the typical significance level of 0.05. Therefore, the test does not reject the null hypothesis and concludes that the data are drawn from the same distribution.

$$s_p = \frac{M}{h} \tag{3.31a}$$

$$M \sim \text{LN}(37.0\,\text{kips} \cdot \text{ft/ft}, 0.40) \tag{3.31b}$$

$$e_{2p} = kh^2 \tag{3.31c}$$

Passive Fracture

Due to the lack of experiments of straight backwall with a shear fracture in the literature, a mechanical model for a non-isolated shear key (Figure 3.19(a)) is adapted to create the backwall passive fracture model (Figure 3.21(b)). The similarity between these elements is illustrated in Figure 3.23. Although a backwall is a longitudinal component and a shear key is a transverse component, this adaption is reasonable because: (1) both the backwall and the non-isolated shear key are subjected to impact forces from the deck; (2) the impact forces act at the locations where the shear key and backwall collide with the decks, i.e., the bearing height a in Figure 3.20; and (3) the connection details between the shear key and stem wall are similar to the ones between the backwall and stem wall.

Equation 3.32 are modified from Equation 3.28 and adopted for the calculation of passive fracture capacity s_n of the backwall. It is more reasonable to assume that the orientation of the cracks in the backwall is 45° rather than cutting through to the base of the stem wall because the backwall depth d in Figure 3.23(b) is much smaller than the stem wall height H. Such a 45° cracking has been validated by previous experimental results Megally et al. (2001). Equation 3.32c can be derived from Equation 3.28c because the corresponding reinforcement is not transected by the proposed shear crack. A_{RHW} and A_{RCD} are defined in Table 3.3.

$$s_n = V_c + V_s \tag{3.32a}$$

$$V_c = 2.4wd\sqrt{f'_{co}\text{psi}} \tag{3.32b}$$

$$V_s = \frac{1}{d+a}\left(A_{RHW}f_yd + A_{RCD}f_yd\right) = \frac{f_yd}{d+a}(A_{RHW} + A_{RCD}) \tag{3.32c}$$

The complete mechanical model (Zheng et al., 2021) for the backwall passive fracture is shown in Figure 3.28(a). Displacement parameters are determined by applying the essential formulas of the non-isolated shear key model Megally et al. (2001, 2003). Equation 3.33 expresses the relationship between the horizontal crack width (δ_0) at the RHW level and the strain of the horizontal reinforcement (ε), in which L_d is the reinforcement development length, as given by Equation 3.29f and L_a is the horizontal distance of the crack region (see Figure 3.23(a)). Experimental results indicate that such a crack region approximately equals the bending wall width (Megally et al., 2001).

$$\delta_0 = \varepsilon(L_d + L_a) \tag{3.33}$$

When the backwall fractures and rotates as a rigid body, displacement compatibility is obtained and given by Equation 3.34a. The left-hand side describes the rotation angle at the impact level relative to the bottom-left end of the crack, namely the backwall displacement en divided by the impact level height of $(a + d)$. The right-hand side calculates the crack width at the RHW level divided by the corresponding height of $(d - c)$, in which c is the concrete cover for the RHW. Substituting Equation 3.33 into Equation 3.34a yields Equation 3.34b, which represents the passive fracture displacement en. The backwall starts to yield when ε reaches the yield strain ε_y and loses strength when ε reaches $\varepsilon_u = 0.7\%$ (Megally et al., 2001, 2003).

$$\frac{e_n}{a+d} = \frac{\delta_0}{d-c} \tag{3.34a}$$

$$e_n = \varepsilon \frac{(L_a + L_d)(a+d)}{d-c} \tag{3.34b}$$

A procedure similar to that used to develop the generic backwall active bending model is also employed to develop a model for passive fracture response. Here, application of LHS to Equation 3.32 and Equation 3.34 is used to generate 320 probabilistic backbone curves. Figure 3.28(a) shows a sample backbone curve, in which s_n is calculated by Equation 3.32, and e_{1n} and e_{2n} are calculated by substituting ε_y and ε_u into Equation 3.34b, respectively. The generic model is then summarized in Equation 3.35 for the two controlling parameters s_n and e_{1n}. The displacement e_{2n}, where the strength starts to decrease, is assumed to be 3.5 times of e_{1n} for simplicity as $\varepsilon_u/\varepsilon_y \approx 3.5$.

$$s_n \sim \text{LN}(52.0\,\text{kips}\cdot\text{ft}, 0.20) \tag{3.35a}$$

$$e_{1n} = \frac{s_n}{6.35 s_n + 130} \tag{3.35b}$$

The same procedure is also applied to early-ductile (era-2) straight backwall designs, which differ slightly from the modern (era-3) designs by the inclusion of additional reinforcement stirrups at the base of the wall as shown in Figure 3.29. This increases the fracture capacity of the backwall connection. The applicable model for era-2 designs is

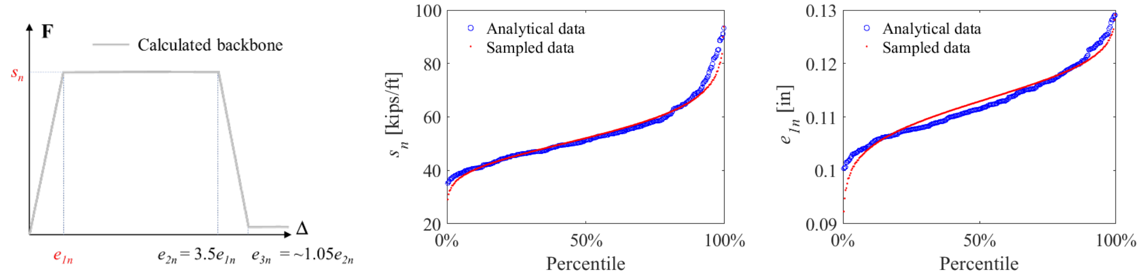

(a) (b) (c)

Figure 3.28: Backwall passive fracture model (Zheng et al., 2021): (a) backbone curve, comparison of distribution between analytical results and samples from the generic model for pre-ductile bridges: (b) s_n , and (c) e_{1n}

summarized in Equation 3.36.

$$s_n \sim \text{LN}(89.0\,\text{kips} \cdot \text{ft}, 0.20) \tag{3.36a}$$

$$e_{1n} = \frac{s_n}{1.25 s_n + 520} \tag{3.36b}$$

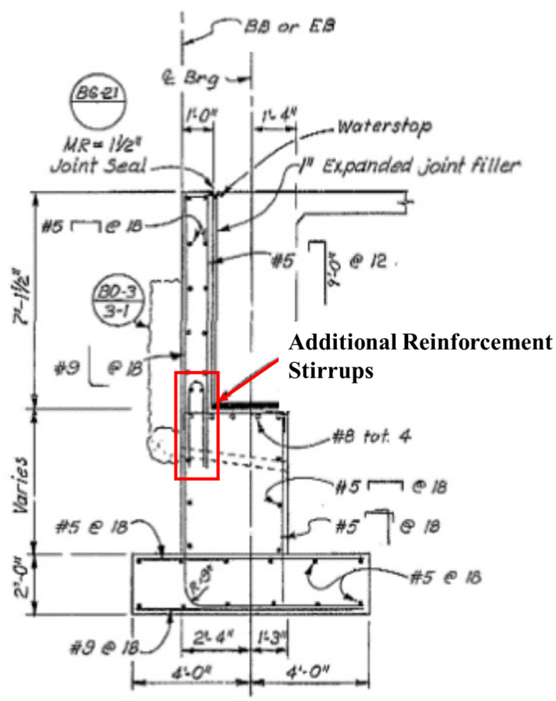

Figure 3.29: Straight backwall designed in early-ductile (era-2) bridges.

Haunched Backwall

As detailed in Table 2.1 and Figure 2.6, many pre-ductile bridges (era-1) backwalls incorporate a haunch detail, commonly on the backwall, but sometimes alternatively or also on the deck. For these haunched cases, the failure mode in both loading directions is flexural bending. The difference with the straight backwall in the passive direction is that the point of loading application is now at the backwall top. For simplicity of application, the response model for haunched backwall is taken as symmetric in both active and passive directions, following the model described in Equation 3.31.

3.3.4 Pounding

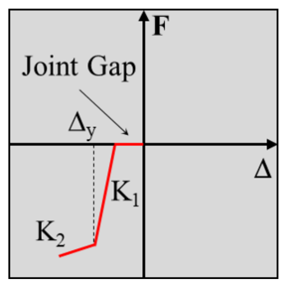

Figure 3.30: Response model for pounding

The study by Muthukumar and DesRoches (2006) indicated that pounding between bridge components causes energy dissipation and therefore can have a significant impact on the overall bridge response.

The adopted pounding model is established by determining two stiffness K_1 and K_2 as the initial stiffness and post-yield stiffness, respectively (Muthukumar, 2003; Nielson, 2005). Derived from a two-degree-of-freedom system, the contact force due to pounding is based on the Hertz contact model with nonlinear hysteresis damper. The adjacent pounding components are assumed to be two spheres with the density of concrete material. With this assumption, calculating the volume of two pounding objects leads to the radii of the two spheres noted as R_1 and R_2. Then the stiffness parameter K_h of the Hertz model can be derived using the following equation:

$$K_h = \frac{4}{3\pi(h_1 + h_2)}\sqrt{\frac{R_1 R_2}{R_1 + R_2}} \tag{3.37}$$

where h_1 and h_2 are material parameters also representative of the same concrete material:

$$h_1 = h_2 = h = \frac{1 - \nu^2}{\pi E_c} \tag{3.38}$$

where ν and E_c are the poisson ratio and elastic modulus of concrete, respectively. The energy dissipated during the pounding procedure ΔE is calculated as:

$$\Delta E = \frac{K_h \delta_m^{n+1}(1 - e^2)}{n + 1} \tag{3.39}$$

Incorporating several constant parameter values (maximum penetration displacement δ_m =1.0 inch, $n = 1.5, e = 0.6$), Equation 3.39 is further simplified into $\Delta E = 0.256 K_h$. Effective stiffness then determined as $K_{eff} = \Delta E \sqrt{\delta_m}$ and used to compute the two desired stiffness's with Equation 3.40 with $a = 0.1$:

$$K_1 = K_{eff} + \frac{\Delta E}{a\delta_m^2} \tag{3.40a}$$

$$K_2 = K_{eff} - \frac{\Delta E}{a\delta_m^2} \tag{3.40b}$$

OpenSees modeling of the hysteresis properties of this material is accomplished by incorporating two *ElasticPPGap* elements in parallel. Note that this model considers the mass of two pounding structures, and thus, the force and stiffness scale of the material used in the abutment system will be different from the one used in the pounding of adjacent decks in an in-span hinge. Figure 3.31 compares the responses for pounding between decks versus deck-to-abutment pounding for the bridge in Appendix A. Both responses take the gap size as 0.5 inches. The figure indicates that the pounding force between decks is significantly higher than that between deck and abutment.

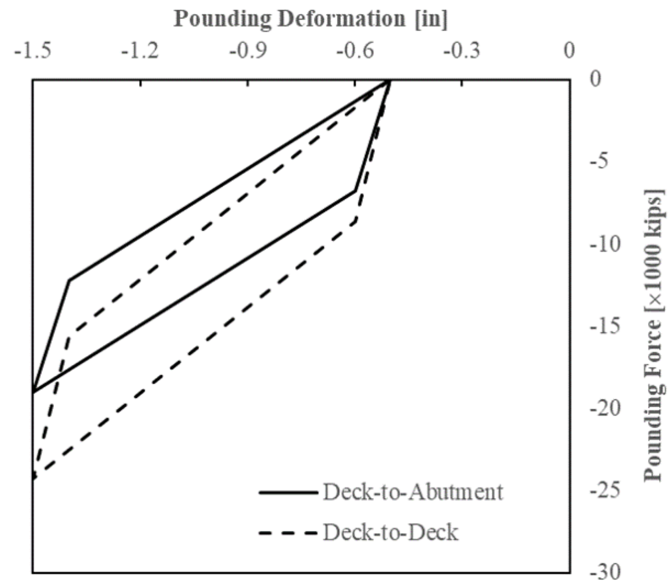

Figure 3.31: Pounding models hysteretic loops for different adjacent objects

3.3.5 Bearing

Elastomeric pads are used in all ductile (era-3) and early-ductile (era-2) designed bridges. Steel rocker bearings are very common for non-ductile (era-1) designed bridges, although a few late-era bridges adopted elastomeric pads.

This research models elastomeric pads as having a simple bilinear response as illustrated in Figure 3.32(a). This is done within OpenSees using the *Steel01* material with zero strain hardening. Two parameters K_e and μ are used to construct a pad's constitutive model, in which K_e is the initial stiffness, and μ is the friction coefficient that generates the yield strength F_y by multiplying by axial load N on the pad.

While elastomeric pads have the same constitutive model in both directions, steel rocker bearings have very different responses in the longitudinal and transverse directions. Figure 3.33(a) shows the rocker bearing most commonly used in early California bridge designs. The bearing has a curved surface at the top and bottom in the longitudinal direction, which accommodates translational movement. However, in the transverse

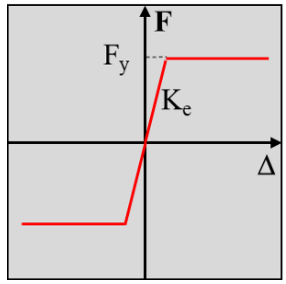

(a)

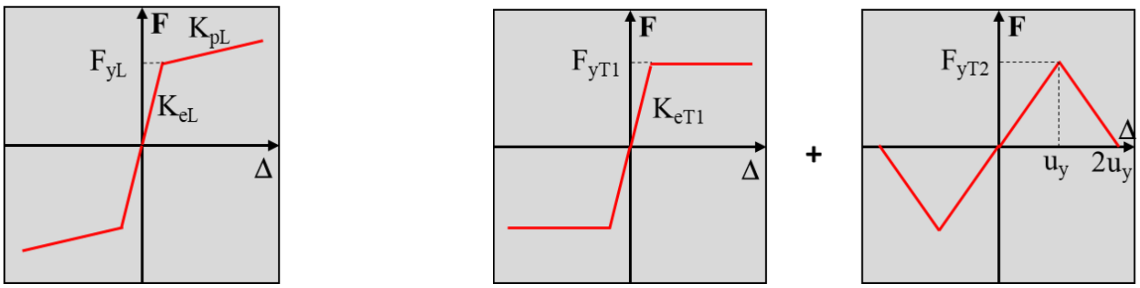

(b) (c)

Figure 3.32: Response models for bearings: (a) elastomeric pads; and rocker bearings in (b) longitudinal direction; and (c) transverse direction. The transverse rocker bearing model includes both a frictional and a fuse component.

direction, the bearing must first fail a pair of retainer bracket bolts before responding as a frictional connection. In these designs, the transverse restraint provided by the bearing retainer assembly serves to limit transverse deck movement similar to a shear key.

This research adapts a model by Nielson (2005), developed for high expansion steel bearings as shown in Figure 3.33(c), to the modeling of the typical California bridge bearing assembly shown in Figure 3.33(a). The failure modes are comparable with the exception that the transverse restraint is provided by a pair of pintles rather than retainer-bracket bolts. However, once the pintles are sheared, all transverse restraint is lost, whereas the shearing of any pair of the retainer-bracket bolts only allows movement in one direction. Responses are considered comparable in the longitudinal direction.

In the longitudinal direction, Nielson (2005) validated the model against an experimental test by using *Steel01* material with parameters $K_{eL} = 80.0\,\text{kips/in}$, $K_{pL} = 0.018K_{eL}$, and $F_{yL} = \mu N$, in which $\mu = 0.04$ is the friction coefficient and N is

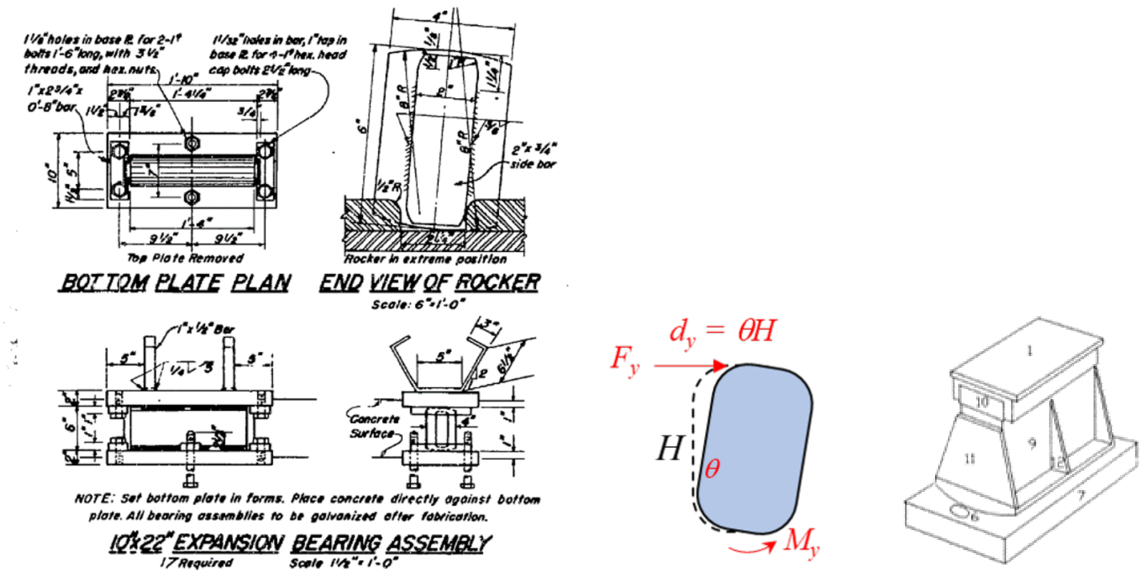

(a) (b) (c)

Figure 3.33: (a) Typical rocker bearings used in era-1 California bridges (6.0 inch height with 2 nuts on each side in the transverse direction); (b) simplified diagram for force calculation; and (c) high expansion steel bearings (Mander et al., 1996).

the axial load acting on the bearing. The dimension used by Nielson (2005) for validation is 16.7 inch, which is different from the 6.0 inch bearing height used in California concrete box-girder bridges. In order to adapt this validated model, it is assumed that the overturning moment provided by the pintle (or the flat surface in Figure 3.33(b)) is the yield base moment M_y. A bearing rocks to the yield base moment M_y when it reaches the same tilted angle θ. Under this assumption, Equation 3.41 derives the relationship of variables with bearing height H:

$$F_y = \frac{M_y}{H} \tag{3.41a}$$

$$\mu = \frac{F_y}{N} = \frac{M_y}{HN} \tag{3.41b}$$

$$K_e = \frac{F_y}{d_y} = \frac{M_y}{\theta H^2} \tag{3.41c}$$

Consequently, the model for typical rocker bearings used in California concrete box-girder bridges is defined used the parameters: $K_{eL} = 620.0\,\text{kips/in}$, $K_{pL} = 0.018K_{eL}$, and

$F_{yL} = \mu N$, in which $\mu = 0.11$ is the friction coefficient and N is the axial load acting on the bearing.

In the transverse direction, two springs are used parallel to capture the complete response, namely the fuse and friction springs. The fuse spring models the failure of retainer pintles (or retainer bracket bolts), whereas the fiction spring models the kinetic frictional movement between the rocker and the base plate after the failure of pintle (or retainer bracket bolts). The friction spring is modeled using $K_{eT1} = 1440\,\mathrm{kips/in}$ (Nielson, 2005) , and $F_{yT1} = 0.30N$, where N is the axial load acting on the bearing. The yield deformation of fuse spring is assumed to be 10 mm or 0.39 inch. The model proposed by Steelman et al. (2014) is used to estimate the capacity of retainer pintles (or bolts):

$$F_{yT2} = n_b(0.6f_u)A_{gb} \tag{3.42}$$

where n_b is the number of retainer pintles or bolts; the 0.6 coefficient reflects the assumption that pure shear controls capacity; f_u is ultimate tensile strength of steel; and A_{gb} is the effective cross-section area of a pintles or bolts, and it's recommended to be taken as 80% of the nominal cross-section area for threaded nuts. Validation of the high expansion steel bearing with pintles design against the experimental tests by Steelman et al. (2014) is shown below. To adapt this model to rocker bearings used in California concrete bridges, the bolt number n_b in Equation 3.42 is changed to 2, accounting for the pair of bolts are sheared in the transverse direction.

3.3.6 Foundations

Two general classes of foundations, piles and spread footings, are commonly used to support both abutments and bents of California bridges. Figure 3.35 illustrates parameterized models for the translational response of these two foundation types. Note that large-diameter drilled shafts of various designs are also used at bent locations, but these are treated as special cases of column-bent modeling.

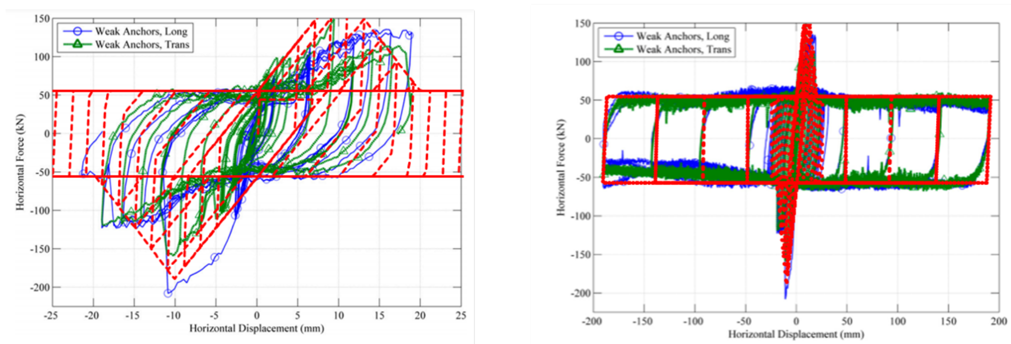

Figure 3.34: Validation of the OpenSees model (red lines) against experimental tests by Steelman et al. (2014).

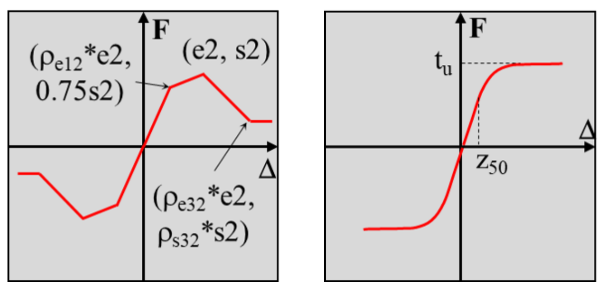

(a) (b)

Figure 3.35: Response models for foundation translational springs: (a) piles; and (b) spread footings.

Pile Foundation

A multi-linear model, defined by *Hysteretic* material in OpenSees, is used to capture the seismic response of various pile foundation types using a set of models developed by Xie et al. (2021, 2020). These transverse-response models all require five parameters as illustrated in Figure 3.35(a): the ultimate strength s_2 and corresponding deformation e_2, the ratio ρ_{e12} between yield deformation and e_2, ratio ρ_{s32} between degraded strength and s_2, and the ratio ρ_{e32} between the deformation at onset of degraded strength and e_2.

The modeled s_2 value represents the ultimate lateral resistance of a single pile. Most pile foundations involve an array of multiple rows and/or columns of piles, and their interactions typically reduce pile-group capacity below that of the simple summation of individual pile capacities. This is commonly handled with 'group factors' or capacity-reduction ratios. These factors, herein denoted f_m, are applied to individual piles based on pile spacing and pile position within the group and relative to the direction of motion.

(Xie et al., 2021) suggested the following procedure, based on Rollins et al. (2006), for computing a group amplification factor g_f to scale up the backbone response of a single pile to that for a group of piles. This process is performed separately for each loading direction. Note that the amplification factor g_f incorporates the impact of multiple group factor f_m applied to individual rows of piles. Figure 3.36 shows a 4×6 pile group representative of a typical pile cap which might underlie a single column bent of a modern bridge. For procedure illustration purposes, the amplification factor is only considered for the longer axis undergoing a leftward direction of motion. In the direction of motion, there are $n_r = 6$ rows and $n_p = 4$ piles at each row. S in the figure represents the center-to-center spacing of piles, and D is the pile dimension. The group factors are largest for the leading row of piles in the direction of motion, which engage the largest volume of soil, and become smaller for trailing rows that are in the shadow of the leading row. The Rollins et al. (2006) procedure assigns the larges group-factor value f_{m1} to the first row, a reduced value f_{m2} to the second row, and the smallest value f_{m3} to the third and all subsequent rows as follows:

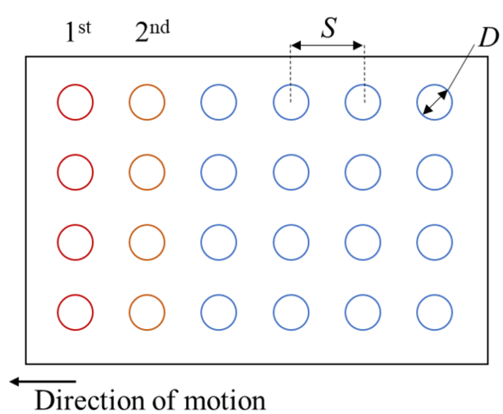

Figure 3.36: Illustration for calculating pile group effect.

$$0.0 \leq f_{m1} = 0.26 \ln \frac{S}{D} + 0.50 \leq 1.0 \tag{3.43a}$$

$$0.0 \leq f_{m2} = 0.52 \ln \frac{S}{D} + 0.00 \leq 1.0 \tag{3.43b}$$

$$0.0 \leq f_{m3} = 0.60 \ln \frac{S}{D} - 0.25 \leq 1.0 \tag{3.43c}$$

The final amplification factor g_f for this direction of motion sums up the individual pile contributions by row and can be written as follows, where $\mathbb{I}(\cdot)$ is the indicator function that equals 1 if the condition is true and 0 otherwise.

$$g_f = f_{m1} n_p + f_{m2} n_p \mathbb{I}(n_r > 1) + f_{m3} n_p (n_r - 2) \mathbb{I}(n_r > 2) \tag{3.44}$$

Spread Footing Foundation

In this research OpenSees modeling of footing sliding behavior uses the *TzSimple2* material (Raychowdhury and Hutchinson, 2008). This model requires two controlling parameters: ultimate capacity t_u and a deformation value z_{50} corresponding to 50% of t_u. The distributions adopted for this research are summarized in the Chapter 5.

3.3.7 Soil Loads on Structural Elements

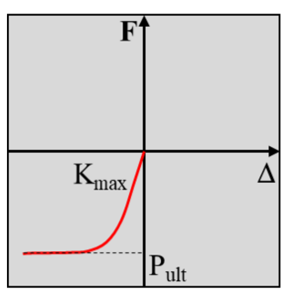

Figure 3.37: Response model for passive soil loads.

The passive resistance of soil on a structural element, such as the backfill load on an abutment, is typically modeled using nonlinear springs with a hyperbolic shape

(Shamsabadi et al., 2007; Shamsabadi and Yan, 2008; Xie et al., 2019), where the soil resistance is a function of the contact dimensions and embedment depth of the structural element. Active soil resistance is not modeled. The probabilistic hyperbolic backfill-soil model with depth effects developed by Xie et al. (2019) is adopted herein and modeled in OpenSees using *HyperbolicGap* material. This same hyperbolic model formulation used for backfill loads is also used to characterize passive loads acting on the front and side of the abutment as well as on the sides of pile caps and footings. Depending on location, these soil loads may be referred to as backfill, frontfil, or sidefill loads.

An important feature of abutment modeling adopted in this research per Figure 3.20 is isolating the different soil loads acting on the backwall and stem wall after backwall fracture. To implement this, the Xie et al. (2019) model is extended used to allow separation of backwall reactions into the backfill-A and backfill-B components. Equation 3.45 are the general formulae for the backbone model where P is the unit reaction force for wall displacement y, H is the wall height, $H_0 = 5.5\,\text{feet}$, and the parameters $P_{ult,0}$, $K_{max,0}$, α_1, and α_2 are model coefficients which depend on backfill soil type. R_f is back-calculated for the sampled values of P_{ult} and K_{max}.

$$P = \frac{y}{\dfrac{1}{K_{max}} + R_f \dfrac{y}{P_{ult}}} \tag{3.45a}$$

$$P_{ult} = P_{ult,0} \left(\frac{H}{H_0} \right)^{\alpha_1} \tag{3.45b}$$

$$K_{max} = K_{max,0} \left(\frac{H}{H_0} \right)^{\alpha_2} \tag{3.45c}$$

Equation 3.46 show the implementation for backfill-A response where the parameters $P_{ult,A}$ and $K_{max,A}$ are scaled from the total-height (i.e., backfill-A and backfill-B) response parameters which are initially specified.

$$P_{ult,A} = P_{ult,T} \left(\frac{H_A}{H_T} \right)^{\alpha_1} \tag{3.46a}$$

$$K_{max,A} = K_{max,T} \left(\frac{H_A}{H_T} \right)^{\alpha_2} \tag{3.46b}$$

$$R_{f,A} = 1 - \frac{P_{ult,A}}{0.05 K_{max,A} H_T} \tag{3.46c}$$

As a first approximation considering the two backfill loads as parallel springs, Equation 3.47 show that backfill-B response parameters $P_{ult,B}$ and $K_{max,B}$ are taken as the difference between values for the total height and backwall height. For both the backfill-A and backfill-B calculations, the R_f term is back-calculated assuming the ultimate resistance is attained at the same mobilized deformation, which is taken as 5% of the total wall height (H_T).

$$P_{ult,B} = P_{ult,T} - P_{ult,A} \tag{3.47a}$$

$$K_{max,B} = K_{max,T} - K_{max,A} \tag{3.47b}$$

$$R_{f,B} = 1 - \frac{P_{ult,B}}{0.05 K_{max,B} H_T} \tag{3.47c}$$

An alternative strategy is adopted to address two minor deficiencies in parallel spring simplification to separate the backfill-A and backfill-B. First, the $R_{f,A}$ calculation in Equation 3.46c is a function of the total height H_T. The assumption means the response model for the backfill-A soil depends on the height of the backfill-B soil, which is not rigorously defined. Second, in the simplified approach, the resistance calculated by subtracting backfill-A from total ($P_T - P_A$) is about 10% less than the backfill-B model calculated by Equation 3.47 (Figure 3.38(a)); or in other words, the total resistance from the two parallel springs (backfill-A and backfill-B) is not the same as modeling the combined backfill directly.

To better address this problem, Equation 3.46c is first modified to use $0.05H_A$ as the

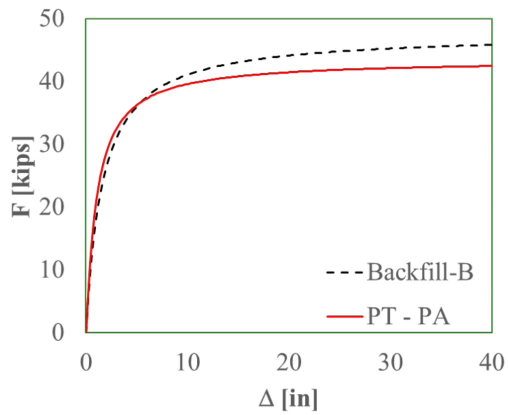

(a)

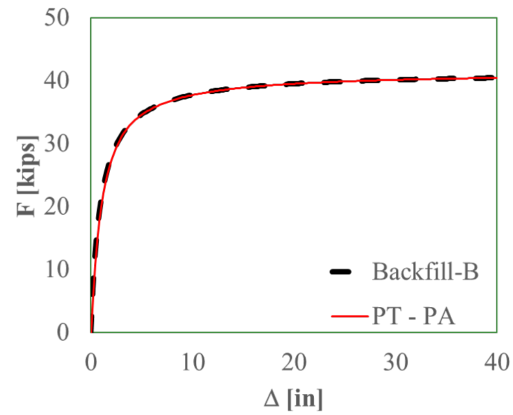

(b)

Figure 3.38: (a) Difference between calculation of backfill-B model by subtracting backfill-A from total and by Equation 3.47; (b) same comparison using Appendix D.

deformation attaining ultimate capacity in Equation 3.48. The remainder of the modification uses polynomial equality to calculate the backfill-B parameters as detailed Appendix D. Figure 3.38(b) shows this modified strategy addresses the deficiency in the parallel spring approximation and produces compatible response values for backfills T, A, and B.

$$R_{f,A} = 1 - \frac{P_{ult,A}}{0.05K_{max,A}H_A} \tag{3.48}$$

3.3.8 Skew Effects on Backfill Soil Response

Bridge skew has long been recognized to have an impact on bridge response and is routinely incorporated into fragility assignments (FEMA, 2003). Accurate prediction of overall skew effects must include consideration of the impact which skew has on backfill soil response. This research adopts two modifications to backfill response models resulting from skew: 1) an overall reduction factor, and 2) a non-uniform distribution factor as illustrated in Figure 3.39.

The overall reduction factor, identified by Shamsabadi and Rollins (2014), reduces the total backfill response acting on a skewed abutment relative to an unskewed (or straight) abutment per Figure 3.39(a). The reduction factor $R(\theta)$ is applied to the strength/stiffness of the response model of a straight bridge. An exponential decay relationship was proposed by Shamsabadi and Rollins (2014) and then updated by Shamsabadi et al. (2020). This project adopts the median reduction-factor model proposed in Shamsabadi et al. (2020) where θ in Equation 3.49 is the bridge skew angle. Note that dispersion in this reduction factor model is not considered since the Xie et al. (2019) backfill response model already incorporates probabilistic effects.

$$R(\theta) = e^{-0.021\theta} \tag{3.49}$$

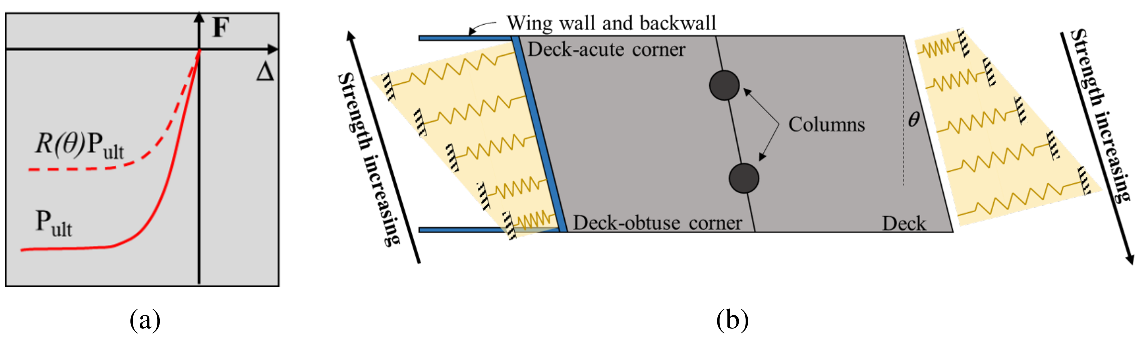

Figure 3.39: Skew effects on soil behaviors: (a) overall reduction factor; and (b) non-uniform distribution of soil resistance.

The second factor pertains to the local distribution of the soil capacity in a skew bridge. As illustrated in Figure 3.39(b), the skewed abutment develops an asymmetric passive soil wedge when the abutment is rotated. Moreover, the backfill soil volume, mobilized per unit length of abutment wall, increases from the deck-obtuse corner toward the deck-acute corner, as more soil is engaged at the deck-acute corner than at the deck-obtuse corner. Equation 3.50 is the model proposed by Kaviani et al. (2012) which is adopted for this research. The $\beta(\theta)$ value represents the maximum difference in response over the full width of the abutment. Thus, the combination of the two skew factors on backfill response becomes $R(\theta)(1 + \beta(\theta)/2)$ at the deck-acute corner, and $R(\theta)(1 - \beta(\theta)/2)$ at the deck-obtuse corner. These response modifiers are applied individually to both strength and stiffness values of each soil response in the finite-element model and are assumed to vary linearly with position along the abutment.

$$\beta(\theta) = 0.3\frac{\tan\theta}{\tan 60°} \tag{3.50}$$

3.4 Ground Motion Set and Structural Damping Model

3.4.1 Ground Motions

To develop fidelity in the PSDM, it is important to have a wide range of ground motions with a large variation of S_{a1} (spectral acceleration at 1.0 second) values or PGA (peak ground accelerations) to ensure the evaluation of a sufficient range of bridge responses. The current study utilizes the T1780 ground motions specified by Roblee (2015*c*,*b*), selected from the NGA-2 database (Bozorgnia et al., 2014) and assembled by Mangalathu (2017) and Soleimani (2017). These motions were developed specifically to be broadly representative of a wide range of California bridge sites, and consist of the 320 scaled recorded ground motions listed in Appendix B. As illustrated in Figure 3.40(a), the distribution of the S_{a1} values for the T1780 ground motions (from 0.01 g to 2.72 g) is wider than that of Baker et al. (2011) used in early feasibility phase of this project. Further, a greater proportion of the T1780 records have high S_{a1} values to better assess bridge responses in the nonlinear regime. These T1780 ground motions were specified as 20 sets with 16 ground motions in each set having an ensemble average S_{a1} which closely approximates a target S_{a1} value for the set. As shown in Figure 3.40(b), the median S_{a1} increases from set-20 to set-1 with a progressively higher concentration of motions from the elastic to the highly-nonlinear structural response regimes. All 320 downloaded excitations have two orthogonal components and are randomly oriented and applied to the longitudinal and transverse directions of bridge models.

Although the original T1780 set shown here included several motions in the high nonlinear response region, project experience showed that these alone were insufficient to accurately constrain the high-demand response of modern ductile bridges having

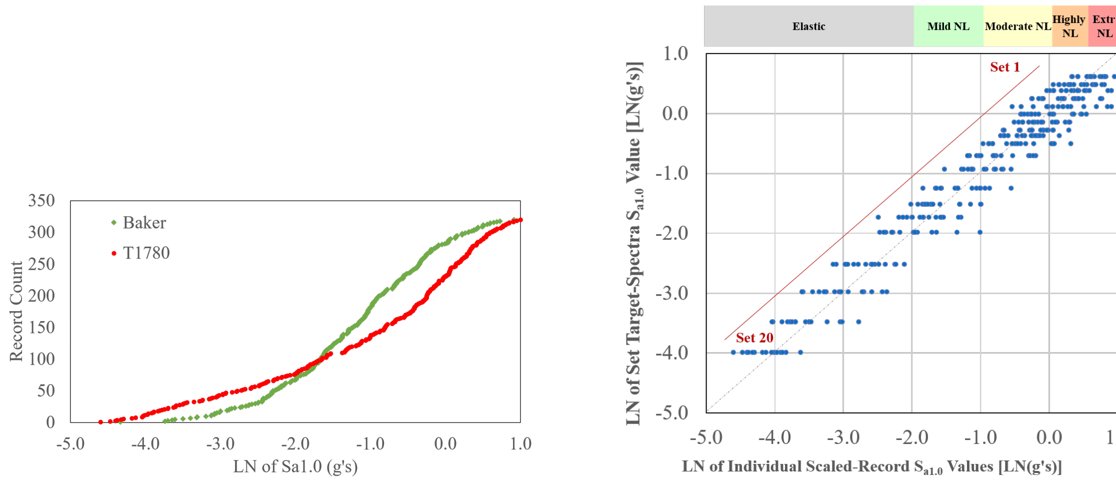

(a) (b)

Figure 3.40: Features of the T1780 (Roblee, 2015*c*,*b*, 2016*d*) ground motion sets: (a) comparison of S_{a1} distributions used in earlier feasibility studies (from Baker et al. (2011)) with T1780 set used in this study; and (b) distribution of S_{a1} values for each of the 20 T1780 sets relative to the target spectrum for each set.

high-capacity components. Therefore, an additional set of even high-level motions was created by uniformly scaling set-1 and set-2 of the T1780 motions to 3.00 g to improve the prediction accuracy of the demand models of modern bridges.

Finally, note that the selection of S_{a1} as the intensity measurement (IM) in the PSDM model is based on the work of Ramanathan (2012), which indicated that S_{a1} is the optimal intensity measure for the class of California concrete box-girder bridges.

3.4.2 Damping Model

Rayleigh damping (Rayleigh, 1896) is one of the most commonly used damping models that is adopted in this research. The frequency characterizes Rayleigh damping within two bounding structural frequencies ω_i and ω_j, where the damping ratio within this range is smaller than ξ. For a mode shape involving oscillation of only a small part of the structure (a local mode), the corresponding frequency is usually substantial, which results in a substantial damping ratio. Those high-frequency modes are overdamped and thus limit the considered modes to lower frequencies.

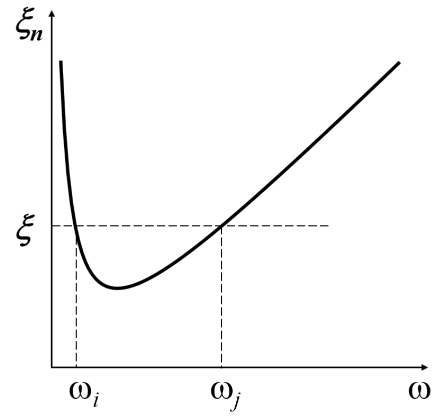

Figure 3.41: Rayleigh damping model.

Two parameters are needed to specify a Rayleigh damping model. These two parameters correspond to the structure mass matrix (M) and tangent stiffness matrix (K_T), respectively, and the damping matrix for an element (D) is specified as a combination of M and K_T by the following equation:

$$D = \alpha M + \beta K_T \tag{3.51}$$

where $\alpha = \dfrac{2\xi\omega_i\omega_j}{\omega_i + \omega_j}$ and $\beta = \dfrac{2\xi}{\omega_i + \omega_j}$. ω_i and ω_j are the structure frequencies corresponding to the i^{th} and j^{th} mode shapes. Based on the established rules for use of of Rayleigh damping, in order to damp out higher modes, the modes considered in this research are specified as the 1^{st} and the 5^{th} modes. This assumption is based on simulation results which show that most analyzed concrete bridges have a local mode shape after the 5^{th} mode. An example verification of dynamic modeling using this strategy for Rayleigh dampling specification can be found in section C.5.

3.5 Deterministic Example Illustration (OSB-1 Bridge)

Simulated deterministic responses for the two-span box-girder multi-column bent bridge with seat-type abutment shown in Appendix A are used in this section to demonstrate the effects of several of the adopted modeling strategies described earlier in this chapter.

3.5.1 Abutment Models

This first section explores the impact of adopting the abutment model illustrated in Figure 3.20 by contrasting its responses for primary bridge components with those produced by two conventional models. The identical bridge model is analyzed using the adopted abutment model (Figure 3.20), referred to as Model-A hereafter, and two conventional abutment modeling schemes (Figure 2.7) called Model-C1 and Model-C2 used in prior research. Model-C1 and Model-C2 differ only in the value assigned to the backfill spring. Model-C1 assumes the backfill height to be limited to the backwall height (i.e., considers only backfill-A) throughout loading. Model-C2 assumes the backfill height to extend the total wall height (i.e., considers both backfill-A and backfill-B) throughout loading. Model-A also considers response contributions of both backfill-A and backfill-B but allows for decoupling during loading upon backwall fracture. Note that the C2 model assumption of using total abutment-wall height for estimating backfill reaction force is not commonly used for design. Its inclusion in this paper is primarily to illustrate end-member modeling options which produce results that bracket and provide context to the responses produced by the adopted model. All models use the same transverse configuration as Model-A to isolate the difference in longitudinal response caused solely by backwall fracture.

Pushover Analysis in Longitudinal Direction

Longitudinal pushover responses of the primary components of the bridge system are compared in Figure 3.42 for the three alternative abutment models (Model-A, Model-C1, and Model-C2). Figure 3.42(a) compares the total abutment reaction, which consists of the forces in springs backfill-A, backfill-B, and foundations in Figure 3.20. Figure 3.42(b)-(d) compare the passive responses of the backfill, bearings, and longitudinal foundations in the abutment, respectively. Before the closure of the joint gap between the backwall and deck (at 2.0 inches), the deck response is controlled only by the bearings. In this stage, all three models exhibit the same behavior. After the gap is closed, the three models start to behave differently. Each model is separately discussed below.

For Model-C1, the abutment is laterally supported by backfill-A and the foundation. Figure 3.42(a) shows that the abutment reaction reaches the 2350 kips peak at about 3.0 inches and then starts to decrease due to failure of the abutment foundation. The backfill provides an ultimate resistance of about 1550 kips (Figure 3.42(b)), but provides only about 1250 kips when the piles reach peak capacity at about 1.7 inch deformation. The bearings deform by only 2.0 inches (Figure 3.42(c)) before "locking" due to closure of the 2.0 inches joint gap and minor deformation of the impact element. Since this model does not consider the backwall fracture, the deck continues pushing the backwall, stem wall, and abutment foundation. Thus, the abutment foundation experiences a large post-peak deformation (Figure 3.42(d)), whereas the bearings experience only a small deformation controlled by the joint gap.

For Model-C2, the abutment has an additional resistance from backfill-B compared to Model-C1. Due to the large and increasing capacity of backfill-B, the abutment reaction continues increasing (Figure 3.42(a)) even as the foundation fails. At a displacement of 10.0 inches, the Model-C2 reaction is larger than those of the other two models by about 4000 kips (Figure 3.42(b)). Again, since Model-C2 does not consider backwall fracture, bearing deformation remains in the elastic range reaching only 2.4 inches (Figure 3.42(c)), and large foundation deformation is also observed in this model (Figure 3.42(d)).

Unlike Model-C1 and Model-C2, the backwall fracture mechanism is considered in Model-A to decouple the responses of backfill-A and backfill-B accurately. As shown in Figure 3.42(a), the Model-A reaction includes both backfills and the foundations before the backwall fracture at approximately 3.1 inches. Once the backwall fractures, the Model-A reaction loses the support of both backfill-B and the foundations and is suddenly

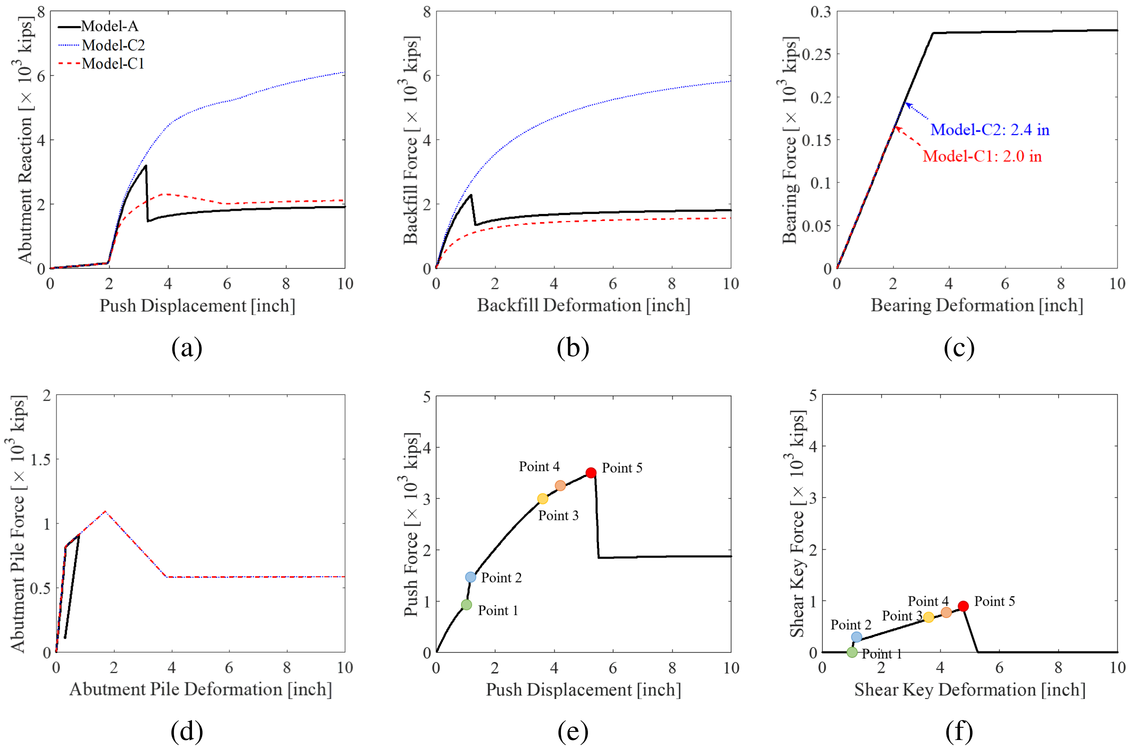

Figure 3.42: Bridge responses in both the longitudinal direction: (a) east abutment, (b) backfill, (c) bearing, and (d) abutment foundation; and the transverse direction: (e) entire bridge and (f) shear key.

reduced to nearly the capacity of backfill-A alone. Note that after the backwall completely fractures, only limited force from the deck can be transferred to backfill-B and the foundations through the bearings and the 5% residual strength of the backwall connection, which is the reason why the total backfill force in Model-A is slightly higher than that in Model-C1 seen in Figure 3.42(b). Figure 3.42(d) highlights the difference in abutment-foundation response where Model-A, because of the backwall-fracture mechanism, protects the foundation and limits its deformation to roughly 0.8 inch. Further, the foundation response in Model-A is primarily within the elastic range and well below its ultimate capacity. In contrast, the other two models show that the foundations exceed peak-strength capacity and undergo substantial residual displacements. However, Figure 3.42(c) shows that Model-A places the highest demand on the bearings, which experience considerable displacement and failure as the bridge deck moves relative to the abutment stem wall. The combination of allowing backwall and bearing failure is consistent with modern design strategies focused on protecting expensive foundation elements in favor of replacing inexpensive and accessible backwall and bearings.

Pushover Analysis in Transverse Direction

In the transverse direction, shear keys can play a similar sacrificial role as the breakaway backwalls did in the longitudinal direction – shear keys are allowed to fracture to protect the abutment foundations. In order to illustrate this behavior, the Model-A bridge deck is uniformly pushed in the transverse direction. Responses for the conventional abutment models are identical since all use the same transverse spring-element configuration. Figure 3.42(e) highlights the main stages of overall bridge response associated with the isolated external shear key response shown in Figure 3.42(f). Point-1 corresponds to key-gap closure. Before that point, lateral resistance to deck movement arises only from the abutment bearings and bent columns, both responding elastically. The lateral response increases rapidly from Point-1, where the key and abutment foundation is engaged, are Point-2, where the key yields. The response from Point-2 to Point-5 corresponds with the ascending inelastic segment of the shear key response. The abutment foundation remains engaged but to a limited, softer degree. Point-3 corresponds to bearing yield along that portion of the response, and Point-4 corresponds to the initial yielding of the foundation. As the shear-key fails at Point-5, the abutment foundation reaction is released, and the deck is entirely supported by the bent columns and minimal abutment resistance transferred through the bearings to the abutment foundation.

3.5.2 Deck Models

Per Figure 3.1, two alternative strategies – spine and grillage – were considered for modeling the elastic deck component. Figure 3.43 illustrates differences arising from these alternatives. To illustrate the effects on the column behavior, the two-column bridge in Appendix A is modified to be a three-column bent bridge with each column section being 48 inches diameter having 24#11 longitudinal reinforcements. Upon application of axial loading (bridge self-weight), the column axial-load and transverse movements are recorded per Figure 3.43 where the ’analysis factor’ is the proportion of full gravity load.

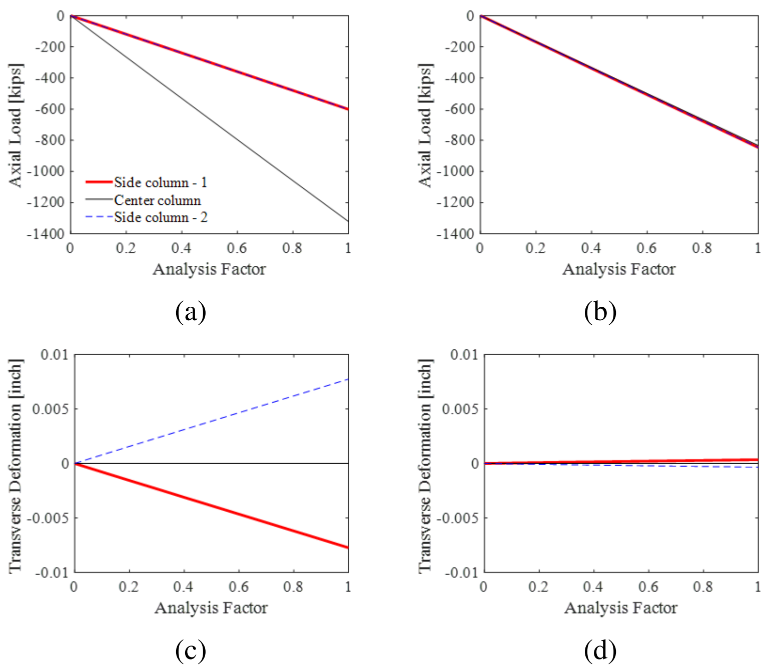

Figure 3.43: Comparison of axial load behavior of three-column bent for (a) spine model and (b) grillage model; and initial transverse deformation for (c) spine model and (d) grillage model.

Figure 3.43(a) shows that the use of the spine model causes a significant difference between the axial load of the center column (1300 kips) and side columns (600 kips). In contrast, the use of the grillage model results in a uniform 830 kips axial load across all three columns as shown in Figure 3.43(b). Figure 3.43(c) and (d) show a tenfold difference in the transverse deformation at the column base between the two models. The spline model generates an initial displacement of about 0.01 inches upon application of the axial loading protocol, while the grillage model shows negligible deformation. The phantom added deformations of using the spine model impact the PSDM in a low S_{a1} region, which in turn alters the trend of the regression models.

3.5.3 Column Failure Mode

This case study compares pushover performance of the ductile column design for the bridge in Appendix A with two pre-ductile designed (era-1) columns. The two era-1 columns have the same longitudinal reinforcement ratio but are modeled using a fixed base and #4@12" transverse reinforcements to facilitate the lap-splice and shear failures. The lap-splice case has a 2.0 feet lap length. Figure 3.44 presents monotonic pushover results for the three design cases. The response is expressed in terms of normalized shear force versus displacement ductility.

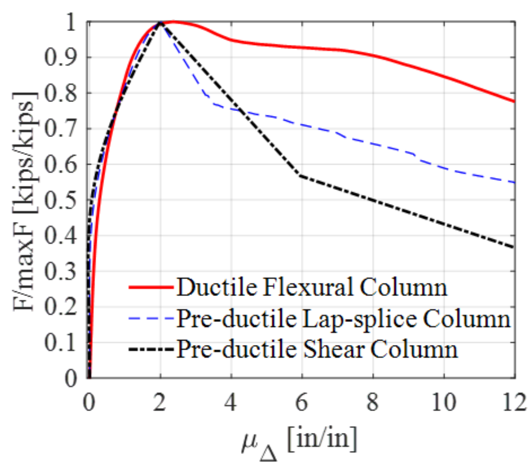

Figure 3.44: Comparison of column failure with pushover analysis

The ductile flexural column outperforms the two pre-ductile columns in terms of column ductility. Adopting a typical design definition for failure as 80% remaining force capacity, the flexural column reaches ductility of 11, while the other two quickly lose capacity after attaining the peak strength and reach the failure state at ductility of about 3.5. Comparing the two pre-ductile column designs, the lap-splice column shows relatively higher ductility than the shear column.

3.5.4 Transverse Constraints: Shear Keys and Rocker Bearings

Finally, a dynamic simulation is used in this section to illustrate the impact of alternative transverse constraints on bridge motion. The S07_R03 ground motion listed in Appendix B is used as the free-field input motion for this simulation.

Results comparing the two types of external keys are shown in Figure 3.45(a). For the modern ductile design era, non-isolated external shear keys are commonly used. The non-isolated shear key has a higher capacity, and while its response exceeds peak strength (Figure 3.45(b)), it does not entirely fail during this loading and thus limits deck-center displacements to approximately 7.0 inches. In contrast, the emerging isolated shear key (the per-plan design in Appendix A), has a lower capacity and releases completely, allowing deck-center displacement to reach approximately 17.0 inches. The higher non-isolated shear key capacity also produces larger abutment foundation loads (Figure 3.45(c)), but in this instance, the foundation remains in the elastic range.

Combining internal shear keys with external non-isolated shear keys is often used in early-ductile designed (era-2) bridges. Figure 3.3(d) to (f) compare the performance of this design to that discussed above using the external non-isolated key only. Here, the deck center displacement slightly decreases due to the additional internal shear key. The internal shear keys also share the resistance with the external shear keys and thus reduce deformation. The internal shear key hysteresis loop is illustrated in Figure 3.45(f) and shows the key to be near complete failure in one direction while the external key has remaining capacity.

Lastly, substantial shear keys are not found in pre-ductile designed (era-1) California bridges. Instead, the retainer brackets of the rocker bearings serve to provide a transverse constraint. However, as illustrated in Figure 3.45(g) to (h), the capacity of this bracket is typically lower than an external non-isolated shear key capacity; hence the deformation is more significant than the era-3 bridges. Bearing damage in Figure 3.45(h) shows that the elastomeric bearing in era-3 bridges remains in the elastic range, while the rocker bearing has failed and slides about 12 inches.

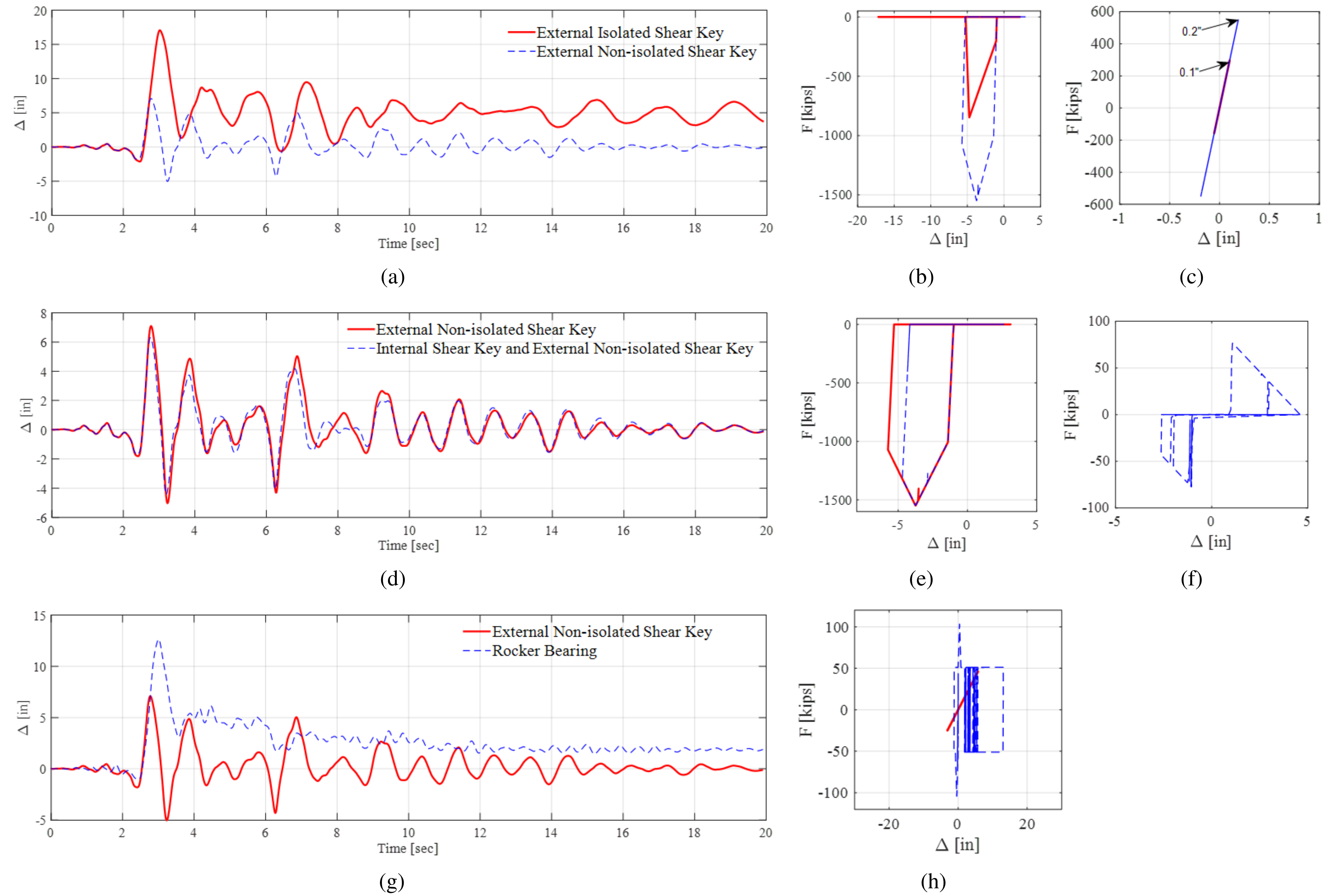

Figure 3.45: Comparison of transverse constraints. External isolated shear key v.s. non-isolated shear key: (a) deck center displacement time-history; (b) shear key hysteresis; and (c) abutment foundation deformation. External isolated shear key v.s. with internal shear key: (d) deck center displacement time-history; (e) shear key hysteresis; and (f) internal shear key hysteresis. External non-isolated shear key v.s. rocker bearings: (g) deck center displacement time-history; and (h) bearing hysteresis.

3.6 Closure

This chapter described the techniques used in this research for establishing three-dimensional nonlinear dynamic models for concrete box-girder bridges. Modeling strategies adopted for various bridge components are covered, including superstructure, columns, and abutment. A grillage model is adopted to simulate the superstructure. As for the column, modeling procedures for flexural, flexural-shear, shear, and lap-splice columns are discussed. Modeling of flexure critical column uses emerging concrete and steel models and considers strain-penetration effects, reduced sections, and approximately address the numerical localization issue. To model flexural-shear/shear critical columns, a new shear capacity is developed, and the shear spring is extended to the collapsed stage with a bilinear model. All column models are validated against an extensive set of experimental tests. The flexural column model is also used in dynamic analysis and found to compare favorably with experimental results.

Another innovative model is adopted herein to incorporate a backwall fracture mechanism in the abutment models. An advanced spring system was described, and the full backwall fracture model was developed for application within a probabilistic framework. Strategies for modeling techniques for other abutment components such as bearings, and shear keys, and soil responses were also presented. Specifically, the backfill-B model is optimized based on the framework of Xie et al. (2019).

This chapter concludes with case studies based on variations of the OSB1 bridge. First, the newly adopted abutment modeling scheme was compared with two conventional models and shown to provide more complete and realistic responses and component interactions. Pushover responses comparing column failure modes showed the ductile column to have higher ductility than the lap-splice or shear column. Finally, a comparison of transverse constraints showed that the isolated external shear key conveys smaller lateral forces to the abutment foundation than the non-isolated external shear key; the internal shear key combination has minimal impact on the overall bridge performance; and that rocker bearings have much lower strength than external shear keys and result in significantly larger deck displacement.

CHAPTER 4

EMERGING COMPONENT CAPACITY LIMIT STATE MODELS

A 'limit state model' establishes a direct relationship between a qualitative named condition, or 'state', and quantitative metrics expected to predict that state. Limit state models can be implemented at both the 'component level' and at higher 'subsystem' or 'system' levels.

At the component level, a state definition is expressed in terms of specific expected damage to a single component type, and this is coupled with a 'Component Capacity Limit State (CCLS) model', or the statistical distribution of a specific 'Engineering Demand Parameter (EDP)', which is expected to predict that state. In this research, all CCLS models are expressed as lognormal distributions having median and dispersion terms.

At the higher subsystem/system levels, the state definition is expressed in broader terms indicative of the more generalized performance of the combination of included components. These higher-level models must consider the CCLS models of each included component and 'roll up', or logically combine, the likelihood that the damage state of any single component corresponds with the generalized subsystem/system performance definition. This roll-up procedure requires an 'alignment' of the individual component damage states to have common performance implications that are described in the generalized subsystem/system state definition.

Whether deployed at the component or subsystem/system level, a complete set of limit state models typically considers multiple states which specify a progression of damage or performance from least to most impactful. The preponderance of existing fragility literature is organized around a framework of four damage states (plus a no-damage state). This corresponds with the widely adopted loss-estimation framework of HAZUS (FEMA, 2003) which defines a progression of generalized system-level damage states listed as none (ds1), slight/minor (ds2), moderate (ds3), extensive (ds4), and complete (ds5).

For the development of the ’2nd-Generation Fragility (g2F)’ models considered herein, Caltrans (Roblee, 2017*d*) outlined a refined limit-state framework consisting of seven damage states (plus a no-damage state) intended for consistent application from the component to the system levels. This 7-state framework was better aligned with Caltrans’ emerging probabilistic bridge-design methodologies (Saini and Saiidi, 2014; Bromenschenkle et al., 2015), and met recognized needs for added granularity at both ends of the damage spectrum to better define secondary-component damage at the low end and to better characterize operational implications of failure at the high end. Taken together, this enhanced limit state framework facilitates improved post-earthquake situational awareness and response operations, supports better damage and loss estimates, and provides planners and bridge designers with information needed to advance seismic mitigation and transportation-network reliability initiatives.

It is *critical* to note, as this dissertation is written, the g2F project is actively underway and important details of the CCLS models, and their alignment within the 7-state framework, have *not* been finalized nor vetted through Caltrans review processes. Nevertheless, this chapter presents several *emerging* CCLS models and alignments which represent current concepts. These, in turn, are used in the remaining chapters to illustrate the complete methodology for development of g2F fragility models at the component, subsystem and system levels. Although the CCLS models and fragility results presented herein cannot be viewed as final and authoritative, they are considered reasonably representative of general trends in expected seismic performance for the modern bridge classes considered. However, these results are subject to change as the details and alignment of the CCLS models are finalized. Caltrans serves as the sole source for final authoritative models and information regarding the g2F project.

The remainder of this chapter describes the emerging CCLS models used herein to compute fragility models in the remaining chapters. Discussion begins with an overview of the g2F state framework which aligns component damage CCLS models to whole-bridge system level states. Next is an extended overview of the research completed to define CCLS models for the most critical component in a bridge system - columns. This includes compilation of experimental column test data from the research literature into a data set called 'Resource Package 1 (RP1)' (Zheng et al., 2020) and supplemental analyses conducted to extend the experimentally-based models to higher states and for consideration of bent-frame or redundancy effects. Finally, this chapter covers the development of CCLS models for several other bridge components, including several expressed in terms of ranges of performance-backbone response.

4.1 g2F State Framework

The g2F project establishes an overarching framework for alignment of top-level 'Bridge System States (BSS)' through to underlying 'Component Damage States (CDS)' for multiple bridge components and their groupings. The BSS are expressed in terms of post-earthquake operational considerations including traffic state and potential emergency repairs per Table 4.1.

This framework is structured around seven aligned earthquake-impacted states, BSS_1 through BSS_7 at the system level, and CDT_1 through CDT_7 at the component level, plus an assessed no-observable damage state (BSS_0 and CDT_0). Table 4.1 also shows an approximate mapping of the g2F system-level states to those of HAZUS (FEMA, 2003) which attempts to balance differences in g2F-HAZUS state mapping relationships which vary by bridge component (Roblee, 2020*d*).

Comparison of the two state frameworks (i.e. g2F vs. HAZUS) in Table 4.1 reveals similar concepts expressed and grouped somewhat differently. The first two g2F states separate the 'slight/minor (ds2)' state of HAZUS into 'observable damage (BSS_1)' (such as observable concrete hairline cracking not likely to require emergency repair) and the lower portion of 'repairable minor damage (BSS_2)' (such as minor open cracking that can be simply repaired using epoxy injection). The exact positioning of the g2F separation relative to the HAZUS state varies by g2F component and is approximate. The 'moderate (ds3)' HAZUS state overlaps with all or portions of several g2F states (BSS_2 through BSS_4) which involve repairable damage having varied impact on bridge-system function, but where the bridge remains open to at least some level of traffic. The 'extensive (ds4)' HAZUS state overlaps with all or portions of the g2F states (BSS_4 through BSS_6) mainly associated with a severely damaged bridge likely to be closed to public traffic for an extended period. The g2F state BSS_5 is intended to encompass 'design failure' corresponding to the ultimate state in most design procedures where the bridge system has failed from a design point of view, but is considered stable with roughly 80% of ultimate lateral force capacity remaining. The 'complete (ds5)' state in the HAZUS model encompasses the remainder of the g2F states (BSS_6 and BSS_7). The g2F framework seeks to differentiate degrees of "failure" having different operational implications. While states BSS_5 through BSS_7 all denote failure and bridge closure of some kind, BSS_5 is considered stable requiring little immediate attention (beyond closure), while BSS_6 denotes an unstable bridge requiring site security and rapid demolition, and BSS_7 denotes bridge collapse which may involve search and recovery operations.

Table 4.2 extends the bridge-system state descriptions in Table 4.1 downward to lower-level groupings of components identified as primary and secondary components. Primary components are those components that have a significant impact on bridge stability and life safety. Among all components considered in this research, only the internal supports (i.e. column hinge and overturning damage and single-column-bent foundation-rotation damage) and deck unseating are considered primary components; and all other components (e.g. the abutment backwall and shear keys, abutment and bent foundations, joint components such as seals and bearings, etc.) are taken as secondary components as their failure will not cause bridge collapse. In the capacity model, primary components are defined through the final state (CDS_7), while CDS_5 is the highest defined state for secondary components. Note that secondary components are aligned to the g2F framework based on system-level operational consequences, so complete failure of any specific component may align with any one of multiple states (i.e. CDS_1 through CDS_5).

Table 4.1: g2F bridge-system level state definitions in terms of post-earthquake operational impacts (Roblee, 2021*c*) and approximate alignment with HAZUS bridge-system level damage states (Roblee, 2020*d*).

	BSS_0	T_01	BSS_1	T_12	BSS_2	T_23	BSS_3	T_34	BSS_4	T_45	BSS_5	T_56	BSS_6	T_67	BSS_7
Proposed Bridge-System State:	Assessed- No Damage		Observable Damage Intact System Function		Repairable Minor Damage To System Function		Repairable Moderate Damage To System Function		Repairable Major Damage To System Function		Failed, But Stable System "Design Failure" (~80% RemCap)		Unstable System (~50% RemCap)		Collapsed System (~20% RemCap)
Impact Level:	None		Very Low Potential Impact		Low Potential Impact		Low-Medium Potential Impact		Medium Potential Impact		Medium-High Potential Impact		High Potential Impact		Extreme Potential Impact
Likely Traffic State:	Public w/ Near- Normal Ride Quality		Public w/ Reduced Ride Quality		Public w/ Speed Restrictions		Public w/ Lane or Weight Restrictions		Emergency Vehicles Only w/ Restrictions		Closed (At Least) Temporarily		Closed Long-Term (Demo Equip Access)		Closed Long-Term Emergency Response
Potential Emergency Repair:	None		Inspection & Debris Clean-Up		Traffic Controls, Minor Grade Leveling		Major Grade Leveling, Lane Barriers		Precautionary Shoring/Bracing		Shoring/Bracing Required to Re-Open		Secure Site for Demolition/Safety		Controls/Services for Search/Recovery/Safety

	ds1 (None)		ds2 (Slight/Minor)		ds3 (Moderate)		ds4 (Extensive)		ds5 (Complete)
HAZUS state									

Table 4.2: g2F generic damage state definitions in terms of primary and secondary component functionality (Roblee, 2021*c*)

	CDS_0		**CDS_1**		**CDS_2**		**CDS_3**		**CDS_4**		**CDS_5**		**CDS_6**		**CDS_7**
		T_01		**T_12**		**T_23**		**T_34**		**T_45**		**T_56**		**T_67**	
Primary Component Damage:	Undamaged		Incidental Component Damage Full Function Intact		Minor Component Damage Core Function Intact		Moderate Component Damage Core Function Intact		Major Component Damage Restorable Function		Irreparable Component Damage (But System Stable)		Irreparable Component Damage (w System Instability)		Catastrophic Component Damage
Primary Component Repairs:	na		Routine Maintenance		Minor Repairs of Existing Component		Substantial Repairs of Existing Component		Enhancements of Existing Component		Replacement of Components		Replacement of Bridge		Replacement of Bridge
Secondary Component Damage:	Undamaged		Minor Component Damage Core Function OK		Substantial Component Damage Diminished Function		Component Failure Low System Impacts		Component Failure Medium System Impacts		Component Failure High System Impacts				
Secondary Component Repairs:	na		Minor Comp. Repair, Largely Aesthetic		Major Comp. Repair To Restore Function		Replace Component To Restore Function		Replace Component and Minor System Repairs		Replace Comp. & Major System Repairs				

4.2 Column Capacity Limit States

Columns are one of the primary components and have a significant, and often governing impact on the seismic reliability of a bridge system. Therefore, carefully defined column capacity limit states are essential for developing an accurate fragility model. This section reviews the development of a seven-damage-state column capacity model. An extensive experimental column data set is first compiled and analyzed to establish an initial CCLS framework based on physical tests. However, very few of these experimental tests were carried to the unstable and collapse states due to laboratory limitations and safety protocols. To supplement the limited experimental information, a series of finite element analyses were conducted to consider both high-state column damage and load-path redundancy effects of multi-column bents.

4.2.1 Column Types in California Bridges

Researchers have shown that the seismic detailing of bridges in California significantly changed in different periods, and therefore, the responses of different components varied (Ramanathan, 2012). Sensitivity analysis also showed that the design era is a key variable in bridge fragility analysis (Mangalathu, 2017).

Identification of systematic differences in column detailing between design eras was the first step in developing a rational framework for both grouping experimental tests and identification of response trends. Toward that end, Roblee (2017*e*) compiled typical column-design details for three eras of California bridges having both regular and wide sections and having both fixed-base and pinned-base connections to the foundation. Figure 4.1 provides compares typical detailing for three eras of fixed-base regular-section single-column bents.

Era-1 is considered the pre-ductile era of California bridge design before practices incorporated the lessons of the 1971 San Fernando earthquake. Lap spliced longitudinal

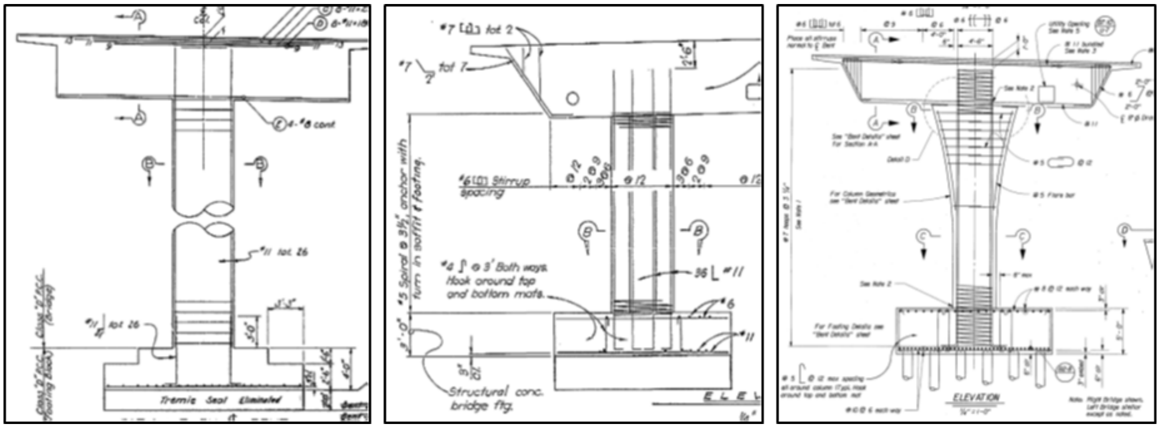

Figure 4.1: Illustration of detailing differences for typical California single-column-bent bridges from design era-1 to era-3 (from left to right) (Roblee, 2017*e*).

reinforcement is typical at the base of columns. The typical transverse reinforcement configuration is $\#4@12''$ hoops with cross-ties for wide sections, and the transverse reinforcement ratio ranged from roughly 0.1% to 0.25%. Rectangular wide sections were frequently employed, often having aspect ratios exceeding 2.0. Transverse reinforcement was typically terminated with 18-inch lap splices or 90-degree hooks.

Era-2 is considered the early-ductile era of California bridge design existing between roughly the 1971 San Fernando and the 1989 Loma Prieta and 1994 Northridge events. This design era saw removal of longitudinal lap-splice connections from the plastic hinges regions and ductile detailing of most columns and some foundation connections. Continuous spiral reinforcement around circular cores became common, and volumetric reinforcement ratio ranged from about 0.3% to 1.0% with spacing from about 3 to 6 inches. Wide sections transitioned from rectangular to oblong sections, typically having an aspect ratio of 1.5 to 2.0. Flared columns were common, but flare detailing is now recognized as poor as it could reduce effective shear-span ratio and lead to mixed flexure-shear failure.

Era-3 is considered the modern ductile era of California bridge design existing since incorporation of lessons from the 1994 Northridge event. Specifications now limit transverse spacing to be less than 6 times the diameter of longitudinal reinforcement and volumetric reinforcement ratio ranges from about 0.55% to 1.35%. Foundation connection details were significantly enhanced with the addition of top mats and by extending column confinement fully into thicker footings/caps. The use of architectural flares diminished, and those that exist typically adopt a flare-isolation detail having a 2 to 4 inches gap between the flared top and the superstructure.

Although columns within a specific design era have similar design details, their responses may differ substantially due to distinctive failure modes arising from different column geometries, fixity conditions, axial loads, and reinforcement detailing. Nearly all era-3 and most era-2 designs fail in flexure mode, with some predicted to fail in mixed shear-flexure mode. In era-1, all column failure modes (flexure, mixed flexure-shear, and brittle shear) can occur. Additionally, the longitudinal lap splice (starter bar) detail can induce a relatively brittle lap-splice failure mode. Also, the existence of lapped-hoop details introduces significant uncertainty into the integrity of lateral confinement.

4.2.2 Column Experiment-Based Performance Dataset, RP1

In an effort to establish a firm physical basis for column CCLS models, experimental results from 198 test specimens were compiled from the research literature and summarized in a column-performance dataset called 'Resource Packet 1 (RP1)' (Zheng et al., 2020).

The dataset adopts column displacement ductility as the recorded engineering demand parameter EDP. Previous methodologies of developing column damage states used curvature ductility as the EDP . However, most experimental tests did not include curvature ductility values in the experimental reports. Some previous researchers converted displacement ductility into curvature ductility using an estimated plastic hinge length. This processing procedure caused an objective bias in the curvature ductility values. Furthermore, in numerical modeling, curvature estimation may not be accurate enough when there is a localization issue, as mentioned in Chapter 3. Moreover, curvature ductility only reflects a column's local flexural damage, compared to displacement ductility that represents the overall global column damage including shear mechanisms. For some tall slender columns, local damage cannot account for overturning hazard due to the P-Δ effect, while this hazard can be expressed in terms of metrics related to displacement ductility. Consequently, in this research, the displacement ductility is used as the primary metric for column damage.

The RP1 column-performance dataset is based on a collection of column tests from the United States and New Zealand which includes column dimensions, materials strength, design codes, reinforcement details, experimental column boundary conditions, experimental lateral strengths, computed shear capacities, damage descriptions, and limit state values in terms of displacement ductility. In addition, the transverse reinforcement spacings are categorized for inside and outside plastic hinge regions, respectively. The spacing inside the plastic hinge regions, and other parameters such as transverse reinforcement ratio, are used to distinguish column design eras.

Classification of column failure modes is based on a combination of the calculated shear capacity, recorded descriptions, and reported specimen damage. Ultimately, the 198 columns are classified into “Era-3 Flexural Columns” (58 columns), “Era-2 Flexural Columns” (48 columns), “Era-1 Flexural Columns” (15 columns), “Era-3 and Era-2 Flexural-Shear Columns” (32 columns), ”Era-1 Flexural-Shear Columns” (18 columns), “Shear Columns” (14 columns), and “Era-1 Lap Spliced Columns” (13 columns).

Adoption of displacement ductility as the primary metric for column CCLS models required identification of a reference displacement for normalization of the test data. Generally, the yield displacement of the column is used as the reference displacement. However, the actual yield point corresponding to the first reinforcement yielding is not always accessible. In order to apply the same rule for all the selected experimental test columns, the idealized yield displacement as defined by Park (1989) was selected for this project. The idealized yield displacement is determined by first identifying the maximum lateral strength Vmax as the envelope of the lateral strength versus displacement response, as demonstrated by the upper horizontal dashed line in Figure 4.2. Then, the elastic linear stiffness branch is defined by passing through the point of 75% Vmax on the column response and extending to the Vmax level on the envelop. The idealized yield displacement is determined as the displacement corresponding to the intersection between the Vmax level and the elastic linear branch.

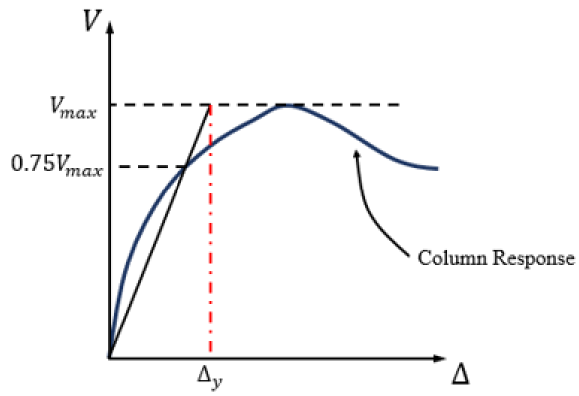

Figure 4.2: Definition of idealized yield displacement (Park, 1989)

4.2.3 High State and Redundancy (HS-R) Study

Although the RP1 dataset established a firm physical basis for the column limit state system, 75% and 95% of these experiments did not extend testing into the last two limit states desired for the g2F project. In order to supplement the experimental dataset, a complementary program of column analyses, herein called 'High State and Redundancy (High State - Redundancy (HS-R))' studies were conducted to analytically extend understanding of column performance through the last three (failure) states and to investigate other effects of both column fixity and bent-frame effects (load-path redundancy). Note that bent-frame effects were only considered for transverse loading of multi-column bents, but both 2-column and 3-column bents were investigated. For single-column bents, the effects of column-top fixity (free or fixed) was investigated. All HS-R analyses were conducted on column designs representative of California bridge columns.

The first step of the HS-R studies was sampling of bridge column designs for each failure type. The sampling procedure and considered uncertainties will be covered in Chapter 5. Next, using the procedure introduced in Chapter 3, finite element models of column bents are constructed in OpenSees. Cyclic pushover analyses were carried out until the column reached 20% remaining lateral force capacity (i.e., 80% degradation of the capacity). Displacement ductilities corresponding to different specified levels of capacity remaining (80%, 50%, and 20%) were then identified from the recorded Δ-F hysteretic curves. These three remaining capacity values (80%, 50%, and 20%) were selected as performance-based states and later merged with the laboratory data for the last three experimentally-observed damage states, respectively, in the capacity model.

The HS-R analyses showed some added displacement-ductility capacity of multi-column bents loaded in the transverse direction relative to single-column bents. This effect is called the 'redundancy effect' herein. Figure 4.3 illustrates the physical basis for the redundancy effect using the example case of era-3 flexural columns subjected to monotonic pushover. The three models represent a single-column, two-column, and three column bent. All columns are 20 feet tall with 2% longitudinal reinforcement ratio, 0.8% transverse reinforcement ratio, and 10% axial load ratio. Due to different column numbers, the regular designed section sizes are different in these three models. The three models have 84, 60, and 48 inches diameter circular sections for the single-column, two-column, and three-column bent, respectively. The results in Figure 4.3 demonstrate that individual column responses are affected by the changes in axial load caused by bent-frame effects, and these varied responses impact the shape of the bent-total response. The total-response displacement ductility values corresponding to the three high states defined in this section show that displacement ductility increases modestly ($\sim$15%) at extreme demand for multi-column versus single-column bents.

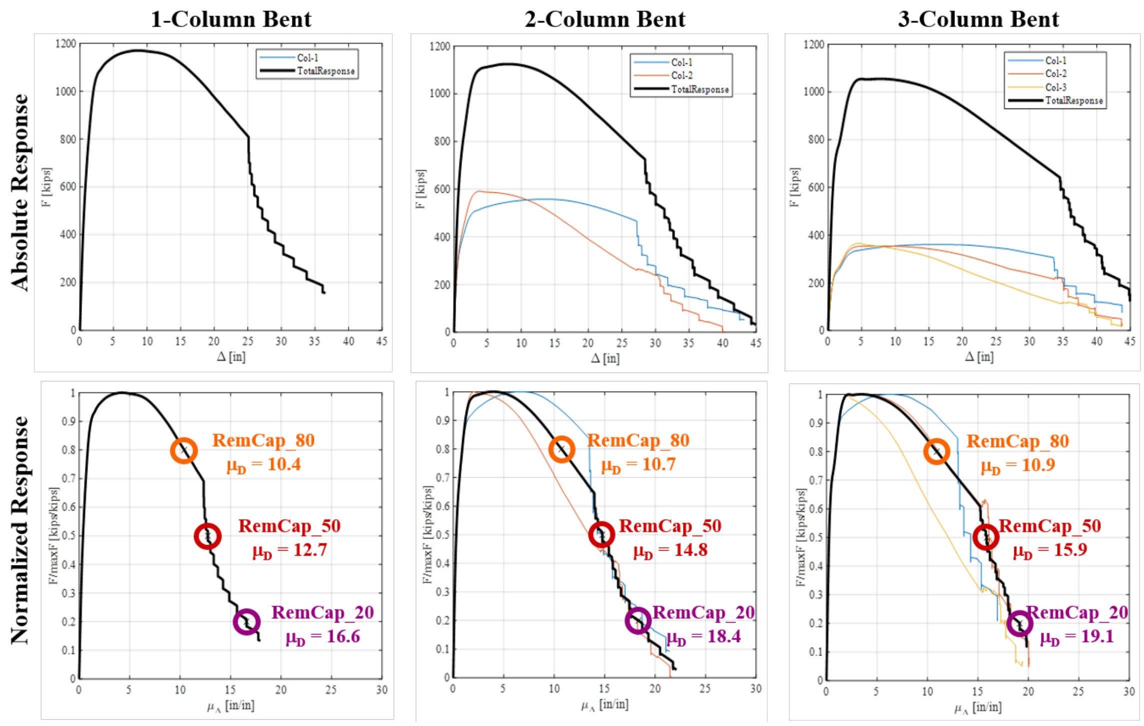

Figure 4.3: Illustration of redundancy effects (Zheng and Roblee, 2021)

4.2.4 Column Capacity Limit State Models

This section outlines emerging column damage state definitions and CCLS model values primarily for the modern (era-3) flexural-mode columns used in the fragility models presented in the remainder of this dissertation. These capacity models are expressed in terms of displacement ductility and the damage described by the state may be observed at various locations in the whole column. Later, localized column-hinge damage models will also be presented.

Table 4.3 provides observation-based damage state definitions used for analysis of RP1 experimental data for the three primary column failure modes, flexure, mixed flexure-shear, and brittle shear. The CDS_1 state for all three failure modes start with an earthquake-related tight cracking of concrete cover. At this level, the typical repair procedure would be to seal or paint the column, perhaps as part of a routine maintenance schedule. The following two states (CDS_2 and CDS_3) are the same for flexural and flexural-shear columns as both column types will develop the full flexural strength during the initial stage. Shear columns behave differently, starting from developing diagonal cracks, then transferring to the formation of a shear plane. The following CDS_4 state defines exposure of core concrete for all of the failure modes. However, this exposure may involve either of two different mechanisms. For both flexural and mixed flexural-shear columns which haven't triggered shear response, core exposure is primarily due to spalling of the cover concrete, which is a type of flexural damage. For shear columns or mixed flexural-shear columns which have triggered shear response, core exposure is associated with widening of diagonal shear cracks. The final three states (CDS_5 to CDS_7) are the same for the flexural-shear and shear failure modes following the intensity of permanent offset, from minor offset to major offset, and ultimately collapse with loss of axial capacity. Flexural column failure is more related to reinforcement performance. In CDS_5, longitudinal reinforcement buckling develops to a visible level, which is a sign of imminent buckling or rupture of multiple reinforcements and is thus taken as an approximation of design failure. If multiple longitudinal bars visibly buckle or rupture, or the core concrete begins to crush, the column is considered to be at the unstable state (CDS_6). The final collapse state (CDS_7) is assigned to cases where axial column capacity, provided by either or both of the core concrete and longitudinal reinforcement, is effectively lost due to either flexural or shear mechanisms.

Table 4.4 and Table 4.5 present the emerging g2F CCLS models for modern (era-3) flexural columns that are used in the remainder of this dissertation. These models are based on a combination of experimental observations at low states from the RP1 data set, and analytical findings for high states from the HS-R studies as described by Roblee (2021*d*). This scheme replaces the RP1 experimentally observed damage states for CDS_5 through CDS_7 appearing in Table 4.3 with the HS-R analytically-based performance definitions, 80%, 50%, 20% remaining lateral force capacity, respectively. This combined experimental-analytical strategy has several benefits including: 1) less reliance on small

Table 4.3: Experimentally observed damage state definitions for columns with different failure modes

CDS_1	Earthquake-related tight cracking of cover
CDS_2	Moderate cracking & minor spalling/flaking
CDS_3	Open cracking or major spalling which reveal the confinement
CDS_4	Exposed core (reveal the longitudinal reinforcement)
CDS_5	Visible bar buckling; confinement loss or core shedding
CDS_6	Multi-bar buckling/rupture; large drift; or core crushing
CDS_7	Column collapse (near-total loss of axial capacity)

a) Flexural Columns

CDS_1	Earthquake-related tight cracking of cover
CDS_2	Moderate cracking & minor spalling/flaking
CDS_3	Open cracking or major spalling which reveal the confinement
CDS_4	Exposed core or initial formation of diagonal shear zones, but no permanent offset
CDS_5	Diagonal shear zone penetrating core with minor offsets and intact confinement
CDS_6	Offset shear plane with core crushing, confinement loss or long-bar buckling
CDS_7	Column collapse (near-total loss of axial capacity)

b) Mixed Flexural-Shear Columns

CDS_1	Earthquake-related tight cracking of cover
CDS_2	Discontinuous web of short diagonal cracks, mostly in cover
CDS_3	Pronounced diagonal cracks forming, partial shear plane with no core offset
CDS_4	Continuous diagonal shear zone with core exposure, but no permanent offset
CDS_5	Diagonal shear plane penetrating core with minor offsets and intact confinement
CDS_6	Offset shear plane with core crushing, confinement loss or long-bar buckling
CDS_7	Column collapse (near-total loss of axial capacity)

c) Shear Columns

RP1 data sets at high states, 2) less ambiguous definitions for high-state column performance, 3) the analytical HS-R studies are based completely on modeling of California bridge columns rather than the assortment of bridge and building columns compiled in RP1, and 4) the analytical HS-R studies could isolate impacts of boundary fixity and bent redundancy that are cannot be considered in the RP1 experimental data set.

Table 4.4 presents a summary of the combined experimental-analytical state definitions for era-3 flexural columns including typical column repair strategies expected for each state. Column retrofit with steel casings is likely for columns in the CDS_4 state, column replacement in the CDS_5 state, and bridge replacement is likely for the CDS_6 and CDS_7 states.

Table 4.4: Emerging g2F CCLS state definitions for era-3 flexural columns (Roblee, 2021*d*).

		CDS_0	T_01	CDS_1	T_12	CDS_2	T_23	CDS_3	T_34	CDS_4	T_45	CDS_5	T_56	CDS_6	T_67	CDS_7
Visible Damage:	Not Assessed	No Visible EQ-Related Damage		EQ-Related Tight Cracking of Cover		Moderate Cracking & Minor Spalling or Flaking		Open Cracking or Major Spalling (Exterior to Confinement)		Exposed Core (Interior of Confinement) But No Visible Bar Buckling		Visible Bar Buckling; Confinement Loss or Core Shedding		Multi-Bar Rupture or Buckling; Large Drift; or Core Crushing		Bent Collapse (Near-Total Loss of Axial Capacity)
Illustrative Damage:	na			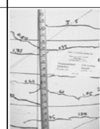				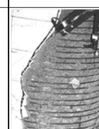				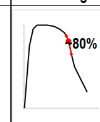		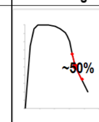		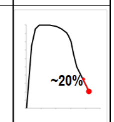
Typical Repair:	na	None		Seal & Paint		Minor Epoxy Inject & Concrete Removal/Patch		Major Epoxy Inject & Concrete Removal/Patch		Steel Column Casing		Column Replacement		Unstable Bridge Replacement		Collapsed Bridge Replacement

Table 4.5 provides CCLS model distribution values for single-column and multi-column bents loaded in the longitudinal and transverse directions. In the transverse direction, single-column bents behave differently in different bridge zones where a bridge zone is defined in terms of a bents proximity to the abutment which provides torsional support to the deck. Zone-1 bents, or those bents adjacent to abutments, have strong constraints that prevent deck rotation in the translational direction, thus resulting in a fixed-top column boundary condition. The other zones are closer to the deck center and less affected by abutment torsional constraints. For example, in a four-span bridge with three internal support bents, the first and third bents next to the abutment are called zone-1 bents in this research and hence use the double-curvature (i.e. fixed top) model in Table 4.5(a). The center bent is called a zone-2 bent which is assigned the single-curvature (i.e. free-top) model. Note, although not considered herein, zone-3 represents bent locations within an isolated frame of a multi-frame bridge having no adjacent abutment.

Multi-column bents in era-3 nearly all have a pinned-base detail, and therefore, only a single-curvature model is needed for multi-column bents loaded in both transverse and longitudinal directions. However, the model for longitudinal direction (Table 4.5(c)) is smaller than that for transverse direction (Table 4.5(a)) due to bent redundancy effects.

Table 4.5: Emerging g2F CCLS lognormal distribution parameters for era-3 flexural column bents in terms of displacement ductility (μ_Δ) (Roblee, 2021*d*): median (σ) and dispersion (β)

Model Matric	**CDS_1**	**CDS_2**	**CDS_3**	**CDS_4**	**CDS_5**	**CDS_6**	**CDS_7**
Single-Curvature (zones 2&3)							
Median (σ)	1.25	2.43	4.05	5.4	6.0	6.8	8.5
LN Dispersion (β)	0.35	0.32	0.26	0.22	0.20	0.20	0.20
Double-Curvature (zone 1)							
Median (σ)	1.25	2.43	4.05	5.5	6.2	7.5	11.0
LN Dispersion (β)	0.35	0.32	0.26	0.22	0.20	0.20	0.22

a) Single-Column Bents Loaded in the Transverse Direction

Model Matric	**CDS_1**	**CDS_2**	**CDS_3**	**CDS_4**	**CDS_5**	**CDS_6**	**CDS_7**
Single-Curvature							
Median (σ)	1.25	2.43	4.05	6.0	7.5	9.2	13.5
LN Dispersion (β)	0.35	0.32	0.26	0.21	0.18	0.18	0.25
Double-Curvature							
Median (σ)	NA	NA	NA	NA	NA	NA	NA
LN Dispersion (β)	NA	NA	NA	NA	NA	NA	NA

b) Multi-Column Bents Loaded in the Transverse Direction

Model Matric	**CDS_1**	**CDS_2**	**CDS_3**	**CDS_4**	**CDS_5**	**CDS_6**	**CDS_7**
Single-Curvature (Multi-Column Bents)							
Median (σ)	1.25	2.43	4.05	5.4	6.0	6.8	8.5
LN Dispersion (β)	0.35	0.32	0.26	0.22	0.20	0.20	0.20
Double-Curvature (Single-Column Bents)							
Median (σ)	1.25	2.43	4.05	5.5	6.2	7.5	11.0
LN Dispersion (β)	0.35	0.32	0.26	0.22	0.20	0.20	0.22

c) Single/Multi-Column Bents Loaded in the Longitudinal Direction

There is no redundancy effect for loading of multi-column bents in the longitudinal direction. Nevertheless, higher capacities are assigned to single-column bents than multi-column bents due to boundary fixity considerations. Deck stiffness functionally fixes column-tops in the longitudinal direction. Single-column bents also have a fixed base which results in a double-curvature condition which simulation results have shown to have higher capacity. Multi-column bents, with a pinned base, have a single-curvature shape associated with somewhat lower capacity at high states. The higher double-curvature capacity may be related to engagement of two hinges to sustain possible damage versus the single hinge engaged in the single-curvature.

4.2.5 Local Column Damage - Fixed Hinge

The models described above define displacement-ductility ranges over which damage is predicted to occur anywhere (globally) within a column bent. There are benefits to also separately characterize damage occurring locally in both fixed and pinned hinge regions of a column. While the global metric for a multi-column bent includes the redundancy (bent framing) effect, a local metric can better capture damage to each individual column. Further, the global metric provides no means to capture hidden damage which occurs in pinned (i.e. reduced section) hinges or from separate mechanisms such as slippage of lapped-splice connections. Therefore, the g2F project has adopted a multiple-complementary-metrics approach to the characterization of bridge columns which, together, capture different damage mechanisms which may occur at various locations on the column, and express these within a common performance framework. This strategy provides additional insight into column and bridge-system behavior, and the additional information regarding damage mechanism and location is beneficial to g2F end-users interested in field-inspection efficiency, repair-strategy selection, and cost/impact estimation.

This section outlines methods developed to characterize localized flexural damage to fixed column hinges. The most applicable EDP for this type of localized damage is curvature ductility. Despite the limitations noted in subsection 4.2.2 for RP1 experimental data-analysis applications, the conceptual advantages of using curvature ductility in analytical studies are fully recognized, and models developed herein serve as a convenient basis for comparison with extensive prior research expressed in these terms.

Here, as a means to maintain full compatibility with the global column-bent capacity models described above, a conversion equation between curvature-ductility (μ_ϕ), and displacement-ductility (μ_Δ) is developed and then applied to the applicable global column capacity model. The single-column bent, single-curvature, global model was selected as most applicable as it directly represents a cantilever beam where performance is primarily controlled by local section damage.

The conversion equation used herein is derived from the following relationship provided by FHWA (Buckle and Friedland, 1995), where l and l_p denotes for the height and plastic hinge length of the column respectively.

$$\mu_\phi = 1 + \frac{\mu_\Delta - 1}{3\frac{l}{l_p}\left(1 - 0.5\frac{l}{l_p}\right)} \tag{4.1}$$

For application to the displacement ductility capacity model, l and l_p are unknown. To approximate these values, three column models were simulated in OpenSees. These models correspond to era-1 through era-3 designs having median height and reinforcement ratios. Cyclic pushover loading to median global-model displacement-ductility values for each era produced the data point pairs in terms of (μ_Δ, μ_ϕ) shown in Figure 4.4, which were then used to regress the conversion model in Equation 4.2. These results estimate the plastic hinge length as approximately 0.1 times of the column height.

$$\mu_\phi = 1 + 3.35(\mu_\Delta - 1) \tag{4.2}$$

The top set of curvature ductility (μ_ϕ) values shown in Table 4.6 are from direct application of the conversion in Equation 4.2 to the single-curvature models in Table 4.5(c)). These models are applicable to prediction of localized damage at fixed hinges of single-column bents and for (simultaneous) bent-average response of multi-column bents. However, additional considerations apply to the case of individual columns within a multi-column bent loaded transversely. Here, the global models (see Table 4.5(b)) account for bent redundancy effects at high (failure) states and allow any

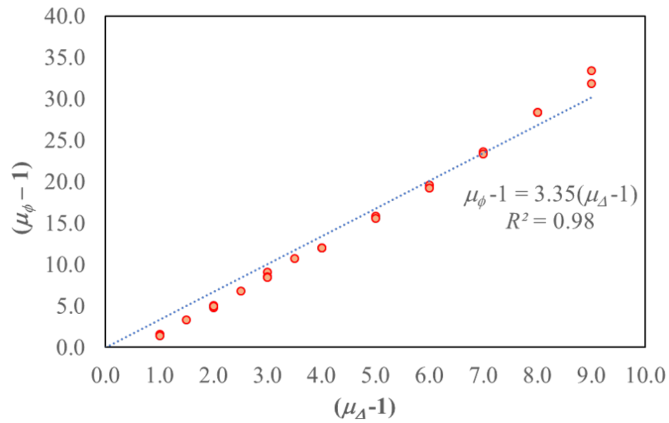

Figure 4.4: Conversion relationship between μ_Δ and μ_ϕ

individual column in the bent to experience higher damage levels than the bent as a whole. To maintain compatibility of the local and global models for this case, a revised state – CCLS model proposed by Roblee (2021*e*) was adopted which shifts the highest possible state for local hinge damage to an individual column to be CDS_6, or that associated with bridge instability. Bridge collapse risk (CDS_7) is only assessed using bent-average metrics for either the global or local criteria. The bottom set of capacity model values in Table 4.6 are applicable to the localized fixed-hinge damage state of individual columns in a multi-column bent loaded transversely.

Table 4.6: Emerging curvature ductility lognormal distribution parameters for fixed-hinge damage in era-3 flexural columns in terms of curvature ductility (μ_ϕ): median (σ) and dispersion (β)

Model Matric	**CDS_1**	**CDS_2**	**CDS_3**	**CDS_4**	**CDS_5**	**CDS_6**	**CDS_7**
Bent-Average							
Median (σ)	1.85	5.8	11.2	15.8	17.8	20.4	26.1
LN Dispersion (β)	0.35	0.32	0.26	0.22	0.20	0.20	0.20
Bent-Maximum¶							
Median (σ)	1.85	5.8	11.2	15.8	20.8	24.8	
LN Dispersion (β)	0.35	0.32	0.26	0.22	0.20	0.20	

¶ Only used for multi-column bents loaded in the transverse direction.

4.2.6 Local Column Damage – Pinned Hinge (Reduced Section)

Unlike the case of fixed hinge damage, no displacement capacity model can be directly adopted to depict localized damage to reduced sections used in pinned column hinges. Therefore, the development of the state - CCLS capacity model for pinned hinges is based on fiber-mechanical responses for the reduced section. Specifically, Table 4.7 summarizes four damage states along with fiber-mechanical criteria used to define those states. For example, the first damage state, CDS_1, is identified as "crushing of cover concrete (outside of confinement) with no/minor reinforcement yield. The threshold for entering that state, CDST_01, is the reduced-section curvature induces compressive strain in the inner-cover concrete of the reduced section that exceeds that corresponding to the compressive strength for cover concrete. Using these thresholds, cyclic pushover analyses were conducted on 50 column realizations and sampled to acquire the curvature-ductility distributions for each threshold. The center-state curvature ductility values were defined as the geometric mean of those for the two adjacent thresholds. Figure 4.5 illustrates a single simulation case, and the state values are denoted with circles. Table 4.8 provides the curvature-ductility models developed from all 50 cases.

Table 4.7: Definition of damage states and associated reduced-section fiber-mechanical thresholds used for pinned-hinge local-damage capacity model.

Damage State	**State Damage and Threshold Condition Description**
CDS_0	**None**
CDST_01	First fiber of inner-cover concrete: compression demand exceeds compressive strength.
CDS_1	**Crushing of Cover Concrete (Outside Confinement) with No/Minor Rebar Yield**
CDST_12	1st fiber of inner-cover concrete: compression demand exceeds spalling strain; and 1st fiber of outer-core concrete: compression demand exceeds compressive strain.
CDS_2	**Initial Core-Concrete Crushing (Inside Confinement) with Moderate Rebar Yield**
CDST_23	1st fiber of inner-core concrete: compression demand exceeds mean of compressive strain and crushing strain; or 1st rebar: tension demand exceeds the end of yield plateau; or 1st rebar: compression demand exceeds visible bar buckling strain ε_b.
CDS_3	**Major Core-Concrete Crushing (Inside Confinement) with Major Rebar Yield or Buckling**
CDST_34	1st fiber of inner-core concrete: compression demand exceeds core-crushing strain; or 1st rebar: tension demand exceeds the mean of peak strength and fracture; or 1st rebar: compression demand exceeds bar buckling strain ε_r.
CDS_4	**Complete Core Crushing and/or Multi-Bar Rupture or Severed Pin Connection**
CDST_45	50% fibers of inner-core concrete: compression demand exceeds crushing strain; or 50% Rebars: tension demand exceeds fracture strain; or 50% Rebars: compression demand exceeds bar buckling strain ε_r

For example, the threshold to define a CDS_1, named CDST_01, is the curvature that the inner cover concrete has compressive strain exceeding the strain corresponding to compressive strength. After carefully defining the thresholds, 50 column realizations are sampled and analyzed to acquire the curvatures for each threshold. The state values are defined by the geometry mean of two adjacent thresholds. Ultimately, the resulting curvature values are converted to curvature ductilities. Figure 4.5 illustrates a single simulation case, and the state values are labeled with circles. Summarizing all 50 simulated cases produces a capacity model in Table 4.8 in terms of curvature ductility.

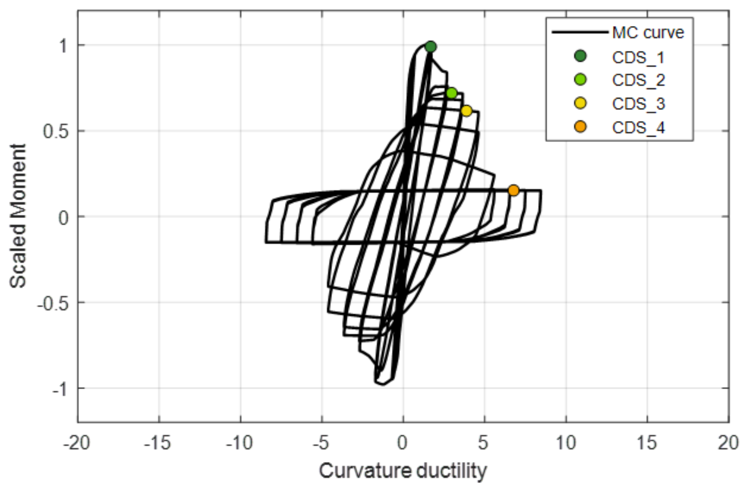

Figure 4.5: Illustration of pin section performance with limit states.

Table 4.8: Emerging curvature ductility lognormal distribution parameters for pinned-hinge (reduced section) damage in era-3 flexural columns in terms of curvature ductility (μ_ϕ): median (σ) and dispersion (β)

<u>**Model Matric**</u>	**CDS_1**	**CDS_2**	**CDS_3**	**CDS_4**	**CDS_5**	**CDS_6**	**CDS_7**
Median (σ)	3.6	7.0	12.0	20.0			
LN Dispersion (β)	0.60	0.40	0.25	0.25			

4.3 Other Components — Simple CCLS

The fragility models developed in this research consider several California era-3 bridge components other than bent columns. This section describes emerging capacity models that are based on simple CCLS models expressed in terms of direct linear relationships to deck displacement at the abutment joint. These include the mechanism of deck unseating and both the bearing and joint seal components. Section 4.4 will consider additional abutment-joint components where the CCLS models are based on response backbones.

4.3.1 Deck Unseating

Besides column failure, deck unseating is the other primary mechanism which can result in bridge collapse. Here, the mechanism of deck unseating is treated as a 'component' where capacity is defined in terms of net seat width, and demand expressed in terms of deck displacement relative to the abutment seat node in the active direction. Net seat width is defined as the nominal total seat with minus the width of the joint gap. California bridge designs employ a range of seat widths depending on the length, height, and skew of the bridge. Roblee (2021*a*) compiled a sample of abutment seat widths for California era-3 box-girder bridge designs and proposed a capacity model in terms of four standard widths: 30-inch, 36-inch, 48-inch, and 60-inch representing 50%, 20%, 25%, and 5% of the era-3 inventory, respectively, as shown in Figure 4.6.

Table 4.9 summarizes emerging g2F capacity models for deck unseating in terms of two complementary metrics which account for different deck responses having comparable bridge-system operational consequences (Roblee, 2021*e*). The '2-corner average displacement' model assigns capacity in terms of standard values for remaining average seat width. The 'peak-1-corner displacement' model provides a complementary check on deck-corner remaining seat width for cases where deck rotation occurs. Differences between these models become more pronounced at lower states where

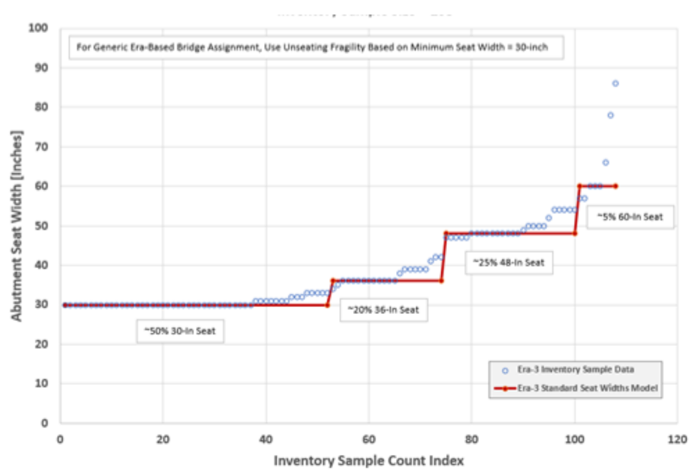

Figure 4.6: Era-3 bridge seat width proportion model (Roblee, 2021*a*)

additional latitude is allowed for deck rotations provided the average displacement remains within the state range. Figure 4.7 is useful for visualizing the concept behind the two metrics. For the scenario presented in Figure 4.7(a), the deck might be considered marginally stable, while the scenario in Figure 4.7(b) is treated as clearly unseated. However, note that the models presented in Table 4.9 limit even peak-corner net remaining seat width to 0-inch at the CDST_67 boundary to account for the limited bearing capacity of cover concrete at abutment lip; thus, even the scenario presented of Figure 4.7(a) would be assigned to CDS_7 using those models.

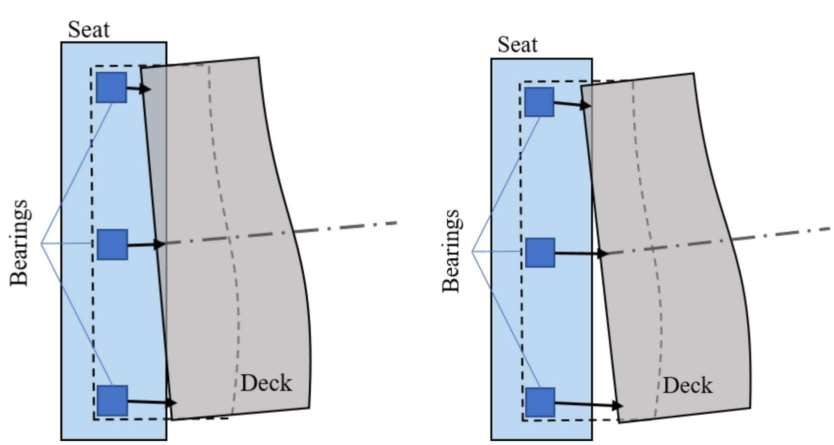

(a) (b)

Figure 4.7: Illustration of two cases of unseating: (a) peak corner is slightly unseated but the deck-average remains (marginally) on the seat; (b) both the peak corner and deck average are considered unseated.

Table 4.9: Emerging active-displacement lognormal distribution parameters for deck unseating damage (Roblee, 2021*e*): median (σ) and dispersion (β)

Model Basis	CDS_1	CDS_2	CDS_3	CDS_4	CDS_5	CDS_6	CDS_7
2-Corner Average Displacement							
Median (σ)			7	13	19	25	30
LN Dispersion (β)			0.25	0.15	0.10	0.08	0.06
Peak 1-Corner Displacement							
Median (σ)			14	18	22	26	30
LN Dispersion (β)			0.08	0.06	0.05	0.04	0.04

a) Design-1: 30-in Seat Width

Model Basis	CDS_1	CDS_2	CDS_3	CDS_4	CDS_5	CDS_6	CDS_7
2-Corner Average Displacement							
Median (σ)			13	19	25	31	36
LN Dispersion (β)			0.15	0.12	0.08	0.06	0.04
Peak 1-Corner Displacement							
Median (σ)			20	24	28	32	36
LN Dispersion (β)			0.06	0.05	0.04	0.03	0.03

b) Design-2: 36-in Seat Width

Model Basis	CDS_1	CDS_2	CDS_3	CDS_4	CDS_5	CDS_6	CDS_7
2-Corner Average Displacement							
Median (σ)			25	31	37	43	48
LN Dispersion (β)			0.08	0.07	0.06	0.05	0.04
Peak 1-Corner Displacement							
Median (σ)			32	36	40	44	48
LN Dispersion (β)			0.04	0.03	0.03	0.03	0.02

c) Design-3: 48-in Seat Width

Model Basis	CDS_1	CDS_2	CDS_3	CDS_4	CDS_5	CDS_6	CDS_7
2-Corner Average Displacement							
Median (σ)			37	43	49	55	60
LN Dispersion (β)			0.07	0.06	0.05	0.04	0.03
Peak 1-Corner Displacement							
Median (σ)			44	48	52	56	60
LN Dispersion (β)			0.03	0.03	0.02	0.02	0.02

d) Design-4: 60-in Seat Width

4.3.2 Elastomeric Bearings

Era-3 bridges in California primarily use elastomeric bearings to support the bridge deck at the abutment joint. The capacity model for this bearing type is characterized in terms of shear strain (i.e. translational displacement normalized by bearing height) so that a consistent metric can be used for bridge realizations having different bearing thicknesses. Table 4.10 describes the two component damage states considered, and Table 4.11 provides the emerging CCLS model values. Note that both states are aligned with having low bridge-system level consequences per Table 4.1. CDS_1, aligned with observable damage, involves initial inelastic performance which may result in bearing degradation and/or minor permanent distortions. Repair of this level of damage would likely be deferred until a routine bridge-maintenance cycle. CDS_2 involves bearing displacements well beyond design limits which may result in elastomer tearing, bearing rollup or distortion, or sliding dislocation. This level of damage typically calls for bearing reset or replacement.

Table 4.10: Emerging CCLS state definitions for damage to elastomeric bearings with illustration of associated absolute shear-strain ranges (Roblee, 2021*e*)

		CDS_1		CDS_2	
	T_01		T_12		T_23
Typical Performance:		Initial Inelastic Deformation		Major Bearing Damage or Dislocation	
Likely Bearing Damage:		Minor Distortions or Degradation of Elastomer		Elastomer Tearing or Bearing Rollup/Distortion; Bearing Sliding Dislocation	
Shear-Strain Range:		150%		300%	

Table 4.11: Emerging lognormal distribution parameters for damage to elastomeric bearings (Roblee, 2021e) : median (σ) and dispersion (β)

Model Basis	**CDS_1**	**CDS_2**	**CDS_3**	**CDS_4**	**CDS_5**	**CDS_6**	**CDS_7**
Absolute Bearing Shear Strain []							
Median (σ)	150%	300%					
LN Dispersion (β)	0.20	0.20					

4.3.3 Joint Seals

Three of the most common types of joint seals used in California bridges are shown in Figure 4.8. Seal type selection is typically based on the design 'Movement Rating (MR)' for the joint which considers thermal-expansion movements and governs the joint gap size. Poured seals can be used in bridges with MR ranging from 0.5 to 1.0 inches; compression seals are commonly used with MR from 1.0 to 2.0 inches; and strip seals are used with MR from 2.0 to 4.0 inches. A variety of assembly seals used for even larger MR are not shown.

Table 4.12 summarizes damage states for the three different seal types, and Table 4.13 provides the emerging CCLS model values applicable to each. Here, the EDP used for damage prediction is gap-size increase (i.e. deck movement in the active direction relative to the abutment seat) normalized by the MR for the joint. Although the state damage descriptions change for each seal type, the same normalized CCLS values are used. Note that the poured seal only involves one damage state, while the others involve two.

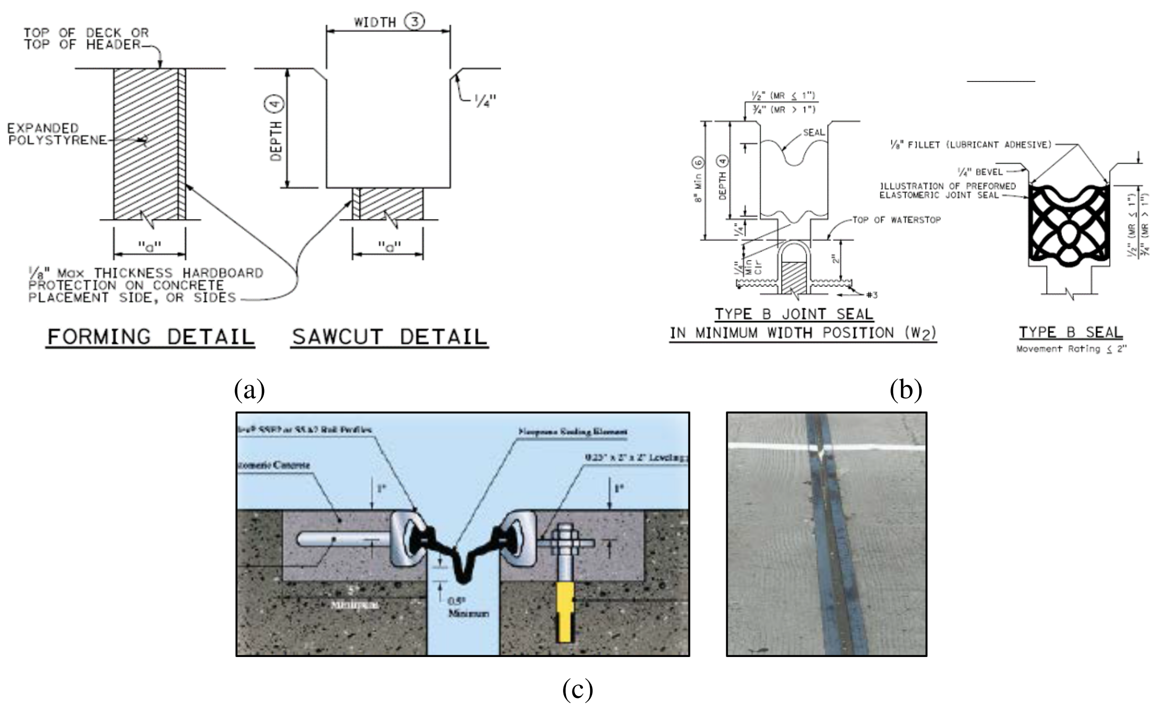

Figure 4.8: Illustration of common joint seal types: (a) poured; (b) compression; and (c) strip

Table 4.12: Emerging CCLS state definitions for damage to three types of joint seals with illustration of associated MR-normalized active joint displacement ranges (Roblee, 2021*e*)

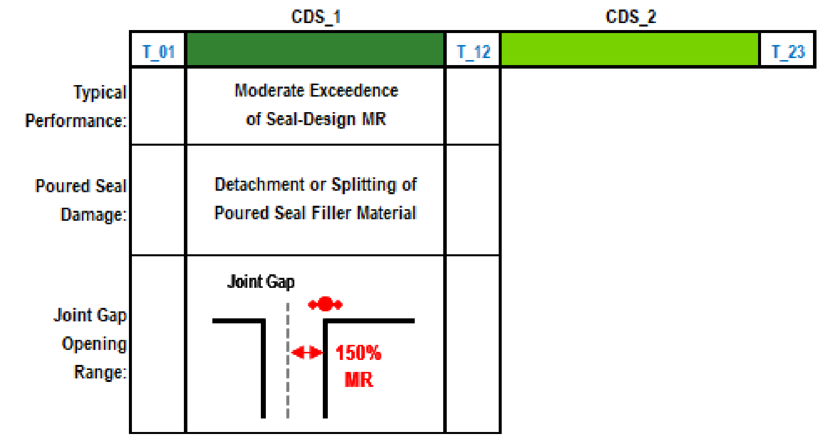

a) Poured Seal

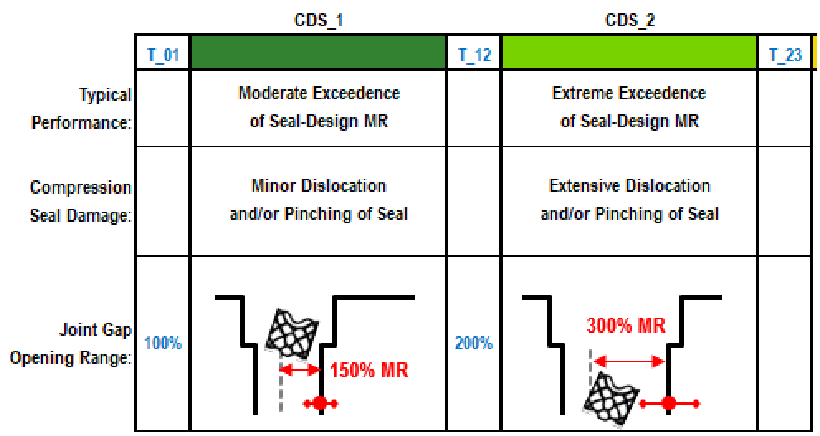

b) Compression Seal

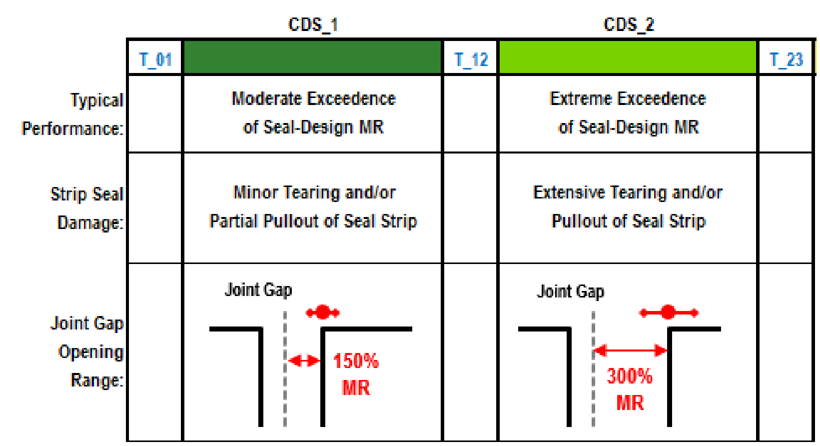

c) Strip Seal

Table 4.13: Emerging lognormal distribution parameters for damage to three types of joint seals (Roblee, 2021e) : median (σ) and dispersion (β)

Model Basis	**CDS_1**	**CDS_2**	**CDS_3**	**CDS_4**	**CDS_5**	**CDS_6**	**CDS_7**
Active MR-Normalized ¶ Joint Displacement []							
Median (σ)	150%	300%					
LN Dispersion (β)	0.20	0.20					

¶ Normalized to design movement rating (MR) of joint.

4.4 Other Components -- Response Based CCLS

The capacity models for the remaining components of the bridge systems considered herein are characterized in terms of expected performance over ranges on an analytical response backbone model. These response-based models address abutment-joint damage associated with shear key and backwall fracture, pounding damage at the abutment-deck interface, and both pile and spread-footing damage occurring at abutment-wall and column-bent foundations. Before describing these specific component models, common aspects of the general response-based CCLS model methodology are first reviewed.

4.4.1 Stochastic Backbone Responses, Performance Points, and Double Normalization

A central feature of analytical fragility models is their ability to capture overall response uncertainty arising from multiple simultaneous component interactions within the bridge-system. Development of a PSDM requires FEM analysis of a large set of bridge configurations representing a bridge class. For each configuration, one realization of the backbone response for each bridge component is stochastically assigned. The PSDM then captures peak responses for the collection of configurations which includes interactions between these varied component combinations.

Stochastic assignment of bridge-component response involves random sampling of correlated parameters of a probabilistic component-response model. Figure 4.9 provides an illustration of 20 such stochastic realizations of the translational response for CIDH piles (bottom) based on the median backbone model (top) and associated tables of dispersion and correlation values for each of five parameters used in that model (Xie et al., 2021). This particular model was explicitly developed for probabilistic application through analysis of an extensive set of simulations which considered variations in soil profiles and pile properties. Response models for other components (e.g. shear keys, backwall connections, backfills, etc.) were developed in a similar fashion and typically validated against available experimental data. It is important to note that while only a single realization of each component backbone is assigned to an analyzed bridge model, the ensemble average of all assigned backbones would closely approximate the median model. It is equally important to note that, due to bridge-system interactions, the median component response of using the stochastic backbone models is not necessarily the same as that of using the median backbone model directly.

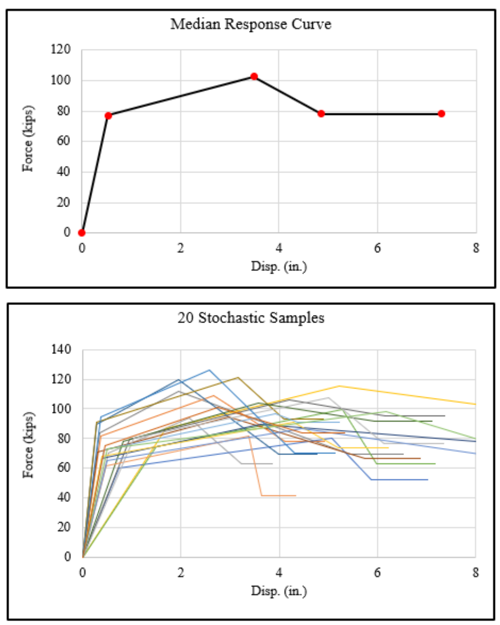

Figure 4.9: Example of stochastic backbone responses for CIDH piles (Xie et al., 2021)

Use of unique component response backbone realizations in each FEM bridge analysis poses a challenge for development of an associated capacity model for that component. This project adopts a novel methodology, herein called ’double normalization’ aimed at assuring consistent use of a stochastic backbone-model realization for both demand and capacity assessment of the component within the analysis. This is implemented by characterizing a backbone as a series of integer-numbered 'performance points' to represent the boundaries between linear segments in the backbone. Response values along the segment are expressed as segment-normalized distances along the horizontal (typically displacement) axis added to the segment's lower endpoint label. Within the FEM demand analysis of each bridge realization, the peak component response is captured and then normalized by the backbone assigned to that realization to yield a result expressed in terms of the performance-point scale. This 'apples to apples' strategy assures that a strong component used in demand analysis is also assessed against the same strong component for purposes of damage assessment. Conversely, it prevents 'apples to oranges' cases where the performance of the same strong component could be assessed using a model for a much weaker component.

The resulting output of a complete set of FEM analyses for multiple bridge realizations then becomes a distribution of performance point values. This distribution incorporates two components of dispersion: 1) that associated with stochastic variation in the backbone shape, and 2) that associated with all other demand-analysis factors such as bridge geometry, ground motion features, and interactions with other stochastically defined component responses. Since the uncertainty in backbone shape is already accounted for within the set of demand-analysis output, there is no need to also include it in the capacity model. Instead, the remaining dispersion on the capacity side primarily relates to the 'state' uncertainty in defining the relationship between backbone response ranges and the damage described in the state definition.

The second normalization is required for proper display and analysis of the distribution cloud of peak component responses on lognormal EDP -IM axes. Recall that each performance-point interval (say 1 to 2, or 2 to 3) represents one linear segment of the backbone response, and in physical-dimension space (say displacement), the segment lengths can vary substantially. Using the example in Figure 4.9, the second segment of the median response curve is roughly six times longer than the first segment. To restore at least a first-order approximation of the fundamental component backbone shape for purposes of display and analysis, the performance-point output is scaled by the relative lengths of the median response backbone. This can be done using either of two approaches. For optimal insight into component performance, it is most beneficial to express models in terms of physical units which can be readily visualized. However, for standardized displays and analysis, it is often more convenient to normalize these rescaled results by a reference value, typically taken as the value of the first performance point (i.e. end of idealized linear-elastic performance). In the remainder of this chapter, component capacity CCLS models are expressed using both approaches.

4.4.2 External Non-Isolated Shear Key

The non-isolated external shear key (see Figure 3.23(a)) is the predominant design used in modern (era-3) California box-girder bridge abutments, and is the sole design considered herein. The backbone response shape adopted for this key's capacity model is illustrated with performance-point labels in Figure 4.10 where the fundamental backbone shape is based on experimental tests by Megally et al. (2001). A stochastic version of this backbone model was developed by varying the geometric and material parameters of Megally's mechanistic model per details found in the California bridge inventory.

Table 4.14 provides state descriptions for four damage levels along with an illustration of the associated ranges in backbone performance. These damage states are based on an interpretation of Megally's experimental damage observations (levels I to V in Figure 4.10) put into the broader context of the bridge-system framework outlined in Table 4.1 and Table 4.2. Table 4.15 provides emerging CCLS model values in terms of center-state performance point values and both absolute and normalized key displacement values.

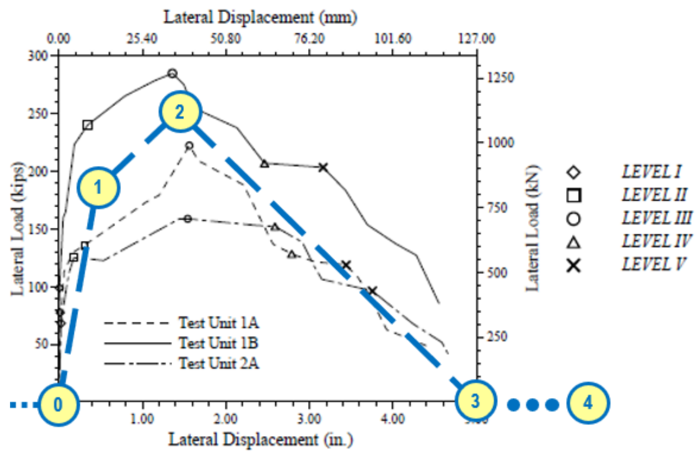

Figure 4.10: Illustration of shear key performance levels (Megally et al., 2001).

Table 4.14: Illustration of capacity limit state definition for external non-isolated shear key.

	T_01	CDS_1	T_12	CDS_2	T_23	CDS_3	T_34	CDS_4	T_45
Typical Performance:		Initial Loss of Lateral Stiffness		Fusing - Near Ultimate Lateral Capacity		Plastic Deformation - Degrading Lateral Capacity		Fully Fused, Diminishing to No Residual Capacity	
Likely Shear Key Damage:		Minor Inclined Cracking in Connection Region; Small Crack Width		Clear Shear-Plane Formation w/ Crack Opening & Minor Spalling w/o Rebar Exposure; Strength Largely Intact		Shear-Plane Gap Opening; Significant Spalling w/ Core Exposure & Some Crushing & Initial Rebar Deformation		Large Displacement and/or Rotation; Large Diagonal Gap w/ Major Core Crushing, Rebar Deformation & Fracture	
Backbone Response Range:		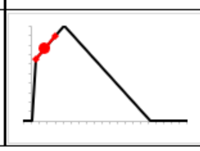		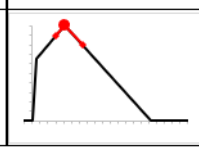		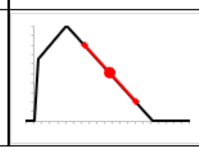		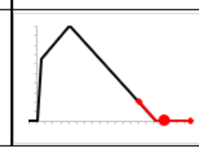	

Table 4.15: Emerging lognormal distribution parameters for damage to external non-isolated shear keys (Roblee, 2021*e*): median (σ) and dispersion (β)

Model Basis	**CDS_1**	**CDS_2**	**CDS_3**	**CDS_4**	**CDS_5**	**CDS_6**	**CDS_7**
Backbone Performance Point []							
Median (σ)	1.3	2.0	2.5	3.1			
LN Dispersion (β)	NA	NA	NA	NA			
Absolute Key Displacement [Inch]							
Median (σ)	1.25	3.3	7.6	12.9			
LN Dispersion (β)	0.45	0.25	0.2	0.15			
Normalized¶ Key Displacement []							
Median (σ)	3.20	8.3	19.6	33.0			
LN Dispersion (β)	0.45	0.25	0.2	0.15			

¶ Normalized to median e1n value of 0.39-inch corresponding to backbone performance point 1.

4.4.3 Straight Abutment-Backwall Connection

Straight backwalls are solely used in modern (era-3) California box-girder bridge abutments, and its connection to the stem wall (see Figure 3.23(b)) is the sole design considered herein. The backbone response shape for shear fracture of the backwall connection is developed in subsection 3.3.3 and illustrated with performance-point labels in Figure 4.11.

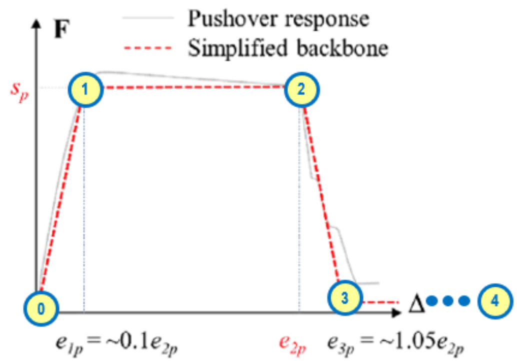

Figure 4.11: Illustration of backbone response shape and performance points for abutment backwall connection relative to sample of analytical data (Zheng et al., 2021)

Table 4.16 provides state descriptions for three damage levels along with an illustration of the associated ranges in backbone performance. Table 4.17 provides emerging CCLS model values in terms of center-state performance point values and both absolute and normalized backwall displacement values. Backwall damage only occurs for deck motion in the passive direction.

Table 4.16: Emerging CCLS state definitions for passive damage to abutment backwall connection with illustration of associated backbone response ranges (Roblee, 2021*e*).

	T_01	CDS_1	T_12	CDS_2	T_23	CDS_3	T_34
Typical Performance:		Initial Plastic Deformation Near Full Lateral Capacity		Fused w/ Rapidly Degradiing Lateral Capacity		Fully Fused, Only Minor Residual Capacity Remaining	
Likely Backwall Connection Damage:		Minor Cracking Along Diagonal Shear Plane in Connection Region		Clear Shear-Plane Formation w/ Major Cracking/Spalling, and Initial Gap Opening		Shear-Plane Gap Opening & Major Rebar Deformation w/ Possible Fracture or Pullout	
Backbone Response Range:		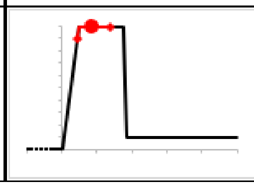		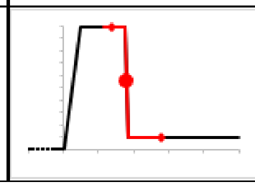		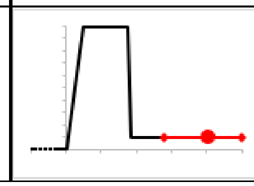	

Table 4.17: Lognormal distribution parameters for backwall passive damage states: median (σ) and dispersion (β)

Model Basis	**CDS_1**	**CDS_2**	**CDS_3**	**CDS_4**	**CDS_5**	**CDS_6**	**CDS_7**
Backbone Performance Point []							
Median (σ)	1.3	2.5	3.7				
LN Dispersion (β)	NA	NA	NA				
Absolute Backwall Displacement [Inch]							
Median (σ)	0.51	1.04	2.35				
LN Dispersion (β)	0.30	0.25	0.20				
Normalized¶ Backwall Displacement []							
Median (σ)	1.75	3.6	8.1				
LN Dispersion (β)	0.30	0.25	0.20				

¶ Normalized to median e1n value of 0.29-inch corresponding to backbone performance point 1.

4.4.4 Pounding

subsection 3.3.4 outlined the analytical basis and development of a pair of pounding models. For the single-frame bridge systems considered herein, only the 'deck-to-abutment' model is considered. Figure 4.12 provides field examples of various types of bridge pounding damage. Figure 4.13 illustrates the backbone response shape for the pounding model along with definitions of performance points. Note that the EDP used in this model is normalized to an assumed maximum penetration value of 0.1-inch per Muthukumar (2003).

Table 4.18 provides state descriptions for three pounding damage levels along with an illustration of the associated ranges in backbone performance. Table 4.19 provides emerging CCLS model values in terms of center-state performance point values and both absolute and normalized pounding displacement values.

(a)

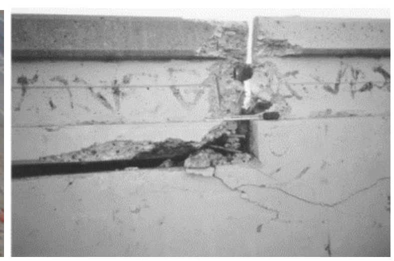

(b)

(c)

Figure 4.12: Illustration of pounding damage: (a) a pounding mark in the bridge backwall (Yen et al., 2011); (b) abutment damage in 1994 Northridge earthquake; and (c) barrier rail pounding damage (Moehle and Eberhard, 2003).

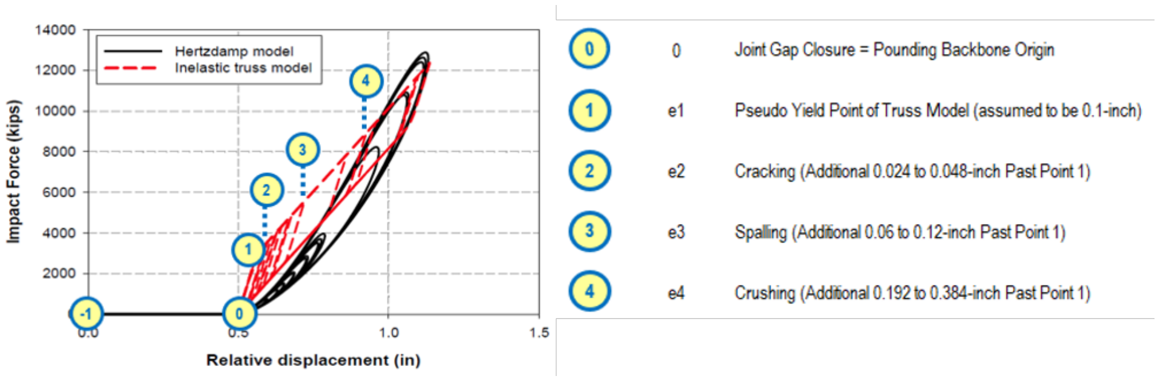

Figure 4.13: Illustration of backbone response shape (red) and performance points (blue) for abutment joint pounding relative to analytical data (Muthukumar, 2003).

Table 4.18: Emerging CCLS state definitions for abutment joint pounding damage with illustration of associated backbone response ranges (Roblee, 2021*e*).

	T_01	CDS_1	T_12	CDS_2	T_23	CDS_3	T_34
Typical Performance:		Initial Pounding Damage		Moderate Pounding Damage		Extensive Pounding Damage	
Pounding Damage To Broad Faces:		Minor Near-Surface Cracking & Chipping of Impacting Elements		Moderate Surface Spalling & Crack Penetration Deeper Into Impacting Elements		Crushing, w/ Major Spalling & Cracking Deep (~12-in) Into Impacting Elements	
Norm Force-Displ. Response Range:		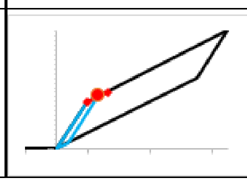		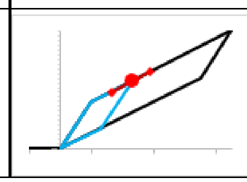		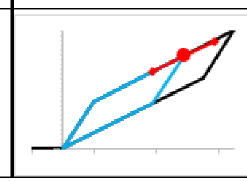	

Table 4.19: Emerging lognormal distribution parameters for abutment joint pounding damage: median (σ) and dispersion (β)

Model Basis	**CDS_1**	**CDS_2**	**CDS_3**	**CDS_4**	**CDS_5**	**CDS_6**	**CDS_7**
Backbone Performance Point []							
Median (σ)	2.0	3.2	4.0				
LN Dispersion (β)	NA	NA	NA				
Absolute Post-Contact Displacement§ [Inch]							
Median (σ)	0.13	0.23	0.39				
LN Dispersion (β)	0.15	0.15	0.15				
Normalized¶ Post-Contact Displacement []							
Median (σ)	1.36	2.3	3.9				
LN Dispersion (β)	0.15	0.15	0.15				

§ Displacement after closure of joint gap;
¶ Normalized to median e1n value of 0.10-inch corresponding to backbone performance point 1.

4.4.5 Foundations

Two general types of foundations, pile/cap systems and spread footings, are used to support both abutment walls and column bents. This research considers damage associated with translational movement of both types of foundations at both locations as well as rotational damage at column-bent locations. Damage is assessed separately for transverse and longitudinal loading.

Pile Foundations

Caltrans employs a variety of 'standard plan pile' designs within foundation systems used at bridge bents and abutments (Caltrans, 2014, 2015*a*,*b*,*c*). Figure 4.14 shows some of the designs used in the modern (era-3) bridges considered herein. These vary in material, section shape and reinforcement, and cap-connection details, and are classified by nominal axial load capacity as Class 90, Class 140, and Class 200 where a larger class number correspond to a higher capacity. Similar and additional standard pile designs were used in earlier (eras 1 and 2) bridges, but these have different section properties and details, particularly as related to the cap-connection.

Xie et al. (2021) completed an extensive program of analytical research into the development of stochastic backbone response models for translational pile-head displacement of California standard plan piles. Figure 4.15 illustrates the generic backbone shape adopted for all models, along with enumerated performance-points used herein for capacity model development. Xie's work developed separate models to specify load and displacement distributions for performance points identified as 1-3 in Figure 4.15 for each pile type, era, and class for five ranges of pile-cap embedment depth.

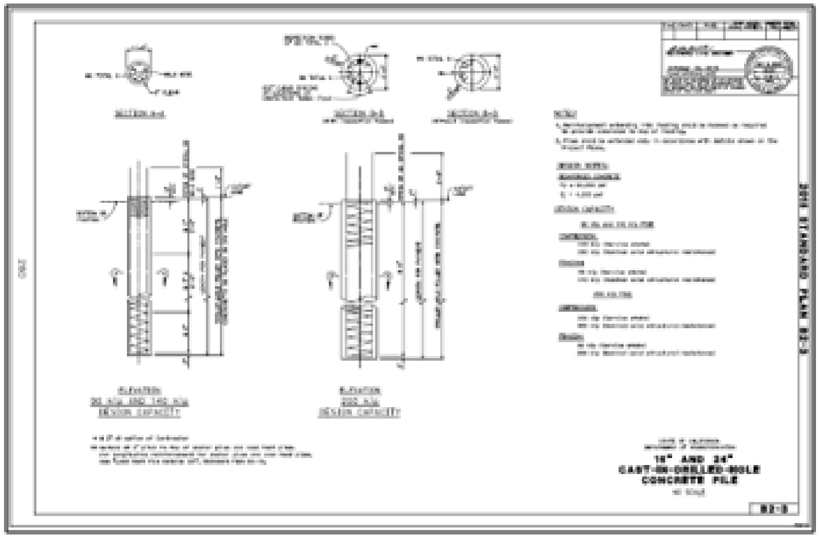

(a)

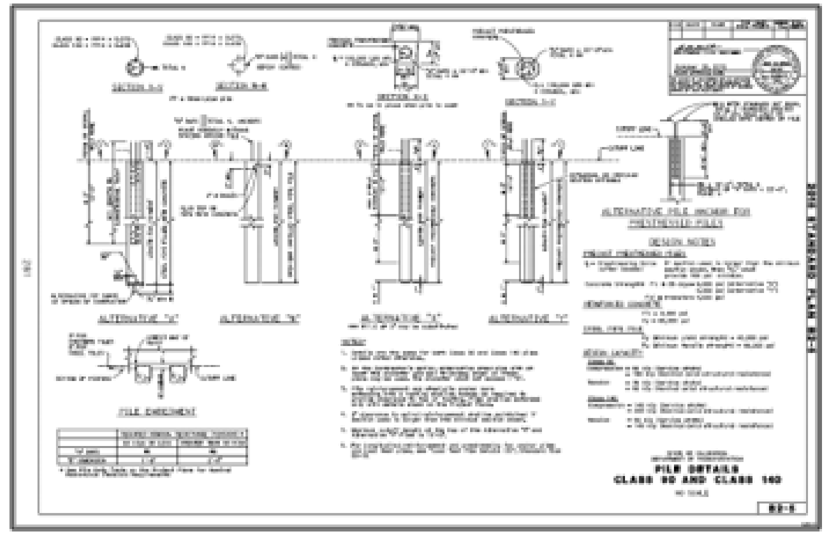

(b)

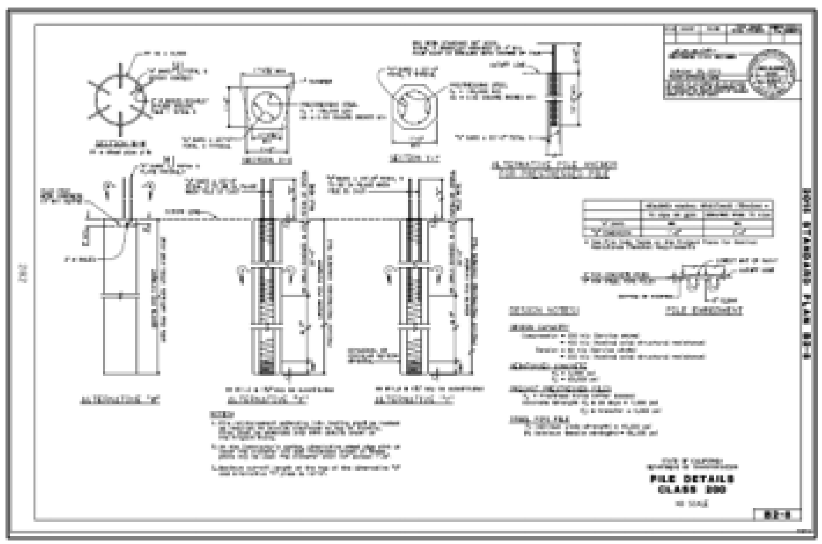

(c)

Figure 4.14: Standard plan pile types used in modern California bridges (Caltrans, 2015*a*,*b*,*c*): (a) CIDH group; (b) Precast group; and (c) Steel group.

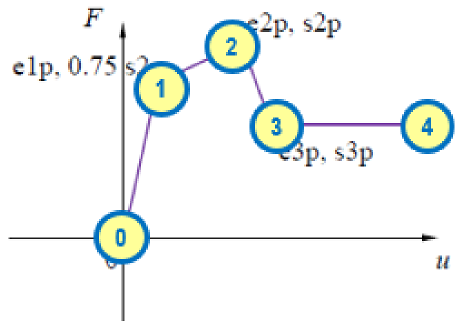

Figure 4.15: Illustration of generalized backbone response shape and performance points for pile-head translational response (Xie et al., 2021)

For purposes of capacity model development herein, three groups of pile designs were identified based on having similar backbone shape: 1) Cast-In-Drilled-Hole (CIDH) concrete piles, 2) precast, prestressed concrete piles (PC), and 3) steel piles including both H-section and open pipe piles (Steel). A fourth group, concrete-filled steel pipes known as Cast-In-Steel-Shell (CISS) piles is also being considered for future development.

A variation of the double normalization strategy outlined in subsection 4.4.1 was used for modeling pile translational response. For FEM demand analysis, each bridge realization was assigned a standard-plan pile design (i.e. type and class), and embedment depth per distributions representative of era-3 bridge designs found in the California inventory. Procedures for this assignment are detailed in Chapter 5. As usual, peak demand output from the FEM analysis was expressed in terms of performance point values to assure the same backbone shape was used for demand and capacity assessment. The variations in the double normalization procedure occur in the handling of the performance point distributions. Here, separate distributions are reported for each of the three pile groups (CIDH, PC, Steel) and separate scaling is used for each to reintroduce physical dimensions back into the backbone shapes. Scaling values for the median backbone shape of each group were defined using the weighted average of the median Xie et al. (2021) backbone model values for the pile types and embedment depths assigned in the demand modeling (Roblee, 2021*b*).

Table 4.20 shows that the backbone shapes for the three pile groups differ substantially. The CIDH group reaches its idealized elastic limit (e1p) at 0.25 inch, while displacements for the other two groups are over four times greater. Differences are even more pronounced for displacements required to achieve peak capacity (e2p). This occurs for the CIDH pile at under 2-inches, while it requires nearly 14-inch and 22-inch for the precast and steel groups, respectively. Broadly, the CIDH system is considered much more brittle in translation response than the remaining systems, and each group undergoes a unique damage sequence.

Table 4.20: Comparison of median era-3 column-bent pile-head displacement values for three pile groups at three response-backbone performance points (Roblee, 2021*b*)

Median Displacement [inch]	**CIDH Group**	**Precast Group**	**Steel Group**
Performance Point 1 (e1p)	0.25	1.10	1.16
Performance Point 2 (e2p)	1.68	13.8	21.9
Performance Point 3 (e3p)	4.14	22.4	30.2

Table 4.21 provides 3 sets of state descriptions, each having five damage levels, for the three pile-type groups (CIDH, PC, Steel) along with illustrations of the associated ranges in backbone performance. Table 4.22 and Table 4.23 provide emerging CCLS model values for column-bent and abutment foundations, respectively, in terms of center-state performance point values and both absolute and normalized pile-head displacement values. The minor difference between the column-bent and abutment model values arises from the different distributions of pile design (type and class) and embedment depth used in these two applications.

Note that different state descriptions and response-backbone performance-point ranges are used in the capacity models for the three pile groups. This arises from the very different displacement responses for the three groups noted in Table 4.20 which can induce damage to the pile-cap and its connection which is not explicitly considered by Xie et al. (2021) Broadly, these three independent capacity models were aligned to have comparable system-level impacts per Table 4.1 and Table 4.2.

Table 4.21: Emerging CCLS state definitions for pile-foundation translational response damage with illustration of associated backbone response ranges for three era-3 pile-type groups (Roblee, 2021*e*)

	T_01	CDS_1	T_12	CDS_2	T_23	CDS_3	T_34	CDS_4	T_45	CDS_5	T_56
Typical Performance:		Initial Loss of Lateral Stiffness		Approaching Lateral Capacity		Degrading Lateral Capacity		Residual Lateral Capacity		Loss of Lateral (& Axial?) Capacity	
Likely Pile-Foundation Damage:		Initial Minor Cracking/Spalling Damage at Pile Head (Future Corrosion)		Initial Pile-Head Hinging w/ Substantial Cracking/Spalling & Minor Rebar Yield		Well Developed Pile-Head Hinge w/ Major Rebar Yield & Core Crushing; Initial 2nd Hinge Below Ground		Buckling & Fracture of Rebar & Hoop Fracture at Pile Head; Fully Formed 2nd Hinge Below Ground		Large Displacement & Pile Rotation; Possible Detachment at Pile Cap; Major Loss of Lateral & Axial Capacity	
Backbone Response Range:	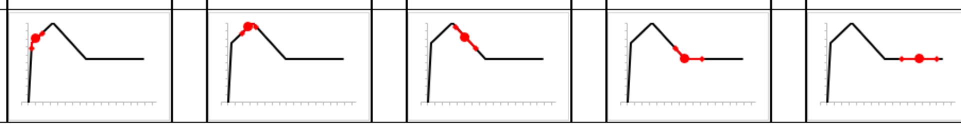										

a) Cast-In-Drill-Hole (CIDH) Pile Group

	T_01	CDS_1	T_12	CDS_2	T_23	CDS_3	T_34	CDS_4	T_45	CDS_5	T_56
Typical Performance:		Initial Loss of Lateral Stiffness		Approaching Lateral Capacity		Degrading Lateral Capacity		Residual Lateral Capacity		Loss of Lateral (& Axial?) Capacity	
Likely Pile-Foundation Damage:		Initial Minor Cracking/Spalling Damage at Pile Head (Future Corrosion)		Initial Pile-Head Hinging w/ Substantial Cracking/Spalling; Initial Yielding of Rebar & Prestress Tendons		Well Developed Pile-Head Hinge w/ Major Yielding of Rebar & Prestress Tendons; Core Crushing; Initial 2nd Hinge Below Ground		Buckling & Fracture of Rebar & Prestress Tendons; Fully Formed 2nd Hinge Below Ground		Large Displacement & Pile Rotation; Possible Detachment at Pile Cap; Major Loss of Lateral & Axial Capacity	
Backbone Response Range:	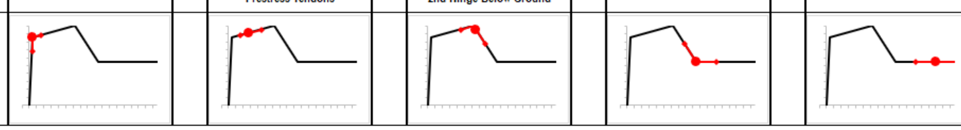										

b) Precast, Prestressed Concrete Pile Group

	T_01	CDS_1	T_12	CDS_2	T_23	CDS_3	T_34	CDS_4	T_45	CDS_5	T_56
Typical Performance:		Initial Pile-Cap Connection Damage		Initial Loss of Lateral Stiffness		Pile Ductile Yielding w/ Cap Damage		Degrading Lateral Capacity		Residual Lateral Capacity	
Likely Pile-Foundation Damage:		Initial Minor Cracking at Pile Cap Connection (Future Corrosion); Low (< ~5-deg) Pile-Head Rotation		Rotational Gap at Cap Connection; Initial Steel Yielding Below Ground; Moderate (5 to 10-deg) Pile-Head Rotation		Increasing Cap Connection Damage; Ductile Steel Yielding Below Ground; High (10 to 30-deg) Pile-Head Rotation		Substantial Cap Connection Damage; Steel Buckling at Below-Ground Hinge; Extreme (30 to 45-deg) Pile-Head Rotation		Extreme Displacement & Pile-Head Rotation (> ~45 deg); Possible Detachment at Pile Cap; Major Loss of Lateral & Possibly Axial Capacity	
Backbone Response Range:	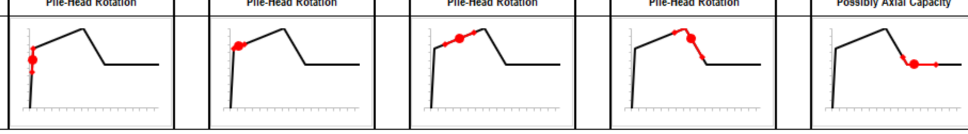										

c) Steel Pile Group (H-Section and Open Pipe)

Table 4.22: Emerging lognormal distribution parameters for *abutment* pile-foundation translational response damage for three era-3 pile-type groups (Roblee, 2021*e*):median (σ) and dispersion (β)

Model Basis	**CDS_1**	**CDS_2**	**CDS_3**	**CDS_4**	**CDS_5**	**CDS_6**	**CDS_7**
Backbone Performance Point []							
Median (σ)	1.2	1.8	2.4	3.0	3.6		
LN Dispersion (β)	NA	NA	NA	NA	NA		
Absolute Pile-Head Displacement§ [Inch]							
Median (σ)	0.6	1.4	2.7	4.1	6.6		
LN Dispersion (β)	0.40	0.25	0.15	0.15	0.15		
Normalized¶ Pile-Head Displacement []							
Median (σ)	2.1	5.5	10.3	15.8	25.3		
LN Dispersion (β)	0.40	0.25	0.15	0.15	0.15		

§ Displacement values based on inventory-averaged pile section and embedment depth for the CIDH group.

¶ Normalized to inventory median e1n value of 0.26-inch corresponding to backbone performance point 1.

a) Cast-In-Drill-Hole (CIDH) Pile Group

Model Basis	**CDS_1**	**CDS_2**	**CDS_3**	**CDS_4**	**CDS_5**	**CDS_6**	**CDS_7**
Backbone Performance Point []							
Median (σ)	1.0	1.4	2.1	3.0	3.6		
LN Dispersion (β)	NA	NA	NA	NA	NA		
Absolute Pile-Head Displacement§ [Inch]							
Median (σ)	1.2	6.4	15.1	21.6	34.6		
LN Dispersion (β)	0.40	0.30	0.15	0.15	0.15		
Normalized¶ Pile-Head Displacement []							
Median (σ)	1.0	5.6	13.1	18.8	30.1		
LN Dispersion (β)	0.40	0.30	0.15	0.15	0.15		

§ Displacement values based on inventory-averaged pile section and embedment depth for the Precast group.

¶ Normalized to inventory median e1n value of 1.15-inch corresponding to backbone performance point 1.

b) Precast, Prestressed Concrete Pile Group

Model Basis	**CDS_1**	**CDS_2**	**CDS_3**	**CDS_4**	**CDS_5**	**CDS_6**	**CDS_7**
Backbone Performance Point []							
Median (σ)	0.8	1.1	1.5	2.3	3.1		
LN Dispersion (β)	NA	NA	NA	NA	NA		
Absolute Pile-Head Displacement§ [Inch]							
Median (σ)	1.3	3.8	12.6	26.4	36.3		
LN Dispersion (β)	0.25	0.35	0.30	0.15	0.15		
Normalized¶ Pile-Head Displacement []							
Median (σ)	0.8	2.4	7.8	16.3	22.3		
LN Dispersion (β)	0.25	0.35	0.30	0.15	0.15		

§ Displacement values based on inventory-averaged pile section and embedment depth for the Steel group.

¶ Normalized to inventory median e1n value of 1.63-inch corresponding to backbone performance point 1.

c) Steel Pile Group (H-Section and Open Pipe)

Table 4.23: Emerging lognormal distribution parameters for *column-bent* pile-foundation translational response damage for three era-3 pile-type groups (Roblee, 2021*e*):median (σ) and dispersion (β)

Model Basis	**CDS_1**	**CDS_2**	**CDS_3**	**CDS_4**	**CDS_5**	**CDS_6**	**CDS_7**
Backbone Performance Point []							
Median (σ)	1.2	1.8	2.4	3.0	3.6		
LN Dispersion (β)	NA	NA	NA	NA	NA		
Absolute Pile-Head Displacement§ [Inch]							
Median (σ)	0.5	1.4	2.7	4.1	6.6		
LN Dispersion (β)	0.40	0.25	0.15	0.15	0.15		
Normalized¶ Pile-Head Displacement []							
Median (σ)	2.1	5.5	10.6	16.4	26.3		
LN Dispersion (β)	0.40	0.25	0.15	0.15	0.15		

§ Displacement values based on inventory-averaged pile section and embedment depth for the CIDH group.

¶ Normalized to inventory median e1n value of 0.25-inch corresponding to backbone performance point 1.

a) Cast-In-Drill-Hole (CIDH) Pile Group

Model Basis	**CDS_1**	**CDS_2**	**CDS_3**	**CDS_4**	**CDS_5**	**CDS_6**	**CDS_7**
Backbone Performance Point []							
Median (σ)	1.0	1.4	2.1	3.0	3.6		
LN Dispersion (β)	NA	NA	NA	NA	NA		
Absolute Pile-Head Displacement§ [Inch]							
Median (σ)	1.1	6.2	14.7	22.4	35.8		
LN Dispersion (β)	0.40	0.30	0.15	0.15	0.15		
Normalized¶ Pile-Head Displacement []							
Median (σ)	1.0	5.6	13.3	20.3	32.4		
LN Dispersion (β)	0.40	0.30	0.15	0.15	0.15		

§ Displacement values based on inventory-averaged pile section and embedment depth for the Precast group.

¶ Normalized to inventory median e1n value of 1.10-inch corresponding to backbone performance point 1.

b) Precast, Prestressed Concrete Pile Group

Model Basis	**CDS_1**	**CDS_2**	**CDS_3**	**CDS_4**	**CDS_5**	**CDS_6**	**CDS_7**
Backbone Performance Point []							
Median (σ)	0.8	1.1	1.5	2.3	3.1		
LN Dispersion (β)	NA	NA	NA	NA	NA		
Absolute Pile-Head Displacement§ [Inch]							
Median (σ)	0.9	3.2	11.5	24.4	33.2		
LN Dispersion (β)	0.25	0.35	0.30	0.15	0.15		
Normalized¶ Pile-Head Displacement []							
Median (σ)	0.8	2.8	10.0	21.0	28.7		
LN Dispersion (β)	0.25	0.35	0.30	0.15	0.15		

§ Displacement values based on inventory-averaged pile section and embedment depth for the Steel group.

¶ Normalized to inventory median e1n value of 1.16-inch corresponding to backbone performance point 1.

c) Steel Pile Group (H-Section and Open Pipe)

Spread Footing Foundation

Spread footing foundations are used for bridge foundations where axial loads are relatively low and/or the native soils have relatively high bearing capacity. A hyperbolic response backbone is used to model their elastoplastic behavior under translational loading. Figure 4.16 illustrates such a backbone along with the set of performance points used herein for capacity model definition. In the multi-segmented backbones considered in previous models, the performance points were defined at segment boundaries and used in the double-normalization procedure. Here, the performance points are simply labels to represent a progression of displacement values. Point 1 represents the z_{50} value in the hyperbolic model where total displacement is comprised of approximately 60%-40% elastic-plastic components, respectively. Points 2 and higher simply represent a specific geometric progression of plastic displacements, 1-inch, 2-inch, 4-inch, 8-inch, etc. obtained through analysis of the OSB-1 column-foundation design. Subsequent analyses for other footing configurations yield similar backbones.

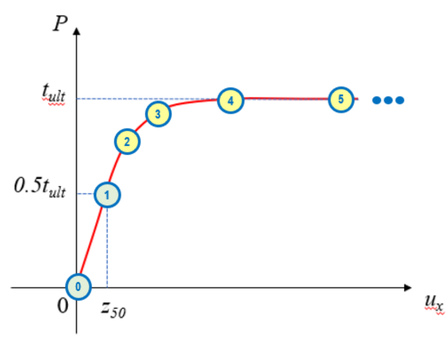

Figure 4.16: Illustration of backbone response shape and performance points for spread-footing translational response

Table 4.24 provides state descriptions for three damage levels along with an illustration of the associated ranges in backbone performance. Table 4.25 provides emerging CCLS model values in terms of center-state performance point values and both absolute and normalized footing translational displacement values. Direct damage to the footing element itself was not modeled and it was assumed that the structural connection was sufficiently robust to mobilize footing slippage relative to the underlying native soil. Instead, damage states were broadly defined in terms of wide ranges in residual plastic displacement values and considered the impacts which such displacements might have on adjacent facilities.

Table 4.24: Emerging CCLS state definitions for spread-footing translational response damage with illustration of associated backbone response ranges (Roblee, 2021*e*)

		CDS_1		CDS_2		CDS_3	
	T_01		T_12		T_23		T_34
Typical Performance:		Observable Residual Displacements (1-4 Inch)		Substantial Residual Displacements (4-16-Inch)		Extreme Residual Displacements (>16-Inch)	
Footing-Area Damage:		Minor Gaps or Dislocations Near Footing at Ground Surface		Potential Distress to Footing Connection or Abuting Facilities/Utilities		Potential Impacts on Column Capacity and/or Alignment	
Norm Force-Displ. Response Range:	~1-In	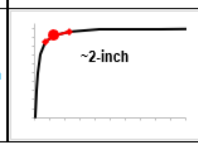	~4-In	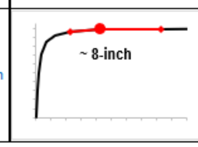	~16-In	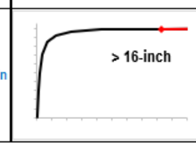	

Table 4.25: Emerging lognormal distribution parameters for spread-footing translational response damage (Roblee, 2021*e*): median (σ) and dispersion (β)

Model Basis	**CDS_1**	**CDS_2**	**CDS_3**	**CDS_4**	**CDS_5**	**CDS_6**	**CDS_7**
Backbone Performance Point []							
Median (σ)	3.0	5.0	7.0				
LN Dispersion (β)	0.35	0.35	0.35				
Residual* Footing Displacement [Inch]							
Median (σ)	2.0	8.0	32.0				
LN Dispersion (β)	0.35	0.35	0.35				
Absolute Total§ Footing Displacement [Inch]							
Median (σ)	2.5	8.6	32.6				
LN Dispersion (β)	0.35	0.35	0.35				
Normalized¶ Total Footing Displacement []							
Median (σ)	5.1	17.6	66.5				
LN Dispersion (β)	0.35	0.35	0.35				

* Residual plastic component of total displacement;
§ Sum of elastic and residual plastic displacement components;
¶ Normalized to the z_{50} value for OSB-1 bridge of 0.49-inch corresponding to backbone performance point 1.

Foundation Rotation

As noted in subsection 3.2.6, foundation rotation is also modeled as a hyperbolic response. A single rotational spring is assigned to represent the weaker of two potential failure mechanisms: 1) 'geotechnical failure' associated with excessive axial displacement of piles at the foundation perimeter, and 2) 'structural' failure associated with excessive rotation of poor column-foundation connection details. Era-3 California foundation designs are quite robust both structurally and geotechnically as they are explicitly designed to have rotational capacities which exceed column-bottom hinge capacity by a specified margin (typically 1.2). Foundation designs for earlier eras were not as robust and either failure mechanism was possible before column fusing. Although foundation-rotation damage risk is low for the era-3 bridge designs considered herein, the following discussion outlines concepts used to develop such models, primarily for application to other eras. This model development is done in the context of geotechnical failure of a pile foundation which is assumed to be also applicable to spread-footing rotation. Similar compatible CCLS models are anticipated for structural failure with different descriptions of damage state.

Table 4.26 summarizes emerging sets of state descriptions developed in conjunction with the emerging CCLS model values listed in Table 4.27. Separate CCLS models were developed for fixed-base and pinned-base column connections as foundations beneath these two systems differ substantially. Further, the fixed-base-column model allows for additional damage states through possible overturning (CDS_7) of single-column bents. In contrast, even severe damage to a pinned-base-column foundation is not associated with a bridge collapse risk, but rather to 'repairable major damage to system function' per Table 4.1.

Table 4.26: Emerging CCLS state definitions for column-foundation rotational response damage for 2 column base-fixity types (Roblee, 2021*f*)

CDS_1		>90% Design Geotech Capacity, ~Elastic (Non-Linear) Pile Response
CDS_2		Initial Minor Residual Pile Displacements
CDS_3		Exceed Geotech Capacity, Observable Residual Pile Displ.
CDS_4		Substantial Residual Pile Displacement & Observable Cap Rotation
CDS_5		Foundation Rotational Failure, Bent Marginally Stable
CDS_6		Excessive Cap Rotation, Column Instability Risk
CDS_7		Extreme Cap Rotation, Column Collapse Risk

a) Fixed-Base Column Connection

CDS_1		>90% Design Geotech Capacity, ~Elastic (Non-Linear) Pile Response
CDS_2		Exceed Geotech Capacity, Observable Residual Pile Displ. & Cap Rotation
CDS_3		Substantial Residual Pile Displacement & Cap Rotation
CDS_4		Foundation Rotational Failure & Excessive Cap Rotation
CDS_5		
CDS_6		
CDS_7		

b) Pinned-Base Column Connection

4.5 Capacity Model Dispersion

Each of the CCLS models presented in this chapter include a lognormal dispersion term to capture uncertainty in the capacity definition. Determination of dispersion values was straightforward for the column-bent damage states where both the RP1 experimental test results and the HS-R analytical programs provided clear and easily modeled distributions of the displacement-ductility EDP used for capacity definition.

However, the definition of the dispersion terms for most other components was less clear, particularly when simple numerical thresholds were used to differentiate states (e.g. deck unseating, bearing strain, foundation rotation, etc.) or for components analyzed within the framework of response-based CCLS and double normalization (e.g. shear keys, backwall connections, translational pile response, etc.). This remains a vexing issue for the project team and the values presented here are subject to change as the issues are more fully addressed. In the interim, a standard approximation was adopted herein whereby the EDP range between adjacent state thresholds was typically assumed to represent four

Table 4.27: Emerging lognormal distribution parameters for column-foundation rotational response damage for 2 column base-fixity types (Roblee, 2021*e*): median (σ) and dispersion (β)

Model Basis	**CDS_1**	**CDS_2**	**CDS_3**	**CDS_4**	**CDS_5**	**CDS_6**	**CDS_7**
Inv-Ave Cap-Edge-Pile* Axial Displ. [Inch]							
Median (σ)	0.6	1.2	2.4	4.8	10	19	38
LN Dispersion (β)	0.27	0.17	0.17	0.17	0.17	0.17	0.17
Inv-Ave Pile-Cap§ Rotation [Degrees]							
Median (σ)	0.3	0.6	1.2	2.4	5	10	19
LN Dispersion (β)	0.27	0.17	0.17	0.17	0.17	0.17	0.17
Normalized¶ Pile-Cap Rotation []							
Median (σ)	2	4	8	16	32	64	128
LN Dispersion (β)	0.27	0.17	0.17	0.17	0.17	0.17	0.17

* Approx. axial deflection of outer row of piles based on inventory-average era-3 fixed-column-base foundation design;

§ Approx. pile-cap rotation based on inventory-average era-3 fixed-column-base foundation design;

¶ Normalized by θ_y of 0.15-degrees. (Inventory-ave cap rotation of ~0.07-deg for 50% moment capacity.)

a) Fixed-Base Column-Foundation Connection

Model Basis	**CDS_1**	**CDS_2**	**CDS_3**	**CDS_4**	**CDS_5**	**CDS_6**	**CDS_7**
Inv-Ave Cap-Edge-Pile* Axial Displ. [Inch]							
Median (σ)	0.7	2.3	5	9			
LN Dispersion (β)	0.35	0.27	0.17	0.17			
Inv-Ave Pile-Cap§ Rotation [Degrees]							
Median (σ)	0.6	2.0	4	8			
LN Dispersion (β)	0.35	0.27	0.17	0.17			
Normalized¶ Pile-Cap Rotation []							
Median (σ)	2.5	8	16	32			
LN Dispersion (β)	0.35	0.27	0.17	0.17			

* Approx. axial deflection of outer row of piles based on inventory-average era-3 pinned-column-base foundation design;

§ Approx. pile-cap rotation based on inventory-average era-3 pinned-column-base foundation design;

¶ Normalized by θ_y of 0.25-degrees. (Inventory-ave cap rotation of ~0.124-deg for 50% moment capacity.)

b) Pinned-Base Column-Foundation Connection

standard deviations ($\pm 2\sigma$ from the mean value in the natural logarithm space) under the assumption that component capacity was nearly always within the EDP range defined by half the distance to the adjacent state.

4.6 Closure

A complete set of emerging component capacity models used in this dissertation are presented in this chapter. These models are aligned within an overarching 7-state bridge-system framework where component performance is expected to have comparable operational consequences for bridge traffic capacity and earthquake-emergency repair needs. The 7-state framework provides additional granularity for the definition and progression of component damage, and is intended to provide improved post-earthquake situational awareness and inspection guidance for emergency responders as well as produce more refined bridge damage and cost estimates needed to support mitigation planning.

Special attention was given to development of capacity models for bent columns due to the critical importance of these components to the seismic performance of modern bridges. The extensive RP1 dataset consisting of 198 experimental test columns was compiled and analyzed to identify performance trends based on physical tests. An equally extensive HS-R analysis program was conducted on California-based column designs which allowed extension of the RP1 experimental trends to higher damage states and consideration of both bent framing and column fixity effects. The combination of these two initiatives provides a sound basis for assignment of column capacity models.

Capacity models of various degrees of sophistication were also developed for the other bridge components considered in this research. Each was aligned to the same set of bridge-system states. Some were based on simply specified CCLS criteria such as joint displacement or strain, while others required a more advanced treatment involving development and application of stochastic response backbone models to represent component performance. A double normalization procedure involving backbone response performance points was introduced that allows for consistent use of each component realization for both demand and capacity assessment.

All capacity models presented herein remain under review by Caltrans and are subject to revision. Caltrans serves as the sole source for final authoritative models and information regarding the g2F project.

CHAPTER 5
CALIFORNIA BRIDGE INVENTORY AND SAMPLING TECHNIQUES

Understanding and characterizing the variability in California bridge designs is necessary to establish reasonable and reliable fragility models. This chapter presents an in-depth characterization of modern (era 3) box-girder bridges in the California inventory. Geometric, materials, and design-detail data were developed with Caltrans assistance directly from the National Bridge Inventory (NBI), through queries and interpretations of information held in Caltrans' bridge maintenance database 'SMART', and through manual review of scanned bridge plans available through Caltrans 'BIRIS' records-archive system.

From these, statistical models were developed and sampled to characterize the design parameters and details needed to specify realistic and representative sets of virtual bridge realizations for FEM demand modeling.

It was recognized that completely random pairing of multiple distributed variables could generate bridge realizations that would not reflect realistic bridge designs. Therefore, this study also develops rational procedures to address three inherent correlations between components embedded in the design process: namely the relationships between column section size and contributing deck area, between column moment capacity and foundation design, and for reasonable pairing of design and applied ground motions. Extensive effort was focused on developing the sampling procedures to capture these design constraints.

5.1 Initial System of Representative Bridge Systems (RBS)

Through taxonomic characterization and analysis of California's 2013 inventory of 7839 concrete box-girder bridges, representing roughly 30% of California's total bridge inventory, Roblee (2016*f*)developed an initial set of 129 ‘Representative Bridge Systems (RBS)’ needing separate PSDM model development. Identification of these RBS was based on: 1) an initial set of taxonomic assumptions regarding populations of bridge types expected to have similar performance (i.e. single-column vs. multi-column bent, or seat vs. diaphragm abutment type), 2) the number of bridges found in the California inventory for each taxonomic combination, 3) findings from a program of sensitivity analyses (Mangalathu, 2017; Soleimani, 2017) using ANOVA analysis to investigate potential taxonomic combinations expected to perform similarly (e.g. 2-column bents are combined with other multi-column bents rather than being treated separately), and 4) judgement regarding the optimal balance between RBS granularity, modeling workload, and fragility model application needs. As the project advanced, it became apparent that additional RBS would be needed to better represent unique performance expectations of originally combined bridge systems (i.e. separating era 2 from era 3; shaft bents from pile/footing supported bents, cantilever from seat-type abutments). Recent versions of the RBS work plan (Roblee, 2020*a*) have 176 base models.

This chapter considers design features of a subset of the taxonomically-based RBS classes noted above, and the following chapter will propose an optimization method to combine these models based on similarity of their fragility models. Table 5.1 summarizes the RBS subset characterized herein which consists of modern (e33) single-frame concrete box girder bridges having no (is0B), single-column (isSB), or multi-column (isMB) bents and seat type abutments (aUS). These are the most common configurations found in the California inventory. Less common multi-frame structures and those having either pier wall or shaft bent interior supports are not considered. Further, diaphragm abutments are extremely uncommon in era-3 designs, and therefore not considered. The multi-column RBS are modeled as having 2 columns to 4 columns, and the span ranges considered are single-span (s11), two-span (s22), three or four-span (s34), and five or six-span (s56).

Table 5.1: Initial bridge categories considered in the analysis.

	Design era	Span number	Column number	Abutment Type
e33_s11_is0B_aUS		1	NA	
e33_s22_isSB_aUS		2	single-column	
e33_s22_isMB_aUS		2	multi-column	
e33_s34_isSB_aUS	>1991	3 or 4	single-column	Seat
e33_s34_isMB_aUS		3 or 4	multi-column	
e33_s56_isSB_aUS		5 or 6	single-column	
e33_s56_isMB_aUS		5 or 6	multi-column	

5.2 Superstructure

Superstructures (or decks) of concrete box-girder bridges in California can have two types of girders, namely reinforced concrete (RC) and prestressed concrete (PC). Inventory data compiled by Roblee (2017*c*) shows overall usage of PC in era-3 bridges is relatively high (70% to 80%). Table 5.2 summarizes the percentage breakout for each span range ID of girder type by span number. These proportions are used for sampling of the deck structure parameters in era-3 bridges.

Table 5.2: Proportion of deck girder types

Span Range ID	Number of Spans	Span Mix (%)	RC Percentage (%)	PC Percentage (%)
s11	1	100	30	70
s22	2	100	20	80
s34	3	70	14	56
	4	30	6	24
s56	5	65	13	52
	6	35	7	28

5.2.1 Span Length

Prestressed concrete beams have higher stiffness than reinforced concrete beams, and therefore can have a longer span length. Table 5.3 summarizes span length models developed by Roblee (2017*c*) from a sample of 390 single-span and 550 single-frame multi-span era-3 box-girder bridges in the California inventory. The span length for single-span RC ranges from 35-feet to 200-feet, whereas single-span PC bridges range from 50-feet to 220-feet. Multi-span minimum lengths are somewhat higher. Broadly, median span length for PC bridges is about 30-feet longer than for RC bridges.

Span ratio is defined as the ratio between the end-span length and the interior-span lengths, and is only defined for bridges with more than two spans. For modeling purposes, all interior spans are assumed to have equivalent length. The span ratio distribution parameters are given in Table 5.3 which show that RC and PC median end-span lengths are 60% and 75% of interior span lengths, respectively.

Table 5.3: Distributions of span length and span ratio (end-span length/interior-span length)

Span Type	Girder Type	Span Length Model Distribution						Span Ratio Distribution					
		Unit	Type§	$\mu^{\dagger}$	$\sigma^{\dagger}$	LB⊕	UB⊕	Unit	Type§	$\mu^{\dagger}$	$\sigma^{\dagger}$	LB⊕	UB⊕
s11	RC	feet	N	105	40	35	200	-	N	-	-	-	-
	PC	feet	N	130	35	50	220	-	N	-	-	-	-
s22	RC	feet	N	135	35	85	200	-	N	-	-	-	-
	PC	feet	N	135	35	75	230	-	N	-	-	-	-
s34	RC	feet	N	110	35	55	190	ft/ft	N	0.6	0.2	0.35	1
	PC	feet	N	155	45	75	250	ft/ft	N	0.75	0.2	0.4	1
s56	RC	feet	N	125	35	75	165	ft/ft	N	0.6	0.2	0.35	1
	PC	feet	N	155	35	95	240	ft/ft	N	0.75	0.2	0.4	1

§ C = constant, LN = lognormal, N = normal, B = binomial, and U = uniform.

† μ denotes the mean and median for normal distribution and lognormal distribution, respectively; σ denotes standard deviation and dispersion (logarithmic standard deviation) for normal distribution and lognormal distribution, respectively.

⊕ LB = lower bound, UB = upper bound.

5.2.2 Deck Width

Typically, there is an increased number of both bent columns and box-girder cells with increased deck width. Modeling distributions capturing the relationships between these transverse bent-profile parameters were developed by Roblee (2016*e*) from a sample of the combined era-2 and era-3 California box-girder bridge inventory comprised of 363 single span and 663 multi-span bridges, 194 having single-column bents and 469 having multi-column bents. Table 5.4 summarizes these models. Note that only odd numbers of cells are considered to accommodate modeling practicalities. For single-span (is0B) bridges, modeled deck width ranges from 22-feet to 110-feet, and can include 3-cell to 11-cell designs in the proportions given in Table 5.4. Two categories of multi-span bridges are considered, those with single-column bents (isSB) and those with multi-column bents (isMB). Bridges with single-column bents are modeled as having deck widths ranging from

22-feet to 60-feet with a maximum of 7-cells. Bridges with multi-column bents consisting of 2 to 4 columns per bent are modeled as having widths that range from 36-feet to 128-feet and have from 3 to 13 cells. Both width range and cell numbers increase with the number of columns, but some overlap occurs per the distributions shown.

Table 5.4: Model distributions for deck widths and cell count as a function of number of bent columns for era-3 box girder bridges.

Internal Support	Column Number	Mix (%)	Span Width Model Distribution						Cell Number Mix (%)					
			Unit	Type§	$\mu^\dagger$	$\sigma^\dagger$	LB⊕	UB⊕	3-cell	5-cell	7-cell	9-cell	11-cell	13-cell
isOB	0	5	feet	N	29	6	22	34	100	0	0	0	0	0
		30	feet	N	41	5	34	48	60	40	0	0	0	0
		25	feet	N	56	8	48	64	0	70	30	0	0	0
		30	feet	N	71	9	64	82	0	25	60	15	0	0
		10	feet	N	88	12	82	110	0	0	50	35	15	0
isSB	1	15	feet	N	28	1.2	22	30	100	0	0	0	0	0
		20	feet	N	34	4	30	38	85	15	0	0	0	0
		55	feet	N	42	2	38	46	75	25	0	0	0	0
		10	feet	N	50	14	46	60	30	50	20	0	0	0
isMB	2	20	feet	N	43	7	36	50	40	60	0	0	0	0
		15	feet	N	57	8	50	66	0	80	20	0	0	0
		10	feet	N	73	22	66	88	0	25	50	25	0	0
	3	10	feet	N	59	18	50	68	0	50	50	0	0	0
		15	feet	N	79	20	68	88	0	0	50	50	0	0
		10	feet	N	98	20	88	108	0	0	20	40	40	0
	4	5	feet	N	75	32	58	90	0	25	40	35	0	0
		15	feet	N	107	38	90	128	0	0	0	40	35	25

§ C = constant, LN = lognormal, N = normal, B = binomial, and U = uniform.
† μ denotes the mean and median for normal distribution and lognormal distribution, respectively; σ denotes standard deviation and dispersion (logarithmic standard deviation) for normal distribution and lognormal distribution, respectively.
⊕ LB = lower bound, UB = upper bound.

5.2.3 Deck-Section Depth

Deck-section structural depth is very closely correlated to the maximum span length but differ between the RC and PC girder types. Table 5.5 summarizes model values for the ratio of structural section depth to maximum span length developed from a sample of 197 cast-in-place box-girder bridges of all eras in California (Roblee, 2016*b*). The means of these inventory-based models closely match standard design values of 0.055 and 0.040 for cast-in-place RC and PC bridge superstructures, respectively. PC decks, due to relatively higher stiffness, have a smaller ratio compared to RC decks. However, considering PC decks are also relatively longer than RC decks, PC decks are only a bit shallower (about 6.0-feet) than the RC decks (about 6.5-feet).

Table 5.5: Models for deck depth to maximum span ratio.

Girder	Span Depth Ratio Model Distribution					
Type	Unit	Type§	$\mu^\dagger$	$\sigma^\dagger$	LB⊕	UB⊕
RC	ft/ft	N	0.054	0.003	0.048	0.061
PC	ft/ft	N	0.041	0.003	0.036	0.046

§ C = constant, LN = lognormal, N = normal, B = binomial, and U = uniform.

† μ denotes the mean and median for normal distribution and lognormal distribution, respectively; σ denotes standard deviation and dispersion (logarithmic standard deviation) for normal distribution and lognormal distribution, respectively.

⊕ LB = lower bound, UB = upper bound.

5.2.4 Other Transverse Cross Section Dimensions

To completely define the shape of a deck, several additional dimensional parameters are needed. In this research, these parameters are the same as defined in Mangalathu (2017): top-flange thickness is related to the spacing of cells following the design policy (Caltrans, 2017), bottom-flange thickness is assumed to be 7.0-inches, and inner-wall flange thickness is taken as 1.0-foot.

5.3 Interior Supports – Column Bents

Column bents are the most common interior support type found in California box-girder bridges, although pier walls and shaft bents are also used. This research considers only column bents.

Column designs in California have evolved from pre-ductile designs in era-1, to early-ductile designs in era-2 due to the 1971 San Fernando earthquake's impact, and more recently to modern-ductile designs in era-3 arising from additional design modifications which emerged from the 1989 Loma Prieta and 1994 Northridge earthquakes. These three eras have distinct designs reflecting changes in design philosophies. Although only era-3 fragility models are developed in this research, some of the column design parameters presented below are for all eras to provide insight into evolving practices.

5.3.1 Average Column Height – Base Models

Bridge column height is a critical parameter in seismic demand modeling of bridges that affects structural periods and can influence the column failure mode. Here, column height is defined as the average clear distance from the top of the bent foundation (footing or pile cap) to the bottom of the bridge deck soffit. When heights vary within or between bents, the average height for the entire bridge frame is used.

Table 5.6 presents base column-height models for the three design eras based on analysis of the California single-frame box-girder bridge inventory (Roblee, 2017*b*). These models were developed from manual plans review of a random sample of 427 bridges including 152 single-column bents and 285 multi-column bents. The 'base' models were developed from the subset of bridges having column height less than 32-feet, representing about 85% of the random sample. Separate models were developed for taller bridges which are considered separately as discussed below. Systematic differences with bent type were not observed, so the base models are applicable to both single- and multi-column bent bridges. However, systematic height differences with era were observed with slight increases in median height occurring in later design eras. While the reasons for this height increase are unclear, one outcome for seismic purposes is that the taller modern bridges have slightly higher ductility capacity.

Table 5.6: Base model distributions for average column height.

Design Era	Span Width Model Distribution					
	Unit	Type§	$\mu^{\dagger}$	$\sigma^{\dagger}$	LB⊕	UB⊕
era-1	feet	N	21.7	0.122	17.0	29.0
era-2	feet	N	22.4	0.122	17.5	30.0
era-3	feet	N	23.6	0.122	18.5	31.0

§ C = constant, LN = lognormal, N = normal, B = binomial, and U = uniform.
† μ denotes the mean and median for normal distribution and lognormal distribution, respectively; σ denotes standard deviation and dispersion (logarithmic standard deviation) for normal distribution and lognormal distribution, respectively.
⊕ LB = lower bound, UB = upper bound.

In addition to the 'base' models listed in Table 5.6, a separate set of 'tall' column-height models were developed from a combination of the base box-girder data set and a targeted sample of all bridge types thought to have reasonably high likelihood of having either tall or unbalanced (TU) longitudinal profiles. The plans-selection criteria for this targeted set included bridges identified as ‘stream crossings’ and bridges where names included the words ‘ramp’, ‘connector’ or ‘viaduct’. Related studies by Soleimani (2017) used this TU data set to explore development of adjustment factors for tall and unbalance effects which are not considered herein. Rather, this research only considers bridges of uniform height as specified by the era-3 model in Table 5.6.

5.3.2 Column-Section Types

A large variety of column-section shapes and sizes are used in California bridges. These include various sized ‘regular’ sections having circular, square, hexagonal, and octagonal shapes with equivalent nominal size in both directions, and various sized ‘wide’ sections including transversely elongated versions of the same basic shapes. Roblee (2018*a*) characterized a representative range in column-section types through manual plans review of 438 California single-frame box-girder bridges designed over all three design eras. For modern (era-3) multi-column bridges, 16 unique regular-section types and an additional 12 unique wide section types were observed in the sample of 75 bridges. For era-3 single-column bridges, 10 unique regular-section types and 10 unique wide section types were observed the sample of 30 bridges. Similar levels of section-type variability were observed in era-2, and even greater variability occurs in era-1.

For purposes of fragility analysis, it was deemed impractical to set up FEM models for all of these unique section types. Therefore, a smaller representative set was selected to broadly reflect the variability in section size, shape, and aspect ratio found in the inventory. Table 5.7 summarizes the section types and inventory-mix proportions selected to represent modern (era-3) bridges modeled herein. Note that single-column designs use larger sections and a larger proportion of wide type than multi-column designs.

Table 5.7: Proportion of modern (era 3) section types used in analyses

Section Shape	Section Size [Inch]	CDA Group	isSB Mix (%)	isMB Mix (%)
Regular/Circular	48	2	0	25
	60	3	0	10
	66	3	20	30
	84	4	10	5
	108	5	10	0
Wide/Oblong	48×72	3	10	15
	48×96	3	10	0
	66×99	4	25	10
	72×108	4	15	0
	84×126	5	0	5

All era-3 regular shapes are modeled as circular columns with spiral or welded hoop reinforcement surrounding a circular core. All era-3 wide shapes are modeled as oblong shapes containing overlapping sets of circular reinforcement. All single-column bents are modeled as having fixed-base connections to the foundation, while all multi-column bents have nominally pinned-base connections to the foundation through use of a reduced section size (i.e., column key).

Table 5.7 also lists a value for the 'CDA Group' of each column section. The CDA classification was developed as part of the inventory plans review (Roblee, 2018*a*) as a means to loosely associate larger column sizes with bridge designs having larger 'contributing deck area (CDA)' to support. The CDA group value ranges from 1 to 5 where larger numbers correspond to larger sections and higher CDA. This topic is further developed in section 5.7.1 where the CDA designation is used as one sampling constraint to assure more realistic bridge designs.

5.3.3 Material Properties

Table 5.8 and Table 5.9 summarize materials strength models for concrete and reinforcement steel that are adopted herein for structural demand modeling. These values were obtained by scaling nominal values by factors to account for overstrength. A factor of 1.25 was applied to concrete materials, and 1.15 to steel materials. The nominal values were assigned by (Roblee, 2016*a*) based on data compiled from manual review of 201 bridge plans of all three eras. Separate values of concrete strength are assigned to the superstructure and column concrete for both RC and PC designs. Similarly, separate steel strength values are assigned to the longitudinal and transverse reinforcing elements. Materials strengths increase modestly with design era.

Table 5.8: Distributions of column and superstructure concrete strength model.

Design Era	Girder Type	Column Concrete Model						Superstructure Concrete Model					
		Unit	Type§	$\mu^\dagger$	$\sigma^\dagger$	LB⊕	UB⊕	Unit	Type§	$\mu^\dagger$	$\sigma^\dagger$	LB⊕	UB⊕
era-1	RC	ksi	N	3.750	0.375	3.000	4.500	ksi	N	3.750	0.375	3.000	4.500
	PC	ksi	N	4.000	0.400	3.200	4.800	ksi	N	4.500	0.450	3.600	5.400
era-2	RC	ksi	N	4.000	0.400	3.200	4.800	ksi	N	4.000	0.400	3.200	4.800
	PC	ksi	N	4.000	0.400	3.200	4.800	ksi	N	4.500	0.450	3.600	5.400
era-3	RC	ksi	N	4.000	0.400	3.200	4.800	ksi	N	4.000	0.400	3.200	4.800
	PC	ksi	N	4.500	0.450	3.600	5.400	ksi	N	5.000	0.500	4.000	6.000

§ C = constant, LN = lognormal, N = normal, B = binomial, and U = uniform.
† μ denotes the mean and median for normal distribution and lognormal distribution, respectively; σ denotes standard deviation and dispersion (logarithmic standard deviation) for normal distribution and lognormal distribution, respectively.
⊕ LB = lower bound, UB = upper bound.

Table 5.9: Distributions of longitudinal and transverse reinforcement strength model.

Design Era	Column Longitudinal Reinforcement Model						Column Transverse Reinforcement Model					
	Unit	Type§	$\mu^\dagger$	$\sigma^\dagger$	LB⊕	UB⊕	Unit	Type§	$\mu^\dagger$	$\sigma^\dagger$	LB⊕	UB⊕
era-1	ksi	N	57.500	3.750	50.000	65.000	ksi	N	57.500	3.750	50.000	65.000
era-2	ksi	N	69.000	4.500	60.000	78.000	ksi	N	63.250	4.125	55.000	71.500
era-3	ksi	N	69.000	4.500	60.000	78.000	ksi	N	69.000	4.500	60.000	78.000

§ C = constant, LN = lognormal, N = normal, B = binomial, and U = uniform.
† μ denotes the mean and median for normal distribution and lognormal distribution, respectively; σ denotes standard deviation and dispersion (logarithmic standard deviation) for normal distribution and lognormal distribution, respectively.
⊕ LB = lower bound, UB = upper bound.

5.3.4 Column Reinforcement Ratios

Simple uniform distribution models were developed for characterization of both longitudinal and transverse column reinforcement ratios for each design era based on a review of 431 column designs in the California bridge inventory (Roblee and Zheng, 2017). These models are depicted as red lines in Figure 5.1 and Figure 5.2, respectively, and model bounds are summarized in Table 5.10. While longitudinal reinforcement ratios are comparable through all eras, the transverse reinforcement ratio increased significantly from era-1 to era-3. Note that the high-reinforcement tails in the data distributions are typically associated with unusual column designs and are ignored as outliers for purposes of demand modeling.

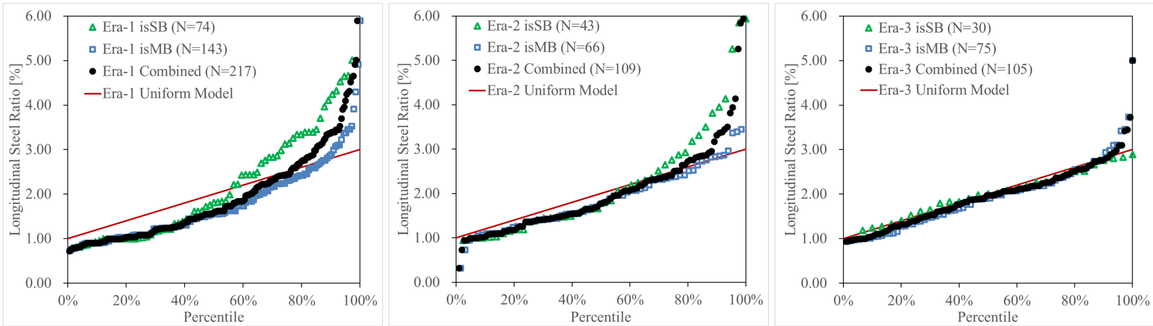

(a) (b) (c)

Figure 5.1: Longitudinal reinforcement ratio for (a) era-1; (b) era-2; and (c) era-3.

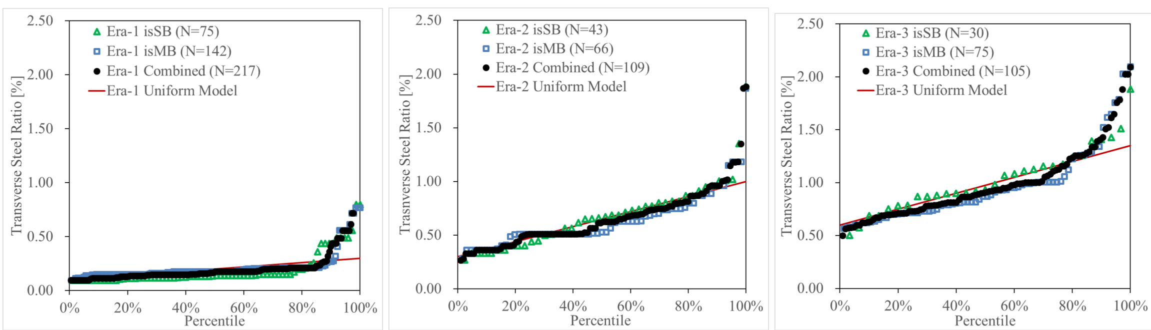

(a) (b) (c)

Figure 5.2: Transverse reinforcement ratio for (a) era-1; (b) era-2; and (c) era-3.

Table 5.10: Uniform distribution bounds for longitudinal (ρ_{sl}) and transverse (ρ_{sv}) reinforcement ratios for bridge columns of three eras .

Model	Reinforcement Ratio Model					
	Unit	Type§	$\mu^{\dagger}$	$\sigma^{\dagger}$	LB$\oplus$	UB$\oplus$
era-1 ρ_{sv}	%	U	-	-	0.10	0.25
era-2 ρ_{sv}	%	U	-	-	0.30	1.00
era-3 ρ_{sv}	%	U	-	-	0.55	1.35
All eras ρ_{sl}	%	U	-	-	1.00	3.00

§ C = constant, LN = lognormal, N = normal, B = binomial, and U = uniform.

† μ denotes the mean and median for normal distribution and lognormal distribution, respectively; σ denotes standard deviation and dispersion (logarithmic standard deviation) for normal distribution and lognormal distribution, respectively.

$\oplus$ LB = lower bound, UB = upper bound.

5.3.5 Reduced Sections for Pinned Column Connections

Reduced sections (or column keys) are used for pinned-base connections at the base of multi-column bents. While multi-column bents of era 1 used both pinned-base and fixed-base connections in similar numbers, the fixed-base detail became less common in era-2 and was virtually eliminated from era-3 bridges not supported on shaft foundations. This section reviews development of a model for specifying reduced section design details needed for creating virtual bridges for demand modeling.

Figure 3.11 shows an example detail for a modern reduced section (or pin or column key) connection at the base of a column. There are three variables needed to specify such a design: the concrete bearing size of the reduced section, the diameter of the pin's reinforced core, and the longitudinal reinforcement ratio (or bar diameters and count) for the pin. Figure 5.3 presents data distributions for related variables obtained through manual plans review of pin details of 63 column designs in the era-3 California box-girder bridge inventory (Zheng, 2020*b*). The three distributions include breakouts into seven groups, categorized by section types (regular/wide) and CDA groups.

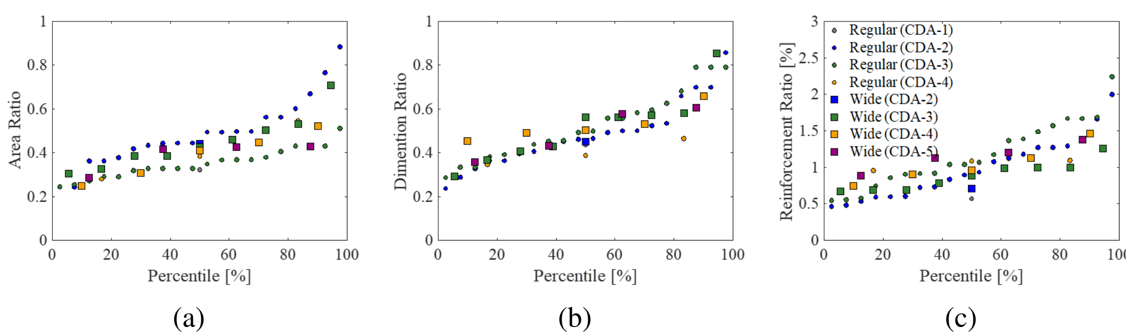

Figure 5.3: Reduced section parameters (Zheng, 2020*b*): (a) area ratio; (b) dimension ratio; and (c) longitudinal reinforcement ratio.

The first variable, called the area ratio, determines the concrete bearing size. It describes the ratio between the concrete bearing area in the reduced section and that in the main section (column main body section). These data reveal three distinct subgroups corresponding to, from bottom to top: regular sections with CDA $\leq$ 2; wide sections; and regular sections with CDA ≥ 3. Lognormal models fit to these subgroups are summarized in Table 5.11. For modeling purposes, it is assumed that the concrete bearing area is a circular section for regular columns and a rectangular section for wide columns where the rectangle has the same aspect ratio as the main section. The additional assumption coupled with the area defines the dimension of a reduced section.

The inventory cases show that the reinforcement used in a reduced section are arranged circularly regardless of the section types. Thus, the second variable named 'dimension ratio' defines the ratio between the pin-core diameter and the 'critical dimension' of concrete bearing. This critical dimension equals either the diameter of a regular-column section or the shorter dimension of a wide-column section. Based on the data in Figure 5.3(b), the two section-types and different CDA groups all have comparable distributions. Therefore, the specification model for the 'dimension ratio' is assumed to be the same for all types of sections considered in this research.

Table 5.11: Distributions of multiple reduced section parameters.

Variables	Distribution Models					
	Unit	Type§	$\mu^\dagger$	$\sigma^\dagger$	LB⊕	UB⊕
Area Ratio for Regular Sections (CDA ≤ 2)	in^2/in^2	LN	0.450	0.300	0.250	0.800
Area Ratio for Regular Sections (CDA ≥ 2)	in^2/in^2	LN	0.350	0.200	0.250	0.500
Area Ratio for Wide Sections	in^2/in^2	LN	0.400	0.250	0.250	0.700
Dimension Ratio	in/in	LN	0.500	0.300	0.250	0.850
Reinforcement Ratio for Regular Sections	%	LN	1.000	0.400	0.500	2.250
Reinforcement Ratio for Wide Sections	%	LN	0.950	0.250	0.500	1.500

§ C = constant, LN = lognormal, N = normal, B = binomial, and U = uniform.
† μ denotes the mean and median for normal distribution and lognormal distribution, respectively; σ denotes standard deviation and dispersion (logarithmic standard deviation) for normal distribution and lognormal distribution, respectively.
⊕ LB = lower bound, UB = upper bound.

The last variable is the longitudinal reinforcement ratio for the reduced section, defined as reinforcement area per unit concrete bearing area. Based on the inventory cases, the reinforcement sizes used in the reduced section tend to be somewhat smaller than those used in the main section. This study assumes the longitudinal reinforcement used in main sections to be evenly split between #11 and #14 bars, and uses 20%, 20%, 20%, and 40% for #8, #9, #10, and #11 bars, respectively, for the reduced sections.

5.3.6 Column Axial Load Ratio

Column axial load ratio is an influential design parameter, and its evaluation here serves as an independent check on the reasonableness of the set of virtual bridges specified using combinations the deck, column and material variables noted in previous sections. Axial load ratio values easily computed after specifying all the geometric variables considered in a box-girder bridge. The column axial load ratio is estimated using a uniformly-distributed deck gravity load and assuming a fixed-pin boundary condition for a two-span bridge. The resistance or axial load acting on the column is $3/8$ of the total deck load. Considering other variables such as deck dimensions, column section size and concrete strength, the axial load ratio distribution for a simulated set of era-3, 2-span concrete box-girder bridges is shown in Figure 5.1. Note that very similar distributions for single-column and multi-column bent are achieved regardless of the substantive differences in specified deck geometries and column-section sizes. Overall, the resulting axial load ratio distributes with a median of about 10% and ranges from 5% to 30% with 0.40 dispersion. This is reasonably consistent with design experience.

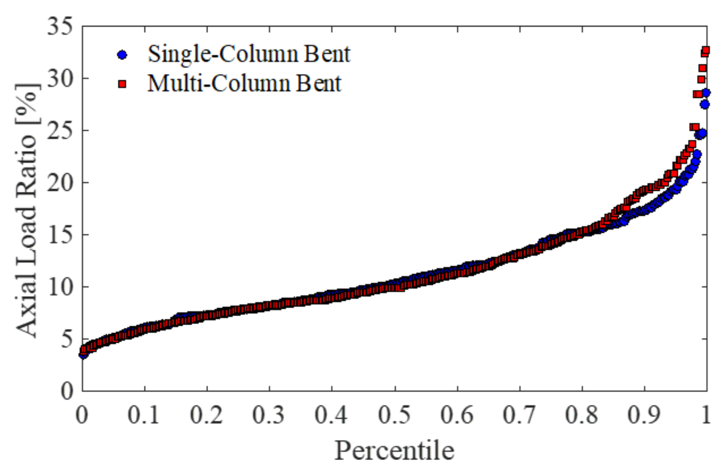

Figure 5.4: Column axial load ratio distribution for simulated set of era-3 bridges

5.4 Abutment

Virtually all era-3 concrete box-girder bridges have seat-type abutments which accommodate thermal movement better than older diaphragm systems. Seat-type abutments provide bearing support to the superstructure and constrain deck movement longitudinally by the abutment backwall and transversely by the shear key. This section reviews the parameter distributions used for the specification of seat-type abutments, except for the more complicated foundation elements which are addressed in section 5.5.

5.4.1 Backfill, Side-fill, and Front-fill

subsection 3.3.7 described the hyperbolic backbone response model proposed by Xie et al. (2019) which is used in this research to characterize soil loads acting on the back, side and front surfaces of the abutment. Table 5.12 provides distribution parameters for the two base model parameters ($P_{ult,0}$, $K_{max,0}$)) which apply specifically to a 5.5-foot soil height. Scaling factors described in subsection 3.3.7 are used to compute parameter values (P_{ult}, K_{max}) for other soil heights. Only the 'sand' model is considered for the era-3 bridges modeled herein. This is based on revised Caltrans backfill specifications for the era which largely eliminated fine-grained and clayey materials. The 'all' model, which incorporates both soil types is used for analyses of earlier eras.

Table 5.12: Distributions for Xie et al. (2019) hyperbolic backfill response model parameters ($P_{ult,0}$ and $K_{max,0}$) for the 5.5-foot soil height base case (per foot width).

Soil	$P_{ult,0}$						$K_{max,0}$						Other parameters		
Type	Unit	Type§	$\mu^\dagger$	$\sigma^\dagger$	LB⊕	UB⊕	Unit	Type§	$\mu^\dagger$	$\sigma^\dagger$	LB⊕	UB⊕	$\rho^\dagger$	α_1	α_2
Sand	kips/ft	LN	35.0	0.25	22.0	55.0	kips/ft/in	LN	85.0	0.20	60.0	120.0	0.45	1.60	0.70
Clay	kips/ft	LN	29.0	0.25	18.0	47.0	kips/ft/in	LN	45.0	0.20	30.0	70.0	0.95	1.40	0.60
All	kips/ft	LN	32.0	0.25	20.0	51.0	kips/ft/in	LN	65.0	0.35	30.0	120.0	0.65	1.50	0.65

§ C = constant, LN = lognormal, N = normal, B = binomial, and U = uniform.
† μ denotes the mean and median for normal distribution and lognormal distribution, respectively; σ denotes standard deviation and dispersion (logarithmic standard deviation) for normal distribution and lognormal distribution, respectively. ρ is correlation between the two parameters.
⊕ LB = lower bound, UB = upper bound.

Table 5.13 provides model distributions for two abutment dimensions, the backwall and stem wall , for each of the three design eras. All eras have comparable backwall heights which are largely tied to deck structural depth. However, median stem wall height increases over the three design eras. In era-1, the backwall is higher than the stem wall, while in era-3 backwall is shorter than the stem wall. The changes in stem wall height increase the probability of backwall-connection fracture in era-3 bridges because the shorter stem walls of earlier eras might provide insufficient backfill-B resistance to fail the backwall.

Table 5.13: Distributions of abutment dimensions.

Design Era	Backwall Height (Backfill-A) Model						Stem Wall Height (Backfill-B) Model					
	Unit	Type§	$\mu^{\dagger}$	$\sigma^{\dagger}$	LB⊕	UB⊕	Unit	Type§	$\mu^{\dagger}$	$\sigma^{\dagger}$	LB⊕	UB⊕
era-1	feet	LN	6.10	0.221	3.90	9.50	feet	LN	4.10	0.400	1.80	9.70
era-2	feet	LN	6.20	0.217	4.00	9.60	feet	LN	7.40	0.300	4.00	13.60
era-3	feet	LN	6.10	0.262	3.60	10.30	feet	LN	10.20	0.200	6.40	16.20

§ C = constant, LN = lognormal, N = normal, B = binomial, and U = uniform.
† μ denotes the mean and median for normal distribution and lognormal distribution, respectively; σ denotes standard deviation and dispersion (logarithmic standard deviation) for normal distribution and lognormal distribution, respectively.
⊕ LB = lower bound, UB = upper bound.

The ‘frontfill’ is the soil resistance acting on the front of the stem wall in the longitudinal direction, whereas backfill-B was acting on the back of the stem wall). The frontfill soil depth is estimated as $H_{FF} = H_A + H_B - H_{deck} - 3.0\,\text{feet} - 1.0\,\text{feet}$ where H_A and H_B are the heights of the backwall and stem wall, respectively. This equation assumes the frontfill contact at the abutment is 3.0-feet below the bottom of the deck, and has a slope that reduces the soil capacity assumed to be approximately equivalent to 1.0-foot of front-fill height. This approximation is based on the design shown in the ’Section A-A’ detail in Figure A.3.

The ‘sidefill’ is the soil resistance acting in the transverse direction on the side of the stem wall. For rough estimation purposes, the height of the sidefill is assumed to be the mean of backfill and frontfill given that there is typically a uniform soil slope from the back to the front. While the frontfill resistance applies to the same abutment width as the backfill, sidefills have a different width model which roughly approximates the stem wall width plus some portion of connected wingwalls. The crude relationship adopted for sidefill width is a lognormal distribution with median = 3.7-feet and dispersion = 0.20 which again is based on the design in Figure A.3.

5.4.2 Elastomeric Bearing

California seat-type abutment design underwent substantial change late in era 1, and the design evolution included a change in bearing type from rocker bearings to elastomeric bearings. Virtually all of era-2 and era-3 designs, and a small proportion of era-1 designs use elastomeric bearings. Roblee (2018*h*) compiled bearing dimensional data from manual review of bridge plans for 19 era-1, 52 era-2 and 66 era-3 bridges which was used to develop the era-based height and unit stiffness models shown in Table 5.14. Unit elastomeric bearing stiffness is a function of bearing thickness, area, average spacing and temperature-dependent modulus of the elastomeric material (Roblee, 2015*a*) and represents linear-elastic stiffness per unit width of abutment. In the development of these models, elastomeric modulus was computed for a randomized temperature range from -20 to +120 degrees Fahrenheit to represent the wide range of environmental conditions in California. Note that the unit stiffness value for era-3 is lowest as it is associated with thicker pads. A uniform range for friction coefficient was assumed for all eras.

Table 5.14: Distributions of modeling parameters for elastomeric bearings. Stiffness value is normalized by abutment length.

Parameters	Design Era	Parameter Model					
		Unit	Type§	$\mu^{\dagger}$	$\sigma^{\dagger}$	UB⊕	LB⊕
Height	era-1	inch	LN	1.50	0.200	1.00	2.00
	era-2			1.70	0.300	1.00	3.00
	era-3			3.00	0.300	1.50	5.50
Unit Stiffness	era-1	(kips/in)/ft	LN	1.50	0.350	0.30	7.00
	era-2			2.00	0.550	0.70	6.00
	era-3			1.00	0.450	0.40	2.50
Friction Coefficient	all eras	kips/kips	N	0.30	0.100	0.10	0.50

§ C = constant, LN = lognormal, N = normal, B = binomial, and U = uniform.
† μ denotes the mean and median for normal distribution and lognormal distribution, respectively; σ denotes standard deviation and dispersion (logarithmic standard deviation) for normal distribution and lognormal distribution, respectively.
⊕ LB = lower bound, UB = upper bound.

5.4.3 Backwall

Seat-type abutments with straight backwalls, as illustrated in Figure 3.25 , are virtually the only design used in era-3 California bridge inventory and considered in the analyses herein. Figure 3.25 provides an illustration of this design and subsection 3.3.3 discusses design parameters. Backwall height models are provided in subsection 3.3.3, and subsection 3.3.3 discusses reinforcement details affecting the shear-failure fusing mechanism.

5.4.4 External Non-Isolated Shear Key

California box-girder bridges in era-3 are typically designed with external non-isolated shear keys. Subsection 3.3.2 illustrated the response backbone shape using methods proposed by Megally et al. (2001). Figure 5.5 summarizes results of applying these methods to key designs for 22 inventory bridges . To generalize a key-response specification procedure, a four-variable model (Zheng, 2019) is used to specify the first two points in the shear key model shown in Figure 3.21 namely F_{sk2}, Δ_2, F_{sk1}/F_{sk2}, and Δ_1/Δ_2. Lognormal distribution parameters for this model are provided in Table 5.15. There is an internal correlation between these variables as shear keys with higher strength (F_{sk2}) tend to have larger corresponding deformation at peak strength (Δ_2). The correlation models between these four variables is also provided in Table 5.15. The last parameter needed for the shear key response model is Δ_3, which is assumed to be 3.35 times of Δ_2 as a result of the relationship between Equation 3.29b and Equation 3.29c.

5.4.5 Abutment Joint Gaps

Abutment joint gaps, longitudinally between the deck and abutment backwall, and transversely between the deck and the shear key, play an important role in whole-bridge response as they govern how much deck deflection needs to occur before abutment responses are engaged. Large gaps tend to transfer more load to the internal supports, while small gaps quickly engage abutment responses.

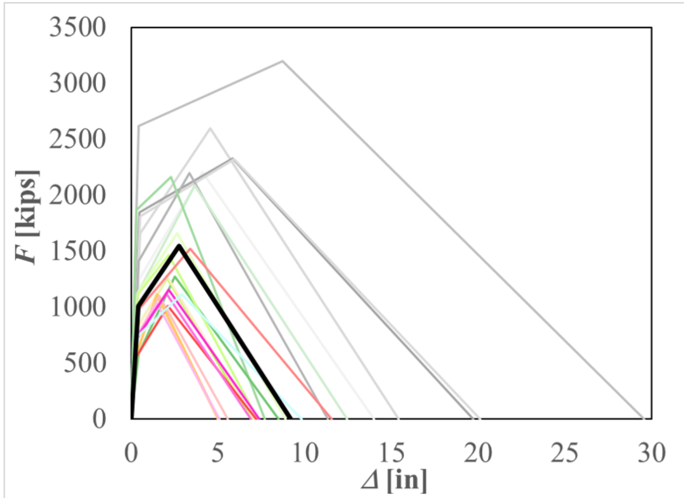

Figure 5.5: Shear key model samples.

Table 5.15: Distributions of modeling parameters for specifying external non-isolated shear keys (Zheng, 2019).

Variable	Shear Key Model						Correlation			
	Unit	Type§	$\mu^{\dagger}$	$\sigma^{\dagger}$	LB⊕	UB⊕	F_{sk2}	Δ_2	F_{sk1}/F_{sk2}	Δ_1/Δ_2
F_{sk2}	kips	LN	1550.0	0.350	1000.0	3200.0	1.00	0.85	0.45	-0.85
Δ_2	inch	LN	2.75	0.500	1.50	8.50	0.85	1.00	0.45	-0.85
F_{sk1}/F_{sk2}	kips/kips	LN	0.65	0.150	0.45	0.85	0.45	0.45	1.00	-0.30
Δ_1/Δ_2	inch/inch	LN	0.15	0.350	0.05	0.25	-0.85	-0.85	-0.30	1.00

§ C = constant, LN = lognormal, N = normal, B = binomial, and U = uniform.
† μ denotes the mean and median for normal distribution and lognormal distribution, respectively; σ denotes standard deviation and dispersion (logarithmic standard deviation) for normal distribution and lognormal distribution, respectively.
⊕ LB = lower bound, UB = upper bound.

Table 5.16 summarizes the lognormal distribution parameters for joint gaps adopted herein. The longitudinal values are based on inventory analysis of movement rating data for 145 era-1, 132 era-2, and 338-era bridges (Roblee, 2018c). Generally, median values for longitudinal joint gap size increase from era-1 to era-3. Era-2 has the largest dispersion in values as this represents a transitional period in design practices. The model for transverse joint size is assumed and applies only to eras 2 and 3 when external keys were used. For these eras, median longitudinal gap size is larger than transverse gap size. Constraints on lateral movement of era-1 designs is provided by rocker bearing assemblies which are not considered herein.

Table 5.16: Distributions of longitudinal joint gap sizes for three eras (Roblee, 2018*c*) and assumed transverse joint model for eras 2 and 3.

Direction	Design Era	Joint Gap Size Model					
		Unit	Type[§]	$\mu^{\dagger}$	$\sigma^{\dagger}$	UB[⊕]	LB[⊕]
Longitudinal	era-1	inch	LN	0.85	0.5	0.31	2.31
	era-2			1.55	0.6	0.47	5.14
	era-3			2.1	0.45	0.85	5.17
Transverse	eras 2 & 3	inch	LN	1	0.08	0.85	1.15

[§] C = constant, LN = lognormal, N = normal, B = binomial, and U = uniform.
[†] μ denotes the mean and median for normal distribution and lognormal distribution, respectively; σ denotes standard deviation and dispersion (logarithmic standard deviation) for normal distribution and lognormal distribution, respectively.
[⊕] LB = lower bound, UB = upper bound.

5.5 Foundations

In era-3 bridges, responses of both column-bent and abutment foundations are modeled with lateral springs in the longitudinal and transverse direction. Column-bent foundations also consider rotational springs in each direction.

5.5.1 Pile-Cap and Spread-Footing Dimensions

The first step in the process of specifying a foundation system for a virtual bridge realization is to sample models of pile-cap or footing dimensions. Pile cap dimensions affect the geotechnical group-effects factor of pile foundations and also the lateral soil resistance acting on the sides of the cap/footing of both types of column foundations. Spread footing response models also highly depend on the footing dimension.

Column Bents

The dimensions of both pile caps and spread footings beneath column bents are primarily defined by four parameters: length (L), breadth (B), thickness (T), and embedment depth (D), as illustrated in Figure 5.6. Additionally, two dimensional constraints, total area and aspect ratio, are adopted to assure realistic cap/footing sizes and shapes. For multiple column bents, footing dimensions are also somewhat constrained by the column spacing (see Chapter 3).

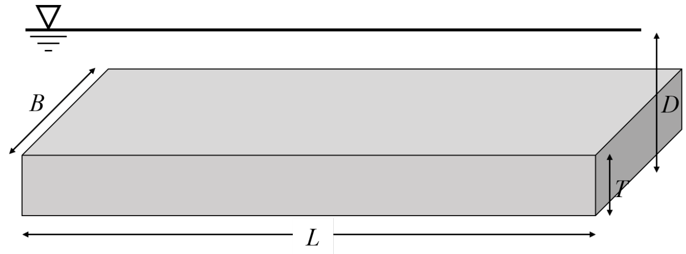

Figure 5.6: Primary Pile-Cap/Footing Dimensions..

The cap/footing dimensional models presented in Table 5.17 through Table 5.18 were developed from analysis of a sample of 77 era-3 box-girder bridges in the California inventory (Roblee, 2020*b*). Separate models were developed for single-column and multi-column bents and further broken out by column-section shape (i.e. regular/wide) and column-section size category (i.e. CDA Group). Note that spread footings are not typically used with single-column bent designs due to low rotational capacity, and usage is limited to multi-column bents having smaller column-section sizes and pinned-base connections.

Table 5.17: Distributions of column pile-cap/footing dimensions (length and breadth) by bent type and both column-section size and shape (Roblee, 2018*d*, 2020*b*).

Support Type	CDA	Type	Cap/Footing Length (L) Model						Cap/Footing Breadth (B) Model					
			Unit	Type§	μ†	σ†	LB⊕	UB⊕	Unit	Type§	μ†	σ†	LB⊕	UB⊕
isSB Regular	3	Pile-Cap	inch	N	261.0	38.0	216.0	328.0	inch	N	260.0	39.0	216.0	328.0
	4	Pile-Cap	inch	N	312.0	36.0	276.0	348.0	inch	N	319.0	27.0	204.0	360.0
	5	Pile-Cap	inch	N	378.0	30.0	348.0	408.0	inch	N	378.0	30.0	348.0	408.0
isSB Wide	3	Pile-Cap	inch	N	293.0	21.0	264.0	315.0	inch	N	222.0	26.0	197.0	258.0
	4	Pile-Cap	inch	N	299.0	67.0	204.0	407.0	inch	N	237.0	48.0	180.0	335.0
isMB Regular	2	Pile-Cap	inch	N	152.0	49.0	106.0	288.0	inch	N	134.0	30.0	106.0	216.0
		Footing	inch	N	182.0	20.0	153.0	216.0	inch	N	174.0	26.0	134.0	216.0
	3	Pile-Cap	inch	N	158.0	33.0	108.0	228.0	inch	N	152.0	27.0	138.0	228.0
		Footing	inch	N	188.0	11.0	177.0	207.0	inch	N	188.0	11.0	177.0	207.0
	4	Pile-Cap	inch	N	216.0	10.0	204.0	228.0	inch	N	204.0	20.0	180.0	228.0
		Footing	inch	N	-	-	-	-	inch	N	-	-	-	-
isMB Wide	3	Pile-Cap	inch	N	170.0	25.0	144.0	216.0	inch	N	154.0	18.0	134.0	180.0
		Footing	inch	N	213.0	25.0	181.0	242.0	inch	N	197.0	14.0	181.0	216.0
	4	Pile-Cap	inch	N	228.0	44.0	192.0	288.0	inch	N	187.0	27.0	144.0	228.0
		Footing	inch	N	-	-	-	-	inch	N	-	-	-	-
	5	Pile-Cap	inch	N	294.0	42.0	252.0	336.0	inch	N	243.0	21.0	222.0	264.0
		Footing	inch	N	-	-	-	-	inch	N	-	-	-	-

§ C = constant, LN = lognormal, N = normal, B = binomial, and U = uniform.
† μ denotes the mean and median for normal distribution and lognormal distribution, respectively; σ denotes standard deviation and dispersion (logarithmic standard deviation) for normal distribution and lognormal distribution, respectively.
⊕ LB = lower bound, UB = upper bound.

As shown in Table 5.17, both the length and breadth of pile-caps and footings are larger for single-column bents (isSB) than for multi-column bents (isMB), and increase with the column-section size range (i.e. represented by CDA value). For regular sections, these two dimensions are distributed in a comparable range, while wide-section columns generally have a larger breadth dimension in the bent-transverse direction. Note that spread footing usage in the era-3 inventory sample was limited to use in multi-column bents with CDA-2 or CDA-3 columns.

Table 5.18 provides inventory values used to constrain dimensional sampling of the values in Table 5.17. Oversampling of plan dimensions was used as needed when a pair of randomized values did not meet both constraint criteria.

Table 5.18: Column pile-cap/footing size constraints by bent type and both column-section size and shape (Roblee, 2018*d*, 2020*b*).

Support Type	CDA	Type	Area Constraints			Aspect Ratio Constraints		
			Unit	LB⊕	UB⊕	Unit	LB⊕	UB⊕
isSB Regular	3	Pile-Cap	in^2	47000.0	108000.0	in/in	1.00	1.00
	4	Pile-Cap	in^2	56000.0	133000.0	in/in	1.00	1.35
	5	Pile-Cap	in^2	121000.0	166000.0	in/in	1.00	1.00
isSB Wide	3	Pile-Cap	in^2	55000.0	77000.0	in/in	1.16	1.60
	4	Pile-Cap	in^2	41000.0	136000.0	in/in	1.00	2.00
isMB Regular	2	Pile-Cap	in^2	11000.0	62000.0	in/in	1.00	1.56
		Footing	in^2	23000.0	47000.0	in/in	1.00	1.35
	3	Pile-Cap	in^2	16000.0	52000.0	in/in	0.75	1.36
		Footing	in^2	31000.0	43000.0	in/in	1.00	1.00
	4	Pile-Cap	in^2	39000.0	52000.0	in/in	1.00	1.20
		Footing	in^2	-	-	in/in	-	-
isMB Wide	3	Pile-Cap	in^2	21000.0	39000.0	in/in	1.00	1.25
		Footing	in^2	33000.0	47000.0	in/in	1.00	1.24
	4	Pile-Cap	in^2	28000.0	66000.0	in/in	1.00	1.53
		Footing	in^2	-	-	in/in	-	-
	5	Pile-Cap	in^2	56000.0	89000.0	in/in	1.14	1.27
		Footing	in^2	-	-	in/in	-	-

⊕ LB = lower bound, UB = upper bound.

Table 5.19 provides models for footing thickness and embedment depth. As illustrated in Figure 5.6, embedment depth is measured from ground surface to the base of the cap/footing. Generally, both thickness and embedment depth values increase with larger column-section size (i.e. CDA value).

Table 5.19: Distributions of column pile-cap/footing dimensions (thickness and embedment depth) by bent type and both column-section size and shape (Roblee, 2018*d*, 2020*b*).

Support Type	CDA	Type	Cap/Footing Thickness (T) Model						Cap/Footing Embedment Depth (D) Model					
			Unit	Type[§]	$\mu^{\dagger}$	$\sigma^{\dagger}$	LB[⊕]	UB[⊕]	Unit	Type[§]	$\mu^{\dagger}$	$\sigma^{\dagger}$	LB[⊕]	UB[⊕]
isSB Regular	3	Pile-Cap	inch	N	59.0	8.0	47.0	69.0	inch	N	88.0	8.0	71.0	96.0
	4	Pile-Cap	inch	N	69.0	9.0	60.0	78.0	inch	N	119.0	9.0	84.0	128.0
	5	Pile-Cap	inch	N	83.0	5.0	78.0	87.0	inch	N	150.0	10.0	140.0	160.0
isSB Wide	3	Pile-Cap	inch	N	69.0	7.0	60.0	78.0	inch	N	96.0	13.0	84.0	115.0
	4	Pile-Cap	inch	N	58.0	10.0	42.0	72.0	inch	N	94.0	12.0	80.0	120.0
isMB Regular	2	Pile-Cap	inch	N	44.0	7.0	36.0	60.0	inch	N	81.0	18.0	60.0	120.0
		Footing	inch	N	42.0	4.0	36.0	48.0	inch	N	80.0	14.0	55.0	96.0
	3	Pile-Cap	inch	N	47.0	4.0	39.0	55.0	inch	N	82.0	14.0	60.0	100.0
		Footing	inch	N	47.0	4.0	42.0	51.0	inch	N	88.0	16.0	65.0	115.0
	4	Pile-Cap	inch	N	62.0	1.0	60.0	63.0	inch	N	103.0	5.0	100.0	110.0
		Footing	inch	N	-	-	-	-	inch	N	-	-	-	-
isMB Wide	3	Pile-Cap	inch	N	48.0	5.0	42.0	57.0	inch	N	89.0	15.0	70.0	115.0
		Footing	inch	N	50.0	2.0	48.0	52.0	inch	N	87.0	19.0	60.0	100.0
	4	Pile-Cap	inch	N	57.0	5.0	48.0	60.0	inch	N	103.0	11.0	90.0	120.0
		Footing	inch	N	-	-	-	-	inch	N	-	-	-	-
	5	Pile-Cap	inch	N	60.0	1.0	59.0	61.0	inch	N	110.0	10.0	100.0	120.0
		Footing	inch	N	-	-	-	-	inch	N	-	-	-	-

[§] C = constant, LN = lognormal, N = normal, B = binomial, and U = uniform.
[†] μ denotes the mean and median for normal distribution and lognormal distribution, respectively; σ denotes standard deviation and dispersion (logarithmic standard deviation) for normal distribution and lognormal distribution, respectively.
[⊕] LB = lower bound, UB = upper bound.

Abutment Walls

Unlike for columns, dimensional models for pile-cap/footing foundations supporting abutment walls require only two parameters. Values used for era-3 abutment wall foundations are provided in Table 5.12. Here, it is assumed that the sampled bridge width defines the abutment length model, and the embedment depth is taken to be equal to the frontfill depth.

5.5.2 Spread Footings – Inventory Proportions and Response Modeling Parameters

Inventory analyses of era-3 bridge foundation design suggest usage of spread footings is less common than pile foundations. Roblee (2018*d*) shows spread footing usage for column foundations is extremely rare for single-column bents and for multi-column bents having very large column-section size (CDA 4 or 5). For multi-column bents having smaller column sections (CDA $\leq$ 3), only about 40% are supported on spread footings

Table 5.20: Distributions of pile-cap/footing dimensions used for era-3 abutment-wall foundations (Roblee, 2018*b*).

Parameters	Abutment Dimension Model					
	Unit	Type§	$\mu^\dagger$	$\sigma^\dagger$	LB⊕	UB⊕
Length (L)	Deck Width					
Breadth (B)	feet	LN	9.3	0.2	6.8	12.5
Thickness (T)	feet	LN	2.0	0.2	1.5	2.7
Embedment Depth (D)	Front-fill Depth					

§ C = constant, LN = lognormal, N = normal, B = binomial, and U = uniform.
† μ denotes the mean and median for normal distribution and lognormal distribution, respectively; σ denotes standard deviation and dispersion (logarithmic standard deviation) for normal distribution and lognormal distribution, respectively.
⊕ LB = lower bound, UB = upper bound.

based on a sample size of 45 bridges.

Roblee (2018*e*) shows approximately 30% of abutment walls are founded on spread footings in an inventory sample of 89 bridges. There may also be a positive correlation between spread footing usage at both the column and abutment locations for bridge sites underlain by firmer soil/rock materials. For example, spread footing usage for abutment foundations is very rare for single-column bents and for multi-column bents having very large column-section size (CDA 4 or 5). In multi-column bents bridges, there are 60% of abutments seating on spread footing for those having CDA-2 column sections, and the proportion decreases to 40% for bridges having CDA-3 column sections.

Spread-footing response is modeled as a hyperbolic backbone shape as noted in subsection 3.3.7. Table 5.21 provides model-parameter distributions developed by Xie (2021) for separate application to column and abutment locations based on analysis of typical era-3 bridge-foundation designs. Differences in these models is due to differences in the foundation shape and embedment at the two locations.

5.5.3 Pile Layout

subsection 5.5.1 described models and constraints for the dimensioning of pile caps. This and the next sections describe considerations for the specification of both the layout and type of piles. subsection 5.7.2 will describe the iterative process used for pile-foundation

Table 5.21: Distributions of response-backbone parameters for spread-footing foundations at column bents and abutment walls (Xie, 2021).

Location	Spread Footing Unit Strength (t_u/BL) Model						Spread Footing Unit Yield Deformation (z_{50}/B) Model					
	Unit	Type§	$\mu^\dagger$	$\sigma^\dagger$	LB⊕	UB⊕	Unit	Type§	$\mu^\dagger$	$\sigma^\dagger$	LB⊕	UB⊕
Column	ksi	LN	3.05	0.40	1.40	6.80	in/in	LN	0.0040	0.5000	0.0015	0.0110
Abutment	ksi	LN	1.95	0.33	1.00	3.75	in/in	LN	0.0050	0.5000	0.0015	0.0135

§ C = constant, LN = lognormal, N = normal, B = binomial, and U = uniform.
† μ denotes the mean and median for normal distribution and lognormal distribution, respectively; σ denotes standard deviation and dispersion (logarithmic standard deviation) for normal distribution and lognormal distribution, respectively.
⊕ LB = lower bound, UB = upper bound.

specification at column-bent locations to assure the foundation capacity is commensurate with the column moment capacity.

Column Bents

Table 5.22 presents the models for the layout of a pile foundation beneath a column-bent based on the inventory analysis noted earlier in subsection 5.5.1. These models define the number of pile rows in both the longitudinal and transverse directions as a function of bent type and column shape and size. The total-pile count model provides a constraint to assure the separately sampled pile-row models yield a realistic total.

Table 5.22: Distributions of pile layout parameters for era-3 column-bent pile foundations by bent type and both column-section size and shape (Roblee, 2018*d*, 2020*b*).

Support Type	CDA	Longitudinal Pile Number Model					Transverse Pile Number Model					Total Number Constraints	
		Type§	$\mu^\dagger$	$\sigma^\dagger$	LB⊕	UB⊕	Type§	$\mu^\dagger$	$\sigma^\dagger$	LB⊕	UB⊕	LB⊕	UB⊕
isSB Regular	3	N	5.0	0.8	4	6	N	5.0	0.8	4	6	16	32
	4	N	7.0	0.5	3	8	N	7.0	1.0	4	8	12	46
	5	N	7.5	1.5	6	9	N	7.5	1.5	6	9	36	68
isSB Wide	3	N	5.0	0.8	4	6	N	6.7	1.2	5	8	20	36
	4	N	5.0	0.7	4	6	N	6.3	1.0	5	8	20	42
isMB Regular	2	N	3.2	0.6	2	4	N	3.5	0.7	3	5	6	16
	3	N	3.9	0.6	3	5	N	4.0	0.5	3	5	12	16
	4	N	5.0	0.0	5	5	N	5.3	0.5	5	6	25	30
isMB Wide	3	N	3.8	0.7	3	5	N	4.2	0.7	3	5	8	25
	4	N	3.8	0.7	3	5	N	4.4	0.8	3	5	8	25
	5	N	4.5	0.5	4	5	N	5.5	0.5	5	6	20	30

§ C = constant, LN = lognormal, N = normal, B = binomial, and U = uniform.
† μ denotes the mean and median for normal distribution and lognormal distribution, respectively; σ denotes standard deviation and dispersion (logarithmic standard deviation) for normal distribution and lognormal distribution, respectively.
⊕ LB = lower bound, UB = upper bound.

Abutment Walls

Piles within foundations beneath seat-type abutments are typically arranged as two rows along the length of abutment, where pile spacing within the row is variable. Figure 5.7 presents inventory data and a model for relationship between total piles and abutment length. The lognormal model has median $\mu = \exp(\ln L - 1.2)$. and dispersion $\beta = 0.35$ where L is the abutment length in feet. This model is directly sampled to specify the total number of piles in a virtual bridge realization.

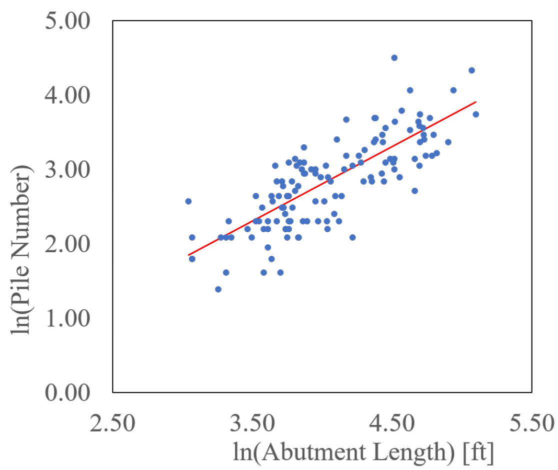

Figure 5.7: Relationship between the total pile number and abutment length in natural logarithm space.

5.5.4 Pile Types and Inventory Proportions

Caltrans defines a ‘Class’ of piles to include a variety of standard pile designs that meet the same nominal design requirement for axial load capacity. Figure 4.14(a-c) show the variety of era-3 designs used in California bridges, though only Class-140 and Class-200 designs are commonly found in era-3 box-girder designs. By definition, the Class-200 piles have a higher axial capacity than Class-140 piles, but there is some overlap in the lateral performance of various piles within these two classes.

Inventory analysis of era-3 box-girder bridges shows that the usage proportions of Class-140 and Class-200 piles varies between the column-bent and abutment-wall locations, and also by the bent type and column size at the bent location. At abutment walls, approximately 65% of pile-supported foundations are on Class-140 designs. At single-column bent locations, Class-140 pile usage decreases from approximately 40% for CDA-3, to 30% for CDA-4, and lastly, to 0% for CDA-5 column sections. Similarly, at multi-column bent locations, Class-140 pile usage decreases from approximately 75% for CDA-2, to 60% for CDA-3, to 25% for CDA-4, and again, 0% for CDA-5 column sections.

Next, one must identify the usage proportions of specific pile designs within each class. Roblee (2018*f*) summarized design distinctions of Caltrans standard piles used in each of the three design eras, and also developed the approximate inventory-usage proportions shown in Table 5.23 for the most commonly used era-3 design variations within the two classes. Separate proportions are provided for foundations supporting column-bents and abutment walls.

The translational backbone response of each individual pile selection is specified using stochastic models developed by Xie et al. (2021, 2020) for each Caltrans standard pile design of all three eras. The median value for peak strength from these models was used to rank order the 11 types of standard piles of both classes as noted at the left of Table 5.23. This rank order is used in the iterative column-foundation specification procedure discussed in subsection 5.7.2. A lower rank in the list indicates a relatively lower peak strength for the pile type.

5.5.5 Column-Foundation Rotation

As discussed in subsection 3.2.6 and subsection 4.4.5, damage associated with column-foundation rotation is being considered as a separate column component model in the g2F framework. The controlling case of two possible rotational failure mechanisms, 'geotechnical' (i.e. edge-pile axial failure) or 'structural' (i.e. connection bending failure), is being modeled using the same hyperbolic parametric form. Table 5.24 presents model

Table 5.23: Approximate inventory proportions of pile types for column and abutment foundations for era-3 bridges (Roblee, 2018*f*, 2020*c*)

Pile Type	Class	Pile Size [inch]	Column Piles		Abutment Piles		Ranking
			% of Cl-140	% of Cl-200	% of Cl-140	% of Cl-200	
CIDH, 16”, Era 33	140	16	30%		30%		1
CIDH, 24”, Era 33	200	24		30%		25%	6
CISS 14x0.438	140	PP14 x 0.438	10%		5%		11
Steel Pipe, 14x0.438	140	PP14 x 0.438	10%		5%		7
Steel Pipe, 16x0.500	200	PP16 x 0.500		15%		10%	10
Prestr Conc, Alt-X	140	12 (+- 3/8)	15%		20%		2
Prestr Conc, Alt-X	200	14 (+- 3/8)		25%		25%	5
Prestr Conc, Alt-Y	140	15	15%		20%		4
Prestr Conc, Alt-Y	200	15		20%		25%	8
Steel HP, HP 10x57	140	HP10x57	20%		20%		3
Steel HP, HP 14x89	200	HP14x89		10%		15%	9

parameters developed by Yang (2020*a*,*b*) which involves three parameters, the initial stiffness K, and two strength-ratio models corresponding to the two damage modes: geotechnical (R_G) and structural (R_S). R_G and R_S are the strength ratio between the rotational strength (t_u) and the column section moment capacity. These models were developed through analysis of 24 fixed-base single-column bent, and 36 pinned-base multi-column bent bridges from the era-3 California box-girder bridge inventory. As seen by the median strength ratio values in Table 5.24, both the geotechnical and structural designs of typical era-3 foundations provide ample rotational capacity which exceeds column-hinge capacity. However, the lower bound values indicate there is some minor risk of foundation-rotation damage exceeding column-fusing damage, particularly for the fixed-base case. It is unclear if this result is an artifact of the analysis strategy, but because of the large median ratios, it is not expected to have significant impact on which component controls fragility near the base of era-3 columns. Implementation of the 2-mechanism rotation model involves randomly sampling both strength-ratio models for each bridge realization, then selecting the controlling value for use in demand analysis. The proportion of total realizations controlled by each mechanism is tracked and used to assign the proper capacity model.

Table 5.24: Distributions of model parameters used for column foundation rotational springs (Yang, 2020*a*,*b*).

Variable	Foundation Rotation Model						Correlation		
	Unit	Type§	$\mu^{\dagger}$	$\sigma^{\dagger}$	LB⊕	UB⊕	R_G	R_S	K
Pin-Based Columns									
R_G	kip-in/kip-in	LN	4.50	0.40	2.10	16.50	1.00	0.35	0.50
R_S	kip-in/kip-in	LN	5.50	1.00	1.30	100.00	0.35	1.00	0.55
K	10^6 kip-ft/rad	LN	2.50	0.95	0.50	20.00	0.50	0.55	1.00
Fix-Based Columns									
R_G	kip-in/kip-in	LN	2.30	0.40	0.80	6.50	1.00	0.65	0.15
R_S	kip-in/kip-in	LN	16.00	1.35	0.75	180.00	0.65	1.00	0.25
K	10^6 kip-ft/rad	LN	17.00	0.75	5.00	80.00	0.15	0.25	1.00

§ C = constant, LN = lognormal, N = normal, B = binomial, and U = uniform.
† μ denotes the mean and median for normal distribution and lognormal distribution, respectively; σ denotes standard deviation and dispersion (logarithmic standard deviation) for normal distribution and lognormal distribution, respectively.
⊕ LB = lower bound, UB = upper bound.

5.6 Miscellaneous

Several other miscellaneous parameters are required to specify a FEM bridge-model realization. Model values such as damping ratio and mass factor are taken to be the same as used in prior work by Mangalathu (2017); Soleimani (2017); Ramanathan (2012). Ground motion components are assigned randomly as these models are intended for generic application where orientation to the fault is unknown. The effects of vertical acceleration are not considered in this study.

5.7 Design Constraints

The stochastic analysis strategy generally involves simultaneous consideration of multiple variables which are randomly sampled. This research adopts the Latin-Hypercube Sampling (LHS) technique (McKay et al., 2000). LHS is found to be an efficient way of capturing the uncertainties in fragility analysis (Nielson, 2005). Nevertheless, a completely random sampling approach ignores inherent correlations in parameter specification that naturally arise from bridge design practices. Some correlations are directly embedded within the component models, such as in the case of pile models. However, some exist between multiple components that are normally considered separately and are difficult to identify.

This section describes three important constraints incorporated into the sampling process herein which address several recognized bridge-component parameter correlations arising from standard design practices. Taken together, these assure more realistic and proportional virtual bridge designs.

5.7.1 Contributing Deck Area (CDA) Group Constraint

The CDA-group constraint aims to broadly align the deck area supported by a column with an appropriate column-section size so as to generate a realistic axial load ratio. Bridge design practices do not allow overloading (extremely high axial load) of columns. However, completely random sampling of span-length, deck width, and column section size could result in unrealistic outlier combinations where a large deck area is supported by a small column section or vice versa. The CDA-group constraint on column sampling addresses this issue.

Figure 5.8 illustrates the CDA-group constraints adopted herein. These are based on analysis of inventory data from 434 California single-frame box-girder bridges of all design eras (Roblee, 2016*c*). Each data point relates a bridges' column-section gross area to its contributing deck area (CDA) value, where CDA is approximated as the product of the average deck width per bent column and the average span length. Breakouts of these data by design era and bent configuration were also explored. While the data for multi-column bents of each era, and era-1 bridges of either bent configuration, all had smaller columns (i.e. section area) and lower CDA values, clear trends in their ratios could not be differentiated from the overall trends in the combined data shown here.

The data in Figure 5.8 show that the same column section size can be used to support a wide range of deck areas; a single value for deck area might be supported on a range of column sizes; and there is a broad but clear trend for larger columns being used to support larger deck areas as one would expect from proportional bridge designs. The red boxes

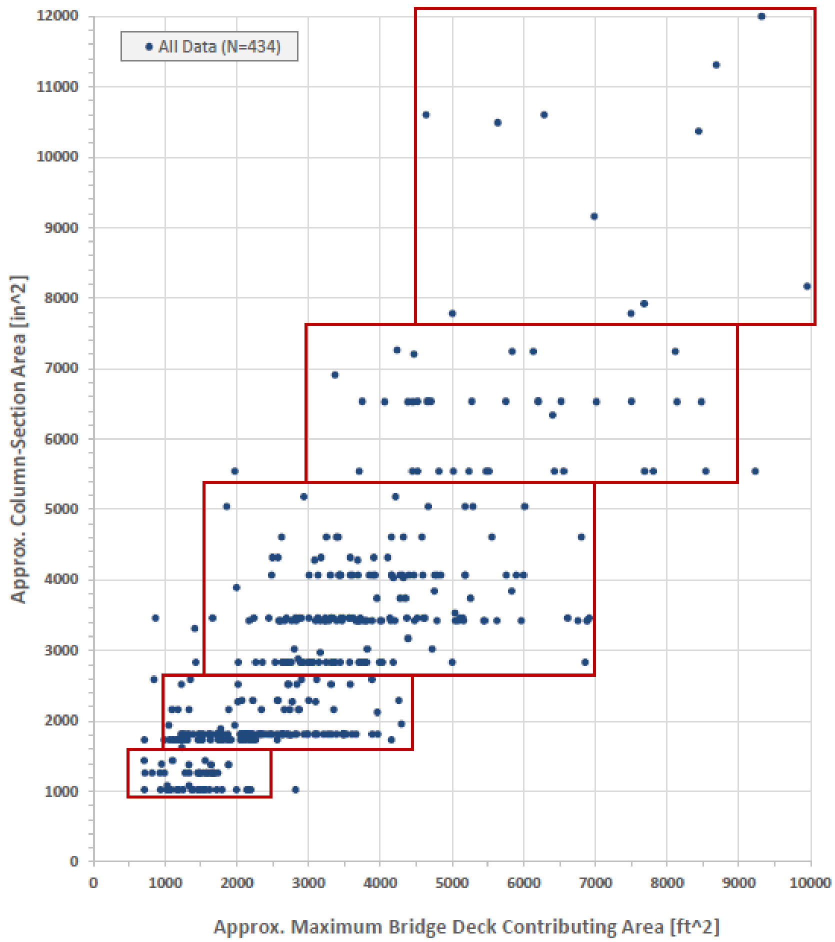

Figure 5.8: California bridge inventory data and illustration of CDA-group constraints used in virtual bridge sampling processes (Roblee, 2016*c*).

in Fig. 5.8 define the set of loose CDA-group constraints adopted herein with boundary values listed in Table 5.25. These are defined in terms of overlapping ranges of deck area for distinct ranges of column section size.

Table 5.25: CDA-Group constraints used for virtual bridge proportioning and assignment of column-related components (Roblee, 2016*c*).

CDA	Column Area [inch^2]		Contributed Deck Area [feet^2]	
	Low	High	Low	High
1	1000	1600	500	2500
2	1600	2600	1000	4500
3	2600	5400	1500	7000
4	5400	7600	3000	9000
5	7600	12000	4500	10000

The CDA-group values identify the five column-section ranges as CDA-1 to CDA-5 with larger numbers representing larger column sizes. These ranges are used directly to constrain overall bridge geometry using an acceptance/rejection procedure with oversampling as needed. The CDA-groups are also used as breakout categories for other component-parameter specification models for items related to column design. These include the size of the pinned-base reduced section (see Table 5.11) and various foundation parameters including cap/footing dimensions (see Table 5.17 thru Table 5.19), pile-array layout parameters (see Table 5.22), the proportions of column foundations having footings (see subsection 5.5.2), and assignment of specific pile classes and types (see subsection 5.5.4). They are also used to differentiate ranges of design moment capacity in the ground-motion pairing procedure described in Section 5.7.3.

5.7.2 Pile-Foundation Design Constraints

The second adopted constraint on virtual bridge specification assures that pile-foundation systems used at bent columns are well matched to the specified column. As outlined in earlier sections, specification of a pile foundation system includes multiple parameters including overall cap size and embedment as well as the quantity, layout, and type of piles. Random specification of all these parameters can result in an inadequate foundation capacity. Specifically, modern bridge design practices in California take steps to assure that column-foundation is stronger than the column so the preferred damage mechanism of column fusing occurs before foundation damage during an earthquake.

Based on discussions with Caltrans designers, this study assumes that the total capacity of a modern (era-3) pile-foundation system (i.e. pile-group lateral resistance plus sidesoil resistance on the cap) has 20% higher capacity ($\phi = 1.2$) than the column. However, completely random sampling of the various parameters of the pile foundation models described herein yields column-foundation combinations that do not meet this criterion. In the worst case, as many as 30% of randomly sampled single-column bridge realizations violated this criterion by varying amounts.

Therefore, a more sophisticated iterative re-sampling process, as outlined in the flowchart shown in Figure 5.9, was adopted for specification of pile-foundation systems at column bents. The process first compares foundation and column capacities of each bridge to identify the N_f cases which fail to meet the ($\phi = 1.2$) criteria. For those cases which fail, the embedment depth is resampled first as it retains the specified proportions of pile types. Increases in embedment depth typically increases pile capacity. Therefore, the procedure updates pile capacities correspondingly.

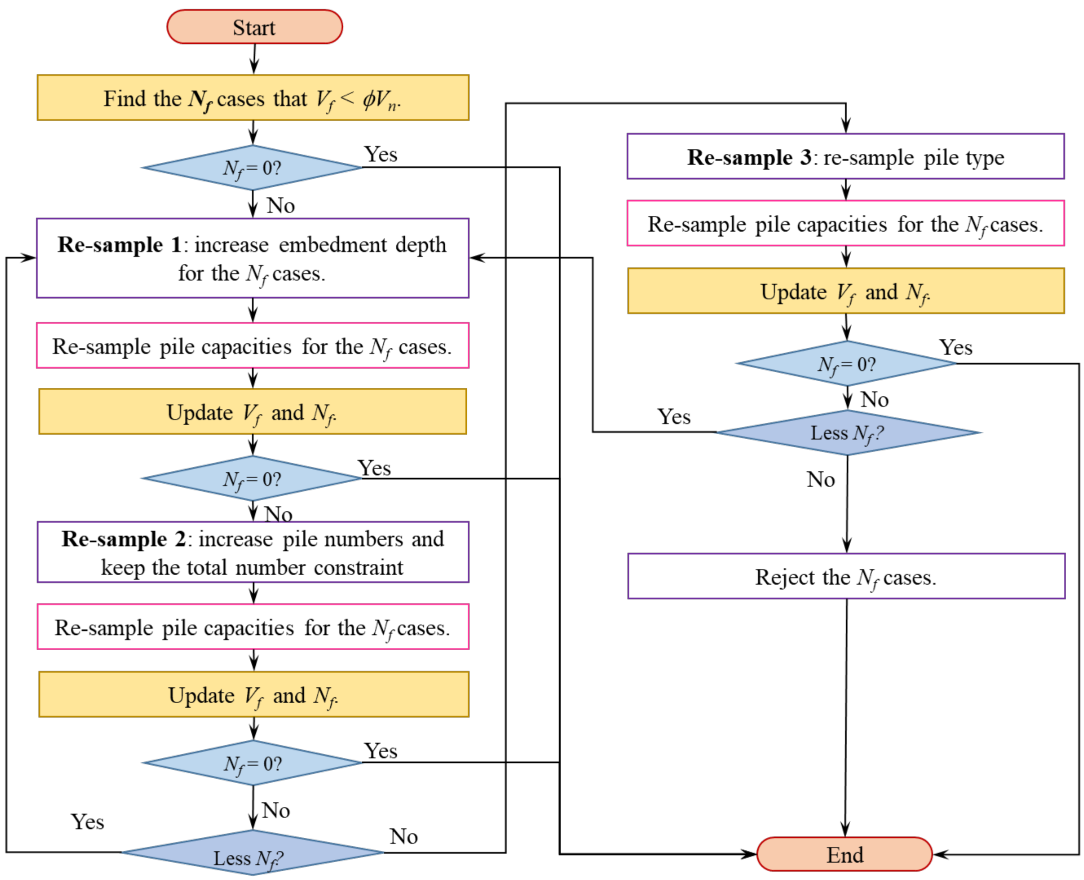

Figure 5.9: Flowchart for sampling pile foundations.

For the set of remaining failure cases not addressed by embedment-depth re-sampling, the second step is to increase the number of pile rows in the failure direction within model constraint limits. Similarly, the pile capacities are re-sampled and the failure cases are updated. A decreasing the number of failure cases N_f indicates the current pile type has sufficient capacity. When that strategy is exhausted, the third step in the re-sampling procedure is applied to the remaining cases. Here, an increased pile-type rank is assigned per Table 5.23 which results in selection of a new pile type with increased peak pile capacity. Overall, the three stages of re-sampling and iteration outlined in the flowchart are followed until N_f stops decreasing. Any remaining failure cases are accepted as substandard, but within the parameter bounds set by inventory analysis. In actual design practice, those cases would likely consider using other foundation types such as shaft or mat foundations. Note that for the single-column-bent case noted earlier as having a 30% failure rate, application of iterative resampling procedure reduced the failure rate to 0.6%.

5.7.3 Ground Motion Pairing Constraints

Perhaps the most fundamental principle of earthquake engineering is to design higher capacity into bridges expected to undergo higher levels of ground shaking. However, most prior analytically based fragility methodologies randomly pair any one of a wide range of ground motions to a random virtual-bridge selection for purposes of capturing peak responses used in the PSDM. However, this random pairing process violates the noted fundamental seismic design principle by allowing the lowest-capacity bridges to be subjected to the highest level of motions, thereby incorporating unrealistically high peak responses into the PSDM model. This issue is addressed herein with the introduction of a combination of two new methodological steps together referred to as ‘ground motion pairing constraints’.

The ground motion pairing procedure seeks to avoid an inappropriate pairing of strong earthquake shaking with a weak bridge design. Here, the term ‘applied ground motion (AGM)’ is that specified for use in the demand analysis. Seismic bridge design practice involves the selection, proportioning and detailing of components to withstand a ‘design ground motion (DGM)’ typically specified in terms of a site-specific response spectrum.

For purposes herein, both the AGM and DGM are taken as 1-second spectral acceleration (S_{a1}). Bridges designed for a high DGM have higher capacities (i.e. are "stronger") than bridges designed for low DGM (i.e. "weaker"). In the field, strong bridges can be subjected to either high or low AGM whereas weak bridges are unlikely to be subjected to high AGM. The ground motion pairing procedures introduced here serve to implement this fundamental seismic design principle into the otherwise random pairing process.

Pairing Step 1: Moment Capacity (or DGM) with Column Section Size

This first pairing step establishes and enforces realistic ranges of seismic capacity for different sized bridge-column sections. Here, seismic capacity is defined in terms of column moment capacity which mirrors seismic design practices where column sections are initially sized and detailed to resist moments arising from a specified shaking hazard. The determination of realistic capacity ranges for each column size is based on analysis of a sample of 420 column designs from the California box-girder bridge inventory. For each design, an approximate design moment was computed as the product of the superstructure mass, the column height, and a design ground motion. The design motion for each case was approximated using current probabilistic shaking hazard values for S_{a1} at each bridge location. Superstructure mass was approximated using column-section properties and applying a median axial-load ratio value of 10%.

Figure 5.10 presents results of this inventory-column analysis in terms of the total longitudinal reinforcement area, approximate design moment, and the CDA group (which conveniently represents groups of column sections having similar size). The total longitudinal reinforcement area parameter captures the combined effects of column section size and reinforcement ratio. These results show a clear positive proportional relationship between approximate design moment and longitudinal reinforcement. It also shows how ranges in both parameters increase with column section size (as represented by the CDA-group value). Ranges in approximate design moment for each CDA-group are summarized in Table 5.26.

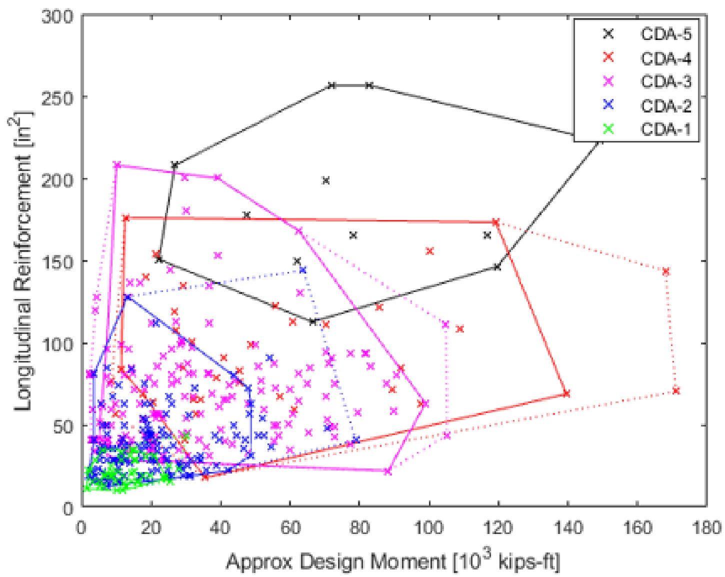

Figure 5.10: Relationship between total longitudinal reinforcement and approximate design moment by CDA group for 420 CA bridge column designs (Zheng, 2020*a*): solid-line boundaries are generated by removing outliers in dashed-line boundaries

Table 5.26: Approximate design moment ranges for CDA groups (Zheng, 2020*a*).

CDA	Approximate Designed Moment Range [10^3 kip-ft]
1	<25
2	<50
3	5 to 100
4	10 to 150
5	25 to 200

Recall that the overall goal of the ground-motion pairing procedure is to associate strong bridge designs (i.e. configured to withstand high design moment) with high applied ground motions. Toward that end, the information in Table 5.26 allows for the creation of proportional virtual bridge designs to withstand the full range of seismic demands. For average column height and superstructure mass, the largest column sections are required to handle the largest demands while smaller demands can be accommodated by a range of smaller section sizes.

Implementation of this first paring step in the virtual-bridge specification process occurs within the bridge-model sampling sequence. First, separate candidate pools for design moment and column section are specified. Each candidate design moment is computed as the product of randomly sampled values for column height, superstructure mass and DGM. Column sections are classified by CDA group. The superstructure mass value requires separate sampling of the deck width, span length, section depth distributions.

The DGM is sampled from the distribution of ground motions used in the California inventory analysis of Figure 5.10. Note that a minimum DGM value of 0.5g is assigned because smaller values have been found to have little impact on bridge designs which then become governed by other load combinations and design requirements. Next, the two pools are paired by assigning the pool of design moments in reverse rank order (i.e. highest to lowest) to a random selection from the largest available CDA pool of column sections. For example, the highest design moments are first assigned to CDA-5 sections until that pool is exhausted, then to the CDA-4 and so forth. Once this process is complete, the moment-section pairs are checked against the ranges shown in Table 5.26. Experience to date has shown the entire virtual bridge set is within the inventory-based boundaries using this process.

Pairing Step 2: DGM and AGM

The second pairing step assures realistic assignment of a virtual bridge design, having a design capacity represented by a DGM, with an AGM value in the demand analysis. Note, the DGM for each virtual bridge design was specified as part of the moment-section pairing procedure discussed above.

The core of the AGM-DGM pairing procedure used herein is tied to an assumed probability distribution for r, defined as the ratio of a Target AGM (TAGM) to the DGM. The distribution assigns any TAGM below the DGM (i.e. $0 \leq r \leq 1$) to have equal probability. TAGM values above the DGM (i.e. $r > 1.0$) have decreasing probability per the form of an assumed lognormal distribution until a hard truncation limit of that distribution is imposed where the TAGM reaches 1.5 times the DGM (i.e. $r = 1.5$). Appendix E outlines the development of the r distribution.

The AGM-DGM pairing process is implemented by first assigning a TAGM value to each virtual bridge realization by multiplying its DGM by a randomly sampled value of r and then sorting the bridge designs by their TAGM value. The AGM's for the set of ground motions used in the demand analysis (e.g. the T1780 set defined in Appendix B) are then sorted by S_{a1} value. Pairing of a virtual bridge design to a ground motion is then finalized by using the same rank from the ordered lists of TAGM and AGM. Note that while the ratio of TAGM to DGM in the r distribution was truncated at 1.5, the ratio of AGM (in the demand analysis) to DGM depends on the ground motion set adopted for the demand analysis. The T1780 set yields maximum AGM/DGM ratios of approximately 2.

Figure 5.11 illustrates the impact of the ground-motion pairing process. The figure on the left shows AGM-DGM pairing combinations of the T1780 set resulting from a random pairing process as adopted by most other research. The data points on the upper left represent highly unrealistic combinations where applied motions are as much as five times design values. In contrast, the figure on the right shows the same set of motions paired using the procedures outlined above. Here, the unrealistic combinations are eliminated, and applied motions are systematically limited to roughly two times the design values, while lower motions can be applied to all designs.

Another way to consider the results in Figure 5.11 is to look at bands of applied motion. At low AGM, both methods consider similar DGM ranges, or similar bridge designs. However, at high AGM, the ground motion pairing method described herein assigns stronger bridges compared to the randomly sampled case where both strong and weak bridges are assigned. Thus, it is anticipated that the ground motion pairing will reduce the probability of higher damage states since more of the bridges subjected to high motions were designed with higher capacities per fundamental seismic design principles.

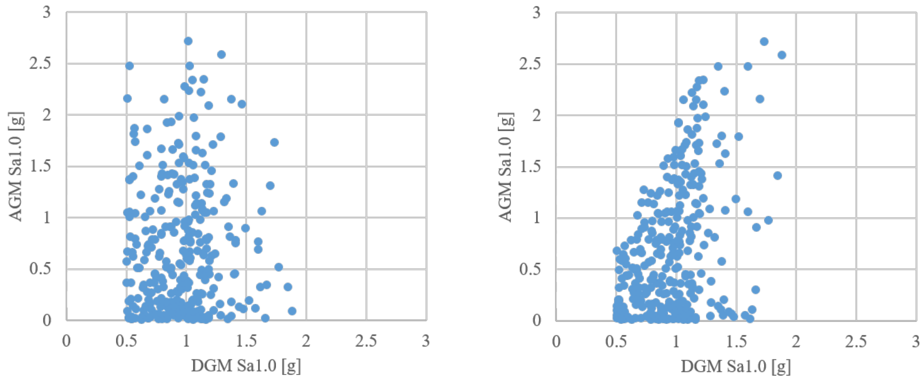

(a) (b)

Figure 5.11: Illustration of ground motion sampling results: (a) without ground motion pairing; and (b) with ground motion pairing.

Figure 5.12 illustrates the overall impact of this ground motion pairing procedure by contrasting two sets of fragility curves for column damage from a case study simulation. Both sets of curves show similar median S_{a1} for damage states CDS_1 to CDS_3, but the sets using ground motion pairing show lower failure probability for the remaining states. For the CDS_7 collapse state, the increase of median S_{a1} is nearly 20%, from roughly 2.25g to 2.70g.

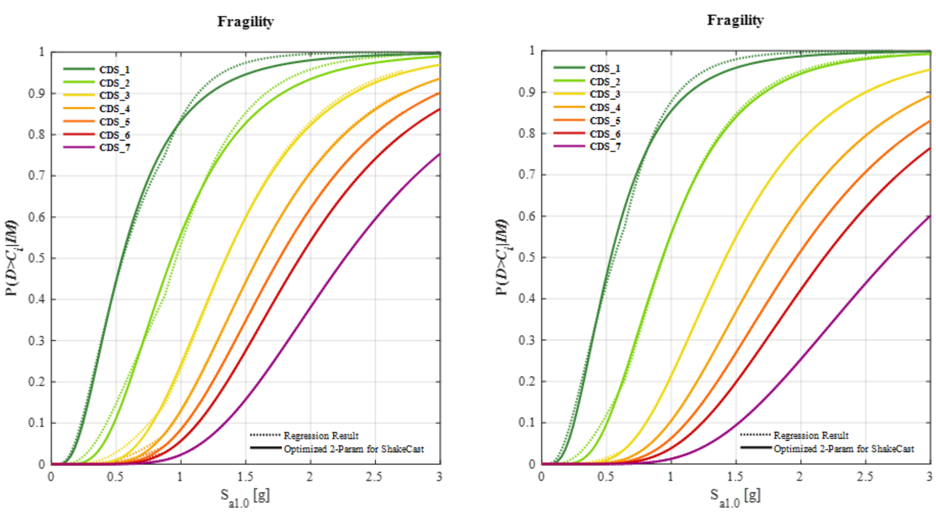

(a) (b)

Figure 5.12: Illustration of the effect of ground motion sampling: (a) without ground motion pairing; and (b) with ground motion pairing.

5.8 Closure

This chapter outlined details of a wide range of distributed variables that are sampled for the specification of virtual bridges used in the demand analyses herein. Variability in superstructure, column-bent, and abutment component designs are identified and quantified. The distributions adopted are well grounded through the extensive use of California bridge inventory data.

Equally important, three types of design constraints are introduced and discussed in detail. CDA grouping constrains column section sizes to have realistic axial load ratios when combined with sampled superstructures; the pile-foundation design procedure constrains the foundation to be stronger than the column (for era-3 bridges); and the ground motion pairing procedures both assure proportional bridge designs and align the overall strength of the bridge design with the amplitude of the applied ground motion. This is demonstrated to have significant impact on high-state fragility models.

CHAPTER 6

ADVANCED PROBABILISTIC SEISMIC DEMAND MODELS AND FRAGILITY CURVES

The generation of fragility models involves the convolution of demand models and capacity models. Using the component models and methods described in Chapter 3, dynamic nonlinear finite-element models are constructed in the analytical platform OpenSees (McKenna et al., 2000). Specific EDP's described in Chapter 4 were recorded during the dynamic analysis. Probabilistic Seismic Demand Models (PSDM's) are then used to establish a relationship between the EDPs and the ground motion IM. A linear relationship is commonly used to represent the EDP-IM relationship in the PSDM and this method is both mature and well used for the development of fragility models through these years (Cornell et al., 2002; Nielson, 2005; Padgett, 2007; Ramanathan, 2012; Mangalathu, 2017; Soleimani, 2017). However, as both more nonlinear component behavior and higher IM levels are considered, the conventional assumptions are not always valid and higher order regression models are needed to address the increased nonlinearity. Additional methodological refinements are warranted to support the more demanding g2F framework involving more components, states, and EDPs for refined assessment of both high and low-damage conditions.

As component fragility models offer valuable detailed information about component damage, higher-stage fragility models are also needed to identify generalized damage for a specific bridge region (e.g. column bent or abutment), zone (e.g. interior bents, base of column) or the operational condition of the whole system. While elements of the procedures needed to handle multi-level fragility models have been widely used since Nielson (2005), these strategies are extended herein for generation of fragility model for various meaningful combinations of component groups. Additionally, formal consideration is given herein to the construction of a correlation matrix between different components, which to the best of the author's knowledge, has not been previously addressed.

This chapter starts with the discussion of conventional methods for constructing the PSDM and component fragility models. After outlining limitations of these, this chapter proposes strategies to address them. Next, a detailed comparison of different methodologies is presented. The remainder of this chapter introduces the methodology used to construct fragility models for multiple component groups and the whole bridge system.

6.1 Conventional PSDM Model - Linear Regression Model

It is suggested by Cornell et al. (2002) that the estimate of the median of seismic demand S_D has a power relationship with IM as shown in Equation 6.1.

$$S_D = a \cdot (IM)^b \tag{6.1}$$

This relationship indicates that the seismic demand D, discussed in Chapter 3 has a linear relationship with the IM. Transformation of the relationship into natural logarithm simplifies the parameters estimation into simple linear regression model concerning data pair of $(x = \ln IM, y = \ln D)$ following Equation 6.2.

$$\ln D = \ln a + b \cdot \ln IM + \varepsilon \tag{6.2}$$

where $\varepsilon \overset{iid}{\sim} \mathcal{N}(0, \sigma^2)$.

As illustrated in Figure 6.1, the linear regression model estimates the seismic demand D as a conditional lognormal (LN) distribution with median S_D and dispersion, or lognormal standard deviation, $\beta_{D|IM}$. Given an IM, for example when $\ln IM = x_0$, while the median estimation $\hat{S}_D$ is trivial, and the calculation of variance for dispersion estimation is per

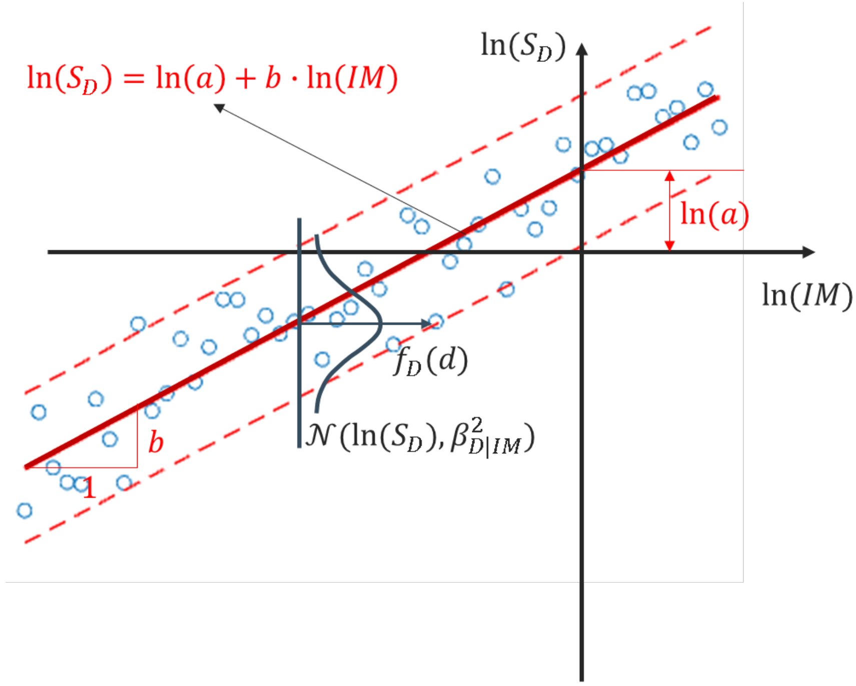

Figure 6.1: PSDM illustration in natural logarithm space.

Equation 6.3.

$$\beta_{D|IM=x_0} = \sqrt{\hat{\sigma}^2 \left[1 + \frac{1}{N} + \frac{(x_0 - \bar{x})^2}{\sum_{i=1}^{N}(x_i - \bar{x})^2}\right]} \tag{6.3}$$

Here, N is the total number of the regression data points, $\bar{x}$ is the mean of x, and $\hat{\sigma}$ is the unbiased estimation of σ, or the root mean square error (RMSE) measurement of the regression model, which is calculated by Equation 6.4.

$$\hat{\sigma} = \sqrt{\frac{\sum_{i=1}^{N}(y_i - \hat{y}_i)^2}{N - 2}} \tag{6.4}$$

where y_i is the i^{th} seismic demand $\ln D_i$, and $\hat{y}_i$ is the estimation of the $\ln D_i$, or $\ln \hat{S}_D$.

With the knowledge that both of the seismic demand and capacity models are lognormal distributions conditioned on a specific IM (Chapter 4), fragility curves for the component can be developed. As indicated before, fragility curves depict the probability of seismic demands larger than capacities given an IM, which is represented in Equation 6.5.

$$
\begin{aligned}
P(D \geq C|IM) &= P(\ln D \geq \ln C|IM) \\
&= P(\ln C - \ln D \leq 0|IM).
\end{aligned}
\tag{6.5}
$$

Notate $(Z|IM) = \ln C - \ln(D|IM)$, then $(Z|IM)$ is a normal distribution $\mathcal{N}\left(\ln(S_C/S_{D|IM}), \sqrt{\beta_C^2 + \beta_{D|IM}^2}\right)$. This indicates the fragility can be evaluated by Equation 6.6, in which $\Phi(\cdot)$ is the cumulative probability function (CDF) of the standard normal distribution.

$$
\begin{aligned}
P(D \geq C|IM) &= P\left[(Z|IM) \leq 0\right] \\
&= \Phi\left(\frac{0 - \ln(S_C/S_{D|IM})}{\sqrt{\beta_C^2 + \beta_{D|IM}^2}}\right) \\
&= \Phi\left(\frac{\ln(S_{D|IM}/S_C)}{\sqrt{\beta_C^2 + \beta_{D|IM}^2}}\right)
\end{aligned}
\tag{6.6}
$$

To this end, a fragility model using the conventional linear regression model is established. However, this study identifies that some components do not follow a linear relationship between seismic demand and intensity measurement. By using linear regression, the resulting residuals also violate the normal assumption. This is illustrated in Figure 6.2 which comes from a simulation for the era-3 two-span multi-column bent bridges. The first figure is the PSDM for the column hinge curvature ductility in the transverse direction. After column yielding, there is a significant change in the data distribution slope. The linear model underestimates the response in the low S_{a1} region (say $\ln S_{a1} < -1.5$) and then first overestimates (to say $\ln S_{a1} \approx 0$), then again underestimates (say $\ln S_{a1} > 0$) response in the high S_{a1} region. It can be seen in the residual plot that the normal assumption for linear regression is violated. The case on the right is for longitudinal displacement of the abutment foundation. As previous described, abutment foundations provide only a small force after backwall fracture, and their deformations are limited to a low level by design to prevent damage. The linear model, as illustrated here, cannot model this phenomenon. Similar to the first case, the residual of this regression model is not uniformly distributed. Therefore, linear regression is not a good choice to describe these two components, and it indicates the need for a better statistical strategy to represent the PSDM.

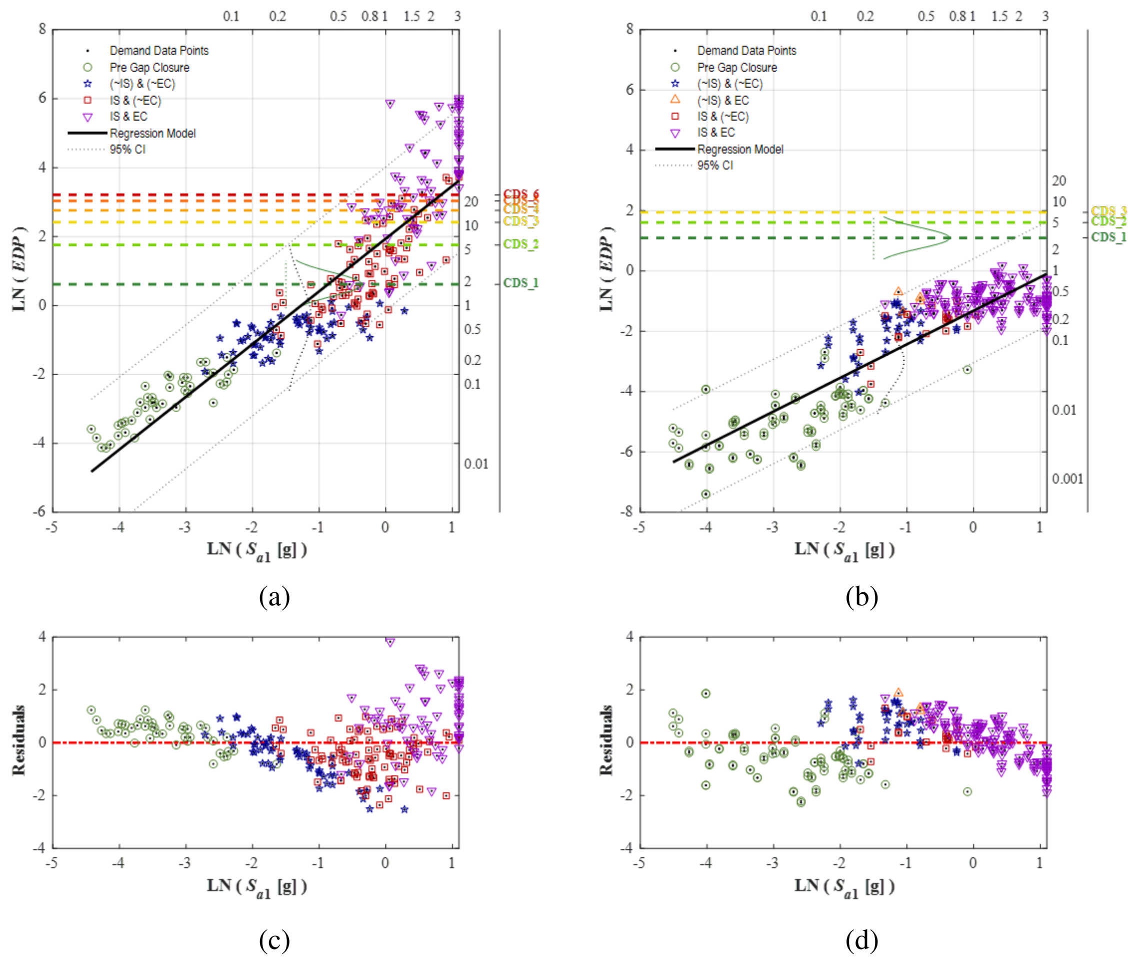

Figure 6.2: Illustration of linear regression. (a) and (c): PSDM and residual plots for hinge curvature ductility in transverse direction; (b) and (d): PSDM and residual plots for abutment footing foundation displacement in longitudinal direction.

6.2 Emerging Methods to Capture High Non-linearity in PSDM

As mentioned before, the research community has recognized the nonlinearity of PSDM's constructed in lognormal space. Additionally, heteroscedasticity (i.e. non-uniform standard deviation) of the data violates the basic assumption of linear regression. This section reviews three methods that seek to address these issues.

6.2.1 Quadratic Model

Work by Pan et al. (2007) attempted to represent the high non-linearity of the seismic demand data with quadratic models. It was assumed that the seismic demand and IM follows quadratic relationship in the following form. Dispersion can be calculated based on Equation 6.3.

$$\ln D = \ln a + b_1 \cdot \ln IM + b_2 \cdot (\ln IM)^2 + \varepsilon \tag{6.7}$$

6.2.2 Bi-linear Model

A similar technique was proposed by Jeon (2013) for handling high PSDM nonlinearity. It was assumed that the seismic demand is represented by two linear segments as shown in Equation 6.8, where the breaking point (IM_0) between segments is determined by minimizing the errors between actual and fitted values. The original work by Jeon (2013) indicates the dispersions were calculated with Equation 6.4 for each segment. However, as stated before, predicted dispersion using Equation 6.3 is preferable and will be used for comparison.

$$\ln D = \begin{cases} \ln a + b_1 \cdot \ln IM + \varepsilon_1, & IM \leq IM_0 \\ \ln a + b_1 \cdot \ln IM_0 + b_2 \cdot (\ln IM - \ln IM_0) + \varepsilon_2, & IM > IM_0 \end{cases} \tag{6.8}$$

The study by Jeon et al. (2015a) also identified that dispersion is not constant across the IM range for linear regression. Comparison of the linear and bi-linear models showed that the bi-linear regression model addressed the heteroscedasticity issue.

6.2.3 Multi-Phase Model (M-PARS)

Unlike the two aforementioned studies where nonlinearity was handled with regression techniques, Zareian et al. (2015) proposed a model combining regression with explicit consideration of the causes for the multi-phases of seismic demand. The fundamental idea of this method, named Multiphase Performance Assessment of structural Response to Seismic Excitations (M-PARS), is total probability is represented as a combination of separate mechanism-dependent models per Equation 6.9, where BS represents "Bridge Survival", BC represents "Bridge Collapse", SKS represents "Shear Key Survival", and SKF represents "Shear Key Failure". The four terms (BS, BC, SKS, and SKF) represent different phases of the bridge behavior.

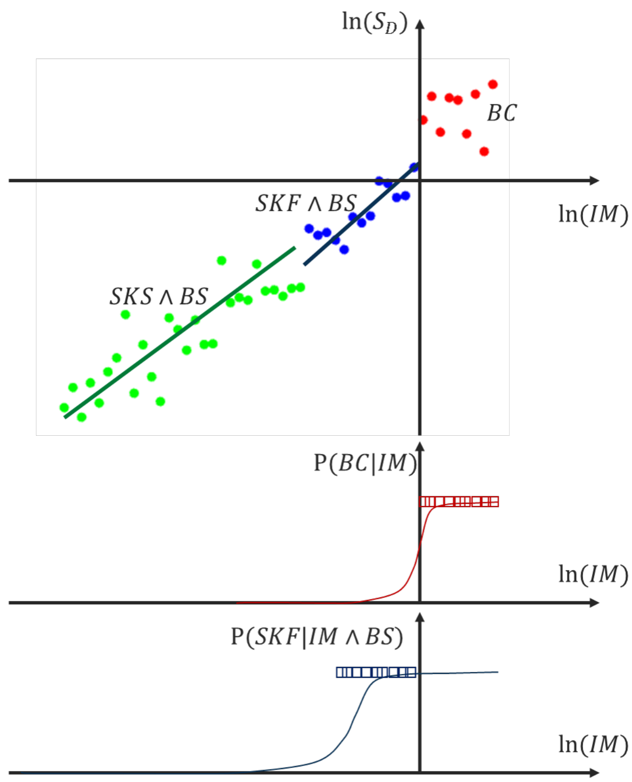

Figure 6.3: Illustration of M-PARS method.

$$
\begin{aligned}
P(D \geq C|IM) = P(D \geq C|IM \wedge BS \wedge SKS)P(BS \wedge SKS|IM) \\
+ P(D \geq C|IM \wedge BS \wedge SKF)P(BS \wedge SKF|IM) \\
+ P(D \geq C|IM \wedge BC)P(BC|IM)
\end{aligned}
\tag{6.9}
$$

To calculate the failure probability by Equation 6.9, the three equations below are evaluated which considers that the two pairs of phases (BS and BC, SKS and SKF) are collectively exhaustive, and the fragility is always equated to 1.0 given bridges collapse, i.e., $P(D \geq C|IM \wedge BC) \equiv 1$.

$$P(BS \wedge SKS|IM) = [1 - P(SKF|IM \wedge BS)][1 - P(BC|IM)] \tag{6.9a}$$

$$P(BS \wedge SKF|IM) = P(SKF|IM \wedge BS)[1 - P(BC|IM)] \tag{6.9b}$$

$$P(D \geq C|IM \wedge BC)P(BC|IM) = P(BC|IM) \tag{6.9c}$$

As illustrated in Figure 6.3, the two terms $P(D \geq C|IM \wedge BS \wedge SKS)$ and $P(D \geq C|IM \wedge BS \wedge SKF)$ in Equation 6.9 are determined using linear regression (Equation 6.2 to Equation 6.6). The other two critical terms $P(SKF|IM \wedge BS)$ and $P(BC|IM)$ are determined using logistic regression as suggested by Zareian et al. (2015).

In practice, this study did not consider possible application of this method to multi-phase response in the longitudinal direction. An additional limitation is that the linear regressions for the two phases, $SKS \wedge BS$, and $SKF \wedge BS$, sometimes cannot accurately capture the trend if the data leverage is too short; or in other words, this method cannot consider data continuity between different phases.

6.3 Modified Multivariate Adaptive Regression Spline (M-MARS) for PSDM

Multivariate Adaptive Regression Spline (MARS) is a non-parametric regression method (Friedman, 1991). Employing multiple segments, MARS is frequently used to model a nonlinear data set. In this research, the standard MARS model is modified to meet specific engineering requirements of this project. Specifically, the segments in this method are fixed so that each segment represents one recognized phase in the seismic demand data. The procedure is presented in four steps.

First, seismic demand data points are separated into the five bridge-system response phases listed in Table 6.1. These phases focus on three mechanistic causes for PSDM data non-linearity: abutment-joint gap closure, the yielding of the internal supports (e.g. column bents, pier walls), and the fusing of the end constraint (e.g. abutment backwall in longitudinal direction and shear key in transverse direction). The phases in Table 6.1 represent pre-gap-closure (PGC) and four post-closure phases: the internal supports have not yielded and end constraint has not failed ($\overline{IS} \wedge \overline{EC}$); the internal supports have yielded but the end constraint has not failed ($IS \wedge \overline{EC}$); the internal supports have not yielded but the end constraint have fused ($\overline{IS} \wedge EC$); and both the internal support has yielded and the end constraint has fused ($IS \wedge EC$). For bridges with multiple internal supports, internal support yielding is taken to represent yielding (i.e., displacement ductility larger than 1.0-in/in) occurring at all of the internal supports across all the bents. End constraint failure is taken as failure of either one of the end constraint components. As indicated in Chapter 4, abutment components are modeled by multiple spring elements. Failure of either one of the elements indicates end constraint failed (EC) in this context. For backwall or shear keys, failure of the component represents the seismic demand exceeds e3n in the material backbone stated in Chapter 4. Figure 6.4(a) uses unique color and symbol designations to illustrate the five phases of column-response data for a 2-span bridge case.

Table 6.1: Definition for five phases used in M-MARS

Notation	Gap Closure	Internal Support(s) Yielded	End Constraint(s) Failed
PGC	No	No	No
$\overline{IS} \wedge \overline{EC}$	Yes	No	No
$IS \wedge \overline{EC}$	Yes	Yes	No
$\overline{IS} \wedge EC$	Yes	No	Yes
$IS \wedge EC$	Yes	Yes	Yes

Second, the boundaries between each pair of adjacent phases are located, which are called ”knots” by the MARS method. These knots are illustrated by the large colored dots in Figure 6.4(b). In this example, the $IS \wedge \overline{EC}$ and $\overline{IS} \wedge EC$ data are combined together as a single transitional phase. Therefore, four phases remain to be considered to determine three internal knots and one end knot. The end knot could be taken at either the lower bound or upper bound of the data set. To avoid overfitting (i.e. use of too many small segments), especially at the edge of the data set, spacings between the edge knots are checked. If the length of the edge phase (i.e., PGC and $IS \wedge EC$) is smaller than a threshold IM value, the corresponding internal knot would be removed. In this study, the threshold is set as $0.5 \ln g$.

Next, similar basis functions $B_i(x)$ are applied to these pre-determined knots to enable segmentation per the MARS method. As shown in Equation 6.10, a linear function is used for the edge knot, and a hinge function is used for internal knots. At this stage in the process, seismic demand is ready for regression (in lognormal space) with respect to no more than four basis functions $B_i(x)$ of IM.

$$B_i(x) = \begin{cases} x - c_i, & \text{if } c_i \text{ is an edge knot;} \\ max(0, x - c_i), & \text{if } c_i \text{ is an internal knot.} \end{cases} \tag{6.10}$$

Finally, the problem becomes a multivariate linear regression with variable selection, during which one would regress the data and consider a fair number of base functions to avoid overestimation. Stepwise regression or best-subset selection could be used here. In this study, forward and backward stepwise regression is adopted (Figure 6.4(c)).

To address possible heteroscedasticity, dispersion is represented by a separate regression model as a function of IM. In this research, a linear relationship (Figure 6.4(d)) is established for the residual. Under such an assumption, the residual still follows a conditional normal distribution.

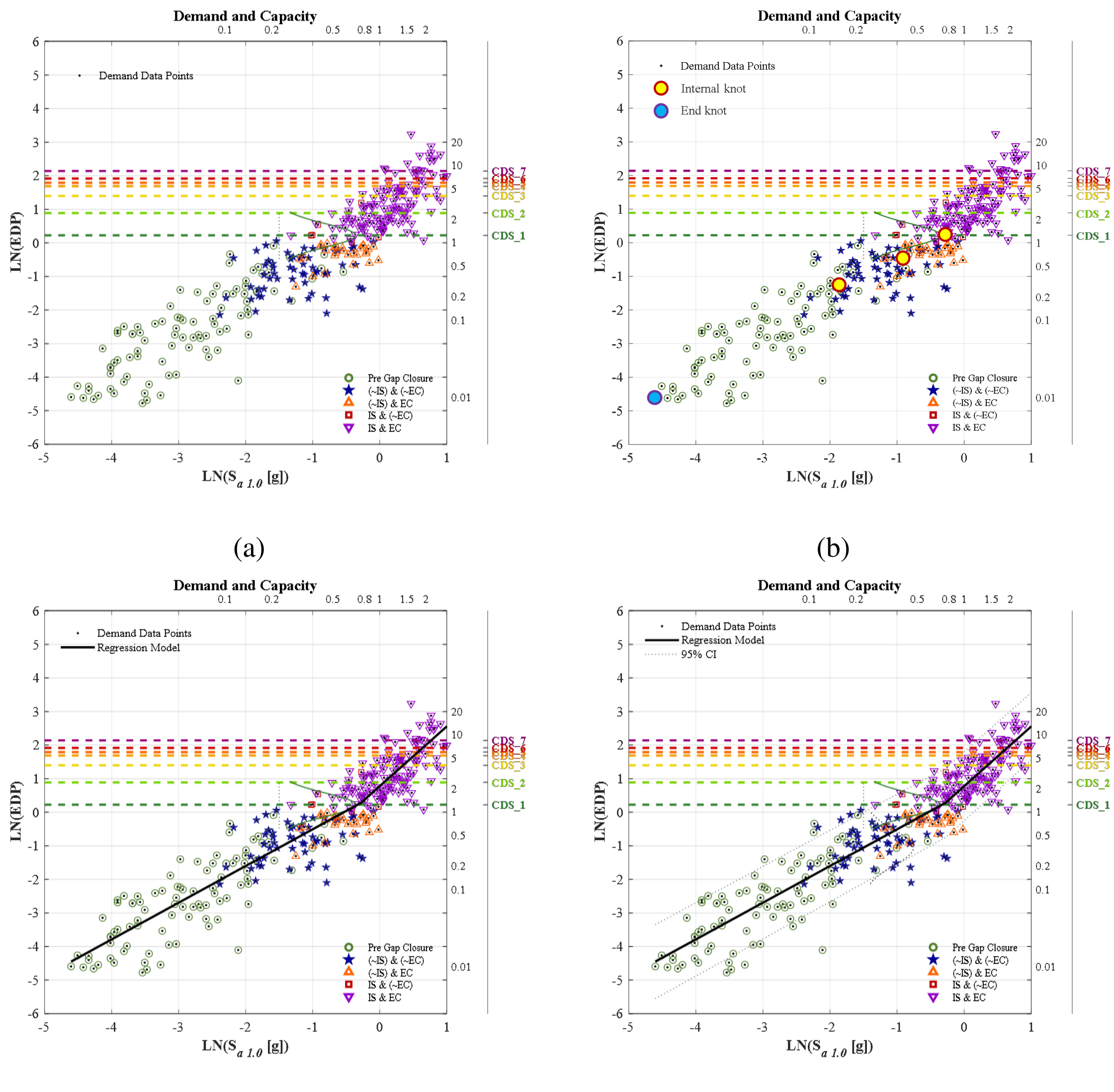

(a) (b) (c) (d)

Figure 6.4: Procedure of constructing M-MARS model: (a) Definition of phases; (b) Locate knots; (c) Stepwise regression to fit the mean response; and (d) Linear model of dispersion.

6.4 Filtered Adaptive Regression with Logistic Incorporation of Omitted Data (FAR+) for PSDM

In the previous section, the Modified Multivariate Adaptive Regression Spline (Modified Multivariate Adaptive Regression Spline (M-MARS)) was introduced, and it is used to handle nonlinearity in the PSDM data for most components herein. However, as the bridge-system model has become more comprehensive with the engagement and fusing of components at different IM levels, the resulting PSDM seismic demand data may not be ideal enough to use M-MARS directly for all components. Therefore for application, it is recommended to first review the data and determine the most appropriate approach for constructing the PSDM. This section presents an alternative method for handling two types of exceptions to the use of the M-MARS method.

6.4.1 Two Types of Exceptions

The first "low-end exception" refers to components that have extremely low responses under small ground motions. Components directly engaged by gap closure or those connected to them are good examples of this exceptional group.

For example, the impact element model (Chapter 4) includes the gap-closure process. Under small ground motions that do not cause gap closure, there is no pounding between adjacent components, and thus no damage to the component [1]. Other components, including shear key and residual joint deformation, sometimes contain non-positive values in the low-IM portions of the PSDM that should not be considered with regular regression in logarithm space. However, these data points do contain important information that component response is negligible for the applied IM, and therefore should be considered for evaluation of the failure probability; otherwise, the generated fragility model would overestimate failure probability based only on cases having high responses.

Another example for the low-end exception is the backwall-connection element which connects to the impact element. Under small ground motion and before gap closure, the backwall generates very small, randomly fluctuating seismic demand data associated with small inertial loads of the backwall or numerical noise (Figure 6.5(a)). These data points represent seismic demand on the order of 10^{-4} which is far below that associated with any damage. So, while the EDP values in such cases should not be considered in the assessment

[1] In this research, impact damage describes possible pounding-caused damage in the contacting surface of adjacent structures. Although the strip-seal element in this research use the same recorded data as the impact element, "damage" in this context does not refer to the possible strip-seal damage.

of fragility, the IM values from these cases contain important information regarding the level of excitation required engage these components in a way that may induce damage.

The second "high-end exception" is similar to the low-end exception but refers to seismic demand data under high ground motion where the EDP value no longer has significant meaning. For example, after column demand exceeds a realistic range of its capacity (say 99^{th} percentile of CCLS model), the important information is to simply know the column has failed, but not by how much. Demand data in this range can be treated as a "separate set" representing cases of complete component failure.

6.4.2 FAR+ Methodology for Handling Data Exceptions

This research introduces a new methodology called "Filtered Adaptive Regression - Logistic Incorporation of Omitted Data (FAR+)" to handle the two types of exceptions mentioned before. The basic concept of FAR+ involves total probability in a way that is similar to M-PARS. Construction of a FAR+ model involves four steps as outlined below.

First, the exceptional low-end/high-end data points are filtered out from the set to be considered using regular regression methods. For the low-end exception, a low-pass filter is applied for separation of the low-end data set ($\mathcal{S}_L$) from the regular regression data set ($\mathcal{S}_R$). Similarly, a high-pass filter is used to separate the high-end data ($\mathcal{S}_H$) from ($\mathcal{S}_R$). In order to classify the two sets of data, the K-Means clustering (Lloyd, 1982) for data pairs $(\ln IM, \ln EDP)$s is adopted. The start point can be set at the center of the pre-gap closure (PGC) phase in the low-end exceptions, or the center of the all fused ($IS \wedge EC$) phase in high-end exceptions, and the center of the remaining points for $\mathcal{S}_R$. Figure 6.5(a) illustrates this first step in the FAR+ method using response data for the backwall connection which contains a large amount of 'low exception' data mostly related to pre-gap closure. Here, the large colored dots identify the start points for the K-Means clustering algorithm which were taken as the center of phase PGC and the rest of the data. After clustering, data points are split into the $\mathcal{S}_L$ and $\mathcal{S}_R$ sets shown in Figure 6.5(b).

Second, apply the M-MARS regression to the data points in the $\mathcal{S}_R$ set as illustrated in Figure 6.5(c).

Third, apply Logistic Regression to the $\mathcal{S}_L$ or $\mathcal{S}_H$ sets to establish the probability of data points located in low-end/high-end. With this model, the probability that the remaining demand data points are located in SR can be derived from the theory of complementary events. The dashed line (”Low-Pass Filter”) shown in Figure 6.5(d) is the logistic regression result, representing the probability that the data point is located in $\mathcal{S}_R$ given IM.

Finally, incorporation of omitted data is accomplished using the total probability equation below, where $P_L(IM) = P((IM, D) \in \mathcal{S}_L|IM)$ and $P_H(IM) = P((IM, D) \in \mathcal{S}_H|IM)$ are the two logistic regression models derived before. Figure 6.5(d) presents the three-state fragility models for backwall connection failure incorporating the omitted data.

$$P(D \geq C|IM) = P(D \geq C|IM \wedge (IM, D) \in \mathcal{S}_R) \cdot (1 - P_L(IM) - P_H(IM)) + P_H(IM) \tag{6.11}$$

6.5 Comparison of Different Regression Models for Establishing Component Fragility

This section compares fragility models generated using the adopted M-MARS model relative to those from the regular linear regression model, the quadratic model, and the bilinear model, all introduced in section 6.2. The PSDM and fragility results are for the case of displacement ductility response in the longitudinal direction for regular-section columns in era-3 two-span multi-column bent bridges.

Figure 6.6 shows that the adopted M-MARS model captures three segments of response. From left to right, the first segment represents the initial pre-gap closure stage, where columns must absorb virtually all seismic demand, the second segment represents

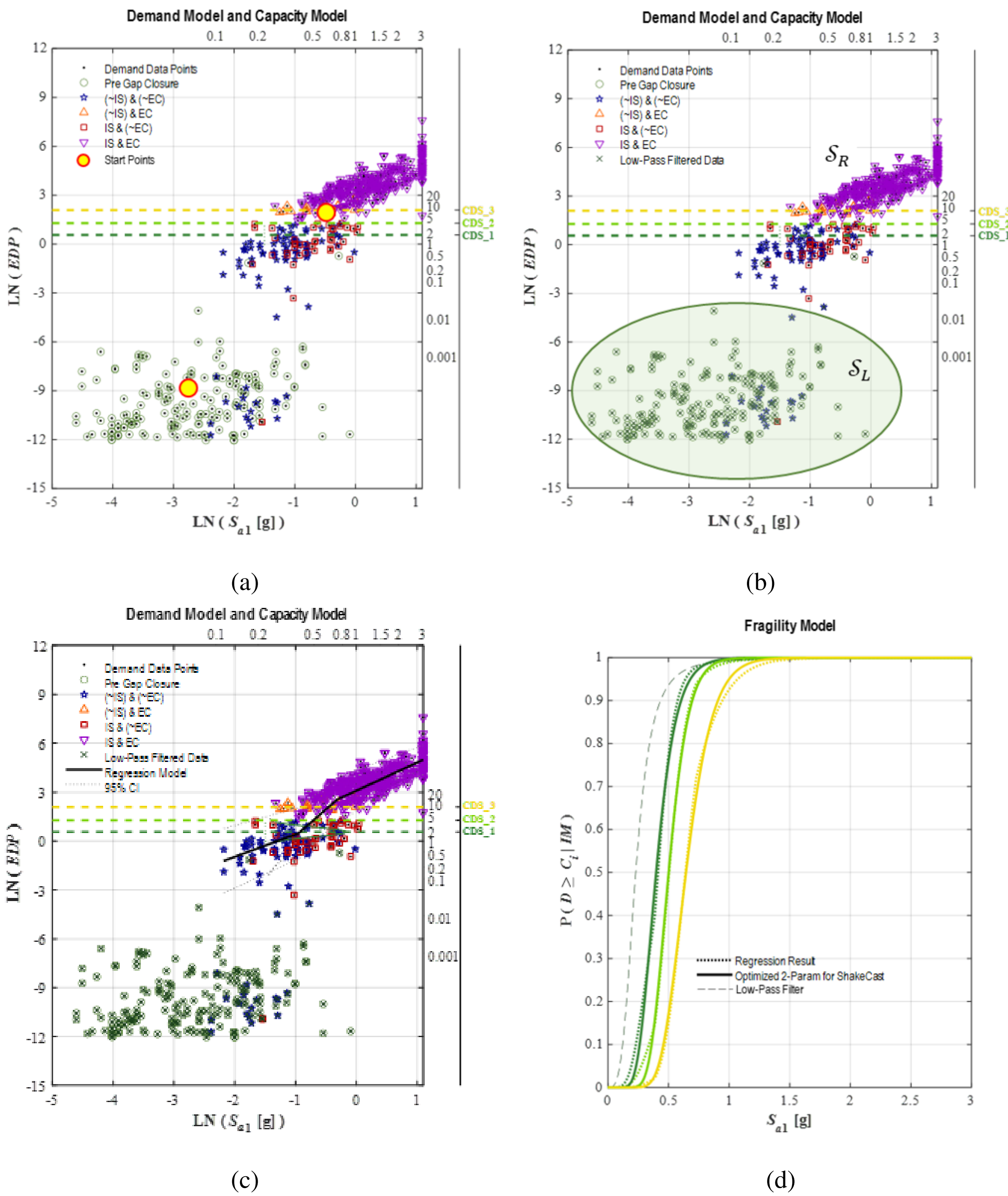

Figure 6.5: Procedure of constructing FAR+ model: (a) Define initial K-means center points; (b) K-means clustering result; (c) M-MARS regression; and (d) Fragility model.

the transition stage where the backwall is engaged and fuses, and the last segment having the largest slope (or highest nonlinearity) represents progressive column failure due to high ground motions. Thus, the segment boundaries in the PSDM using the M-MARS method occur at physically meaningful points in the response. Median fragility values for the seven states are listed in Table 6.2 with the highest CDS_7 value of 2.07 g. Comparable results using the other regression strategies are presented in Figure 6.7 through Figure 6.9 with fragility model values also summarized in Table 6.2.

The linear model is illustrated in Figure 6.7. This single-slope model provides a reasonable match to the data, but the fragility results show that dispersion has increased significantly. Table 6.2 shows the linear produces the smallest median S_{a1} at CDS_1 and the largest at CDS_7 with median values crossing in the mid-state region between states CDS_3 and CDS_4. The difference in the median CDS_7 is roughly 12%, and differences in failure probability at the very-high IM of 3.0 g are about 15% to 20%, both in the non-conservative direction.

The quadratic model, illustrated in Figure 6.8, performs somewhat better than the linear model as it can capture more nonlinearity at high S_{a1} region. As such, its median S_{a1} for CDS_7 is smaller than the linear model, indicating the quadratic model is modestly more conservative relative to the linear model.

The bilinear model, illustrated in Figure 6.9, produces results closest to the adopted M-MARS model. In this case, the difference in median fragility model median values is negligible suggesting two segments are sufficient in this instance. However, as seen in the response data chart on the left of Figure 6.9, the slope-change point $\ln(IM_0)$ is determined by the data alone and therefore lacks a physical explanation for why it is located at 1.0 g.

Table 6.2: Comparison of the fragility median S_{a1} for the four regression models: the red (green) color highlights overestimation (underestimation) of failure probability.

CDS	M-MARS	Linear	Quadratic	Bi-linear
1	0.52	0.46	0.48	0.50
2	0.91	0.8	0.83	0.89
3	1.28	1.24	1.24	1.29
4	1.55	1.58	1.55	1.56
5	1.65	1.73	1.67	1.66
6	1.79	1.92	1.84	1.80
7	2.07	2.32	2.18	2.07

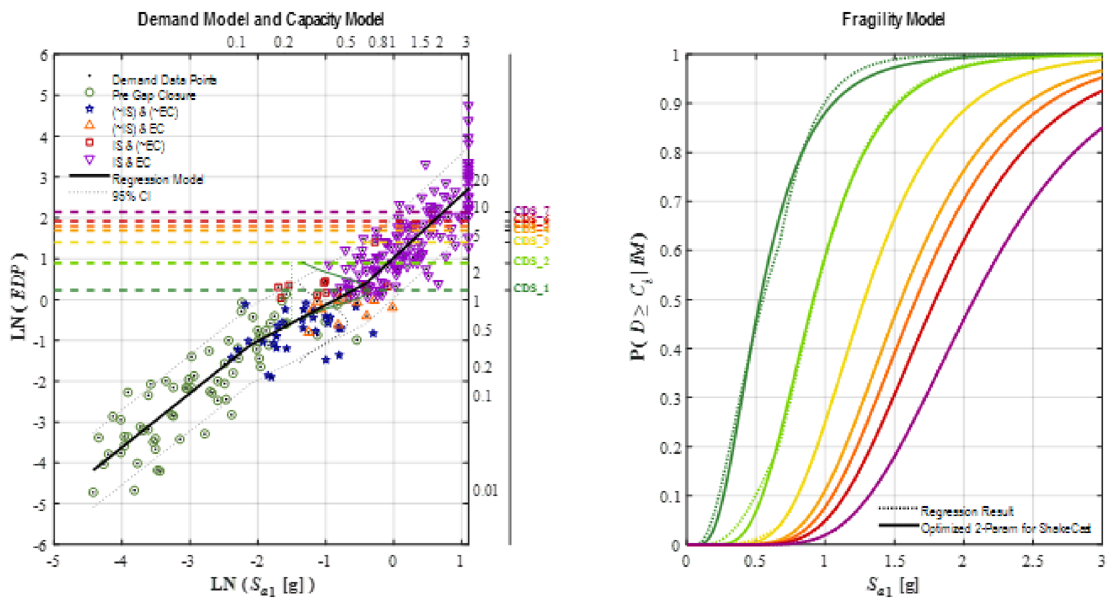

Figure 6.6: Comparison of different regression models: M-MARS model.

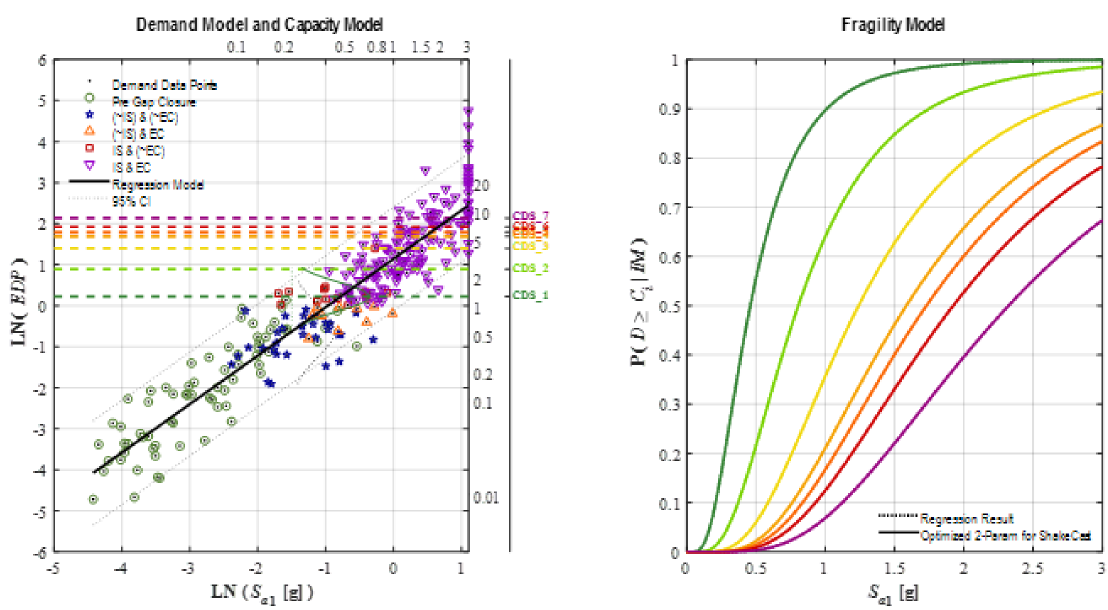

Figure 6.7: Comparison of different regression models: Linear model.

Table 6.4 provides a comparison of mean-squared error (MSE) values from the alternative regression models for several additional components. It shows that the linear model always has the highest error (i.e. 'worst' accuracy). The proposed M-MARS model does not always produce the 'best' model in terms of the MSE. The components where

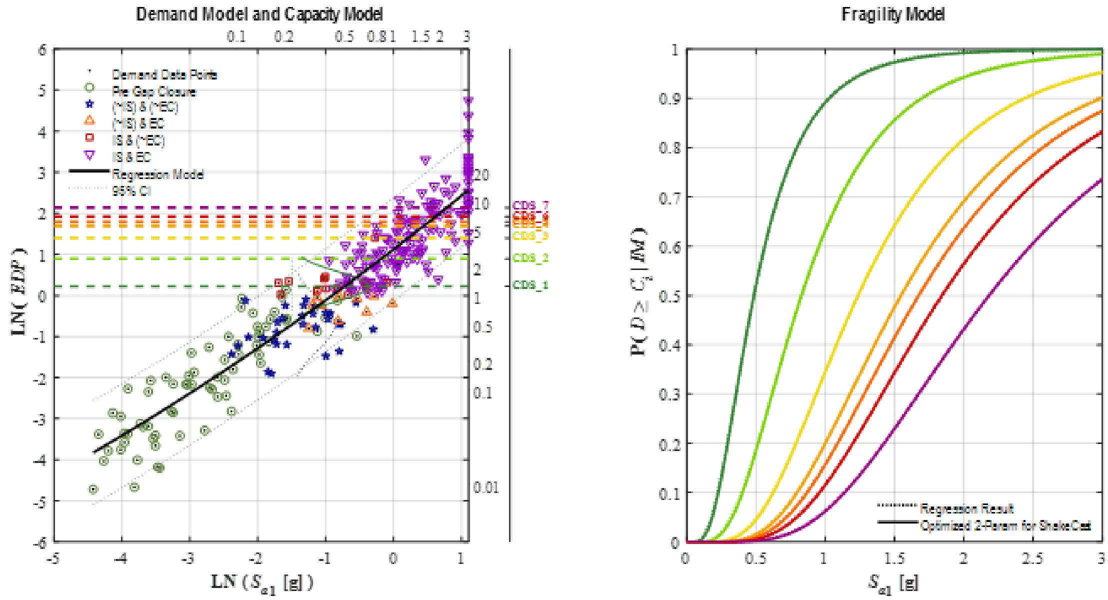

Figure 6.8: Comparison of different regression models: Quadratic model.

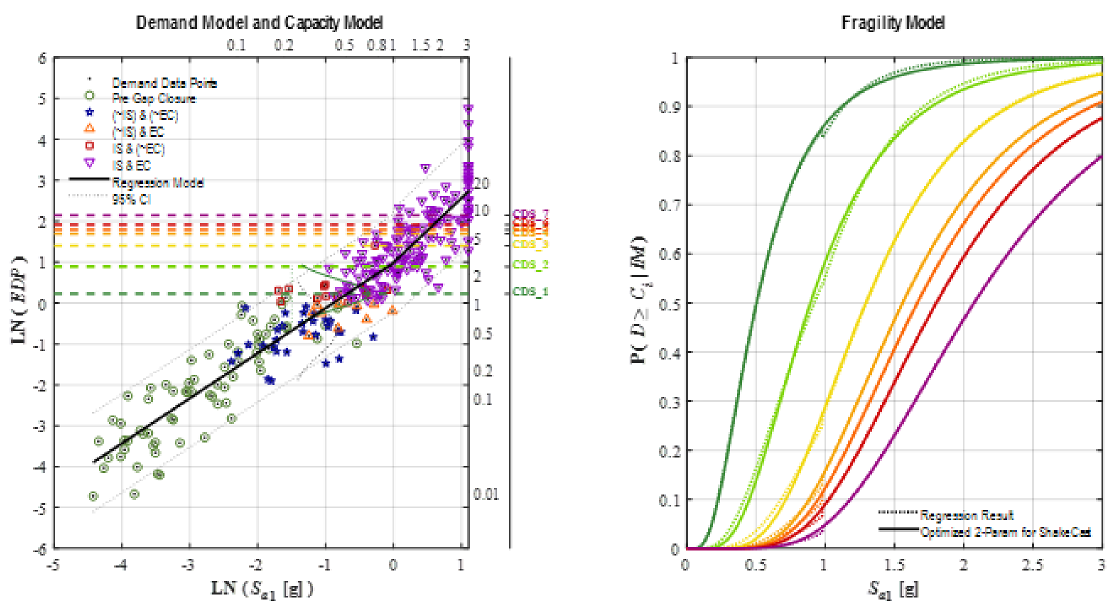

Figure 6.9: Comparison of different regression models: Bilinear model.

higher MSE is observed for M-MARS compared with bilinear or quadratic models are all cases where the PSDM data are readily represented as bilinear. For components requiring higher-order estimation (tri-linear or quad-linear), M-MARS outperforms other models in these terms. The additional benefit of M-MARS is that the segment boundaries, at least initially, correspond with physically significant events in the overall bridge response.

Table 6.3: Comparison of MSE for various methods for PSDM generation.

MSE	**COL_RL** §	**COL_RT**	**maxCTH_WL**	**CFF_L**	**maxUNS_30**	**SEAL_T3**	**AFP_HPL**	**AFP_HPT**
Linear	0.636	0.728	0.838	0.558	0.435	0.495	0.930	0.831
Quadratic	0.631	0.712	0.683	0.546	0.424	0.492	0.912	0.817
Bilinear	0.622	**0.686**	**0.657**	0.537	0.435	0.483	0.851	**0.807**
M-MARS	**0.615**	0.688	0.661	**0.529**	**0.397**	**0.482**	**0.833**	0.811
M-MARS Segments	3	2	2	3	3	3	3	2

§ See Appendix F for abbreviation of components.

6.6 Component-Groups/System Fragility Models and Roll-Up Procedure

Using the methodologies discussed above, one can establish fragility models for different individual components and responses. Some use cases for fragility model application such as inspection guidance, cost estimation, and assessment of bridge-subsystem performance require simultaneous consideration of multiple components. This section details so called 'roll up' processes used to assemble higher-stage fragility models representing various groupings of components.

6.6.1 Multi-Stage Framework for Roll-Up of Fragility Models

The base fragility models developed using methods outlined in prior sections are called ”Stage-0” models in this research. These apply to a single bridge component assessed with a single EDP acting in a single direction, and can only be developed based on a PSDM. Table 6.4 outlines a larger multi-stage framework for the roll-up of the Stage-0 models to represent ever larger groupings of components categorized as Stage-A through Stage-E roll-ups, each of which is described below.

The “Stage-A” roll-up is referred to as “omni-directional”, and represents the overall multi-directional damage state probability developed from separate Stage-0 PSDM models for the two orthogonal directions. As described in Chapter 4, some component responses, such as the backwall-connection and shear key elements are specified in only

Table 6.4: Multi-stage framework for roll-up of base (Stage 0) fragility models

Roll-up Stage	Roll-up objects	Roll-up type	Example
0	NA	NA	backfill-A
A	orthogonal directions	Type-II	regular section column displacement ductility
B.1	multiple sub-types	Type-I	pile-foundations
B.2	multiple EDP's	Type-II	columns
C	multiple components within zone	Type-II	abutment, bent
D	all components in one system	Type-II	e33_s22_isMB_aUS bridges
E	multiple RBS's	Type-II	all e33 bridges

one direction. An elastomeric bearing is an example of an omni-directional component where the maximum recorded EDP (shear strain) could happen in any direction. In this case, the demand model itself could be simply expressed in terms of the omnidirectional peak value and a Stage-0 fragility model developed directly since the capacity model is identical in all directions. However, other components, such as columns, may have separate capacity models for each orthogonal direction (i.e. for a multi-column bent where transverse capacity includes bent-frame effects). The State-0 fragility models for each loading direction thereby reflects only part of the failure probability. Hence, a roll-up procedure is needed for combining the pair of one-directional models into a "Stage-A" fragility model to represent omni-directional damage to a component. Figure 6.10 provides an illustration of a Stage-A roll-up for the case of regular-section column response in the longitudinal and transverse directions. These results show that damage in both directions contribute to the combined fragility model for column performance. In this case, the transverse direction, represented with the dotted line, is seen to control the response (has a smaller median) for the first few states, while the longitudinal direction, represented by the dashed line, has increasing influence at higher states.

The two "Stage-B" roll-ups involves more complicated component assessments where either multiple component subtypes/subgroups are considered, or multiple EDP's are involved in the performance assessment. A "Stage-B.1" roll-up captures overall damage probability to multiple types of the same basic component. Pile foundations provide a good example of multiple component types where separate CCLS models were defined for each of three subgroups (CIDH, PC, Steel) which themselves are combinations of a larger set of individual standard pile types. The capacity models for each subgroup have different values and correspond to distinct failure mechanisms. It is therefore unreasonable to put these subgroups together in a single PSDM. The illustration in Figure 6.11 provides another example, where in this case, the Stage-B.1 rollup combines damage for the two column section-types (regular and wide).

Note that the relationship between individual component fragilities and the combined fragility results in the Stage-B.1 case in Figure 6.11 differs from the pattern observed for Stage-A rollups in Figure 6.10. In the Stage-A case, both Stage-0 curves contribute to combined hazard and the combination always exceeds either part. However, in the Stage-B.1 case, the two Stage-0 curves represent mutually-exclusive component types, so the combined curve represents some mixture of the two hazards and the fragility curve is always in the middle of those for the two subgroups. The precise position of the combined curve is dependent on the mix of subtypes considered in the analysis. In this research, subtype proportions are selected to be consistent with the California bridge inventory.

"Stage-B.2" roll-up captures overall damage probability to one physical component implied by multiple EDPs and capacity models used to assess performance of that component. The g2F framework allows for multi-metric assessment of components, particularly for vital components having multiple failure mechanisms having life-safety implications. For example, column failure could be identified by either global-column damage from excessive displacement ductility demand or local hinge-section damage from excessive curvature ductility demand (or by other mechanisms such as column overturning due to P-Δ effects or lap-splice reinforcement failures in earlier era designs). Under these situations, the Stage-B.2 roll-up procedure is used to establish a combined model considering different failure modes. Figure 6.12 illustrates this using the example of global and local column damage. Both the global and local metrics contribute to the assessment of overall column damage state, thus the combined fragility model is always larger than those for the two individual metrics. Broadly, this multi-metric strategy allows different recognized mechanisms of component failure to be recognized and become the controlling parameter as conditions warrant. In the case shown in Figure 6.12, the global damage controls all of the states and the local damage contributes very little additional hazard.

One of the ShakeCast use cases envisioned for g2F model application is to provide field inspectors with additional guidance for where to look for damage starting with specific bridge regions or zones. A "Stage-C" roll-up is designed to support this use case. This stage of fragility model combines multiple components within a bridge zone. Typically, a bridge can be segmented into three regions: 1) the abutment wall region considering damage to abutment stem walls, wing walls, and foundations; 2) the abutment joint region including the unseating mechanism, the backwall and shear-key fusing mechanisms, and miscellaneous joint component such as bearings and joint seals; and 3) the interior support (e.g. column bent) region considering damage to bent columns and their foundation systems. The interior support region can be further subdivided into zones. In the g2F framework, zone-1 bents refers to those adjacent to the abutment, zone-2 bents are the remaining bents in a single- or dual-frame bridge, and zone-3 bents are those on a freestanding frame having no adjacent abutment. For these regions and zones, Stage-C fragility models reflect damage to all components within the zone. Armed with Stage-C roll-up information, field inspectors could quickly locate likely damage regions or zones and thus improve the inspection efficiency. Figure 6.13 provides an example of a State-C roll-up for zone-1 bent damage including damage contributed by column, foundation rotation connection, and foundation translation. The two foundation damage mechanisms are secondary components with damage models extending only to CDS_5. Thus, for higher states, column damage is the sole contributor to bent damage. In this era-3 bridge case having well-designed foundation systems, column damage controls combined damage for all the states.

A “Stage-D” roll-up generates the overall bridge-system fragility model used to depict the operational state of the bridge. Figure 6.14 shows the State-D roll-up for the case of an era-3 two-span multi-column box-girder bridge. It includes damage to the bent (per Figure 6.13) as well as to the abutment joint and abutment wall regions. The abutment joint damage is further detailed in Appendix F which presents separate and combined fragility models for unseating, backwall, shear key, bearing, and pounding. In this case, the backwall and shear key control abutment joint damage for the respective loading directions as might be expected for these sacrificial elements designed to protect the foundation. These abutment-region damage types control the first three states of the bridge-system fragility model. Beyond that, column-bent damage governs the higher system states. In this study of era-3 abutment design, the abutment wall considers only abutment foundation damage – a component that is not vulnerable due to the fusing action of the backwall and shear key – and thus has only a minor contribution to the overall bridge-system damage state.

Appendix F presents the complete set of 92 fragility models created at all stages for this case study. Note that Table 6.4 includes a “Stage-E” roll-up which is a placeholder for envisioned potential future development of more generic fragility models (e.g. era-3 box girder) which combine multiple RBS for applications where bridge-type information is limited.

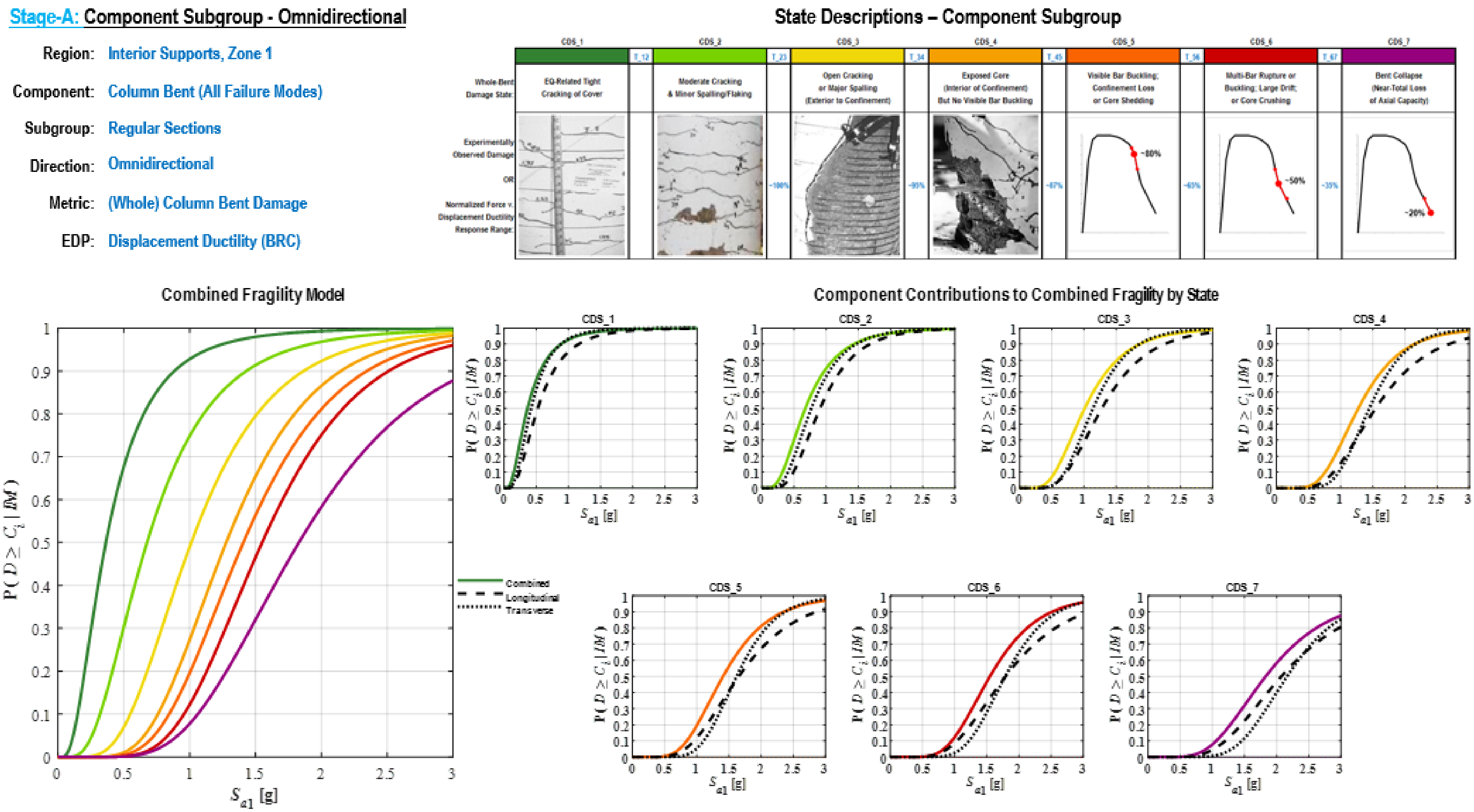

Figure 6.10: Stage-A roll-up: column regular section global displacement ductility response

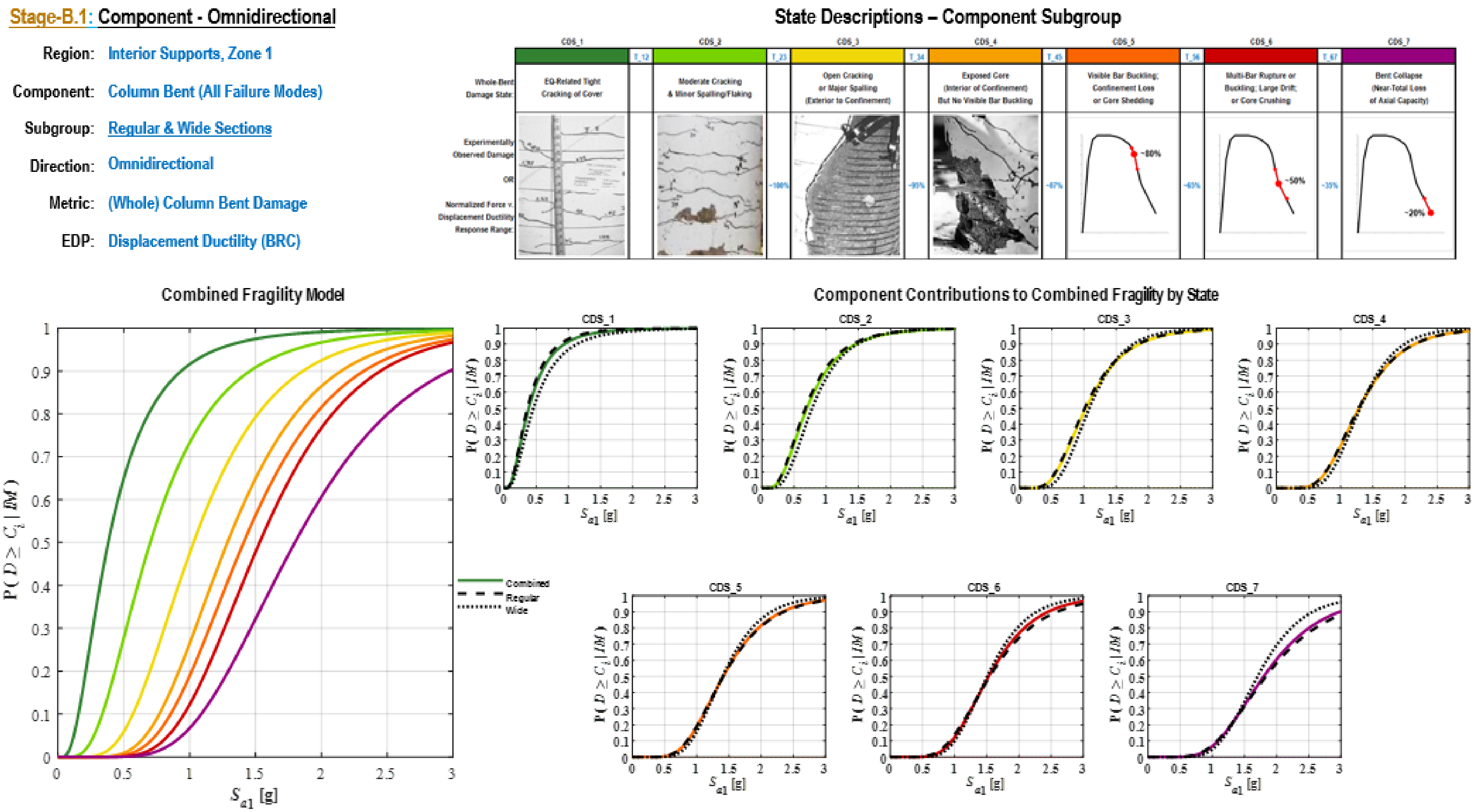

Figure 6.11: Stage-B.1 roll-up: column global displacement ductility response

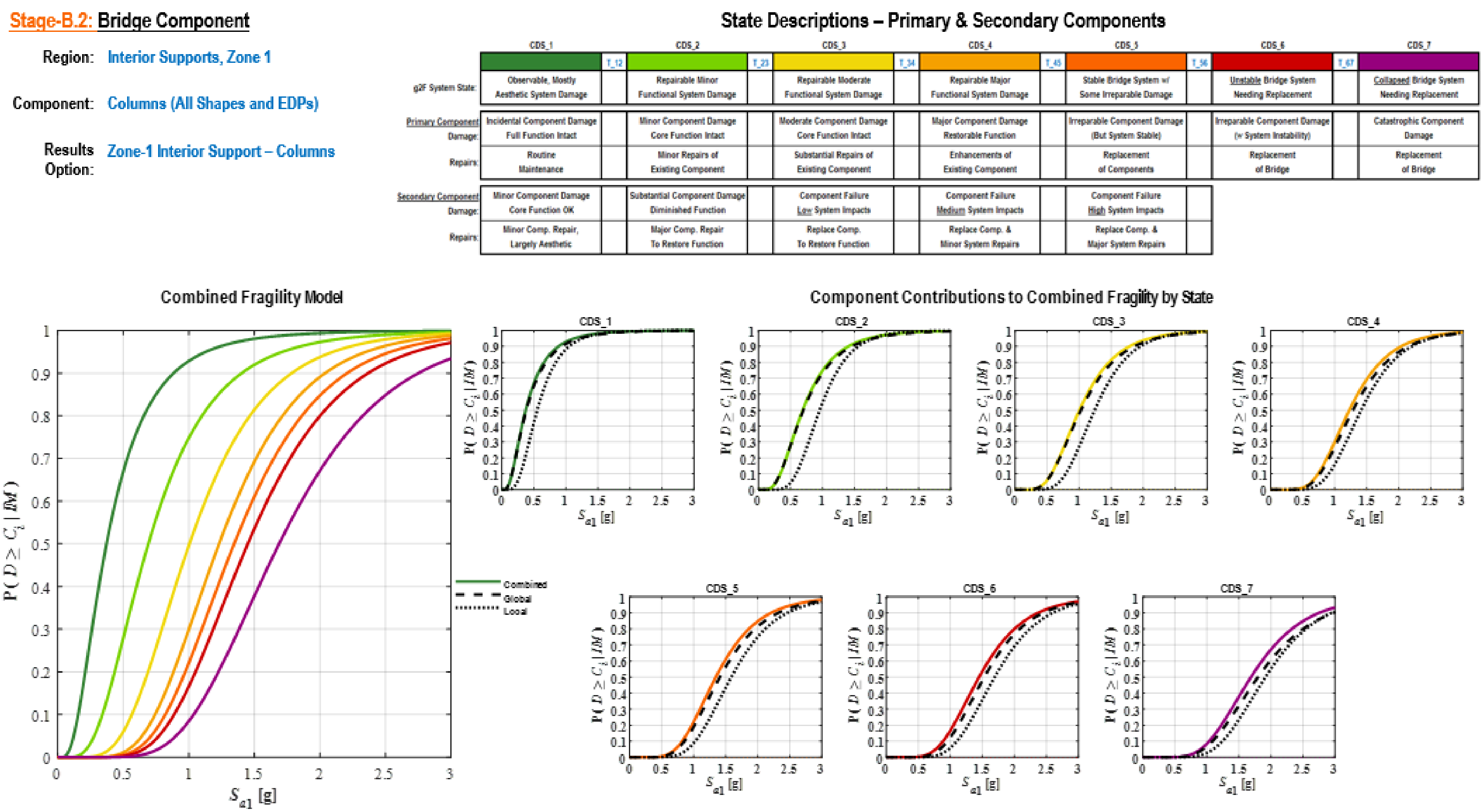

Figure 6.12: Stage-B.2 roll-up: column response

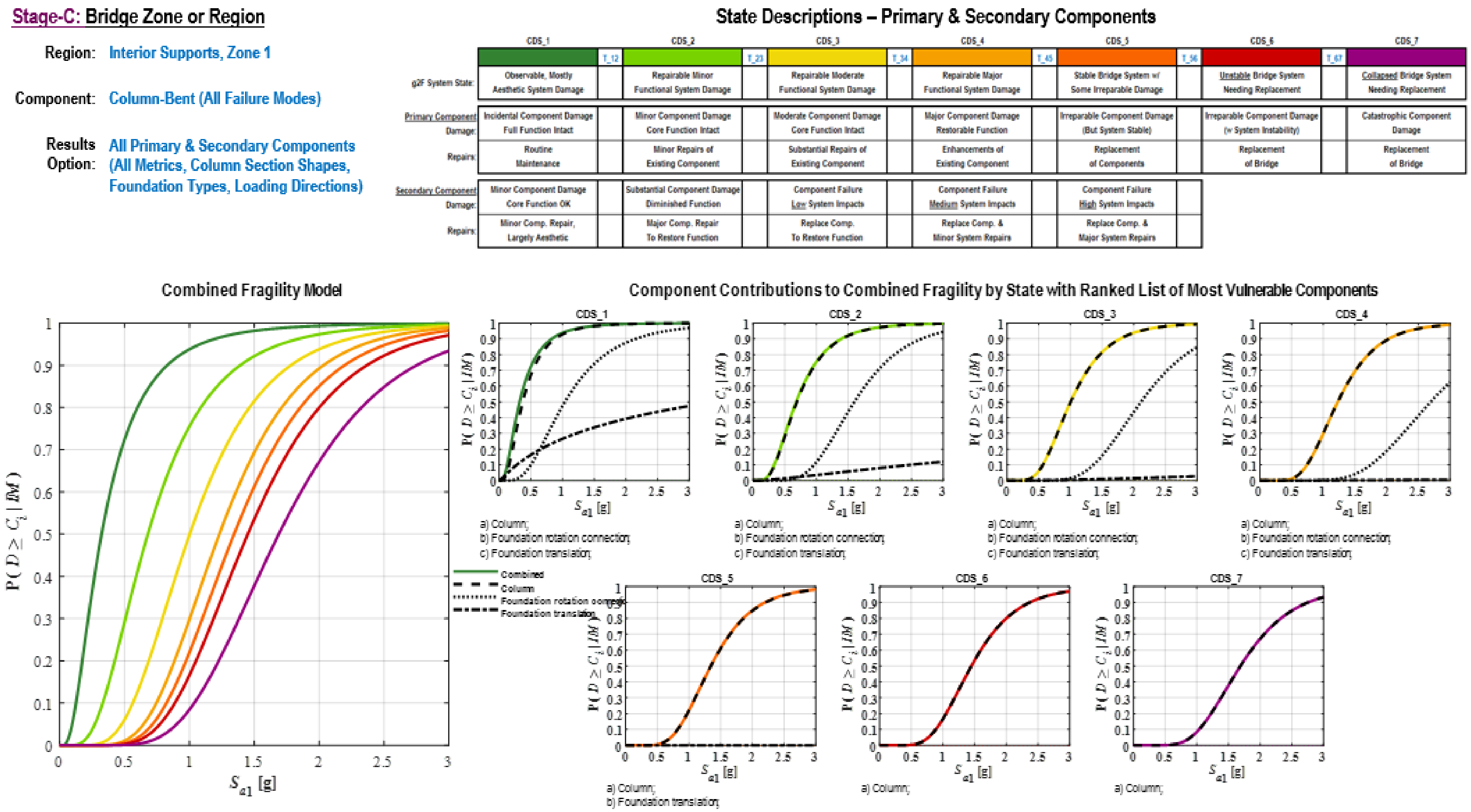

Figure 6.13: Stage-C roll-up: bent response

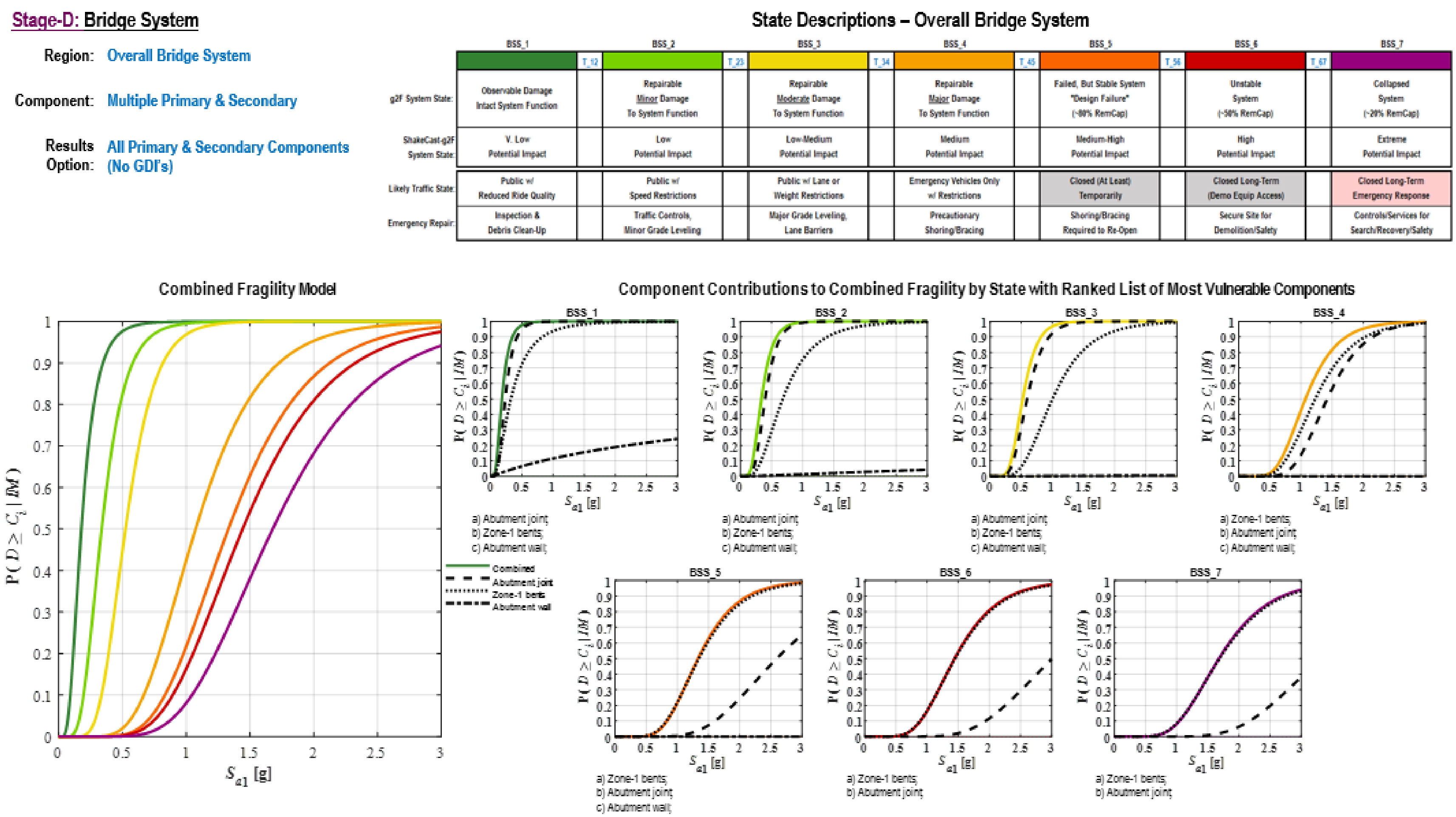

Figure 6.14: Stage-D roll-up: system response

6.6.2 Roll-Up Types and General Methods

As detailed in the last section, there are multiple stages in the overall roll-up process, each serving its own objectives. To implement these roll-ups, two different roll-up procedures are used herein called Type-I and Type-II. As noted in Table 6.4, most roll-ups uses the Type-II procedure, the exception here being for ”Stage-B.1” roll-ups. These two procedures are detailed below.

Type-I roll-up

The “Type-I” roll-up in this research refers to those cases involving the combination of multiple sub-types of the same component. For instance, two subtypes of column sections, regular and wide, each have their own PSDM. Similarly, pile-foundations have three separate PSDM’s corresponding to CIDH concrete, precast concrete, and steel piles. These three types of piles have distinct damage mechanisms and capacity models. While detailed insight on performance can only be provided by considering these subtypes separately, a roll-up of all three types can provide useful a general sense of the approximate component damage if the sub-type is unknown. Using the total probability concept, a simple procedure for implementing the Type-I roll-up is shown in Equation 6.12, where the proportion of each type is written as $P(Type_i)$ and there are T subtypes in total. The failure probability $P(D_i \geq C_i|IM \wedge Type_i)$ is the fragility model developed in ”Level-0”.

$$P(D \geq C|IM) = \sum_{i=1}^{T} P(D_i \geq C_i|IM \wedge Type_i) \cdot P(Type_i). \tag{6.12}$$

Figure 6.11 was an example of the Type-I roll-up. It can be seen that the two mutually exclusive subgroups generate a combined fragility curve located in the middle. Therefore, the boundary for a Type-I roll-up is the minimum and maximum probability of all the considered subgroups.

Type-II roll-up

The “Type II” roll-up in this research refers to a mature procedure to generate system fragility curves using Monte-Carlo simulations as per the work by Nielson (2005) which is adopted herein. Type-II roll-ups provide a means to combine fragility for different loading directions, EDP’s, components regions.

To generate a fragility model using Type-II roll-up, first step is to determine a sample space consisting of multiple steps for the IM of interest, and then also set the number of samples N at each step. A small number of samples N may cause instability of fragility curves, especially when it includes multiple components, while a large number slows down the computation time. In this research, 60 sample steps are set from $S_{a1} = 0\,\mathrm{g}$ to 3.0 g with 5000 samples at each step.

Next, sample N number of seismic demands and capacities for all components at each step of IM. Estimation of the mean and dispersion vectors for seismic demands is calculated by the regression model (PSDM). It is easy to see that both seismic demand and capacity are multivariate normal distributions in logarithm space. Correlation is a crucial part of this sampling procedure and will be discussed separately below. Note that the demand samples included components with sub-types should keep the same proportion of missing data. After generating the N samples at each sample step, the fragility is calculated by averaging the sample number that any of the demands are greater than the corresponding capacities. To represent it mathematically, note that for each component j, there are N sample points, and their corresponding demands and capacities are denoted as D_{ij} and C_{ij}, where $1 \leq i \leq N$ and $1 \leq j \leq M$ given there are total M components in this roll-up procedure. Then the roll-up procedure is written as:

$$P(D \geq C|IM) = \sum_{i=1}^{N} \frac{\max\limits_{1 \leq j \leq M} [\mathbb{I}(D_{ij} \geq C_{ij}|IM)]}{N}, \tag{6.13}$$

where $\mathbb{I}(\cdot)$ is the indicator function, which equals to 1 if the condition is true and 0 otherwise.

Similar to the Type-I roll-up, there is a boundary for the Type-II roll-up in terms of the underlying fragility curves used to create the combined curve. The lower bound is the maximum probability (or envelope) of all underlying components. This represents the idealized case when responses of all underlying components are fully correlated. In contrast, the upper bound is the calculated probability for the opposite idealized case when all roll-up components are fully independent and uncorrelated. For these purposes, the expression 'fully correlated' components indicate that both their demand and capacity models are fully correlated. Similarly, 'independent' applies to both the demand and capacity models. In real-world applications, most components are neither fully correlated nor fully independent. The next section discusses how to determine correlation for such cases.

6.6.3 Demand Correlation: Pearson Correlation and Partial Correlation

In order to properly sample seismic demands for multiple components at each IM step, it is critical to determine the correlation matrix for components and/or EDPs considered in the roll-up procedure.

However, to the knowledge of the author, prior studies have directly calculated the correlation based on the original data, which is the Pearson correlation (Freedman et al., 2020). Pearson correlation does not remove the effect of a set of controlling random variables, i.e., the intensity measurement, which would result in significant over-estimation of the correlation coefficient. Statistically, the sampling procedure of seismic demand data indicates that these data are conditioned on a given IM, or in other words, that the correlation is a measurement with the controlling variable removed. For a sampling procedure that is going to use the correlation matrix, the calculation of the correlation matrix should also be conditioned on a given IM.

To illustrate this problem from an engineering point of view, consider the seismic demands of a component in two orthogonal directions. Given a ground motion intensity, any knowledge of the seismic response in the longitudinal direction cannot improve the prediction accuracy of the response in the transverse direction. On the other hand, if one has no idea of the ground motion, the situation is different because a large seismic response in the longitudinal direction would indicate a relatively large ground motion, which will consequently cause a large response in the transverse direction with relatively high probability. This example illustrates that the seismic responses in two orthogonal directions are indeed conditionally independent given the ground motion intensity.

To address this problem, it is proposed to calculate the correlation matrix using partial correlation (Baba et al., 2004). Partial correlation is calculated based on the residual of the regression model, reflecting the conditional correlation of seismic demands. Using partial correlation is an approximation of the intrinsic value by averaging the correlation through the whole range of IM.

The second issue arises due to the existence of components with sub-types, non-positive responses, and different seismic demand data between abutment components and other components. It is not an easy practice to calculate the correlation matrix directly using the residual data. For example, in a roll-up procedure with K bridge realization, abutment components (e.g., elastomeric bearing pad elements) include $2K$ (two sides of abutment) data points while internal bent components (e.g., column displacement ductility) have only K data points. It is therefore suggested to calculate the correlation matrix pair-wisely. However, it would fail to construct a positive semi-definite matrix. In order to resolve this issue, one would like to compute the nearest positive semi-definite matrix (Higham, 1988) for the covariance matrix.

A comparison of the correlation matrices using the Pearson correlation and Partial correlation is shown in Table 6.5. The matrices shown here includes multiple components including column displacement ductility in longitudinal (COL_L) and transverse (COL_T) directions, column spread footing foundation response in longitudinal (CFF_L) and transverse (CFF_T) directions, and abutment spread footing foundation response in longitudinal (AFF_L) and transverse (AFF_T) directions.

Table 6.5: Demand correlations for damage states

Pearson Correlation						
	COL_L	COL_T	CFF_L	CFF_T	AFF_L	AFF_T
COL_L	1.00	0.94	0.86	0.85	0.85	0.82
COL_T	0.94	1.00	0.79	0.84	0.81	0.80
CFF_L	0.86	0.79	1.00	0.96	0.81	0.78
CFF_T	0.85	0.84	0.96	1.00	0.82	0.83
AFF_L	0.85	0.81	0.81	0.82	1.00	0.91
AFF_T	0.82	0.80	0.78	0.83	0.91	1.00
Partial Correlation						
	COL_L	COL_T	CFF_L	CFF_T	AFF_L	AFF_T
COL_L	1.00	0.60	0.47	0.30	0.29	0.29
COL_T	0.60	1.00	0.15	0.36	0.21	0.33
CFF_L	0.47	0.15	1.00	0.79	-0.02	-0.02
CFF_T	0.30	0.36	0.79	1.00	0.10	0.23
AFF_L	0.29	0.21	-0.02	0.10	1.00	0.63
AFF_T	0.29	0.33	-0.02	0.23	0.63	1.00

As indicated above, the Pearson correlation generates correlation coefficients that are mostly larger than 0.75, while the partial correlation coefficients have large variance ranging from -0.02 to 0.79. Based on the partial correlation coefficient result, the same component in different directions has a correlation value of approximately 0.60 to 0.70; and for different components in the same zone, the correlation value is about 0.10 to 0.50. Responses of the column foundation are only loosely correlated to the responses of abutment foundation, but column response has about 0.30 correlation to the abutment foundation.

6.6.4 Capacity Correlation

Capacity correlations are defined in two parts, namely the correlation between components and the correlation between states. Prior research typically applied a 0% correlation between components and 100% correlation between states.

In this research, the state correlation is formally established using the dataset developed in Chapter 4 and shown below. Although the state correlation is developed based on the column dataset, this correlation is also assumed to be applicable for other components. It can be seen from Table 6.6 that the correlation between states is large when states are adjacent and then degrades as their separation increases.

Table 6.6: Capacity correlations for damage states

	CDS_1	CDS_2	CDS_3	CDS_4	CDS_5	CDS_6	CDS_7
CDS_1	1.00	**0.85**	**0.60**	**0.50**	**0.45**	**0.40**	**0.40**
CDS_2	0.85	1.00	**0.85**	**0.60**	**0.50**	**0.50**	**0.50**
CDS_3	0.60	0.85	1.00	**0.85**	**0.60**	**0.60**	**0.60**
CDS_4	0.50	0.60	0.85	1.00	**0.85**	**0.80**	**0.80**
CDS_5	0.45	0.50	0.60	0.85	1.00	**0.95**	**0.95**
CDS_6	0.40	0.50	0.60	0.80	0.95	1.00	**1.00**
CDS_7	0.40	0.50	0.60	0.80	0.95	1.00	1.00

To avoid the violation of rank order between states, the demand samples need to be sampled separately for each damage state. The resulting fragility models are the same as long as the sample number is sufficient.

Determine the correlation between components is more complex. Table 6.7 lists some values used in this research, which separates the components and/or EDP 's into multiple categories. When sampling the capacity data points for an abutment component on the east and west sides, their capacities are assumed to be the same. The same EDP's in two orthogonal directions, such as column responses in longitudinal and transverse directions, are highly correlated. Capacity correlation between different components is then all assumed to be 15%.

Table 6.7: Capacity correlations for different components

Category	Value	Example
same components in a different zones	1.00	BKW in east and west abutment
same EDP but in orthogonal direction	0.90	zone_1_COL_RL & zone_1_COL_RT
different components in a same zone and same direction	0.15	zone_1_COL_RL & zone_1_CFF_L
different components in a same zone but different direction	0.15	BKW & SKY
different components in different zones	0.15	zone_1_COL_RL & BKW

6.7 Smoothing of Fragility Curves: Re-Sampling for Two-Parameter Model

The primary application now envisioned for the g2F models is implementation within the ShakeCast platform, where two-parameter lognormal fragility model values are required. Therefore, all generated fragility models are further simplified into two-parameter lognormal models. This provides a clear and consistent basis for comparing median fragility model values, or the IM corresponding to 50% failure probability.

6.7.1 Generic Form of Two-Parameter Component Fragility Models

This section outlines the process to compute two-parameter models for component fragility curves. Equation 6.6 depicts the generic form of a fragility model that the $S_{D|IM}$ and $\beta_{D|IM}$ are only constrained by normal assumption of the conditional demand response: $D|IM \sim \mathcal{N}(S_{D|IM}, \beta_{D|IM})$. Assume $\ln S_{D|IM} = f(\ln IM)$ is any function of $\ln IM$ that satisfies the conditional normal assumption. Then Equation 6.6 can be rewritten as below.

$$P(D \geq C|IM) = \Phi\left(\frac{\ln IM - \ln S_F}{\beta_{F|IM}}\right). \tag{6.14}$$

where S_F is the estimation of median for the fragility model that satisfies the relation in Equation 6.14a. The S_F value defines the intersection point of the regression and capacity lines as the fragility median. The fragility model dispersion changes with IM but can approximated as Equation 6.14b using RMSE.

$$f(\ln S_F) = \ln S_C \tag{6.14a}$$

$$\beta_{F|IM} = \sqrt{\beta_C^2 + \beta_{D|IM}^2} \approx \sqrt{\beta_C^2 + \hat{\sigma}^2} \tag{6.14b}$$

6.7.2 Optimization Method

The model discussed above does not include M-PARS or FAR+ because they violate the conditional normal assumption at some IM. For example, in any PSDM that needs to use the FAR+ method, the demand data is a mixture distribution given an IM. In addition, there is no closed form solution for roll-up fragility models. In order to represent the model as two parameters in the form of Equation 6.14, one can use linear regression to approximate the fragility model by rewritting Equation 6.14 into the following form, where $\Phi^{-1}(\cdot)$ is the inverse normal function.

$$\ln IM = \beta_F \cdot \Phi^{-1}\big(P(D \geq C|IM)\big) + \ln S_F \tag{6.15}$$

However, this equation will produce a fragility model that is dominated by the most extended segment. Since the longest segment predicts about 100% failure probability, the regression model gives a poor estimation on the more important transient portion (i.e., from 0% to 100%) of the curve.

Therefore, this research adopts an optimization procedure to minimize the error between the original (multi-segmented) curve and the approximated (2-parameter) curve where the median of the fragility model is the primary emphasis. If available, the median is first determined by Equation 6.14a or interpolation using data around the median. The problem then becomes a one-parameter optimization problem. The other situation is where the median is not available or the failure probability does not reach 50% at the high end of the IM range considered (e.g., 3.0g S_{a1} in this research). In this case, two-parameter optimization is applied to approximate the fragility model.

6.8 Fragility Based Bridge Grouping

The overarching goal of bridge-type grouping is to find the minimum number of unique fragility models needed to reasonably represent truly unique performance characteristics at all base and roll-up fragility levels. Based on review of initial fragility results, this project has begun investigating grouping methods based directly on the fragility models. Unlike the previous studies that are based on performance (PSDM), grouping based on fragility models considers both demand and capacity models. In addition, while some components may reveal unique fragility from a component-damage perspective, they may not significantly impact the system fragility model. In such situations, bridge types are combined using the proposed grouping method.

Given multiple fragility models representative of different subgroups (e.g., regular section columns or wide section columns; four designs of seat width) with multiple states (7 states in this study), these can be rolled up to generate an inventory average model (Type-I roll-up). The proposed method first tests whether the inventory average model can represent all the subgroup fragility models for all states. If the answer is yes, then bridges with these subgroup designs can be grouped. Otherwise, the second step of the proposed method is to investigate whether those subgroups can be grouped again. For example, if the inventory average of seat width models can not represent the four designs (seat width is 30 inches, 36 inches, 48 inches, and 60 inches), it is proposed to continue testing whether the four subgroups can be combined into fewer groups (e.g., one group with seat width = 30 inches and one group with seat width $>$ 30 inches).

The testing method follows the two-sample KS-test (Kolmogorov, 1933; Smirnov et al., 1948). Fragility models are cumulative distribution functions. The maximum difference between two fragility models in the desired range are denoted as the $D_n = \sup |F_i - F_j|$. As a continuous functions, it is discretized with n data points (e.g., n = 1000 used in the following studies). Then the null hypothesis is rejected at level α if:

$$D_n > \sqrt{-\ln{(0.5\alpha)}/n} \tag{6.16}$$

The first step in the proposed grouping method results in multiple indicator vector for each subgroup when comparing them to the inventory average. Denote the indicator vector as $A_i = \{a_{ij}\}$, where i is the index for various subgroups ($1 \leq i \leq I$), j is for different states ($1 \le j \le J$), and

$$a_{ij} = \begin{cases} 1, & \text{the null hypothesis is rejected at state } j \text{ for the } i^{th} \text{ subgroup;} \\ 0, & \text{otherwise.} \end{cases} \tag{6.17}$$

The null hypothesis in this step is subgroup fragility model is the same as the inventory average model. One can conclude that the inventory average model cannot represent different subgroup models if $\max(A) = 1$ where $A = [A_1, \cdots, A_I]^T$.

The second step uses graph theory to determine whether the subgroups can be grouped again. Define an adjacency matrix $G = \{g_{ik}\}$ by calculating $\max(A_i)$ for each possible combination pair of subgroups (i,k). In other word, when picking the k^{th} subgroup ($1 \le k \le I$) as a test model, g_{ik} is defined as the following:

$$g_{ik} = \max(A_i). \tag{6.18}$$

The adjacency matrix G is then used to find the connected graph components, representing these subgroups' possible grouping.

A representative era-3 bridge in California with two-span and multi-column bents is used to illustrate the procedure. After calculating the system fragility models as stated above, the grouping procedure is applied to various subgroups, including seat width designs (four types of designs), section types (regular or wide), joint seal types (compression or strip seal), bent foundation types (pile or footing, and pile material types), abutment foundation types (pile or footing, and pile material types), and bent foundation rotational control types (structural damage or geotechnical damage). Fragility results for these cases are presented in Appendix G. At the bridge-system level, this method indicates there are only two distinct bridge groups out of all the design variations considered: bridges with regular-section columns and bridges with wide-section columns

6.9 Closure

This chapter described the various statistical methods used in establishing PSDM's, both base component fragility models and various types of roll-up fragility models, and a procedure for grouping bridge subtypes having comparable risk.

For constructing a PSDM, the M-MARS and FAR+ methods are adopted. The M-MARS is well suited to handle the highly nonlinear seismic demand data for the varied components. Compared with other methods, it allows for up to 4 segments which provides the flexibility to aligns well with physically-based stages of bridge response. The development and adoption of the FAR+ method provides an effective strategy for handling PSDM's that contain either extremely low or extremely high responses.

Methods to establish a two-parameter lognormal distribution from the higher-order initial models were presented. This is critical for deployment of the g2F models in ShakeCast which is the overall intent. The optimization procedure presented in that section is implemented using the *fconmin* function in the *Matlab* platform.

A four-stage framework for the roll-up of base component fragility models is developed which allows grouping of loading directions, varied component subtypes, multiple damage metrics for the same component, regional/zonal based groupings of component, and finally to bridge-system level performance. A pair of procedures need to implement the various roll-ups are presented. An important contribution here is enumeration of various correlation models needed for appropriate sampling of the demand and capacity models. Also, methods are identified to make the correlation between demand data conditioned on intensity measurement.

A grouping procedure is proposed splitting the system-level fragility curves into subgroups having unique performance traits. This will be useful for assignment of refined bridge categories expected to perform differently. Compared with prior grouping methods based solely on use of the demand data, the proposed bridge-grouping method also accounts for the capacity model.

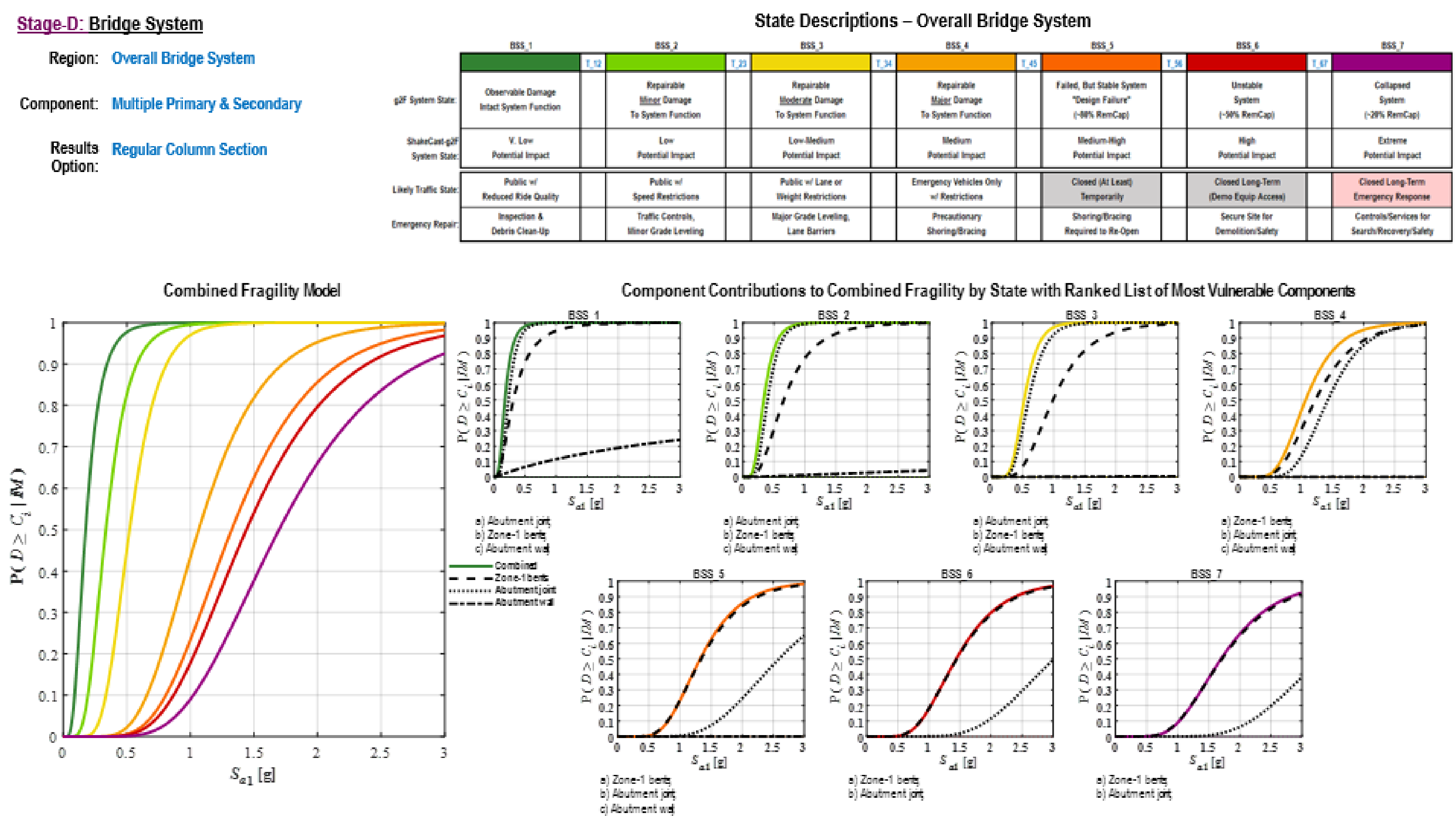

Figure 6.15: Bridge grouping results: regular section model

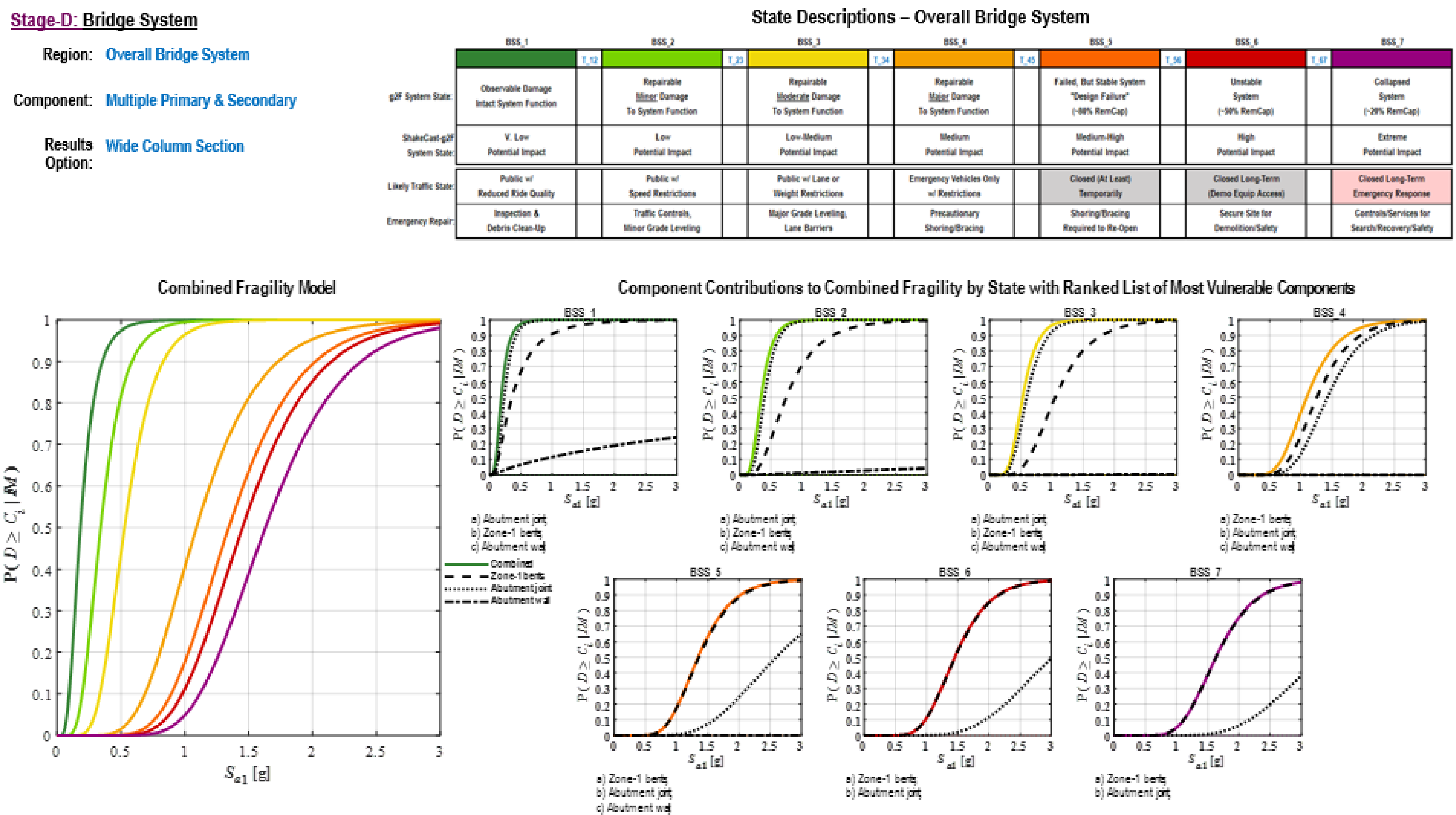

Figure 6.16: Bridge grouping results: wide section model

CHAPTER 7

CONCLUSIONS AND FUTURE WORK

7.1 Summary and Conclusions

This dissertation provides a comprehensive summary of an emerging methodology for the development of a new generation of seismic fragility curves for highway bridges, and details several important new research contributions to this overall methodology. These fragility models are being designed primarily for deployment in the ShakeCast platform, and will be used in the planning of mitigation strategies for, and supporting emergency response immediately after, a damaging earthquake. The methodology and models developed herein are systematically illustrated in the context of a modern California concrete box-girder bridge.

This study makes several significant advances toward increasing the accuracy and utility of seismic risk estimation including the following:

- Improvements in modeling fidelity:

  Multiple new modeling strategies are proposed in this study. Specifically, the adopted column model is shown to overcome the localization issue and refinements in column-response models provides more accurate simulation of various failure mechanisms such as buckling, shear, and lap-splice damage. Validation of a variety of the column models is also included in this study. Additionally, a new abutment response model is developed to account for the backwall fracture mechanism within a larger context of deck-abutment interactions. A case study illustration for the OSB1 bridge shows the proposed abutment modeling scheme produces more realistic results compared to prior models. Through an in-depth review of component modeling strategies, improved three-dimensional nonlinear finite element models are established for dynamic seismic analysis.

- Refinement of capacity models:

  An emerging seven-state framework for consistent sets of component and bridge-system level fragility models is established. Within this framework, component capacity models are proposed for various primary and secondary bridge components. In particular, this study significantly advanced the development of column capacity models by harmonizing an extensive set of experimental tests (i.e. the RP1 dataset) with results from a systematic program of finite element simulations focused on high state performance and the effects of alternate bent-configurations (i.e. the HS-R study). The resulting capacity models provide a refined and well-grounded vision for bridge damage assessment.

- Identification of uncertainties and design constraints in creating virtual bridge realizations:

  The study develops probabilistic models for specifying all major components of modern single-frame concrete box-girder bridges where the component models are based on a comprehensive review of the California bridge inventory. Moreover, three types of design constraints are developed and implemented within the sampling procedure to reflect inherent bridge design correlations. The combination of inventory-based stochastic component models and design-based sampling constraints support the creation of realistic virtual bridge realizations used for production simulations.

- Methodology improvements for integrating demand and capacity to generate fragility models:

  The maximum/average responses (demand data) are obtained through conduct of nonlinear dynamic numerical simulations on the virtual bridges created using the adopted modeling strategies. This study examined multiple methods of integrating demand data and capacity models and concluded that the adopted M-MARS and FAR+ methods are capable of not only representing highly nonlinear data but also allows consideration of the PSDM data in terms of physical phenomena controlling highly non-linear bridge response. Furthermore, this study develops four stages of fragility models to facilitate various engineering applications. To generate more accurate component-group fragility models, this study carefully examined the correlation between demand components and concludes that the use of partial correlation is more appropriate than Pearson correlation. Ultimately, the study seeks to develop an innovative method to group bridges by distinguishing different system fragility models.

As part of these endeavors to establish more useful and reliable seismic bridge fragility models, several important findings emerged including:

1. Accurate modeling of the straight backwall fracture mechanism has a significant impact on bridge performance. The comparison of static pushover results in Chapter 3 indicates that the newly-developed model accurately simulates the protective effect of backwall fusing on the abutment foundation. In contrast to the conventional model — in which abutment foundations completely fail -– the new model shows that the abutment foundation is protected by the backwall-fracture mechanism, resulting in only minor damage to the lower portion of the abutment. The new model also shows that columns must resist larger loads and bearings undergo fully elasto-plastic behavior which is all consistent with modern bridge design principles.

2. The newly developed column capacity models introduce a redundancy effect to account for framing behavior of flexural columns in multi-column bents loaded transversely. Inclusion of this effect results in about 15% improvement in the displacement ductility capacity of multi-column bents relative to single-column

bents for the safety-related states (CDS_5 to CDS_7).

3. In Chapter 5, the incorporation of three design constraints on the bridge-component sampling procedure, most notably the ground motion pairing strategy, is shown to have significant influence on the resulting column and bridge fragility models for the last three safety-related states. Compared with the fragility model without ground motion pairing, the median S_{a1} of the proposed model (with ground motion pairing) increases nearly 20% (2.25g to 2.70g) for the collapse state (CDS 7) and causes the failure probability at 2.00g to decrease from about 39% to 25%.

4. Comparison of multiple PSDM development methodologies is shown in Chapter 6. The regular linear regression model fails to accurately predict the median. In contrast, the proposed M-MARS and FAR+ provide better estimation to the data median, generate a smaller MSE, and allow a clear physical interpretation of the PSDM model.

5. A complete set of base and roll-up fragility models for the case study of a modern ductile designed bridge are provided in Appendix F. The stage-3 roll-up indicates that the vulnerability sequence of components in a column bent is: column, foundation rotation connection, and lastly the foundation transition. In the abutment joint region, the backwall and shear key control the fragility models of the first four damage states. It also demonstrates that unseating is not as likely as damage to other components for CDS_1 to CDS_4 (CDS_5 to CDS_7 have only the unseating component). In the system fragility model, the abutment joint region is found to control vulnerability for the first three states, while the column bent region controls the last four states as fewer components are included in the abutment joint. For this modern bridge design, the abutment foundation is always the least vulnerable component as a result of the designed protective effect from the abutment backwall fracture.

6. Appendix G shows the bridge grouping results for this studied case (era-3 two-span multi-column-bent bridge). Except for the column section shapes, the maximum difference of the failure probability between various subgroups and inventory average models is only about 5%, concluding that the studied case could be subdivided into two unique bridge models, ones with either regular or wide column sections.

7.2 Research Impact

Contributions of this study include:

- Development of a new abutment modeling scheme to capture the abutment straight backwall fracture mechanism and thereby more fully characterize the resulting interactions between deck, column, abutment components and backfill;
- Advanced component modeling techniques in several ways including: better modeling of columns with different failure modes (flexural, flexural-shear, shear, and lap-splice failures); usage of deck grillage model (instead of spine model) for more accurate bent responses, and development of component backbone models for abutment straight backwall connections; and three types of shear keys (isolation, external, and internal);
- Validated modeling of columns and other components' against experimental tests;
- Compiled, characterized and documented specimen, test, and experimental performance data for 198 columns in a column performance dataset;
- Supported development of component damage definitions compatible with the emerging seven-damage-state framework;
- Defined initial emerging capacity model values for various components within the scope of the damage-state framework;

- Developed a double normalization strategy for internally consistent processing of demand data and capacity models for components such as foundation piles, backwalls, and shear keys which are modeled using response backbones;
- Developed a comprehensive procedure for the sampling and constraining of component models for specification of virtual bridges used in seismic demand simulations;
- Developed the M-MARS and FAR+ methods for more accurate regression of PSDM's and improved fragility curves;
- Compared multiple multiple classical and contemporary methodologies for generating component fragility curves;
- Outlined a comprehensive framework for four-stage roll-up of base component fragility models to facilitate various engineering applications
- Summarized extensive studies into the correlation of demands among various bridge components;
- Proposed a bridge grouping method for isolating unique-performance subgroups of bridge system fragility models.

7.3 Recommendations for Future Work

The following is a list of potential topics where this work can be extended through additional research:

- Immediate research needs now underway include: refinement and finalization of component capacity models; refinement and streamlining of the number of fragility models; development and consistent application of adjustment factors on base system response; and extension of this emerging methodology to a wide variety of concrete bridge designs, particularly for earlier design eras and other design types (i.e. I-girder, T-girder, slab, etc.).

- Near-future research needs include: exploration and iterative refinement of processes to effectively assign fragility models (system through component levels) to bridges in the California inventory (and beyond) within the ShakeCast platform; and validation of the performance of these fragility models against field observations from real earthquakes.

- In the longer term, similar compatible fragility models need to be developed for steel bridge types. This includes characterization of damage mechanisms unique to these bridges and development and/or adaptation of component response models needed to develop demand, capacity and fragility models.

- At the more fundamental research level, work should continue on compiling experimental test data for columns and other bridge components, and using these data to guide development of refinements in the response models used for both demand and capacity assessment.

- As a separate focus, efficient means of developing bridge-specific fragility models from basic design-floor information should be explored.

Appendices

APPENDIX A

BRIDGE PLAN FOR OSB1

The following is a generic bridge plan representative of modern Caltrans design practices called Ordinary Standard Bridge 1 (OSB1). OSB1 is a two-span bridge with a two-column bent. The bridge superstructure has a span length of 150.0 ft, deck width of 47.5 ft, and section depth of 6.0 ft. The columns are 20.0 ft height. The circular column section has 66 inch diameter with #8@6-inch transverse reinforcement, which corresponds to approximately 0.85% transverse reinforcement ratio. Note that the column reinforcing detail (Section H-H) was modified slightly to be 44 rather than 36#11 reinforcements such that the longitudinal reinforcement ratio is approximately 2.0%.

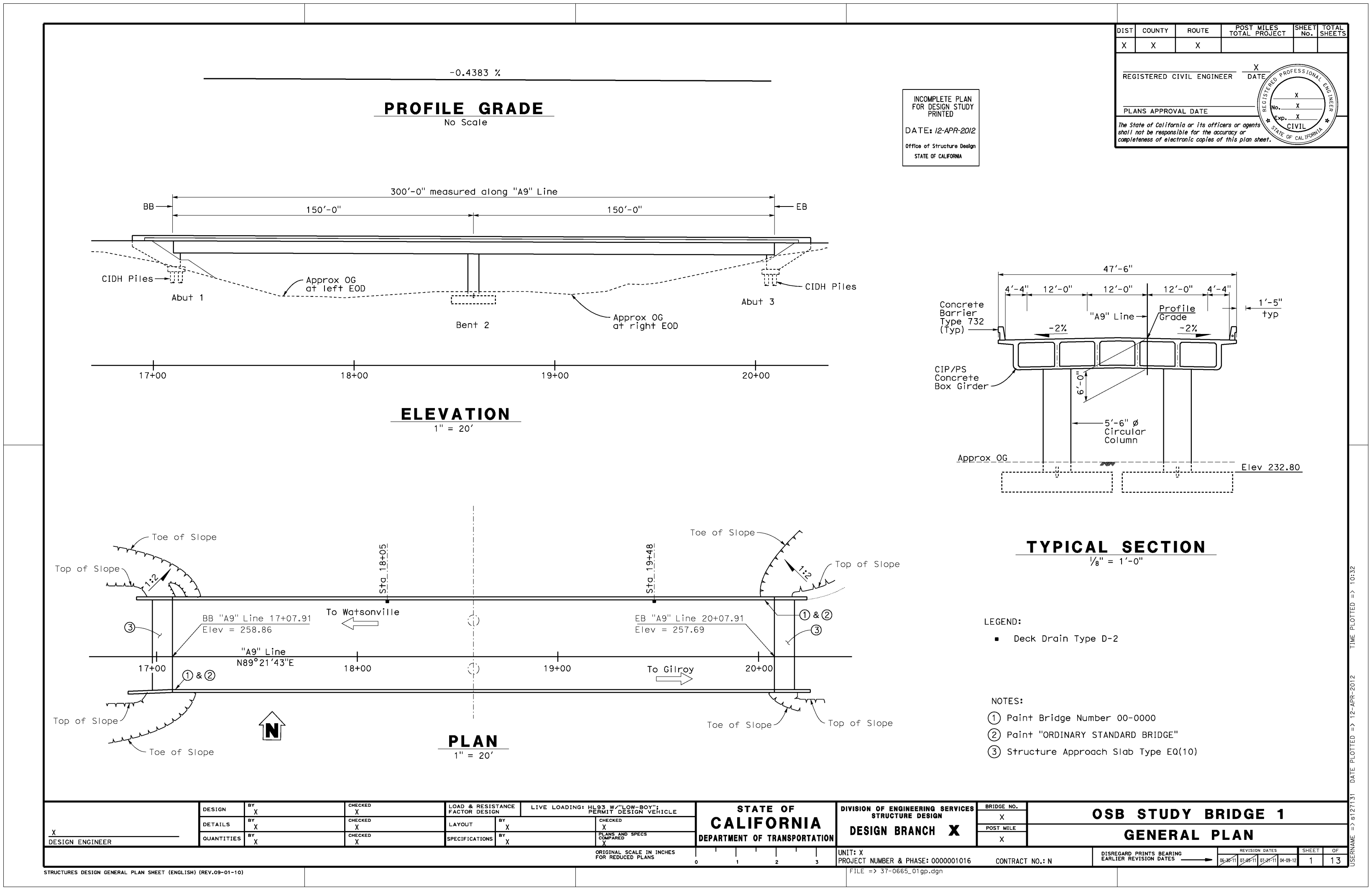

Figure A.1: OSB1 bridge plan drawing page-01

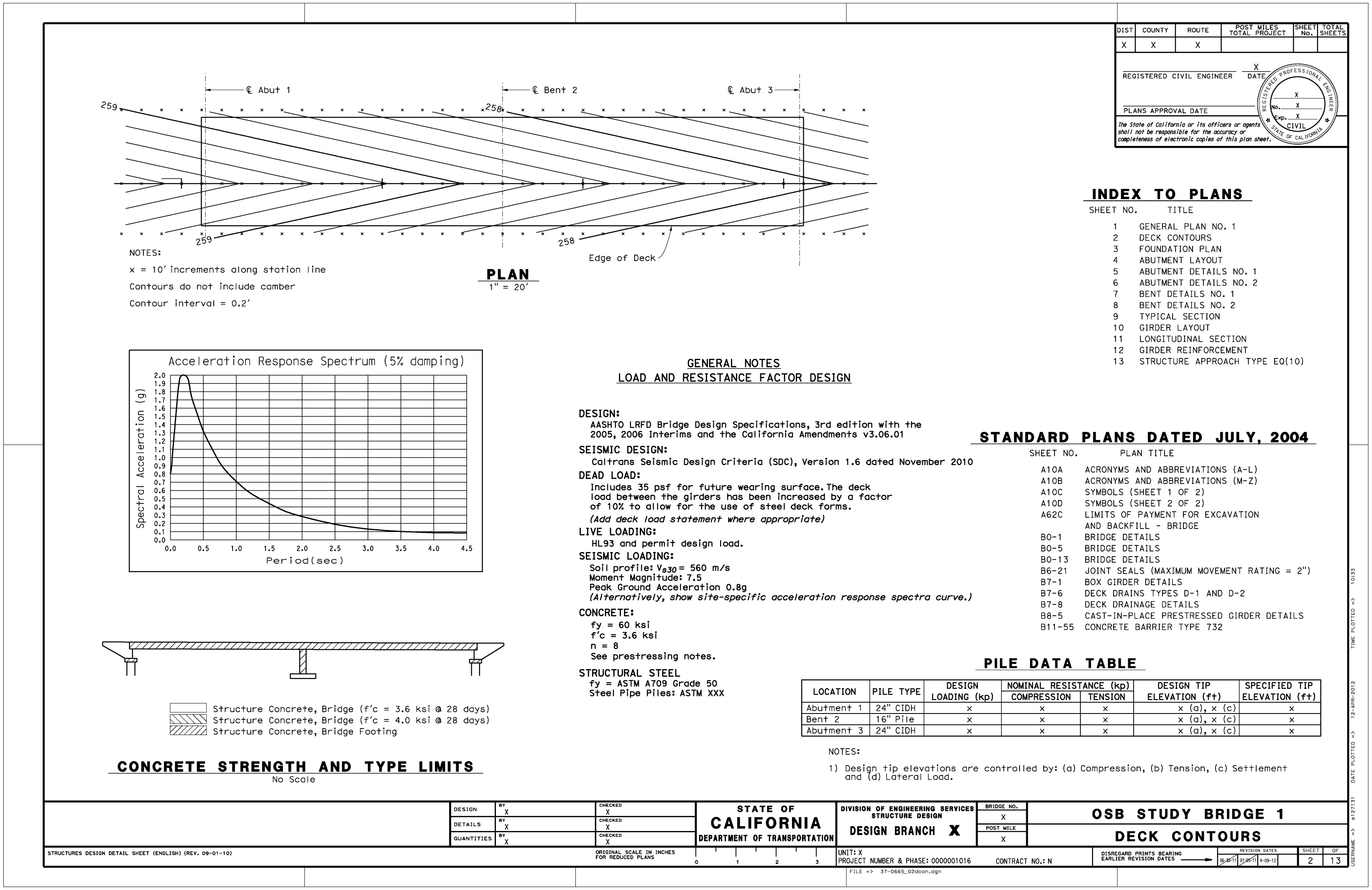

Figure A.2: OSB1 bridge plan drawing page-02

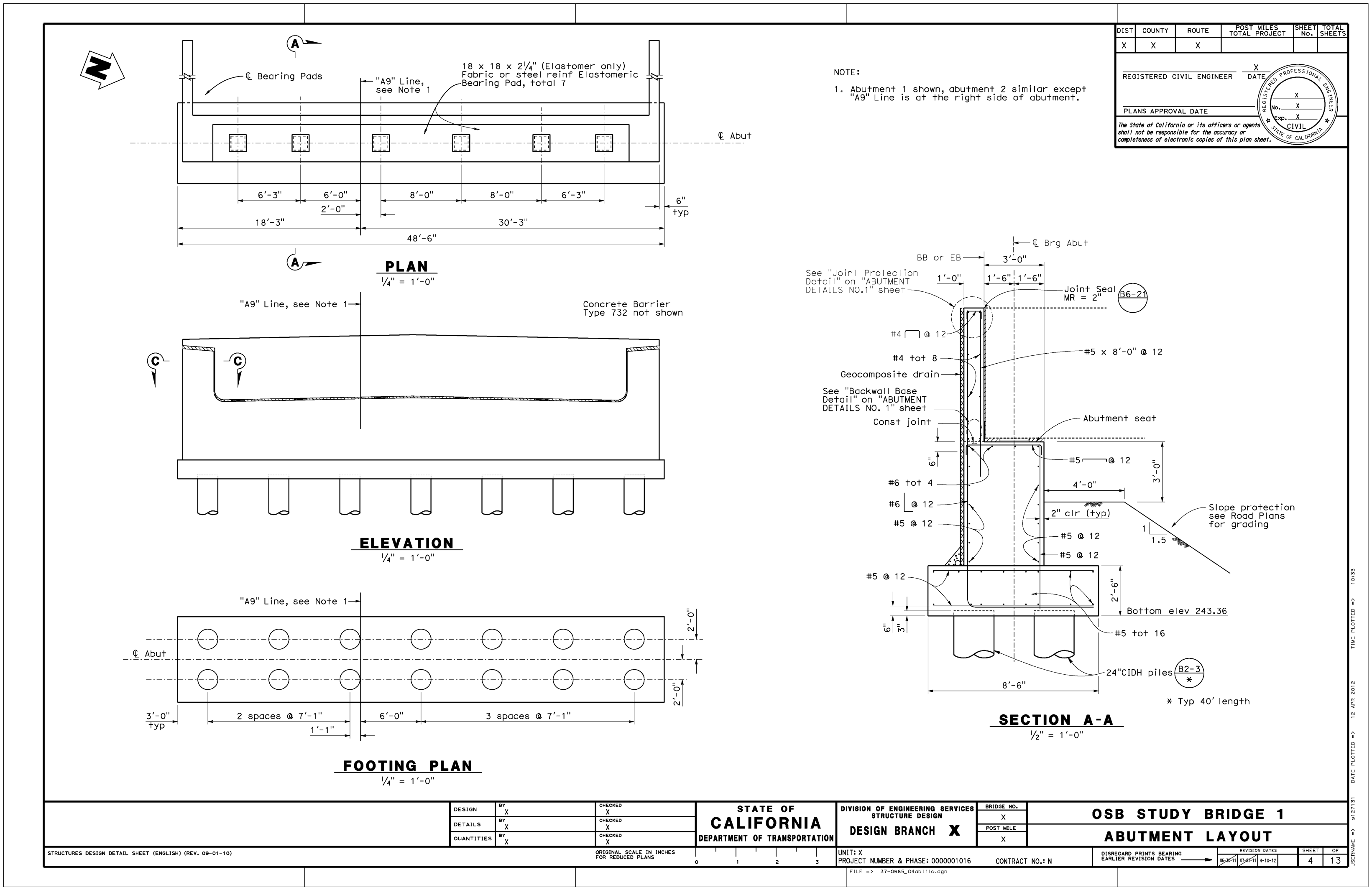

Figure A.3: OSB1 bridge plan drawing page-03

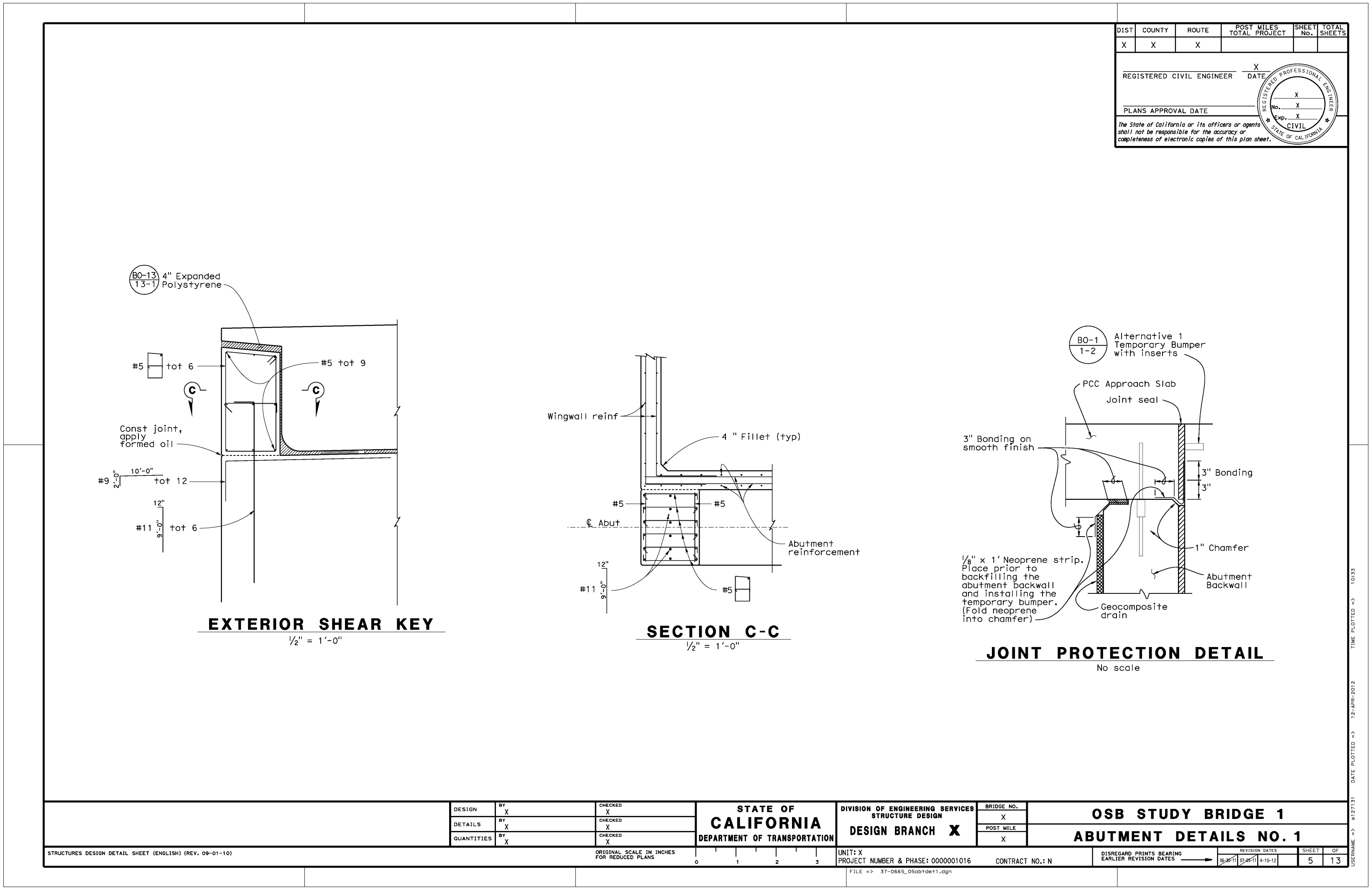

Figure A.4: OSB1 bridge plan drawing page-04

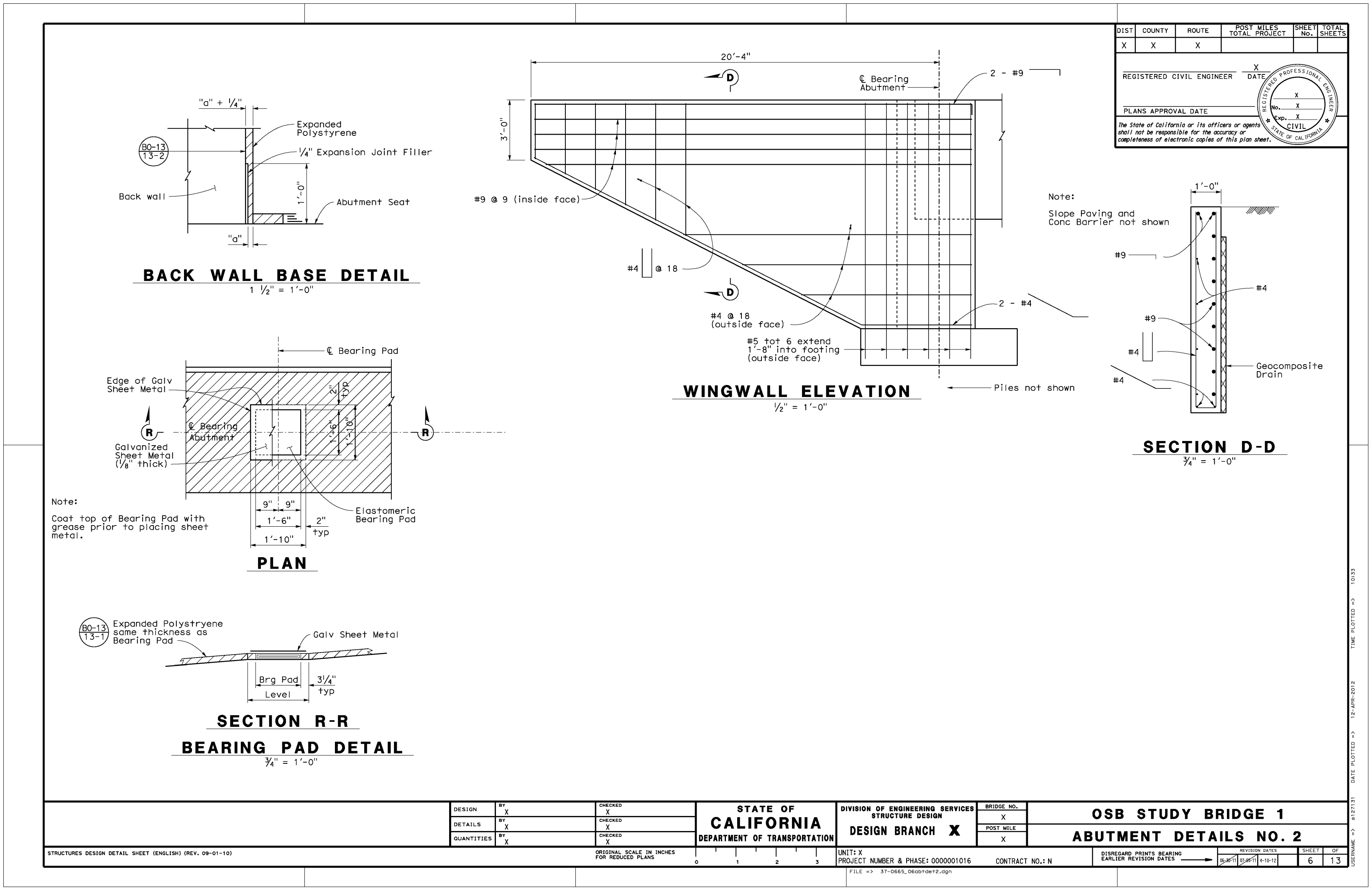

Figure A.5: OSB1 bridge plan drawing page-05

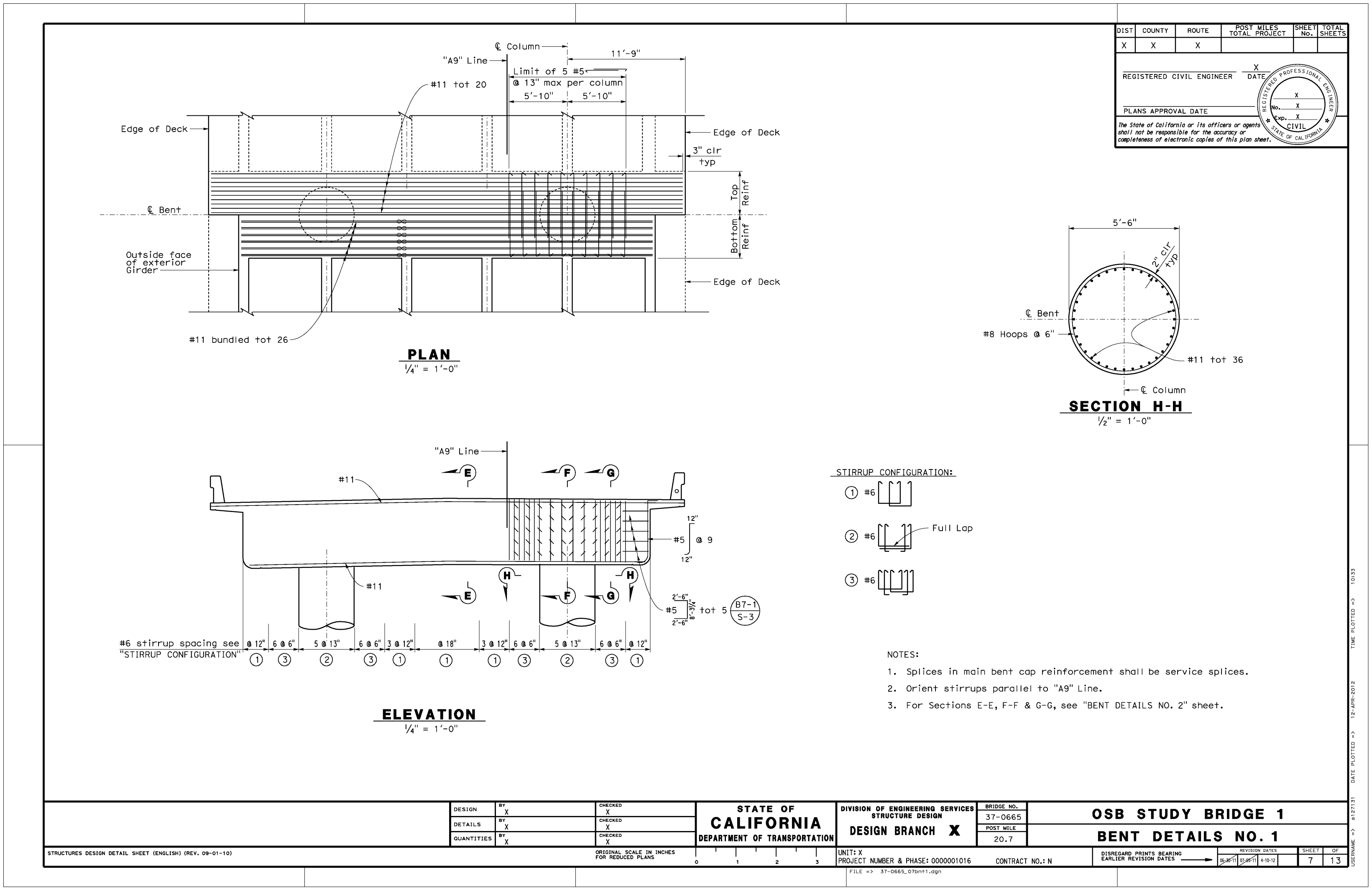

Figure A.6: OSB1 bridge plan drawing page-06

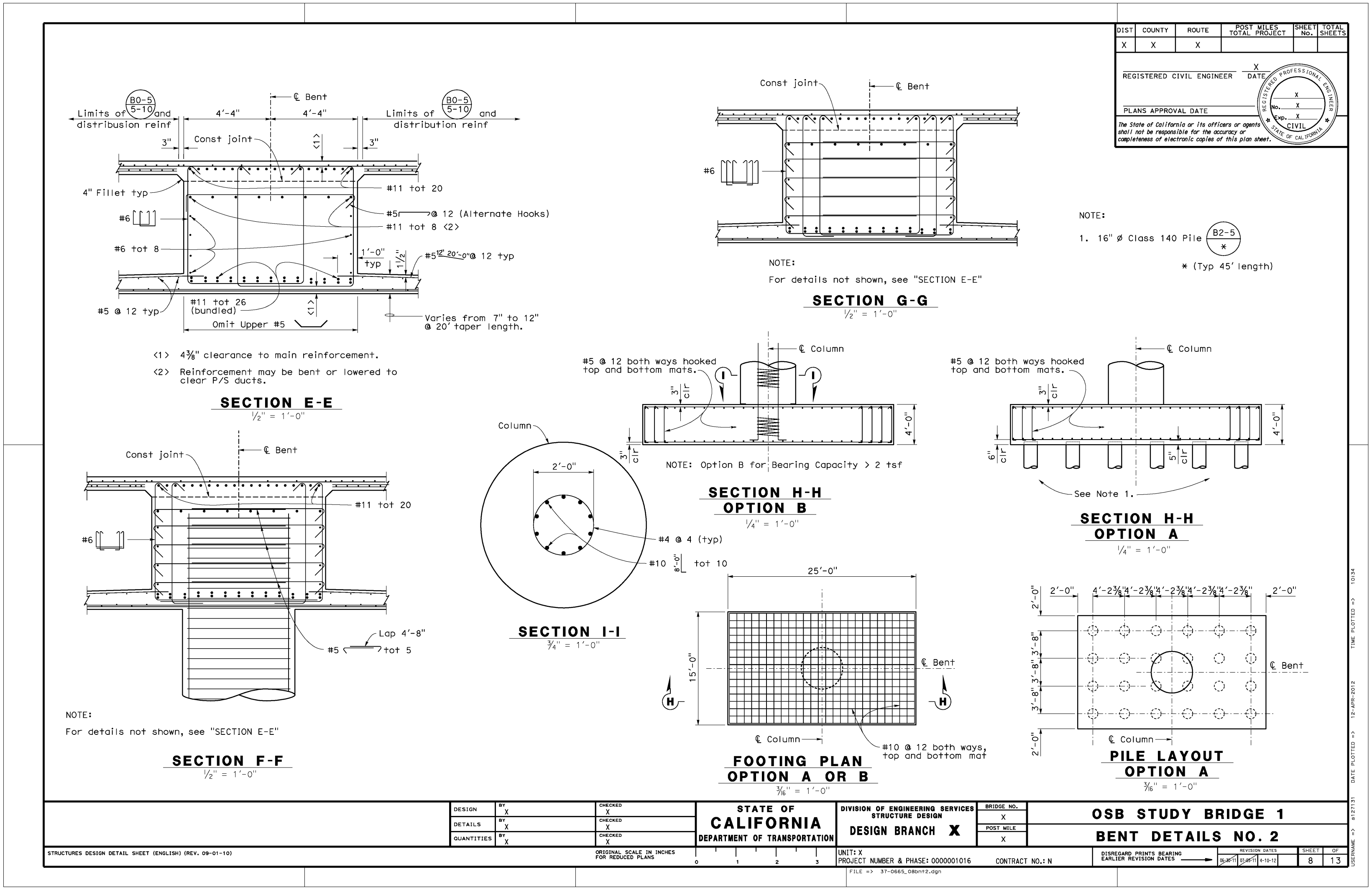

Figure A.7: OSB1 bridge plan drawing page-07

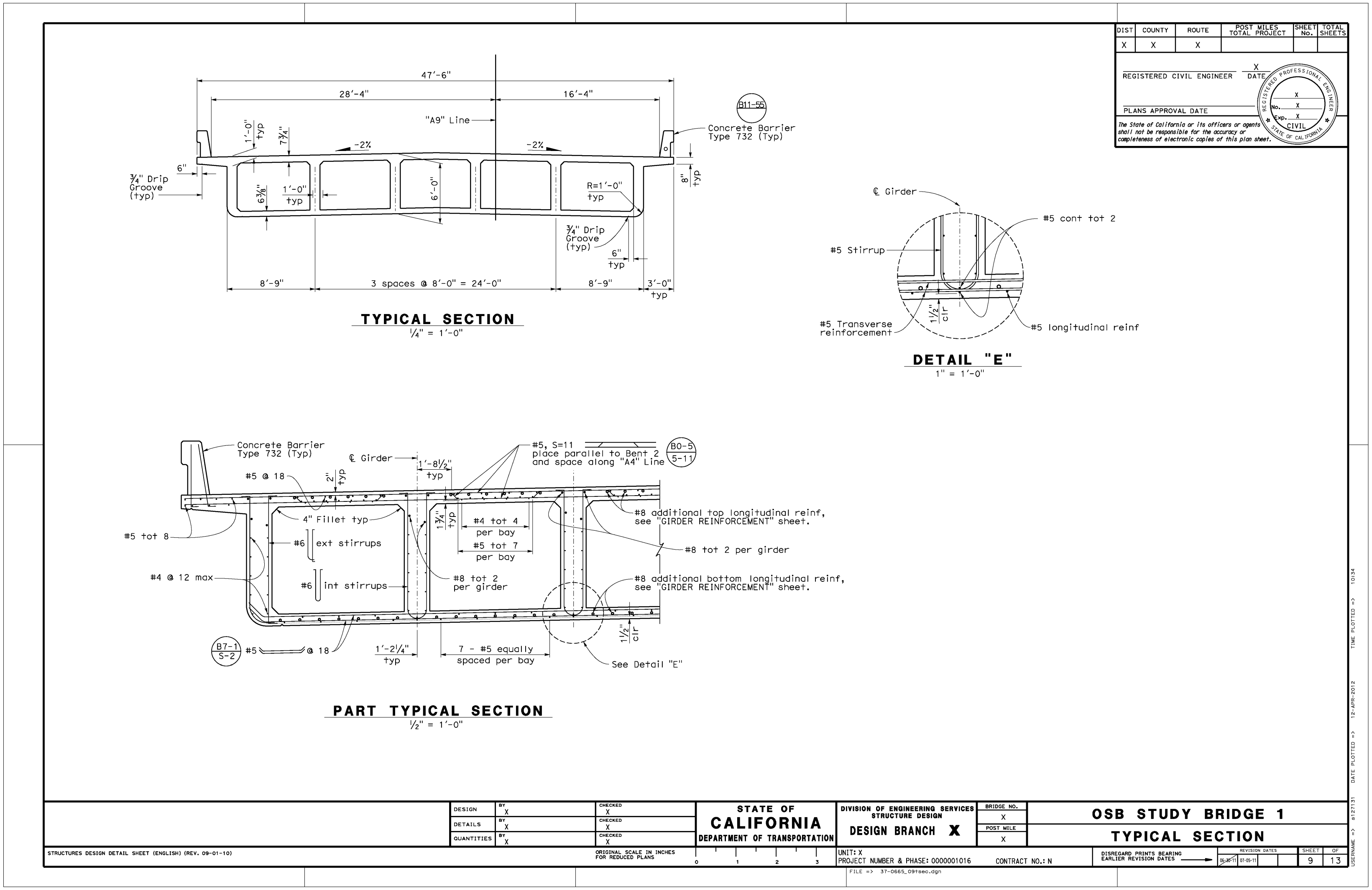

Figure A.8: OSB1 bridge plan drawing page-08

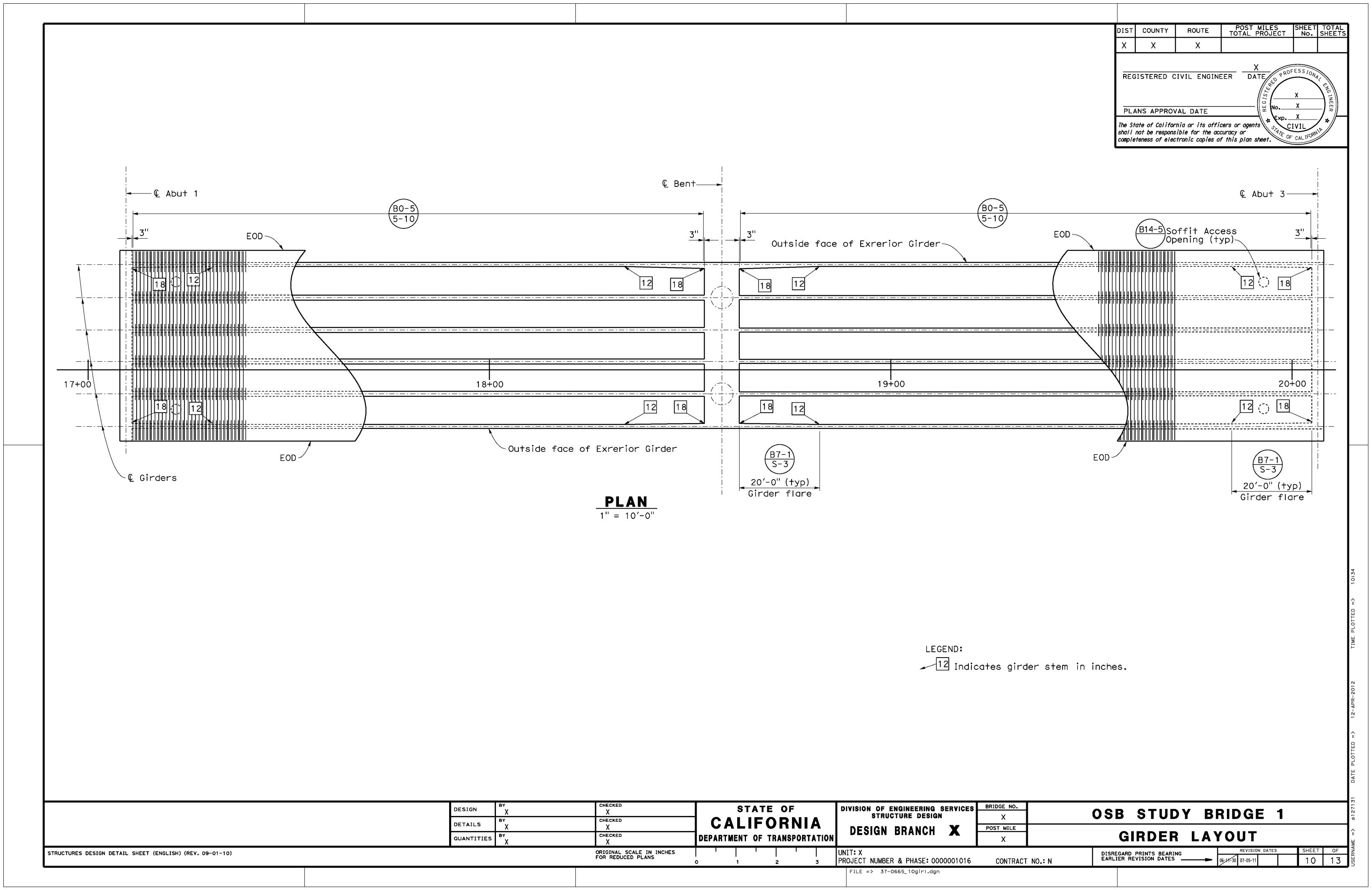

Figure A.9: OSB1 bridge plan drawing page-09

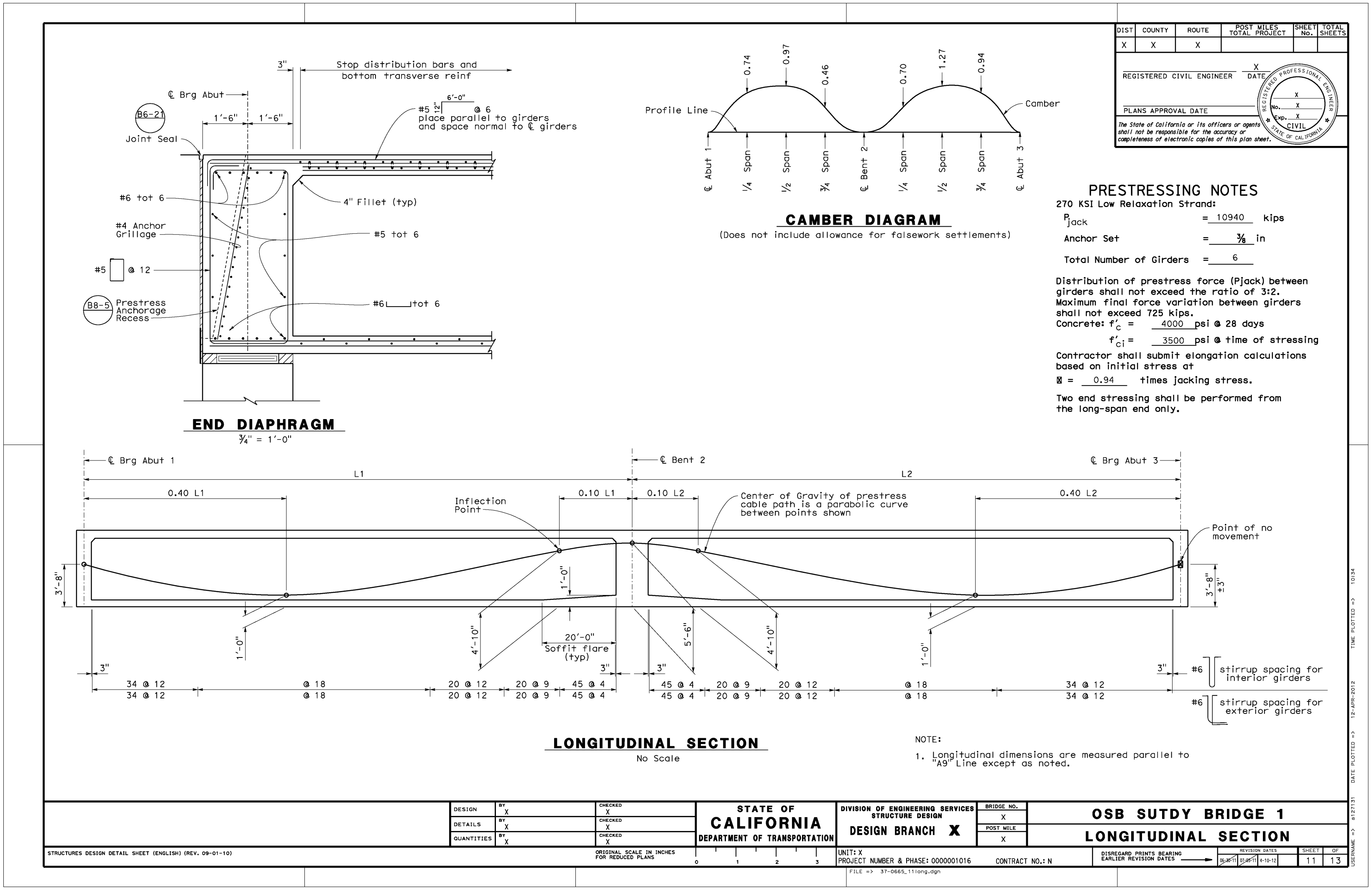

Figure A.10: OSB1 bridge plan drawing page-10

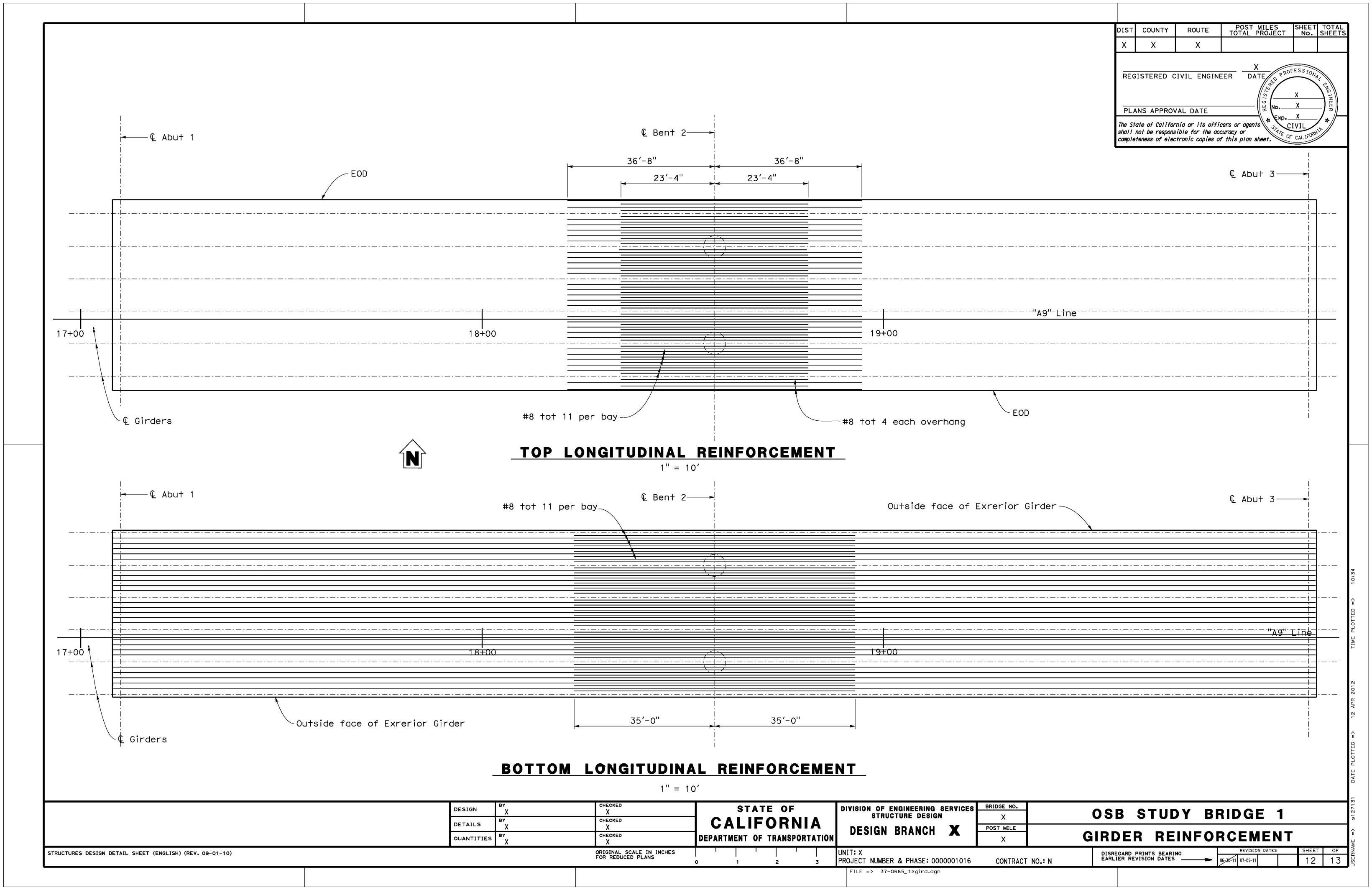

Figure A.11: OSB1 bridge plan drawing page-11

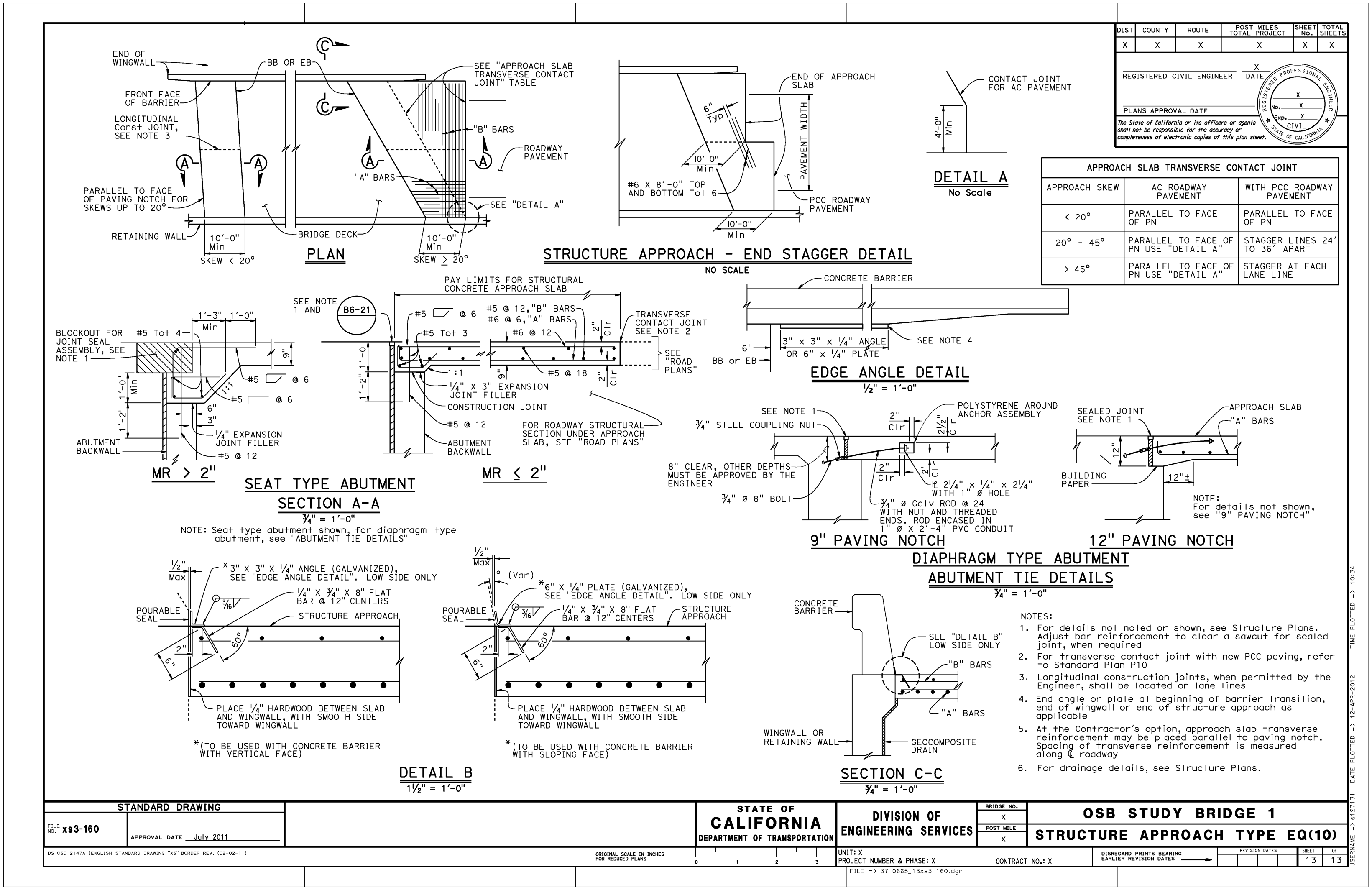

Figure A.12: OSB1 bridge plan drawing page-12

APPENDIX B

LIST OF GROUND MOTIONS FOR FRAGILITY ANALYSIS

The T1780 ground motion sets provided by Caltrans (Roblee, 2015*c*,*b*) are listed in this appendix. There are 20 sets of recorded time histories with 16 ground motions per set, resulting in a total of 320 ground motions. Records were selected such that the ensemble average spectra of each set approximated a specified target spectrum. The target-spectrum S_{a1} value decreases from set-1 to set-20, ranging from approximately 1.870 g to 0.018 g. The S_{a1} values for individual records in all sets range from 0.010 g to 2.716 g. However, only 14 ground motions in the list have a S_{a1} larger than 2.000 g, with two larger than 2.500 g. The lack of high S_{a1} ground motions limits the accuracy of regression in PSDM at high S_{a1}, and this, in turn, limits the accuracy of fragility models for modern bridges having high component capacities. Therefore, for the simulation of modern ductile bridges, the first two ground motion sets are also scaled to 3.000 g to achieve higher prediction accuracy in the high S_{a1} region.

GM_ID	PEER Record Sequence Number	Scale Factor	RotD50 S_{a1} [g]	V_{s30} [m/sec]	Earthquake Name	Year	Station Name	Magnitude	Mechanism
S01_R01	0825	2.2944	1.3880	567.78	Cape Mendocino	1992	Cape Mendocino	7.01	Reverse
S01_R02	0983	1.9298	1.9254	525.79	Northridge-01	1994	Jensen Filter Plant Generator Building	6.69	Reverse
S01_R03	1063	1.8567	2.7159	282.25	Northridge-01	1994	Rinaldi Receiving Sta	6.69	Reverse
S01_R04	1119	2.2672	1.8626	312	Kobe Japan	1995	Takarazuka	6.9	strike slip
S01_R05	1120	1.6166	2.0883	256	Kobe Japan	1995	Takatori	6.9	strike slip
S01_R06	1492	2.2163	2.2741	579.1	Chi-Chi Taiwan	1999	TCU052	7.62	Reverse Oblique
S01_R07	1503	1.8964	2.2239	305.85	Chi-Chi Taiwan	1999	TCU065	7.62	Reverse Oblique
S01_R08	1605	2.3620	1.5102	281.86	Duzce Turkey	1999	Duzce	7.14	strike slip
S01_R09	3968	1.8432	2.5842	310.21	Tottori Japan	2000	TTRH02	6.61	strike slip
S01_R10	4040	2.2834	1.7395	487.4	Bam Iran	2003	Bam	6.6	strike slip
S01_R11	4219	2.2457	1.7233	480.4	Niigata Japan	2004	NIGH01	6.63	Reverse
S01_R12	4856	2.1655	1.7974	294.38	Chuetsu-oki Japan	2007	Kashiwazaki City Center	6.8	Reverse
S01_R13	4894	1.3610	2.1513	329	Chuetsu-oki Japan	2007	Kashiwazaki NPP Unit 1: ground surface	6.8	Reverse
S01_R14	5657	1.8484	1.3997	506.44	Iwate Japan	2008	IWTH25	6.9	Reverse
S01_R15	5992	2.4994	1.5150	196.25	El Mayor-Cucapah Mexico	2010	El Centro Array #11	7.2	strike slip
S01_R16	6906	1.7853	1.8152	344.02	Darfield New Zealand	2010	GDLC	7	strike slip
S02_R01	0126	2.1058	1.3320	259.59	Gazli USSR	1976	Karakyr	6.8	Reverse
S02_R02	0180	2.2452	1.3260	205.63	Imperial Valley-06	1979	El Centro Array #5	6.53	strike slip
S02_R03	0181	2.3701	1.1521	203.22	Imperial Valley-06	1979	El Centro Array #6	6.53	strike slip
S02_R04	0723	2.2238	1.5962	348.69	Superstition Hills-02	1987	Parachute Test Site	6.54	strike slip
S02_R05	0821	2.4202	1.8739	352.05	Erzican Turkey	1992	Erzincan	6.69	strike slip
S02_R06	0828	2.3571	1.9311	422.17	Cape Mendocino	1992	Petrolia	7.01	Reverse

S02_R07	1084	1.6212	2.2358	251.24	Northridge-01	1994	Sylmar - Converter Sta	6.69	Reverse
S02_R08	1086	1.7538	1.1434	440.54	Northridge-01	1994	Sylmar - Olive View Med FF	6.69	Reverse
S02_R09	1244	2.3459	1.7328	258.89	Chi-Chi Taiwan	1999	CHY101	7.62	Reverse Oblique
S02_R10	1549	2.4168	1.3715	511.18	Chi-Chi Taiwan	1999	TCU129	7.62	Reverse Oblique
S02_R11	1602	2.2344	2.1573	293.57	Duzce Turkey	1999	Bolu	7.14	strike slip
S02_R12	4876	2.1144	1.9752	655.45	Chuetsu-oki Japan	2007	Kashiwazaki Nishiyamacho Ikeura	6.8	Reverse
S02_R13	5264	1.7743	1.6631	198.26	Chuetsu-oki Japan	2007	NIG018	6.8	Reverse
S02_R14	5658	2.3663	1.0599	371.06	Iwate Japan	2008	IWTH26	6.9	Reverse
S02_R15	5818	2.3537	1.2385	512.26	Iwate Japan	2008	Kurihara City	6.9	Reverse
S02_R16	6911	2.0410	1.4244	326.01	Darfield New Zealand	2010	HORC	7	strike slip
S03_R01	0160	2.2724	1.0064	223.03	Imperial Valley-06	1979	Bonds Corner	6.53	strike slip
S03_R02	0182	2.2703	1.5345	210.51	Imperial Valley-06	1979	El Centro Array #7	6.53	strike slip
S03_R03	0779	1.5782	1.1880	594.83	Loma Prieta	1989	LGPC	6.93	Reverse Oblique
S03_R04	0982	1.7438	2.4752	373.07	Northridge-01	1994	Jensen Filter Plant Administrative Building	6.69	Reverse
S03_R05	1044	1.7056	1.7100	269.14	Northridge-01	1994	Newhall - Fire Sta	6.69	Reverse
S03_R06	1106	1.6933	2.3427	312	Kobe Japan	1995	KJMA	6.9	strike slip
S03_R07	1505	1.5083	1.0614	487.34	Chi-Chi Taiwan	1999	TCU068	7.62	Reverse Oblique
S03_R08	1507	2.0460	1.4320	624.85	Chi-Chi Taiwan	1999	TCU071	7.62	Reverse Oblique
S03_R09	2114	2.3968	1.7911	329.4	Denali Alaska	2002	TAPS Pump Station #10	7.9	strike slip
S03_R10	4874	2.4248	1.2791	561.59	Chuetsu-oki Japan	2007	Oguni Nagaoka	6.8	Reverse
S03_R11	4895	1.3258	1.5058	265.5	Chuetsu-oki Japan	2007	Kashiwazaki NPP Unit 5: ground surface	6.8	Reverse
S03_R12	5663	2.3817	0.9608	479.37	Iwate Japan	2008	MYG004	6.9	Reverse
S03_R13	5664	2.3788	1.0683	361.24	Iwate Japan	2008	MYG005	6.9	Reverse
S03_R14	5827	2.3508	1.3769	242.05	El Mayor-Cucapah Mexico	2010	MICHOACAN DE OCAMPO	7.2	strike slip
S03_R15	6927	2.2644	1.2785	263.2	Darfield New Zealand	2010	LINC	7	strike slip
S03_R16	8161	2.4903	1.6684	196.88	El Mayor-Cucapah Mexico	2010	El Centro Array #12	7.2	strike slip

S04_R01	0179	2.1278	1.1400	208.91	Imperial Valley-06	1979	El Centro Array #4	6.53	strike slip
S04_R02	0183	2.2374	0.7756	206.08	Imperial Valley-06	1979	El Centro Array #8	6.53	strike slip
S04_R03	0753	2.4659	1.2448	462.24	Loma Prieta	1989	Corralitos	6.93	Reverse Oblique
S04_R04	1004	1.6596	1.4154	380.06	Northridge-01	1994	LA - Sepulveda VA Hospital	6.69	Reverse
S04_R05	1013	2.3259	1.4570	628.99	Northridge-01	1994	LA Dam	6.69	Reverse
S04_R06	1114	2.3096	2.1524	198	Kobe Japan	1995	Port Island (0 m)	6.9	strike slip
S04_R07	1176	2.3332	0.8957	297	Kocaeli Turkey	1999	Yarimca	7.51	strike slip
S04_R08	1197	1.4877	1.5145	542.61	Chi-Chi Taiwan	1999	CHY028	7.62	Reverse Oblique
S04_R09	1509	1.8506	2.1059	549.43	Chi-Chi Taiwan	1999	TCU074	7.62	Reverse Oblique
S04_R10	3748	2.4770	1.6312	387.95	Cape Mendocino	1992	Ferndale Fire Station	7.01	Reverse
S04_R11	4886	2.2196	1.1903	338.32	Chuetsu-oki Japan	2007	Tamati Yone Izumozaki	6.8	Reverse
S04_R12	4894	0.9684	1.5306	329	Chuetsu-oki Japan	2007	Kashiwazaki NPP Unit 1: ground surface	6.8	Reverse
S04_R13	5656	2.3398	0.7813	486.41	Iwate Japan	2008	IWTH24	6.9	Reverse
S04_R14	5825	2.3359	0.9142	242.05	El Mayor-Cucapah Mexico	2010	CERRO PRIETO GEOTHERMAL	7.2	strike slip
S04_R15	5837	2.2679	1.2229	229.25	El Mayor-Cucapah Mexico	2010	El Centro - Imperial & Ross	7.2	strike slip
S04_R16	6962	2.2290	0.8534	295.74	Darfield New Zealand	2010	ROLC	7	strike slip
S05_R01	0174	2.4477	0.5827	196.25	Imperial Valley-06	1979	El Centro Array #11	6.53	strike slip
S05_R02	0184	1.8524	0.7914	202.26	Imperial Valley-06	1979	El Centro Differential Array	6.53	strike slip
S05_R03	0741	2.2993	1.2275	476.54	Loma Prieta	1989	BRAN	6.93	Reverse Oblique
S05_R04	0803	2.2728	1.3710	347.9	Loma Prieta	1989	Saratoga - W Valley Coll.	6.93	Reverse Oblique
S05_R05	1054	2.1164	2.4748	325.67	Northridge-01	1994	Pardee - SCE	6.69	Reverse
S05_R06	1080	2.3163	1.6550	557.42	Northridge-01	1994	Simi Valley - Katherine Rd	6.69	Reverse
S05_R07	1111	2.3132	0.6613	609	Kobe Japan	1995	Nishi-Akashi	6.9	strike slip
S05_R08	1120	1.0150	1.3111	256	Kobe Japan	1995	Takatori	6.9	strike slip
S05_R09	1158	2.0056	0.9817	281.86	Kocaeli Turkey	1999	Duzce	7.51	strike slip
S05_R10	1231	1.1141	2.3362	496.21	Chi-Chi Taiwan	1999	CHY080	7.62	Reverse Oblique

S05_R11	1517	1.0584	1.9886	665.2	Chi-Chi Taiwan	1999	TCU084	7.62	Reverse Oblique
S05_R12	3746	2.2317	0.9690	459.04	Cape Mendocino	1992	Centerville Beach Naval Fac	7.01	Reverse
S05_R13	4228	2.4179	0.9634	375	Niigata Japan	2004	NIGH11	6.63	Reverse
S05_R14	4895	1.0324	1.0504	265.5	Chuetsu-oki Japan	2007	Kashiwazaki NPP Unit 5: ground surface	6.8	Reverse
S05_R15	5985	2.1850	1.2177	202.26	El Mayor-Cucapah Mexico	2010	El Centro Differential Array	7.2	strike slip
S05_R16	6906	1.1209	1.1397	344.02	Darfield New Zealand	2010	GDLC	7	strike slip
S06_R01	0721	2.2656	0.6605	192.05	Superstition Hills-02	1987	El Centro Imp. Co. Cent	6.54	strike slip
S06_R02	0767	2.1105	0.6676	349.85	Loma Prieta	1989	Gilroy Array #3	6.93	Reverse Oblique
S06_R03	0779	1.0845	0.8163	594.83	Loma Prieta	1989	LGPC	6.93	Reverse Oblique
S06_R04	0983	1.0692	1.0668	525.79	Northridge-01	1994	Jensen Filter Plant Generator Building	6.69	Reverse
S06_R05	1084	1.0143	1.3988	251.24	Northridge-01	1994	Sylmar - Converter Sta	6.69	Reverse
S06_R06	1101	1.8653	1.5789	256	Kobe Japan	1995	Amagasaki	6.9	strike slip
S06_R07	1106	1.1635	1.6098	312	Kobe Japan	1995	KJMA	6.9	strike slip
S06_R08	1505	1.0364	0.7294	487.34	Chi-Chi Taiwan	1999	TCU068	7.62	Reverse Oblique
S06_R09	1510	1.9862	0.6925	573.02	Chi-Chi Taiwan	1999	TCU075	7.62	Reverse Oblique
S06_R10	3968	1.0212	1.4317	310.21	Tottori Japan	2000	TTRH02	6.61	strike slip
S06_R11	4031	2.2820	0.7604	410.66	San Simeon CA	2003	Templeton - 1-story Hospital	6.52	Reverse
S06_R12	4451	1.9679	1.7131	462.23	Montenegro Yugoslavia	1979	Bar-Skupstina Opstine	7.1	Reverse
S06_R13	5264	1.1101	1.0405	198.26	Chuetsu-oki Japan	2007	NIG018	6.8	Reverse
S06_R14	5657	1.0241	0.7755	506.44	Iwate Japan	2008	IWTH25	6.9	Reverse
S06_R15	5991	1.7633	1.0066	202.85	El Mayor-Cucapah Mexico	2010	El Centro Array #10	7.2	strike slip
S06_R16	6893	2.1415	0.8574	344.02	Darfield New Zealand	2010	DFHS	7	strike slip
S07_R01	0776	1.7656	1.2586	282.14	Loma Prieta	1989	Hollister - South & Pine	6.93	Reverse Oblique
S07_R02	0825	1.1218	0.6786	567.78	Cape Mendocino	1992	Cape Mendocino	7.01	Reverse
S07_R03	1063	0.9077	1.3278	282.25	Northridge-01	1994	Rinaldi Receiving Sta	6.69	Reverse
S07_R04	1086	0.9682	1.1211	440.54	Northridge-01	1994	Sylmar - Olive View Med FF	6.69	Reverse

S07_R05	1119	1.1084	0.9106	312	Kobe Japan	1995	Takarazuka	6.9	strike slip
S07_R06	1197	1.0223	1.0407	542.61	Chi-Chi Taiwan	1999	CHY028	7.62	Reverse Oblique
S07_R07	1503	0.9272	1.0873	305.85	Chi-Chi Taiwan	1999	TCU065	7.62	Reverse Oblique
S07_R08	1605	1.1548	0.7383	281.86	Duzce Turkey	1999	Duzce	7.14	strike slip
S07_R09	3749	2.0583	0.6795	355.18	Cape Mendocino	1992	Fortuna Fire Station	7.01	Reverse
S07_R10	4219	1.0979	0.8425	480.4	Niigata Japan	2004	NIGH01	6.63	Reverse
S07_R11	4863	1.9954	1.3493	514.3	Chuetsu-oki Japan	2007	Nagaoka	6.8	Reverse
S07_R12	4875	1.0774	0.8864	282.57	Chuetsu-oki Japan	2007	Kariwa	6.8	Reverse
S07_R13	5780	1.9118	0.8099	345.55	Iwate Japan	2008	Iwadeyama	6.9	Reverse
S07_R14	5975	1.8672	0.5995	231.23	El Mayor-Cucapah Mexico	2010	Calexico Fire Station	7.2	strike slip
S07_R15	6911	1.1268	0.7864	326.01	Darfield New Zealand	2010	HORC	7	strike slip
S07_R16	6953	2.1580	0.6390	206	Darfield New Zealand	2010	Pages Road Pumping Station	7	strike slip
S08_R01	0126	1.0259	0.6489	259.59	Gazli USSR	1976	Karakyr	6.8	Reverse
S08_R02	0180	1.0938	0.6460	205.63	Imperial Valley-06	1979	El Centro Array #5	6.53	strike slip
S08_R03	0723	1.0834	0.7776	348.69	Superstition Hills-02	1987	Parachute Test Site	6.54	strike slip
S08_R04	0900	2.1828	0.9177	353.63	Landers	1992	Yermo Fire Station	7.28	strike slip
S08_R05	0982	0.9331	1.3244	373.07	Northridge-01	1994	Jensen Filter Plant Administrative Building	6.69	Reverse
S08_R06	1044	0.9126	0.9150	269.14	Northridge-01	1994	Newhall - Fire Sta	6.69	Reverse
S08_R07	1492	0.9562	0.9811	579.1	Chi-Chi Taiwan	1999	TCU052	7.62	Reverse Oblique
S08_R08	1513	1.3912	0.8789	363.99	Chi-Chi Taiwan	1999	TCU079	7.62	Reverse Oblique
S08_R09	1602	1.0885	1.0510	293.57	Duzce Turkey	1999	Bolu	7.14	strike slip
S08_R10	3750	2.0797	0.5091	515.65	Cape Mendocino	1992	Loleta Fire Station	7.01	Reverse
S08_R11	4040	0.9851	0.7504	487.4	Bam Iran	2003	Bam	6.6	strike slip
S08_R12	4458	1.9486	1.0610	318.74	Montenegro Yugoslavia	1979	Ulcinj - Hotel Olimpic	7.1	Reverse
S08_R13	4856	0.9342	0.7755	294.38	Chuetsu-oki Japan	2007	Kashiwazaki City Center	6.8	Reverse
S08_R14	4876	1.0301	0.9623	655.45	Chuetsu-oki Japan	2007	Kashiwazaki Nishiyamacho Ikeura	6.8	Reverse

S08_R15	5658	1.1528	0.5164	371.06	Iwate Japan	2008	IWTH26	6.9	Reverse
S08_R16	5992	1.0783	0.6536	196.25	El Mayor-Cucapah Mexico	2010	El Centro Array #11	7.2	strike slip
S09_R01	0160	1.1090	0.4912	223.03	Imperial Valley-06	1979	Bonds Corner	6.53	strike slip
S09_R02	0181	1.0531	0.5119	203.22	Imperial Valley-06	1979	El Centro Array #6	6.53	strike slip
S09_R03	0821	1.0754	0.8327	352.05	Erzican Turkey	1992	Erzincan	6.69	strike slip
S09_R04	0828	1.0474	0.8581	422.17	Cape Mendocino	1992	Petrolia	7.01	Reverse
S09_R05	0953	1.1756	1.1547	355.81	Northridge-01	1994	Beverly Hills - 14145 Mulhol	6.69	Reverse
S09_R06	1004	0.9179	0.7828	380.06	Northridge-01	1994	LA - Sepulveda VA Hospital	6.69	Reverse
S09_R07	1244	1.0424	0.7700	258.89	Chi-Chi Taiwan	1999	CHY101	7.62	Reverse Oblique
S09_R08	1507	0.9985	0.6988	624.85	Chi-Chi Taiwan	1999	TCU071	7.62	Reverse Oblique
S09_R09	2114	1.1697	0.8741	329.4	Denali Alaska	2002	TAPS Pump Station #10	7.9	strike slip
S09_R10	4874	1.1834	0.6242	561.59	Chuetsu-oki Japan	2007	Oguni Nagaoka	6.8	Reverse
S09_R11	4896	0.9299	0.9119	201	Chuetsu-oki Japan	2007	Kashiwazaki NPP Service Hall Array 2.4 m depth	6.8	Reverse
S09_R12	5664	1.1609	0.5214	361.24	Iwate Japan	2008	MYG005	6.9	Reverse
S09_R13	5818	1.0459	0.5503	512.26	Iwate Japan	2008	Kurihara City	6.9	Reverse
S09_R14	5827	1.1472	0.6720	242.05	El Mayor-Cucapah Mexico	2010	MICHOACAN DE OCAMPO	7.2	strike slip
S09_R15	6927	1.1051	0.6239	263.2	Darfield New Zealand	2010	LINC	7	strike slip
S09_R16	8161	1.2153	0.8142	196.88	El Mayor-Cucapah Mexico	2010	El Centro Array #12	7.2	strike slip
S10_R01	0182	0.9770	0.6604	210.51	Imperial Valley-06	1979	El Centro Array #7	6.53	strike slip
S10_R02	0184	1.0238	0.4374	202.26	Imperial Valley-06	1979	El Centro Differential Array	6.53	strike slip
S10_R03	0753	1.2026	0.6071	462.24	Loma Prieta	1989	Corralitos	6.93	Reverse Oblique
S10_R04	1013	1.1343	0.7106	628.99	Northridge-01	1994	LA Dam	6.69	Reverse
S10_R05	1054	1.1697	1.3677	325.67	Northridge-01	1994	Pardee - SCE	6.69	Reverse
S10_R06	1114	1.1264	1.0497	198	Kobe Japan	1995	Port Island (0 m)	6.9	strike slip
S10_R07	1176	1.1379	0.4368	297	Kocaeli Turkey	1999	Yarimca	7.51	strike slip
S10_R08	1509	0.9025	1.0270	549.43	Chi-Chi Taiwan	1999	TCU074	7.62	Reverse Oblique

S10_R09	1549	0.9470	0.5374	511.18	Chi-Chi Taiwan	1999	TCU129	7.62	Reverse Oblique
S10_R10	3748	1.2080	0.7955	387.95	Cape Mendocino	1992	Ferndale Fire Station	7.01	Reverse
S10_R11	4451	1.2325	1.0729	462.23	Montenegro Yugoslavia	1979	Bar-Skupstina Opstine	7.1	Reverse
S10_R12	4886	1.0825	0.5805	338.32	Chuetsu-oki Japan	2007	Tamati Yone Izumozaki	6.8	Reverse
S10_R13	5656	1.1411	0.3810	486.41	Iwate Japan	2008	IWTH24	6.9	Reverse
S10_R14	5663	1.0250	0.4135	479.37	Iwate Japan	2008	MYG004	6.9	Reverse
S10_R15	5991	1.1044	0.6304	202.85	El Mayor-Cucapah Mexico	2010	El Centro Array #10	7.2	strike slip
S10_R16	6962	1.0871	0.4162	295.74	Darfield New Zealand	2010	ROLC	7	strike slip
S11_R01	0179	0.8593	0.4604	208.91	Imperial Valley-06	1979	El Centro Array #4	6.53	strike slip
S11_R02	0183	0.9036	0.3132	206.08	Imperial Valley-06	1979	El Centro Array #8	6.53	strike slip
S11_R03	0767	1.0945	0.3462	349.85	Loma Prieta	1989	Gilroy Array #3	6.93	Reverse Oblique
S11_R04	0776	1.0377	0.7397	282.14	Loma Prieta	1989	Hollister - South & Pine	6.93	Reverse Oblique
S11_R05	1080	1.0600	0.7574	557.42	Northridge-01	1994	Simi Valley - Katherine Rd	6.69	Reverse
S11_R06	1101	0.9674	0.8188	256	Kobe Japan	1995	Amagasaki	6.9	strike slip
S11_R07	1111	1.0586	0.3027	609	Kobe Japan	1995	Nishi-Akashi	6.9	strike slip
S11_R08	1158	0.9179	0.4493	281.86	Kocaeli Turkey	1999	Duzce	7.51	strike slip
S11_R09	1510	1.0301	0.3591	573.02	Chi-Chi Taiwan	1999	TCU075	7.62	Reverse Oblique
S11_R10	1513	0.9265	0.5853	363.99	Chi-Chi Taiwan	1999	TCU079	7.62	Reverse Oblique
S11_R11	3746	1.0213	0.4434	459.04	Cape Mendocino	1992	Centerville Beach Naval Fac	7.01	Reverse
S11_R12	4228	1.1065	0.4409	375	Niigata Japan	2004	NIGH11	6.63	Reverse
S11_R13	4863	1.1727	0.7930	514.3	Chuetsu-oki Japan	2007	Nagaoka	6.8	Reverse
S11_R14	5825	0.9433	0.3692	242.05	El Mayor-Cucapah Mexico	2010	CERRO PRIETO GEOTHERMAL	7.2	strike slip
S11_R15	5837	0.9159	0.4939	229.25	El Mayor-Cucapah Mexico	2010	El Centro - Imperial & Ross	7.2	strike slip
S11_R16	6893	1.1106	0.4447	344.02	Darfield New Zealand	2010	DFHS	7	strike slip
S12_R01	0174	0.9097	0.2166	196.25	Imperial Valley-06	1979	El Centro Array #11	6.53	strike slip
S12_R02	0721	0.9542	0.2782	192.05	Superstition Hills-02	1987	El Centro Imp. Co. Cent	6.54	strike slip

S12_R03	0741	0.8546	0.4562	476.54	Loma Prieta	1989	BRAN	6.93	Reverse Oblique
S12_R04	0803	0.8447	0.5095	347.9	Loma Prieta	1989	Saratoga - W Valley Coll.	6.93	Reverse Oblique
S12_R05	1052	0.9704	0.5005	508.08	Northridge-01	1994	Pacoima Kagel Canyon	6.69	Reverse
S12_R06	1551	1.0399	0.4487	652.85	Chi-Chi Taiwan	1999	TCU138	7.62	Reverse Oblique
S12_R07	3744	1.0644	0.3976	566.42	Cape Mendocino	1992	Bunker Hill FAA	7.01	Reverse
S12_R08	3749	0.9824	0.3243	355.18	Cape Mendocino	1992	Fortuna Fire Station	7.01	Reverse
S12_R09	4031	0.9611	0.3203	410.66	San Simeon CA	2003	Templeton - 1-story Hospital	6.52	Reverse
S12_R10	4207	0.9773	0.3281	274.17	Niigata Japan	2004	NIG017	6.63	Reverse
S12_R11	4218	0.9554	0.3243	430.71	Niigata Japan	2004	NIG028	6.63	Reverse
S12_R12	4458	1.0539	0.5739	318.74	Montenegro Yugoslavia	1979	Ulcinj - Hotel Olimpic	7.1	Reverse
S12_R13	5780	0.9125	0.3865	345.55	Iwate Japan	2008	Iwadeyama	6.9	Reverse
S12_R14	5975	0.8912	0.2861	231.23	El Mayor-Cucapah Mexico	2010	Calexico Fire Station	7.2	strike slip
S12_R15	5985	0.8121	0.4526	202.26	El Mayor-Cucapah Mexico	2010	El Centro Differential Array	7.2	strike slip
S12_R16	6953	1.0300	0.3050	206	Darfield New Zealand	2010	Pages Road Pumping Station	7	strike slip
S13_R01	0020	1.1000	0.3453	219.31	Northern Calif-03	1954	Ferndale City Hall	6.5	strike slip
S13_R02	0161	1.0097	0.2630	208.71	Imperial Valley-06	1979	Brawley Airport	6.53	strike slip
S13_R03	0587	0.9948	0.2070	551.3	New Zealand-02	1987	Matahina Dam	6.6	Normal
S13_R04	0764	1.0589	0.3927	308.55	Loma Prieta	1989	Gilroy - Historic Bldg.	6.93	Reverse Oblique
S13_R05	0900	0.8754	0.3680	353.63	Landers	1992	Yermo Fire Station	7.28	strike slip
S13_R06	0952	0.8821	0.2614	545.66	Northridge-01	1994	Beverly Hills - 12520 Mulhol	6.69	Reverse
S13_R07	1006	1.0908	0.2525	398.42	Northridge-01	1994	LA - UCLA Grounds	6.69	Reverse
S13_R08	1107	0.9747	0.3253	312	Kobe Japan	1995	Kakogawa	6.9	strike slip
S13_R09	1116	1.0195	0.2651	256	Kobe Japan	1995	Shin-Osaka	6.9	strike slip
S13_R10	3750	0.8340	0.2041	515.65	Cape Mendocino	1992	Loleta Fire Station	7.01	Reverse
S13_R11	4456	0.9250	0.4187	543.26	Montenegro Yugoslavia	1979	Petrovac - Hotel Olivia	7.1	Reverse
S13_R12	4849	0.9581	0.3632	342.74	Chuetsu-oki Japan	2007	Kubikiku Hyakken Joetsu City	6.8	Reverse

S13_R13	4879	1.0947	0.5742	265.82	Chuetsu-oki Japan	2007	Yan Sakuramachi City watershed	6.8	Reverse
S13_R14	5774	0.9387	0.1902	276.3	Iwate Japan	2008	Nakashinden Town	6.9	Reverse
S13_R15	6886	1.0034	0.1588	280.26	Darfield New Zealand	2010	Canterbury Aero Club	7	strike slip
S13_R16	8166	1.0093	0.1931	425	Duzce Turkey	1999	IRIGM 498	7.14	strike slip
S14_R01	0068	0.9236	0.1638	316.46	San Fernando	1971	LA - Hollywood Stor FF	6.61	Reverse
S14_R02	0162	0.9207	0.1469	231.23	Imperial Valley-06	1979	Calexico Fire Station	6.53	strike slip
S14_R03	0285	0.9892	0.2717	649.67	Irpinia Italy-01	1980	Bagnoli Irpinio	6.9	Normal
S14_R04	0730	1.0729	0.3167	343.53	Spitak Armenia	1988	Gukasian	6.77	Reverse Oblique
S14_R05	0737	0.9465	0.1569	239.69	Loma Prieta	1989	Agnews State Hospital	6.93	Reverse Oblique
S14_R06	0739	0.9052	0.1625	488.77	Loma Prieta	1989	Anderson Dam (Downstream)	6.93	Reverse Oblique
S14_R07	0881	0.9416	0.2031	396.41	Landers	1992	Morongo Valley Fire Station	7.28	strike slip
S14_R08	0998	1.0039	0.1783	315.06	Northridge-01	1994	LA - N Westmoreland	6.69	Reverse
S14_R09	1115	1.0227	0.1782	256	Kobe Japan	1995	Sakai	6.9	strike slip
S14_R10	1121	0.9052	0.3691	256	Kobe Japan	1995	Yae	6.9	strike slip
S14_R11	1486	1.0989	0.1832	465.55	Chi-Chi Taiwan	1999	TCU046	7.62	Reverse Oblique
S14_R12	1628	0.9661	0.2695	306.37	St Elias Alaska	1979	Icy Bay	7.54	Reverse
S14_R13	4212	1.0955	0.1328	193.2	Niigata Japan	2004	NIG022	6.63	Reverse
S14_R14	4842	0.9588	0.1652	655.45	Chuetsu-oki Japan	2007	Joetsu Uragawaraku Kamabucchi	6.8	Reverse
S14_R15	4859	0.9525	0.3665	274.23	Chuetsu-oki Japan	2007	Mitsuke Kazuiti Arita Town	6.8	Reverse
S14_R16	6928	0.9831	0.1708	649.67	Darfield New Zealand	2010	LPCC	7	strike slip
S15_R01	0175	0.9092	0.1598	196.88	Imperial Valley-06	1979	El Centro Array #12	6.53	strike slip
S15_R02	0724	1.0564	0.1586	316.64	Superstition Hills-02	1987	Plaster City	6.54	strike slip
S15_R03	0827	0.9490	0.1730	457.06	Cape Mendocino	1992	Fortuna - Fortuna Blvd	7.01	Reverse
S15_R04	0990	0.9805	0.1519	365.22	Northridge-01	1994	LA - City Terrace	6.69	Reverse
S15_R05	1001	0.9757	0.1911	285.28	Northridge-01	1994	LA - S Grand Ave	6.69	Reverse
S15_R06	1166	0.9426	0.2069	476.62	Kocaeli Turkey	1999	Iznik	7.51	strike slip

S15_R07	1234	0.9202	0.2141	665.2	Chi-Chi Taiwan	1999	CHY086	7.62	Reverse Oblique
S15_R08	1636	1.0818	0.1256	302.64	Manjil Iran	1990	Qazvin	7.37	strike slip
S15_R09	1794	0.9168	0.2755	379.32	Hector Mine	1999	Joshua Tree	7.13	strike slip
S15_R10	3758	1.0099	0.2050	333.89	Landers	1992	Thousand Palms Post Office	7.28	strike slip
S15_R11	3908	1.0743	0.1345	293.37	Tottori Japan	2000	OKY005	6.61	strike slip
S15_R12	4208	0.9050	0.1361	198.26	Niigata Japan	2004	NIG018	6.63	Reverse
S15_R13	4872	1.0422	0.2661	640.14	Chuetsu-oki Japan	2007	Sawa Mizuguti Tokamachi	6.8	Reverse
S15_R14	5799	1.0360	0.0830	552.38	Iwate Japan	2008	Misato Akita City - Tsuchizaki	6.9	Reverse
S15_R15	5972	0.9103	0.1120	208.71	El Mayor-Cucapah Mexico	2010	Brawley Airport	7.2	strike slip
S15_R16	6965	0.9471	0.1183	263.2	Darfield New Zealand	2010	SBRC	7	strike slip
S16_R01	0070	1.1181	0.3653	425.34	San Fernando	1971	Lake Hughes #1	6.61	Reverse
S16_R02	0078	1.0429	0.1410	452.86	San Fernando	1971	Palmdale Fire Station	6.61	Reverse
S16_R03	0172	1.0360	0.0848	237.33	Imperial Valley-06	1979	El Centro Array #1	6.53	strike slip
S16_R04	0288	1.0039	0.1023	561.04	Irpinia Italy-01	1980	Brienza	6.9	Normal
S16_R05	0726	1.0807	0.1937	191.14	Superstition Hills-02	1987	Salton Sea Wildlife Refuge	6.54	strike slip
S16_R06	0748	0.9886	0.1386	627.59	Loma Prieta	1989	Belmont - Envirotech	6.93	Reverse Oblique
S16_R07	0800	1.0002	0.1006	279.56	Loma Prieta	1989	Salinas - John & Work	6.93	Reverse Oblique
S16_R08	0880	1.0088	0.0920	355.42	Landers	1992	Mission Creek Fault	7.28	strike slip
S16_R09	0968	0.9681	0.1460	271.9	Northridge-01	1994	Downey - Co Maint Bldg	6.69	Reverse
S16_R10	0984	1.0544	0.1383	301	Northridge-01	1994	LA - 116th St School	6.69	Reverse
S16_R11	1162	1.0555	0.1407	347.62	Kocaeli Turkey	1999	Goynuk	7.51	strike slip
S16_R12	1289	1.0727	0.2598	484.97	Chi-Chi Taiwan	1999	HWA041	7.62	Reverse Oblique
S16_R13	3937	1.0936	0.1129	182.3	Tottori Japan	2000	SMN005	6.61	strike slip
S16_R14	3994	1.0456	0.1011	365.15	San Simeon CA	2003	San Luis Obispo - Lopez Lake Grounds	6.52	Reverse
S16_R15	4844	0.9338	0.1812	640.14	Chuetsu-oki Japan	2007	Tokamachi Matsunoyama	6.8	Reverse
S16_R16	5471	1.0835	0.0894	158.16	Iwate Japan	2008	AKT016	6.9	Reverse

S17_R01	0009	1.1686	0.0616	213.44	Borrego	1942	El Centro Array #9	6.5	strike slip
S17_R02	0065	1.2013	0.0745	308.35	San Fernando	1971	Gormon - Oso Pump Plant	6.61	Reverse
S17_R03	0122	0.8143	0.1056	249.28	Friuli Italy-01	1976	Codroipo	6.5	Reverse
S17_R04	0191	0.8770	0.0581	242.05	Imperial Valley-06	1979	Victoria	6.53	strike slip
S17_R05	0745	0.9046	0.0513	422.79	Loma Prieta	1989	Bear Valley #14 Upper Butts Rn	6.93	Reverse Oblique
S17_R06	0860	1.1552	0.1067	328.09	Landers	1992	Hemet Fire Station	7.28	strike slip
S17_R07	0966	0.9956	0.0784	324.79	Northridge-01	1994	Covina - W Badillo	6.69	Reverse
S17_R08	1154	0.9983	0.1211	612.78	Kocaeli Turkey	1999	Bursa Sivil	7.51	strike slip
S17_R09	1626	1.0697	0.0513	649.67	Sitka Alaska	1972	Sitka Observatory	7.68	strike slip
S17_R10	1782	1.0329	0.0833	436.14	Hector Mine	1999	Forest Falls Post Office	7.13	strike slip
S17_R11	2111	0.8824	0.0915	341.56	Denali Alaska	2002	R109 (temp)	7.9	strike slip
S17_R12	3915	1.2281	0.0756	296.96	Tottori Japan	2000	OKY012	6.61	strike slip
S17_R13	4054	0.8284	0.0447	574.88	Bam Iran	2003	Mohammad Abad-e-Madkoon	6.6	strike slip
S17_R14	4222	1.0456	0.0428	244.84	Niigata Japan	2004	NIGH05	6.63	Reverse
S17_R15	5258	1.0028	0.0691	229.95	Chuetsu-oki Japan	2007	NIG012	6.8	Reverse
S17_R16	6933	1.0852	0.0531	342.7	Darfield New Zealand	2010	MAYC	7	strike slip
S18_R01	0007	1.1801	0.0388	219.31	Northwest Calif-02	1941	Ferndale City Hall	6.6	strike slip
S18_R02	0051	1.0168	0.0469	280.56	San Fernando	1971	2516 Via Tejon PV	6.61	Reverse
S18_R03	0056	0.9012	0.0273	235	San Fernando	1971	Carbon Canyon Dam	6.61	Reverse
S18_R04	0188	0.9553	0.0438	316.64	Imperial Valley-06	1979	Plaster City	6.53	strike slip
S18_R05	0294	0.8683	0.0534	496.46	Irpinia Italy-01	1980	Tricarico	6.9	Normal
S18_R06	0897	1.0421	0.0276	635.01	Landers	1992	Twentynine Palms	7.28	strike slip
S18_R07	0975	0.9117	0.0937	362.31	Northridge-01	1994	Glendora - N Oakbank	6.69	Reverse
S18_R08	1061	1.1377	0.0670	580.03	Northridge-01	1994	Rancho Palos Verdes - Hawth	6.69	Reverse
S18_R09	1109	0.9091	0.0349	609	Kobe Japan	1995	MZH	6.9	strike slip
S18_R10	1627	1.0671	0.0318	432.58	Caldiran Turkey	1976	Maku	7.21	strike slip

S18_R11	3583	1.2248	0.0656	309.41	Taiwan SMART1(25)	1983	SMART1 I08	6.5	Reverse
S18_R12	3946	0.9864	0.0480	271.29	Tottori Japan	2000	SMN018	6.61	strike slip
S18_R13	4997	0.9987	0.0875	305.54	Chuetsu-oki Japan	2007	FKS028	6.8	Reverse
S18_R14	5648	1.1235	0.0376	534.71	Iwate Japan	2008	IWTH16	6.9	Reverse
S18_R15	5768	0.9873	0.0274	291.48	Iwate Japan	2008	YMTH09	6.9	Reverse
S18_R16	5864	1.0143	0.0750	384.66	El Mayor-Cucapah Mexico	2010	Frink	7.2	strike slip
S19_R01	0287	0.8610	0.0393	356.39	Irpinia Italy-01	1980	Bovino	6.9	Normal
S19_R02	0432	1.0059	0.0476	267.67	Taiwan SMART1(25)	1983	SMART1 O01	6.5	Reverse
S19_R03	0436	1.0107	0.0178	279.97	Borah Peak ID-01	1983	CPP-601	6.88	Normal
S19_R04	0747	0.8080	0.0288	509.87	Loma Prieta	1989	Bear Valley #7 Pinnacles	6.93	Reverse Oblique
S19_R05	1037	0.9554	0.0301	422.73	Northridge-01	1994	Mojave - Oak Creek Canyon	6.69	Reverse
S19_R06	1097	0.9780	0.0303	506	Northridge-01	1994	Wrightwood - Nielson Ranch	6.69	Reverse
S19_R07	1620	1.1206	0.0221	411.91	Duzce Turkey	1999	Sakarya	7.14	strike slip
S19_R08	1767	0.9701	0.0228	667.42	Hector Mine	1999	Banning - Twin Pines Road	7.13	strike slip
S19_R09	3594	1.0378	0.0622	300.22	Taiwan SMART1(25)	1983	SMART1 M11	6.5	Reverse
S19_R10	3882	1.2227	0.0176	571.63	Tottori Japan	2000	HRS016	6.61	strike slip
S19_R11	3981	0.8611	0.0488	333.61	San Simeon CA	2003	Coalinga - Fire Station 39	6.52	Reverse
S19_R12	3987	0.8661	0.0311	280.64	San Simeon CA	2003	Greenfield - Police Station	6.52	Reverse
S19_R13	4198	0.9814	0.0246	220.65	Niigata Japan	2004	NIG008	6.63	Reverse
S19_R14	5254	0.9642	0.0235	220.65	Chuetsu-oki Japan	2007	NIG008	6.8	Reverse
S19_R15	5467	0.9766	0.0204	449.45	Iwate Japan	2008	AKT012	6.9	Reverse
S19_R16	8163	1.0183	0.0248	483.02	El Mayor-Cucapah Mexico	2010	SANTA ISABEL VIEJO	7.2	strike slip
S20_R01	0058	0.8749	0.0188	477.22	San Fernando	1971	Cedar Springs Pumphouse	6.61	Reverse
S20_R02	0092	0.8077	0.0136	347.67	San Fernando	1971	Wheeler Ridge - Ground	6.61	Reverse
S20_R03	0427	1.0281	0.0216	671.52	Taiwan SMART1(25)	1983	SMART1 E02	6.5	Reverse
S20_R04	0440	0.9071	0.0114	324.2	Borah Peak ID-01	1983	TRA-642 ETR Reactor Bldg(Bsmt)	6.88	Normal

S20_R05	0441	1.0743	0.0153	324.2	Borah Peak ID-01	1983	TRA-670 ATR Reactor Bldg(Bsmt)	6.88	Normal
S20_R06	2093	1.0784	0.0199	382.5	Nenana Mountain Alaska	2002	TAPS Pump Station #09	6.7	strike slip
S20_R07	3899	1.0028	0.0122	617.44	Tottori Japan	2000	HYGH02	6.61	strike slip
S20_R08	3945	0.8604	0.0181	262.19	Tottori Japan	2000	SMN017	6.61	strike slip
S20_R09	5003	0.8012	0.0125	245.88	Chuetsu-oki Japan	2007	FKSH04	6.8	Reverse
S20_R10	5064	1.0319	0.0266	342.36	Chuetsu-oki Japan	2007	GNM005	6.8	Reverse
S20_R11	5461	0.8859	0.0190	279.36	Iwate Japan	2008	AKT006	6.9	Reverse
S20_R12	5490	1.1355	0.0132	232.58	Iwate Japan	2008	AKTH14	6.9	Reverse
S20_R13	5839	1.0089	0.0161	388.01	El Mayor-Cucapah Mexico	2010	El Cajon - Marshall	7.2	strike slip
S20_R14	5970	0.8201	0.0100	619	El Mayor-Cucapah Mexico	2010	Borrego Springs	7.2	strike slip
S20_R15	6515	0.9517	0.0205	279.58	Niigata Japan	2004	FKS016	6.63	Reverse
S20_R16	6783	1.0118	0.0175	265.6	Niigata Japan	2004	TCG008	6.63	Reverse

Table B.1: Earthquake records

APPENDIX C
VALIDATION OF COLUMN MODELS AGAINST LABORATORY TESTS

A subset of the columns summarized in RP1 (Zheng et al., 2020) are validated against the laboratory tests, and results are presented here. The selected subset comprises those experiments where the failure-mode determination was not obvious (e.g., modern flexural column) and represents a wide range of specimen and testing conditions where flexure, mixed flexure-shear, and shear failure could occur. Results are generally organized by section, each representing a unique failure mode. Where applicable, subsection breakouts are provided for results representing different design eras for column detailing. Additional sections are included for special cases of reduced-section (pinned) columns (section C.2), lapped-splice connections (section C.3), and dynamic loading (section C.5).

In all cases, the OpenSees simulation results are presented as *red lines* in the figures atop the black responses reproduced from the original literature.

C.1 Flexural Columns

C.1.1 Pre-Ductile Design (Era-1)

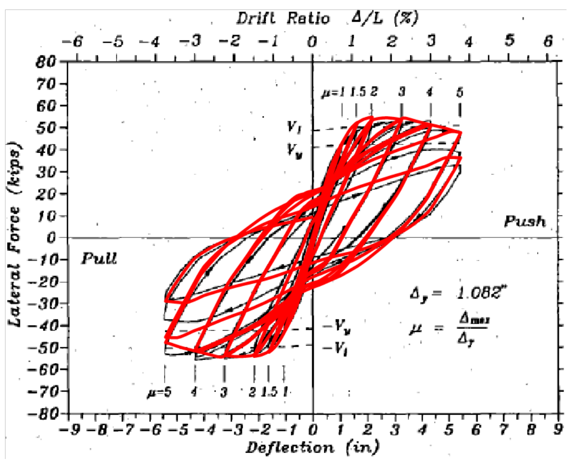

Figure C.1: e1F-1 (Chai et al., 1991)

C.1.2 Early-Ductile Design (Era-2)

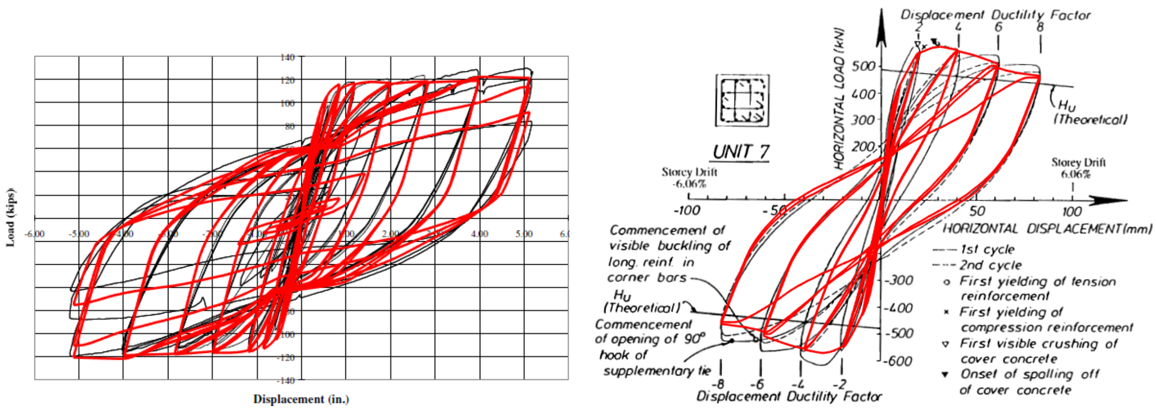

(a) (b)

Figure C.2: (a) e2F-18 (Calderone et al., 2000); (b) e2F-37 (Tanaka, 1990).

C.1.3 Ductile Design (Era-3)

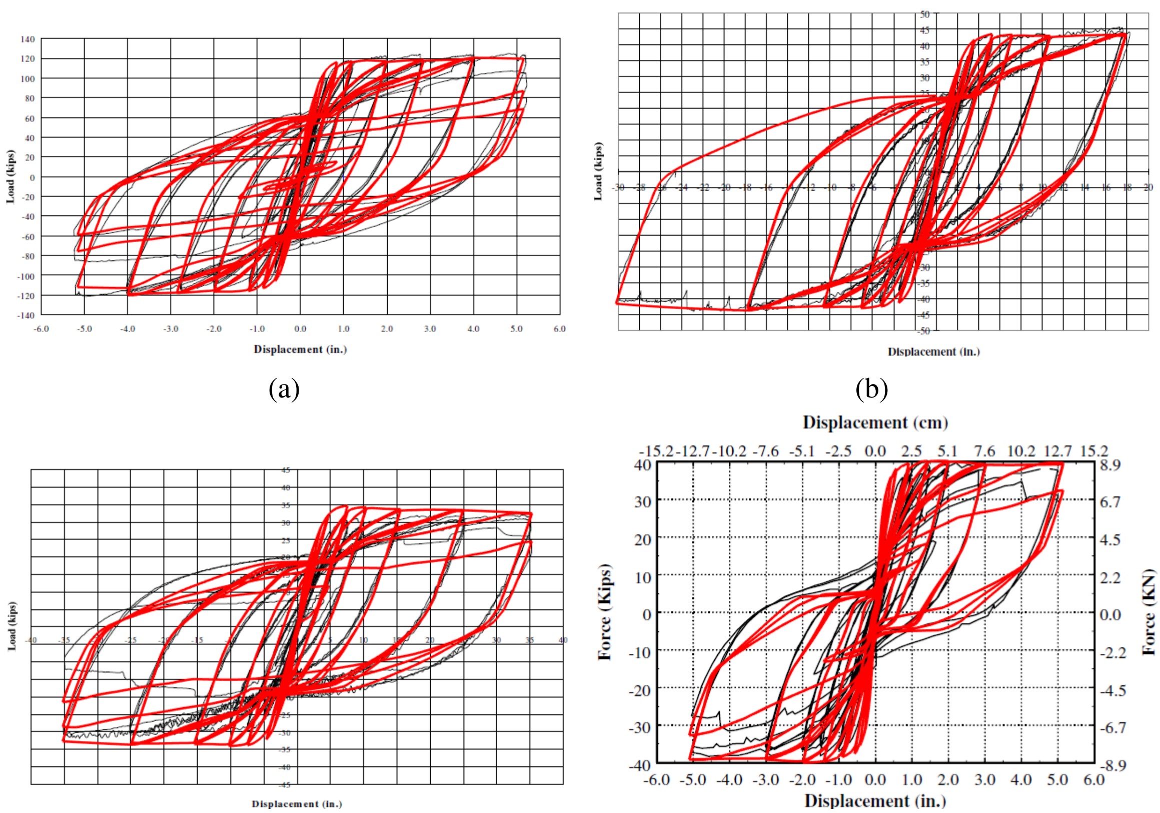

(a) (b)

(c) (d)

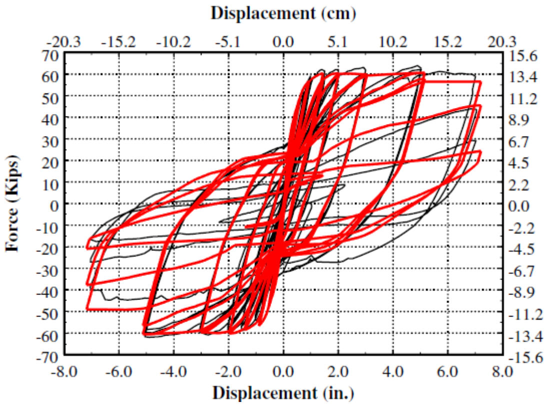

(e)

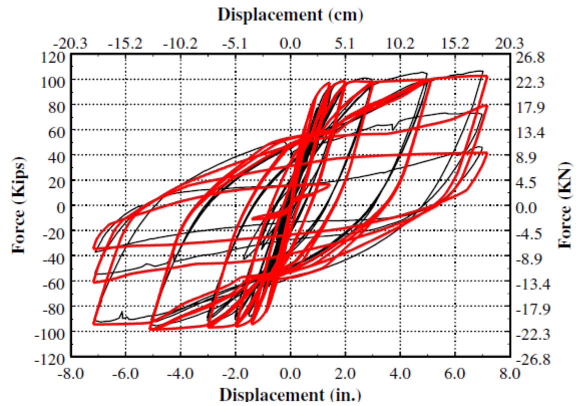

(f)

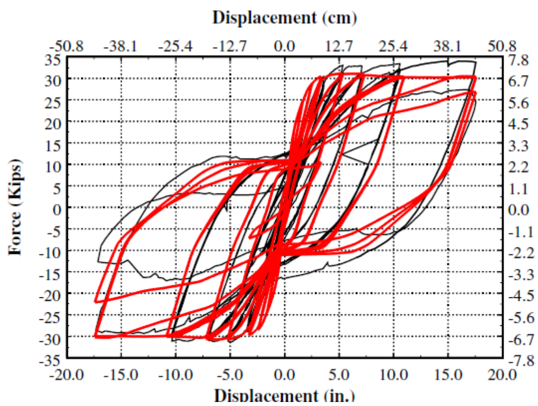

(g)

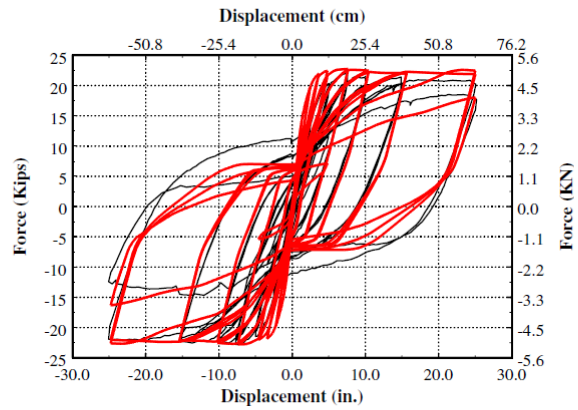

(h)

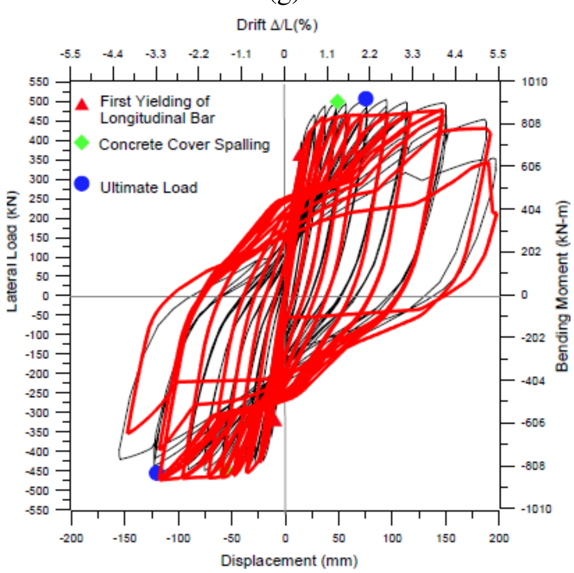

(i)

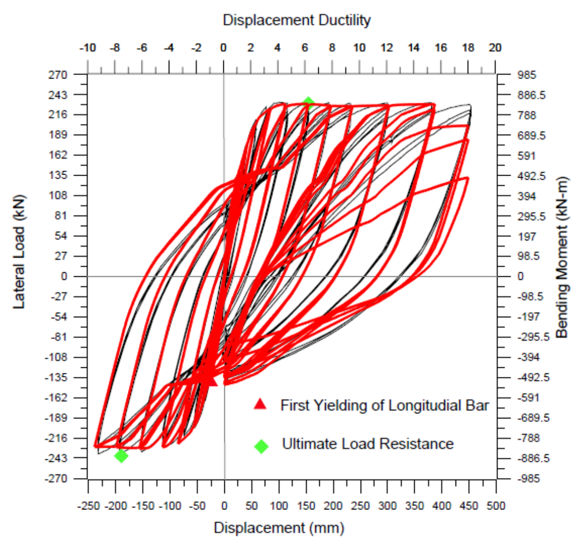

(j)

Figure C.3: Tests by Calderone et al. (2000): (a) e3F-1; (b) e3F-2; (c) e3F-3; tests by Lehman and Moehle (2000): (d) e3F-6; (e) e3F-7; (f) e3F-8; (g) e3F-9; (h) e3F-10; and tests by Prakash (2009): (i) e3F-20; (j) e3F-21.

C.2 Reduced Sections (i.e., Used in Pinned-Base Column Connections)

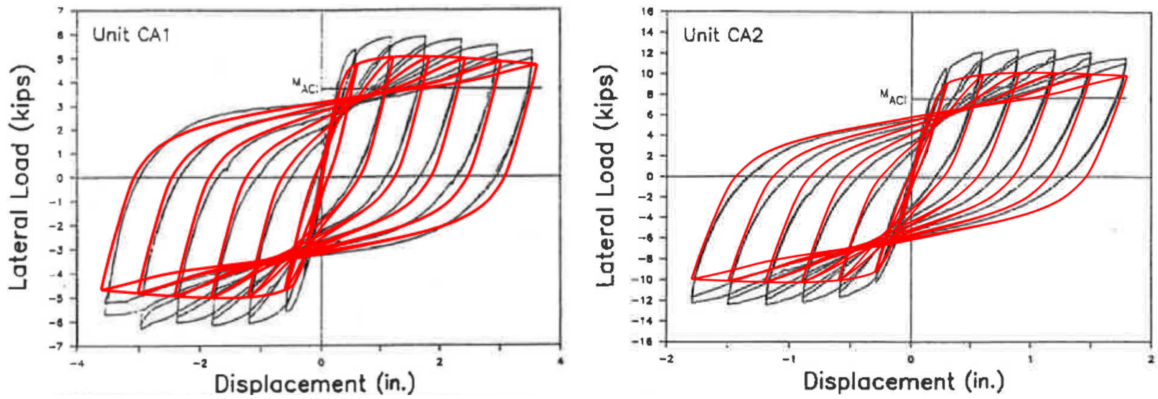

(a) (b)

Figure C.4: Tests by Lim and Mclean (1991): (a) CA1; (b) CA2

C.3 Lap-splice Columns

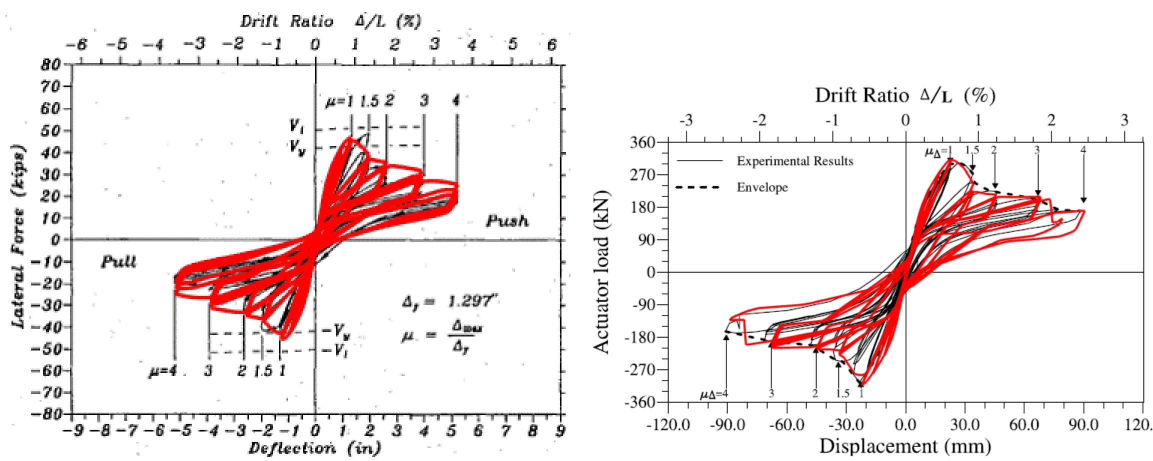

(a) (b)

Figure C.5: (a) e1L-1 (Chai et al., 1991); (b) e1L-6 (Sun et al., 1993).

C.4 Shear/Flexural-Shear Failure Columns

C.4.1 Flexural-Shear Columns in Era-2 and Era-3

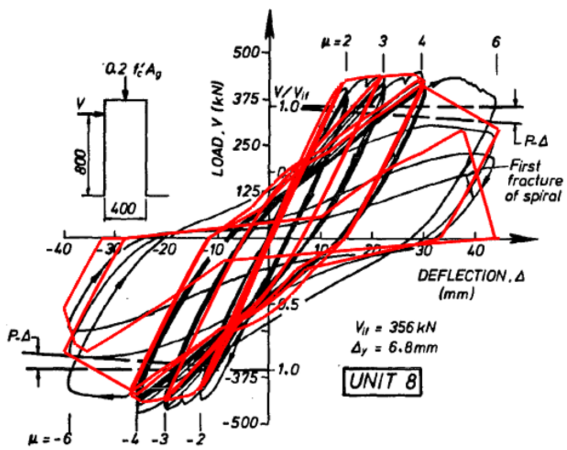

(a)

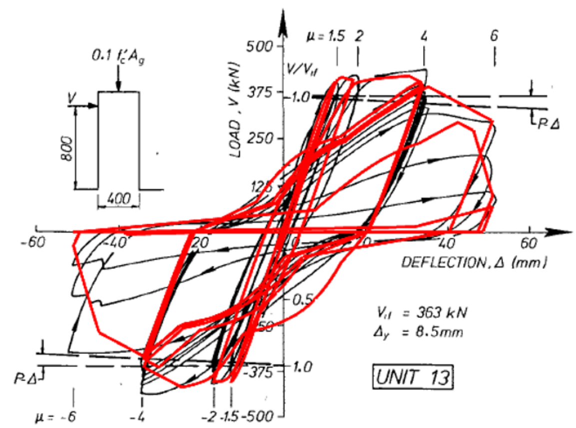

(b)

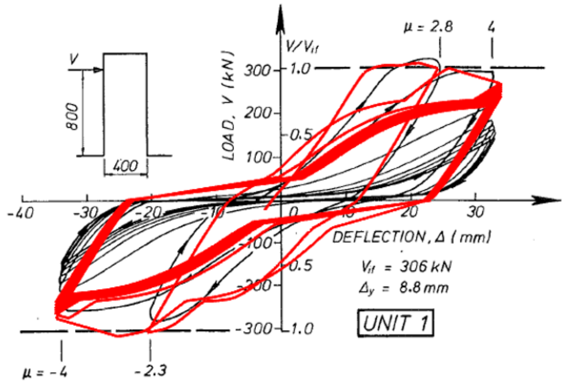

(c)

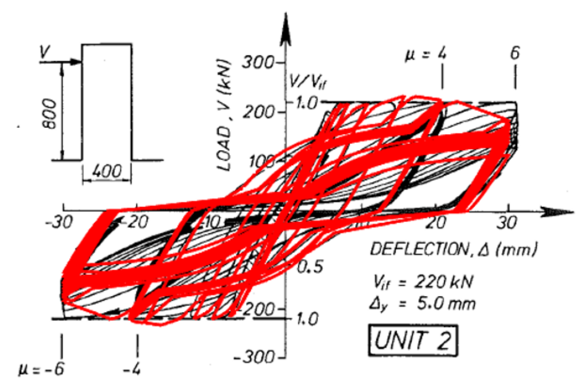

(d)

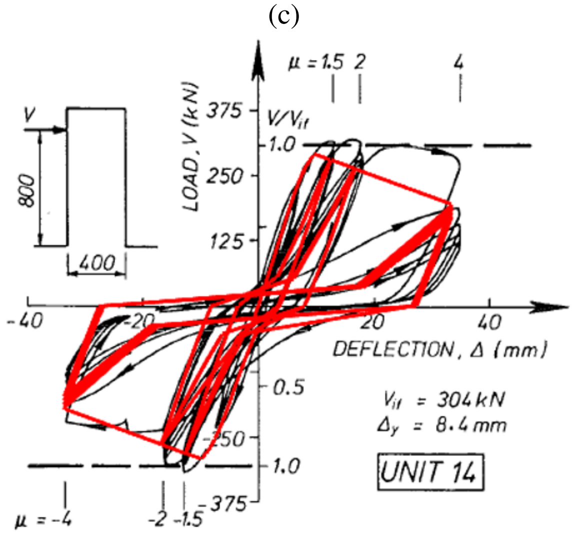

(e)

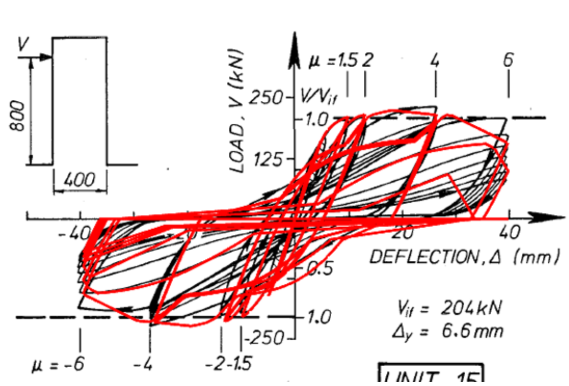

(f)

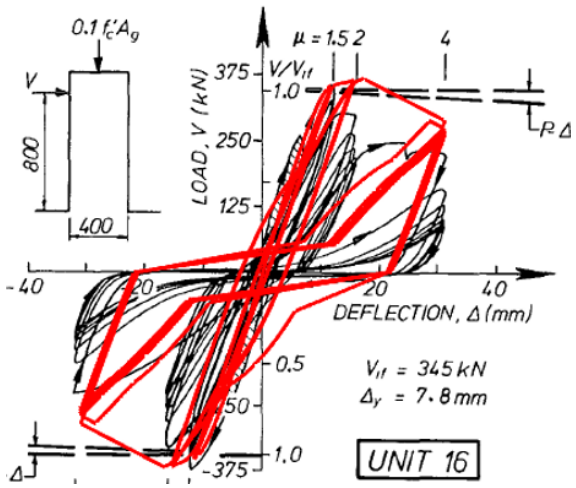

(g)

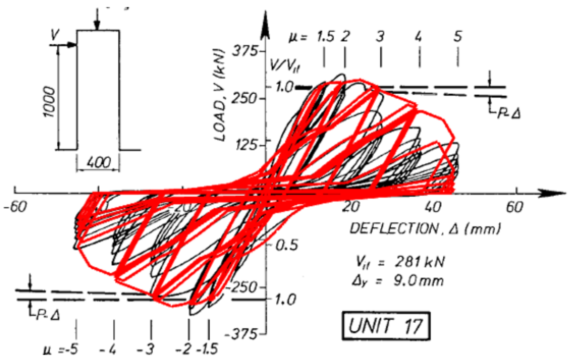

(h)

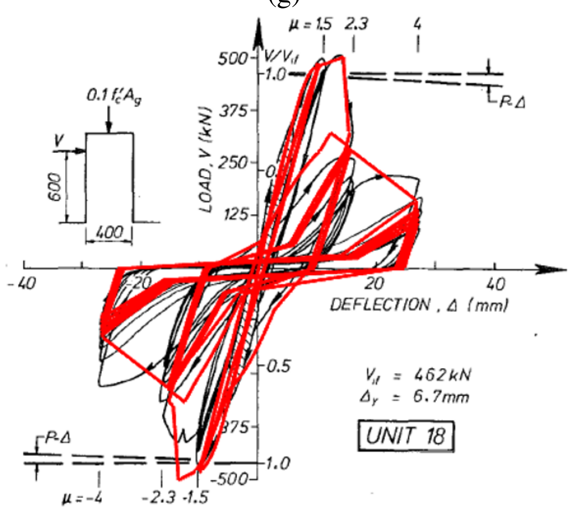

(i)

Figure C.6: Tests by Ang (1985): (a) e23M-1; (b) e23M-3; (c) e23M-13; (d) e23M-14; (e) e23M-15; (f) e23M-16; (g) e23M-17; (h) e23M-18; and (i) e23M-19.

.

C.4.2 Flexural-Shear Columns in Era-1

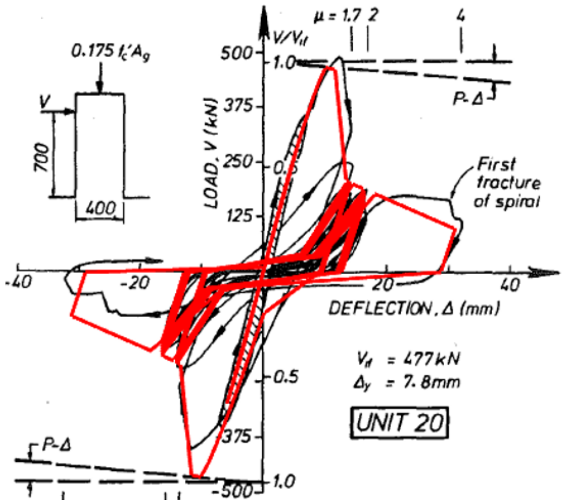

(a)

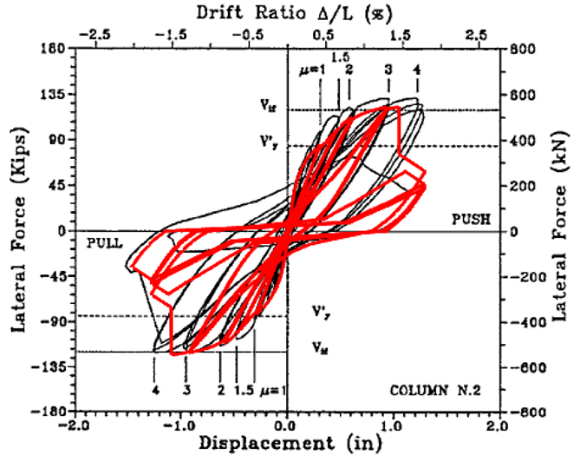

(b)

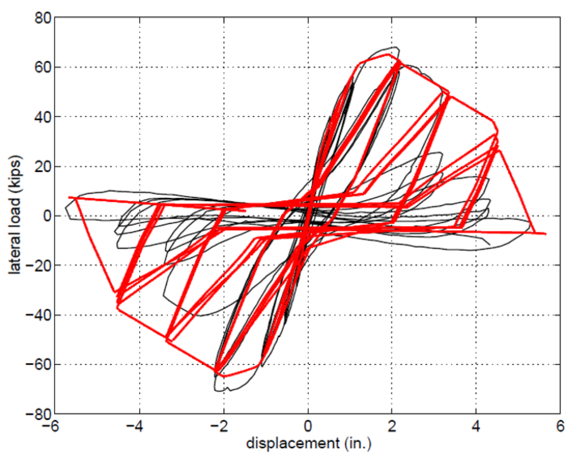

(c)

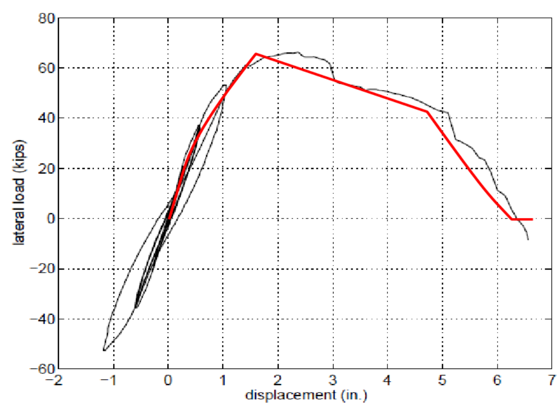

(d)

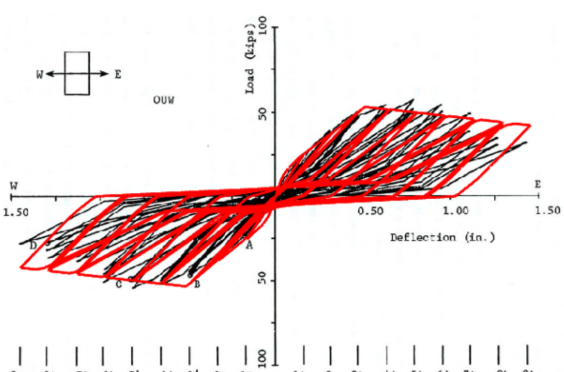

(e)

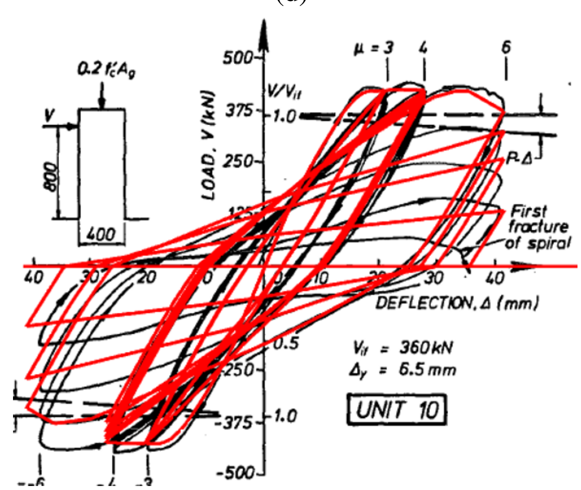

(f)

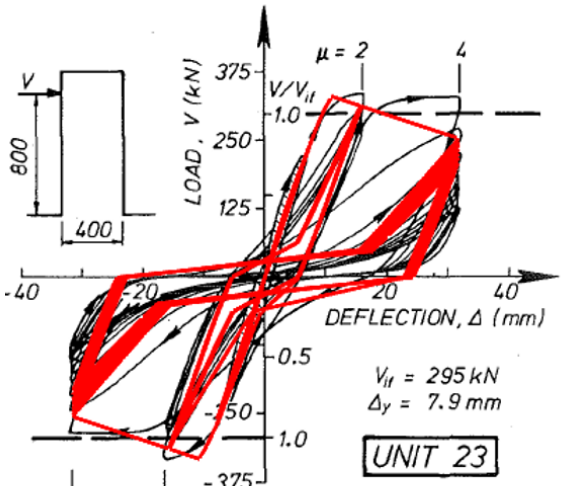

(g)

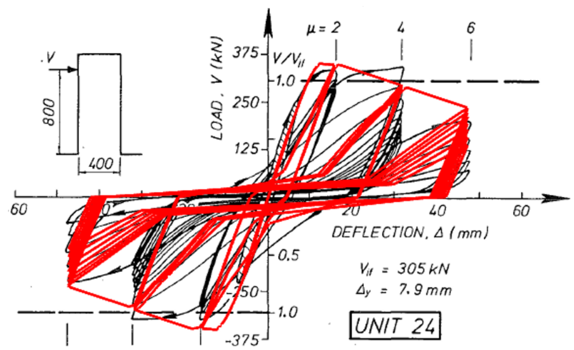

(h)

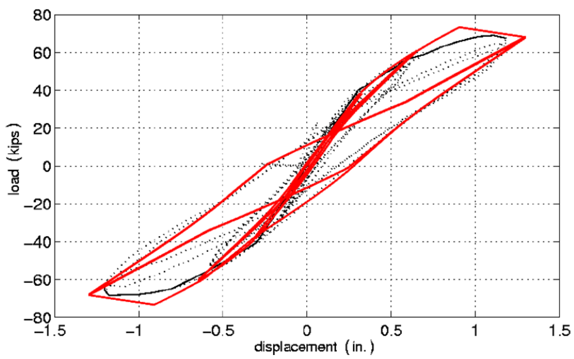

(i)

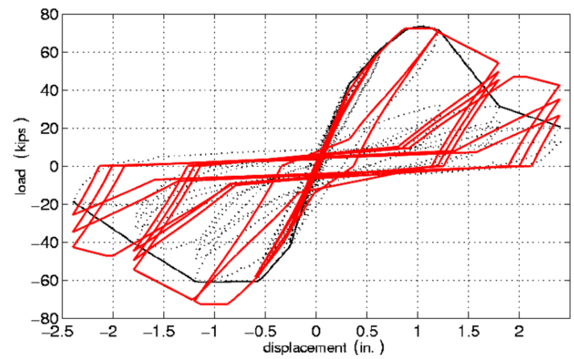

(j)

Figure C.7: (a) e1M-1 (Ang, 1985); (b) e1M-2 (Priestley and Benzoni, 1996); tests by (Sezen, 2002): (c) e1M-3; and (d) e1M-4; (e) e1M-5 (Umehara, 1983); tests by Ang (1985): (f) e1M-6; (g) e1M-7; and (h) e1M-8; tests by Lynn et al. (1996): (i) e1M-9; and (j) e1M-12.

.

C.4.3 Shear Columns

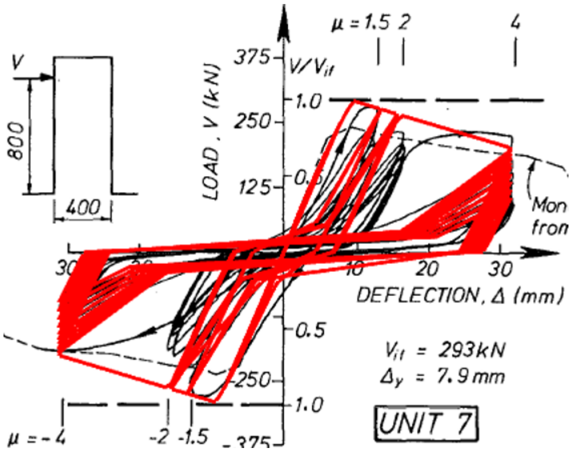

(a)

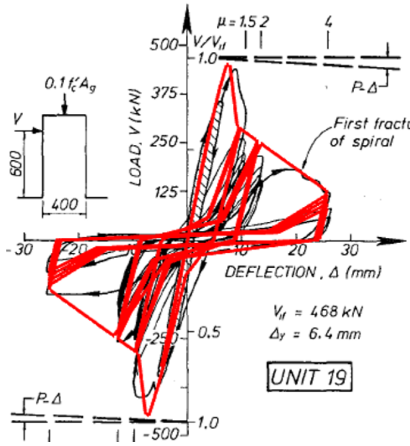

(b)

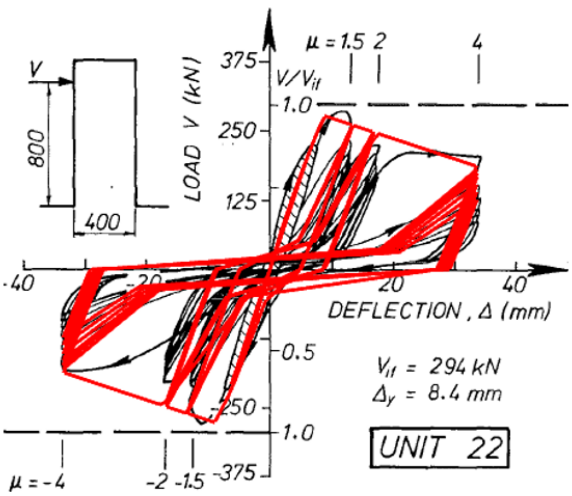

(c)

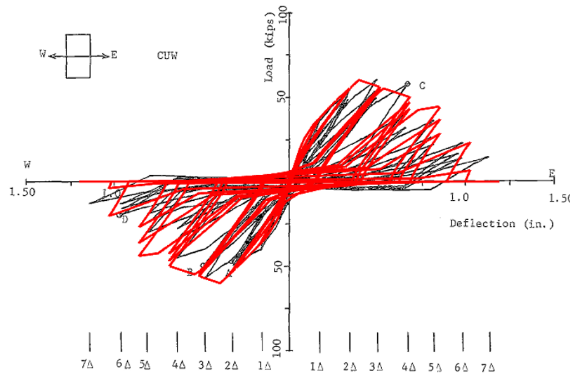

(d)

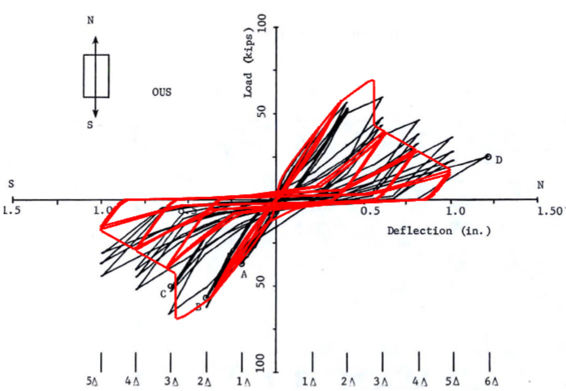

(e)

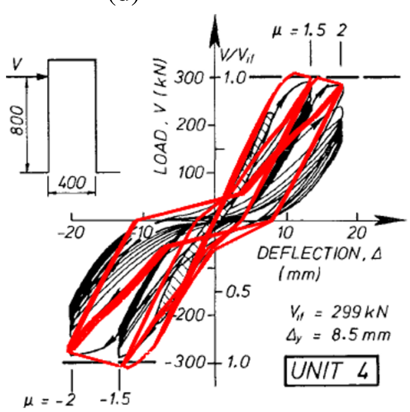

(f)

.

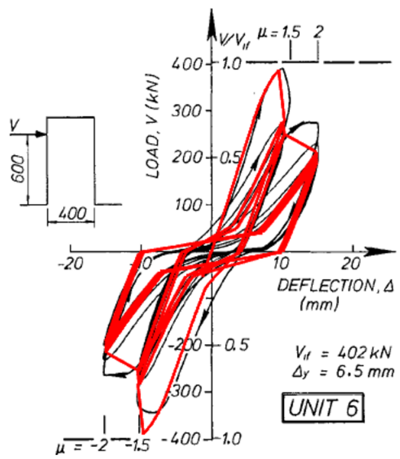

(g)

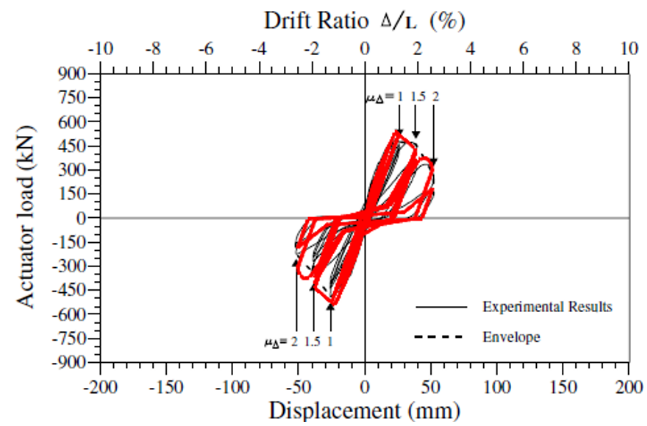

(h)

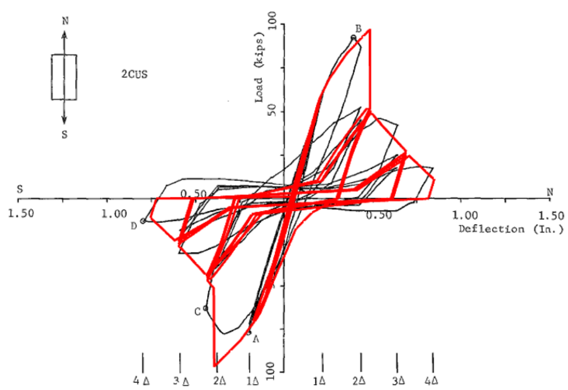

(i)

Figure C.8: Tests by Ang (1985): (a) eXS-1; (b) eXS-2; and (c) eXS-3; tests by Umehara (1983): (d) eXS-8; and (e) eXS-9; Tests by Ang (1985): (f) eXS-10; and (g) eXS-11; (h) eXS-12 (Hose et al., 1997); and (i) eXS-14 (Umehara, 1983).

C.5 Dynamic Analysis

Table C.1: Ground motion parameters in UCSD shake-table tests (Schoettler et al., 2012).

Test	Earthquake	Date	Moment Magnitude	Station	Scale Factor	Table PGA [g]	Table PGV [in./sec]	Feedback Sa1 [g]
EQ1	Loma Prieta	1989	6.9	Agnew State Hospital	1.0	-0.199	6.0	0.25
EQ2	Loma Prieta	1989	6.9	Corralitos	1.0	0.409	15.0	1.00
EQ3	Loma Prieta	1989	6.9	LGPC	1.0	0.526	35.0	1.00
EQ4	Loma Prieta	1989	6.9	Corralitos	1.0	0.454	15.0	1.00
EQ5	Kobe	1995	6.9	Takatori	-0.8	-0.533	38.0	0.80
EQ6	Loma Prieta	1989	6.9	LGPC	1.0	-0.512	34.0	1.00

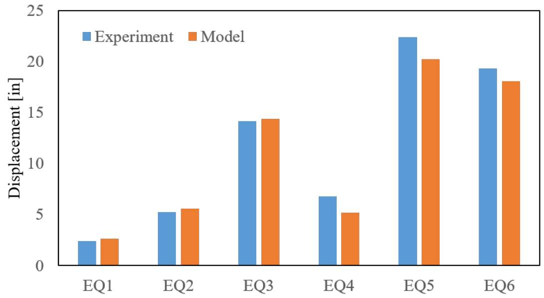
Experiment
Model
Displacement [in]
25
20
15
10
5
0
EQ1
EQ2
EQ3
EQ4
EQ5
EQ6

(a)

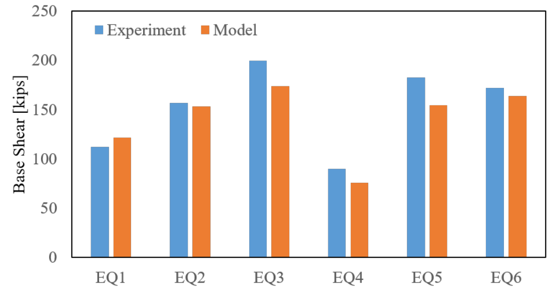
Experiment
Model
Base Shear [kips]
250
200
150
100
50
0
EQ1
EQ2
EQ3
EQ4
EQ5
EQ6

(b)

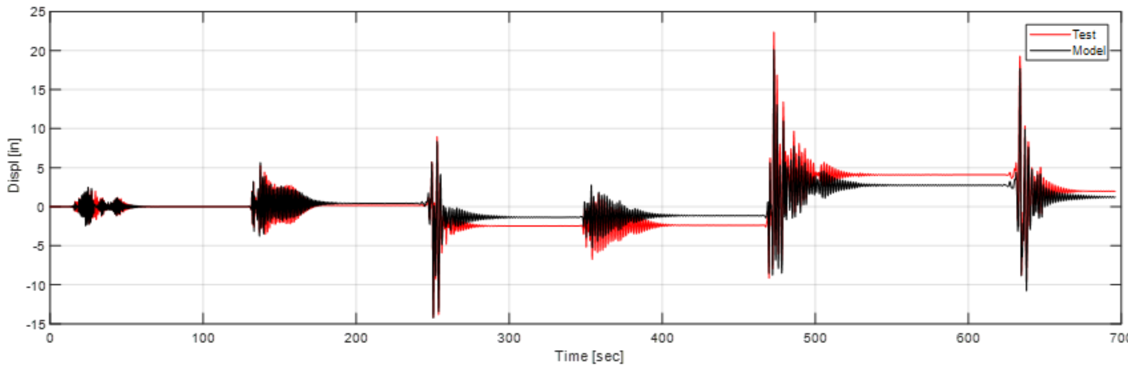
Test
Model
Displ [in]
25
20
15
10
5
0
-5
-10
-15
0
100
200
300
400
500
600
700
Time [sec]

(c)

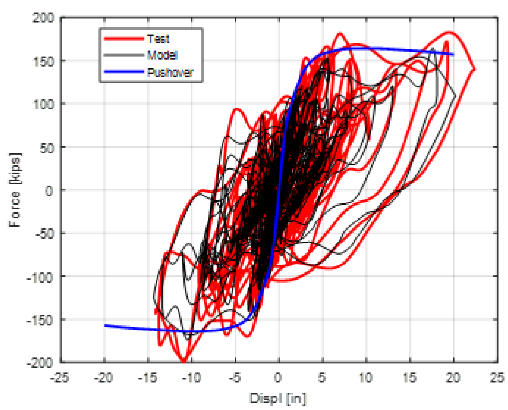
Test
Model
Pushover
Force [kips]
200
150
100
50
0
-50
-100
-150
-200
-25
-20
-15
-10
-5
0
5
10
15
20
25
Displ [in]

(d)

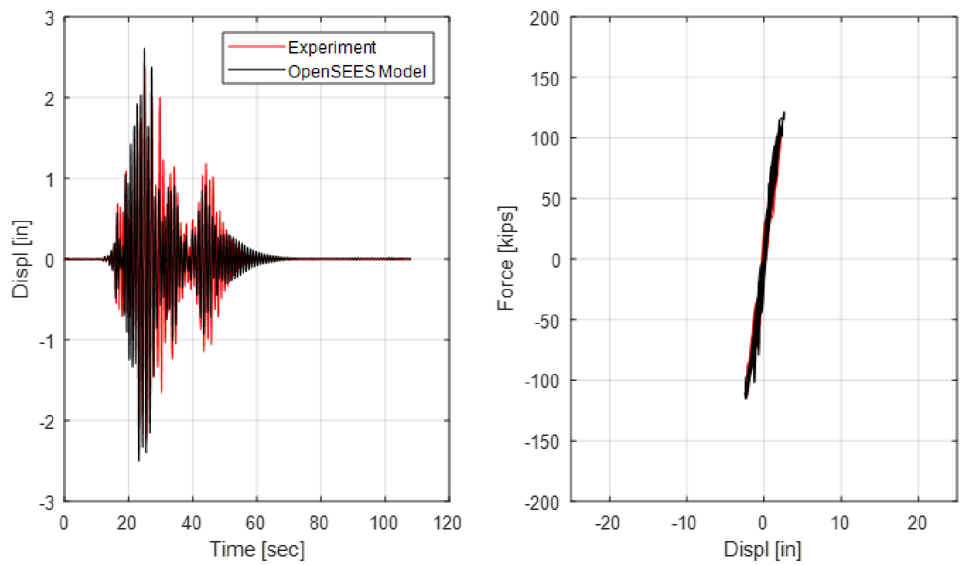

Experiment
OpenSEES Model
Displ [in]
Time [sec]
Force [kips]
Displ [in]

(e)

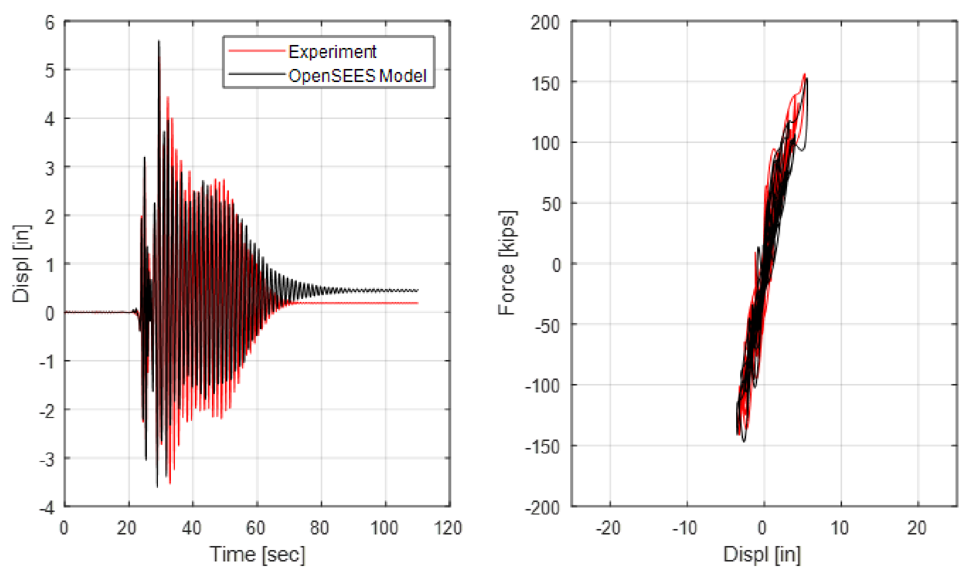

Experiment
OpenSEES Model
Displ [in]
Time [sec]
Force [kips]
Displ [in]

(f)

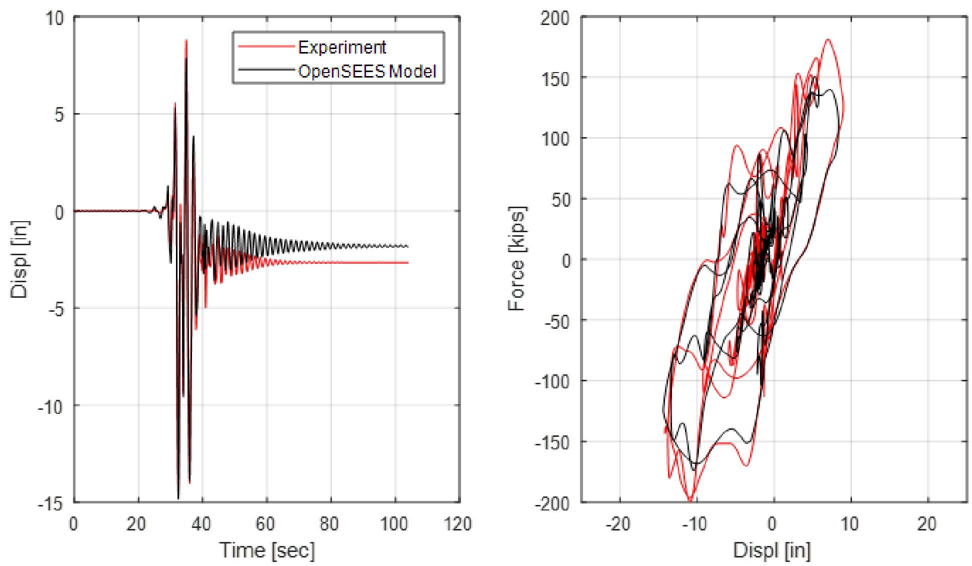
Experiment
OpenSEES Model
Displ [in]
Time [sec]
Force [kips]
Displ [in]

(g)

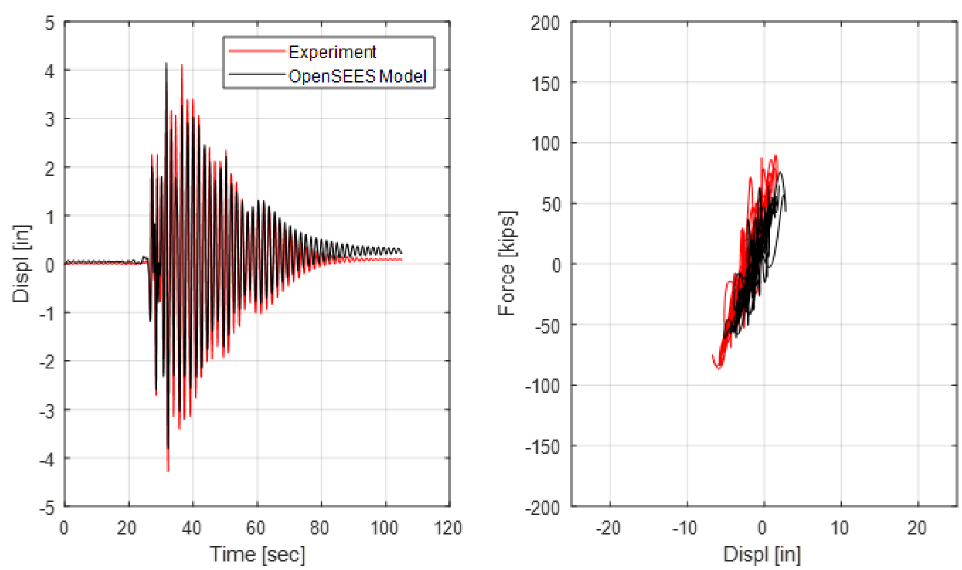
Experiment
OpenSEES Model
Displ [in]
Time [sec]
Force [kips]
Displ [in]

(h)

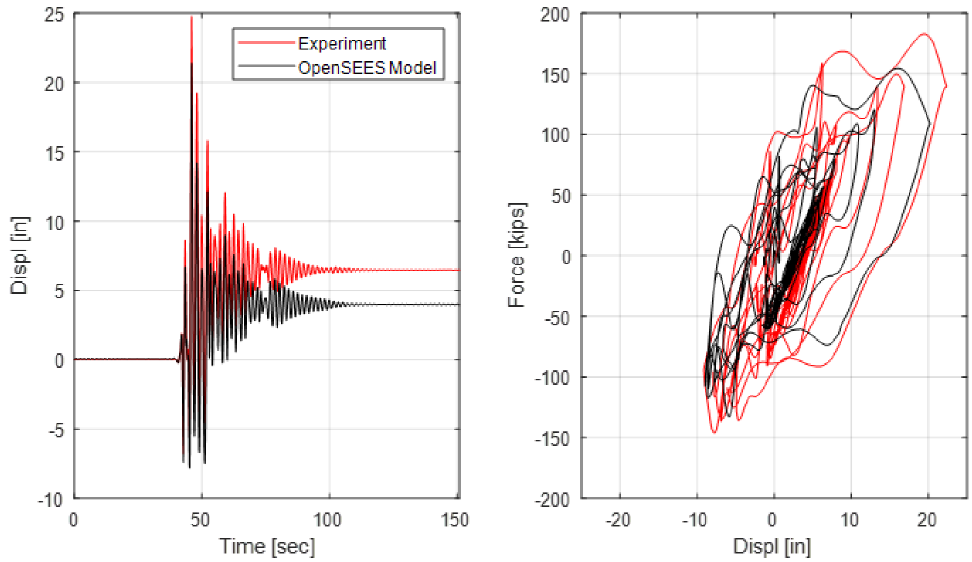

(i)

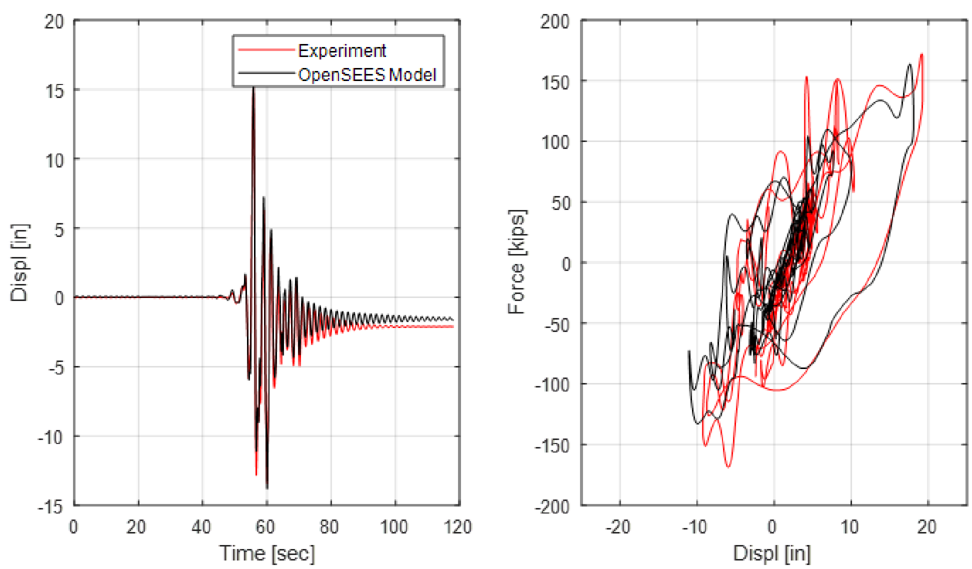

(j)

Figure C.9: Comparison of the UCSD column (Schoettler et al., 2012) and OpenSees modeling results: (a) peak displacement ; (b) peak base shear; (c) time history result; (d) histeretic loops; and (e) to (j) individual ground motion EQ1 to EQ6 simulation results with initial displacement shifted to zero.

APPENDIX D

MODIFIED CALCULATION FOR BACKFILL-B MODEL

This appendix documents the calculation procedure for separating backfill-B introduced near the end of subsection 3.3.7. Before proceeding to the modified calculation procedure, known relationships are first reviewed below, where the variables are described in Chapter 3.

The overall relationship to construct a hyperbolic curve can be written as:

$$P = \frac{y}{\dfrac{1}{K_{max}} + R_f \dfrac{y}{P_{ult}}} \tag{D.1}$$

Substituting H_T or H_A into the following equations provides a model for either the total-backfill (backfill-T) response $P_{ult,T}$ or backfill-A response $P_{ult,A}$. In this manner, these two use a common formula.

$$P_{ult} = P_{ult,0} \left(\frac{H}{H_0}\right)^{\alpha_1} \tag{D.2a}$$

$$K_{max} = K_{max,0} \left(\frac{H}{H_0}\right)^{\alpha_2} \tag{D.2b}$$

$$R_f = 1 - \frac{P_{ult}}{0.05 K_{max} H} \tag{D.2c}$$

Next, denote $a = \dfrac{1}{K_{max}}$ and $b = \dfrac{R_f}{P_{ult}}$. The response of backfill-T and backfill-A is simplified to Equation D.3.

$$P_T = \frac{y}{a_T + b_T y} \tag{D.3a}$$

$$P_A = \frac{y}{a_A + b_A y} \tag{D.3b}$$

Subtracting Equation D.3b from Equation D.3a results in backfill-B's response:

$$\begin{aligned} P_B &= P_T - P_A \\ &= \frac{\left[(a_A + b_A y) - (a_T + b_T y)\right] y}{(a_T + b_T y)(a_A + b_A y)} \\ &= \frac{y}{a_B + b_B y} \end{aligned} \tag{D.4}$$

Rearranging Equation D.4 generates the following relationship:

$$\begin{aligned} & b_B(b_A - b_T)y^2 + \left[b_B(a_A - a_T) + a_B(b_A - b_T)\right]y + a_B(a_A - a_T) \\ = \quad & b_A b_T \quad y^2 + \quad (a_A b_T + a_T b_A) \quad y + \quad a_A a_T \end{aligned} \tag{D.5}$$

Use polynomial equating to equate the coefficients for the two terms with y^2 and y, leaving out the constant term, to yield a function of a_B and b_B with respect to (a_A, b_A, a_T, b_T). This approximation captures the primary effects and does not change with y:

$$b_B \approx \frac{b_A b_T}{b_A - b_T} \tag{D.6a}$$

$$a_B \approx \frac{a_A b_T + a_T b_A - b_B(a_A - a_T)}{b_A - b_T} \tag{D.6b}$$

Finally, these equations can be used to compute $P_{ult,B}$, $K_{max,B}$ and $R_{f,B}$ as follows:

$$K_{max,B} = \frac{1}{a_B} \tag{D.7a}$$

$$P_{ult,B} = P_{ult,T} - P_{ult,A} \tag{D.7b}$$

$$R_{f,B} = P_{ult,B} b_B \tag{D.7c}$$

APPENDIX E

RATIO DISTRIBUTION FOR GROUND MOTION PAIRING

This appendix is documenting the development of distribution for ratio of target applied ground motions (TAGM) to design ground motions (DGM), as well as the sampling procedure.

Denote the ratio of intensity measurement (e.g., $S_{a,1.0}$) as r. It was assumed to distribute with constant probability at the range of 0 to 1, and then with decreasing probability from 1 to 1.5, as demonstrated below in Figure E.1(b).

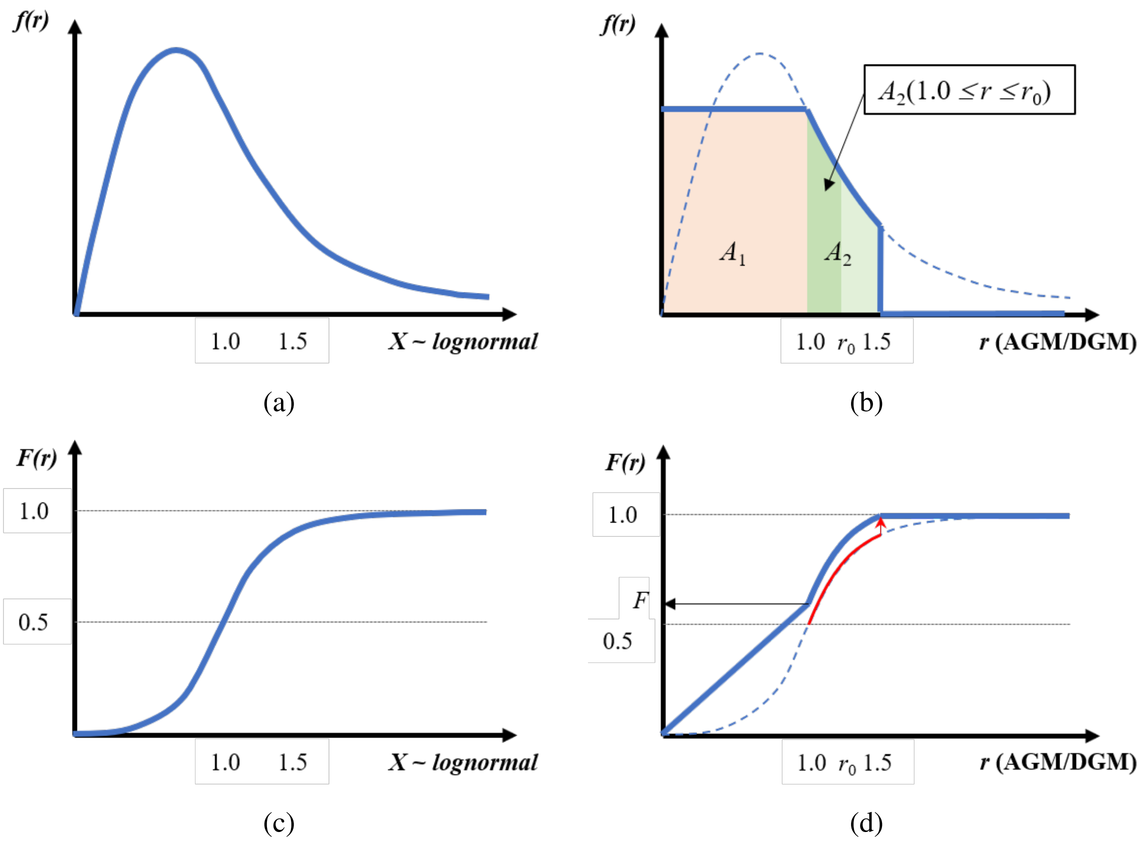

Figure E.1: Illustration of lognormal distribution and desired r distribution.

A lognormal distribution ($F_X(x)$ and $f_X(x)$) is assumed firstly with median = 1.0 and dispersion = d (Figure E.1(a) and (c)). The assumed median is for convenient calculation in the following, which can be changed to any number correspondingly. The assumed lognormal distribution is applied for the decreasing portion in the distribution of r. Correspondingly, non-scaled area in Figure E.1(b) can be calculated as:

$$A_1 = f_X(1.0) \tag{E.1a}$$

$$A_2 = 0.5 - (1 - F_X(1.5)) \tag{E.1b}$$

And therefore, the scaled factor F is derived:

$$F = \frac{A_1}{A_1 + A_2}. \tag{E.2}$$

In Figure E.1(d), the blue line is the scaled from the original lognormal CDF (red line). Thus, for a number $r_0 < 1.5$, the CDF value is calculated the following:

$$F_R(r_0) = \begin{cases} r_0 F, & 0 \leq r_0 \leq 1; \\ [A_1 + A_2(1.0 < r \leq r0)]/(A_1 + A_2), & 1 < r_0 < 1.5. \end{cases} \tag{E.3}$$

where $A_2(1.0 < r \leq r0)$ is demonstrated in Figure E.1(b) as the non-scaled area between 1.0 to r_0.

Considering 1.0 is the median of original lognormal distribution, the corresponding CDF value at $r_0 > 1.0$ is:

$$F_X(r_0) = 0.5 + A_2(1.0 < r \leq r0). \tag{E.4}$$

Combining Equation E.3 and Equation E.4, when $1 < r_0 < 1.5$:

$$F_R(r_0) = (A_1 + F_X(r_0) - 0.5)/(A_1 + A_2) \tag{E.5a}$$

$$F_X(r_0) = (A_1 + A_2)F_R(r_0) - A_1 + 0.5 \tag{E.5b}$$

To this end, a probability p can be transformed to a corresponding r value:

$$r_0 = \begin{cases} p/F, & 0 \leq p \leq F \\ F_X^{-1}((A_1 + A_2)p - A_1 + 0.5), & F < p < 1.0. \end{cases} \tag{E.6}$$

APPENDIX F

FRAGILITY MODELS FOR ERA-3 TWO-SPAN MULTI-COLUMN BENT BOX-GIRDER BRIDGES

This appendix presents the complete set of the fragility models for all three regions and then rolls up these three models into a system model.

Figure F.1 and Figure F.2 outline the roll-up stages for a column bent where Figure F.1 considers Stage-0 models contributing to the Stage-B.2 column model, and Figure F.2 considers the other components leading to a Stage-C bent model.

Figure F.3 through Figure F.33 present all of the underlying fragility models used to create the combined Stage-B.2 column model, while Figure F.34 through Figure F.55 present the additional underlying fragility models used to create the Stage-C bent model in Figure F.56, which is the sole element of the interior support region.

Figure F.57 depicts the roll-up stages for the abutment joint region. Similarly, Figure F.58 through Figure F.80 presents all the underlying fragility models.

Figure F.81 depicts the roll-up stages for the abutment wall region, which in this case, only involves the abutment foundations. Figure F.82 through Figure F.95 present fragility models for the abutment foundation components.

Figure F.96 provides the overall Stage-D roll-up for the entire bridge systems considering hazard contributions from all three regions.

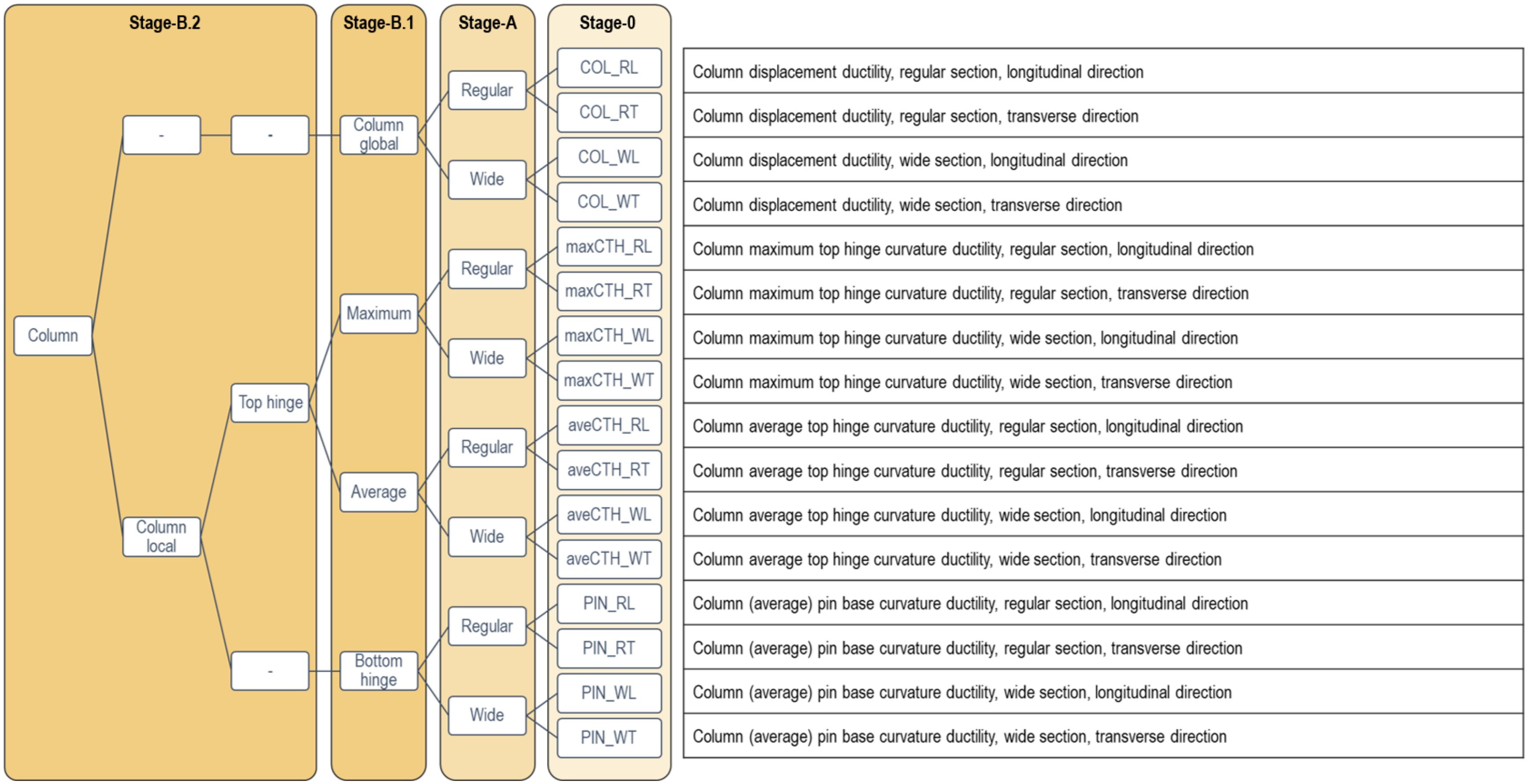

Figure F.1: Roll-up steps to create a Stage-B.2 fragility model for column response.

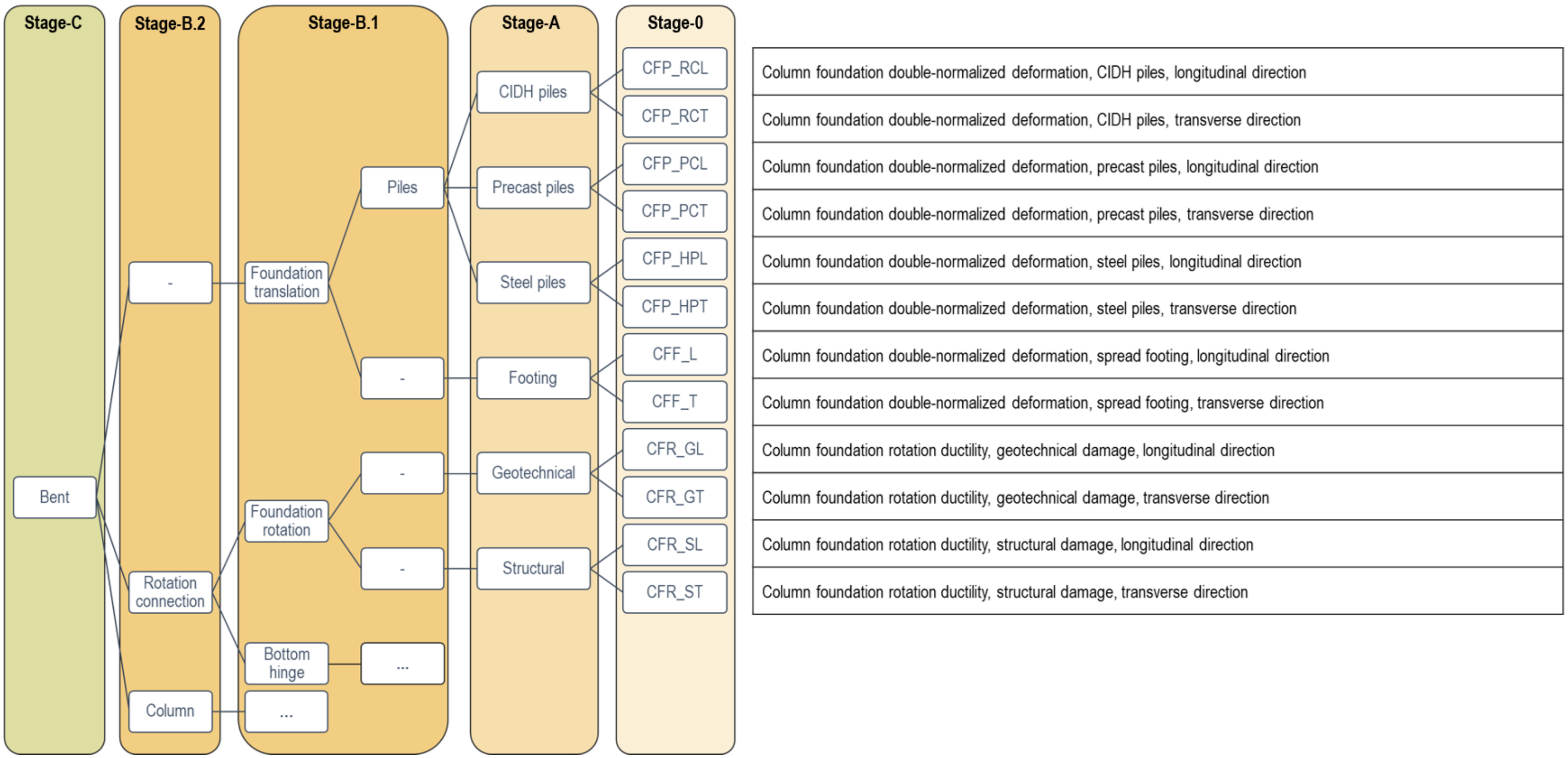

Figure F.2: Additional roll-up steps for a Stage-C bent fragility model.

Stage-0: Component Subgroup - Directional

Region: Interior Supports, Zone 1

Component: Column Bent (All Failure Modes)

Subgroup: Regular Sections

Direction: Longitudinal Rotated (LR), Skew = 0 deg.

Metric: (Whole) Column Bent Damage

EDP: Displacement Ductility (BRC)

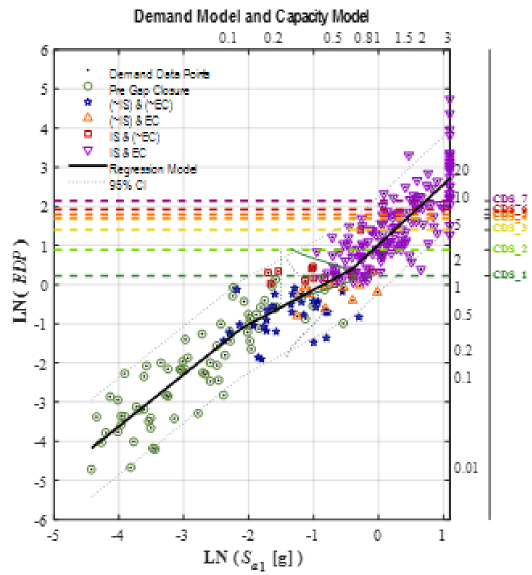

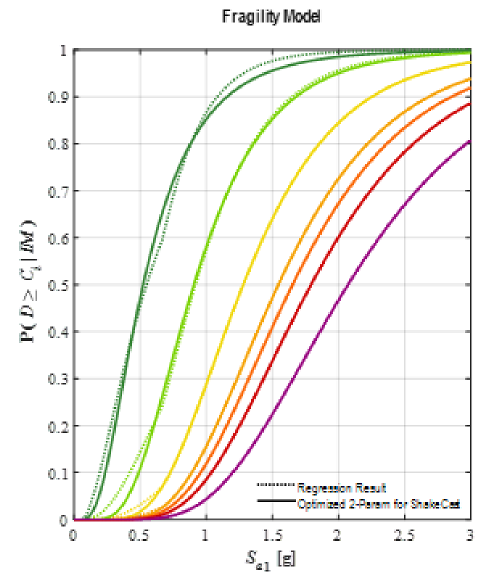

Capacity Model State Descriptions - Component Subgroup

	CDS_1	T_12	CDS_2	T_23	CDS_3	T_34	CDS_4	T_45	CDS_5	T_56	CDS_6	T_67	CDS_7
Whole-Bent Damage State:	EQ-Related Tight Cracking of Cover		Moderate Cracking & Minor Spalling/Flaking		Open Cracking or Major Spalling (Exterior to Confinement)		Exposed Core (Interior of Confinement) But No Visible Bar Buckling		Visible Bar Buckling; Confinement Loss or Core Shedding		Multi-Bar Rupture or Buckling; Large Drift; or Core Crushing		Bent Collapse (Near-Total Loss of Axial Capacity)
Experimentally Observed Damage OR Normalized Force v. Displacement Ductility Response Range:	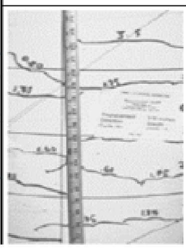		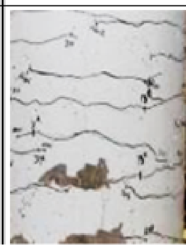	~100%		~95%		~87%	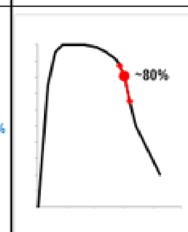 ~80%	~65%	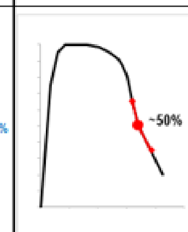 ~50%	~35%	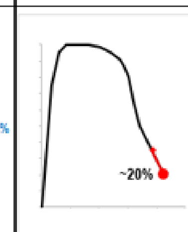 ~20%

Figure F.3: Stage-0: Regular section column displacement ductility in longitudinal direction

Stage-0: Component Subgroup - Directional

Region:	Interior Supports, Zone 1
Component:	Column Bent (All Failure Modes)
Subgroup:	Regular Sections
Direction:	Transverse Rotated (TR), Skew = 0 deg.
Metric:	(Whole) Column Bent Damage
EDP:	Displacement Ductility (BRC)

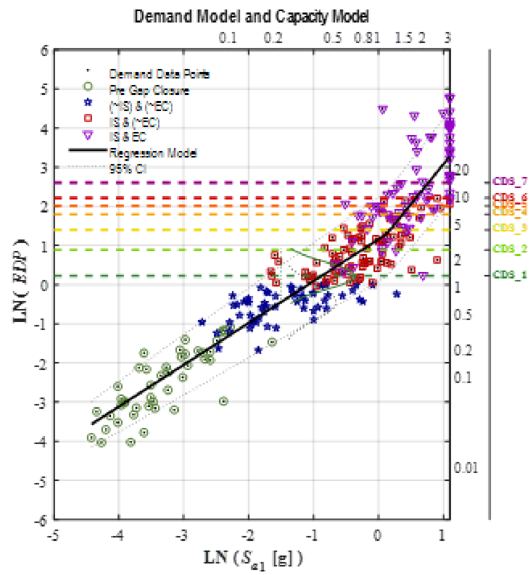

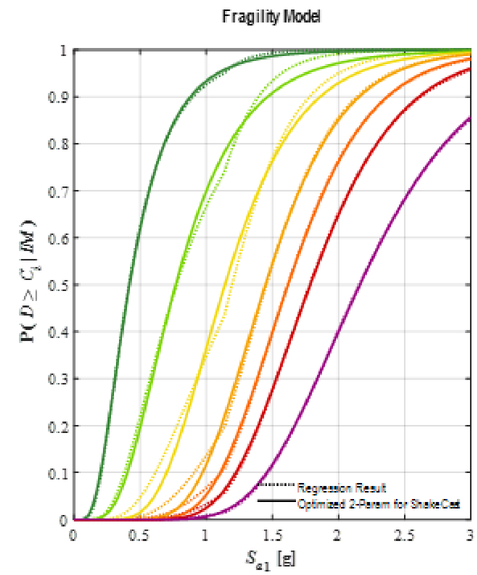

Capacity Model State Descriptions - Component Subgroup

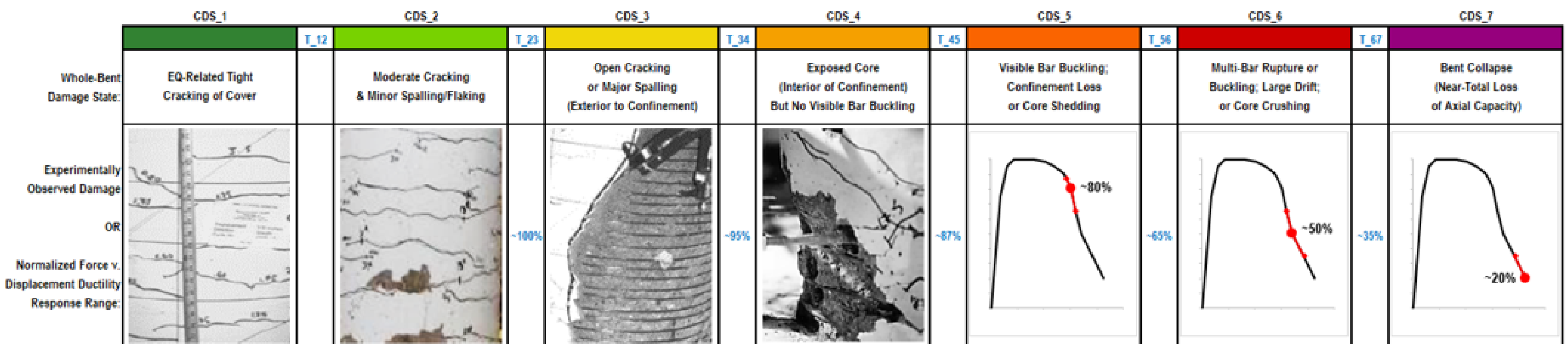

Figure F.4: Stage-0: Regular section column displacement ductility in transverse direction

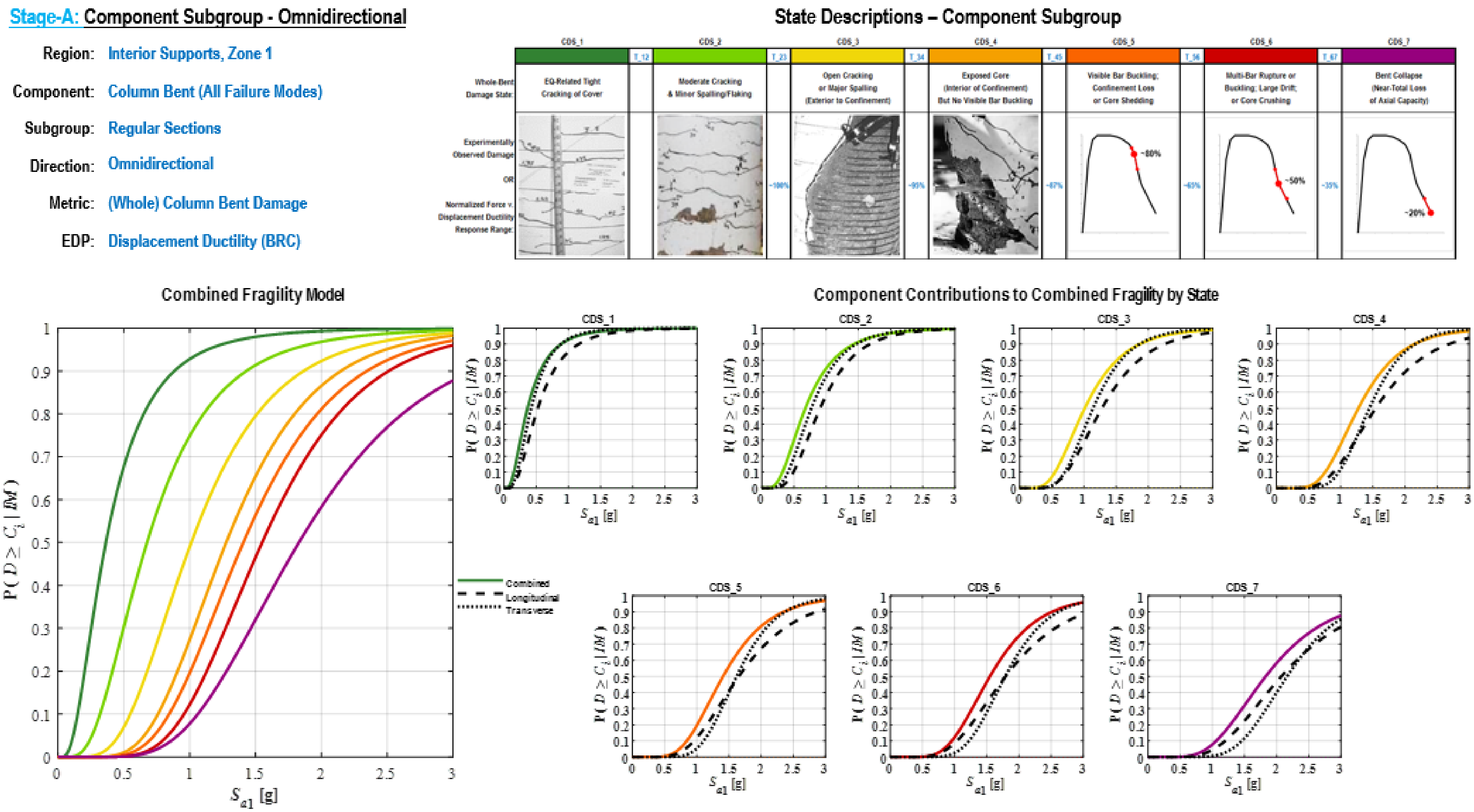

Figure F.5: Stage-A: Regular section column displacement ductility.

Stage-0: Component Subgroup - Directional

Region: Interior Supports, Zone 1

Component: Column Bent (All Failure Modes)

Subgroup: Wide Sections

Direction: Longitudinal Rotated (LR), Skew = 0 deg.

Metric: (Whole) Column Bent Damage

EDP: Displacement Ductility (BRC)

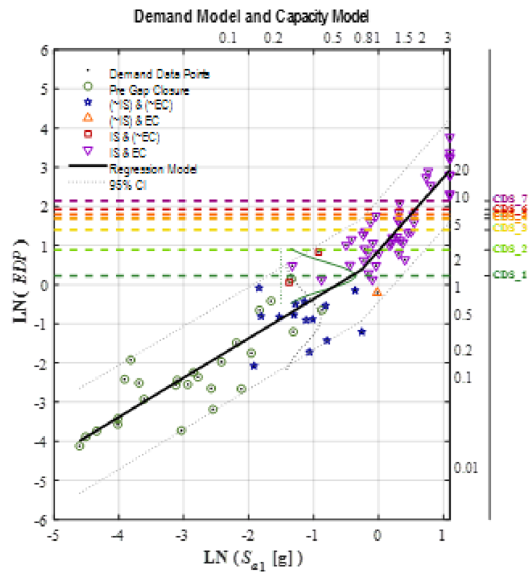

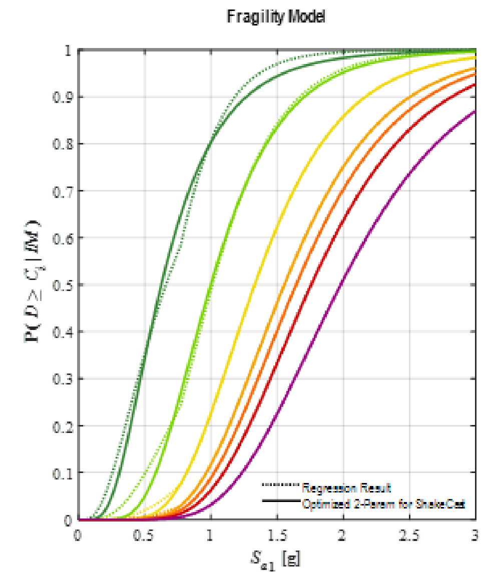

Capacity Model State Descriptions - Component Subgroup

	CDS_1	T_12	CDS_2	T_23	CDS_3	T_34	CDS_4	T_45	CDS_5	T_56	CDS_6	T_67	CDS_7
Whole-Bent Damage State:	EQ-Related Tight Cracking of Cover		Moderate Cracking & Minor Spalling/Flaking		Open Cracking or Major Spalling (Exterior to Confinement)		Exposed Core (Interior of Confinement) But No Visible Bar Buckling		Visible Bar Buckling; Confinement Loss or Core Shedding		Multi-Bar Rupture or Buckling; Large Drift; or Core Crushing		Bent Collapse (Near-Total Loss of Axial Capacity)
Experimentally Observed Damage OR Normalized Force v. Displacement Ductility Response Range:	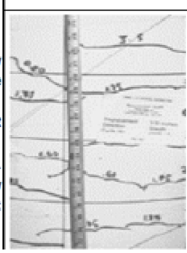		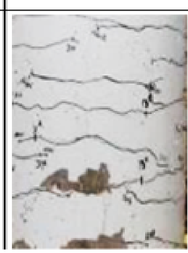	~100%		~95%		~87%	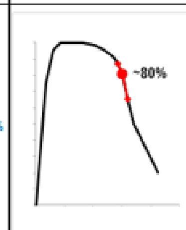 ~80%	~65%	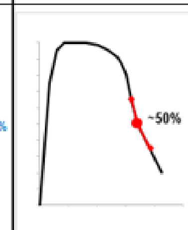 ~50%	~35%	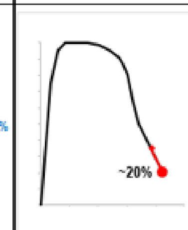 ~20%

Figure F.6: Stage-0: Wide section column displacement ductility in longitudinal direction

Stage-0: Component Subgroup - Directional

Region: Interior Supports, Zone 1

Component: Column Bent (All Failure Modes)

Subgroup: Wide Sections

Direction: Transverse Rotated (TR), Skew = 0 deg.

Metric: (Whole) Column Bent Damage

EDP: Displacement Ductility (BRC)

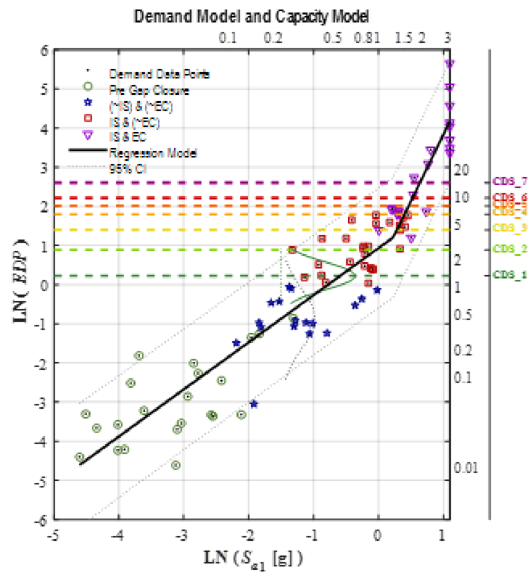

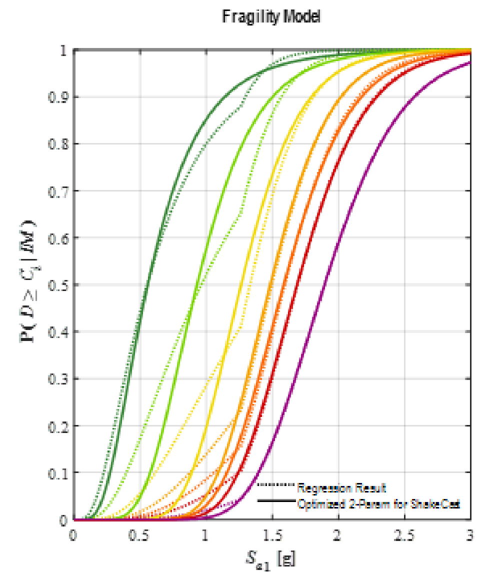

Capacity Model State Descriptions - Component Subgroup

	CDS_1	T_12	CDS_2	T_23	CDS_3	T_34	CDS_4	T_45	CDS_5	T_56	CDS_6	T_67	CDS_7
Whole-Bent Damage State:	EQ-Related Tight Cracking of Cover		Moderate Cracking & Minor Spalling/Flaking		Open Cracking or Major Spalling (Exterior to Confinement)		Exposed Core (Interior of Confinement) But No Visible Bar Buckling		Visible Bar Buckling; Confinement Loss or Core Shedding		Multi-Bar Rupture or Buckling; Large Drift; or Core Crushing		Bent Collapse (Near-Total Loss of Axial Capacity)
Experimentally Observed Damage OR Normalized Force v. Displacement Ductility Response Range:				~100%		~95%		~87%		~65%		~35%	

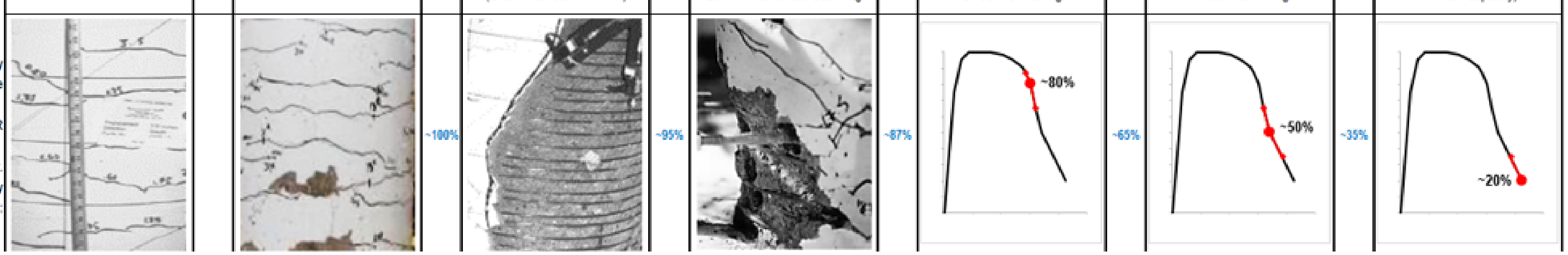

Figure F.7: Stage-0: Wide section column displacement ductility in transverse direction

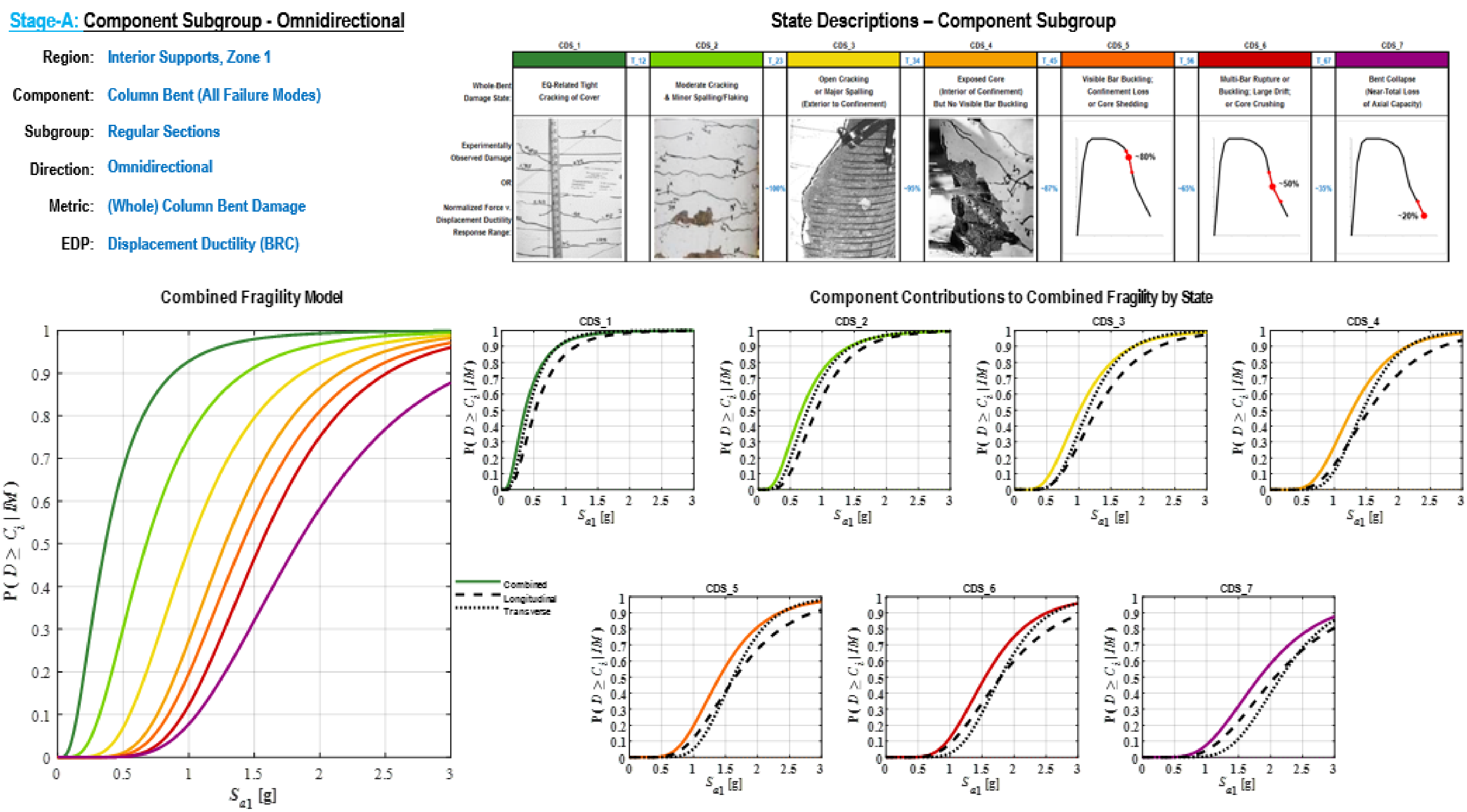

Figure F.8: Stage-A: Wide section column displacement ductility.

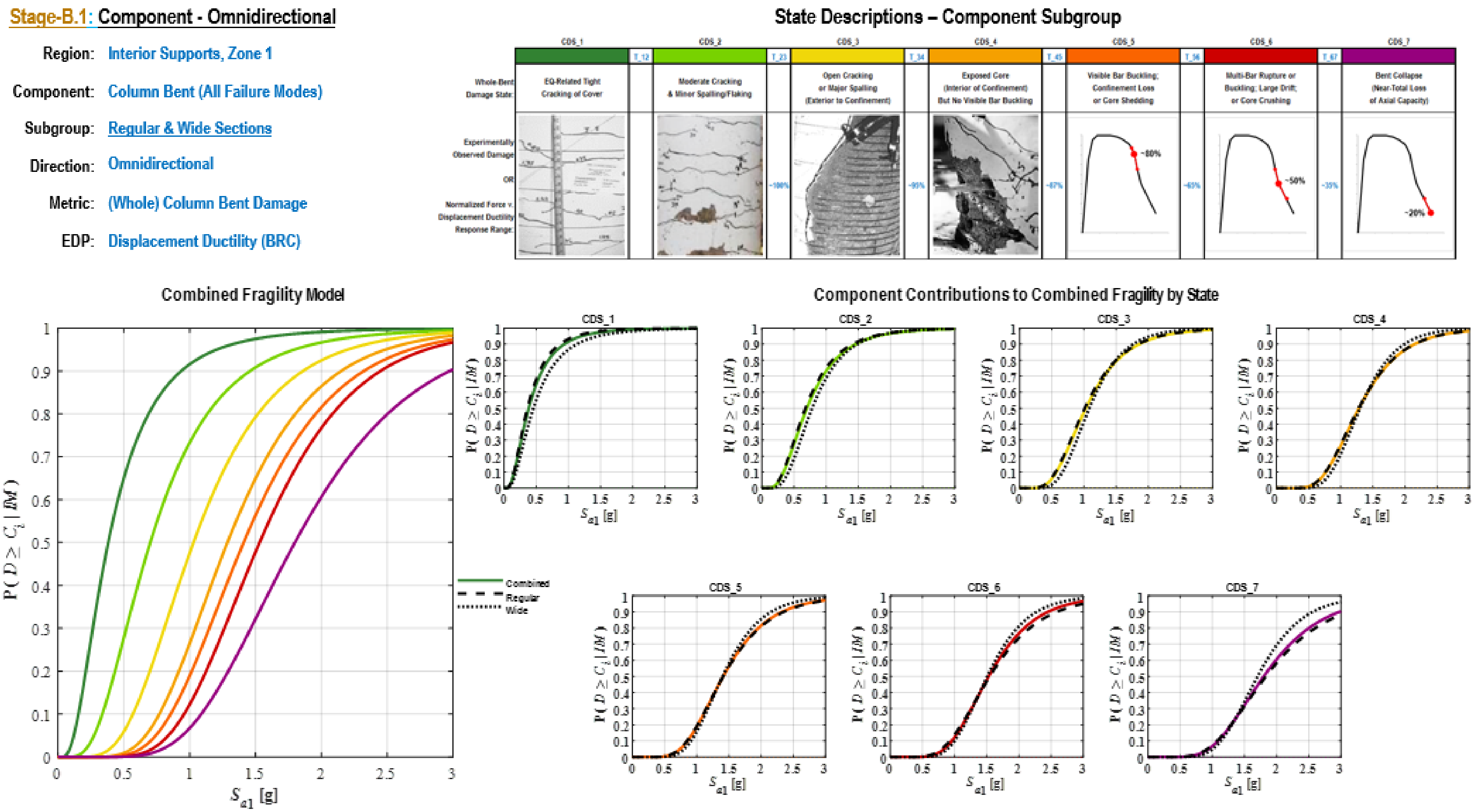

Figure F.9: Stage-B.1: Column displacement ductility (global response).

293

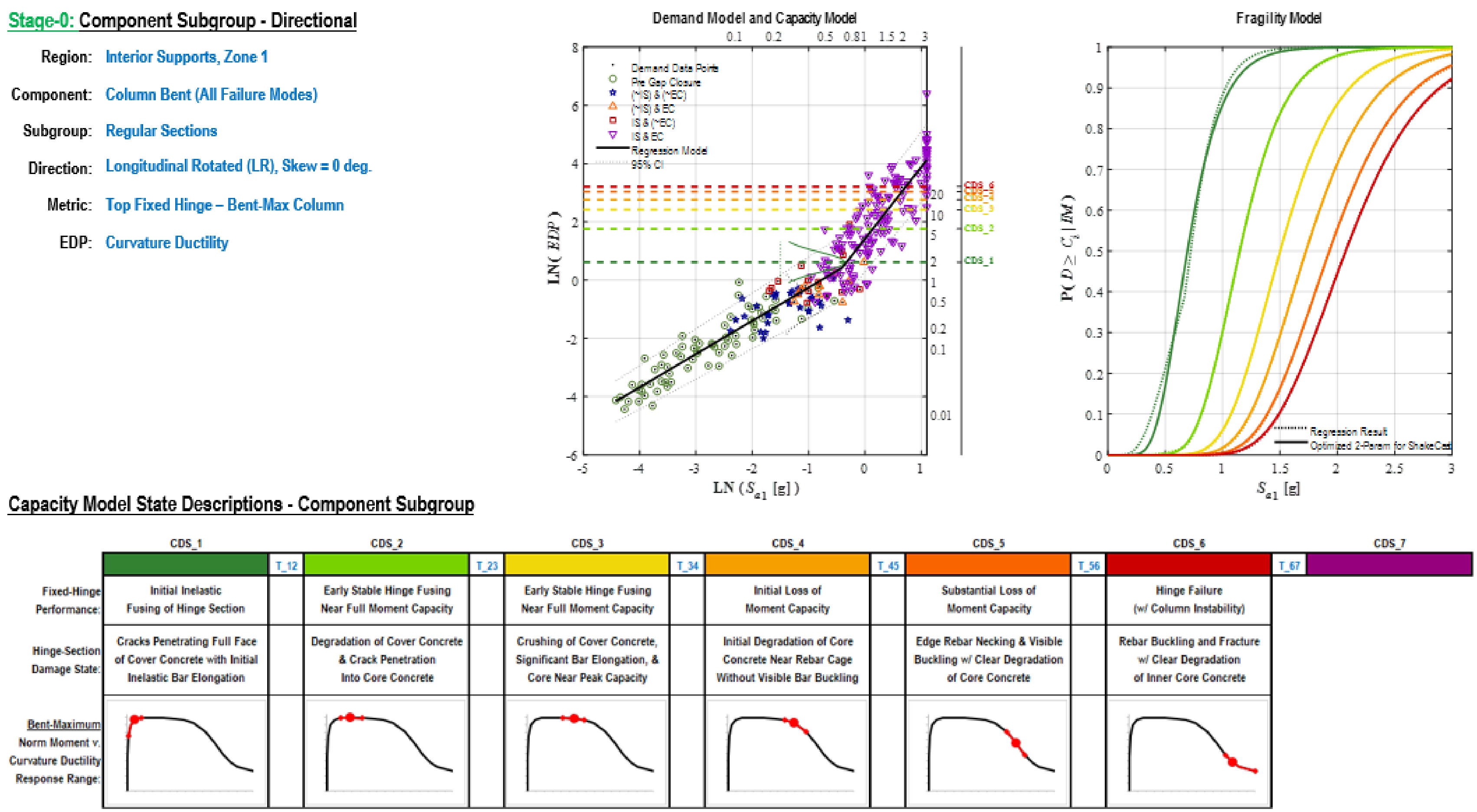

Figure F.10: Stage-0: Regular section column top fixed-section maximum curvature ductility in longitudinal direction

Stage-0: Component Subgroup - Directional

Region: Interior Supports, Zone 1

Component: Column Bent (All Failure Modes)

Subgroup: Regular Sections

Direction: Transverse Rotated (TR), Skew = 0 deg.

Metric: Top Fixed Hinge – Bent-Max Column

EDP: Curvature Ductility

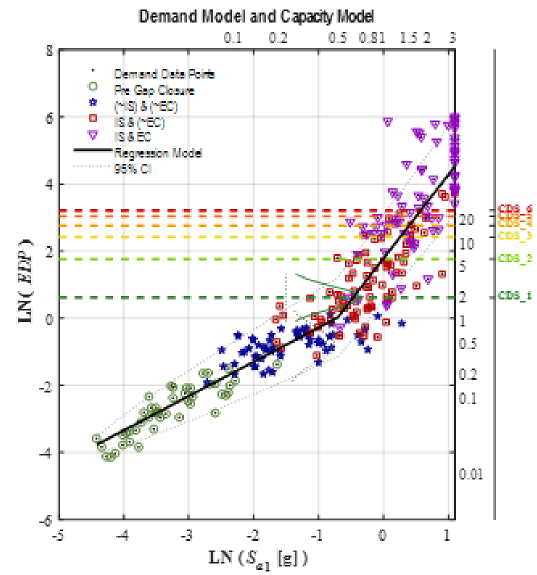

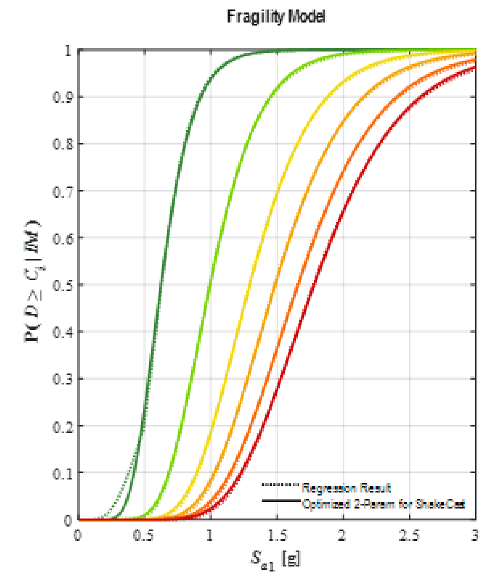

Capacity Model State Descriptions - Component Subgroup

	CDS_1	T_12	CDS_2	T_23	CDS_3	T_34	CDS_4	T_45	CDS_5	T_56	CDS_6	T_67	CDS_7
Fixed-Hinge Performance:	Initial Inelastic Fusing of Hinge Section		Early Stable Hinge Fusing Near Full Moment Capacity		Early Stable Hinge Fusing Near Full Moment Capacity		Initial Loss of Moment Capacity		Substantial Loss of Moment Capacity		Hinge Failure (w/ Column Instability)		
Hinge-Section Damage State:	Cracks Penetrating Full Face of Cover Concrete with Initial Inelastic Bar Elongation		Degradation of Cover Concrete & Crack Penetration Into Core Concrete		Crushing of Cover Concrete, Significant Bar Elongation, & Core Near Peak Capacity		Initial Degradation of Core Concrete Near Rebar Cage Without Visible Bar Buckling		Edge Rebar Necking & Visible Buckling w/ Clear Degradation of Core Concrete		Rebar Buckling and Fracture w/ Clear Degradation of Inner Core Concrete		

Bent-Maximum Norm Moment v. Curvature Ductility Response Range:

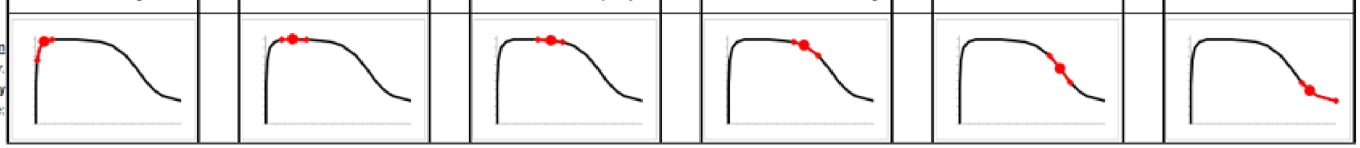

Figure F.11: Stage-0: Regular section column top fixed-section maximum curvature ductility in transverse direction

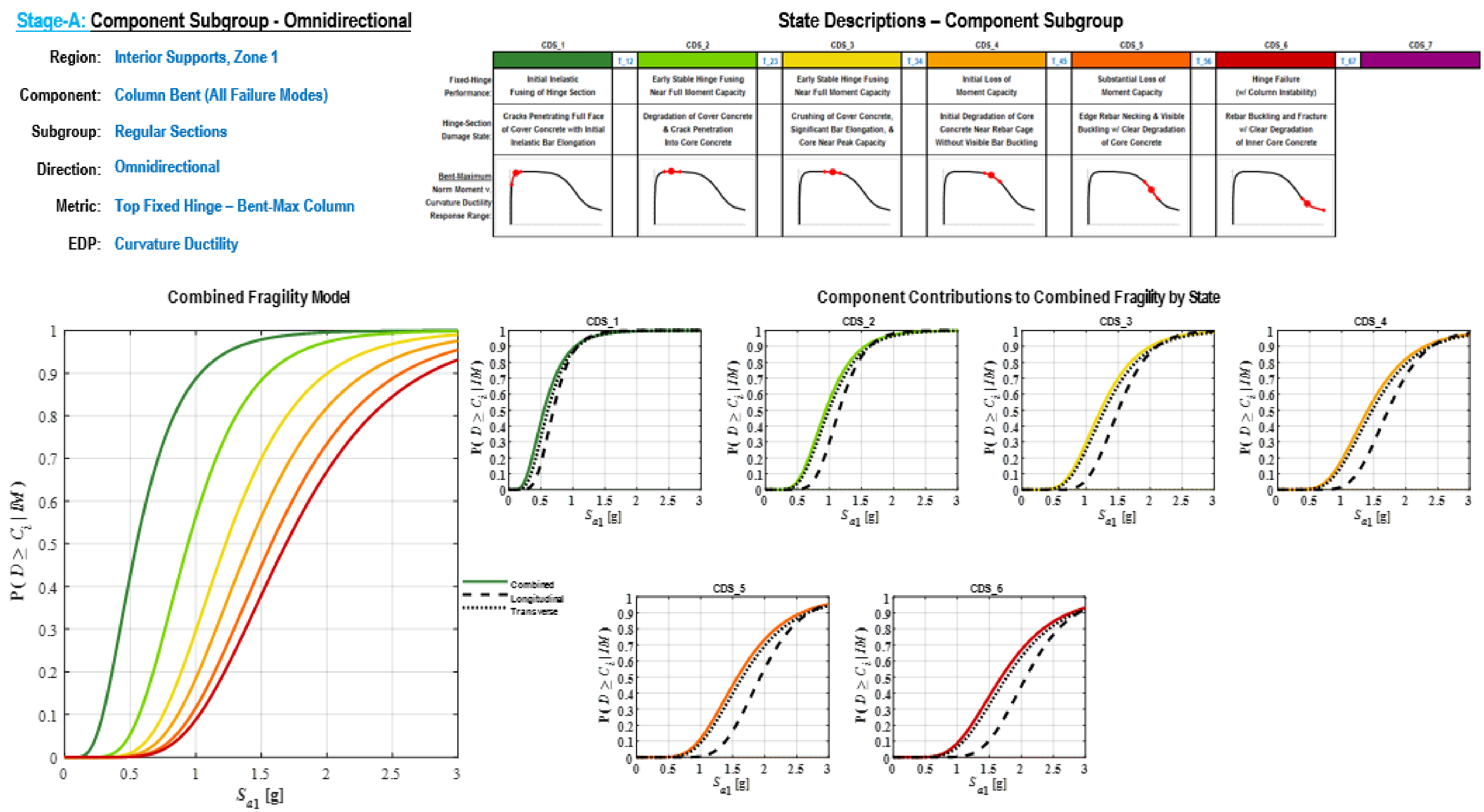

Figure F.12: Stage-A: Regular section column top fixed-section maximum curvature ductility.

Stage-0: Component Subgroup - Directional

Region: Interior Supports, Zone 1

Component: Column Bent (All Failure Modes)

Subgroup: Wide Sections

Direction: Longitudinal Rotated (LR), Skew = 0 deg.

Metric: Top Fixed Hinge – Bent-Max Column

EDP: Curvature Ductility

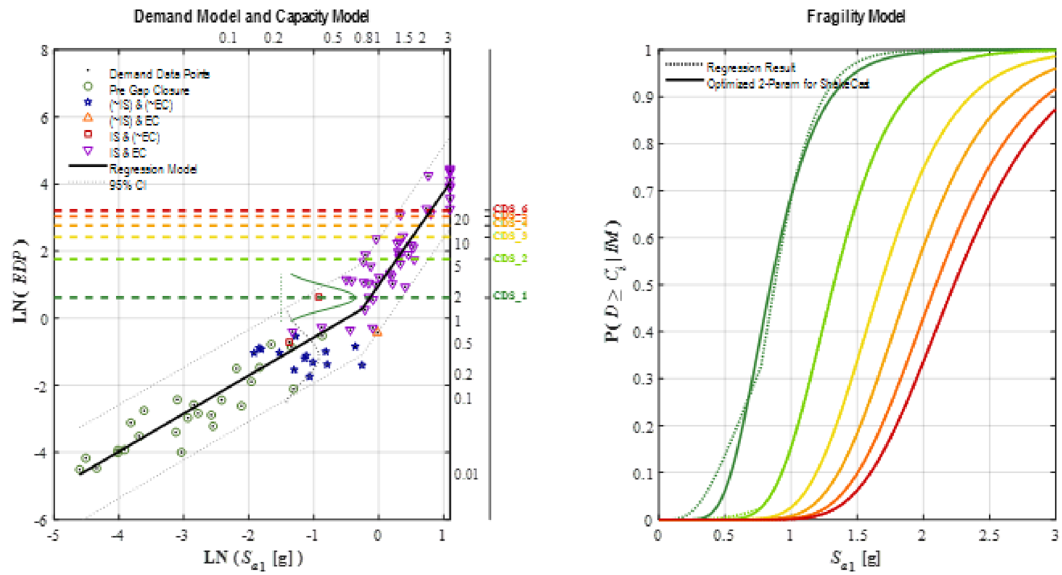

Capacity Model State Descriptions - Component Subgroup

	CDS_1	T_12	CDS_2	T_23	CDS_3	T_34	CDS_4	T_45	CDS_5	T_56	CDS_6	T_67	CDS_7
Fixed-Hinge Performance:	Initial Inelastic Fusing of Hinge Section		Early Stable Hinge Fusing Near Full Moment Capacity		Early Stable Hinge Fusing Near Full Moment Capacity		Initial Loss of Moment Capacity		Substantial Loss of Moment Capacity		Hinge Failure (w/ Column Instability)		
Hinge-Section Damage State:	Cracks Penetrating Full Face of Cover Concrete with Initial Inelastic Bar Elongation		Degradation of Cover Concrete & Crack Penetration Into Core Concrete		Crushing of Cover Concrete, Significant Bar Elongation, & Core Near Peak Capacity		Initial Degradation of Core Concrete Near Rebar Cage Without Visible Bar Buckling		Edge Rebar Necking & Visible Buckling w/ Clear Degradation of Core Concrete		Rebar Buckling and Fracture w/ Clear Degradation of Inner Core Concrete		
Bent-Maximum Norm Moment v. Curvature Ductility Response Range:													

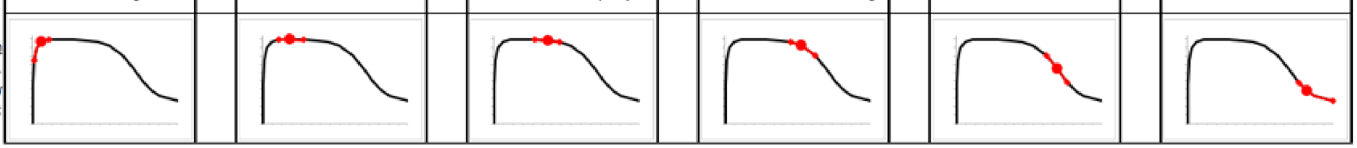

Figure F.13: Stage-0: Wide section column top fixed-section maximum curvature ductility in longitudinal direction

Stage-0: Component Subgroup - Directional

Region: Interior Supports, Zone 1

Component: Column Bent (All Failure Modes)

Subgroup: Wide Sections

Direction: Transverse Rotated (TR), Skew = 0 deg.

Metric: Top Fixed Hinge – Bent-Max Column

EDP: Curvature Ductility

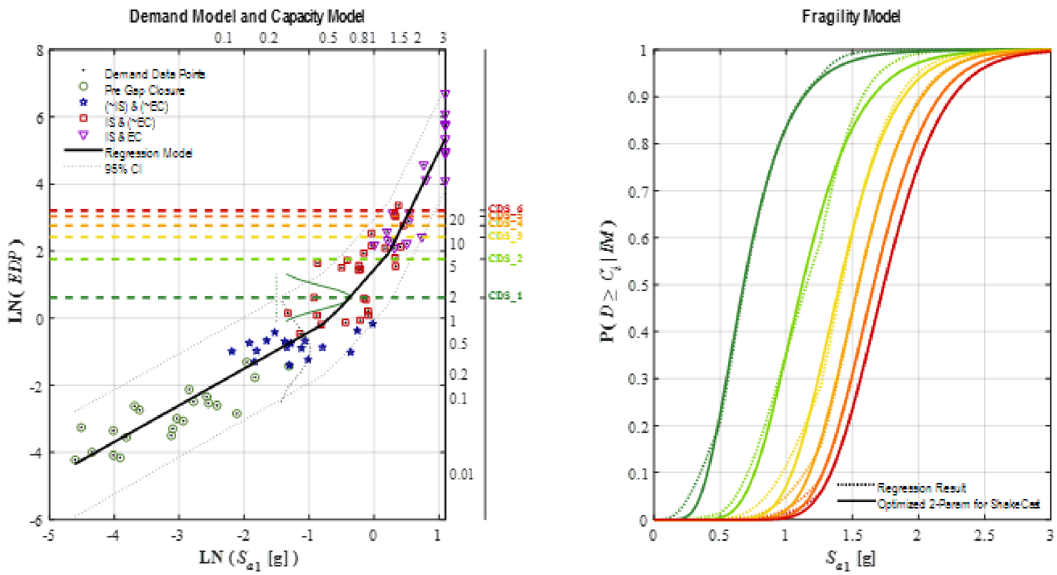

Capacity Model State Descriptions - Component Subgroup

	CDS_1	T_12	CDS_2	T_23	CDS_3	T_34	CDS_4	T_45	CDS_5	T_56	CDS_6	T_67	CDS_7
Fixed-Hinge Performance:	Initial Inelastic Fusing of Hinge Section		Early Stable Hinge Fusing Near Full Moment Capacity		Early Stable Hinge Fusing Near Full Moment Capacity		Initial Loss of Moment Capacity		Substantial Loss of Moment Capacity		Hinge Failure (w/ Column Instability)		
Hinge-Section Damage State:	Cracks Penetrating Full Face of Cover Concrete with Initial Inelastic Bar Elongation		Degradation of Cover Concrete & Crack Penetration Into Core Concrete		Crushing of Cover Concrete, Significant Bar Elongation, & Core Near Peak Capacity		Initial Degradation of Core Concrete Near Rebar Cage Without Visible Bar Buckling		Edge Rebar Necking & Visible Buckling w/ Clear Degradation of Core Concrete		Rebar Buckling and Fracture w/ Clear Degradation of Inner Core Concrete		
Bent-Maximum Norm Moment v. Curvature Ductility Response Range:													

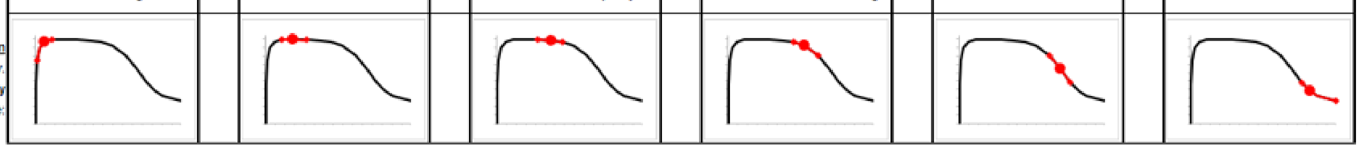

Figure F.14: Stage-0: Wide section column top fixed-section maximum curvature ductility in transverse direction

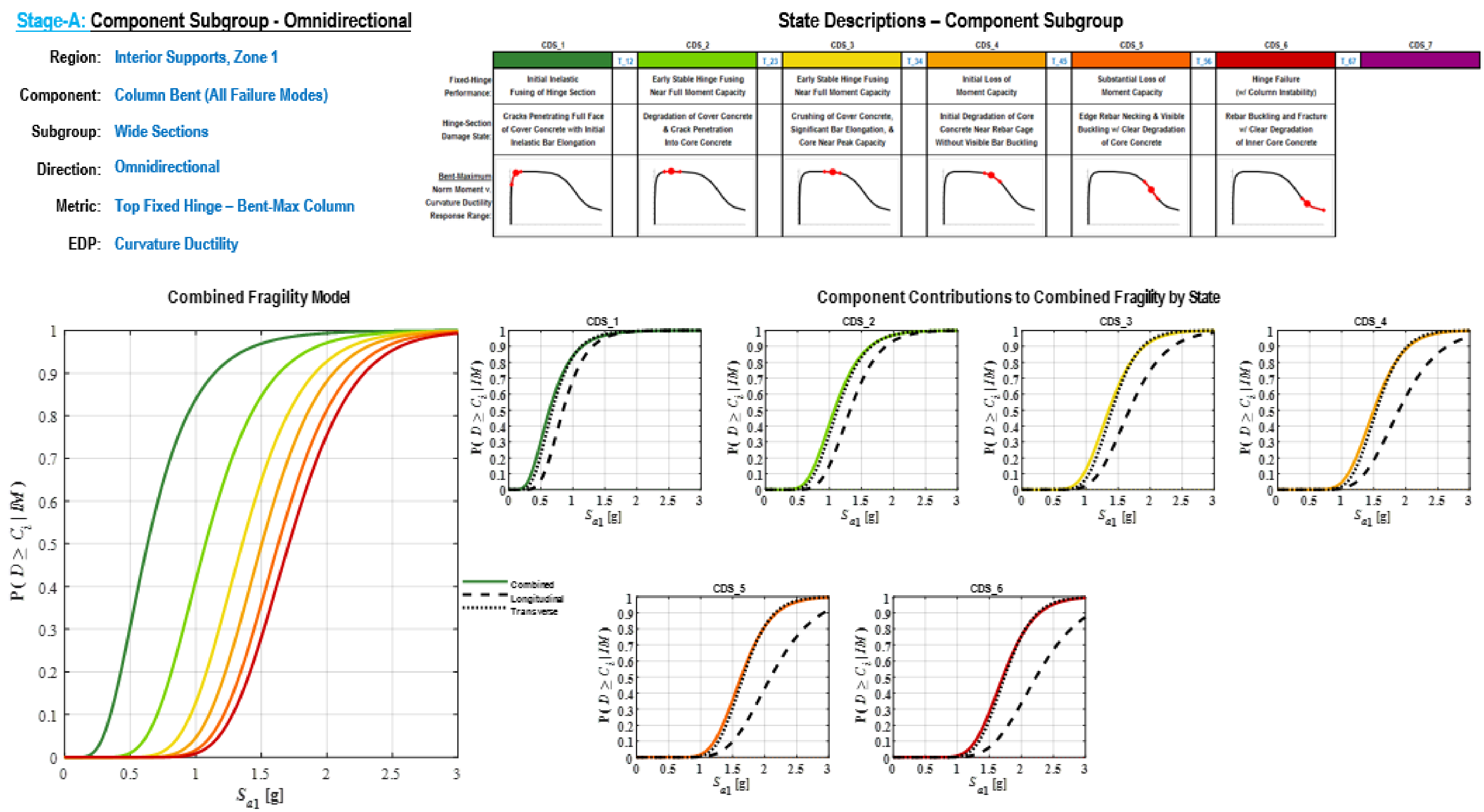

Figure F.15: Stage-A: Wide section column top fixed-section maximum curvature ductility.

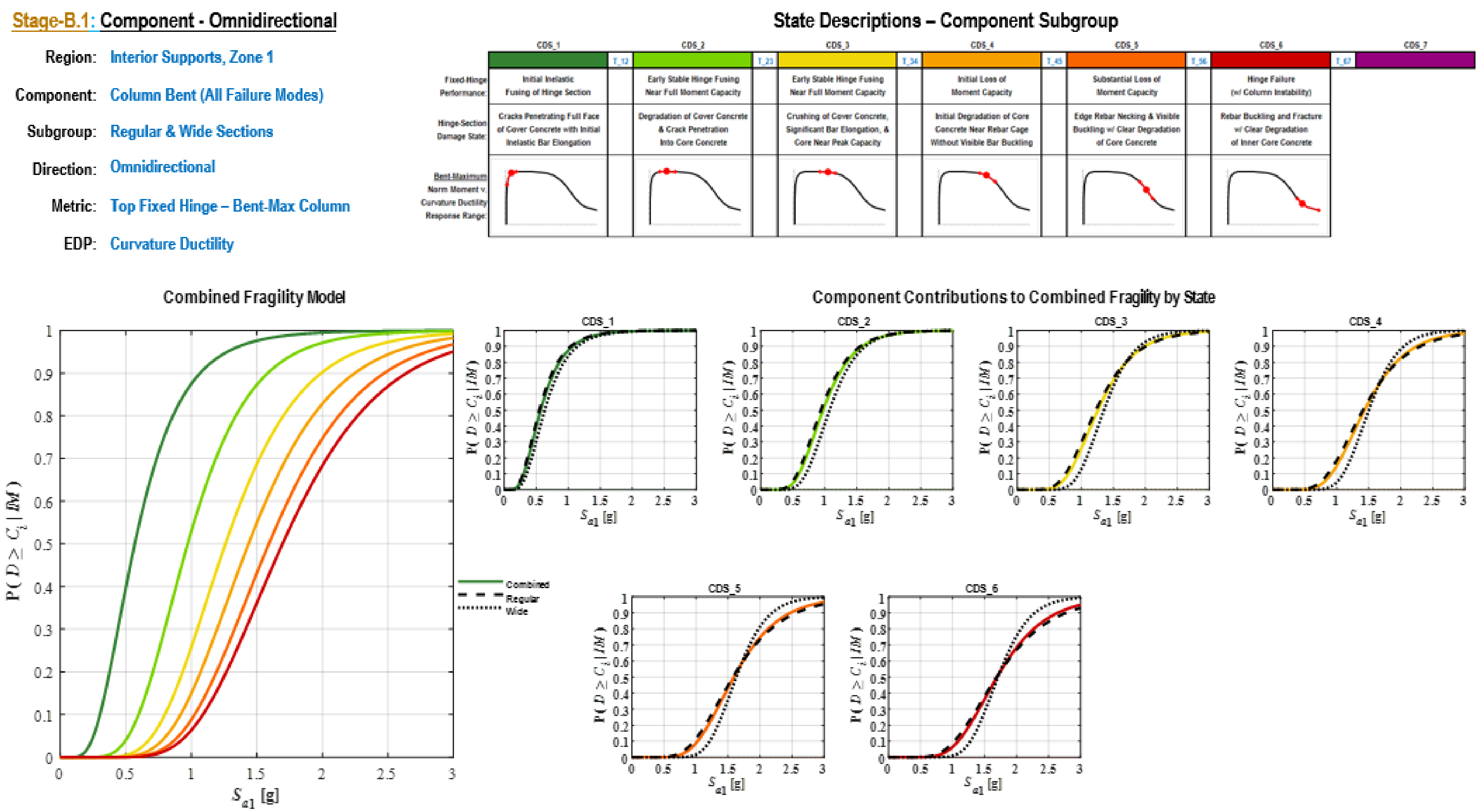

Figure F.16: Stage-B.1: Column top fixed-section maximum curvature ductility.

Stage-0: **Component Subgroup - Directional**

Region:	Interior Supports, Zone 1
Component:	Column Bent (All Failure Modes)
Subgroup:	Regular Sections
Direction:	Longitudinal Rotated (LR), Skew = 0 deg.
Metric:	Top Fixed Hinge – Bent-Ave Column
EDP:	Curvature Ductility

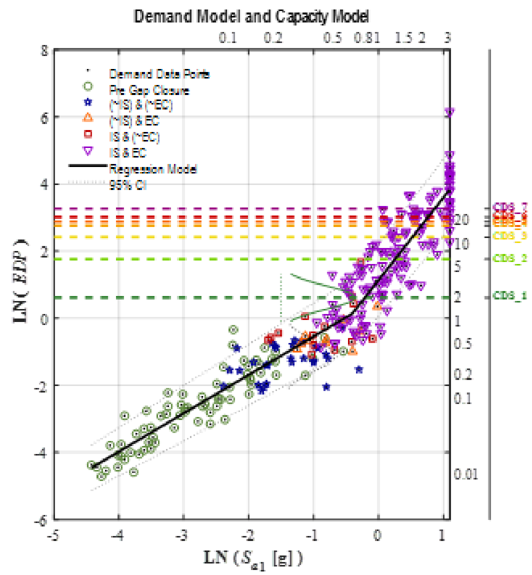

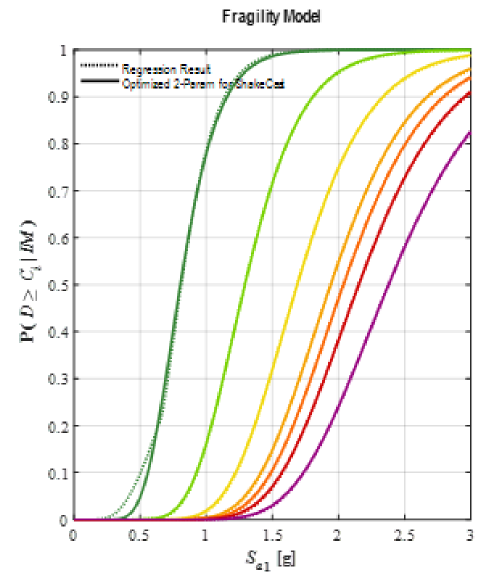

Capacity Model State Descriptions - Component Subgroup

	CDS_1	T_12	CDS_2	T_23	CDS_3	T_34	CDS_4	T_45	CDS_5	T_56	CDS_6	T_67	CDS_7
Fixed-Hinge Performance:	Initial Inelastic Fusing of Hinge Section		Early Stable Hinge Fusing Near Full Moment Capacity		Early Stable Hinge Fusing Near Full Moment Capacity		Initial Loss of Moment Capacity		Partial Hinge Failure (Stable Bent)		Extensive Hinge Failure (Unstable Bent)		Complete Hinge Failure (Bent Collapse Risk)
Hinge-Section Damage State:	Cracks Penetrating Full Face of Cover Concrete with Initial Inelastic Bar Elongation		Degradation of Cover Concrete & Crack Penetration Into Core Concrete		Crushing of Cover Concrete, Significant Bar Elongation, & Core Near Peak Capacity		Initial Degradation of Core Concrete Near Rebar Cage Without Visible Bar Buckling		Edge Rebar Necking & Visible Buckling w/ Clear Degradation of Outer Core Concrete		Widening Rebar Buckling or Fracture w/ Clear Degradation of Inner Core Concrete		Extensive Rebar Fracture & Crushing of Inner Core Concrete
Bent-Average Norm Moment v. Curvature Ductility Response Range:	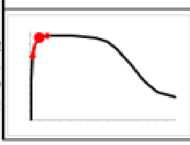		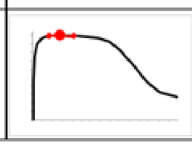		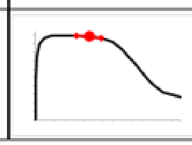		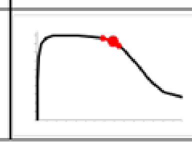		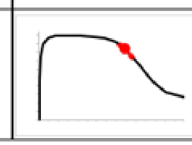		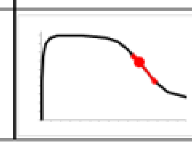		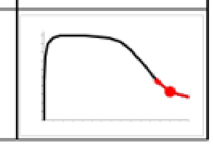

Figure F.17: Stage-0: Regular section column top fixed-section average curvature ductility in longitudinal direction

Stage-0: Component Subgroup - Directional

Region:	Interior Supports, Zone 1
Component:	Column Bent (All Failure Modes)
Subgroup:	Regular Sections
Direction:	Transverse Rotated (TR), Skew = 0 deg.
Metric:	Top Fixed Hinge – Bent-Ave Column
EDP:	Curvature Ductility

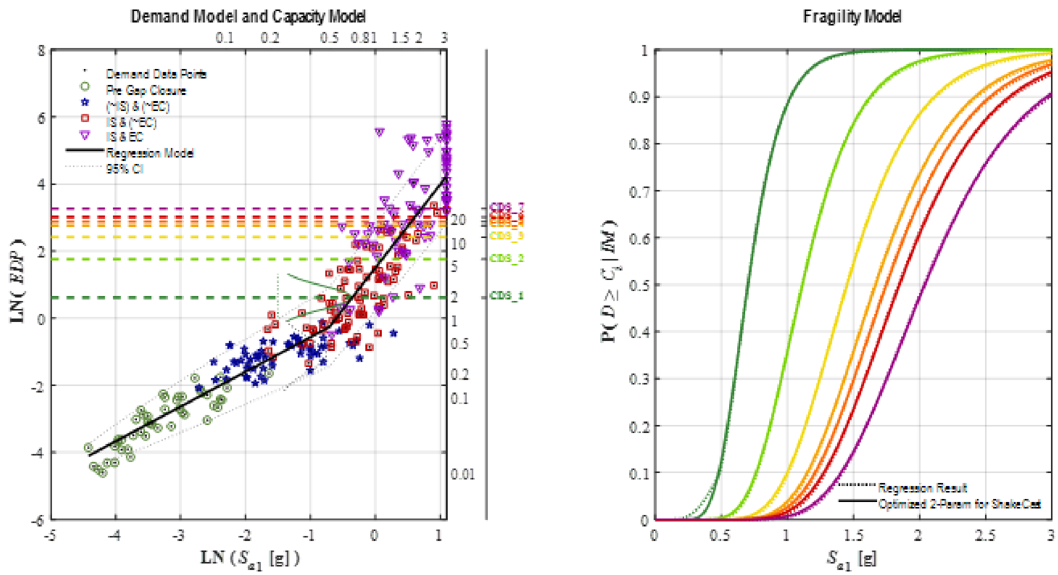

Capacity Model State Descriptions - Component Subgroup

	CDS_1	T_12	CDS_2	T_23	CDS_3	T_34	CDS_4	T_45	CDS_5	T_56	CDS_6	T_67	CDS_7
Fixed-Hinge Performance:	Initial Inelastic Fusing of Hinge Section		Early Stable Hinge Fusing Near Full Moment Capacity		Early Stable Hinge Fusing Near Full Moment Capacity		Initial Loss of Moment Capacity		Partial Hinge Failure (Stable Bent)		Extensive Hinge Failure (Unstable Bent)		Complete Hinge Failure (Bent Collapse Risk)
Hinge-Section Damage State:	Cracks Penetrating Full Face of Cover Concrete with Initial Inelastic Bar Elongation		Degradation of Cover Concrete & Crack Penetration Into Core Concrete		Crushing of Cover Concrete, Significant Bar Elongation, & Core Near Peak Capacity		Initial Degradation of Core Concrete Near Rebar Cage Without Visible Bar Buckling		Edge Rebar Necking & Visible Buckling w/ Clear Degradation of Outer Core Concrete		Widening Rebar Buckling or Fracture w/ Clear Degradation of Inner Core Concrete		Extensive Rebar Fracture & Crushing of Inner Core Concrete
Bent-Average Norm Moment v. Curvature Ductility Response Range:													

Figure F.18: Stage-0: Regular section column top fixed-section average curvature ductility in transverse direction

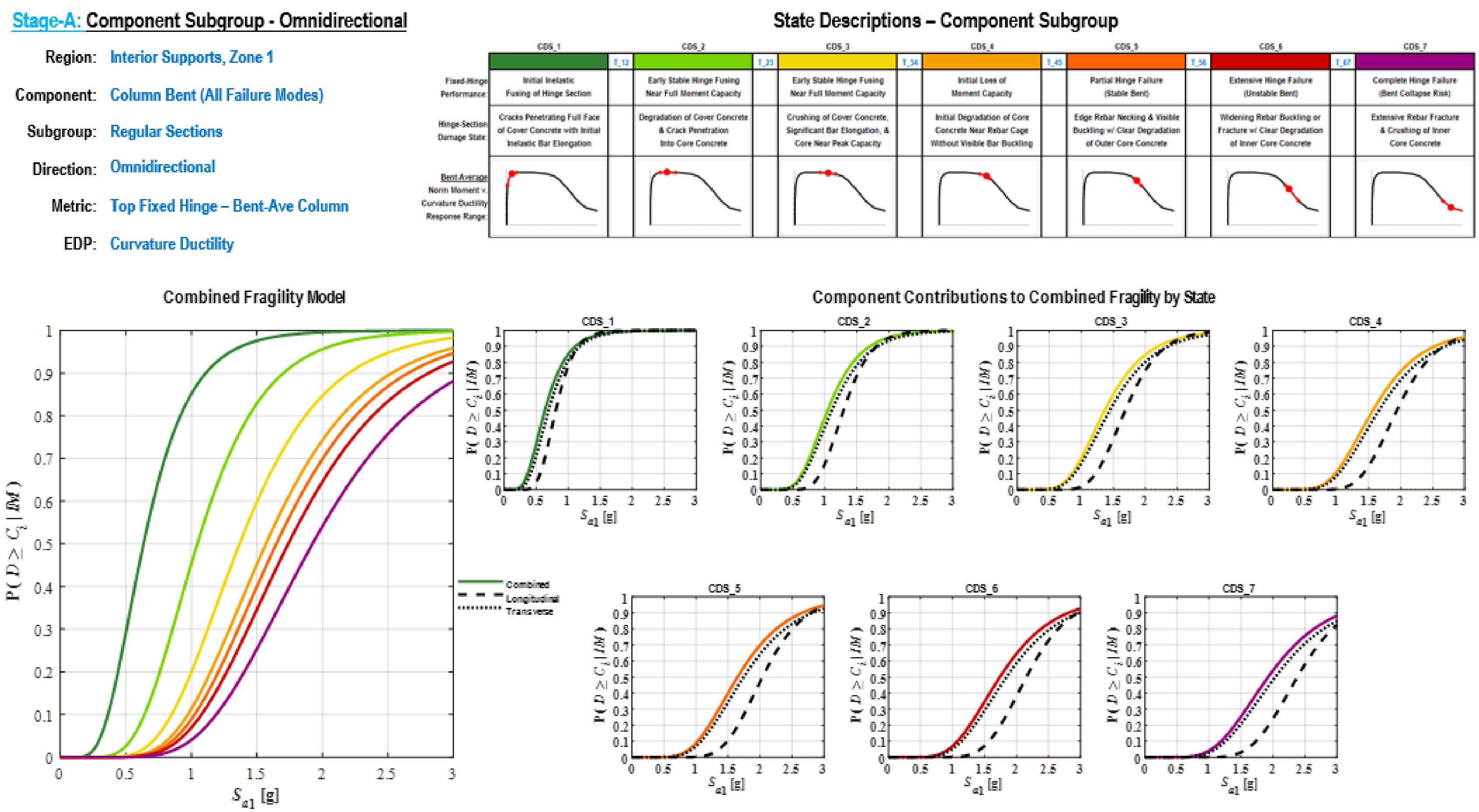

Figure F.19: Stage-A: Regular section column top fixed-section average curvature ductility.

Stage-0: Component Subgroup - Directional

Region: Interior Supports, Zone 1

Component: Column Bent (All Failure Modes)

Subgroup: Wide Sections

Direction: Longitudinal Rotated (LR), Skew = 0 deg.

Metric: Top Fixed Hinge – Bent-Ave Column

EDP: Curvature Ductility

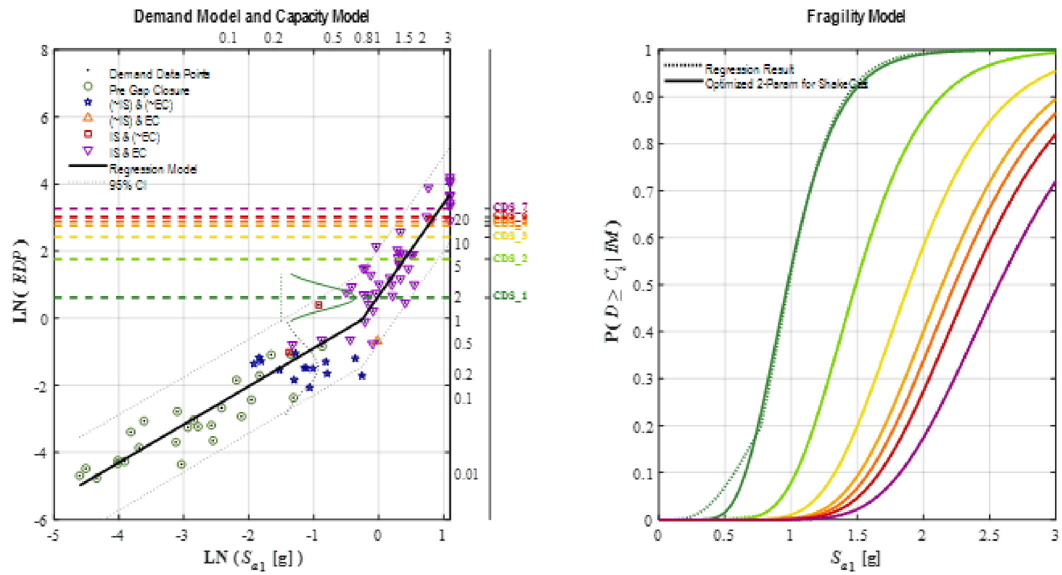

Capacity Model State Descriptions - Component Subgroup

	CDS_1	T_12	CDS_2	T_23	CDS_3	T_34	CDS_4	T_45	CDS_5	T_56	CDS_6	T_67	CDS_7
Fixed-Hinge Performance:	Initial Inelastic Fusing of Hinge Section		Early Stable Hinge Fusing Near Full Moment Capacity		Early Stable Hinge Fusing Near Full Moment Capacity		Initial Loss of Moment Capacity		Partial Hinge Failure (Stable Bent)		Extensive Hinge Failure (Unstable Bent)		Complete Hinge Failure (Bent Collapse Risk)
Hinge-Section Damage State:	Cracks Penetrating Full Face of Cover Concrete with Initial Inelastic Bar Elongation		Degradation of Cover Concrete & Crack Penetration Into Core Concrete		Crushing of Cover Concrete, Significant Bar Elongation, & Core Near Peak Capacity		Initial Degradation of Core Concrete Near Rebar Cage Without Visible Bar Buckling		Edge Rebar Necking & Visible Buckling w/ Clear Degradation of Outer Core Concrete		Widening Rebar Buckling or Fracture w/ Clear Degradation of Inner Core Concrete		Extensive Rebar Fracture & Crushing of Inner Core Concrete
Bent-Average Norm Moment v. Curvature Ductility Response Range:	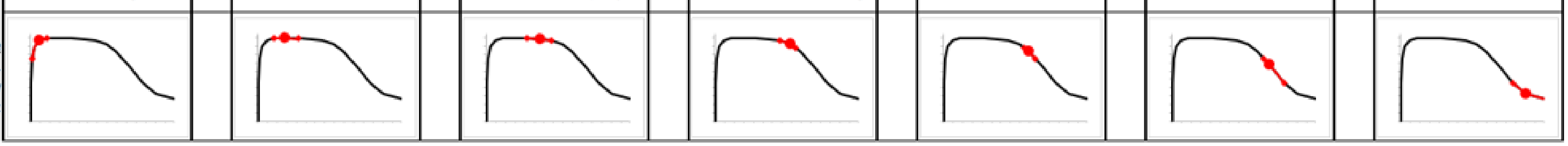												

Figure F.20: Stage-0: Wide section column top fixed-section average curvature ductility in longitudinal direction

Stage-0: **Component Subgroup - Directional**

Region: Interior Supports, Zone 1

Component: Column Bent (All Failure Modes)

Subgroup: Wide Sections

Direction: Transverse Rotated (TR), Skew = 0 deg.

Metric: Top Fixed Hinge – Bent-Ave Column

EDP: Curvature Ductility

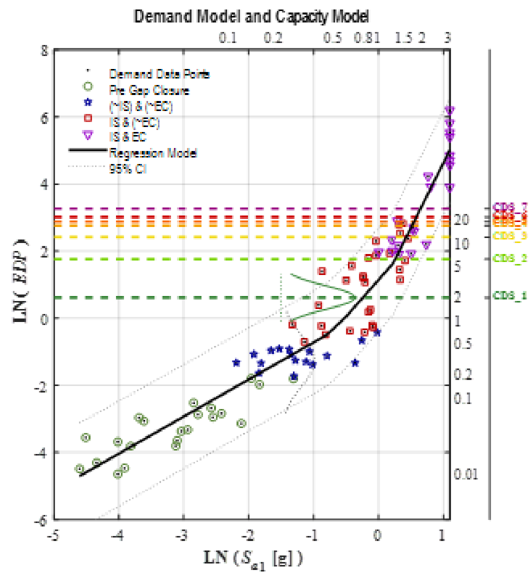

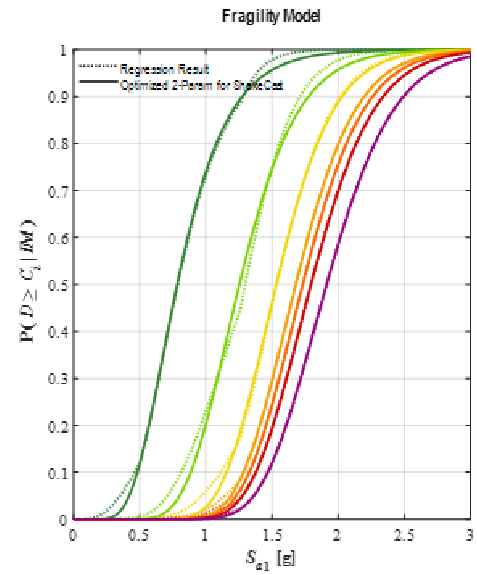

Capacity Model State Descriptions - Component Subgroup

	CDS_1	T_12	CDS_2	T_23	CDS_3	T_34	CDS_4	T_45	CDS_5	T_56	CDS_6	T_67	CDS_7
Fixed-Hinge Performance:	Initial Inelastic Fusing of Hinge Section		Early Stable Hinge Fusing Near Full Moment Capacity		Early Stable Hinge Fusing Near Full Moment Capacity		Initial Loss of Moment Capacity		Partial Hinge Failure (Stable Bent)		Extensive Hinge Failure (Unstable Bent)		Complete Hinge Failure (Bent Collapse Risk)
Hinge-Section Damage State:	Cracks Penetrating Full Face of Cover Concrete with Initial Inelastic Bar Elongation		Degradation of Cover Concrete & Crack Penetration Into Core Concrete		Crushing of Cover Concrete, Significant Bar Elongation, & Core Near Peak Capacity		Initial Degradation of Core Concrete Near Rebar Cage Without Visible Bar Buckling		Edge Rebar Necking & Visible Buckling w/ Clear Degradation of Outer Core Concrete		Widening Rebar Buckling or Fracture w/ Clear Degradation of Inner Core Concrete		Extensive Rebar Fracture & Crushing of Inner Core Concrete
Bent-Average Norm Moment v. Curvature Ductility Response Range:													

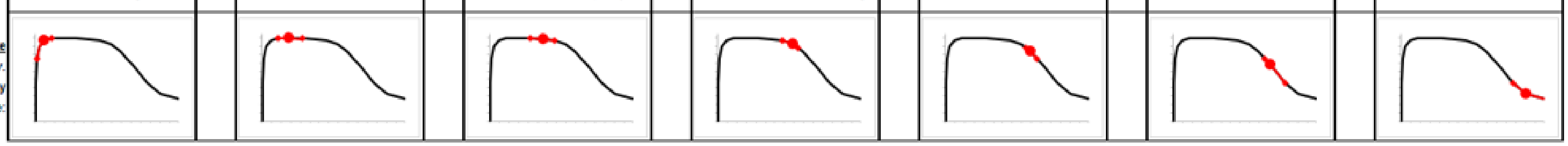

Figure F.21: Stage-0: Wide section column top fixed-section average curvature ductility in transverse direction

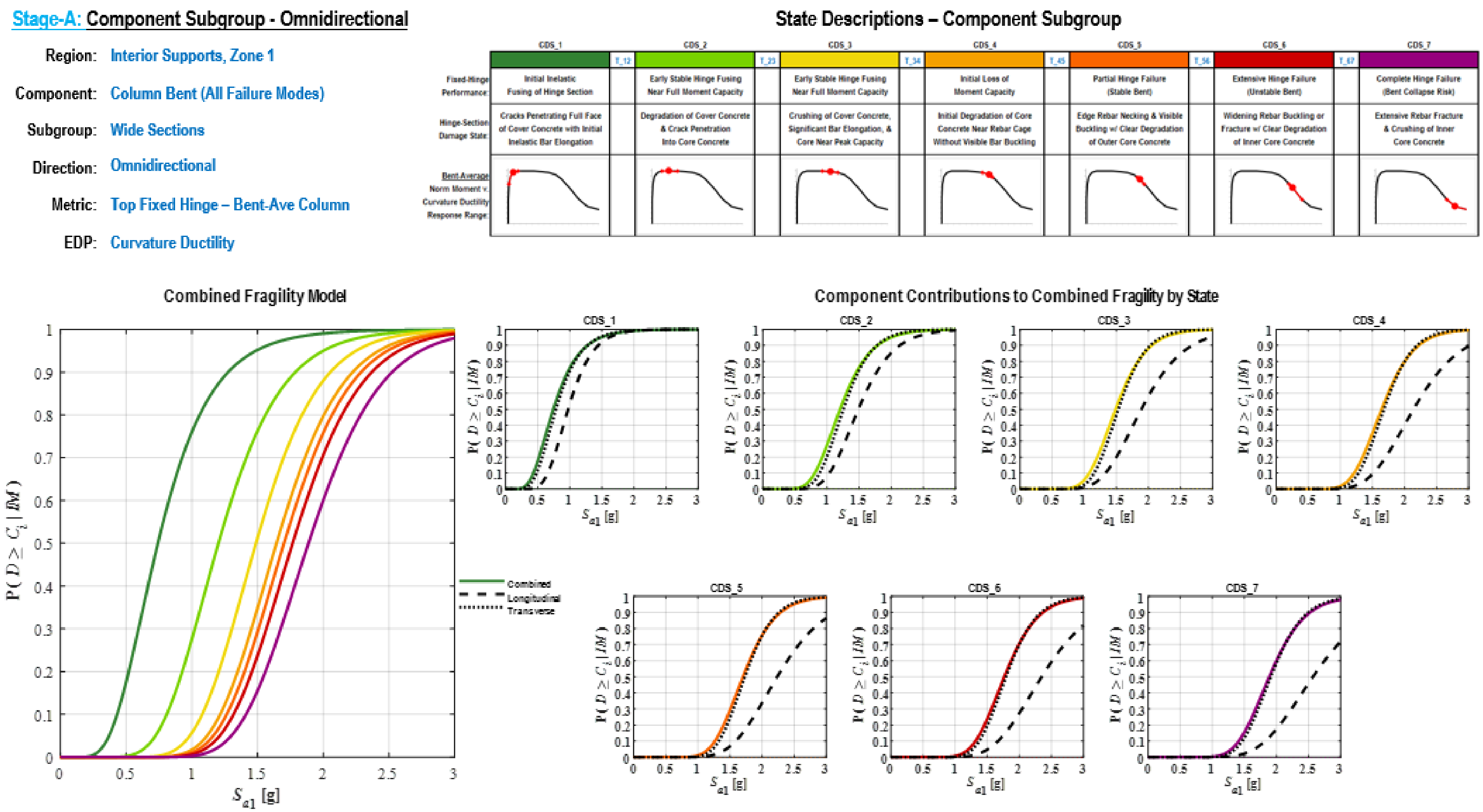

Figure F.22: Stage-A: Wide section column top fixed-section average curvature ductility.

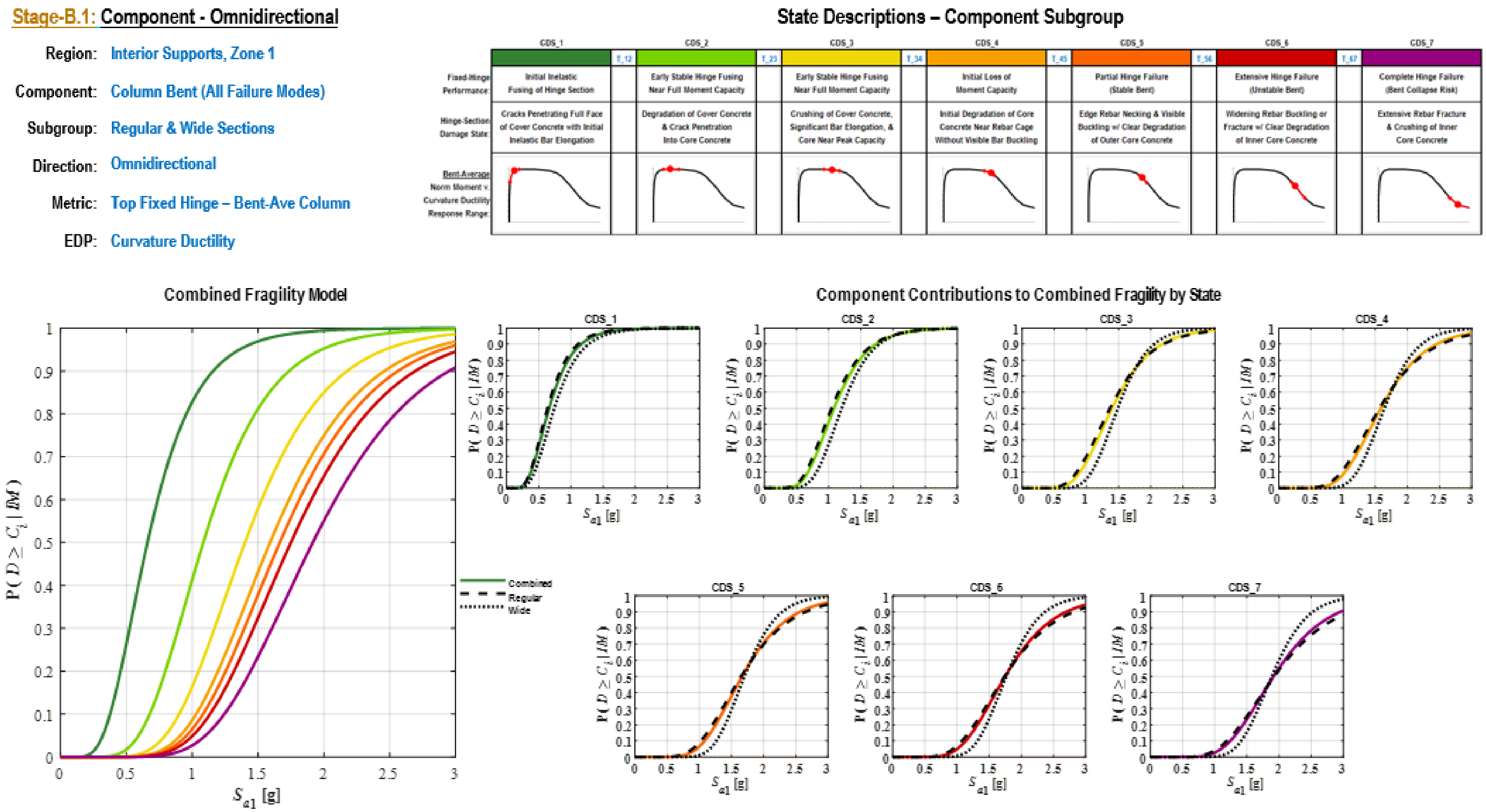

Figure F.23: Stage-B.1: Column top fixed-section average curvature ductility.

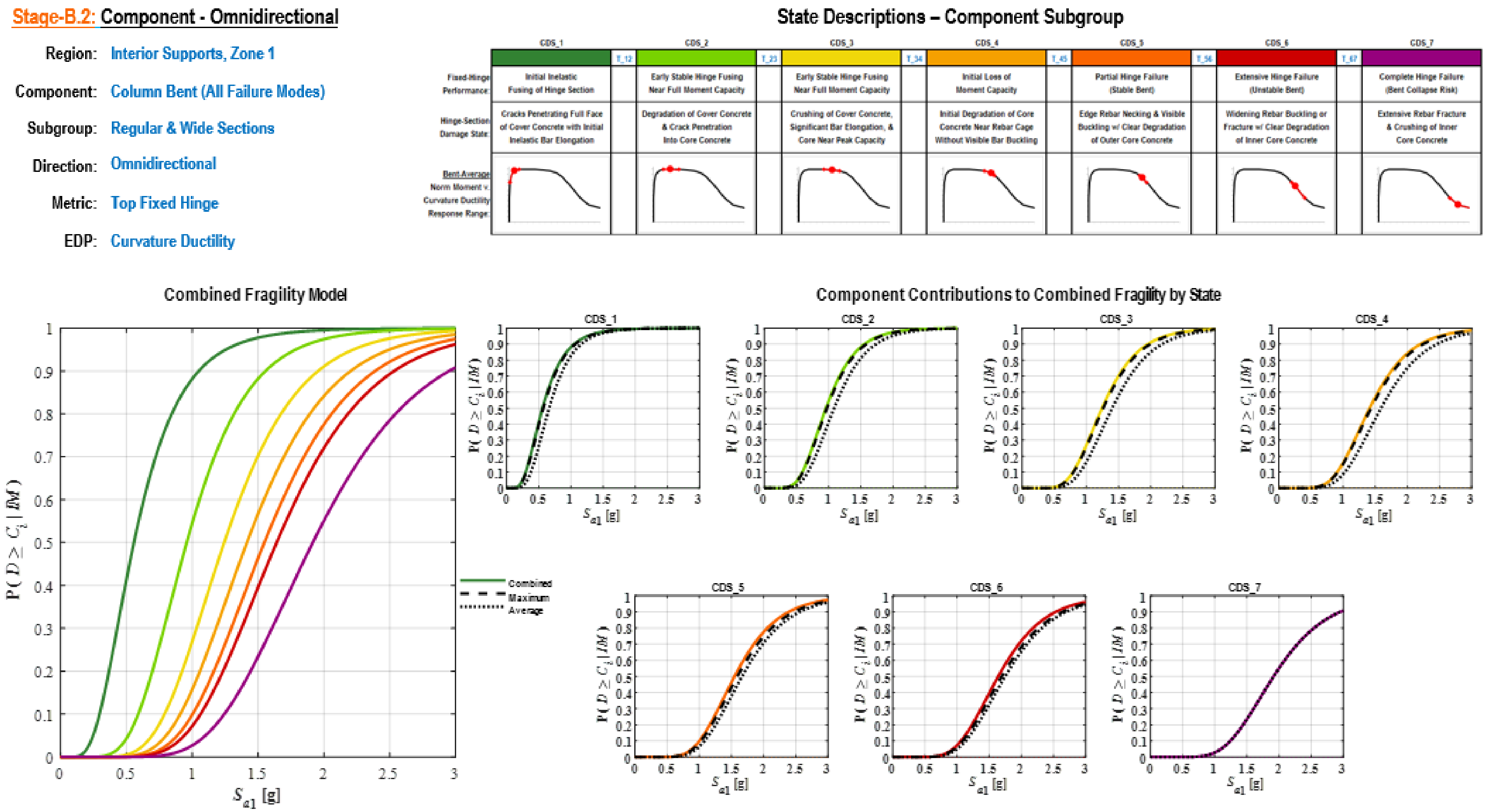

Figure F.24: Stage-B.2: Column top fixed-section curvature ductility.

Stage-0: Component Subgroup - Directional

Region: Interior Supports, Zone 1

Component: Column Bent (All Failure Modes)

Subgroup: Regular Sections

Direction: Longitudinal Rotated (LR), Skew = 0 deg.

Metric: Pin – Bent-Ave Column

EDP: Curvature Ductility

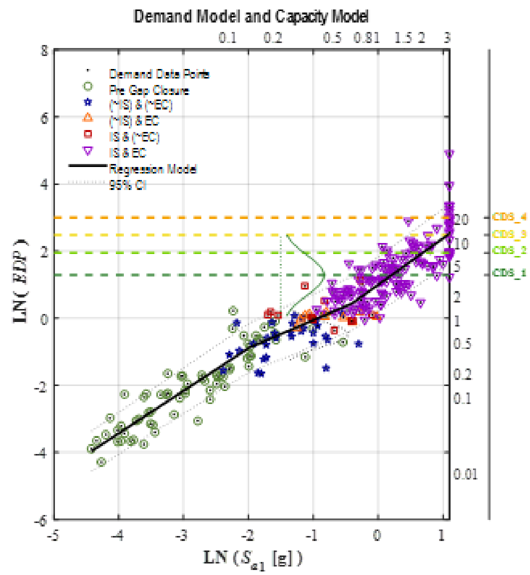

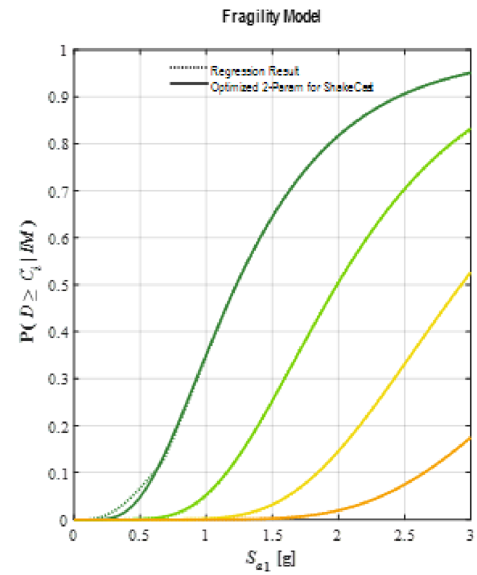

Capacity Model State Descriptions - Component Subgroup

	CDS_1	T_12	CDS_2	T_23	CDS_3	T_34	CDS_4	T_45	CDS_5	T_56	CDS_6	T_67	CDS_7
Pinned-Hinge Performance:	Initial Inelastic Fusing of Pin Section		Stable Pin Fusing (~75% of Undamaged Capacity)		Extreme Pin Fusing (Rapid Degradation)		Complete Pin Failure (w/ Column-Base Impacts)						
Hidden Internal Damage:	Crushing of Cover Concrete (Outside Confinement) with No/Minor Rebar Yield		Initial Core-Concrete Crushing (Inside Confinement) with Moderate Rebar Yield		Major Core-Concrete Crushing (Inside Confinement) with Major Rebar Yield or Buckling		Complete Core Crushing and/or Multi-Bar Buckling/ Rupture or Severed Pin.						
Norm Moment v. Curvature Ductility Response Range:			~75%				Residual Capacity or Rupture						

Figure F.25: Stage-0: Regular section column base pinned-section curvature ductility in longitudinal direction

Stage-0: Component Subgroup - Directional

Region: Interior Supports, Zone 1

Component: Column Bent (All Failure Modes)

Subgroup: Regular Sections

Direction: Transverse Rotated (TR), Skew = 0 deg.

Metric: Pin – Bent-Ave Column

EDP: Curvature Ductility

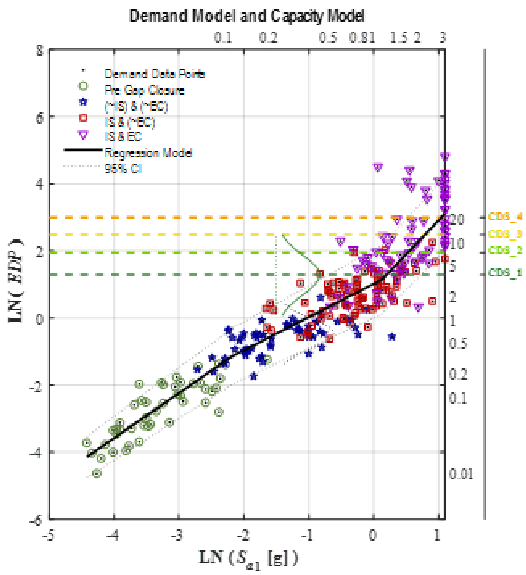

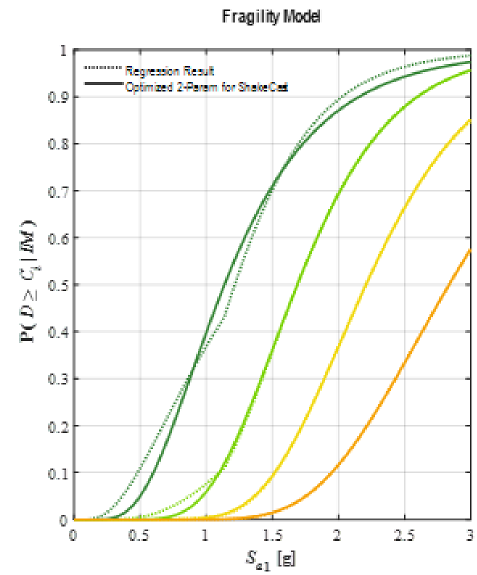

Capacity Model State Descriptions - Component Subgroup

	CDS_1	T_12	CDS_2	T_23	CDS_3	T_34	CDS_4	T_45	CDS_5	T_56	CDS_6	T_67	CDS_7
Pinned-Hinge Performance:	Initial Inelastic Fusing of Pin Section		Stable Pin Fusing (~75% of Undamaged Capacity)		Extreme Pin Fusing (Rapid Degradation)		Complete Pin Failure (w/ Column-Base Impacts)						
Hidden Internal Damage:	Crushing of Cover Concrete (Outside Confinement) with No/Minor Rebar Yield		Initial Core-Concrete Crushing (Inside Confinement) with Moderate Rebar Yield		Major Core-Concrete Crushing (Inside Confinement) with Major Rebar Yield or Buckling		Complete Core Crushing and/or Multi-Bar Buckling/ Rupture or Severed Pin.						
Norm Moment v. Curvature Ductility Response Range:	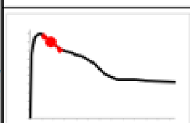		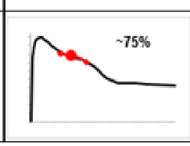 ~75%		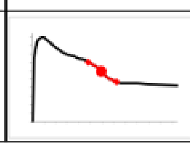		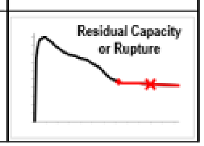 Residual Capacity or Rupture						

Figure F.26: Stage-0: Regular section column base pinned-section curvature ductility in transverse direction

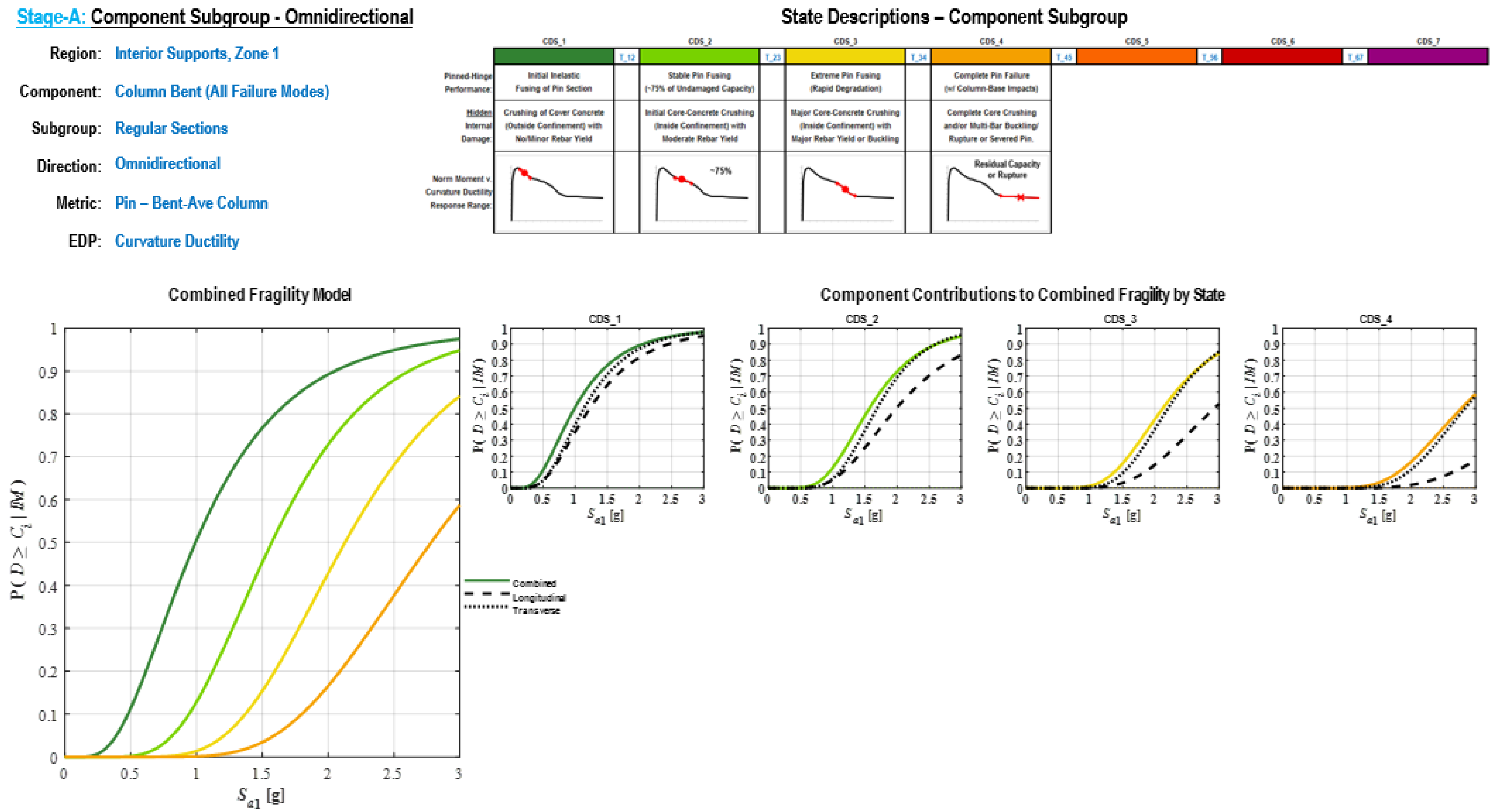

Figure F.27: Stage-A: Regular section column base pinned-section curvature ductility.

Stage-0: Component Subgroup - Directional

Region: Interior Supports, Zone 1

Component: Column Bent (All Failure Modes)

Subgroup: Wide Sections

Direction: Longitudinal Rotated (LR), Skew = 0 deg.

Metric: Pin – Bent-Ave Column

EDP: Curvature Ductility

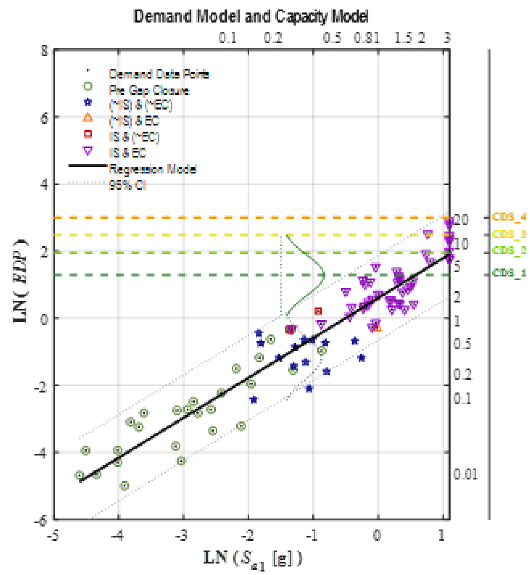

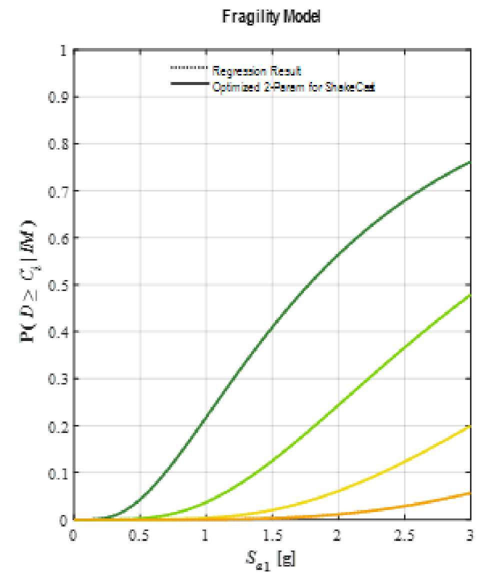

Capacity Model State Descriptions - Component Subgroup

	CDS_1	T_12	CDS_2	T_23	CDS_3	T_34	CDS_4	T_45	CDS_5	T_56	CDS_6	T_67	CDS_7
Pinned-Hinge Performance:	Initial Inelastic Fusing of Pin Section		Stable Pin Fusing (~75% of Undamaged Capacity)		Extreme Pin Fusing (Rapid Degradation)		Complete Pin Failure (w/ Column-Base Impacts)						
Hidden Internal Damage:	Crushing of Cover Concrete (Outside Confinement) with No/Minor Rebar Yield		Initial Core-Concrete Crushing (Inside Confinement) with Moderate Rebar Yield		Major Core-Concrete Crushing (Inside Confinement) with Major Rebar Yield or Buckling		Complete Core Crushing and/or Multi-Bar Buckling/ Rupture or Severed Pin.						
Norm Moment v. Curvature Ductility Response Range:													

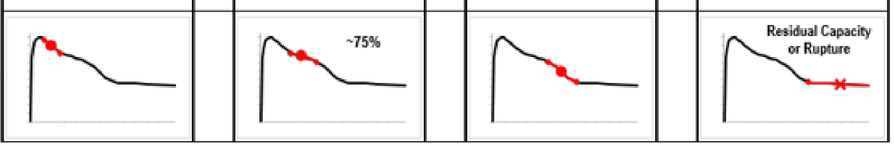

Figure F.28: Stage-0: Wide section column base pinned-section curvature ductility in longitudinal direction

Stage-0: Component Subgroup - Directional

Region: Interior Supports, Zone 1

Component: Column Bent (All Failure Modes)

Subgroup: Wide Sections

Direction: Transverse Rotated (TR), Skew = 0 deg.

Metric: Pin – Bent-Ave Column

EDP: Curvature Ductility

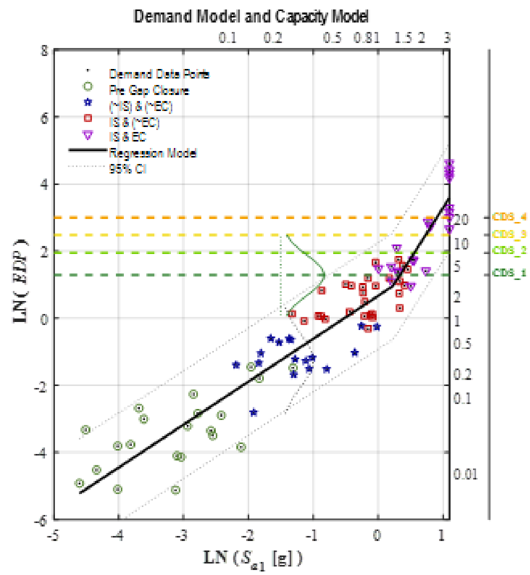

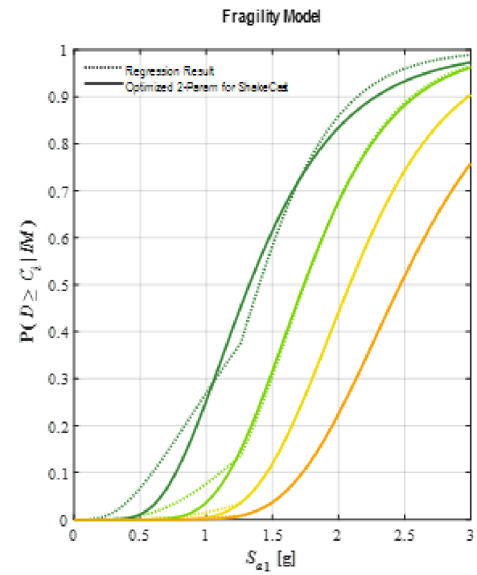

Capacity Model State Descriptions - Component Subgroup

	CDS_1	T_12	CDS_2	T_23	CDS_3	T_34	CDS_4	T_45	CDS_5	T_56	CDS_6	T_67	CDS_7
Pinned-Hinge Performance:	Initial Inelastic Fusing of Pin Section		Stable Pin Fusing (~75% of Undamaged Capacity)		Extreme Pin Fusing (Rapid Degradation)		Complete Pin Failure (w/ Column-Base Impacts)						
Hidden Internal Damage:	Crushing of Cover Concrete (Outside Confinement) with No/Minor Rebar Yield		Initial Core-Concrete Crushing (Inside Confinement) with Moderate Rebar Yield		Major Core-Concrete Crushing (Inside Confinement) with Major Rebar Yield or Buckling		Complete Core Crushing and/or Multi-Bar Buckling/ Rupture or Severed Pin.						
Norm Moment v. Curvature Ductility Response Range:	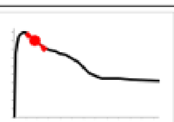		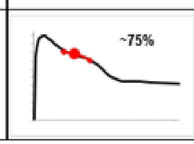		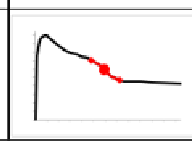		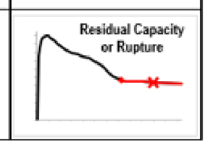						

Figure F.29: Stage-0: Wide section column base pinned-section curvature ductility in transverse direction

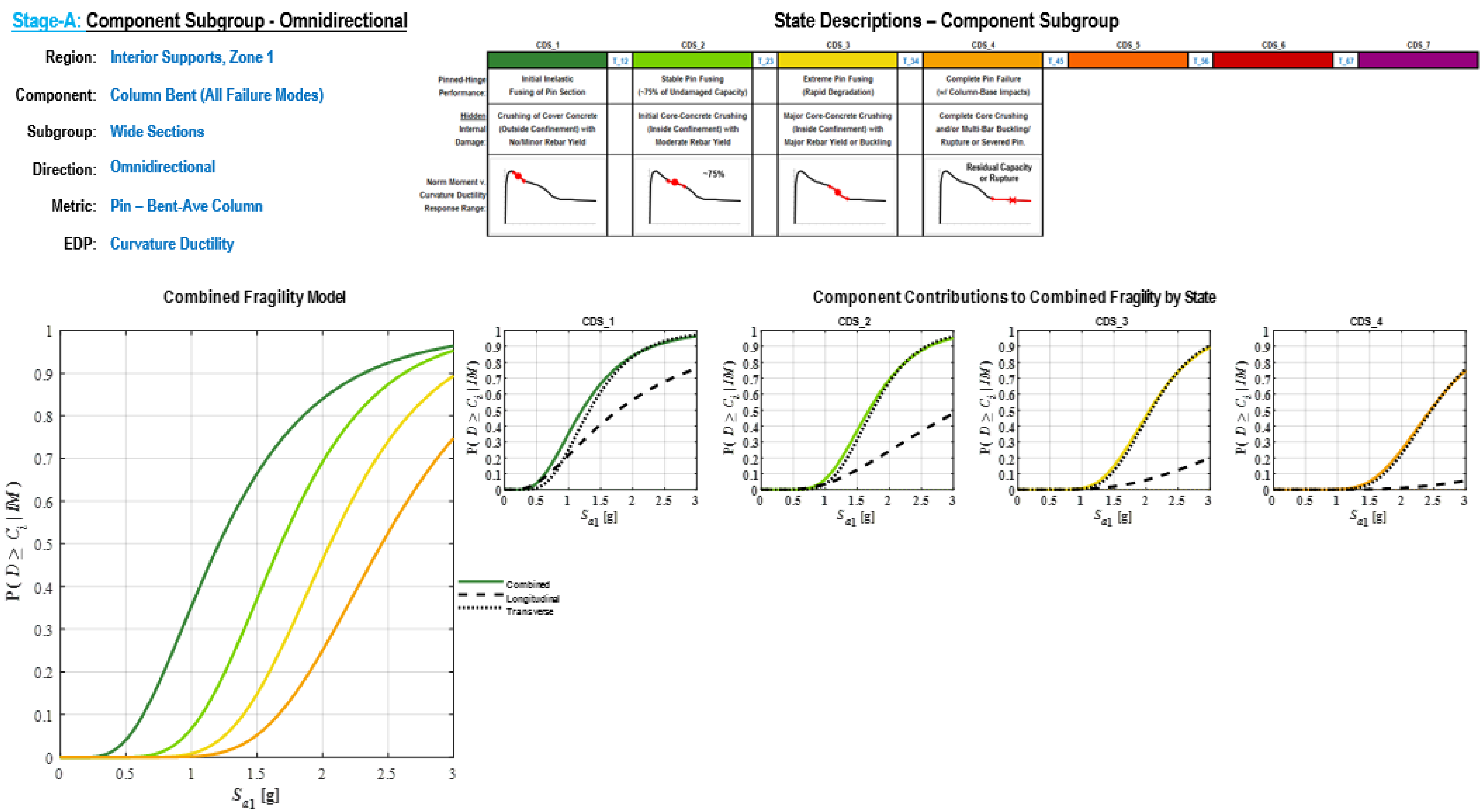

Figure F.30: Stage-A: Wide section column base pinned-section curvature ductility.

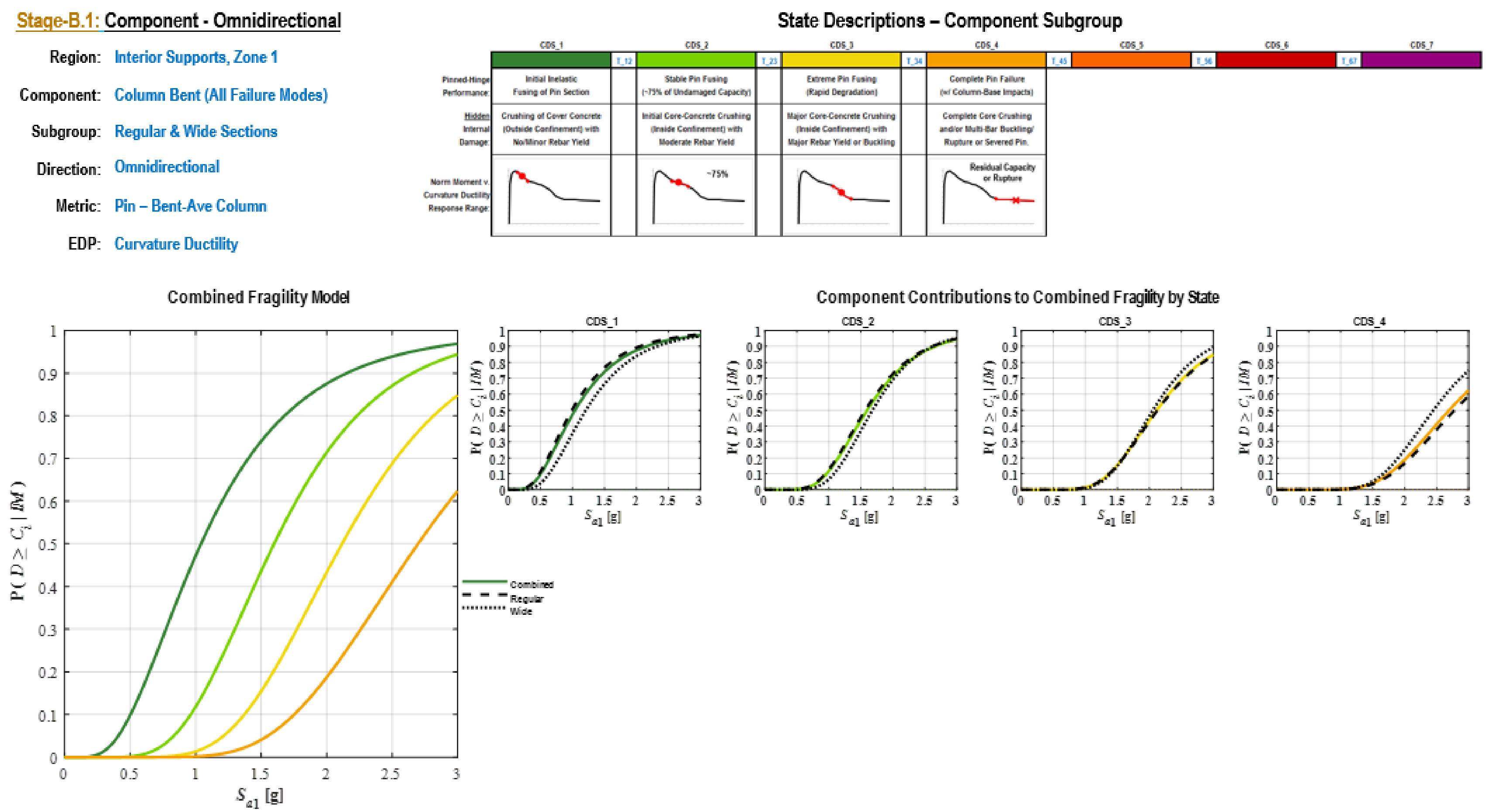

Figure F.31: Stage-B.1: Column base pinned-section curvature ductility.

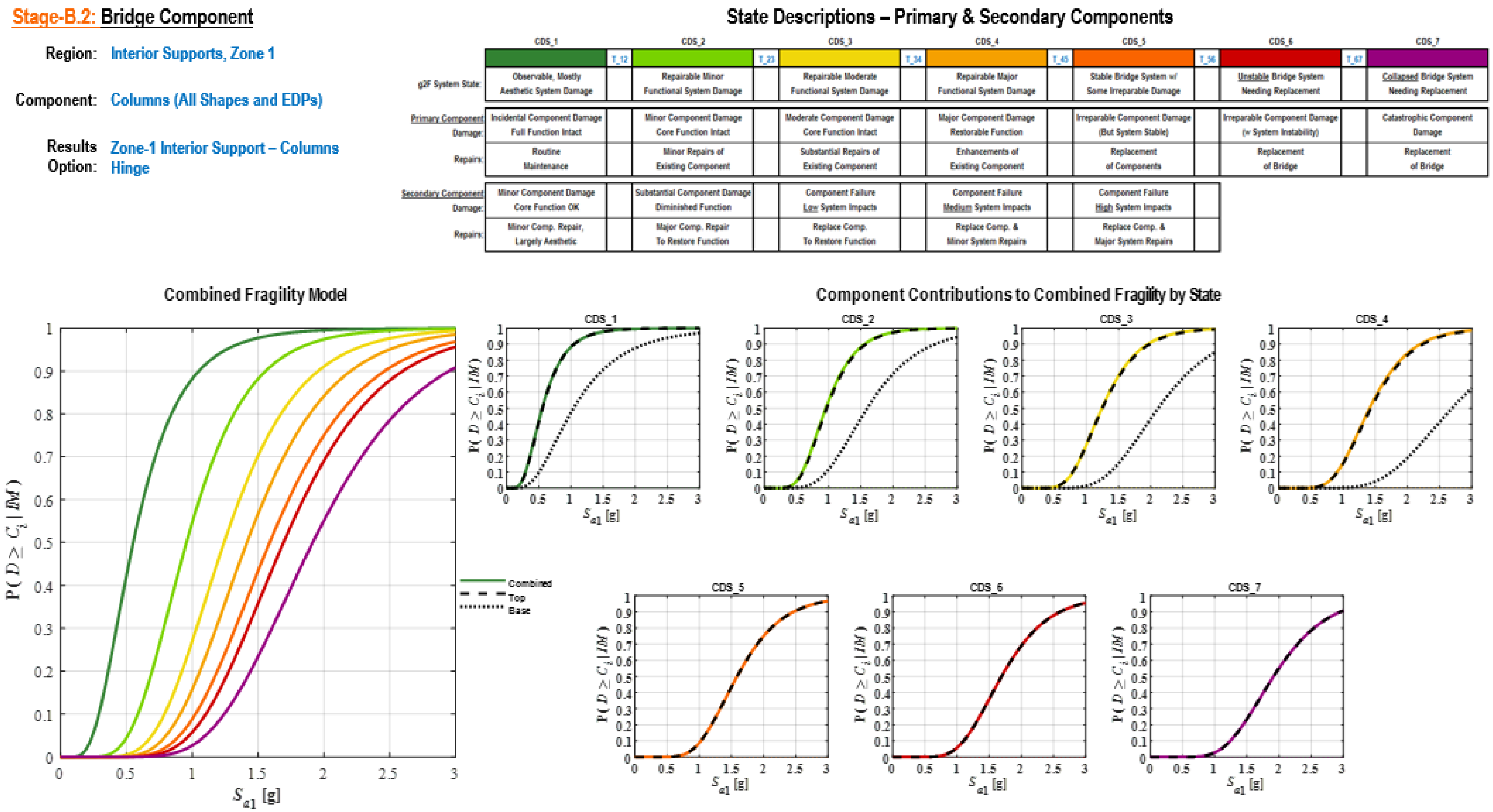

Figure F.32: Stage-B.2: Column curvature ductility (local response).

Stage-B.2: Bridge Component

Region: Interior Supports, Zone 1

Component: Columns (All Shapes and EDPs)

Results Option: Zone-1 Interior Support – Columns

State Descriptions – Primary & Secondary Components

	CDS_1	T_12	CDS_2	T_23	CDS_3	T_34	CDS_4	T_45	CDS_5	T_56	CDS_6	T_67	CDS_7
g2F System State:	Observable, Mostly Aesthetic System Damage		Repairable Minor Functional System Damage		Repairable Moderate Functional System Damage		Repairable Major Functional System Damage		Stable Bridge System w/ Some Irreparable Damage		Unstable Bridge System Needing Replacement		Collapsed Bridge System Needing Replacement
Primary Component Damage:	Incidental Component Damage Full Function Intact		Minor Component Damage Core Function Intact		Moderate Component Damage Core Function Intact		Major Component Damage Restorable Function		Irreparable Component Damage (But System Stable)		Irreparable Component Damage (w System Instability)		Catastrophic Component Damage
Repairs:	Routine Maintenance		Minor Repairs of Existing Component		Substantial Repairs of Existing Component		Enhancements of Existing Component		Replacement of Components		Replacement of Bridge		Replacement of Bridge
Secondary Component Damage:	Minor Component Damage Core Function OK		Substantial Component Damage Diminished Function		Component Failure Low System Impacts		Component Failure Medium System Impacts		Component Failure High System Impacts				
Repairs:	Minor Comp. Repair, Largely Aesthetic		Major Comp. Repair To Restore Function		Replace Comp. To Restore Function		Replace Comp. & Minor System Repairs		Replace Comp. & Major System Repairs				

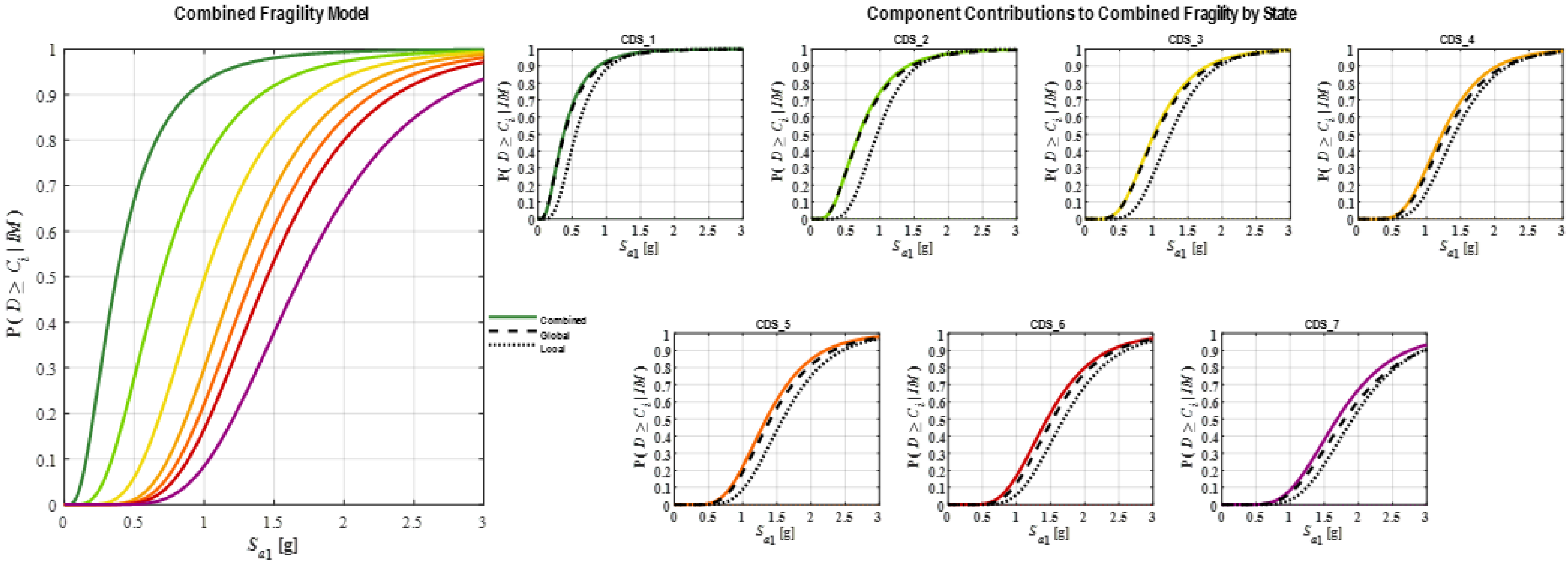

Figure F.33: Stage-B.2: Column response.

Stage-0: Component Subgroup - Directional

Region: Interior Supports, Zone 1

Component: Column Foundation

Subgroup: CIDH-Pile Foundation

Direction: Longitudinal Rotated (LR), Skew = 0 deg.

Metric: Translational Pile Damage

EDP: Normalized R5P Performance Point

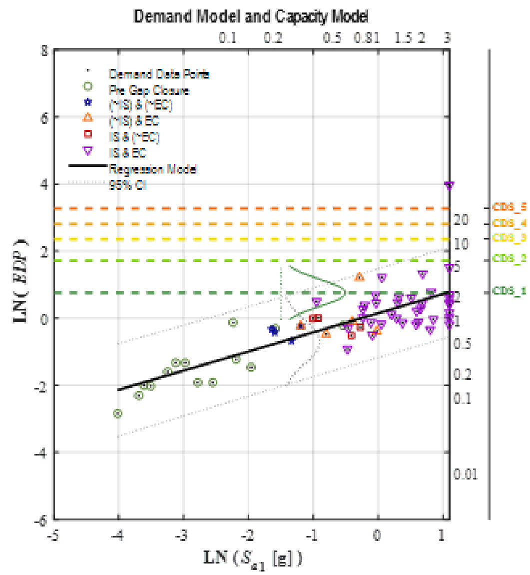

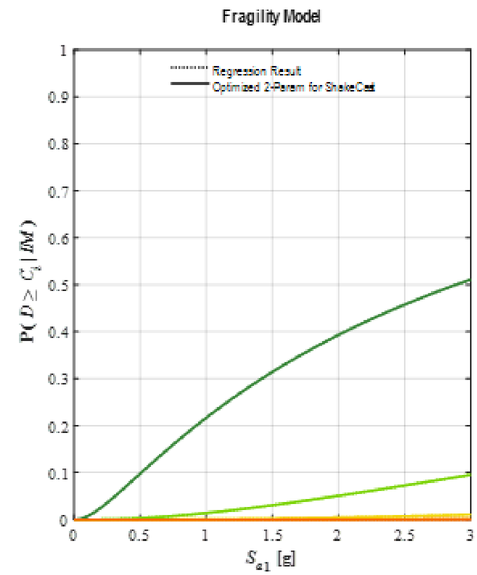

Capacity Model State Descriptions - Component Subgroup

	CDS_1	T_12	CDS_2	T_23	CDS_3	T_34	CDS_4	T_45	CDS_5	T_56	CDS_6	T_67	CDS_7
CIDH-Pile Performance:	Initial Loss of Lateral Stiffness		Approaching Lateral Capacity		Degrading Lateral Capacity		Residual Lateral Capacity		Loss of Lateral (& Axial?) Capacity				
CIDH-Pile Foundation Damage:	Initial Minor Cracking/Spalling Damage at Pile Head (Future Corrosion)		Initial Pile-Head Hinging w/ Substantial Cracking/Spalling & Minor Rebar Yield		Well Developed Pile-Head Hinge w/ Major Rebar Yield & Core Crushing; Initial 2nd Hinge Below Ground		Buckling & Fracture of Rebar & Hoop Fracture at Pile Head; Fully Formed 2nd Hinge Below Ground		Large Displacement & Pile Rotation; Possible Detachment at Pile Cap; Major Loss of Lateral & Axial Capacity				
Normalized Pile-Head Translational Force v. Displacement Response Range	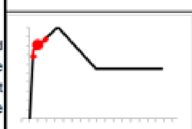		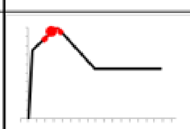		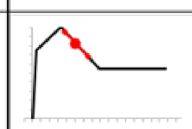		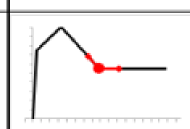		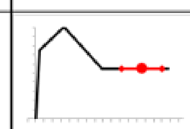				

Figure F.34: Stage-0: CIDH column pile foundation damage in longitudinal direction

Stage-0: Component Subgroup - Directional

Region: Interior Supports, Zone 1

Component: Column Foundation

Subgroup: CIDH-Pile Foundation

Direction: Transverse Rotated (TR), Skew = 0 deg.

Metric: Translational Pile Damage

EDP: Normalized R5P Performance Point

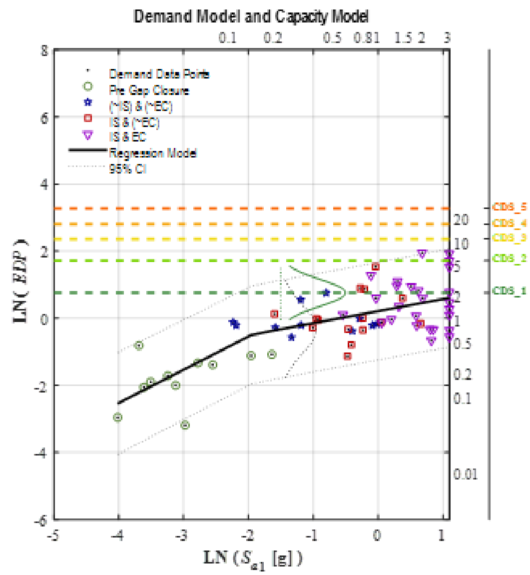

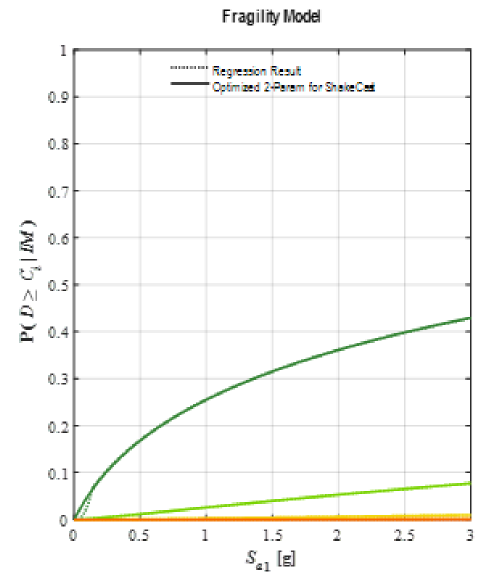

Capacity Model State Descriptions - Component Subgroup

	CDS_1	T_12	CDS_2	T_23	CDS_3	T_34	CDS_4	T_45	CDS_5	T_56	CDS_6	T_67	CDS_7
CIDH-Pile Performance:	Initial Loss of Lateral Stiffness		Approaching Lateral Capacity		Degrading Lateral Capacity		Residual Lateral Capacity		Loss of Lateral (& Axial?) Capacity				
CIDH-Pile Foundation Damage:	Initial Minor Cracking/Spalling Damage at Pile Head (Future Corrosion)		Initial Pile-Head Hinging w/ Substantial Cracking/Spalling & Minor Rebar Yield		Well Developed Pile-Head Hinge w/ Major Rebar Yield & Core Crushing; Initial 2nd Hinge Below Ground		Buckling & Fracture of Rebar & Hoop Fracture at Pile Head; Fully Formed 2nd Hinge Below Ground		Large Displacement & Pile Rotation; Possible Detachment at Pile Cap; Major Loss of Lateral & Axial Capacity				
Normalized Pile-Head Translational Force v. Displacement Response Range	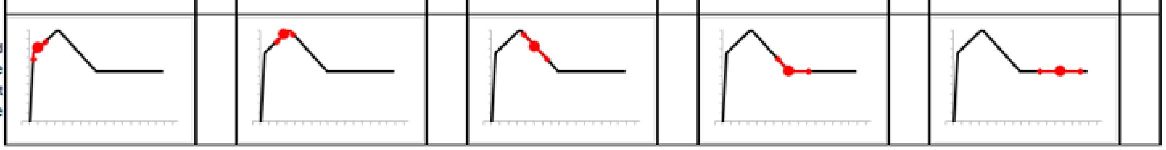												

Figure F.35: Stage-0: CIDH column pile foundation damage in transverse direction

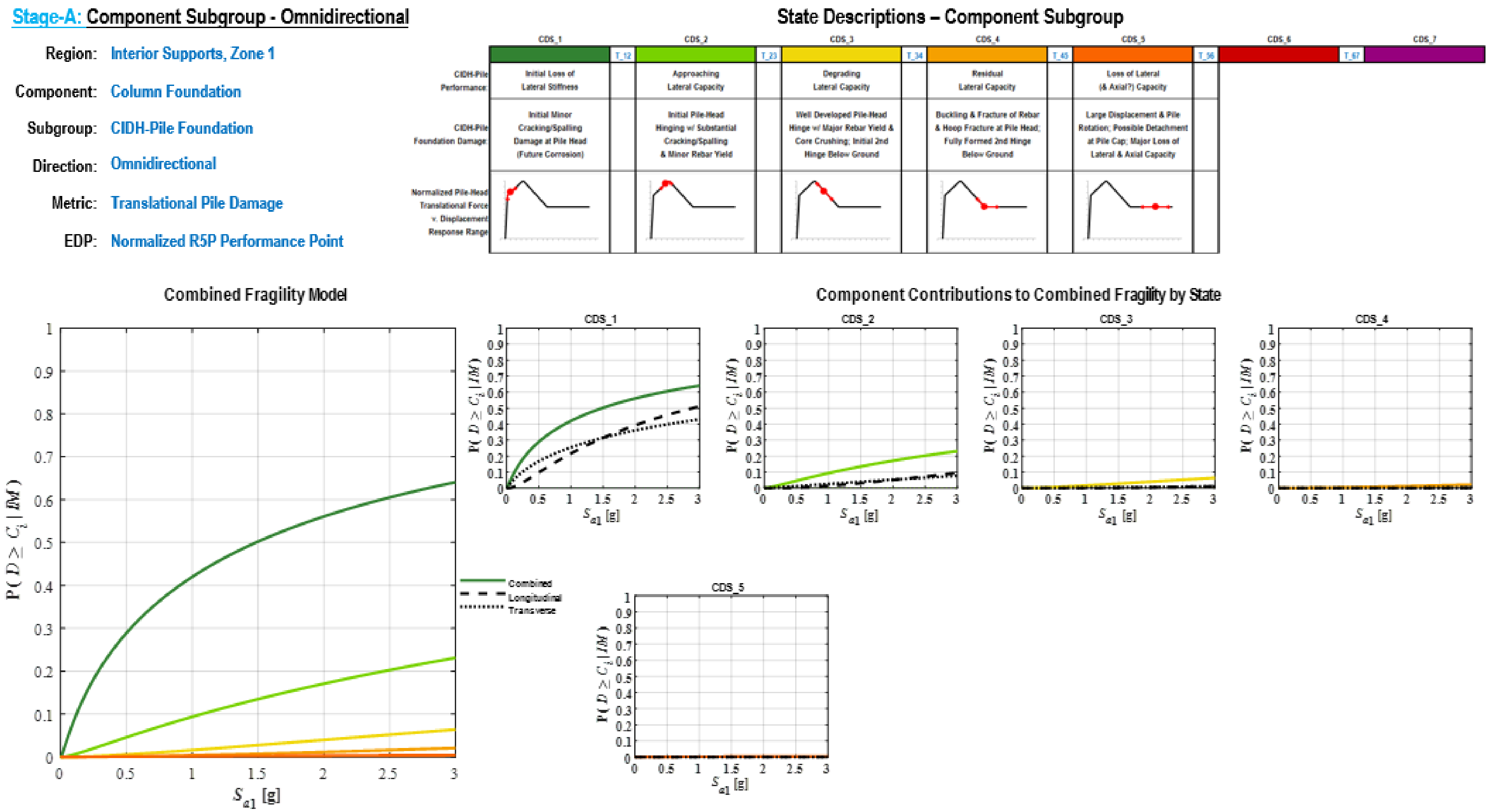

Figure F.36: Stage-A: CIDH column pile foundation damage

Stage-0: Component Subgroup - Directional

Region: Interior Supports, Zone 1

Component: Column Foundation

Subgroup: Precast-Pile Foundation

Direction: Longitudinal Rotated (LR), Skew = 0 deg.

Metric: Translational Pile Damage

EDP: Normalized R5P Performance Point

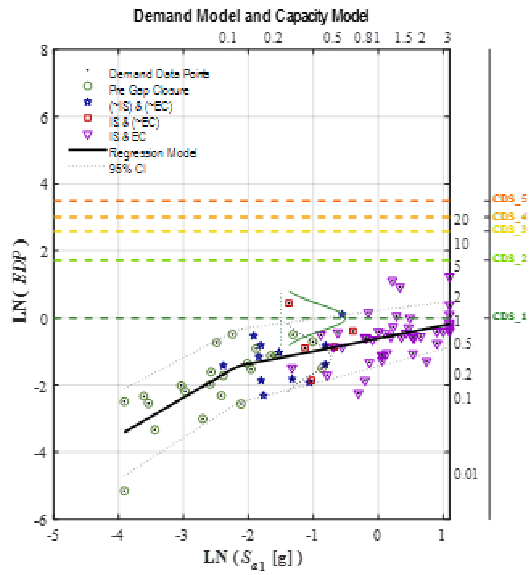

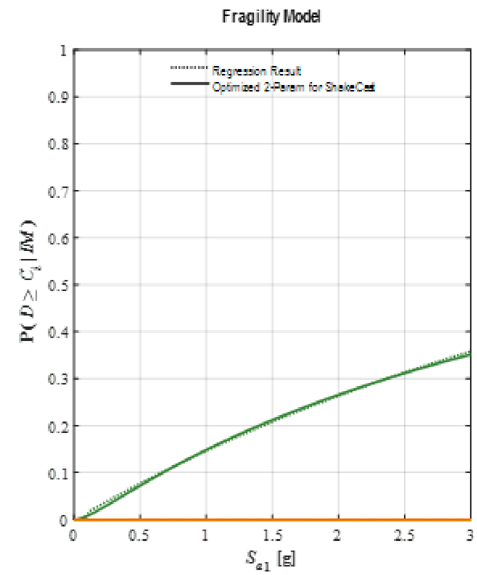

Capacity Model State Descriptions - Component Subgroup

	CDS_1	T_12	CDS_2	T_23	CDS_3	T_34	CDS_4	T_45	CDS_5	T_56	CDS_6	T_67	CDS_7
Precast-Pile Performance:	Initial Loss of Lateral Stiffness		Approaching Lateral Capacity		Degrading Lateral Capacity		Residual Lateral Capacity		Loss of Lateral (& Axial?) Capacity				
Precast-Pile Foundation Damage:	Initial Minor Cracking/Spalling Damage at Pile Head (Future Corrosion)		Initial Pile-Head Hinging w/ Substantial Cracking/Spalling; Initial Yielding of Rebar & Prestress Tendons		Well Developed Pile-Head Hinge w/ Major Yielding of Rebar & Prestress Tendons; Core Crushing; Initial 2nd Hinge Below Ground		Buckling & Fracture of Rebar & Prestress Tendons; Fully Formed 2nd Hinge Below Ground		Large Displacement & Pile Rotation; Possible Detachment at Pile Cap; Major Loss of Lateral & Axial Capacity				
Normalized Pile-Head Translational Force v. Displacement Response Range													

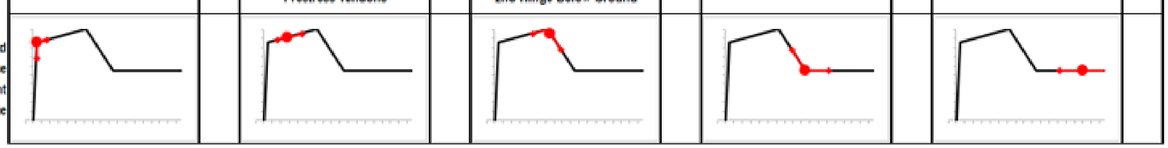

Figure F.37: Stage-0: Precast column pile foundation damage in longitudinal direction

Stage-0: Component Subgroup - Directional

Region: Interior Supports, Zone 1

Component: Column Foundation

Subgroup: Precast-Pile Foundation

Direction: Transverse Rotated (TR), Skew = 0 deg.

Metric: Translational Pile Damage

EDP: Normalized R5P Performance Point

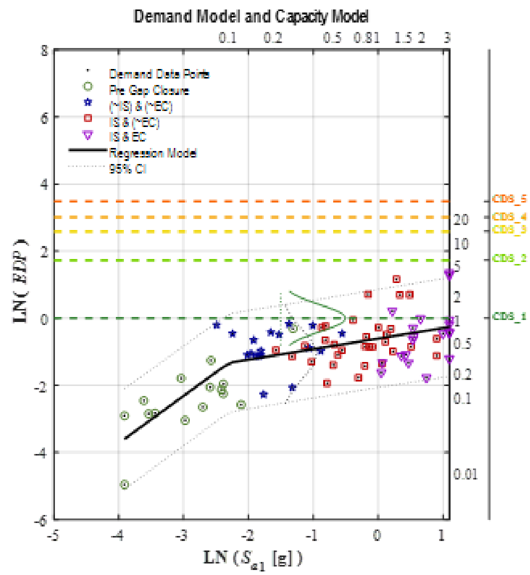

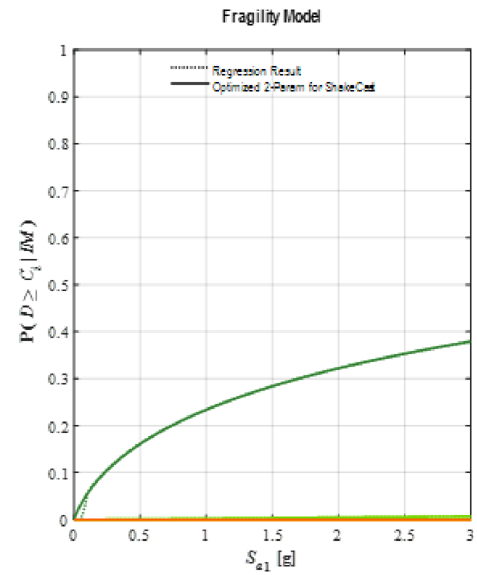

Capacity Model State Descriptions - Component Subgroup

	CDS_1	T_12	CDS_2	T_23	CDS_3	T_34	CDS_4	T_45	CDS_5	T_56	CDS_6	T_67	CDS_7
Precast-Pile Performance:	Initial Loss of Lateral Stiffness		Approaching Lateral Capacity		Degrading Lateral Capacity		Residual Lateral Capacity		Loss of Lateral (& Axial?) Capacity				
Precast-Pile Foundation Damage:	Initial Minor Cracking/Spalling Damage at Pile Head (Future Corrosion)		Initial Pile-Head Hinging w/ Substantial Cracking/Spalling; Initial Yielding of Rebar & Prestress Tendons		Well Developed Pile-Head Hinge w/ Major Yielding of Rebar & Prestress Tendons; Core Crushing; Initial 2nd Hinge Below Ground		Buckling & Fracture of Rebar & Prestress Tendons; Fully Formed 2nd Hinge Below Ground		Large Displacement & Pile Rotation; Possible Detachment at Pile Cap; Major Loss of Lateral & Axial Capacity				
Normalized Pile-Head Translational Force v. Displacement Response Range	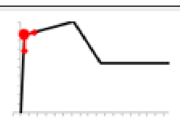		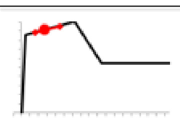		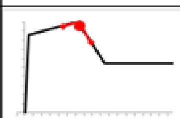		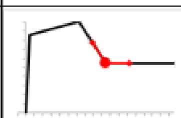		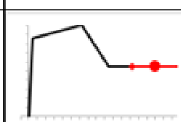				

Figure F.38: Stage-0: Precast column pile foundation damage in transverse direction

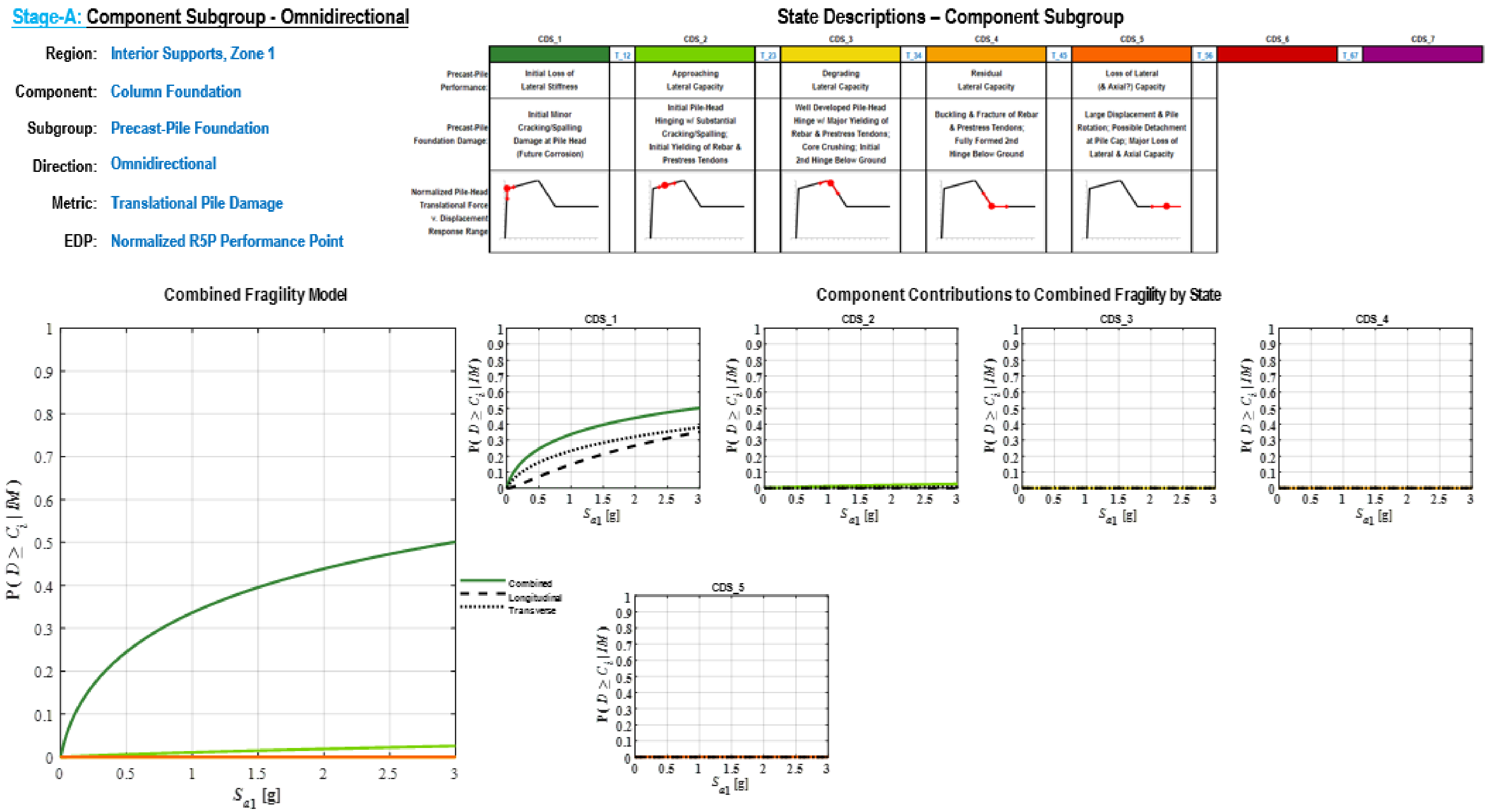

Figure F.39: Stage-A: Precast column pile foundation damage

Stage-0: Component Subgroup - Directional

Region: Interior Supports, Zone 1

Component: Column Foundation

Subgroup: Steel-Pile Foundation

Direction: Longitudinal Rotated (LR), Skew = 0 deg.

Metric: Translational Pile Damage

EDP: Normalized R5P Performance Point

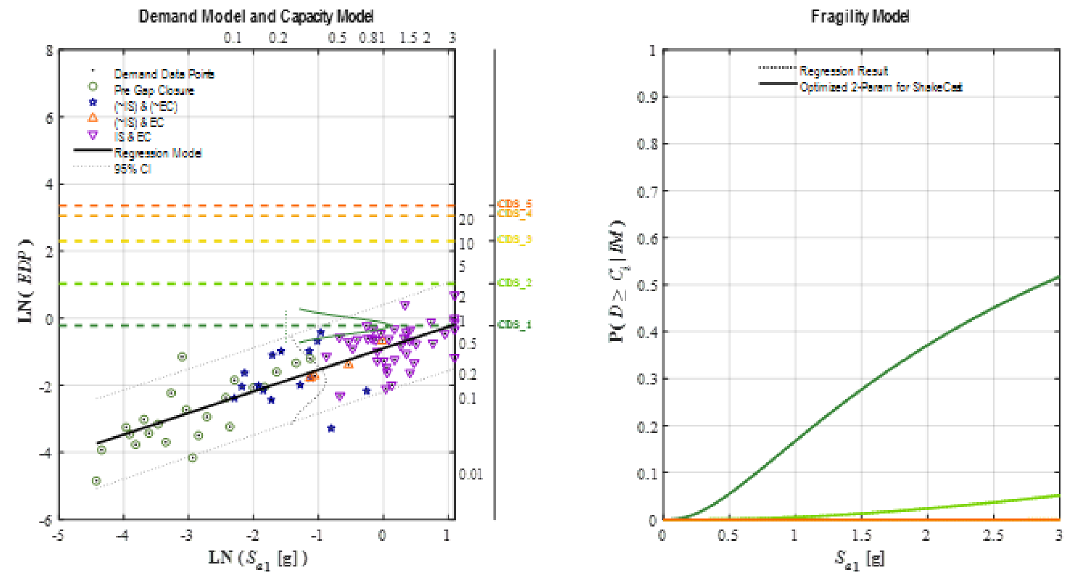

Capacity Model State Descriptions - Component Subgroup

	CDS_1	T_12	CDS_2	T_23	CDS_3	T_34	CDS_4	T_45	CDS_5	T_56	CDS_6	T_67	CDS_7
Steel-Pile Performance:	Initial Pile-Cap Connection Damage		Initial Loss of Lateral Stiffness		Pile Ductile Yielding w/ Cap Damage		Degrading Lateral Capacity		Residual Lateral Capacity				
Steel-Pile Foundation Damage:	Initial Minor Cracking at Pile Cap Connection (Future Corrosion); Low (< ~5-deg) Pile-Head Rotation		Rotational Gap at Cap Connection; Initial Steel Yielding Below Ground; Moderate (5 to 10-deg) Pile-Head Rotation		Increasing Cap Connection Damage; Ductile Steel Yielding Below Ground; High (10 to 30-deg) Pile-Head Rotation		Substantial Cap Connection Damage; Steel Buckling at Below-Ground Hinge; Extreme (30 to 45-deg) Pile-Head Rotation		Extreme Displacement & Pile-Head Rotation (> ~45 deg); Possible Detachment at Pile Cap; Major Loss of Lateral & Possibly Axial Capacity				
Normalized Pile-Head Translational Force v. Displacement Response Range	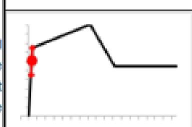		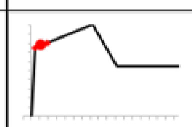		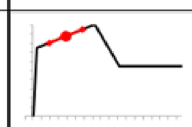		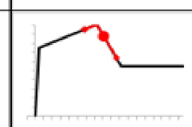		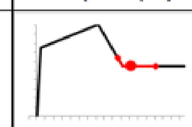				

Figure F.40: Stage-0: Steel column pile foundation damage in longitudinal direction

Stage-0: Component Subgroup - Directional

Region: Interior Supports, Zone 1

Component: Column Foundation

Subgroup: Steel-Pile Foundation

Direction: Transverse Rotated (TR), Skew = 0 deg.

Metric: Translational Pile Damage

EDP: Normalized R5P Performance Point

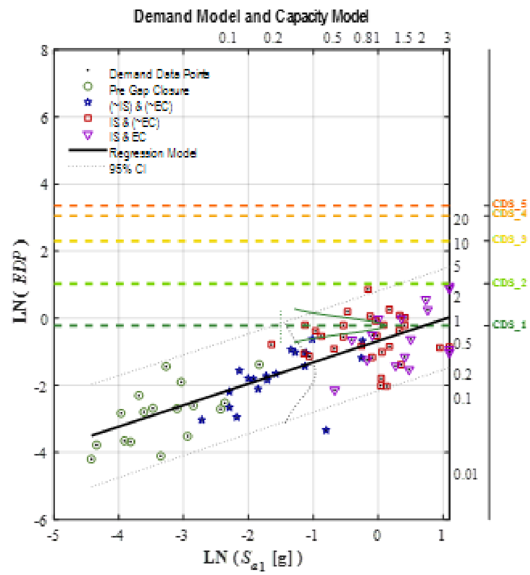

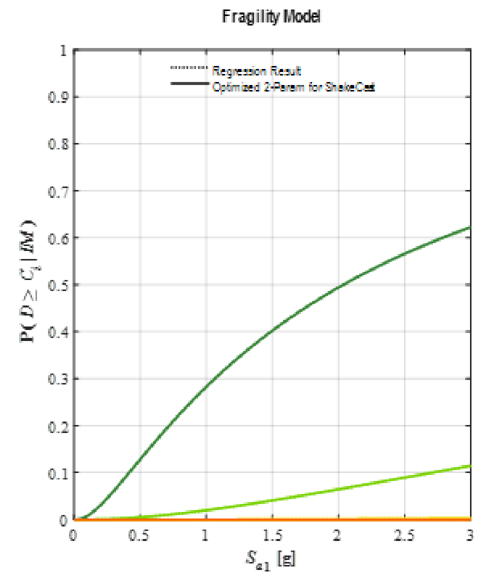

Capacity Model State Descriptions - Component Subgroup

	CDS_1	T_12	CDS_2	T_23	CDS_3	T_34	CDS_4	T_45	CDS_5	T_56	CDS_6	T_67	CDS_7
Steel-Pile Performance:	Initial Pile-Cap Connection Damage		Initial Loss of Lateral Stiffness		Pile Ductile Yielding w/ Cap Damage		Degrading Lateral Capacity		Residual Lateral Capacity				
Steel-Pile Foundation Damage:	Initial Minor Cracking at Pile Cap Connection (Future Corrosion); Low (< ~5-deg) Pile-Head Rotation		Rotational Gap at Cap Connection; Initial Steel Yielding Below Ground; Moderate (5 to 10-deg) Pile-Head Rotation		Increasing Cap Connection Damage; Ductile Steel Yielding Below Ground; High (10 to 30-deg) Pile-Head Rotation		Substantial Cap Connection Damage; Steel Buckling at Below-Ground Hinge; Extreme (30 to 45-deg) Pile-Head Rotation		Extreme Displacement & Pile-Head Rotation (> ~45 deg); Possible Detachment at Pile Cap; Major Loss of Lateral & Possibly Axial Capacity				
Normalized Pile-Head Translational Force v. Displacement Response Range	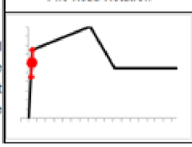		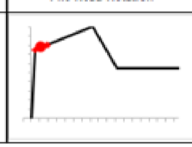		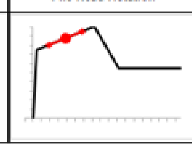		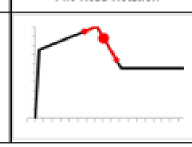		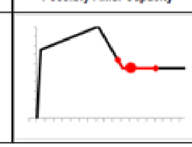				

Figure F.41: Stage-0: Steel column pile foundation damage in transverse direction

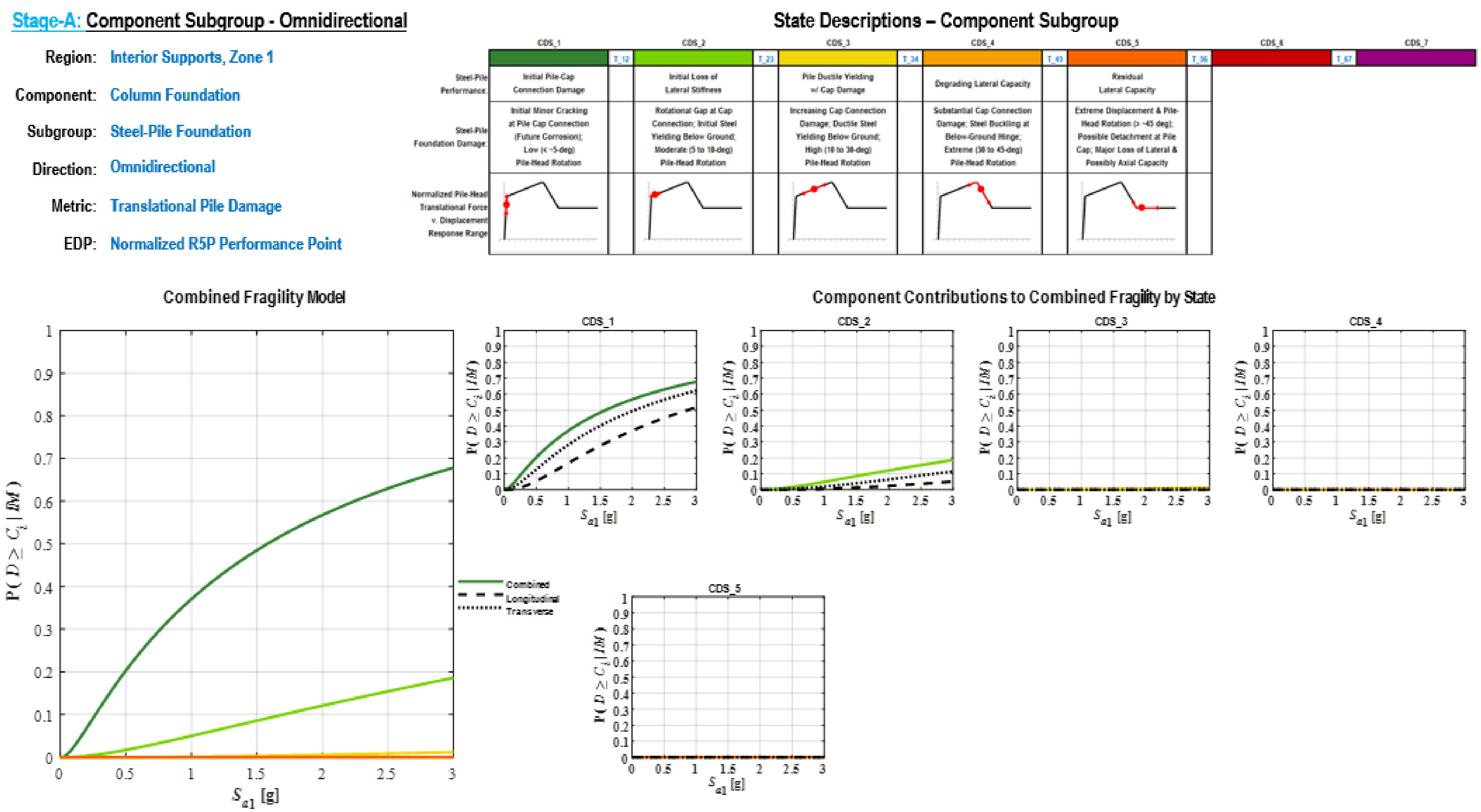

Figure F.42: Stage-A: Steel column pile foundation damage

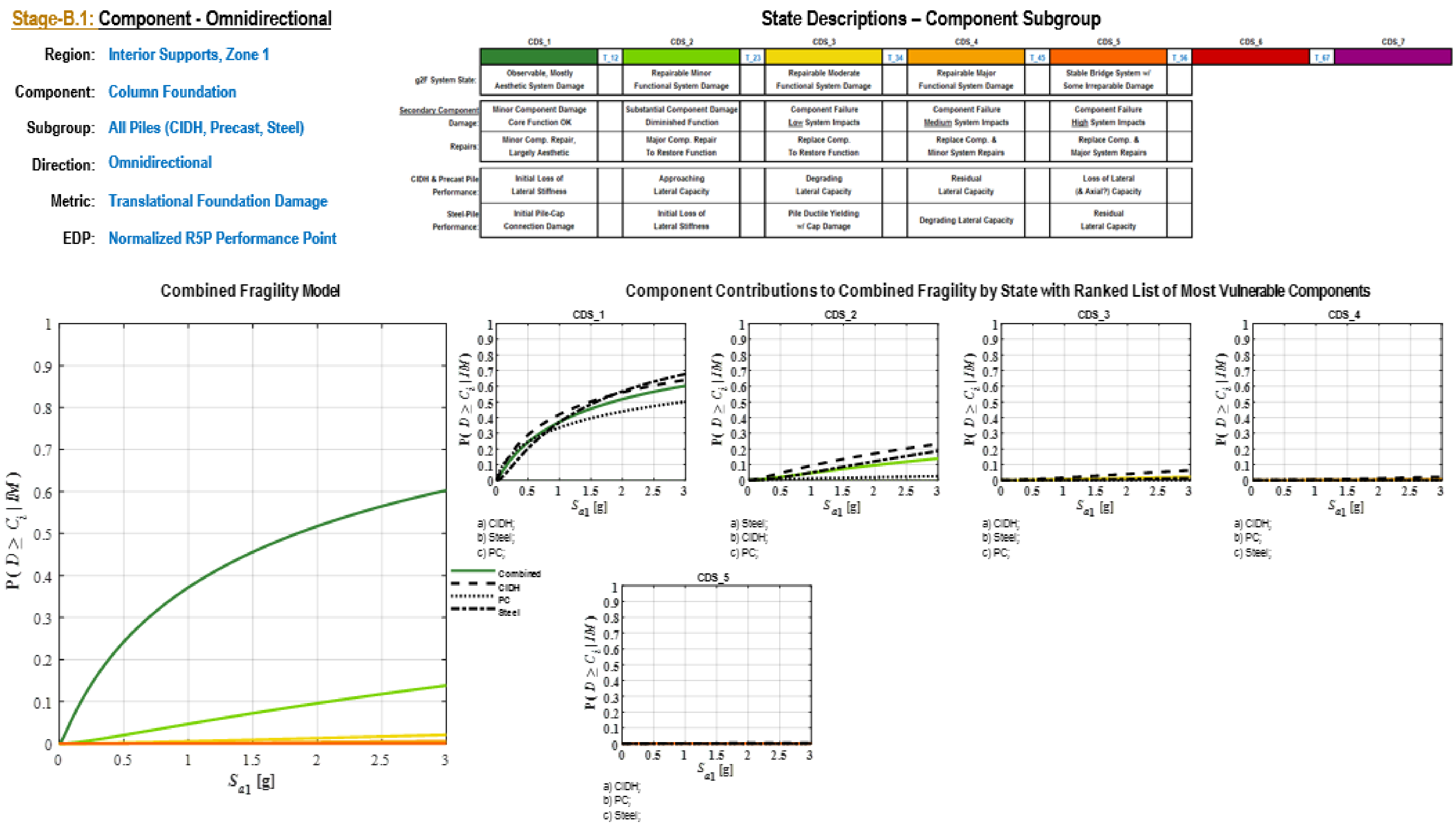

Figure F.43: Stage-B.1: Column pile foundation damage.

Stage-0: Component Subgroup - Directional

Region: Interior Supports, Zone 1

Component: Column Foundation

Subgroup: Spread Footing Foundation

Direction: Longitudinal Rotated (LR), Skew = 0 deg.

Metric: Translational Footing Damage

EDP: Normalized RUUFF Performance Point

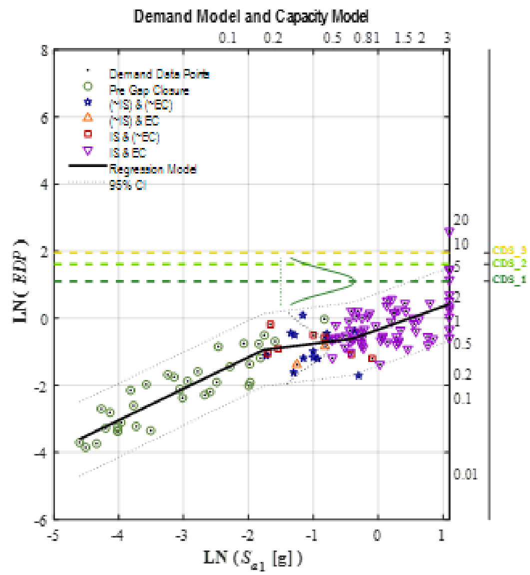

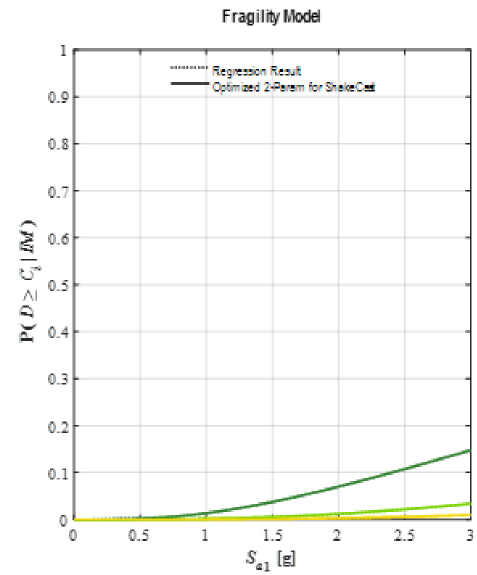

Capacity Model State Descriptions - Component Subgroup

	CDS_1	T_12	CDS_2	T_23	CDS_3	T_34	CDS_4	T_45	CDS_5	T_56	CDS_6	T_67	CDS_7
Typical Performance:	Observable Residual Displacements (1-4 Inch)		Substantial Residual Displacements (4-16-Inch)		Extreme Residual Displacements (>16-Inch)								
Footing-Area Damage:	Minor Gaps or Dislocations Near Footing at Ground Surface		Potential Distress to Footing Connection or Abutting Facilities/Utilities		Potential Impacts on Column Capacity and/or Alignment								
Norm Force-Displ. Response Range:	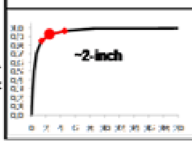	~4-In	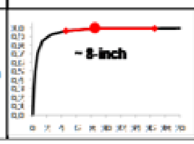	~16-In	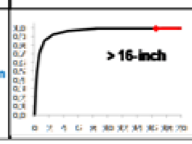								

Figure F.44: Stage-0: Column spread footing foundation damage in longitudinal direction

Stage-0: Component Subgroup - Directional

Region: Interior Supports, Zone 1

Component: Column Foundation

Subgroup: Spread Footing Foundation

Direction: Transverse Rotated (TR), Skew = 0 deg.

Metric: Translational Footing Damage

EDP: Normalized RUUFF Performance Point

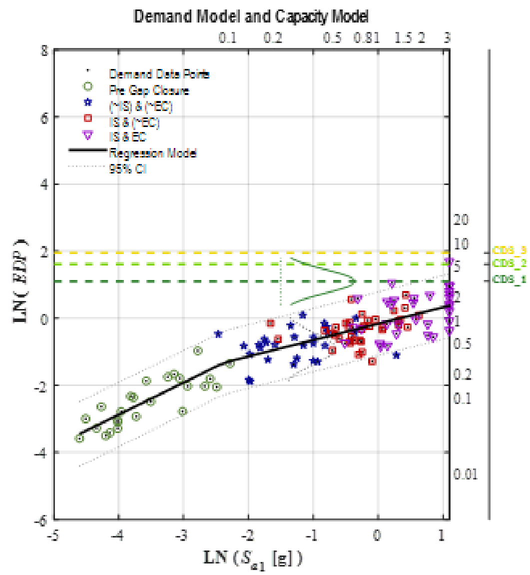

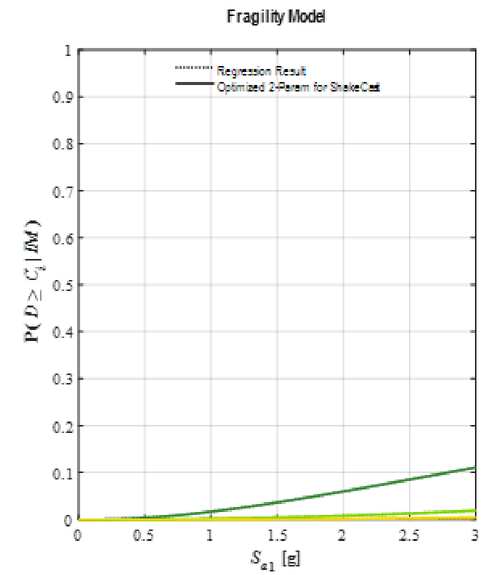

Capacity Model State Descriptions - Component Subgroup

	CDS_1	T_12	CDS_2	T_23	CDS_3	T_34	CDS_4	T_45	CDS_5	T_56	CDS_6	T_67	CDS_7
Typical Performance:	Observable Residual Displacements (1-4 Inch)		Substantial Residual Displacements (4-16-Inch)		Extreme Residual Displacements (>16-Inch)								
Footing-Area Damage:	Minor Gaps or Dislocations Near Footing at Ground Surface		Potential Distress to Footing Connection or Abuting Facilities/Utilities		Potential Impacts on Column Capacity and/or Alignment								
Norm Force-Displ. Response Range:	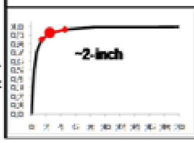 ~2-inch	~4-In	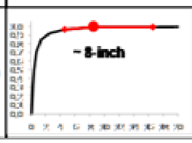 ~8-inch	~16-In	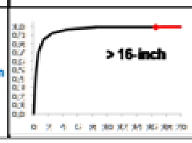 > 16-inch								

Figure F.45: Stage-0: Column spread footing foundation damage in transverse direction

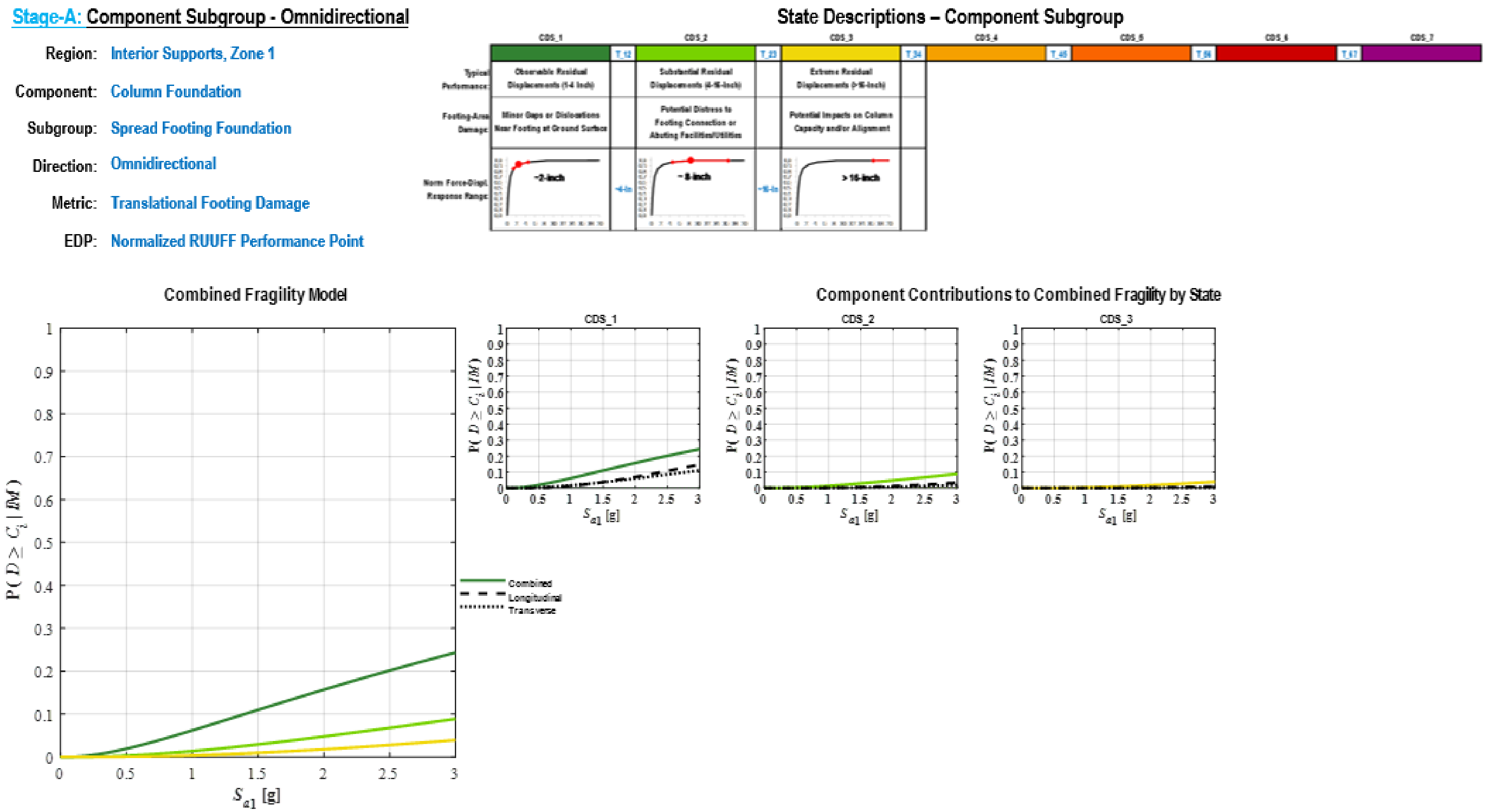

Figure F.46: Stage-A: Column spread footing foundation damage

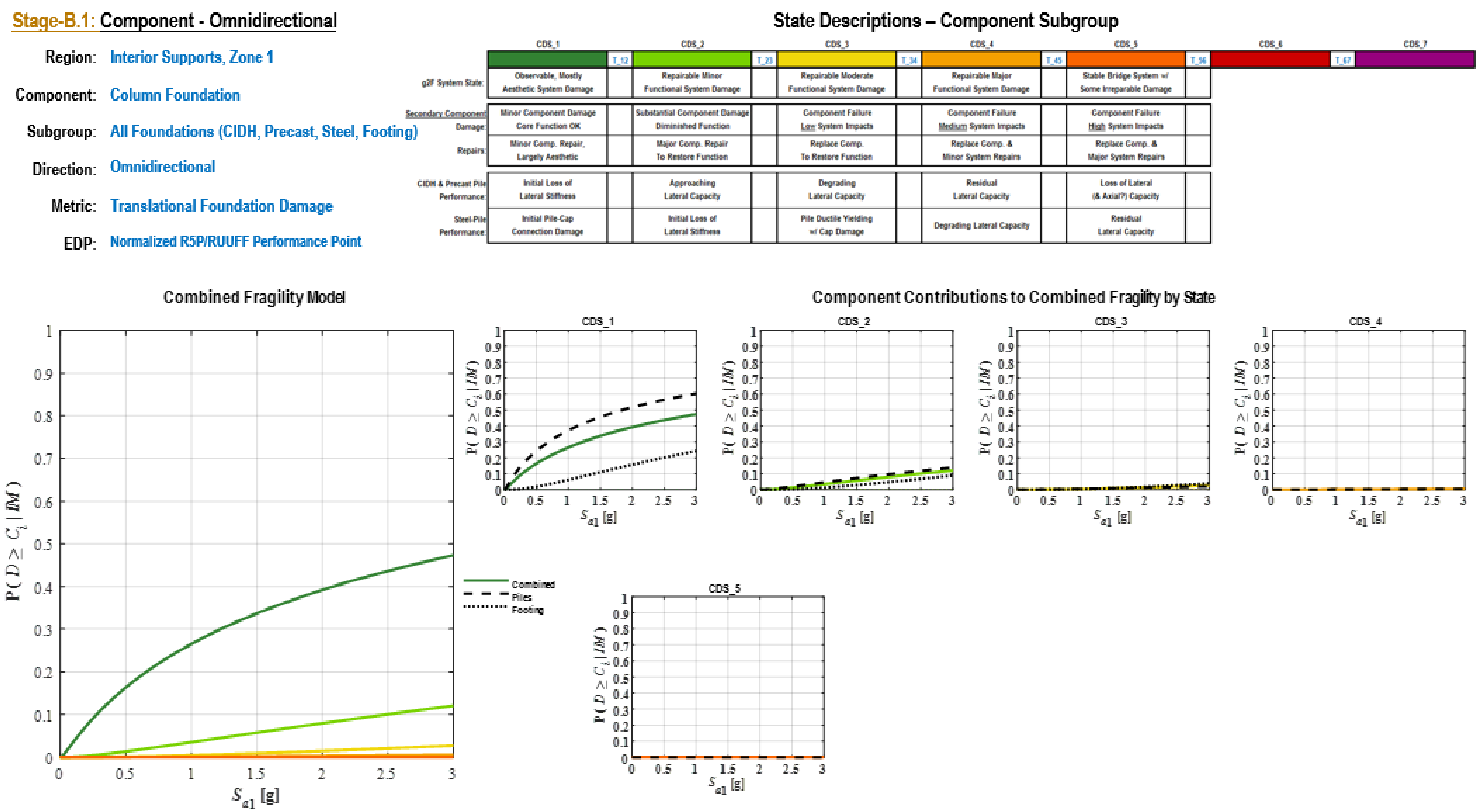

Figure F.47: Stage-B.1: Column foundation translational damage.

Stage-0: Component Subgroup - Directional

Region: Interior Supports, Zone 1

Component: Column Foundation

Subgroup: Geotechnical Damage

Direction: Longitudinal Rotated (LR), Skew = 0 deg.

Metric: Rotational Foundation Damage

EDP: Rotation Ductility

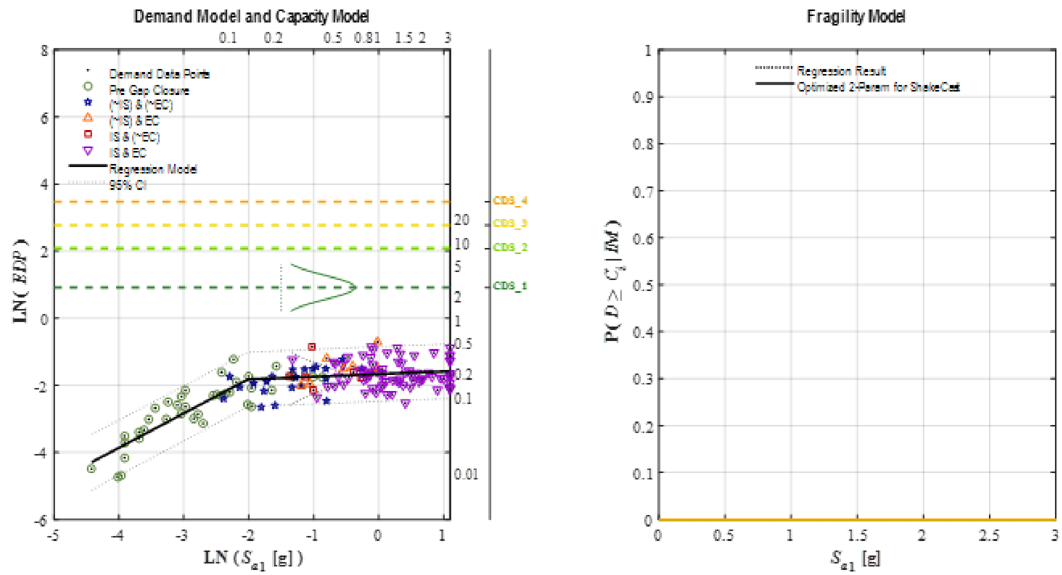

Capacity Model State Descriptions - Component Subgroup

Figure F.48: Stage-0: Column foundation rotational geotechnical damage in longitudinal direction

Stage-0: Component Subgroup - Directional

Region: Interior Supports, Zone 1

Component: Column Foundation

Subgroup: Geotechnical Damage

Direction: Transverse Rotated (TR), Skew = 0 deg.

Metric: Rotational Foundation Damage

EDP: Rotation Ductility

Capacity Model State Descriptions - Component Subgroup

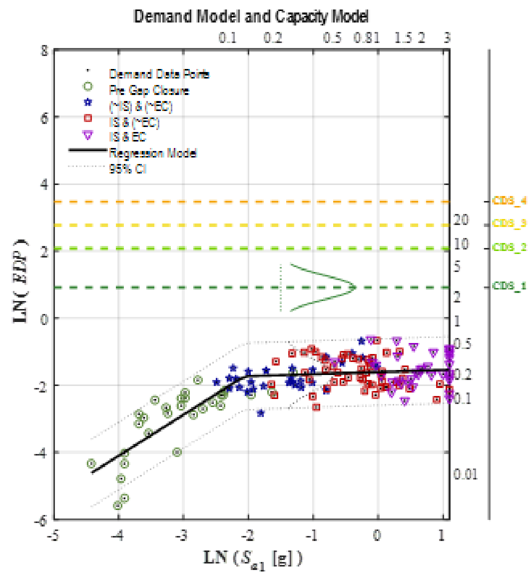

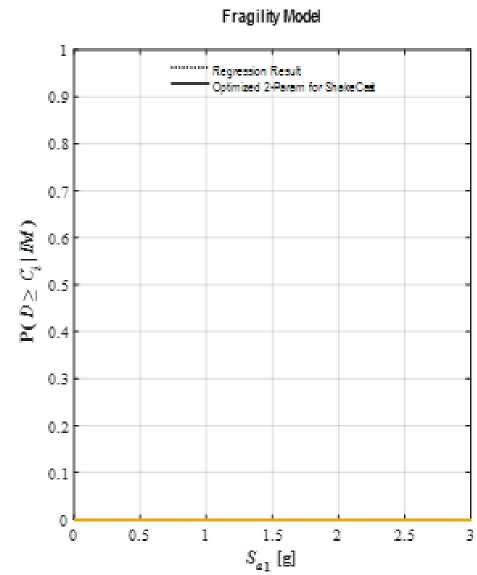

Figure F.49: Stage-0: Column foundation rotational geotechnical damage in transverse direction

Stage-A: Component Subgroup - Omnidirectional

State Descriptions – Component Subgroup

Region:	Interior Supports, Zone 1
Component:	Column Foundation
Subgroup:	Geotechnical Damage
Direction:	Omnidirectional
Metric:	Rotational Foundation Damage
EDP:	Rotation Ductility

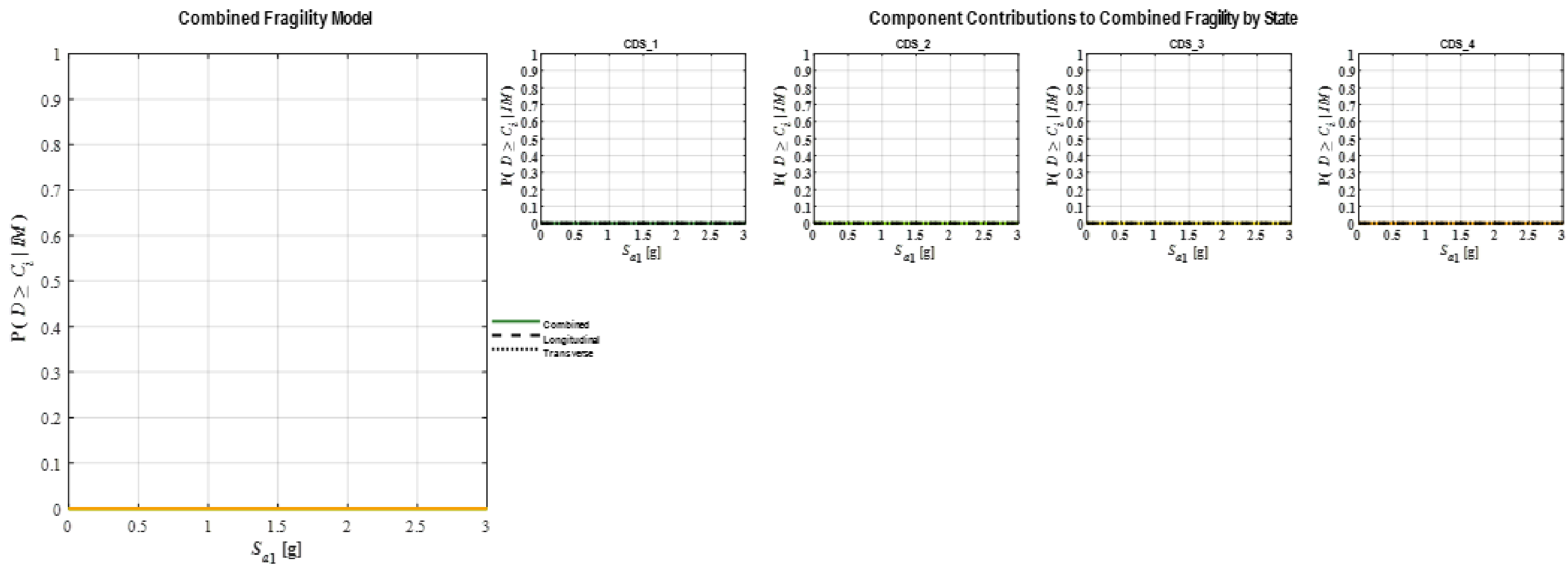

Figure F.50: Stage-A: Column foundation rotational geotechnical damage

Stage-0: Component Subgroup - Directional

Region: Interior Supports, Zone 1

Component: Column Foundation

Subgroup: Structural Damage

Direction: Longitudinal Rotated (LR), Skew = 0 deg.

Metric: Rotational Foundation Damage

EDP: Rotation Ductility

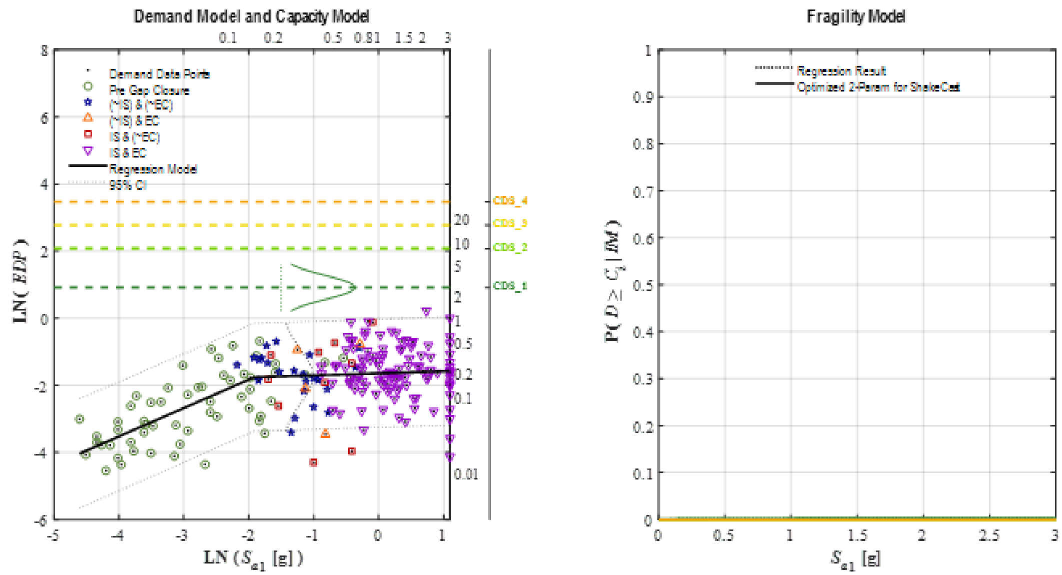

Capacity Model State Descriptions - Component Subgroup

Figure F.51: Stage-0: Column foundation rotational structural damage in longitudinal direction

Stage-0: Component Subgroup - Directional

Region: Interior Supports, Zone 1

Component: Column Foundation

Subgroup: Structural Damage

Direction: Transverse Rotated (TR), Skew = 0 deg.

Metric: Rotational Foundation Damage

EDP: Rotation Ductility

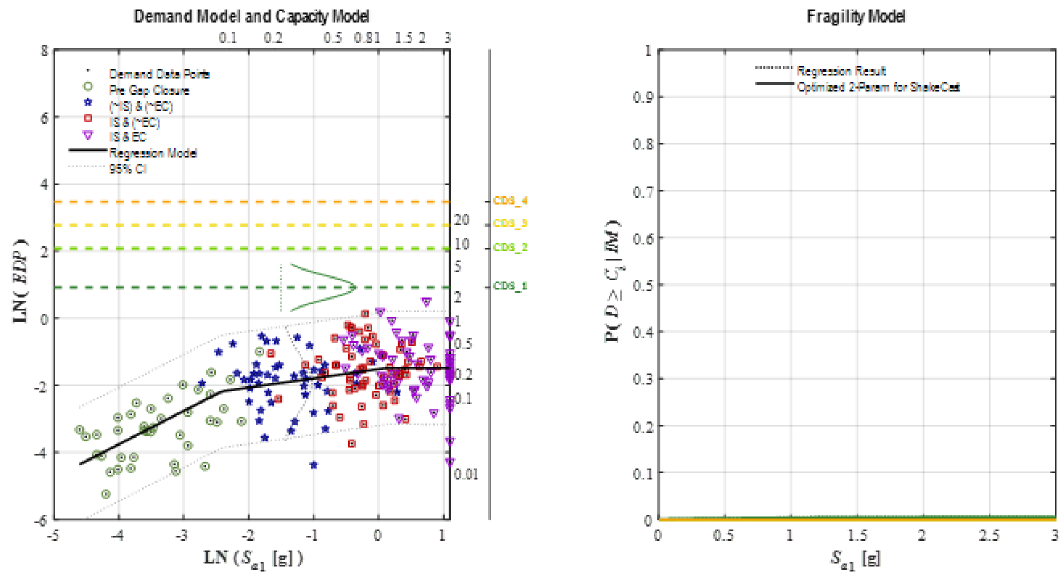

Capacity Model State Descriptions - Component Subgroup

Figure F.52: Stage-0: Column foundation rotational structural damage in transverse direction

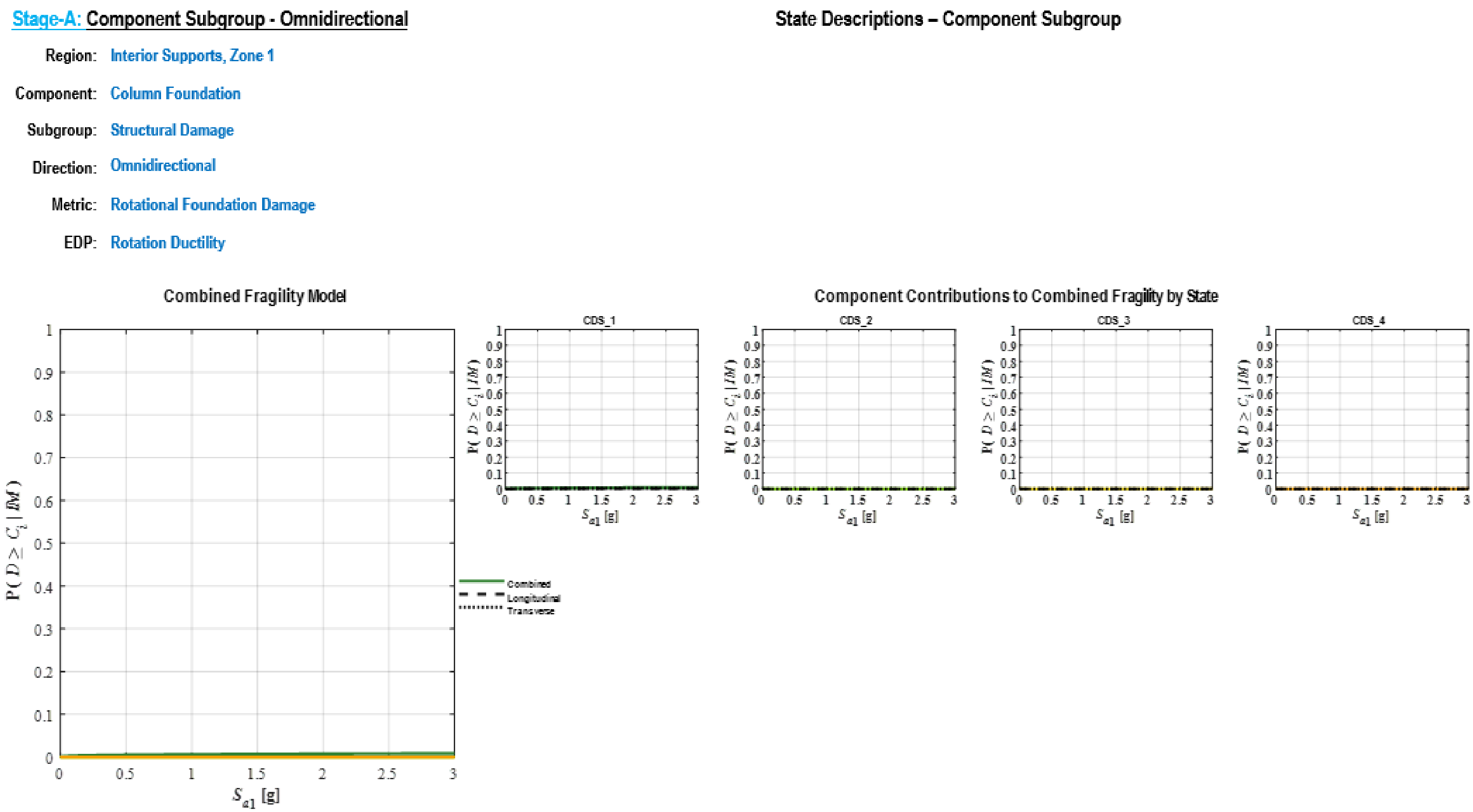

Figure F.53: Stage-A: Column foundation rotational structural damage

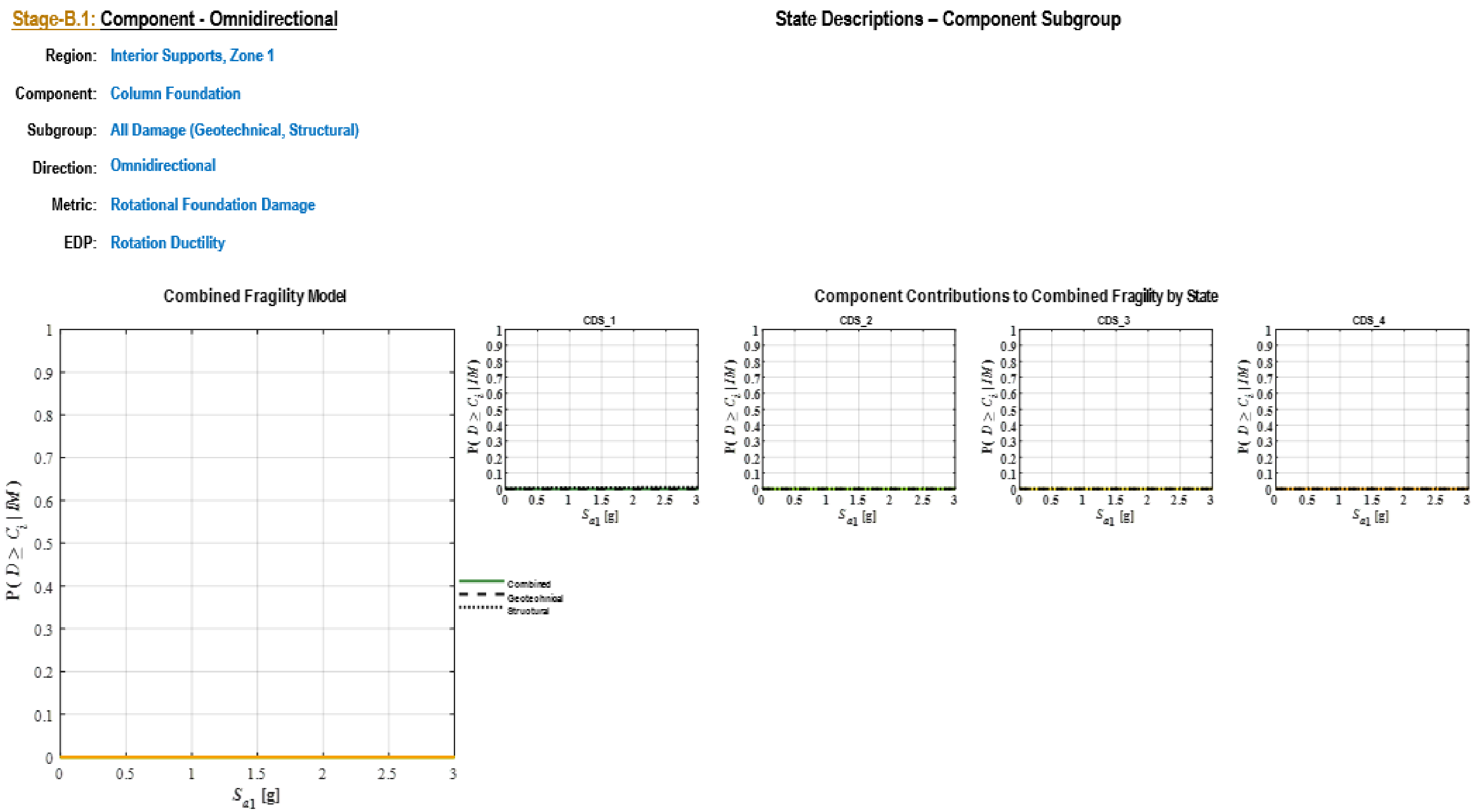

Figure F.54: Stage-B.1: Column foundation rotational damage

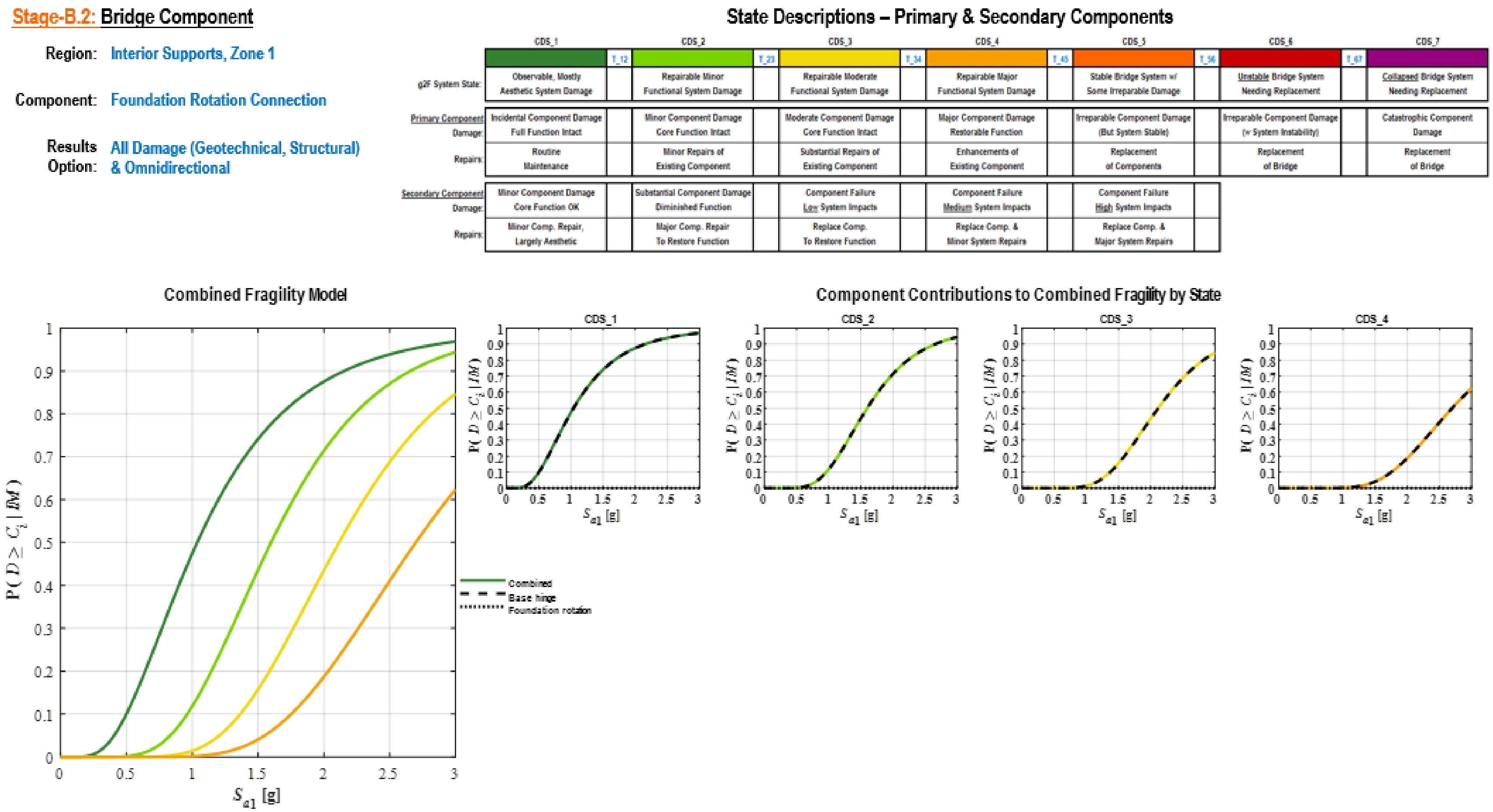

Figure F.55: Stage-B.2: Column foundation rotation connection damage.

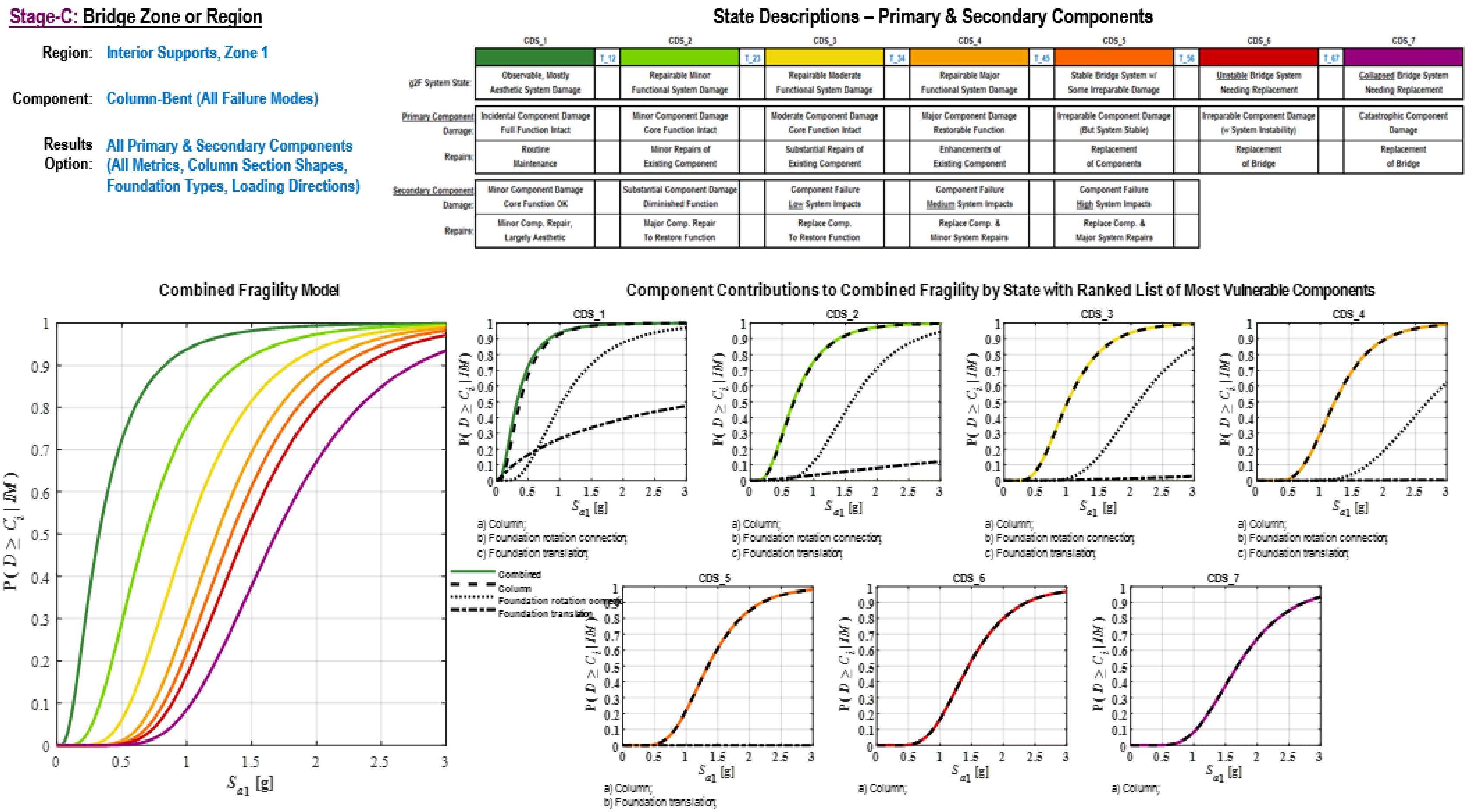

Figure F.56: Stage-C: Column bent damage.

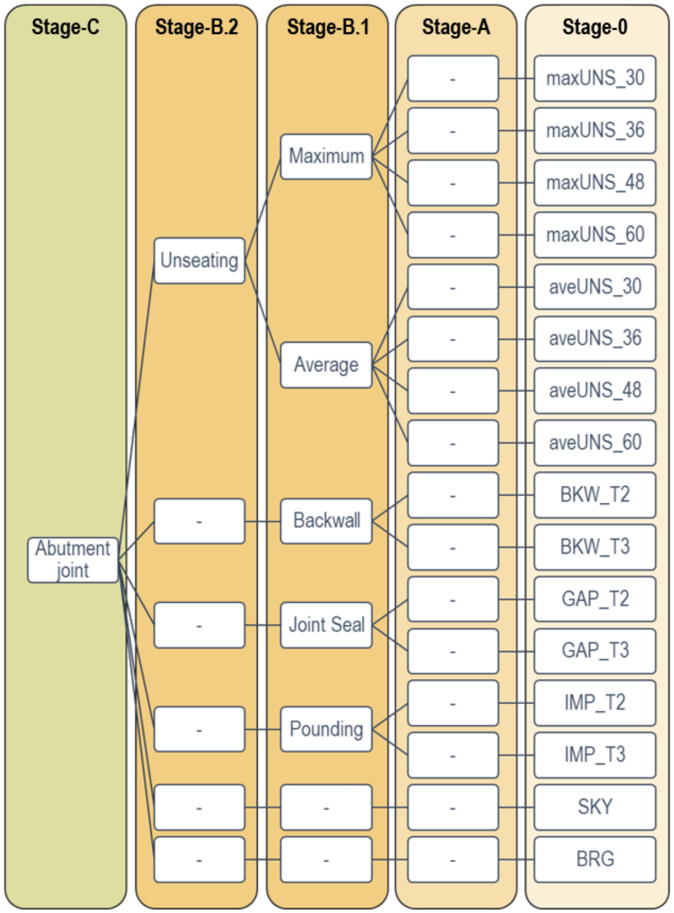

Abutment unseating, maximum response, design-1 with 30-in seat width
Abutment unseating, maximum response, design-1 with 36-in seat width
Abutment unseating, maximum response, design-1 with 48-in seat width
Abutment unseating, maximum response, design-1 with 60-in seat width
Abutment unseating, average response, design-1 with 30-in seat width
Abutment unseating, average response, design-1 with 36-in seat width
Abutment unseating, average response, design-1 with 48-in seat width
Abutment unseating, average response, design-1 with 60-in seat width
Abutment backwall, compression seal
Abutment backwall, strip seal
Abutment joint seal gap, compression seal
Abutment joint seal gap, strip seal
Abutment pounding, compression seal
Abutment pounding, strip seal
Abutment shear key
Abutment bearing

Figure F.57: Roll-up steps to create a Stage-C fragility model for abutment joint response.

Level 0: Component Subgroup - Directional

Region: Abutment Joint

Component: Deck Unseating

Subgroup: Design 1: 30-in Seat w/ 2-in MR (28-in Net Seat)

Direction: Longitudinal Rotated (LR), Skew = 0 deg.

Metric: Minimum Seat Remaining

EDP: Seat Remaining Distance

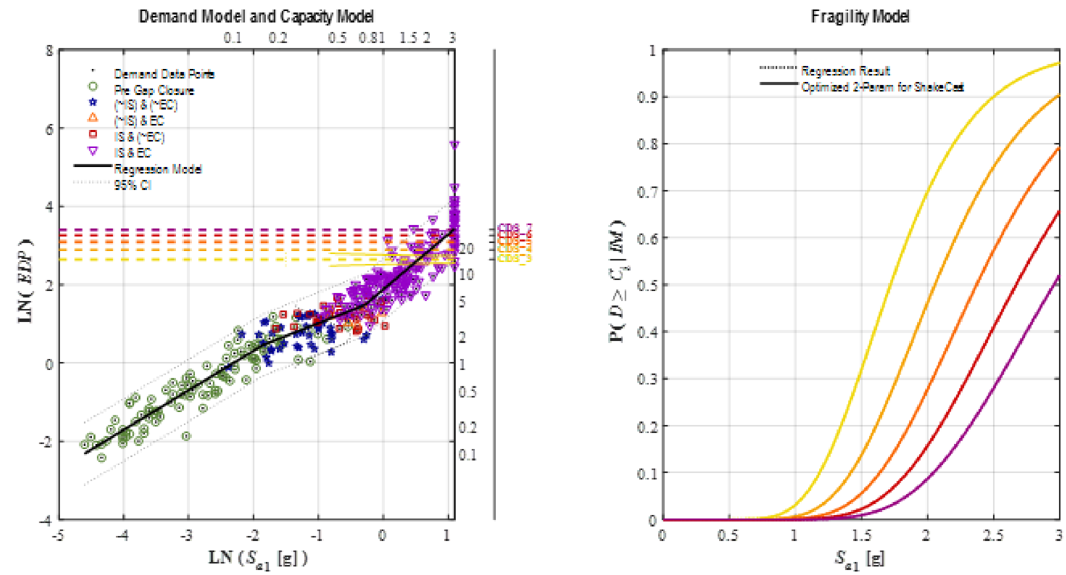

Capacity Model State Descriptions - Component Subgroup

	CDS_1	T_12	CDS_2	T_23	CDS_3	T_34	CDS_4	T_45	CDS_5	T_56	CDS_6	T_67	CDS_7	
Traffic State:	Public w/ Reduced Ride Quality		Public w/ Speed Restrictions		Public w/ Lane or Weight Restrictions		Emergency Vehicles Only w/ Restrictions		Closed (At Least) Temporarily		Closed Long-Term (Demo Equip Access)		Closed Long-Term Emergency Response	
Minimum * Remaining Net** Seat Width Range:	NA		NA	16-in	> 12-in (~14-in) Seat Remaining	12-in	> 8-in (~10-in) Seat Corner Remaining	8-in	> 4-in (~6-in) Seat Corner Remaining	4-in	< 4-in (~2-in) Seat Corner Remaining	0-in	Partially Unseated	-4-in
*Minimum Corner **Plan Seat- MR	NA		NA											

Figure F.58: Stage-0: Abutment maximum unseating damage with 30-in seat width

Level 0: Component Subgroup - Directional

Region: Abutment Joint

Component: Deck Unseating

Subgroup: Design 2: 36-in Seat w/ 2-in MR (34-in Net Seat)

Direction: Longitudinal Rotated (LR), Skew = 0 deg.

Metric: Minimum Seat Remaining

EDP: Seat Remaining Distance

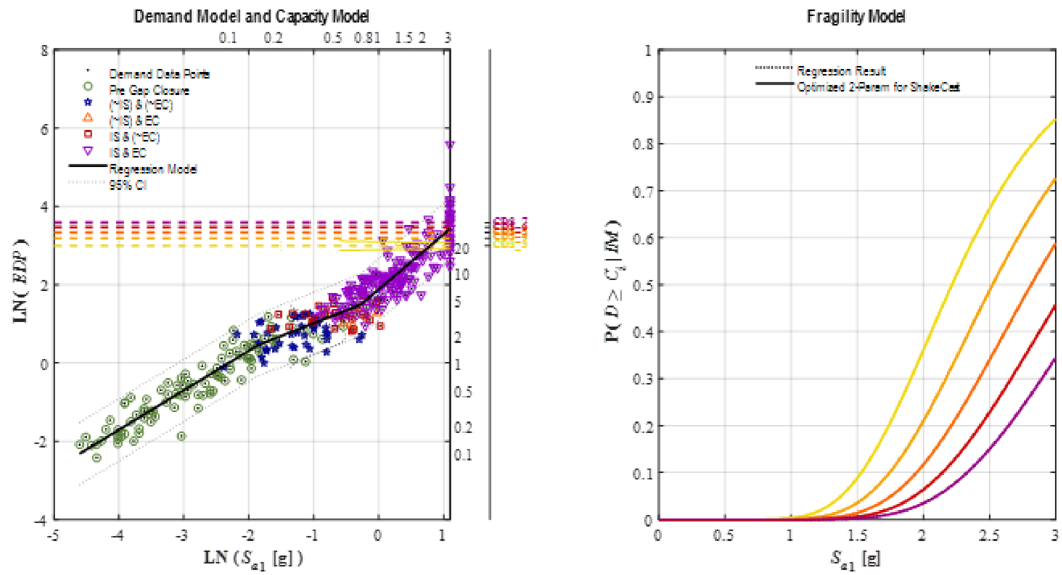

Capacity Model State Descriptions - Component Subgroup

	CDS_1	T_12	CDS_2	T_23	CDS_3	T_34	CDS_4	T_45	CDS_5	T_56	CDS_6	T_67	CDS_7	
Traffic State:	Public w/ Reduced Ride Quality		Public w/ Speed Restrictions		Public w/ Lane or Weight Restrictions		Emergency Vehicles Only w/ Restrictions		Closed (At Least) Temporarily		Closed Long-Term (Demo Equip Access)		Closed Long-Term Emergency Response	
Minimum * Remaining Net** Seat Width Range:	NA		NA	16-in	> 12-in (~14-in) Seat Remaining	12-in	> 8-in (~10-in) Seat Corner Remaining	8-in	> 4-in (~6-in) Seat Corner Remaining	4-in	< 4-in (~2-in) Seat Corner Remaining	0-in	Partially Unseated	-4-in
*Minimum Corner **Plan Seat- MR	NA		NA											

Figure F.59: Stage-0: Abutment maximum unseating damage with 36-in seat width

Level 0: Component Subgroup - Directional

Region: Abutment Joint

Component: Deck Unseating

Subgroup: Design 3: 48-in Seat w/ 2-in MR (46-in Net Seat)

Direction: Longitudinal Rotated (LR), Skew = 0 deg.

Metric: Minimum Seat Remaining

EDP: Seat Remaining Distance

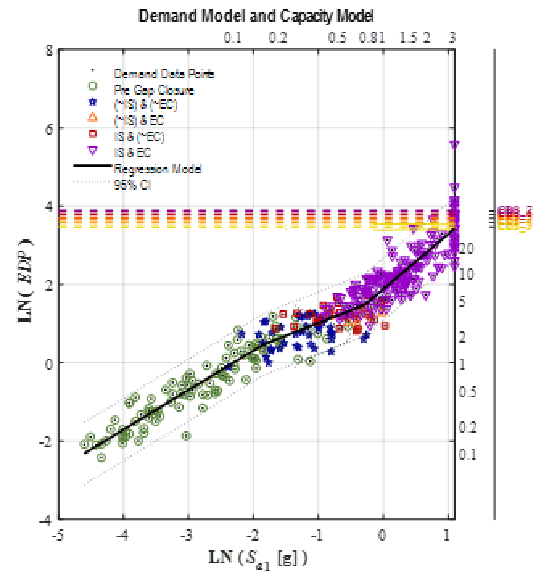

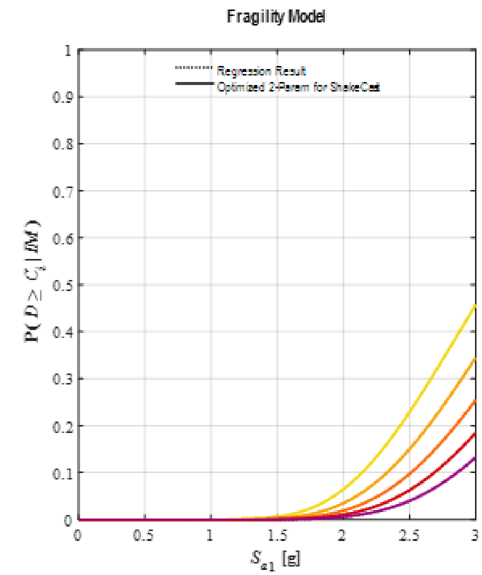

Capacity Model State Descriptions - Component Subgroup

	CDS_1	T_12	CDS_2	T_23	CDS_3	T_34	CDS_4	T_45	CDS_5	T_56	CDS_6	T_67	CDS_7	
Traffic State:	Public w/ Reduced Ride Quality		Public w/ Speed Restrictions		Public w/ Lane or Weight Restrictions		Emergency Vehicles Only w/ Restrictions		Closed (At Least) Temporarily		Closed Long-Term (Demo Equip Access)		Closed Long-Term Emergency Response	
Minimum * Remaining Net** Seat Width Range:	NA		NA	16-in	> 12-in (~14-in) Seat Remaining	12-in	> 8-in (~10-in) Seat Corner Remaining	8-in	> 4-in (~6-in) Seat Corner Remaining	4-in	< 4-in (~2-in) Seat Corner Remaining	0-in	Partially Unseated	-4-in
*Minimum Corner **Plan Seat- MR	NA		NA											

Figure F.60: Stage-0: Abutment maximum unseating damage with 48-in seat width

Level 0: Component Subgroup - Directional

Region: Abutment Joint

Component: Deck Unseating

Subgroup: Design 4: 60-in Seat w/ 2-in MR (58-in Net Seat)

Direction: Longitudinal Rotated (LR), Skew = 0 deg.

Metric: Minimum Seat Remaining

EDP: Seat Remaining Distance

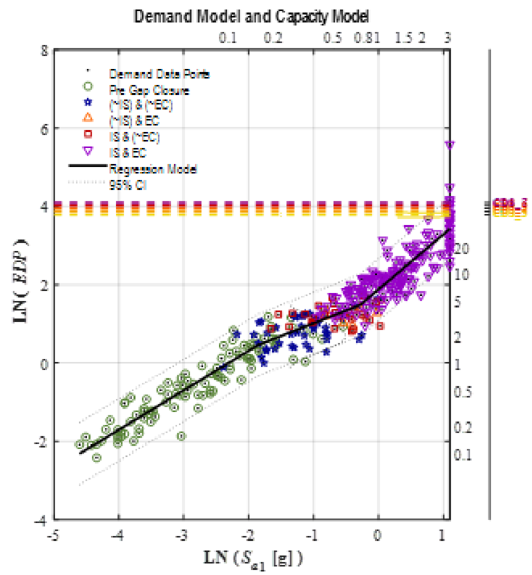

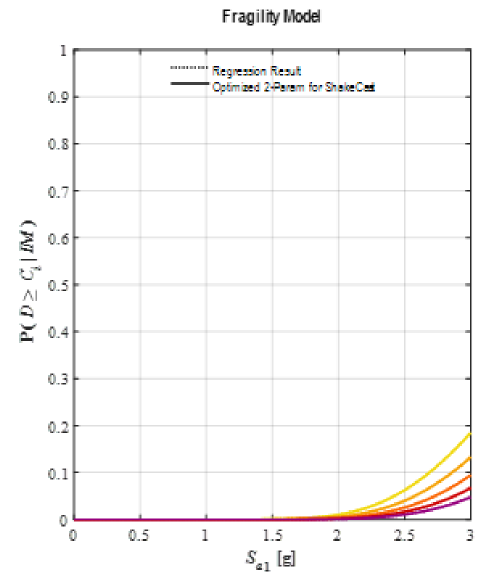

Capacity Model State Descriptions - Component Subgroup

	CDS_1		CDS_2		CDS_3		CDS_4		CDS_5		CDS_6		CDS_7	
		T_12		T_23		T_34		T_45		T_56		T_67		
Traffic State:	Public w/ Reduced Ride Quality		Public w/ Speed Restrictions		Public w/ Lane or Weight Restrictions		Emergency Vehicles Only w/ Restrictions		Closed (At Least) Temporarily		Closed Long-Term (Demo Equip Access)		Closed Long-Term Emergency Response	
Minimum * Remaining Net** Seat Width Range:	NA		NA	16-in	> 12-in (~14-in) Seat Remaining	12-in	> 8-in (~10-in) Seat Corner Remaining	8-in	> 4-in (~6-in) Seat Corner Remaining	4-in	< 4-in (~2-in) Seat Corner Remaining	0-in	Partially Unseated	-4-in
*Minimum Corner **Plan Seat- MR	NA		NA		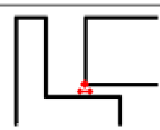		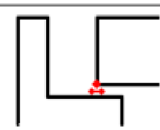		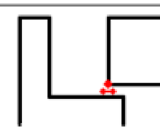		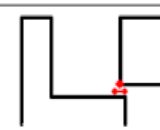		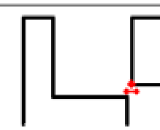	

Figure F.61: Stage-0: Abutment maximum unseating damage with 60-in seat width

Stage-B.1: Bridge Component Metrics

Region: Abutment Joint

Component: Unseating

Results Option: Minimum Seat Remaining

State Descriptions – Primary & Secondary Components

	CDS_1	T_12	CDS_2	T_23	CDS_3	T_34	CDS_4	T_45	CDS_5	T_56	CDS_6	T_67	CDS_7
g2F System State:	Observable, Mostly Aesthetic System Damage		Repairable Minor Functional System Damage		Repairable Moderate Functional System Damage		Repairable Major Functional System Damage		Stable Bridge System w/ Some Irreparable Damage		Unstable Bridge System Needing Replacement		Collapsed Bridge System Needing Replacement
Primary Component Damage:	Incidental Component Damage Full Function Intact		Minor Component Damage Core Function Intact		Moderate Component Damage Core Function Intact		Major Component Damage Restorable Function		Irreparable Component Damage (But System Stable)		Irreparable Component Damage (w System Instability)		Catastrophic Component Damage
Repairs:	Routine Maintenance		Minor Repairs of Existing Component		Substantial Repairs of Existing Component		Enhancements of Existing Component		Replacement of Components		Replacement of Bridge		Replacement of Bridge
Secondary Component Damage:	Minor Component Damage Core Function OK		Substantial Component Damage Diminished Function		Component Failure Low System Impacts		Component Failure Medium System Impacts		Component Failure High System Impacts				
Repairs:	Minor Comp. Repair, Largely Aesthetic		Major Comp. Repair To Restore Function		Replace Comp. To Restore Function		Replace Comp. & Minor System Repairs		Replace Comp. & Major System Repairs				

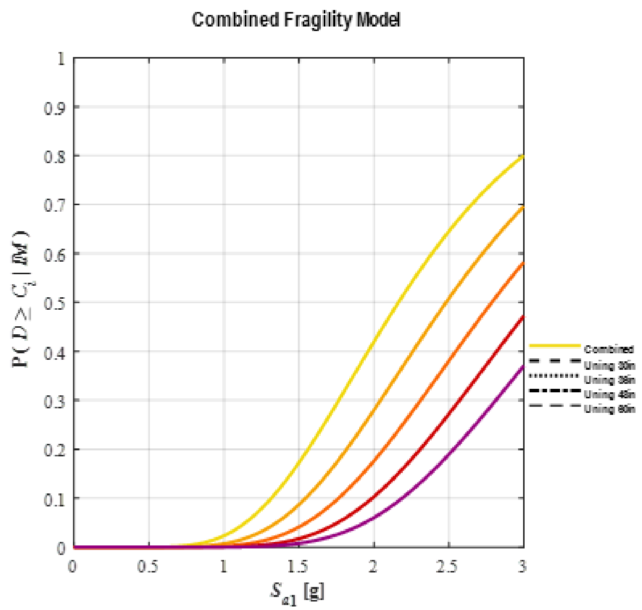

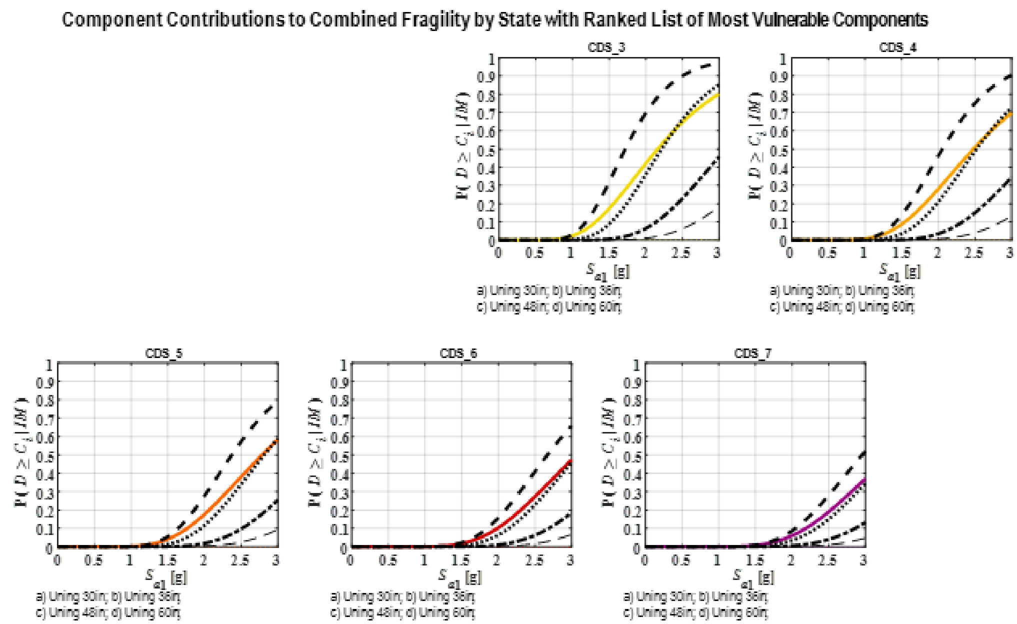

Figure F.62: Stage-B.1: Abutment maximum unseating damage.

Stage-0: Component Subgroup - Directional

Region: Abutment Joint

Component: Deck Unseating

Subgroup: Design 1: 30-in Seat w/ 2-in MR (28-in Net Seat)

Direction: Longitudinal Rotated (LR), Skew = 0 deg.

Metric: Average Seat Remaining

EDP: Seat Remaining Distance

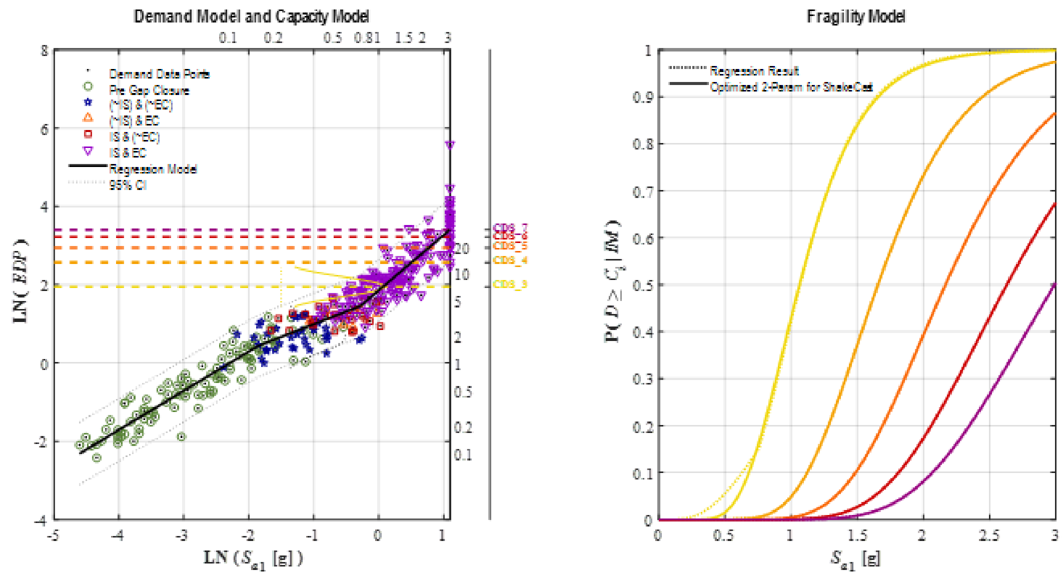

Capacity Model State Descriptions - Component Subgroup

	CDS_1	T_12	CDS_2	T_23	CDS_3	T_34	CDS_4	T_45	CDS_5	T_56	CDS_6	T_67	CDS_7	
Traffic State:	Public w/ Reduced Ride Quality		Public w/ Speed Restrictions		Public w/ Lane or Weight Restrictions		Emergency Vehicles Only w/ Restrictions		Closed (At Least) Temporarily		Closed Long-Term (Demo Equip Access)		Closed Long-Term Emergency Response	
Average * Remaining Net** Seat Width Range:	NA		NA	24-in	> 18-in (~21-in) Seat Remaining	18-in	> 12-in (~15-in) Seat Remaining	12-in	> 6-in (~9-in) Seat Remaining	6-in	< 6-in (~3-in) Seat Rem. (Mostly Cover Concrete)	0-in	Unseated (Or Within MR)	-4-in
*Average of 2 Corners **Plan Seat- MR	NA		NA											

Figure F.63: Stage-0: Abutment average unseating damage with 30-in seat width

Stage-0: Component Subgroup - Directional

Region: Abutment Joint

Component: Deck Unseating

Subgroup: Design 2: 36-in Seat w/ 2-in MR (34-in Net Seat)

Direction: Longitudinal Rotated (LR), Skew = 0 deg.

Metric: Average Seat Remaining

EDP: Seat Remaining Distance

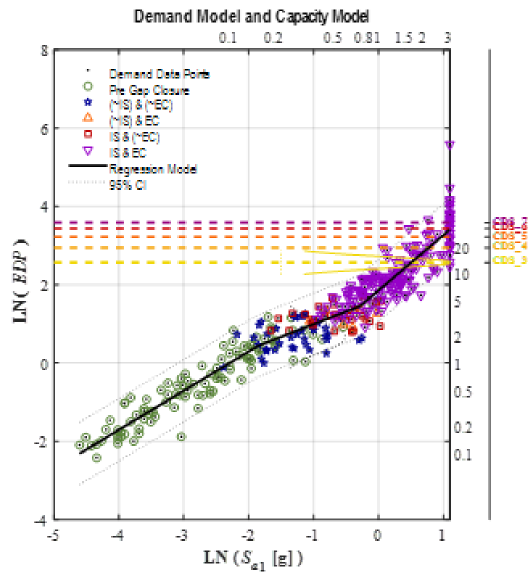

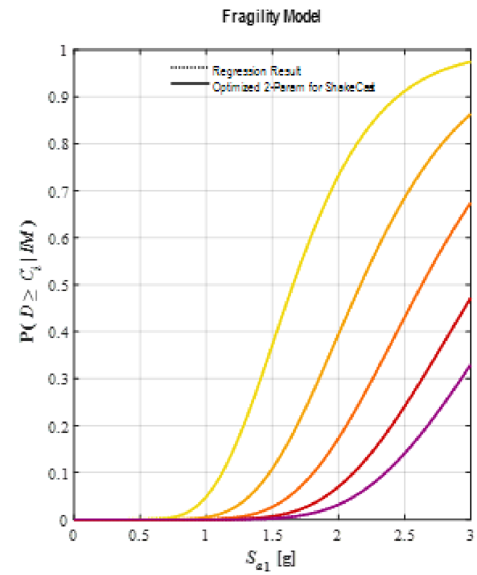

Capacity Model State Descriptions - Component Subgroup

	CDS_1	T_12	CDS_2	T_23	CDS_3	T_34	CDS_4	T_45	CDS_5	T_56	CDS_6	T_67	CDS_7	
Traffic State:	Public w/ Reduced Ride Quality		Public w/ Speed Restrictions		Public w/ Lane or Weight Restrictions		Emergency Vehicles Only w/ Restrictions		Closed (At Least) Temporarily		Closed Long-Term (Demo Equip Access)		Closed Long-Term Emergency Response	
Average * Remaining Net** Seat Width Range:	NA		NA	24-in	> 18-in (~21-in) Seat Remaining	18-in	> 12-in (~15-in) Seat Remaining	12-in	> 6-in (~9-in) Seat Remaining	6-in	< 6-in (~3-in) Seat Rem. (Mostly Cover Concrete)	0-in	Unseated (Or Within MR)	-4-in
*Average of 2 Corners **Plan Seat- MR	NA		NA											

Figure F.64: Stage-0: Abutment average unseating damage with 36-in seat width

Stage-0: **Component Subgroup - Directional**

Region: Abutment Joint

Component: Deck Unseating

Subgroup: Design 3: 48-in Seat w/ 2-in MR (46-in Net Seat)

Direction: Longitudinal Rotated (LR), Skew = 0 deg.

Metric: Average Seat Remaining

EDP: Seat Remaining Distance

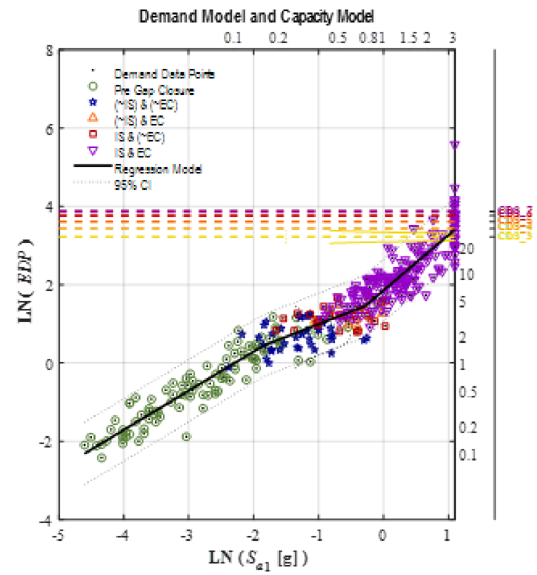

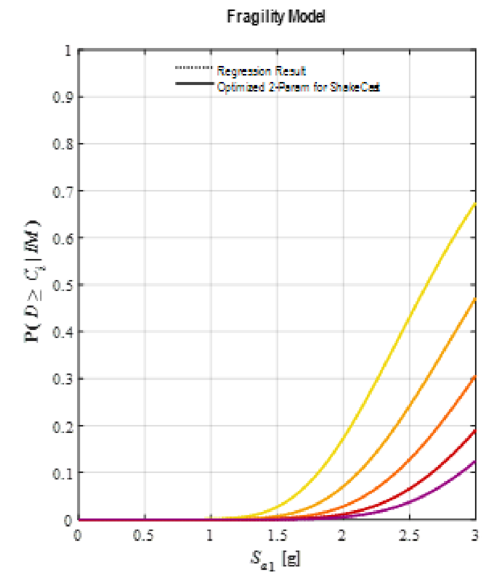

Capacity Model State Descriptions - Component Subgroup

	CDS_1	T_12	CDS_2	T_23	CDS_3	T_34	CDS_4	T_45	CDS_5	T_56	CDS_6	T_67	CDS_7	
Traffic State:	Public w/ Reduced Ride Quality		Public w/ Speed Restrictions		Public w/ Lane or Weight Restrictions		Emergency Vehicles Only w/ Restrictions		Closed (At Least) Temporarily		Closed Long-Term (Demo Equip Access)		Closed Long-Term Emergency Response	
Average * Remaining Net** Seat Width Range:	NA		NA	24-in	> 18-in (~21-in) Seat Remaining	18-in	> 12-in (~15-in) Seat Remaining	12-in	> 6-in (~9-in) Seat Remaining	6-in	< 6-in (~3-in) Seat Rem. (Mostly Cover Concrete)	0-in	Unseated (Or Within MR)	-4-in
*Average of 2 Corners **Plan Seat- MR	NA		NA											

Figure F.65: Stage-0: Abutment average unseating damage with 48-in seat width

Stage-0: Component Subgroup - Directional

Region: Abutment Joint

Component: Deck Unseating

Subgroup: Design 4: 60-in Seat w/ 2-in MR (58-in Net Seat)

Direction: Longitudinal Rotated (LR), Skew = 0 deg.

Metric: Average Seat Remaining

EDP: Seat Remaining Distance

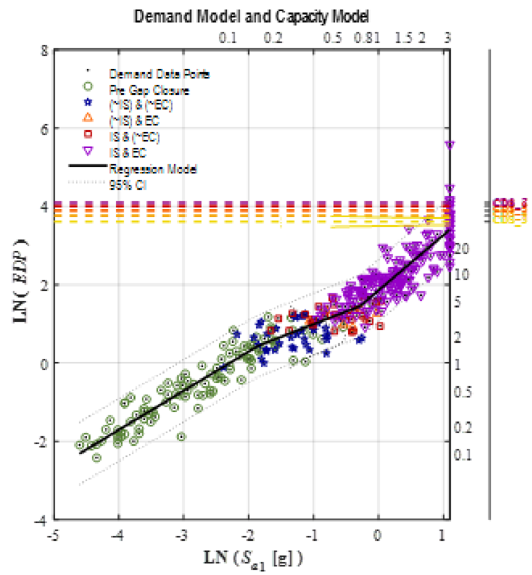

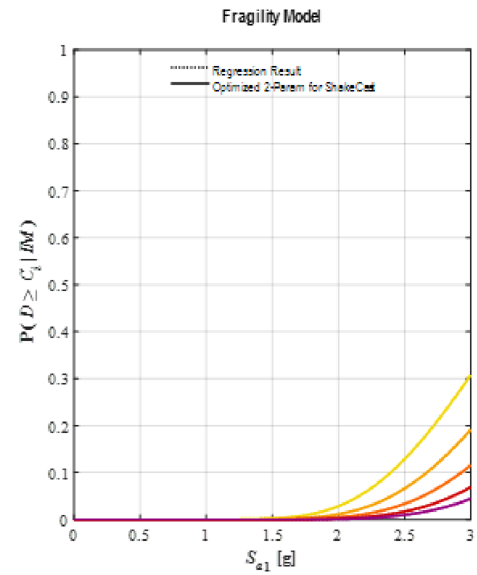

Capacity Model State Descriptions - Component Subgroup

	CDS_1	T_12	CDS_2	T_23	CDS_3	T_34	CDS_4	T_45	CDS_5	T_56	CDS_6	T_67	CDS_7	
Traffic State:	Public w/ Reduced Ride Quality		Public w/ Speed Restrictions		Public w/ Lane or Weight Restrictions		Emergency Vehicles Only w/ Restrictions		Closed (At Least) Temporarily		Closed Long-Term (Demo Equip Access)		Closed Long-Term Emergency Response	
Average * Remaining Net** Seat Width Range:	NA		NA	24-in	> 18-in (~21-in) Seat Remaining	18-in	> 12-in (~15-in) Seat Remaining	12-in	> 6-in (~9-in) Seat Remaining	6-in	< 6-in (~3-in) Seat Rem. (Mostly Cover Concrete)	0-in	Unseated (Or Within MR)	-4-in
*Average of 2 Corners **Plan Seat- MR	NA		NA											

Figure F.66: Stage-0: Abutment average unseating damage with 60-in seat width

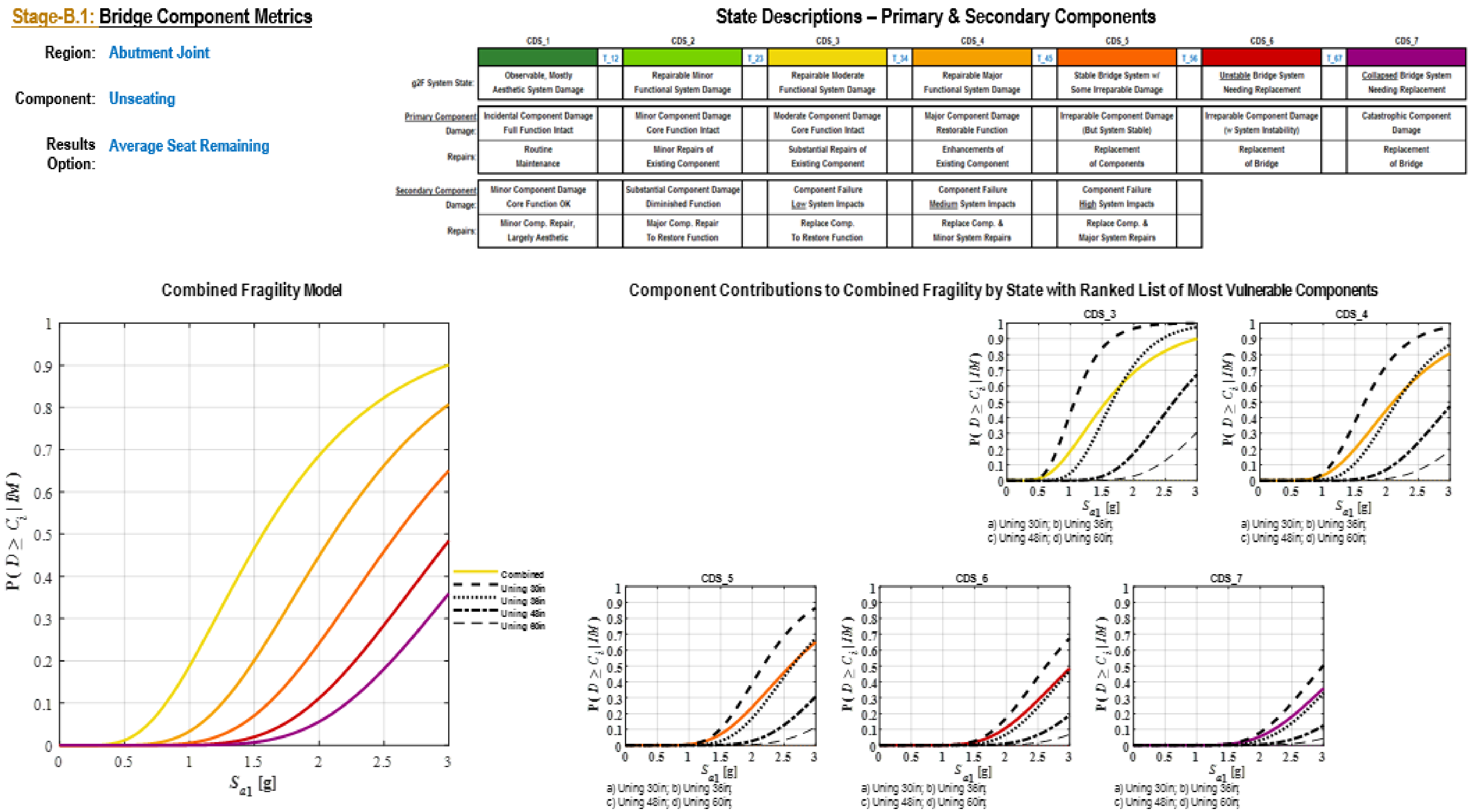

Figure F.67: Stage-B.1: Abutment average unseating damage.

Stage-B.2: **Bridge Component**

Region: Abutment Joint

Component: Deck Unseating

Results Option: Inventory Average

State Descriptions – Primary & Secondary Components

	CDS_1	T_12	CDS_2	T_23	CDS_3	T_34	CDS_4	T_45	CDS_5	T_56	CDS_6	T_67	CDS_7
g2F System State:	Observable, Mostly Aesthetic System Damage		Repairable Minor Functional System Damage		Repairable Moderate Functional System Damage		Repairable Major Functional System Damage		Stable Bridge System w/ Some Irreparable Damage		Unstable Bridge System Needing Replacement		Collapsed Bridge System Needing Replacement
Primary Component Damage:	Incidental Component Damage Full Function Intact		Minor Component Damage Core Function Intact		Moderate Component Damage Core Function Intact		Major Component Damage Restorable Function		Irreparable Component Damage (But System Stable)		Irreparable Component Damage (w System Instability)		Catastrophic Component Damage
Repairs:	Routine Maintenance		Minor Repairs of Existing Component		Substantial Repairs of Existing Component		Enhancements of Existing Component		Replacement of Components		Replacement of Bridge		Replacement of Bridge
Secondary Component Damage:	Minor Component Damage Core Function OK		Substantial Component Damage Diminished Function		Component Failure Low System Impacts		Component Failure Medium System Impacts		Component Failure High System Impacts				
Repairs:	Minor Comp. Repair, Largely Aesthetic		Major Comp. Repair To Restore Function		Replace Comp. To Restore Function		Replace Comp. & Minor System Repairs		Replace Comp. & Major System Repairs				

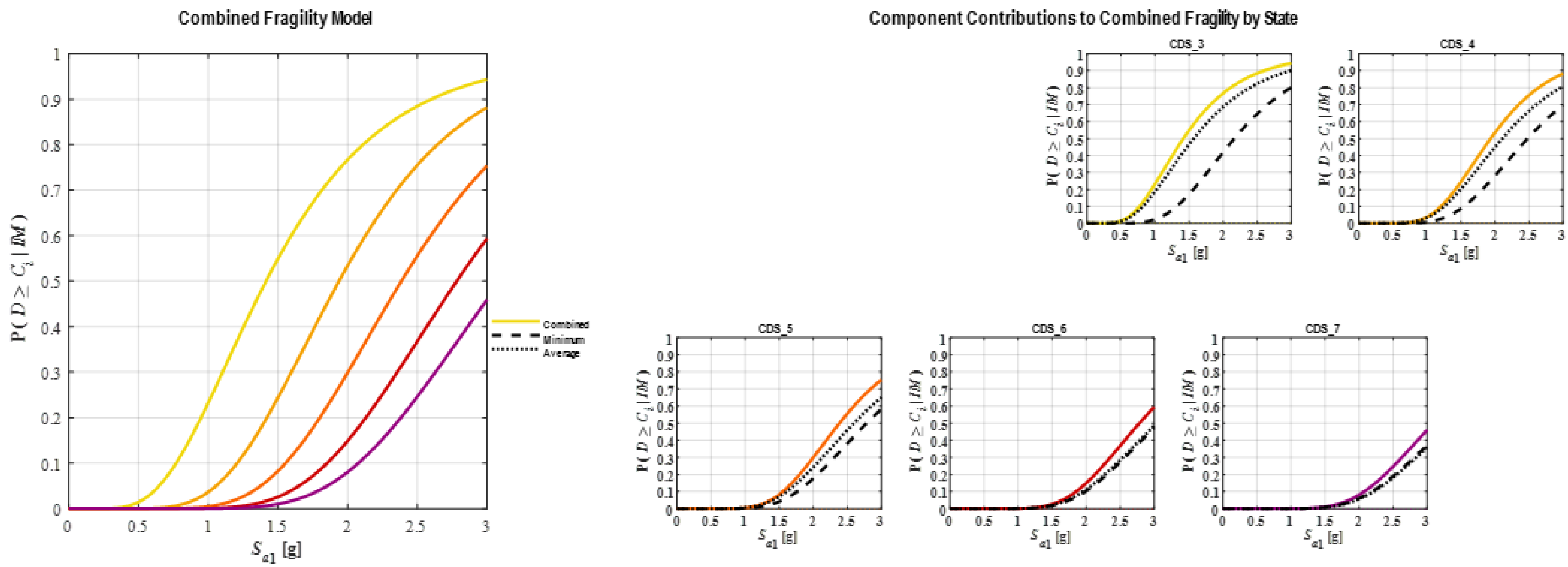

Figure F.68: Stage-B.2: Abutment unseating damage.

Stage-0: Component Subgroup - Directional

Region: Abutment Joint

Component: Backwall w/ compression joint

Subgroup: NA

Direction: Longitudinal Rotated (LR), Skew = 0 deg.

Metric: Lateral Displacement Ductility

EDP: Double-Normalized R5P Performance Point

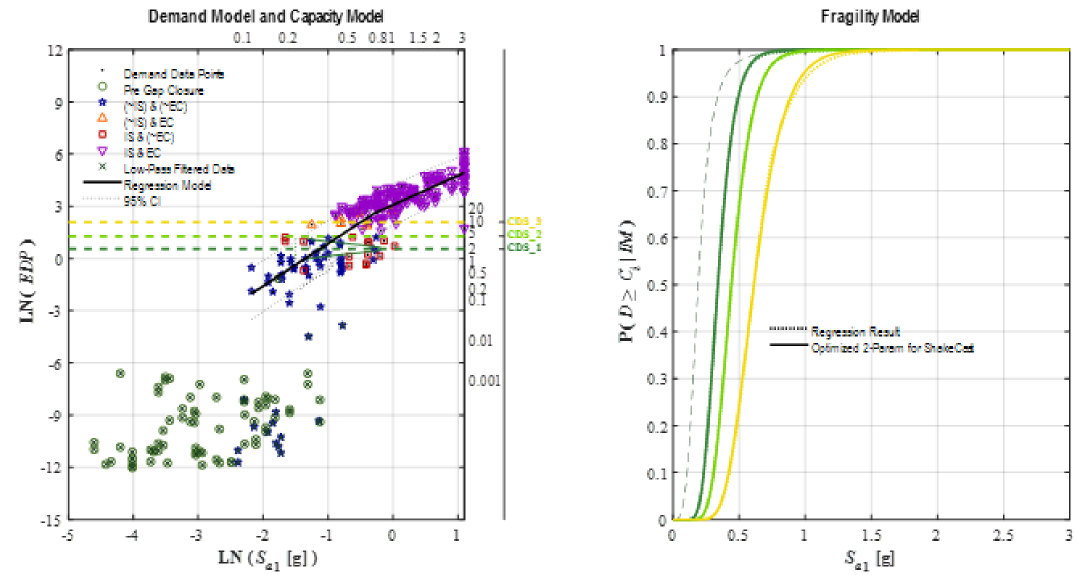

Capacity Model State Descriptions - Component Subgroup

	CDS_1	T_12	CDS_2	T_23	CDS_3	T_34	CDS_4	T_45	CDS_5	T_56	CDS_6	T_67	CDS_7
Typical Performance:	Initial Plastic Deformation Near Full Lateral Capacity		Fused w/ Rapidly Degradiing Lateral Capacity		Fully Fused, Only Minor Residual Capacity Remaining								
Backwall-Connection Damage:	Minor Cracking Along Diagonal Shear Plane in Connection Region		Clear Shear-Plane Formation w/ Major Cracking/Spalling, and Initial Gap Opening		Shear-Plane Gap Opening & Major Rebar Deformation w/ Possible Fracture or Pullout								
Normalized Force-Disp. Backbone Response Range:	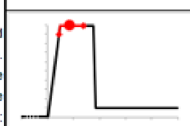		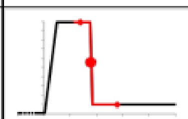		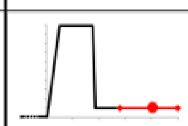								

Figure F.69: Stage-0: Abutment backwall damage with compression seal

Stage-0: Component Subgroup - Directional

Region: Abutment Joint

Component: Backwall w/ strip seal joint

Subgroup: NA

Direction: Longitudinal Rotated (LR), Skew = 0 deg.

Metric: Lateral Displacement Ductility

EDP: Double-Normalized R5P Performance Point

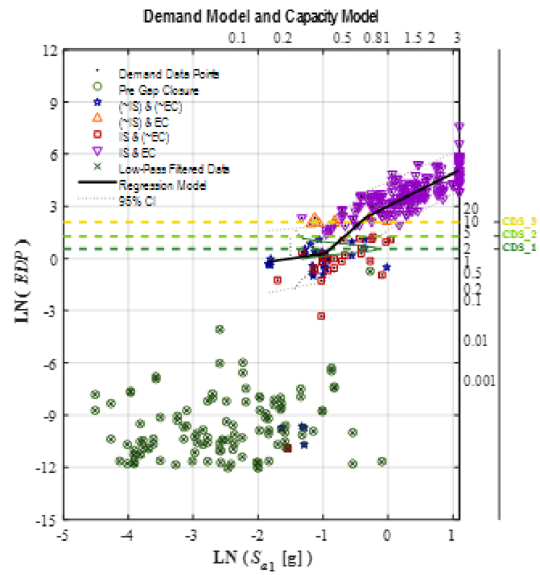

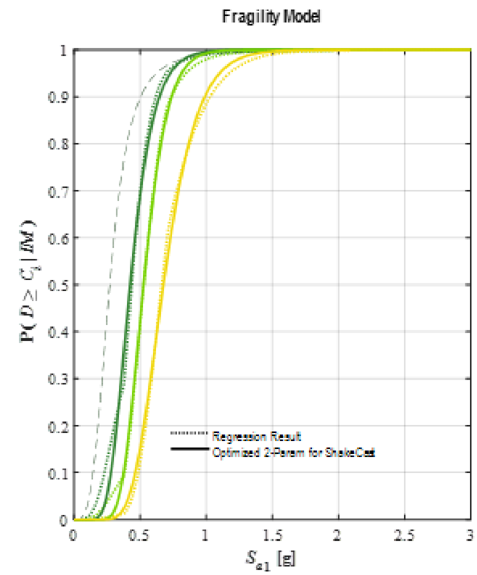

Capacity Model State Descriptions - Component Subgroup

	CDS_1	T_12	CDS_2	T_23	CDS_3	T_34	CDS_4	T_45	CDS_5	T_56	CDS_6	T_67	CDS_7
Typical Performance:	Initial Plastic Deformation Near Full Lateral Capacity		Fused w/ Rapidly Degradiing Lateral Capacity		Fully Fused, Only Minor Residual Capacity Remaining								
Backwall-Connection Damage:	Minor Cracking Along Diagonal Shear Plane in Connection Region		Clear Shear-Plane Formation w/ Major Cracking/Spalling, and Initial Gap Opening		Shear-Plane Gap Opening & Major Rebar Deformation w/ Possible Fracture or Pullout								
Normalized Force-Disp. Backbone Response Range:	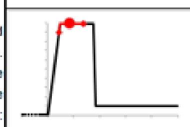		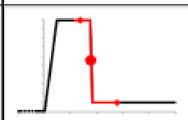		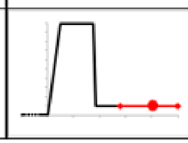								

Figure F.70: Stage-0: Abutment backwall damage with strip seal

Stage-0: Component Subgroup - Directional

Region:	Abutment Joint
Component:	Elastomeric Pad Bearing
Subgroup:	NA
Direction:	Omnidirectional
Metric:	Lateral Bearing Damage
EDP:	Bearing Shear Strain

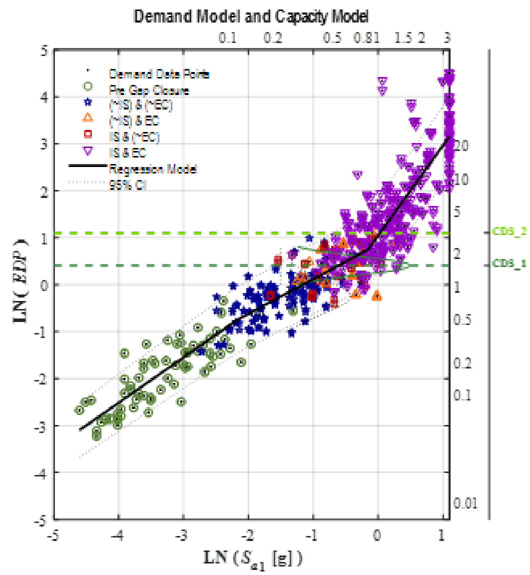

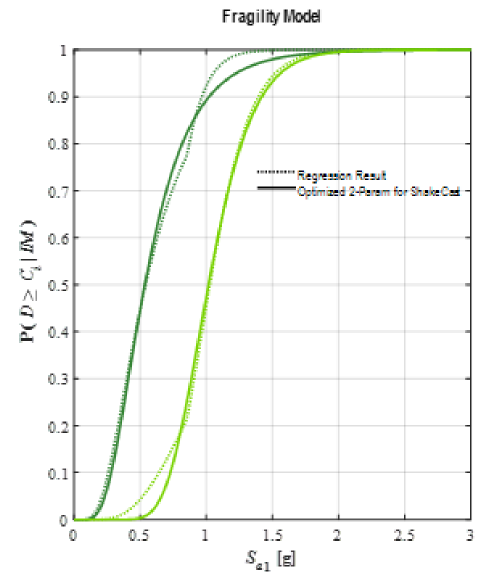

Capacity Model State Descriptions - Component Subgroup

	CDS_1	T_12	CDS_2	T_23	CDS_3	T_34	CDS_4	T_45	CDS_5	T_56	CDS_6	T_67	CDS_7
Typical Performance:	Initial Inelastic Deformation		Major Bearing Damage or Dislocation										
Elastomeric Bearing Damage:	Minor Distortions or Degradation of Elastomer		Elastomer Tearing or Bearing Rollup/Distortion; Bearing Sliding Dislocation										
Shear-Strain Range:	150		300%										

Figure F.71: Stage-B.1: Abutment backwall damage

Stage-0: Component Subgroup - Directional

Region: Abutment Joint

Component: Joint Seal

Subgroup: Compression

Direction: Longitudinal Rotated (LR), Skew = 0 deg.

Metric: Deck Relative to Backwall (Active)

EDP: Movement Rating

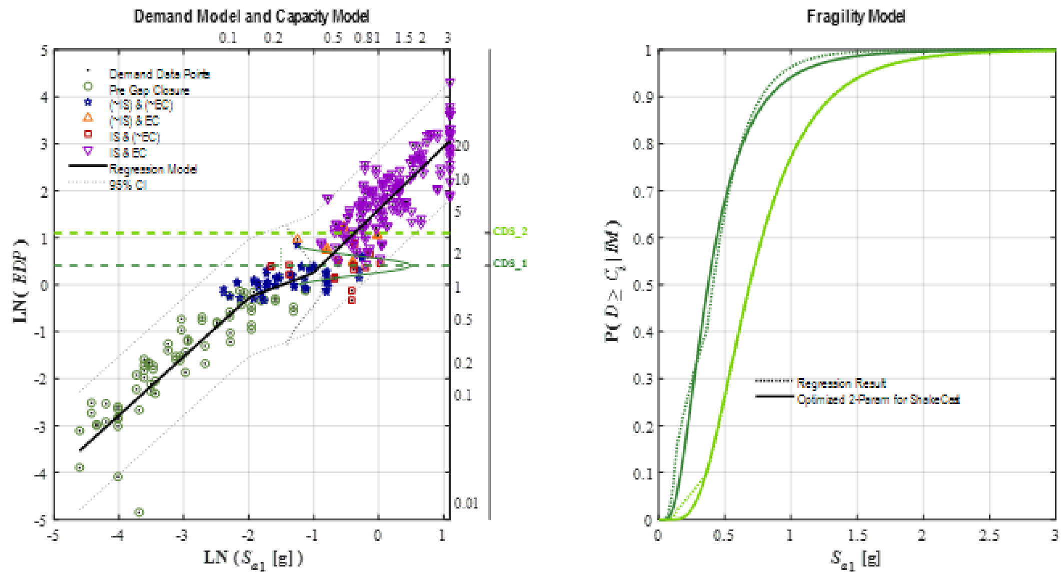

Capacity Model State Descriptions - Component Subgroup

	CDS_1	T_12	CDS_2	T_23	CDS_3	T_34	CDS_4	T_45	CDS_5	T_56	CDS_6	T_67	CDS_7
Typical Performance:	Moderate Exceedence of Seal-Design MR		Extreme Exceedence of Seal-Design MR										
Compression Seal Damage:	Minor Dislocation and/or Pinching of Seal		Extensive Dislocation and/or Pinching of Seal										
Joint Gap Opening Range:	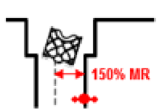 150% MR	200%	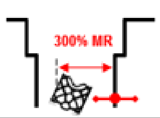 300% MR										

Figure F.72: Stage-0: Abutment joint seal damage with compression seal

Level 0: Component Subgroup - Directional

Region: Abutment Joint

Component: Joint Seal

Subgroup: Strip

Direction: Longitudinal Rotated (LR), Skew = 0 deg.

Metric: Deck Relative to Backwall (Active)

EDP: Movement Rating

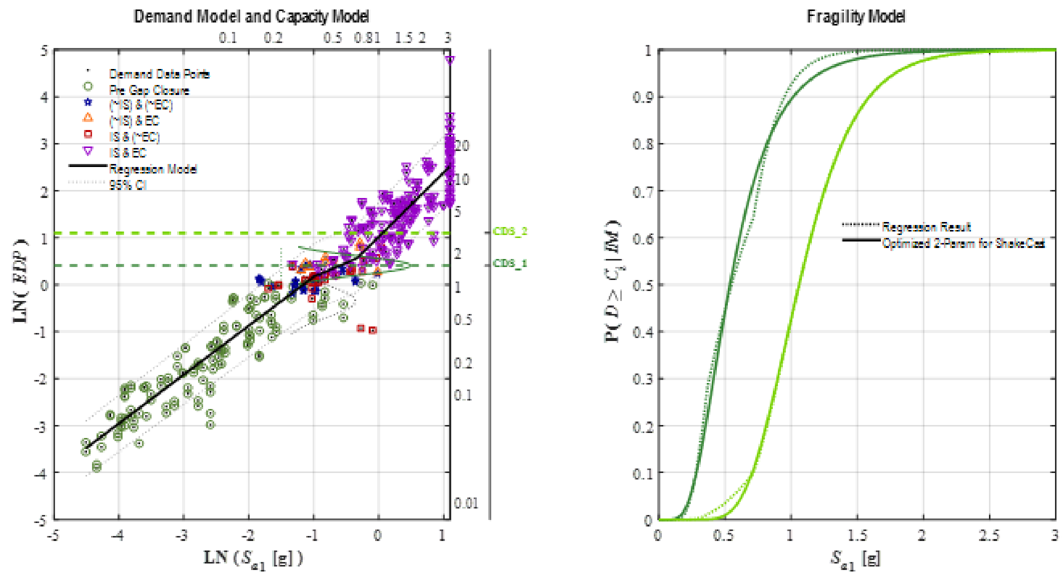

Capacity Model State Descriptions - Component Subgroup

	CDS_1	T_12	CDS_2	T_23	CDS_3	T_34	CDS_4	T_45	CDS_5	T_56	CDS_6	T_67	CDS_7
Typical Performance:	Moderate Exceedence of Seal-Design MR		Extreme Exceedence of Seal-Design MR										
Likely Seal Damage:	Minor Tearing and/or Partial Pullout of Seal Strip		Extensive Tearing and/or Pullout of Seal Strip; Minor Pounding Damage to Assembly										
Joint Gap Opening Range:	MR 150% MR		MR 300% MR										

Figure F.73: Stage-0: Abutment joint seal damage with strip seal

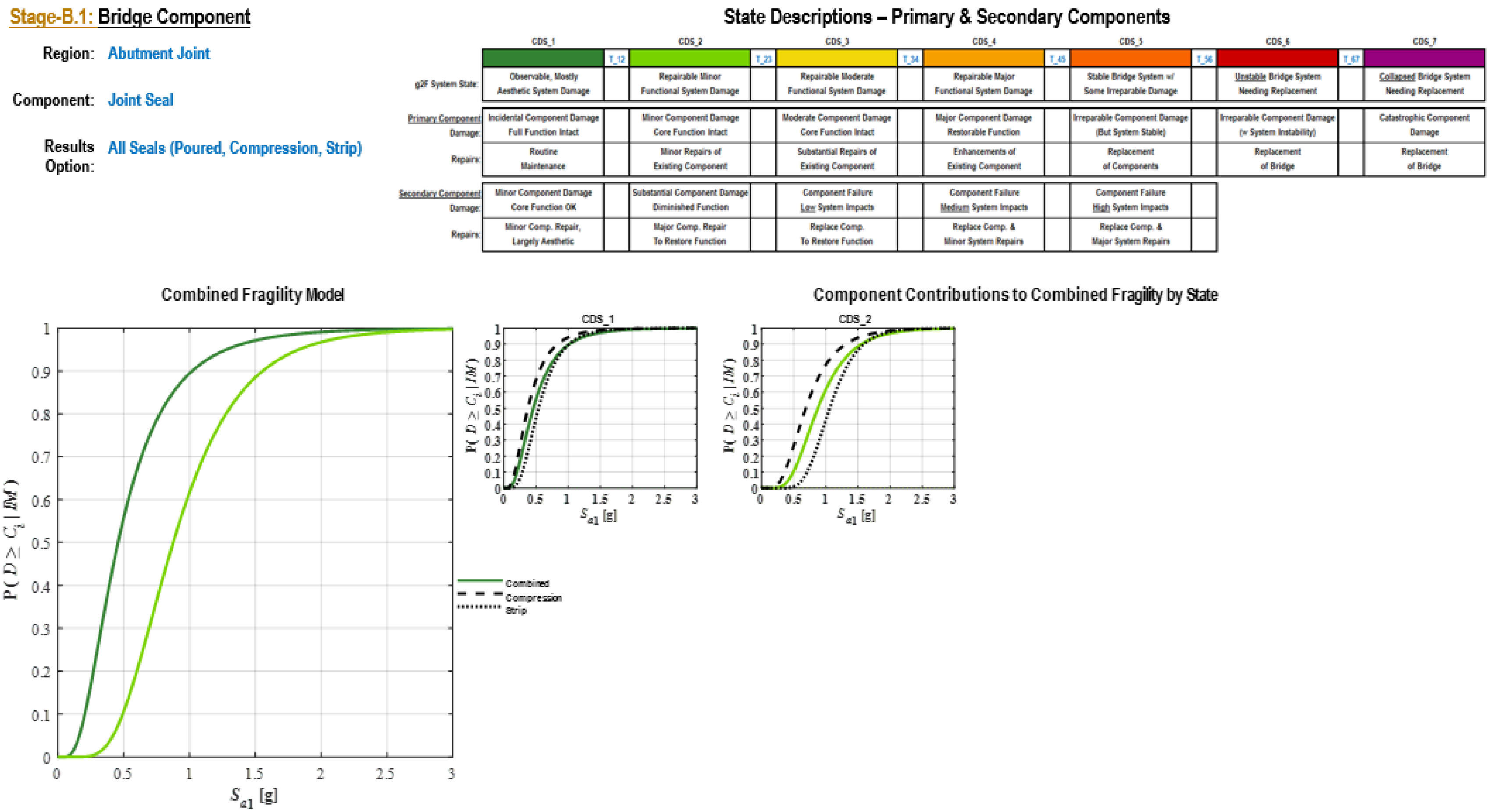

Figure F.74: Stage-B.1: Abutment joint seal damage

Stage-0: Component Subgroup - Directional

Region: Abutment Joint

Component: Pounding - Faces

Subgroup: Compression seal

Direction: Longitudinal Rotated (LR), Skew = 0 deg.

Metric: Abutment Backwall Surface Damage

EDP: Passive Displacement Ductility

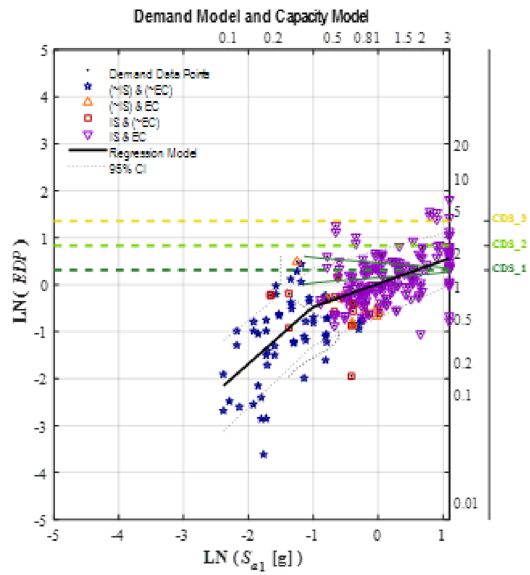

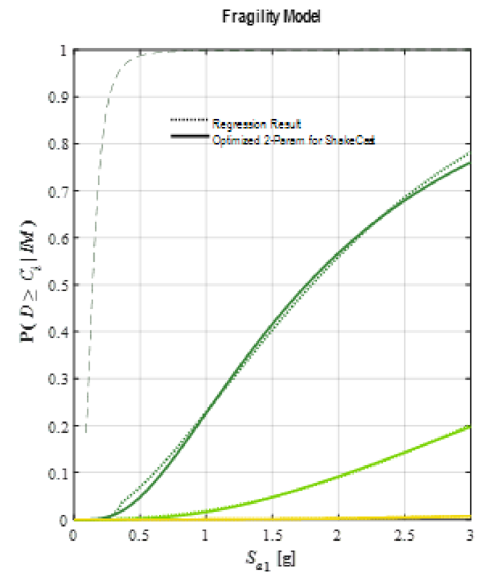

Capacity Model State Descriptions - Component Subgroup

	CDS_1	T_12	CDS_2	T_23	CDS_3	T_34	CDS_4	T_45	CDS_5	T_56	CDS_6	T_67	CDS_7
Typical Performance:	Initial Pounding Damage		Moderate Pounding Damage		Extensive Pounding Damage								
Pounding Damage To Broad Faces:	Minor Near-Surface Cracking & Chipping of Impacting Elements		Moderate Surface Spalling & Crack Penetration Deeper Into Impacting Elements		Crushing, w/ Major Spalling & Cracking Deep (~12-in) Into Impacting Elements								
Norm Force-Displ. Response Range:	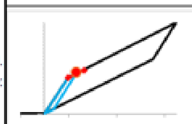		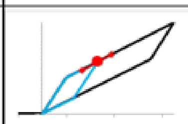		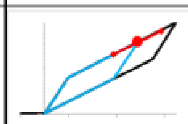								

Figure F.75: Stage-0: Abutment joint pounding damage with compression seal

Stage-0: Component Subgroup - Directional

Region:	Abutment Joint
Component:	Pounding - Faces
Subgroup:	Strip seal
Direction:	Longitudinal Rotated (LR), Skew = 0 deg.
Metric:	Abutment Backwall Surface Damage
EDP:	Passive Displacement Ductility

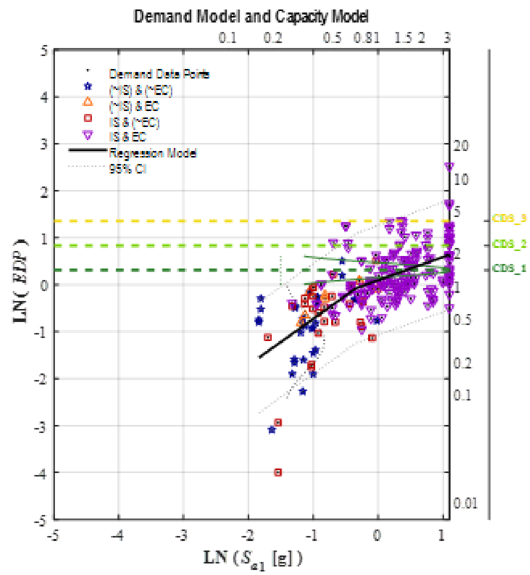

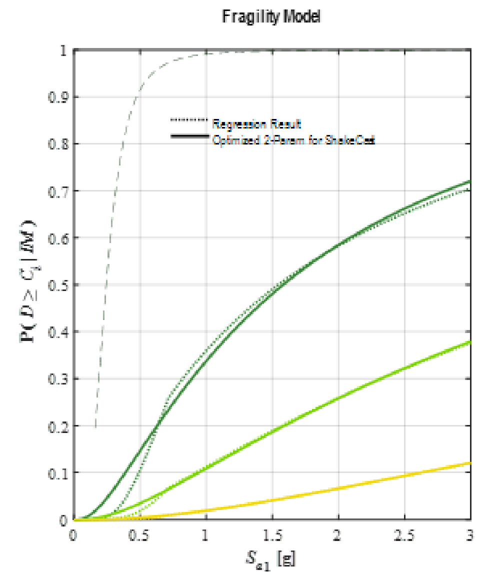

Capacity Model State Descriptions - Component Subgroup

	CDS_1	T_12	CDS_2	T_23	CDS_3	T_34	CDS_4	T_45	CDS_5	T_56	CDS_6	T_67	CDS_7
Typical Performance:	Initial Pounding Damage		Moderate Pounding Damage		Extensive Pounding Damage								
Pounding Damage To Broad Faces:	Minor Near-Surface Cracking & Chipping of Impacting Elements		Moderate Surface Spalling & Crack Penetration Deeper Into Impacting Elements		Crushing, w/ Major Spalling & Cracking Deep (~12-in) Into Impacting Elements								
Norm Force-Displ. Response Range:	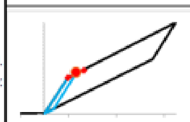		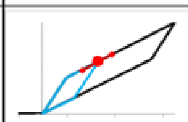		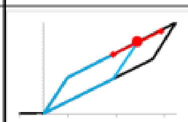								

Figure F.76: Stage-0: Abutment joint pounding damage with strip seal

Stage-B.1: Bridge Component

Region: Abutment Joint

Component: Pounding

Results Option: Inventory Average

State Descriptions – Primary & Secondary Components

	CDS_1	T_12	CDS_2	T_23	CDS_3	T_34	CDS_4	T_45	CDS_5	T_56	CDS_6	T_67	CDS_7
g2F System State:	Observable, Mostly Aesthetic System Damage		Repairable Minor Functional System Damage		Repairable Moderate Functional System Damage		Repairable Major Functional System Damage		Stable Bridge System w/ Some Irreparable Damage		Unstable Bridge System Needing Replacement		Collapsed Bridge System Needing Replacement
Primary Component Damage:	Incidental Component Damage Full Function Intact		Minor Component Damage Core Function Intact		Moderate Component Damage Core Function Intact		Major Component Damage Restorable Function		Irreparable Component Damage (But System Stable)		Irreparable Component Damage (w System Instability)		Catastrophic Component Damage
Repairs:	Routine Maintenance		Minor Repairs of Existing Component		Substantial Repairs of Existing Component		Enhancements of Existing Component		Replacement of Components		Replacement of Bridge		Replacement of Bridge
Secondary Component Damage:	Minor Component Damage Core Function OK		Substantial Component Damage Diminished Function		Component Failure Low System Impacts		Component Failure Medium System Impacts		Component Failure High System Impacts				
Repairs:	Minor Comp. Repair, Largely Aesthetic		Major Comp. Repair To Restore Function		Replace Comp. To Restore Function		Replace Comp. & Minor System Repairs		Replace Comp. & Major System Repairs				

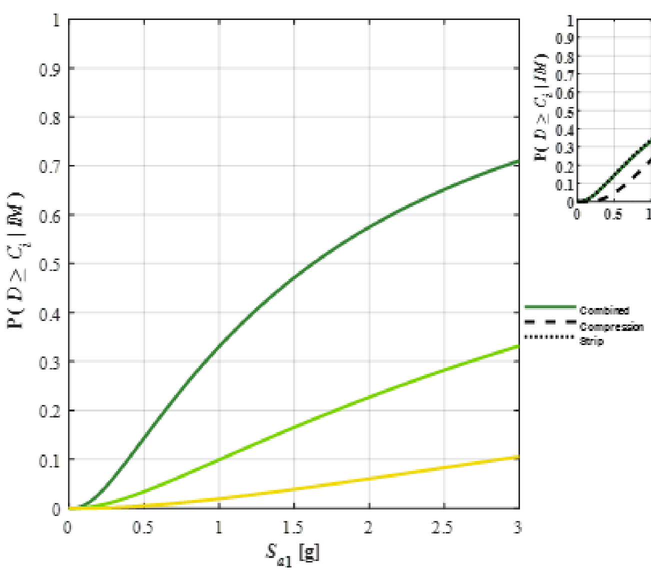

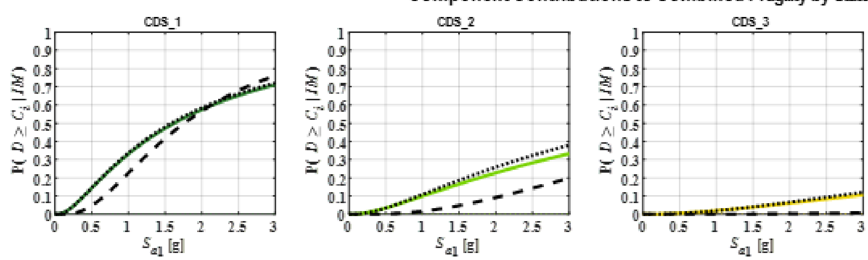

Figure F.77: Stage-B.1: Abutment joint pounding damage

Stage-0: Component Subgroup - Directional

Region:	Abutment Joint
Component:	Shear Key
Subgroup:	External Shear Key
Direction:	Transverse Bridge (TB), Skew = 0 deg.
Metric:	Lateral Displacement Ductility
EDP:	Double-Normalized R5P Performance Point

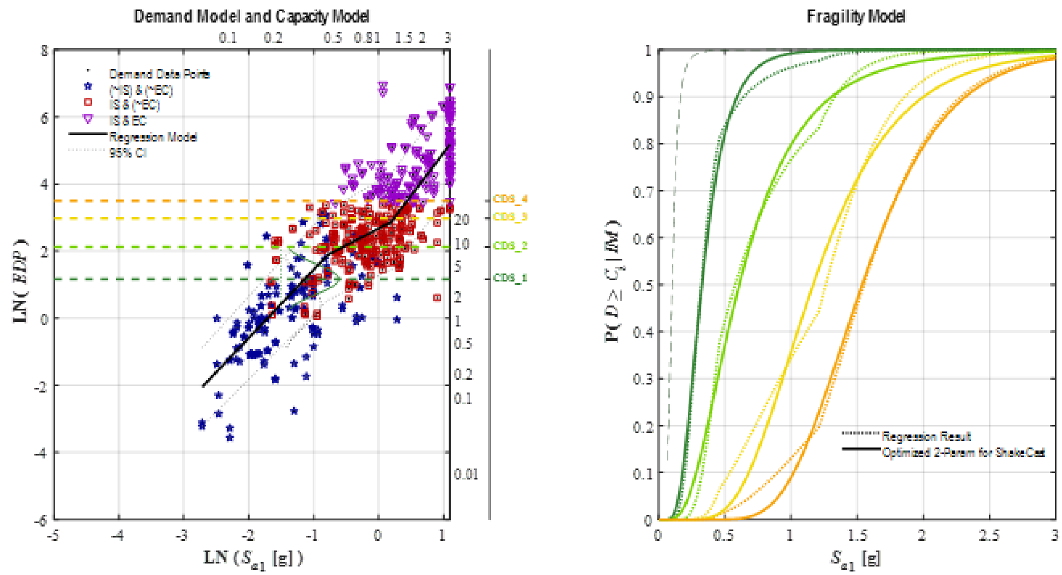

Capacity Model State Descriptions - Component Subgroup

	CDS_1	T_12	CDS_2	T_23	CDS_3	T_34	CDS_4	T_45	CDS_5	T_56	CDS_6	T_67	CDS_7
Typical Performance:	Initial Loss of Lateral Stiffness		Fusing - Near Ultimate Lateral Capacity		Plastic Deformation - Degrading Lateral Capacity		Fully Fused, Diminishing to No Residual Capacity						
Shear Key Damage:	Minor Inclined Cracking in Connection Region; Small Crack Width		Clear Shear-Plane Formation w/ Crack Opening & Minor Spalling w/o Rebar Exposure; Strength Largely Intact		Shear-Plane Gap Opening; Significant Spalling w/ Core Exposure & Some Crushing & Initial Rebar Deformation		Large Displacement and/or Rotation; Large Diagonal Gap w/ Major Core Crushing, Rebar Deformation & Fracture						
Normalized Force-Disp. Backbone Response Range:	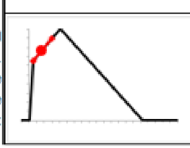				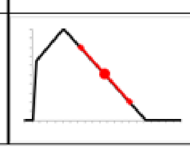		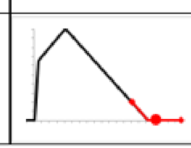						

Figure F.78: Stage-0: Abutment external non-isolated shear key damage

Stage-0: Component Subgroup - Directional

Region: Abutment Joint

Component: Elastomeric Pad Bearing

Subgroup: NA

Direction: Omnidirectional

Metric: Lateral Bearing Damage

EDP: Bearing Shear Strain

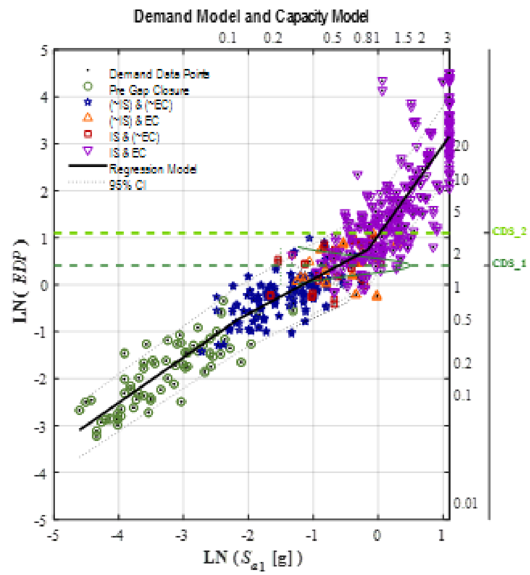

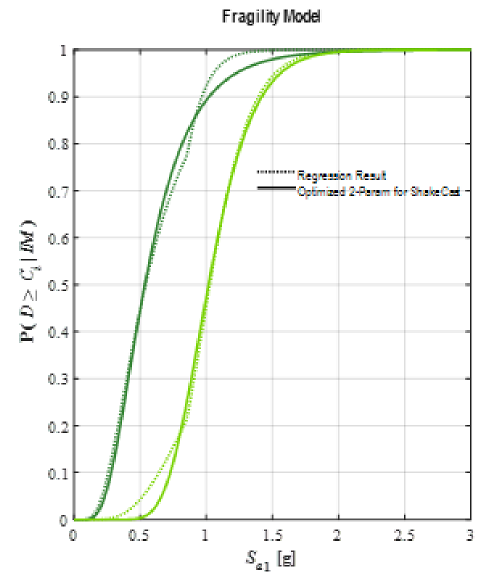

Capacity Model State Descriptions - Component Subgroup

	CDS_1	T_12	CDS_2	T_23	CDS_3	T_34	CDS_4	T_45	CDS_5	T_56	CDS_6	T_67	CDS_7
Typical Performance:	Initial Inelastic Deformation		Major Bearing Damage or Dislocation										
Elastomeric Bearing Damage:	Minor Distortions or Degradation of Elastomer		Elastomer Tearing or Bearing Rollup/Distortion; Bearing Sliding Dislocation										
Shear-Strain Range:	150		300%										

Figure F.79: Stage-0: Abutment elastomeric bearing pads damage

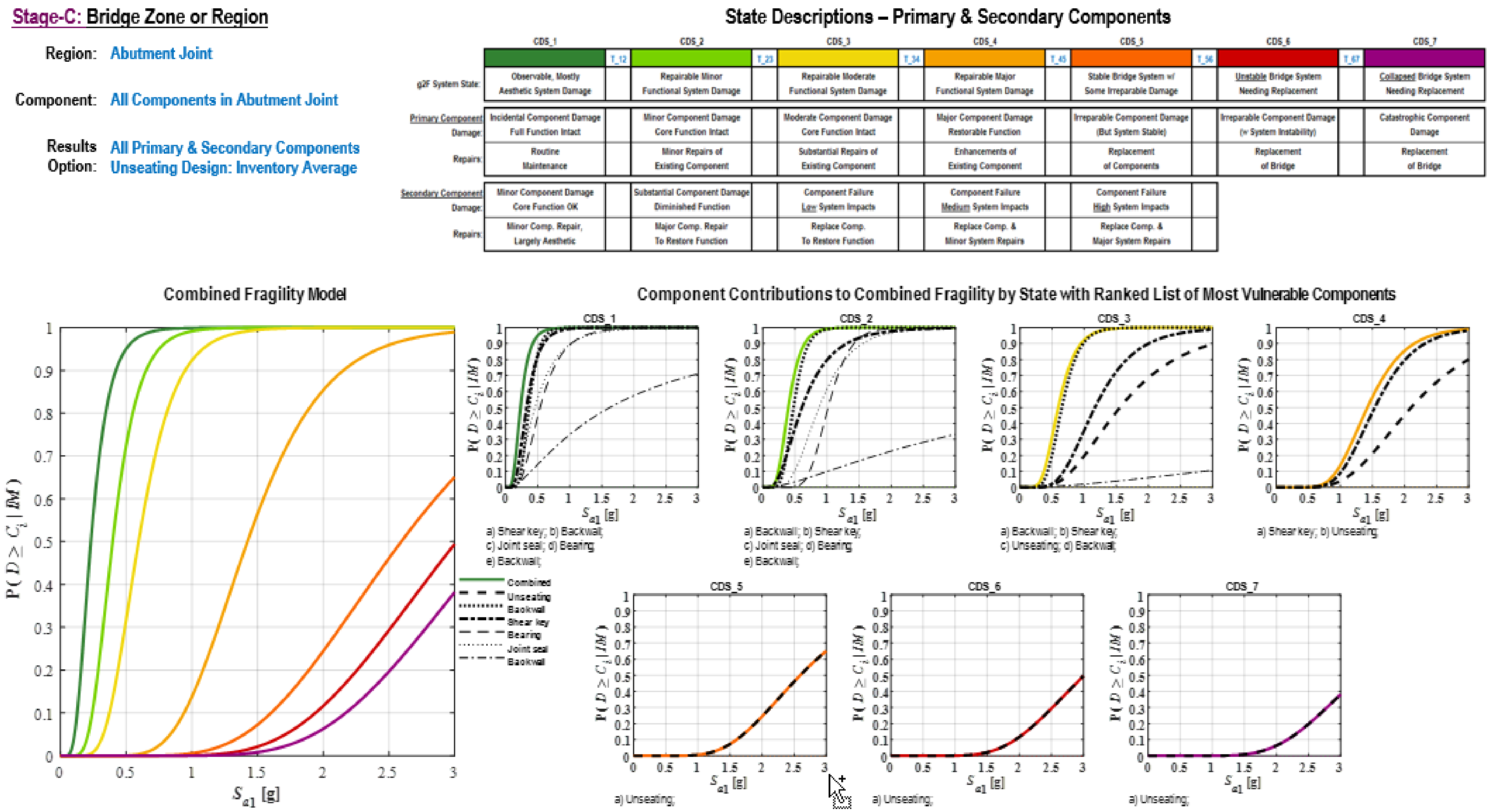

Figure F.80: Stage-C roll-up: Abutment joint damage.

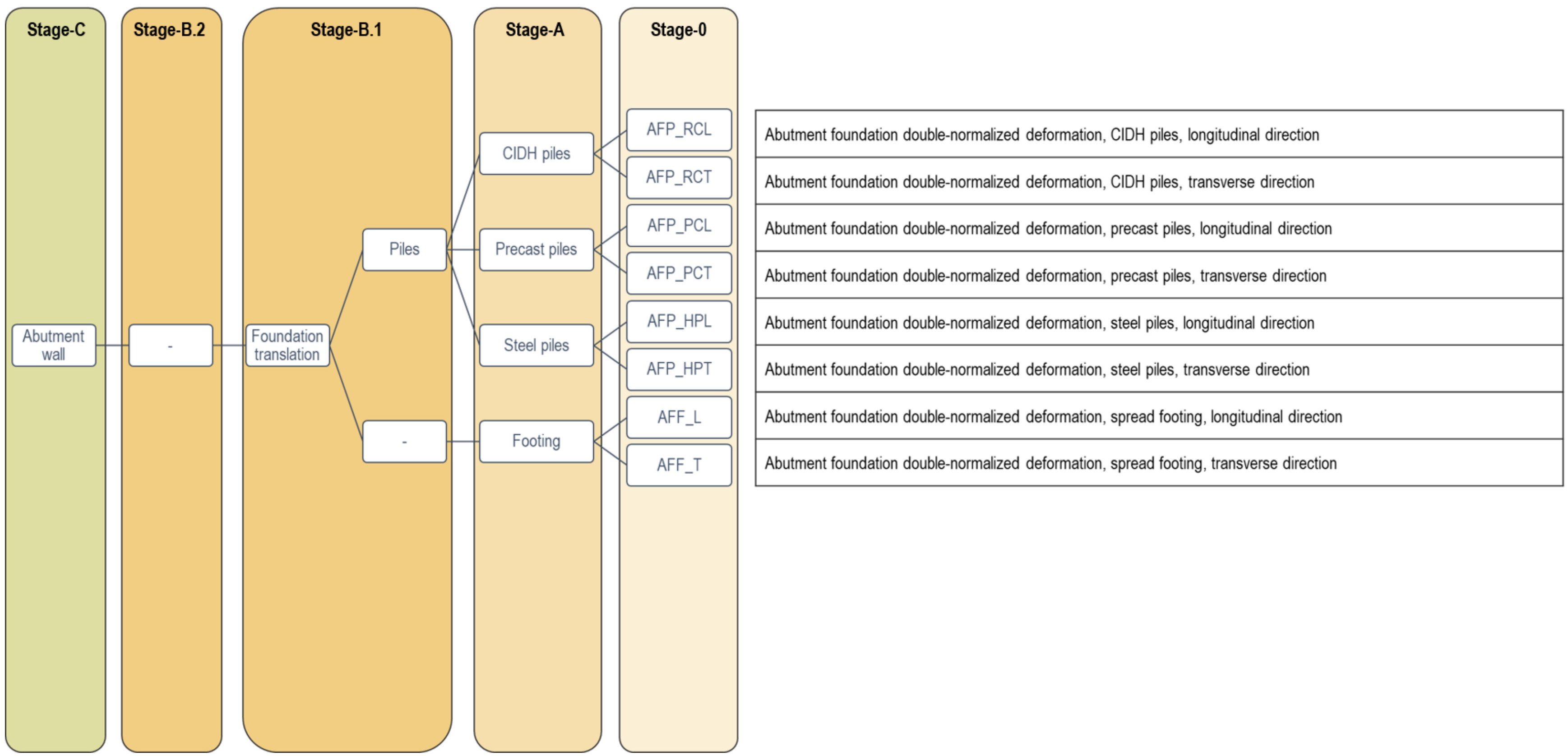

Figure F.81: Roll-up steps to create a Stage-C fragility model for abutment wall response.

Stage-0: Component Subgroup - Directional

Region: Abutment Wall Region

Component: Abutment Wall Foundation

Subgroup: CIDH-Pile Foundation

Direction: Longitudinal Rotated (LR), Skew = 0 deg.

Metric: Translational Pile Damage

EDP: Normalized R5P Performance Point

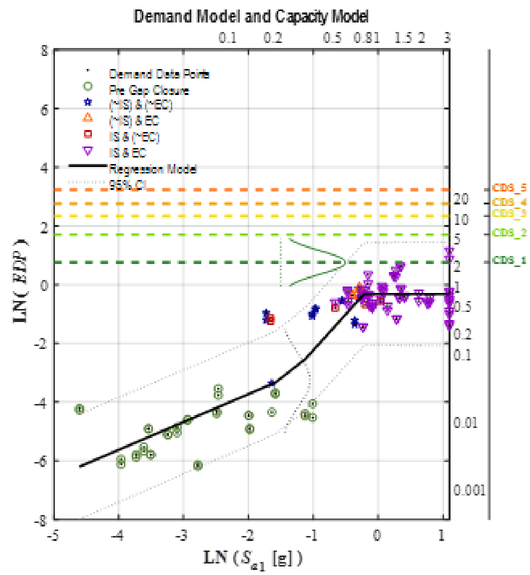

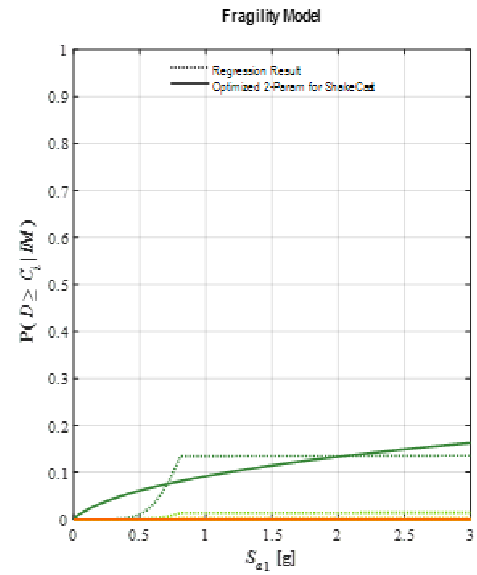

Capacity Model State Descriptions - Component Subgroup

	CDS_1	T_12	CDS_2	T_23	CDS_3	T_34	CDS_4	T_45	CDS_5	T_56	CDS_6	T_67	CDS_7
CIDH-Pile Performance:	Initial Loss of Lateral Stiffness		Approaching Lateral Capacity		Degrading Lateral Capacity		Residual Lateral Capacity		Loss of Lateral (& Axial?) Capacity				
CIDH-Pile Foundation Damage:	Initial Minor Cracking/Spalling Damage at Pile Head (Future Corrosion)		Initial Pile-Head Hinging w/ Substantial Cracking/Spalling & Minor Rebar Yield		Well Developed Pile-Head Hinge w/ Major Rebar Yield & Core Crushing; Initial 2nd Hinge Below Ground		Buckling & Fracture of Rebar & Hoop Fracture at Pile Head; Fully Formed 2nd Hinge Below Ground		Large Displacement & Pile Rotation; Possible Detachment at Pile Cap; Major Loss of Lateral & Axial Capacity				
Normalized Pile-Head Translational Force v. Displacement Response Range	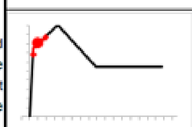		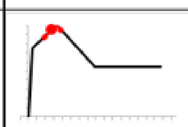		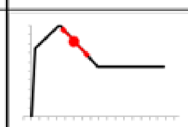		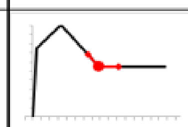		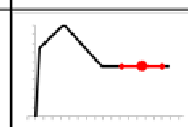				

Figure F.82: Stage-0: CIDH abutment pile foundation damage in longitudinal direction

Stage-0: Component Subgroup - Directional

Region: Abutment Wall Region

Component: Abutment Wall Foundation

Subgroup: CIDH-Pile Foundation

Direction: Transverse Rotated (TR), Skew = 0 deg.

Metric: Translational Pile Damage

EDP: Normalized R5P Performance Point

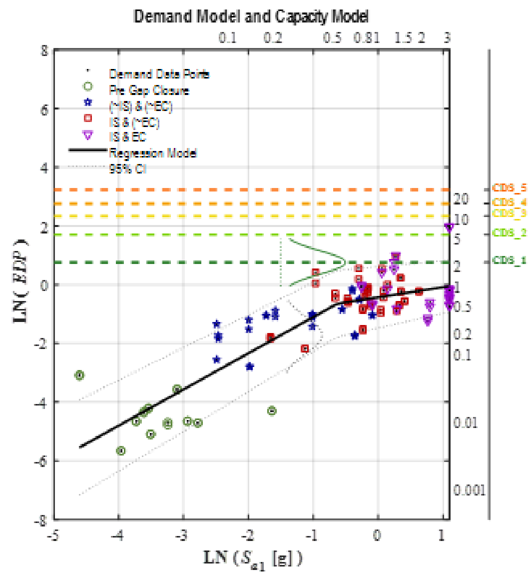

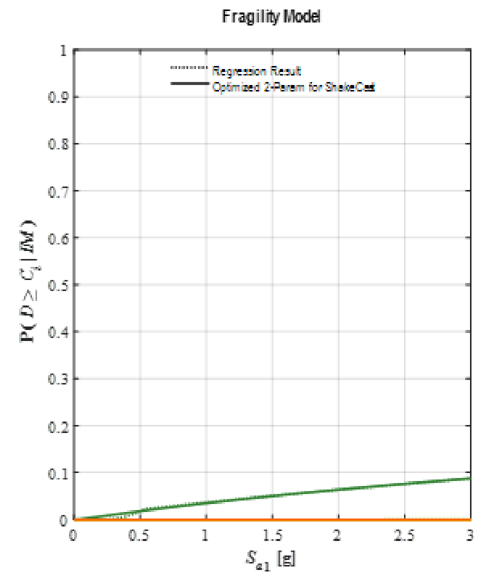

Capacity Model State Descriptions - Component Subgroup

	CDS_1	T_12	CDS_2	T_23	CDS_3	T_34	CDS_4	T_45	CDS_5	T_56	CDS_6	T_67	CDS_7
CIDH-Pile Performance:	Initial Loss of Lateral Stiffness		Approaching Lateral Capacity		Degrading Lateral Capacity		Residual Lateral Capacity		Loss of Lateral (& Axial?) Capacity				
CIDH-Pile Foundation Damage:	Initial Minor Cracking/Spalling Damage at Pile Head (Future Corrosion)		Initial Pile-Head Hinging w/ Substantial Cracking/Spalling & Minor Rebar Yield		Well Developed Pile-Head Hinge w/ Major Rebar Yield & Core Crushing; Initial 2nd Hinge Below Ground		Buckling & Fracture of Rebar & Hoop Fracture at Pile Head; Fully Formed 2nd Hinge Below Ground		Large Displacement & Pile Rotation; Possible Detachment at Pile Cap; Major Loss of Lateral & Axial Capacity				
Normalized Pile-Head Translational Force v. Displacement Response Range	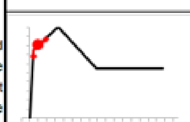		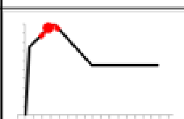		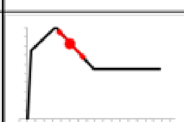		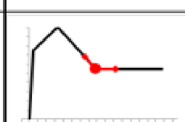		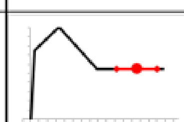				

Figure F.83: Stage-0: CIDH abutment pile foundation damage in transverse direction

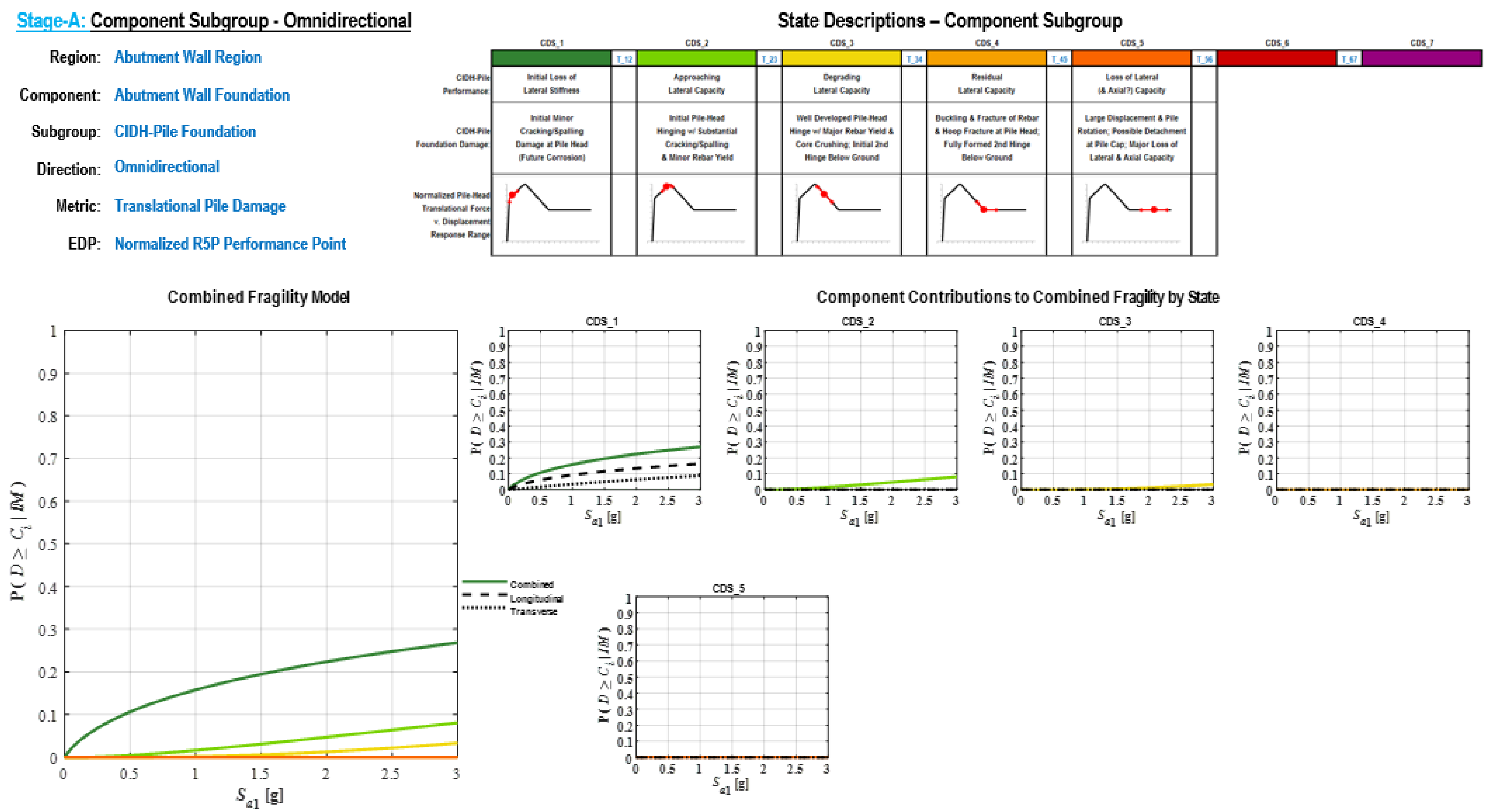

Figure F.84: Stage-A: CIDH abutment pile foundation damage

Stage-0: Component Subgroup - Directional

Region: Abutment Wall Region

Component: Abutment Wall Foundation

Subgroup: Precast-Pile Foundation

Direction: Longitudinal Rotated (LR), Skew = 0 deg.

Metric: Translational Pile Damage

EDP: Normalized R5P Performance Point

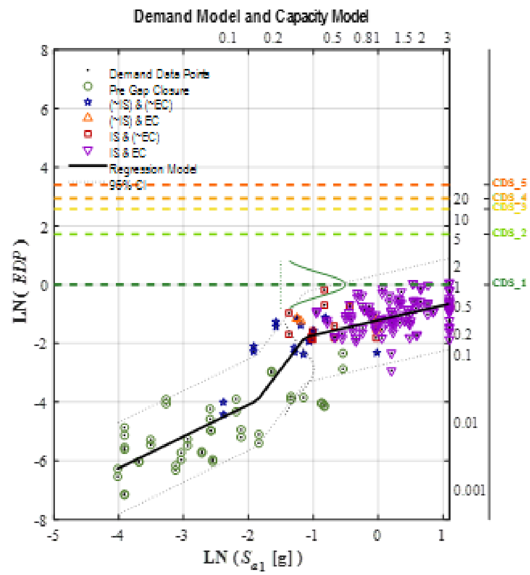

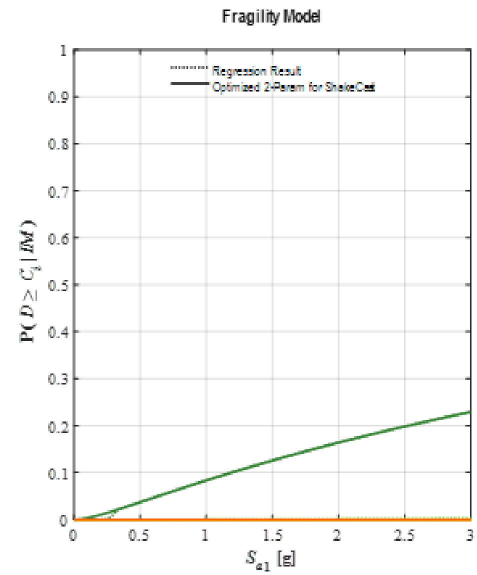

Capacity Model State Descriptions - Component Subgroup

	CDS_1	T_12	CDS_2	T_23	CDS_3	T_34	CDS_4	T_45	CDS_5	T_56	CDS_6	T_67	CDS_7
Precast-Pile Performance:	Initial Loss of Lateral Stiffness		Approaching Lateral Capacity		Degrading Lateral Capacity		Residual Lateral Capacity		Loss of Lateral (& Axial?) Capacity				
Precast-Pile Foundation Damage:	Initial Minor Cracking/Spalling Damage at Pile Head (Future Corrosion)		Initial Pile-Head Hinging w/ Substantial Cracking/Spalling; Initial Yielding of Rebar & Prestress Tendons		Well Developed Pile-Head Hinge w/ Major Yielding of Rebar & Prestress Tendons; Core Crushing; Initial 2nd Hinge Below Ground		Buckling & Fracture of Rebar & Prestress Tendons; Fully Formed 2nd Hinge Below Ground		Large Displacement & Pile Rotation; Possible Detachment at Pile Cap; Major Loss of Lateral & Axial Capacity				
Normalized Pile-Head Translational Force v. Displacement Response Range													

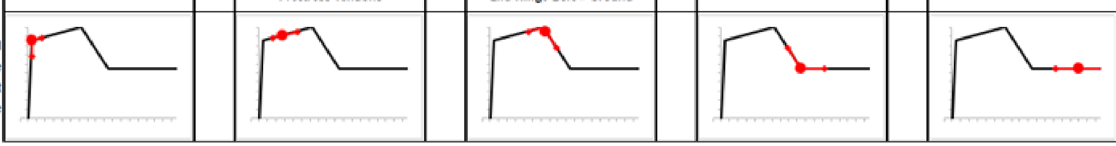

Figure F.85: Stage-0: Precast abutment pile foundation damage in longitudinal direction

Stage-0: Component Subgroup - Directional

Region: Abutment Wall Region

Component: Abutment Wall Foundation

Subgroup: Precast-Pile Foundation

Direction: Transverse Rotated (TR), Skew = 0 deg.

Metric: Translational Pile Damage

EDP: Normalized R5P Performance Point

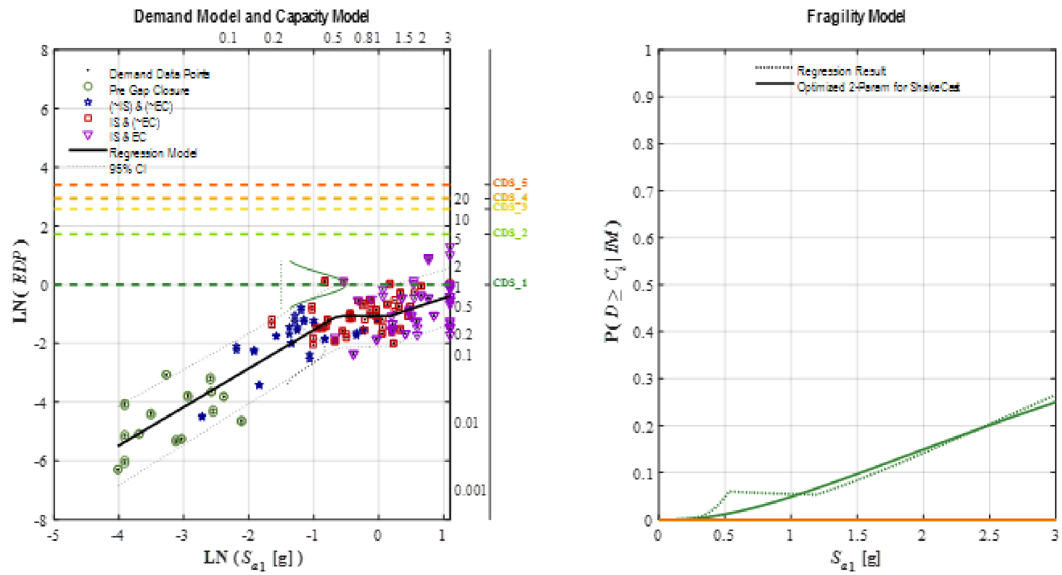

Capacity Model State Descriptions - Component Subgroup

	CDS_1	T_12	CDS_2	T_23	CDS_3	T_34	CDS_4	T_45	CDS_5	T_56	CDS_6	T_67	CDS_7
Precast-Pile Performance:	Initial Loss of Lateral Stiffness		Approaching Lateral Capacity		Degrading Lateral Capacity		Residual Lateral Capacity		Loss of Lateral (& Axial?) Capacity				
Precast-Pile Foundation Damage:	Initial Minor Cracking/Spalling Damage at Pile Head (Future Corrosion)		Initial Pile-Head Hinging w/ Substantial Cracking/Spalling; Initial Yielding of Rebar & Prestress Tendons		Well Developed Pile-Head Hinge w/ Major Yielding of Rebar & Prestress Tendons; Core Crushing; Initial 2nd Hinge Below Ground		Buckling & Fracture of Rebar & Prestress Tendons; Fully Formed 2nd Hinge Below Ground		Large Displacement & Pile Rotation; Possible Detachment at Pile Cap; Major Loss of Lateral & Axial Capacity				
Normalized Pile-Head Translational Force v. Displacement Response Range	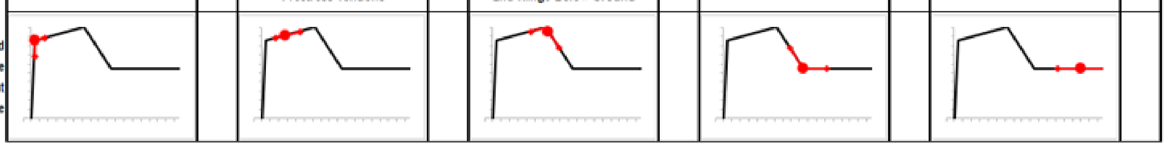												

Figure F.86: Stage-0: Precast abutment pile foundation damage in transverse direction

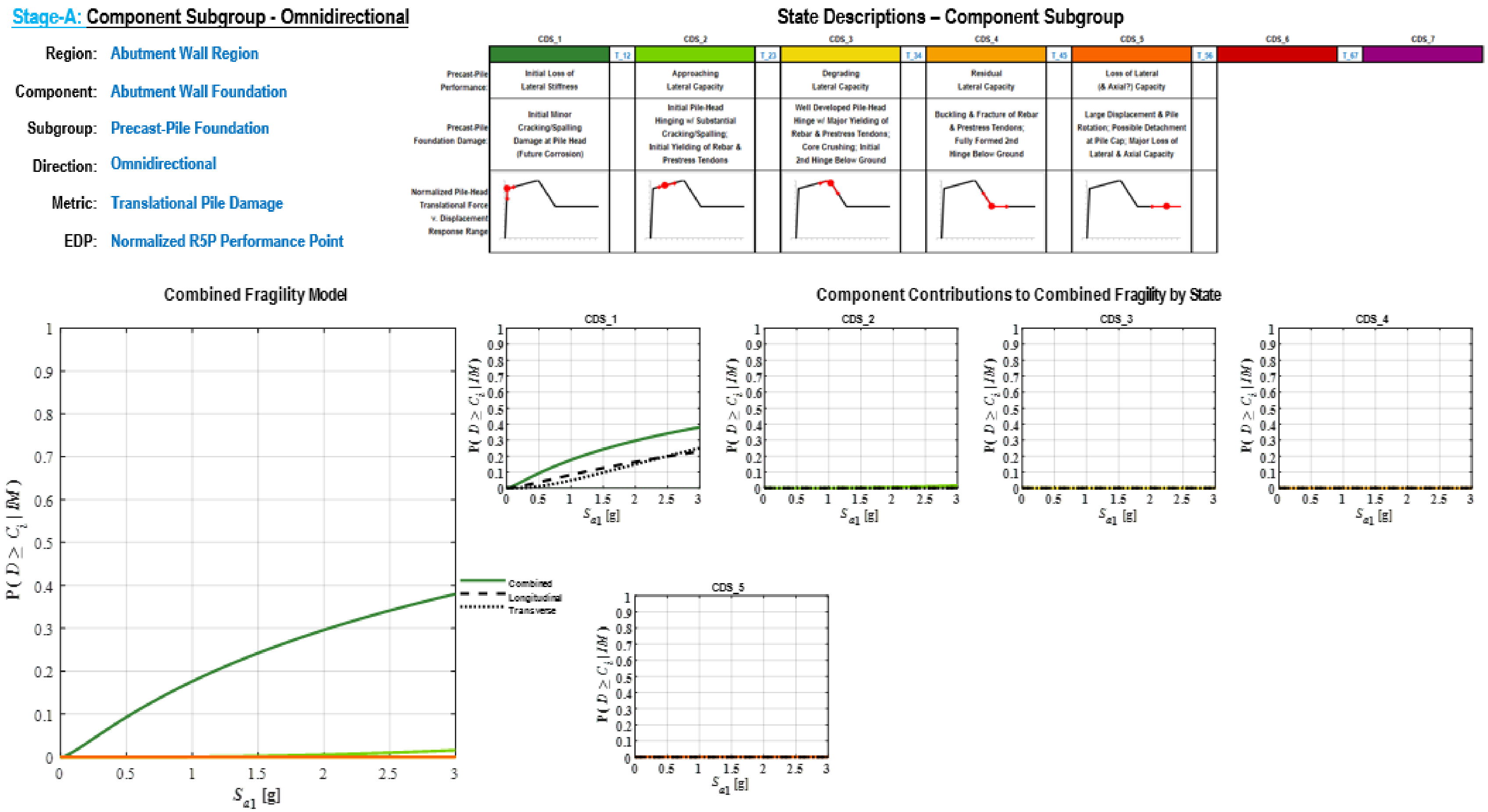

Figure F.87: Stage-A: Precast abutment pile foundation damage

Stage-0: Component Subgroup - Directional

Region: Abutment Wall Region

Component: Abutment Wall Foundation

Subgroup: Steel-Pile Foundation

Direction: Longitudinal Rotated (LR), Skew = 0 deg.

Metric: Translational Pile Damage

EDP: Normalized R5P Performance Point

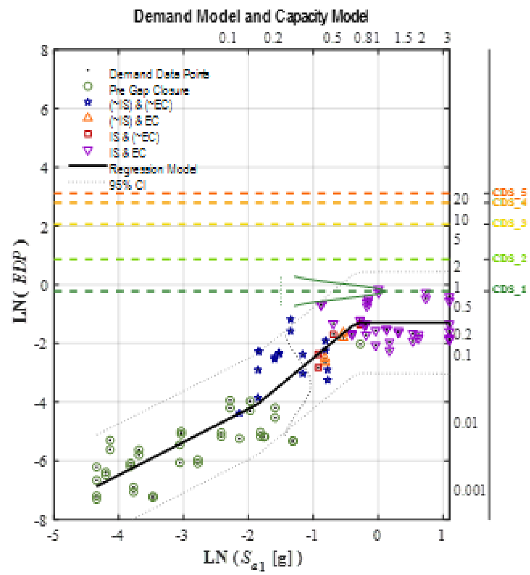

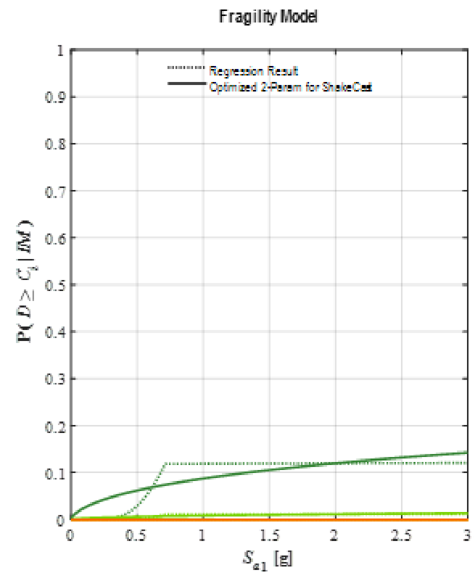

Capacity Model State Descriptions - Component Subgroup

	CDS_1	T_12	CDS_2	T_23	CDS_3	T_34	CDS_4	T_45	CDS_5	T_56	CDS_6	T_67	CDS_7
Steel-Pile Performance:	Initial Pile-Cap Connection Damage		Initial Loss of Lateral Stiffness		Pile Ductile Yielding w/ Cap Damage		Degrading Lateral Capacity		Residual Lateral Capacity				
Steel-Pile Foundation Damage:	Initial Minor Cracking at Pile Cap Connection (Future Corrosion); Low (< ~5-deg) Pile-Head Rotation		Rotational Gap at Cap Connection; Initial Steel Yielding Below Ground; Moderate (5 to 10-deg) Pile-Head Rotation		Increasing Cap Connection Damage; Ductile Steel Yielding Below Ground; High (10 to 30-deg) Pile-Head Rotation		Substantial Cap Connection Damage; Steel Buckling at Below-Ground Hinge; Extreme (30 to 45-deg) Pile-Head Rotation		Extreme Displacement & Pile-Head Rotation (> ~45 deg); Possible Detachment at Pile Cap; Major Loss of Lateral & Possibly Axial Capacity				
Normalized Pile-Head Translational Force v. Displacement Response Range	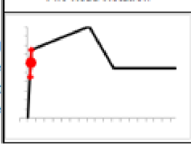		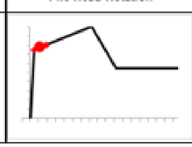		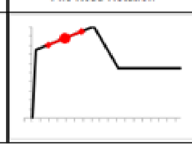		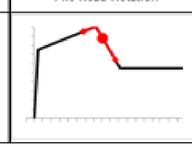		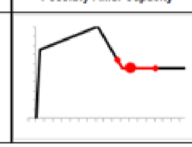				

Figure F.88: Stage-0: Steel abutment pile foundation damage in longitudinal direction

Stage-0: Component Subgroup - Directional

Region: Abutment Wall Region

Component: Abutment Wall Foundation

Subgroup: Steel-Pile Foundation

Direction: Transverse Rotated (TR), Skew = 0 deg.

Metric: Translational Pile Damage

EDP: Normalized R5P Performance Point

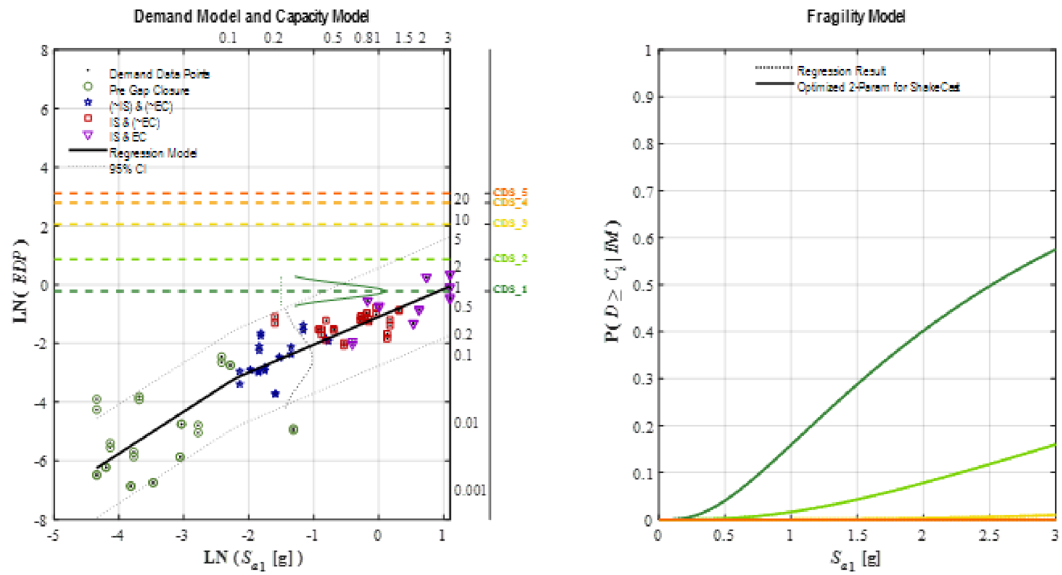

Capacity Model State Descriptions - Component Subgroup

	CDS_1	T_12	CDS_2	T_23	CDS_3	T_34	CDS_4	T_45	CDS_5	T_56	CDS_6	T_67	CDS_7
Steel-Pile Performance:	Initial Pile-Cap Connection Damage		Initial Loss of Lateral Stiffness		Pile Ductile Yielding w/ Cap Damage		Degrading Lateral Capacity		Residual Lateral Capacity				
Steel-Pile Foundation Damage:	Initial Minor Cracking at Pile Cap Connection (Future Corrosion); Low (< ~5-deg) Pile-Head Rotation		Rotational Gap at Cap Connection; Initial Steel Yielding Below Ground; Moderate (5 to 10-deg) Pile-Head Rotation		Increasing Cap Connection Damage; Ductile Steel Yielding Below Ground; High (10 to 30-deg) Pile-Head Rotation		Substantial Cap Connection Damage; Steel Buckling at Below-Ground Hinge; Extreme (30 to 45-deg) Pile-Head Rotation		Extreme Displacement & Pile-Head Rotation (> ~45 deg); Possible Detachment at Pile Cap; Major Loss of Lateral & Possibly Axial Capacity				
Normalized Pile-Head Translational Force v. Displacement Response Range													

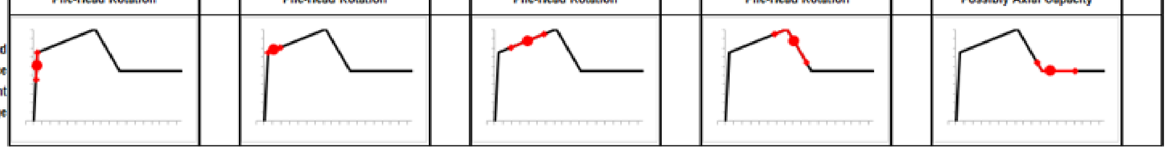

Figure F.89: Stage-0: Steel abutment pile foundation damage in transverse direction

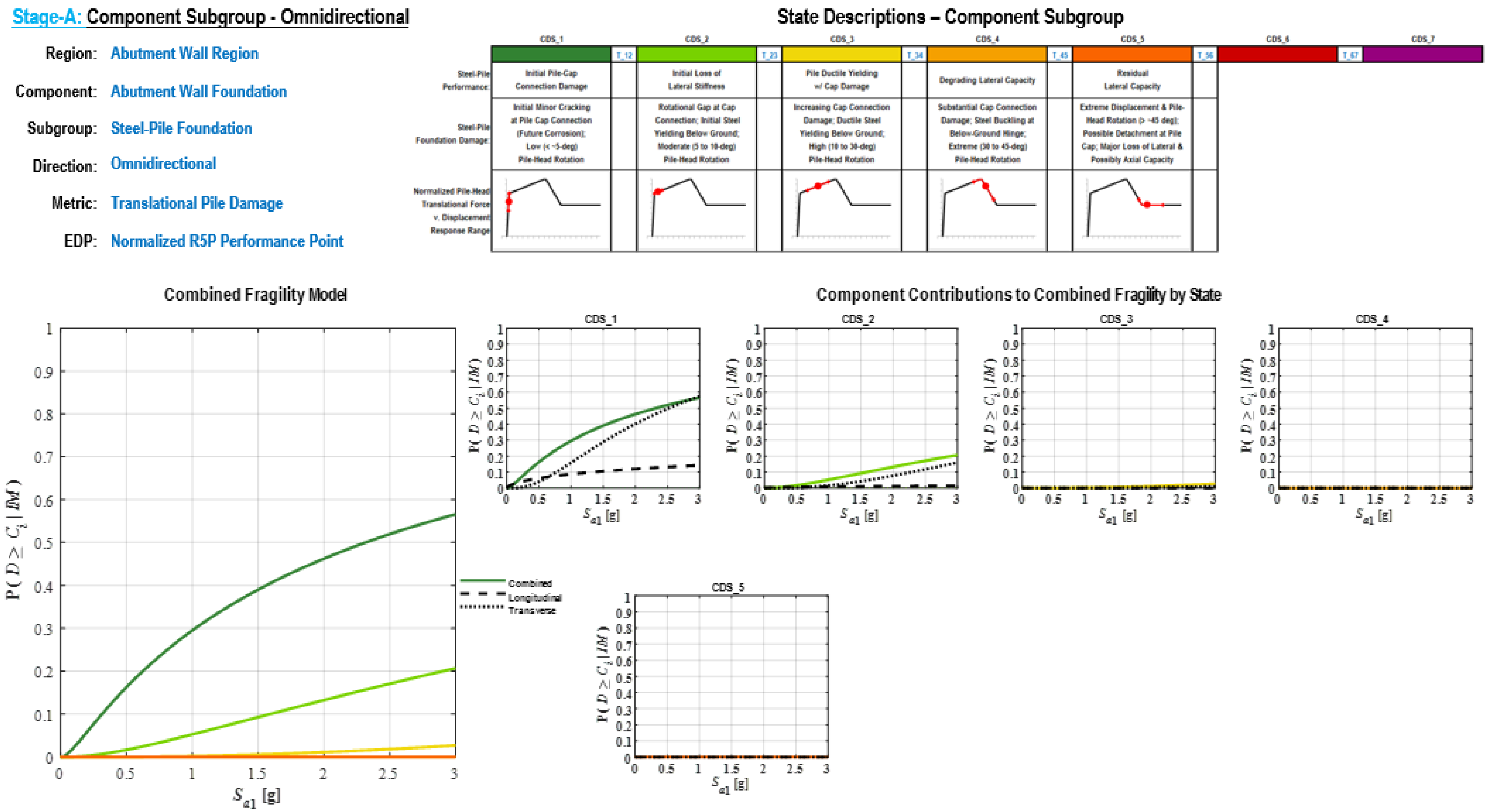

Figure F.90: Stage-A: Steel abutment pile foundation damage

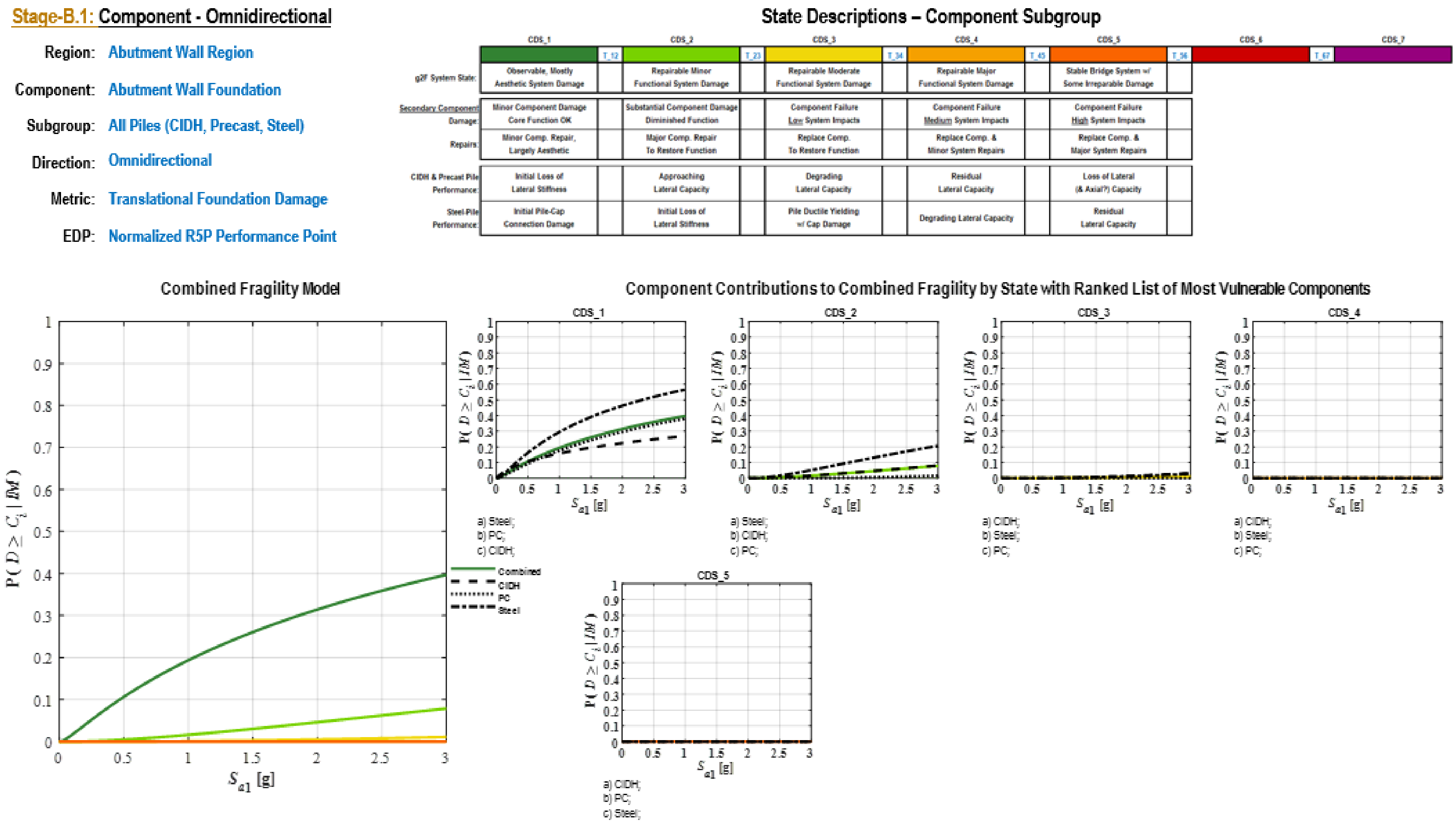

Figure F.91: Stage-B.1: Abutment pile foundation damage.

Stage-0: Component Subgroup - Directional

Region: Abutment Wall Region

Component: Abutment Wall Foundation

Subgroup: Spread Footing

Direction: Longitudinal Rotated (LR), Skew = 0 deg.

Metric: Translational Footing Damage

EDP: Normalized RUUFF Performance Point

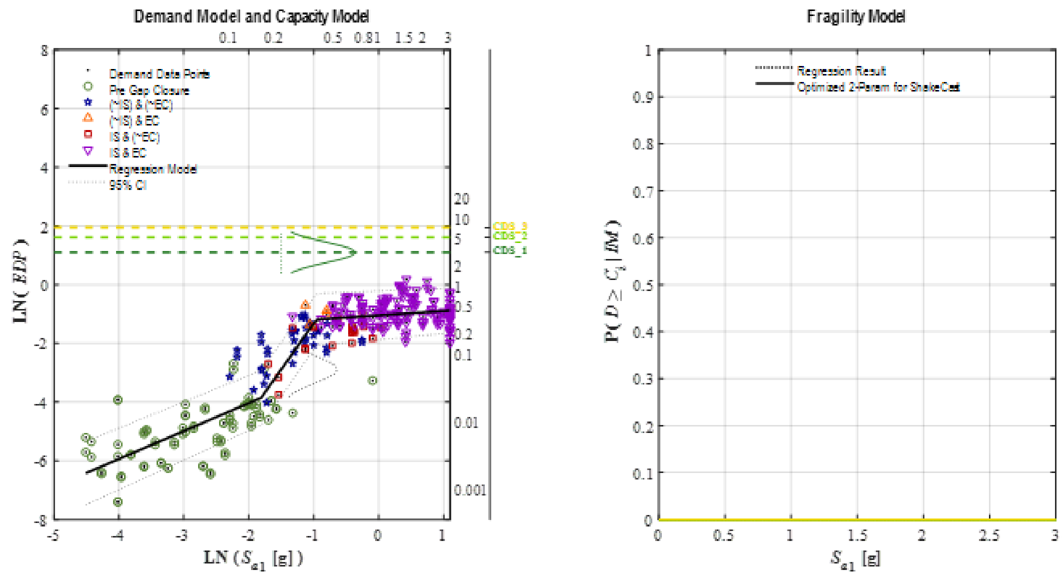

Capacity Model State Descriptions - Component Subgroup

	CDS_1	T_12	CDS_2	T_23	CDS_3	T_34	CDS_4	T_45	CDS_5	T_56	CDS_6	T_67	CDS_7
Typical Performance:	Observable Residual Displacements (1-4 Inch)		Substantial Residual Displacements (4-16-Inch)		Extreme Residual Displacements (>16-Inch)								
Footing-Area Damage:	Minor Gaps or Dislocations Near Footing at Ground Surface		Potential Distress to Footing Connection or Abuting Facilities/Utilities		Potential Impacts on Column Capacity and/or Alignment								
Norm Force-Displ. Response Range:	~2-inch	~4-In	~8-inch	~16-In	> 16-inch								

Figure F.92: Stage-0: Abutment spread footing foundation damage in longitudinal direction

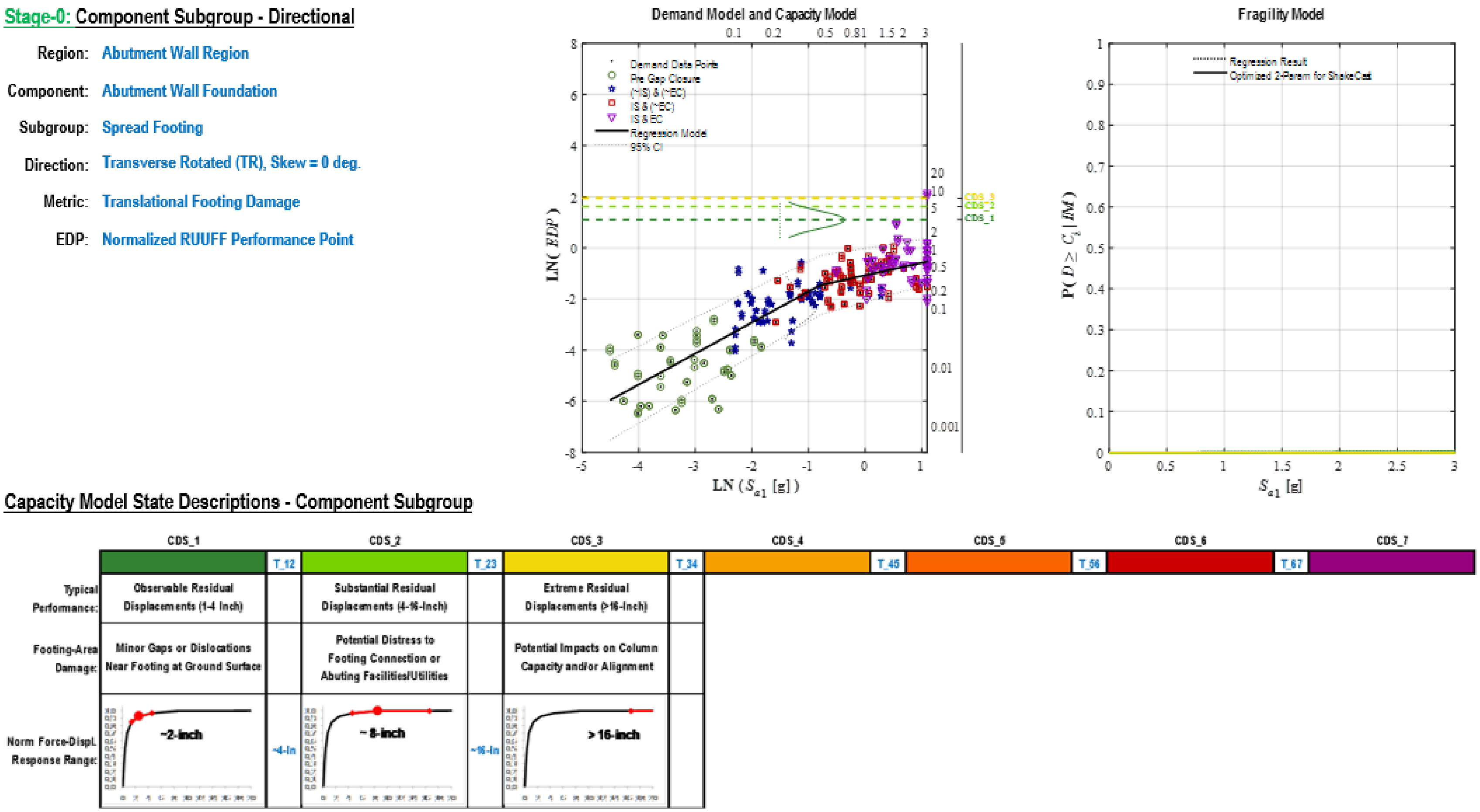

Figure F.93: Stage-0: Abutment spread footing foundation damage in transverse direction

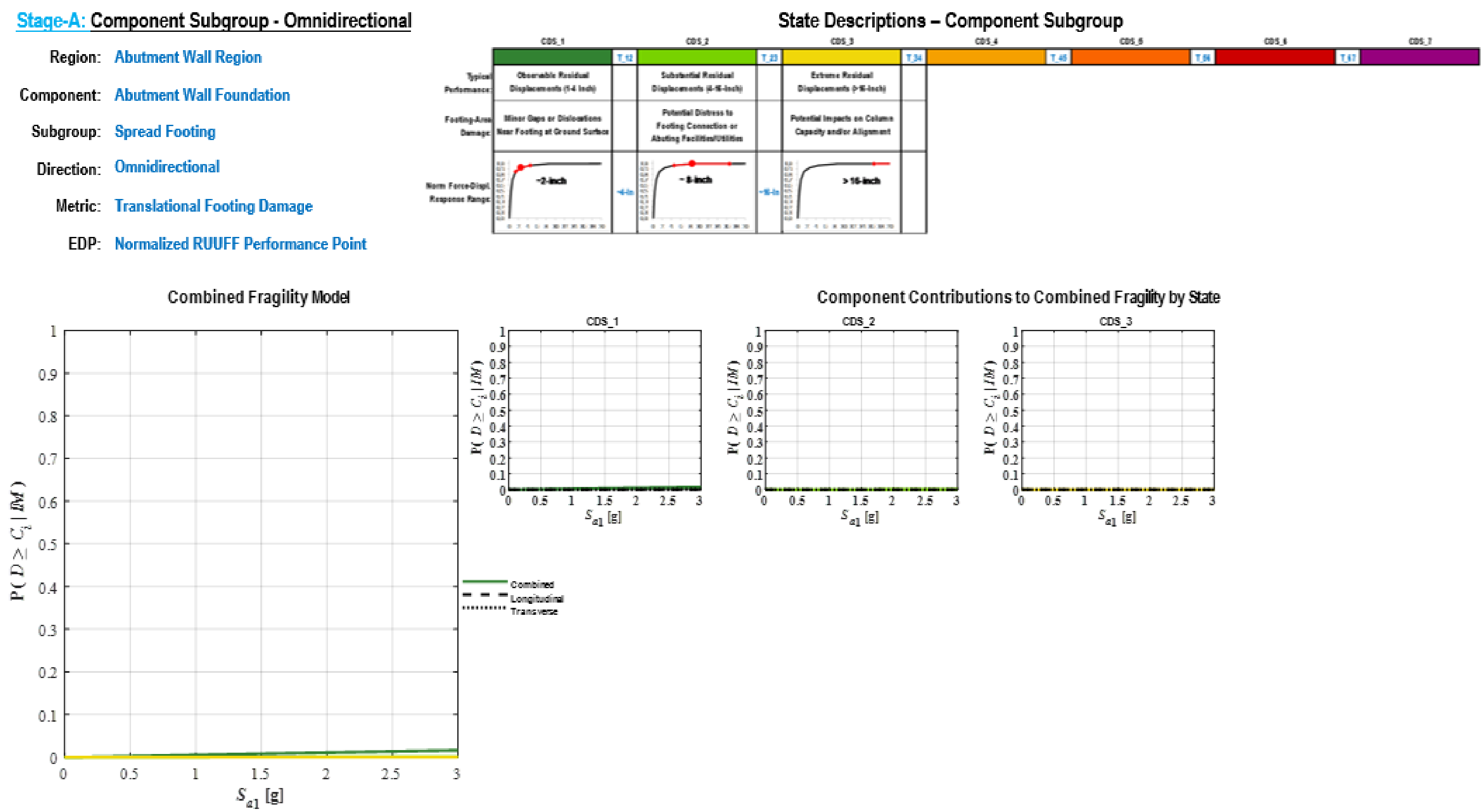

Figure F.94: Stage-A: Abutment spread footing foundation damage

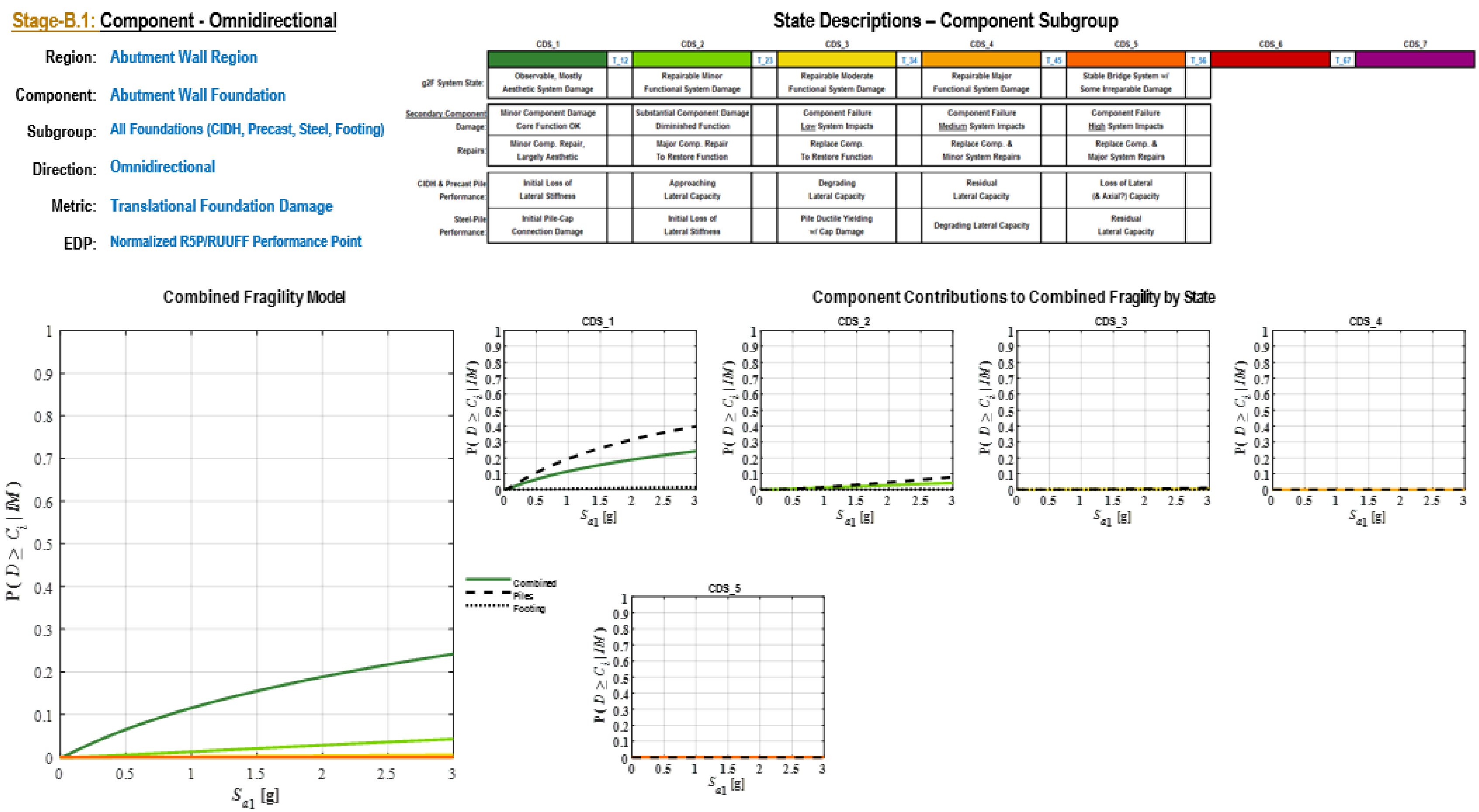

Figure F.95: Stage-B.1: Abutment foundation translational damage (Same as Stage-C roll-up for abutment wall damage).

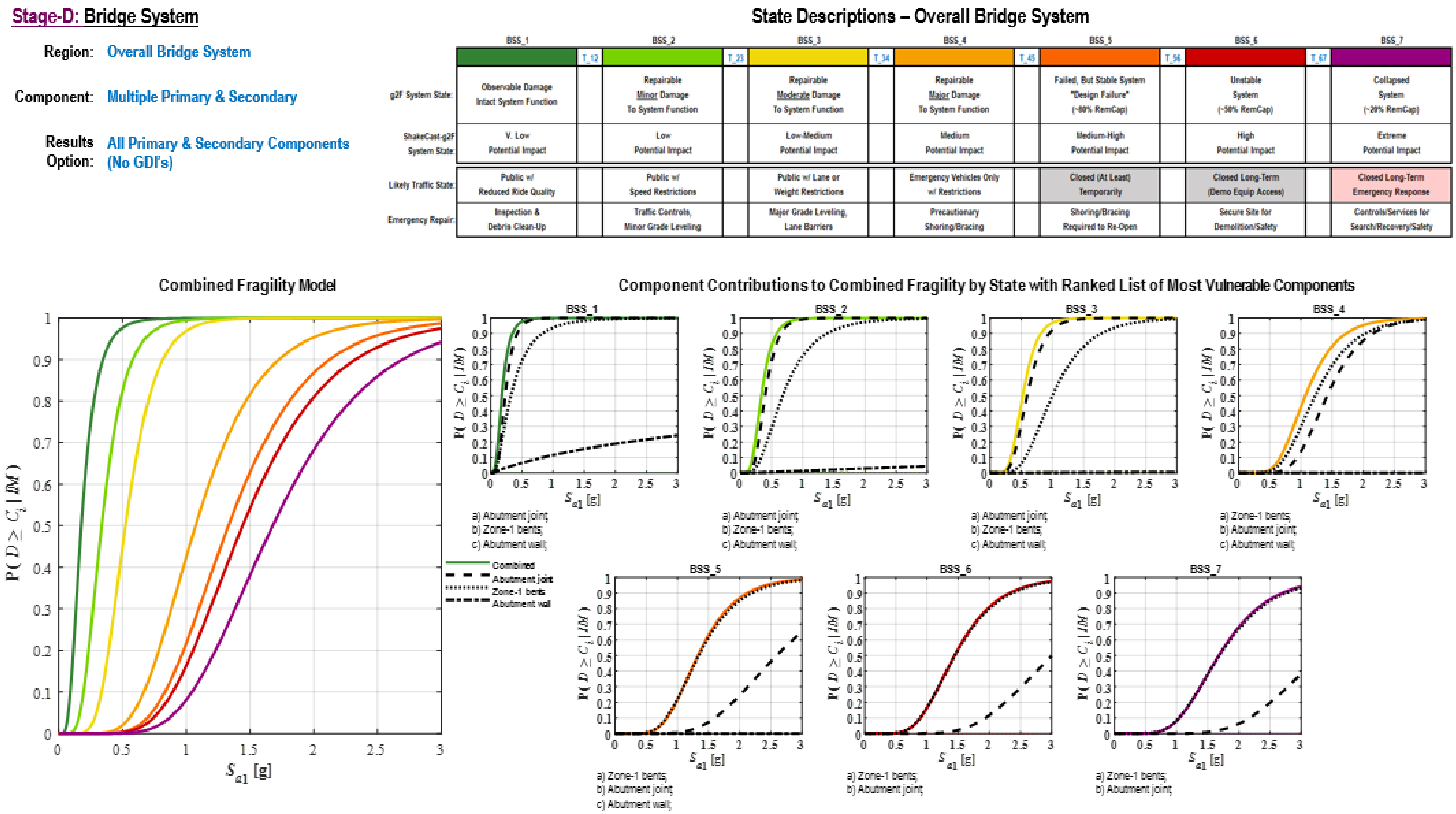

Figure F.96: Stage-D roll-up: System fragility.

APPENDIX G

BRIDGE GROUPING RESULTS FOR ERA-3 TWO-SPAN MULTI-COLUMN BENT BRIDGES

Following a hierarchical structure, the model is first tested in the seat width model, compared to the overall inventory average model. It is shown that the system fragility models with four different seat width designs can be represented by the inventory average model Figure G.1. Then, the grouping procedure is carried down to the next step to test whether the section types affect the system fragility model. The comparison indicates that they are different Table G.2. As a result, the following test is determining bent foundation types having any further influence on the performance of regular section bridges or wide section bridges Table G.3. It is carried down from the system fragility model in Figure F.95 to the base of each subgroup combination. The sequence used here approximately follows the importance of each component: 1) unseating design groups, 2) section types, 3) joint seal types, 4) column foundation types, 5) abutment foundation types, and 6) column foundation rotation damage types. Ultimately, the grouping of this RBS generates two identical models corresponding to regular and wide column sections.

Table G.1: Model comparison for seat width design subgroups.

	CDS_1			CDS_2			CDS_3			CDS_4		
	$\Delta\mu^\dagger$	$\Delta\beta^\dagger$	$\Delta F^\dagger$	$\Delta\mu$	$\Delta\beta$	ΔF	$\Delta\mu$	$\Delta\beta$	ΔF	$\Delta\mu$	$\Delta\beta$	ΔF
IA vs G1 §	0.00	0.00	0.00	0.00	0.00	0.00	0.00	0.00	0.01	0.01	0.01	0.02
IA vs G2	0.00	0.00	0.00	0.00	0.00	0.00	0.00	0.00	0.01	0.01	0.00	0.01
IA vs G3	0.00	0.00	0.00	0.00	0.00	0.00	0.00	0.00	0.01	0.02	0.01	0.02
IA vs G4	0.00	0.00	0.00	0.00	0.00	0.00	0.00	0.00	0.01	0.02	0.01	0.02

	CDS_5			CDS_6			CDS_7			All states		
	$\Delta\mu$	$\Delta\beta$	ΔF	$\Delta\mu$	$\Delta\beta$	ΔF	$\Delta\mu$	$\Delta\beta$	ΔF	$\Delta\mu$	$\Delta\beta$	ΔF
IA vs G1	0.01	0.01	0.01	0.01	0.01	0.01	0.01	0.01	0.01	0.01	0.01	0.02
IA vs G2	0.01	0.00	0.01	0.00	0.00	0.00	0.00	0.00	0.00	0.01	0.00	0.01
IA vs G3	0.01	0.01	0.02	0.01	0.01	0.01	0.01	0.01	0.01	0.02	0.01	0.02
IA vs G4	0.01	0.01	0.02	0.01	0.01	0.01	0.01	0.01	0.01	0.02	0.01	0.02

§ IA = inventory average model; G1 = seat width group design-1 with 30 inch seat width; G2 = seat width group design-2 with 36 inch seat width; G3 = seat width group design-3 with 48 inch seat width; and G4 = seat width group design-4 with 60 inch seat width.

† $\Delta\mu$ = absolute difference of fragility median; $\Delta\beta$ = absolute difference of fragility dispersion; and $\Delta F(IM)$ = maximum absolute difference of fragility probability in S_{a1} = 0 g to 3.0 g.

Table G.2: Model comparison for column section subgroups.

	CDS_1			CDS_2			CDS_3			CDS_4		
	$\Delta\mu^\dagger$	$\Delta\beta^\dagger$	$\Delta F^\dagger$	$\Delta\mu$	$\Delta\beta$	ΔF	$\Delta\mu$	$\Delta\beta$	ΔF	$\Delta\mu$	$\Delta\beta$	ΔF
IA vs G1 §	0.00	0.00	0.01	0.00	0.00	0.00	0.00	0.00	0.00	0.01	0.01	0.01
IA vs G2	0.01	0.00	0.02	0.00	0.00	0.01	0.00	0.01	0.01	0.02	0.01	0.02

	CDS_5			CDS_6			CDS_7			All states		
	$\Delta\mu$	$\Delta\beta$	ΔF	$\Delta\mu$	$\Delta\beta$	ΔF	$\Delta\mu$	$\Delta\beta$	ΔF	$\Delta\mu$	$\Delta\beta$	ΔF
IA vs G1	0.01	0.02	0.02	0.00	0.02	0.01	0.02	0.03	0.02	0.02	0.03	0.02
IA vs G2	0.01	0.05	0.04	0.01	**0.07**	0.05	0.05	**0.07**	**0.08**	0.05	**0.07**	**0.08**

§ IA = inventory average model; G1 = regular column sections; and G2 = wide column sections.

† $\Delta\mu$ = absolute difference of fragility median; $\Delta\beta$ = absolute difference of fragility dispersion; and $\Delta F(IM)$ = maximum absolute difference of fragility probability in S_{a1} = 0 g to 3.0 g.

Table G.3: Model comparison for joint seal gap subgroups given different section types.

Regular sections	**CDS_1**			**CDS_2**			**CDS_3**			**CDS_4**		
	$\Delta\mu^{\dagger}$	$\Delta\beta^{\dagger}$	$\Delta F^{\dagger}$	$\Delta\mu$	$\Delta\beta$	ΔF	$\Delta\mu$	$\Delta\beta$	ΔF	$\Delta\mu$	$\Delta\beta$	ΔF
IA vs G1 §	0.01	0.02	0.03	0.01	0.04	0.04	0.02	0.00	0.04	0.00	0.00	0.00
IA vs G2	0.01	0.02	0.03	0.01	0.03	0.04	0.02	0.01	0.04	0.00	0.00	0.00

Regular sections	**CDS_5**			**CDS_6**			**CDS_7**			**All states**		
	$\Delta\mu$	$\Delta\beta$	ΔF	$\Delta\mu$	$\Delta\beta$	ΔF	$\Delta\mu$	$\Delta\beta$	ΔF	$\Delta\mu$	$\Delta\beta$	ΔF
IA vs G1	0.00	0.00	0.00	0.00	0.00	0.00	0.00	0.00	0.00	0.02	0.04	0.04
IA vs G2	0.00	0.00	0.00	0.00	0.00	0.00	0.00	0.00	0.00	0.02	0.03	0.04

Wide sections	**CDS_1**			**CDS_2**			**CDS_3**			**CDS_4**		
	$\Delta\mu^{\dagger}$	$\Delta\beta^{\dagger}$	$\Delta F^{\dagger}$	$\Delta\mu$	$\Delta\beta$	ΔF	$\Delta\mu$	$\Delta\beta$	ΔF	$\Delta\mu$	$\Delta\beta$	ΔF
IA vs G1	0.01	0.02	0.04	0.01	0.05	0.05	0.02	0.00	0.03	0.00	0.00	0.00
IA vs G2	0.01	0.02	0.04	0.01	0.03	0.03	0.02	0.01	0.03	0.00	0.00	0.00

Wide sections	**CDS_5**			**CDS_6**			**CDS_7**			**All states**		
	$\Delta\mu$	$\Delta\beta$	ΔF	$\Delta\mu$	$\Delta\beta$	ΔF	$\Delta\mu$	$\Delta\beta$	ΔF	$\Delta\mu$	$\Delta\beta$	ΔF
IA vs G1	0.00	0.00	0.00	0.00	0.00	0.00	0.00	0.00	0.00	0.02	0.05	0.05
IA vs G2	0.00	0.00	0.00	0.00	0.00	0.00	0.00	0.00	0.00	0.02	0.03	0.04

§ IA = inventory average model; G1 = compression seal; and G2 = strip seal.

† $\Delta\mu$ = absolute difference of fragility median; $\Delta\beta$ = absolute difference of fragility dispersion; and $\Delta F(IM)$ = maximum absolute difference of fragility probability in S_{a1} = 0 g to 3.0 g.

Table G.4: Model comparison for column-foundation subgroups given different section types.

Regular sections	**CDS_1**			**CDS_2**			**CDS_3**			**CDS_4**		
	$\Delta\mu^{\dagger}$	$\Delta\beta^{\dagger}$	$\Delta F^{\dagger}$	$\Delta\mu$	$\Delta\beta$	ΔF	$\Delta\mu$	$\Delta\beta$	ΔF	$\Delta\mu$	$\Delta\beta$	ΔF
IA vs G1 §	0.01	0.01	0.03	0.00	0.00	0.00	0.00	0.00	0.00	0.00	0.00	0.00
IA vs G2	0.01	0.02	0.04	0.00	0.00	0.01	0.00	0.00	0.01	0.00	0.00	0.00

Regular sections	**CDS_5**			**CDS_6**			**CDS_7**			**All states**		
	$\Delta\mu$	$\Delta\beta$	ΔF	$\Delta\mu$	$\Delta\beta$	ΔF	$\Delta\mu$	$\Delta\beta$	ΔF	$\Delta\mu$	$\Delta\beta$	ΔF
IA vs G1	0.00	0.00	0.00	0.00	0.00	0.00	0.00	0.00	0.00	0.01	0.01	0.03
IA vs G2	0.00	0.00	0.00	0.00	0.00	0.00	0.00	0.00	0.00	0.01	0.02	0.04

Wide sections	**CDS_1**			**CDS_2**			**CDS_3**			**CDS_4**		
	$\Delta\mu^{\dagger}$	$\Delta\beta^{\dagger}$	$\Delta F^{\dagger}$	$\Delta\mu$	$\Delta\beta$	ΔF	$\Delta\mu$	$\Delta\beta$	ΔF	$\Delta\mu$	$\Delta\beta$	ΔF
IA vs G1	0.01	0.04	0.04	0.00	0.00	0.00	0.00	0.00	0.00	0.00	0.00	0.00
IA vs G2	0.01	0.02	0.05	0.00	0.01	0.01	0.00	0.00	0.01	0.00	0.00	0.00

Wide sections	**CDS_5**			**CDS_6**			**CDS_7**			**All states**		
	$\Delta\mu$	$\Delta\beta$	ΔF	$\Delta\mu$	$\Delta\beta$	ΔF	$\Delta\mu$	$\Delta\beta$	ΔF	$\Delta\mu$	$\Delta\beta$	ΔF
IA vs G1	0.00	0.00	0.00	0.00	0.00	0.00	0.00	0.00	0.00	0.01	0.04	0.04
IA vs G2	0.00	0.00	0.00	0.00	0.00	0.00	0.00	0.00	0.00	0.01	0.02	0.05

§ IA = inventory average model; G1 = pile column foundation; and G2 = footing column foundation.

† $\Delta\mu$ = absolute difference of fragility median; $\Delta\beta$ = absolute difference of fragility dispersion; and $\Delta F(IM)$ = maximum absolute difference of fragility probability in S_{a1} = 0 g to 3.0 g.

Table G.5: Model comparison for abutment-foundation subgroups given different section types.

Regular sections	**CDS_1**			**CDS_2**			**CDS_3**			**CDS_4**		
	$\Delta\mu^{\dagger}$	$\Delta\beta^{\dagger}$	$\Delta F^{\dagger}$	$\Delta\mu$	$\Delta\beta$	ΔF	$\Delta\mu$	$\Delta\beta$	ΔF	$\Delta\mu$	$\Delta\beta$	ΔF
IA vs G1 [§]	0.00	0.00	0.00	0.00	0.00	0.00	0.00	0.00	0.00	0.00	0.00	0.00
IA vs G2	0.00	0.00	0.00	0.00	0.00	0.00	0.00	0.00	0.00	0.00	0.00	0.00

Regular sections	**CDS_5**			**CDS_6**			**CDS_7**			**All states**		
	$\Delta\mu$	$\Delta\beta$	ΔF	$\Delta\mu$	$\Delta\beta$	ΔF	$\Delta\mu$	$\Delta\beta$	ΔF	$\Delta\mu$	$\Delta\beta$	ΔF
IA vs G1	0.00	0.00	0.00	0.00	0.00	0.00	0.00	0.00	0.00	0.00	0.00	0.00
IA vs G2	0.00	0.00	0.00	0.00	0.00	0.00	0.00	0.00	0.00	0.00	0.00	0.00

Wide sections	**CDS_1**			**CDS_2**			**CDS_3**			**CDS_4**		
	$\Delta\mu^{\dagger}$	$\Delta\beta^{\dagger}$	$\Delta F^{\dagger}$	$\Delta\mu$	$\Delta\beta$	ΔF	$\Delta\mu$	$\Delta\beta$	ΔF	$\Delta\mu$	$\Delta\beta$	ΔF
IA vs G1	0.00	0.01	0.00	0.00	0.00	0.00	0.00	0.00	0.00	0.00	0.00	0.00
IA vs G2	0.00	0.02	0.01	0.00	0.01	0.01	0.00	0.01	0.01	0.00	0.00	0.00

Wide sections	**CDS_5**			**CDS_6**			**CDS_7**			**All states**		
	$\Delta\mu$	$\Delta\beta$	ΔF	$\Delta\mu$	$\Delta\beta$	ΔF	$\Delta\mu$	$\Delta\beta$	ΔF	$\Delta\mu$	$\Delta\beta$	ΔF
IA vs G1	0.00	0.00	0.00	0.00	0.00	0.00	0.00	0.00	0.00	0.00	0.01	0.00
IA vs G2	0.00	0.00	0.00	0.00	0.00	0.00	0.00	0.00	0.00	0.00	0.02	0.01

§ IA = inventory average model; G1 = pile abutment foundation; and G2 = footing abutment foundation.

† $\Delta\mu$ = absolute difference of fragility median; $\Delta\beta$ = absolute difference of fragility dispersion; and $\Delta F(IM)$ = maximum absolute difference of fragility probability in S_{a1} = 0 g to 3.0 g.

Table G.6: Model comparison for column-foundation-rotation damage subgroups given different section types.

Regular sections	**CDS_1**			**CDS_2**			**CDS_3**			**CDS_4**		
	$\Delta\mu^\dagger$	$\Delta\beta^\dagger$	$\Delta F^\dagger$	$\Delta\mu$	$\Delta\beta$	ΔF	$\Delta\mu$	$\Delta\beta$	ΔF	$\Delta\mu$	$\Delta\beta$	ΔF
IA vs G1 [§]	0.01	0.01	0.02	0.00	0.00	0.00	0.00	0.00	0.01	0.00	0.00	0.00
IA vs G2	0.00	0.01	0.02	0.00	0.00	0.00	0.00	0.00	0.00	0.00	0.00	0.01

Regular sections	**CDS_5**			**CDS_6**			**CDS_7**			**All states**		
	$\Delta\mu$	$\Delta\beta$	ΔF	$\Delta\mu$	$\Delta\beta$	ΔF	$\Delta\mu$	$\Delta\beta$	ΔF	$\Delta\mu$	$\Delta\beta$	ΔF
IA vs G1	0.00	0.00	0.00	0.00	0.00	0.00	0.00	0.00	0.00	0.01	0.01	0.02
IA vs G2	0.00	0.00	0.00	0.00	0.00	0.00	0.00	0.00	0.00	0.00	0.01	0.02

Wide sections	**CDS_1**			**CDS_2**			**CDS_3**			**CDS_4**		
	$\Delta\mu^\dagger$	$\Delta\beta^\dagger$	$\Delta F^\dagger$	$\Delta\mu$	$\Delta\beta$	ΔF	$\Delta\mu$	$\Delta\beta$	ΔF	$\Delta\mu$	$\Delta\beta$	ΔF
IA vs G1	0.00	0.01	0.01	0.00	0.00	0.01	0.00	0.00	0.00	0.00	0.00	0.00
IA vs G2	0.00	0.01	0.01	0.00	0.00	0.01	0.00	0.00	0.00	0.00	0.00	0.00

Wide sections	**CDS_5**			**CDS_6**			**CDS_7**			**All states**		
	$\Delta\mu$	$\Delta\beta$	ΔF	$\Delta\mu$	$\Delta\beta$	ΔF	$\Delta\mu$	$\Delta\beta$	ΔF	$\Delta\mu$	$\Delta\beta$	ΔF
IA vs G1	0.00	0.00	0.00	0.00	0.00	0.00	0.00	0.00	0.00	0.00	0.01	0.01
IA vs G2	0.00	0.00	0.00	0.00	0.00	0.00	0.00	0.00	0.00	0.00	0.01	0.01

[§] IA = inventory average model; G1 = geotechnical damage; and G2 = structural damage.

[†] $\Delta\mu$ = absolute difference of fragility median; $\Delta\beta$ = absolute difference of fragility dispersion; and $\Delta F(IM)$ = maximum absolute difference of fragility probability in S_{a1} = 0 g to 3.0 g.

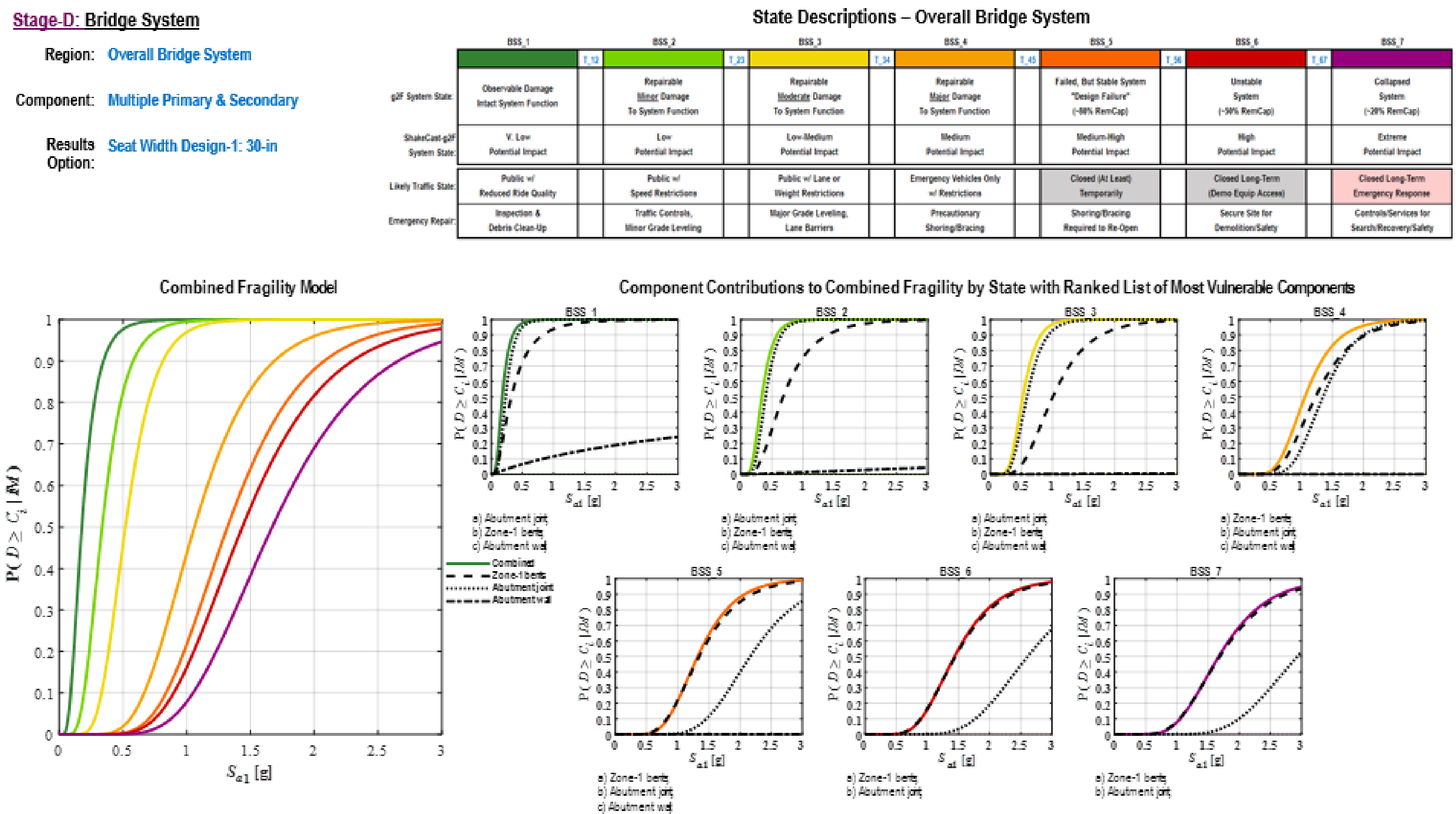

Figure G.1: Stage-D roll-up: system fragility curves with 30 inch seat width.

Stage-D: Bridge System

Region: Overall Bridge System

Component: Multiple Primary & Secondary

Results Option: Seat Width Design-2: 36-in

State Descriptions – Overall Bridge System

	BSS_1	T_12	BSS_2	T_23	BSS_3	T_34	BSS_4	T_45	BSS_5	T_56	BSS_6	T_67	BSS_7
g2F System State:	Observable Damage Intact System Function		Repairable Minor Damage To System Function		Repairable Moderate Damage To System Function		Repairable Major Damage To System Function		Failed, But Stable System "Design Failure" (~80% RemCap)		Unstable System (~50% RemCap)		Collapsed System (~20% RemCap)
ShakeCast-g2F System State:	V. Low Potential Impact		Low Potential Impact		Low-Medium Potential Impact		Medium Potential Impact		Medium-High Potential Impact		High Potential Impact		Extreme Potential Impact
Likely Traffic State:	Public w/ Reduced Ride Quality		Public w/ Speed Restrictions		Public w/ Lane or Weight Restrictions		Emergency Vehicles Only w/ Restrictions		Closed (At Least) Temporarily		Closed Long-Term (Demo Equip Access)		Closed Long-Term Emergency Response
Emergency Repair:	Inspection & Debris Clean-Up		Traffic Controls, Minor Grade Leveling		Major Grade Leveling, Lane Barriers		Precautionary Shoring/Bracing		Shoring/Bracing Required to Re-Open		Secure Site for Demolition/Safety		Controls/Services for Search/Recovery/Safety

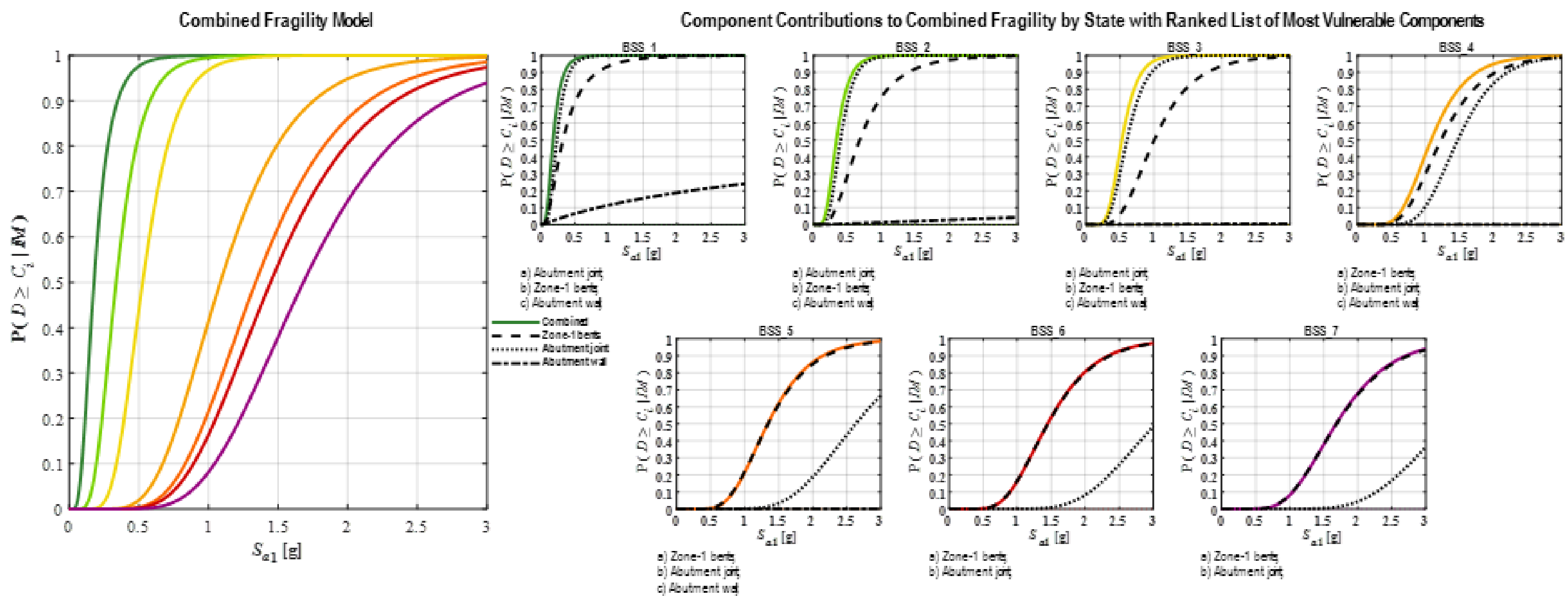

Figure G.2: Stage-D roll-up: system fragility curves with 36 inch seat width.

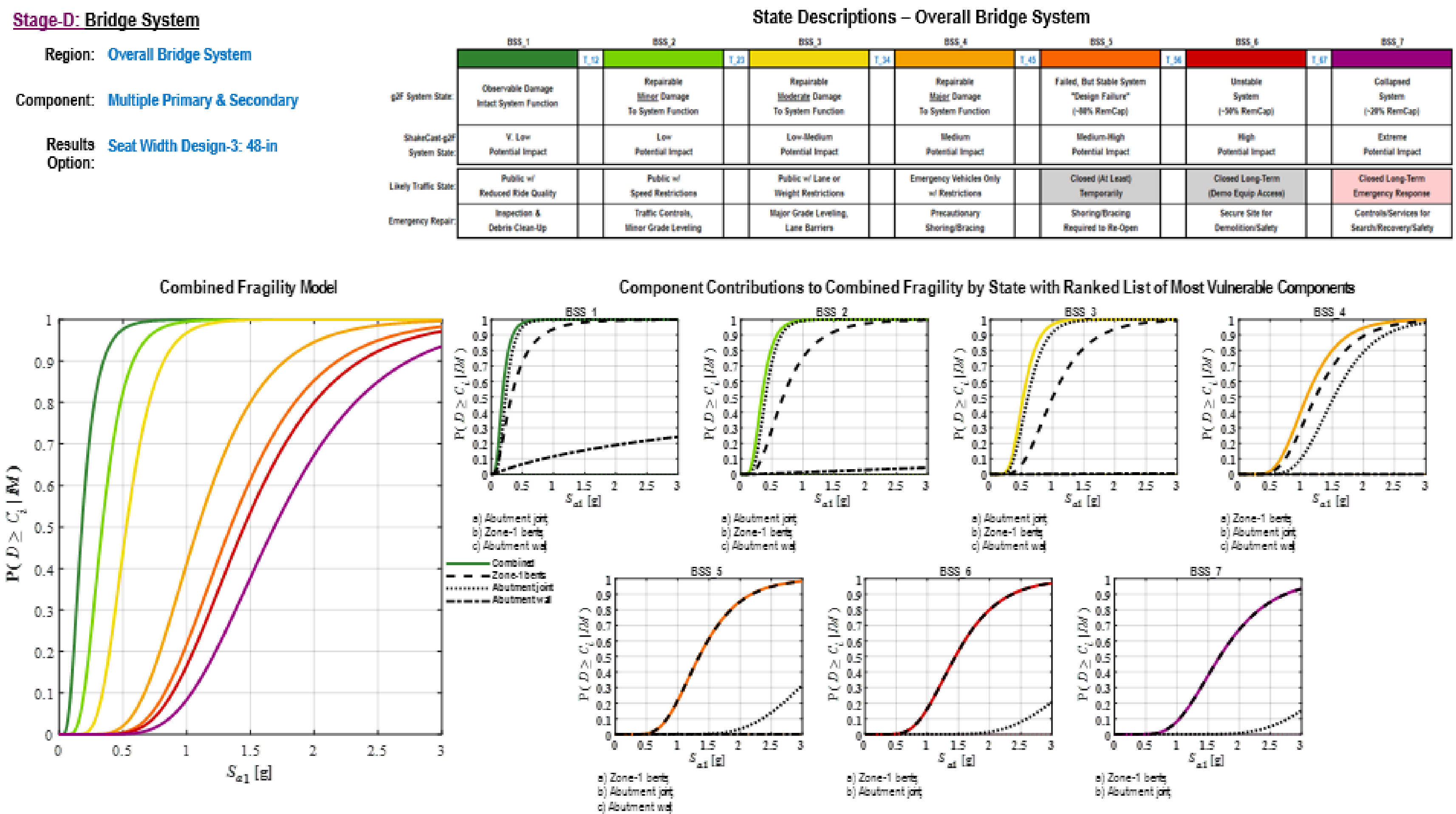

Figure G.3: Stage-D roll-up: system fragility curves with 48 inch seat width.

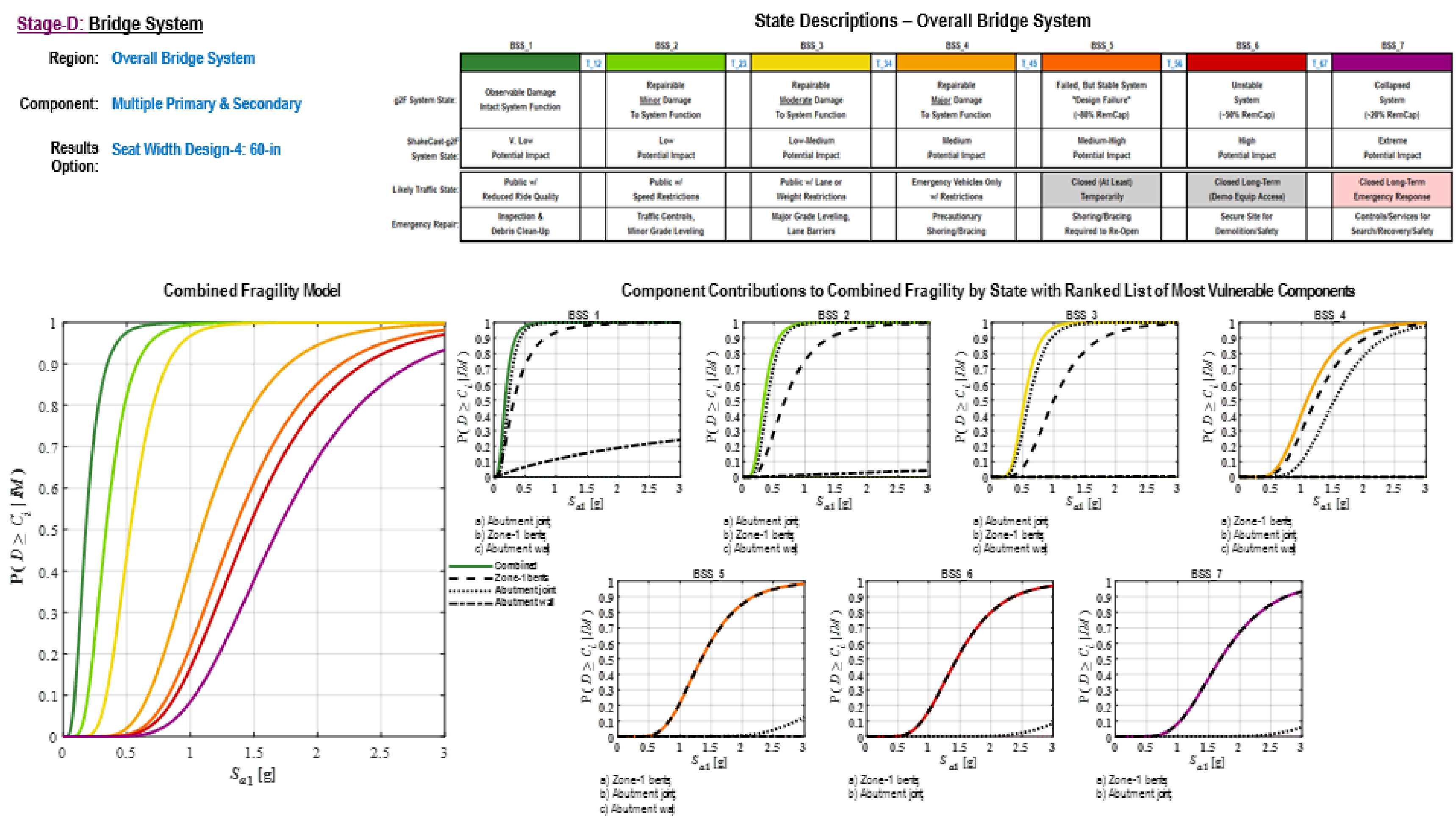

Figure G.4: Stage-D roll-up: system fragility curves with 60 inch seat width.

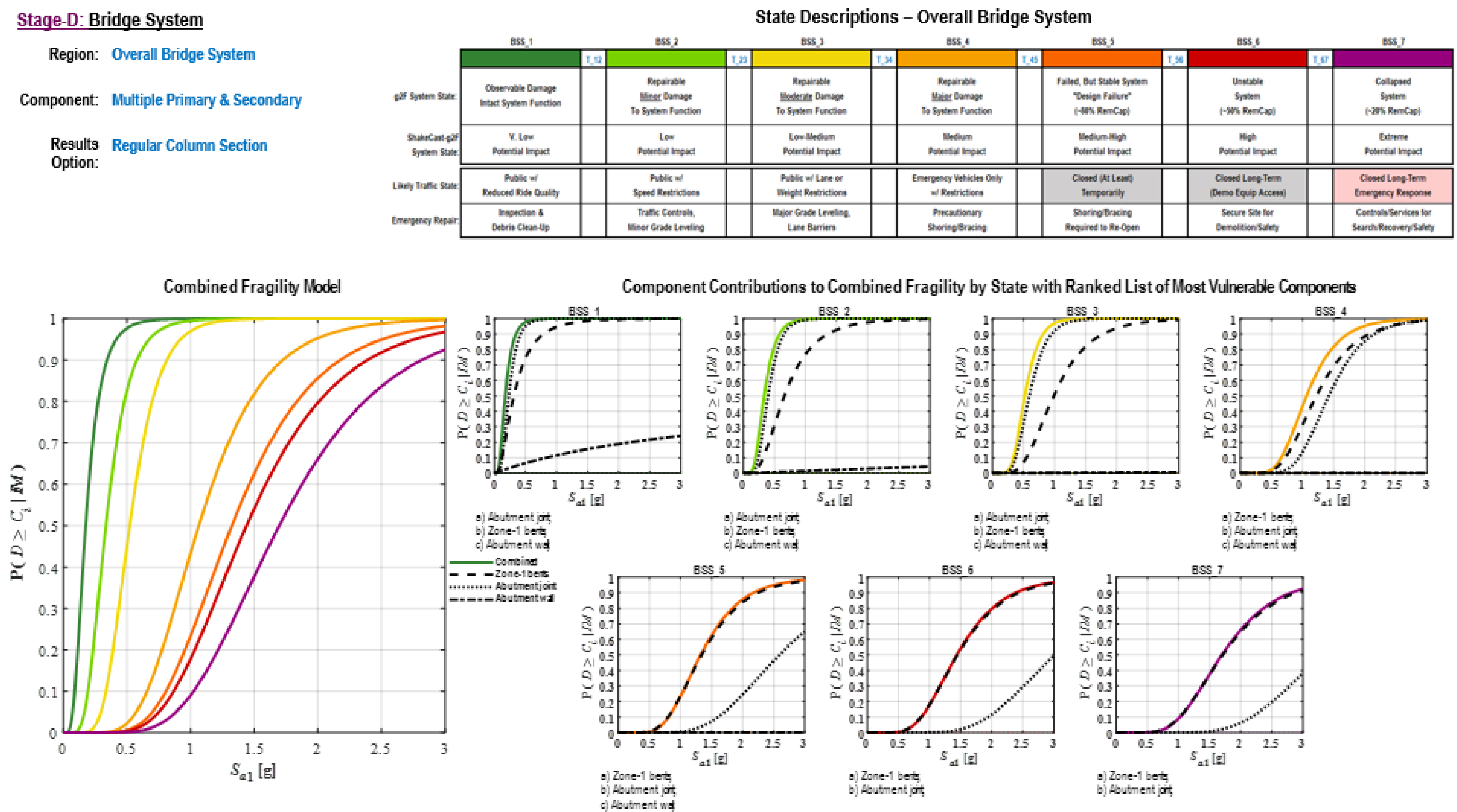

Figure G.5: Stage-D roll-up: system fragility curves with regular column sections.

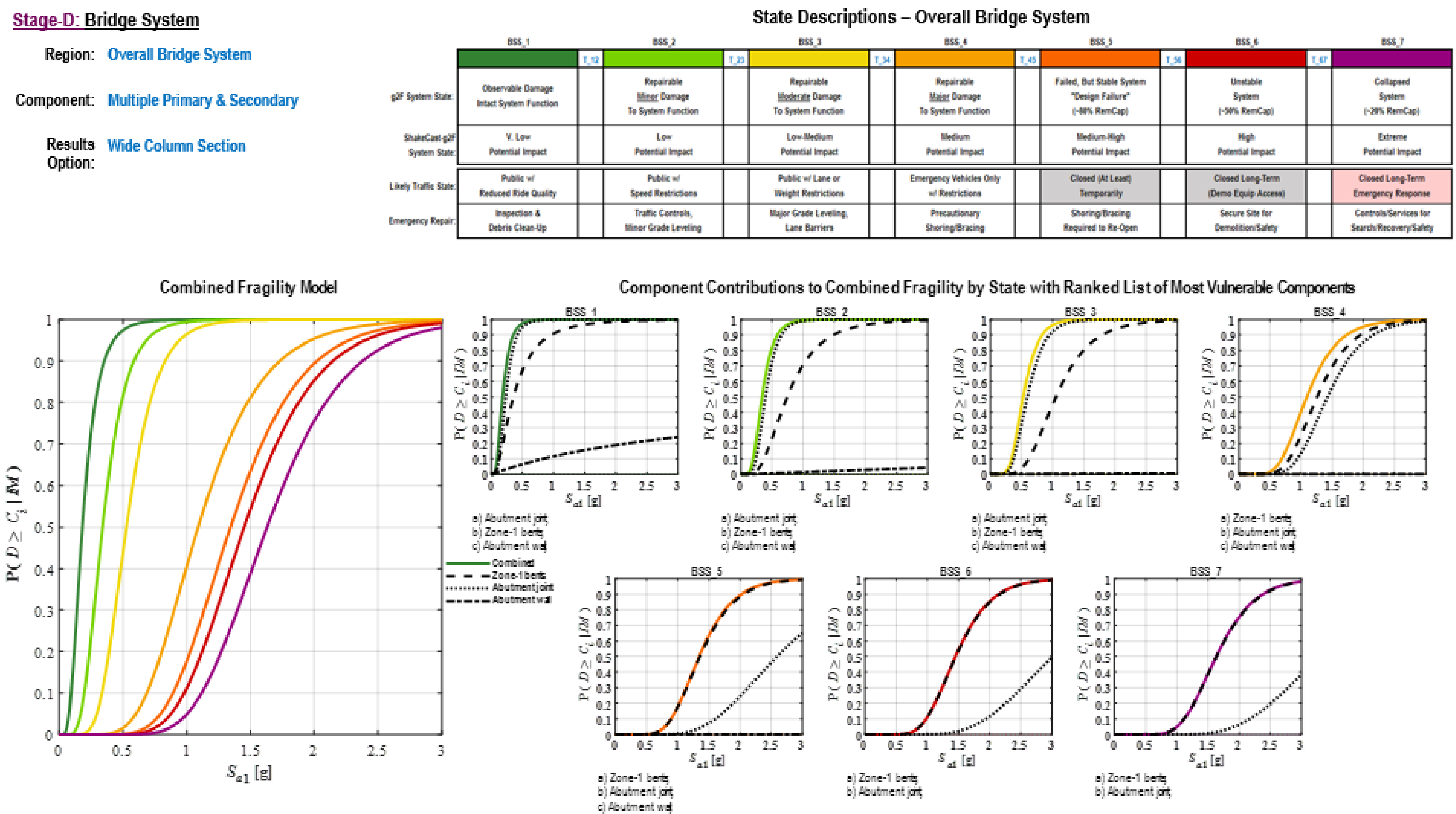

Figure G.6: Stage-D roll-up: system fragility curves with wide column sections.

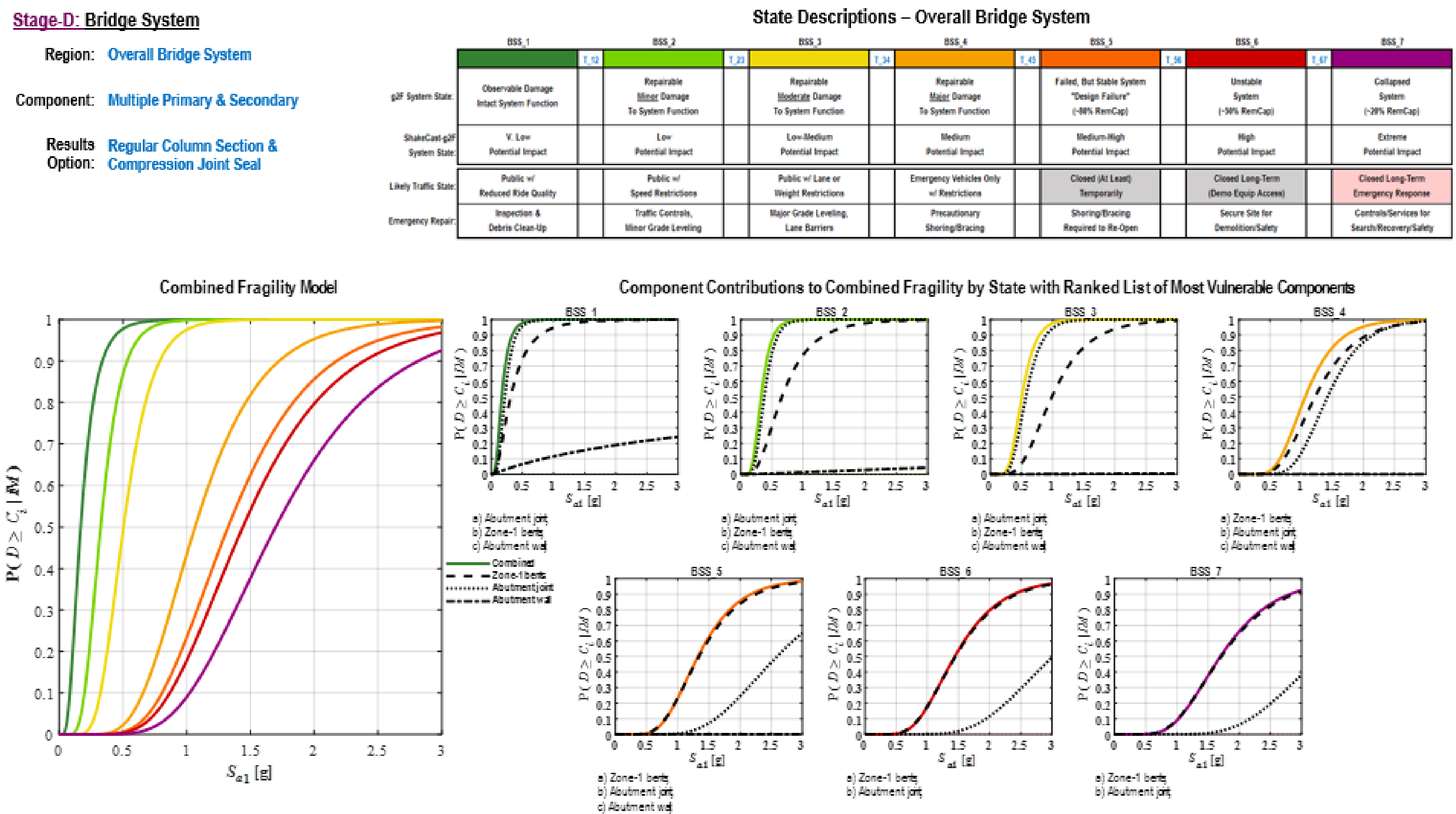

Figure G.7: Stage-D roll-up: system fragility curves with regular column sections and compression joint seal.

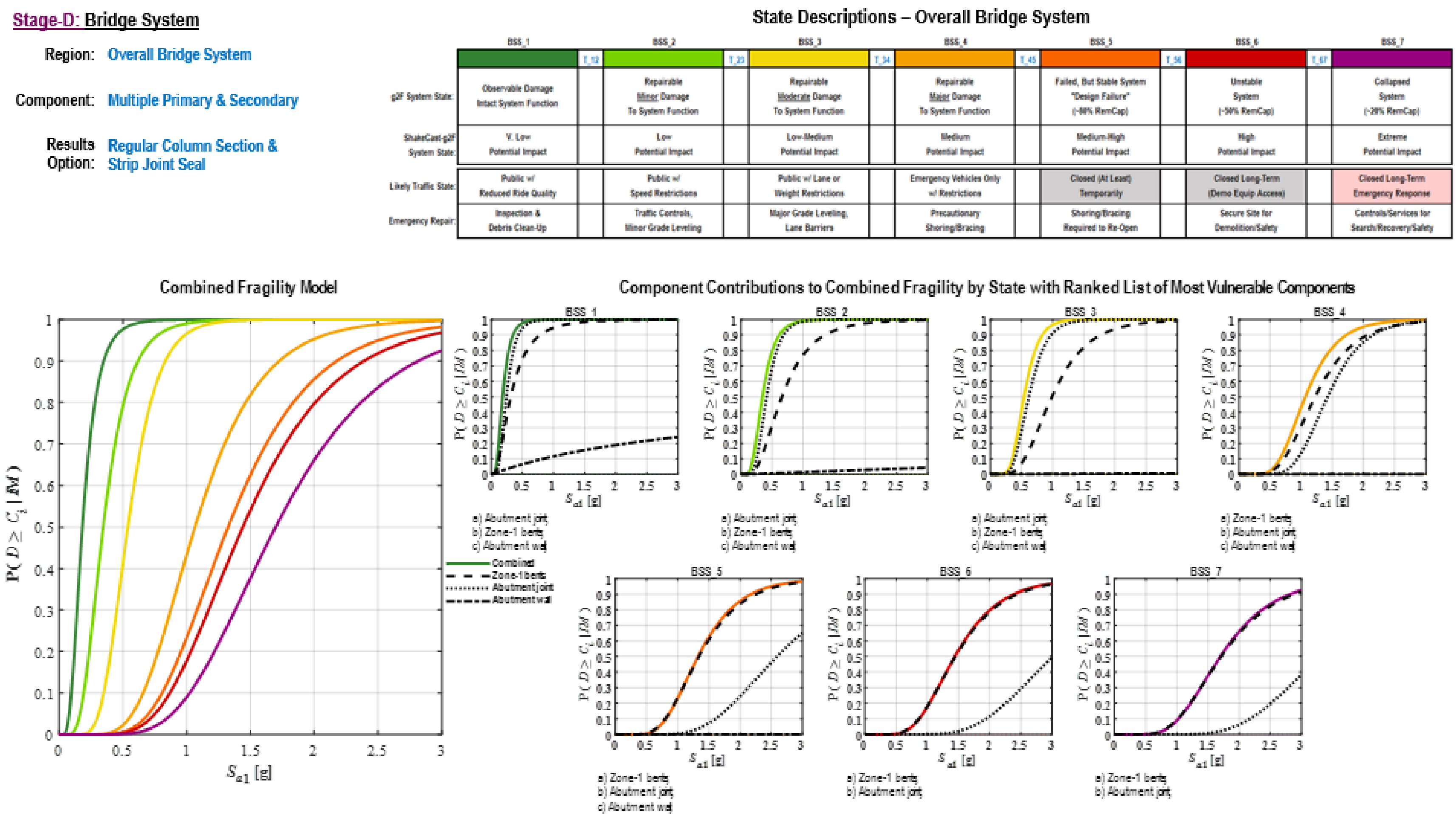

Figure G.8: Stage-D roll-up: system fragility curves with regular column sections and strip joint seal.

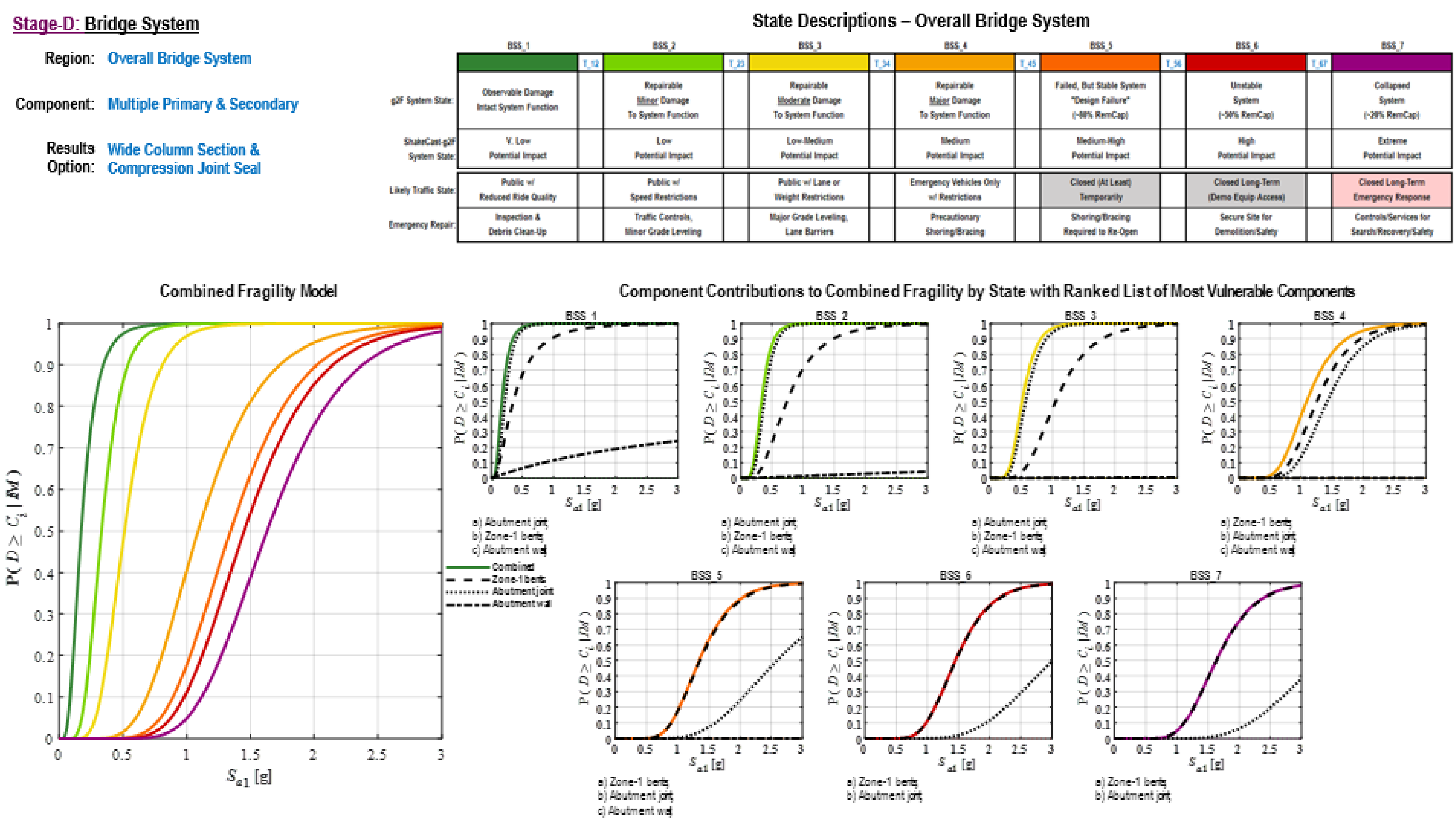

Figure G.9: Stage-D roll-up: system fragility curves with wide column sections and compression joint seal.

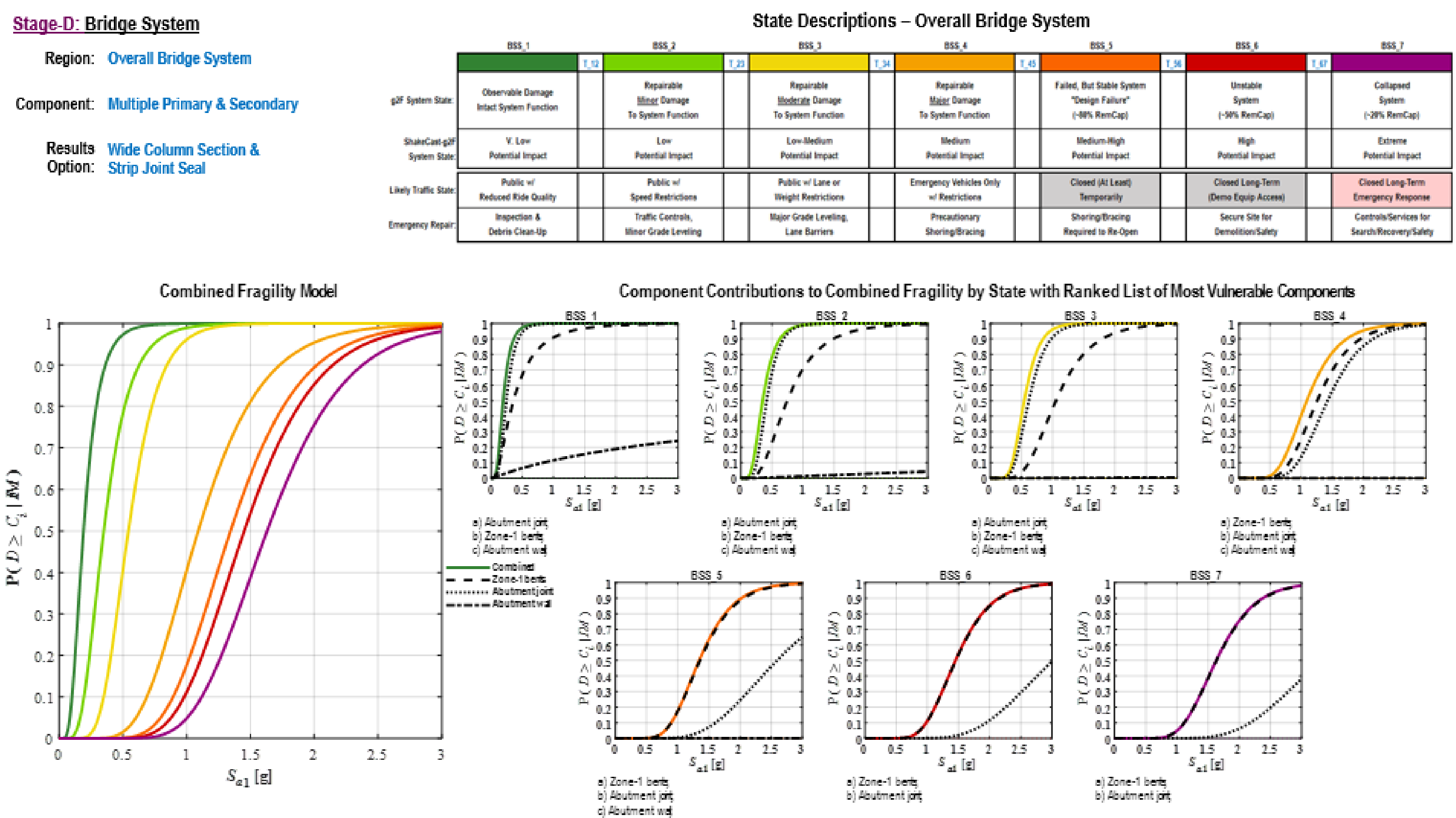

Figure G.10: Stage-D roll-up: system fragility curves with wide column sections and strip joint seal.

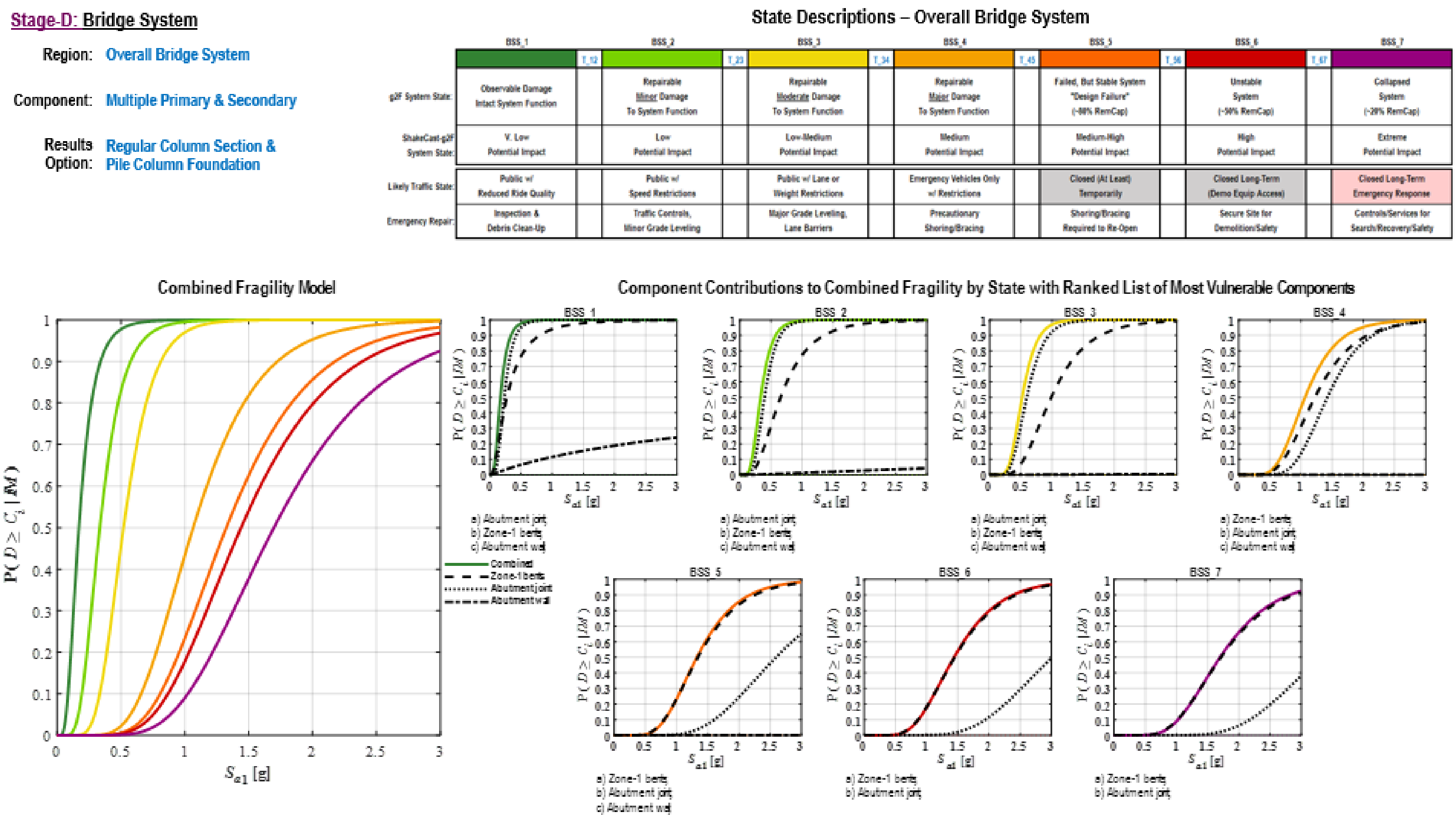

Figure G.11: Stage-D roll-up: system fragility curves with regular column sections and pile column foundations.

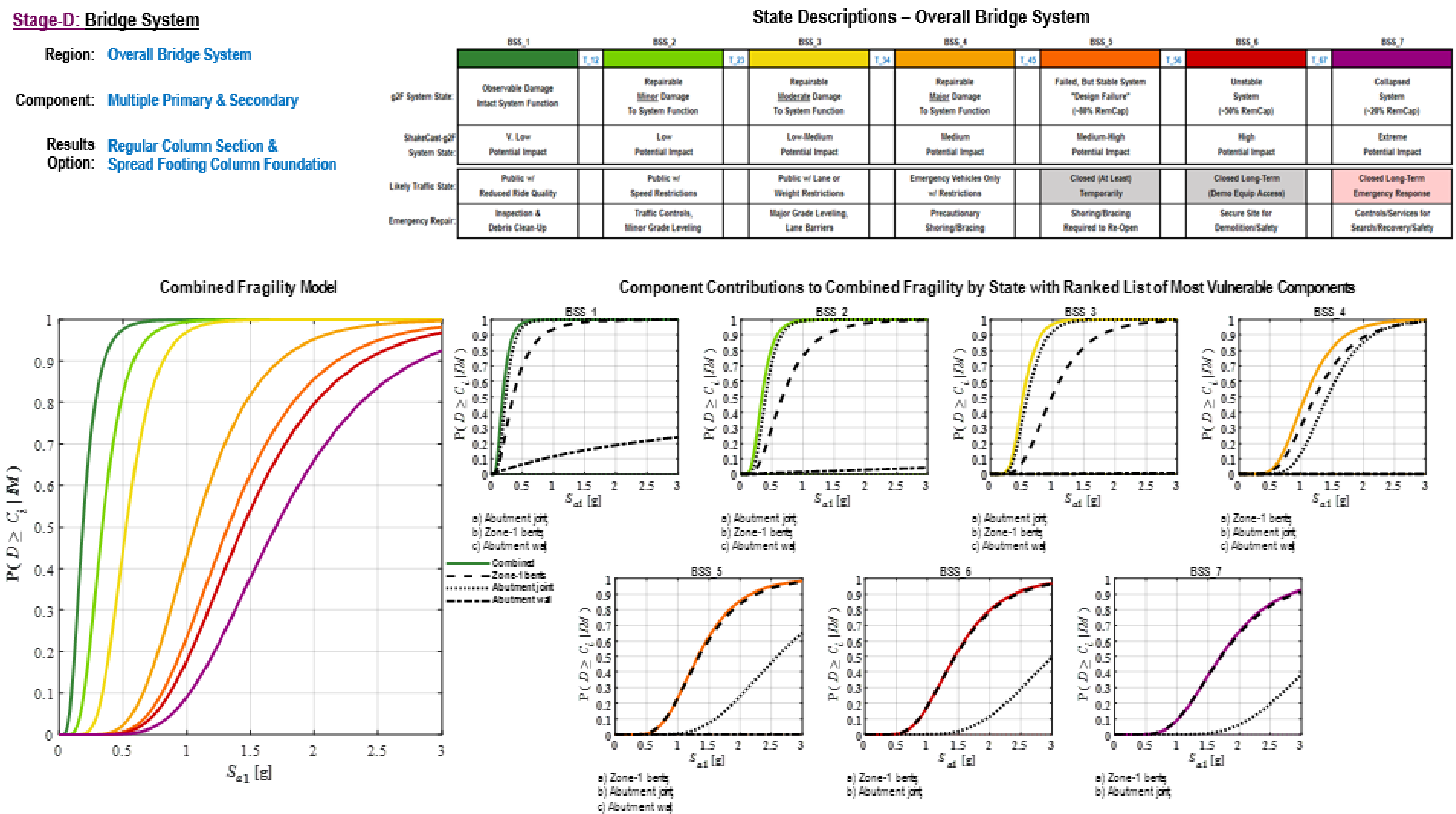

Figure G.12: Stage-D roll-up: system fragility curves with regular column sections and footing column foundations.

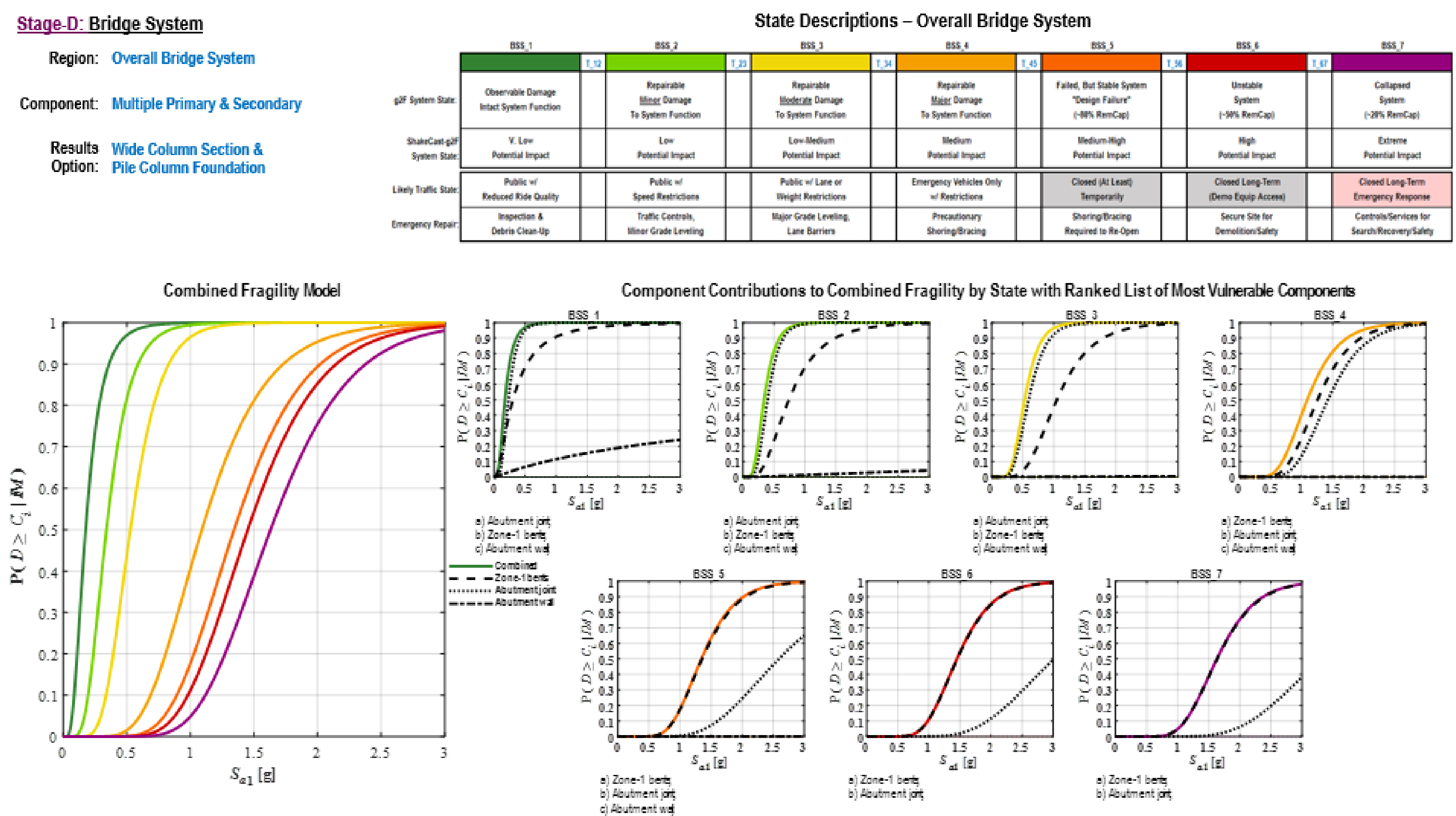

Figure G.13: Stage-D roll-up: system fragility curves with wide column sections and pile column foundations.

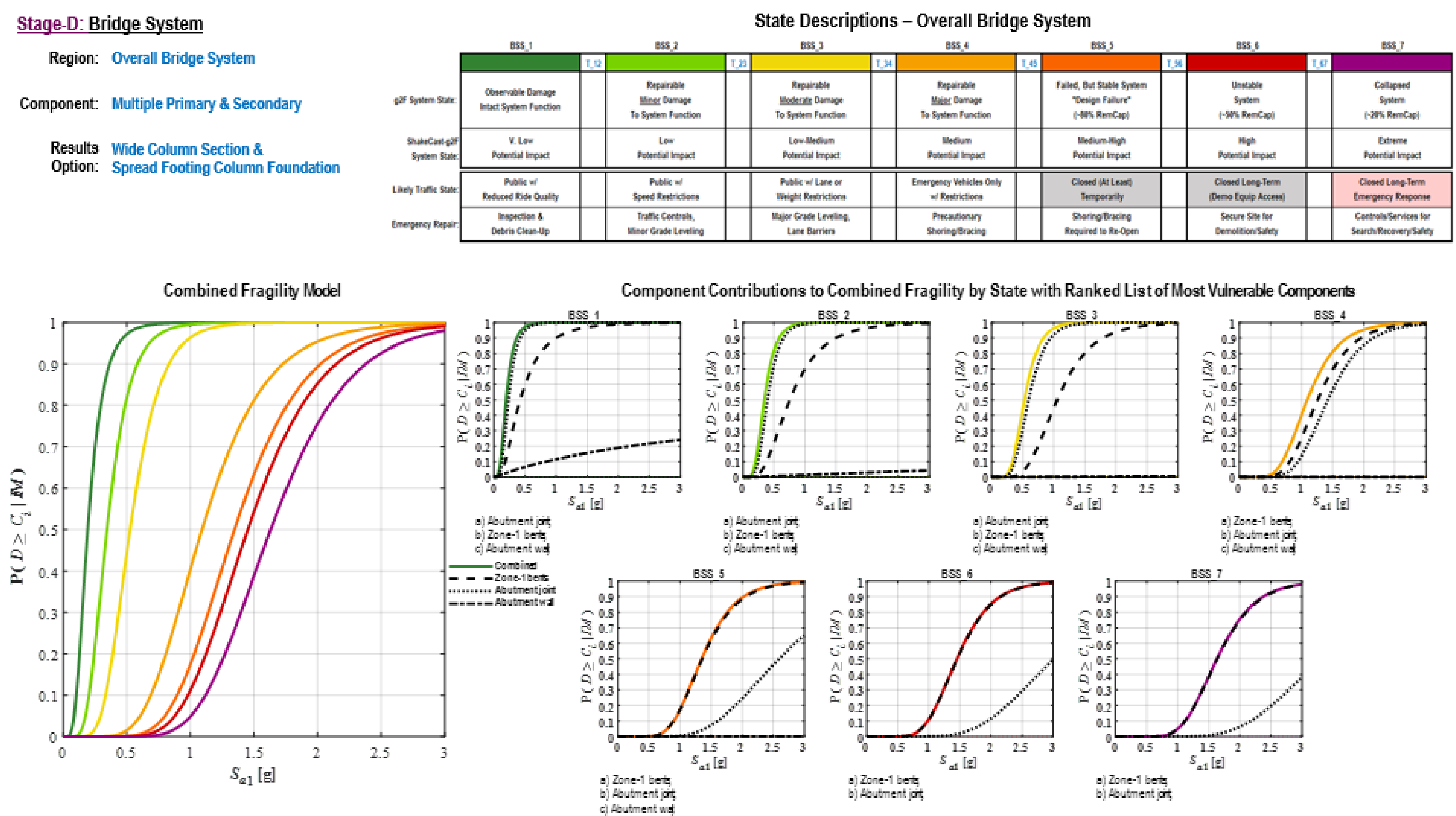

Figure G.14: Stage-D roll-up: system fragility curves with wide column sections and footing column foundations.

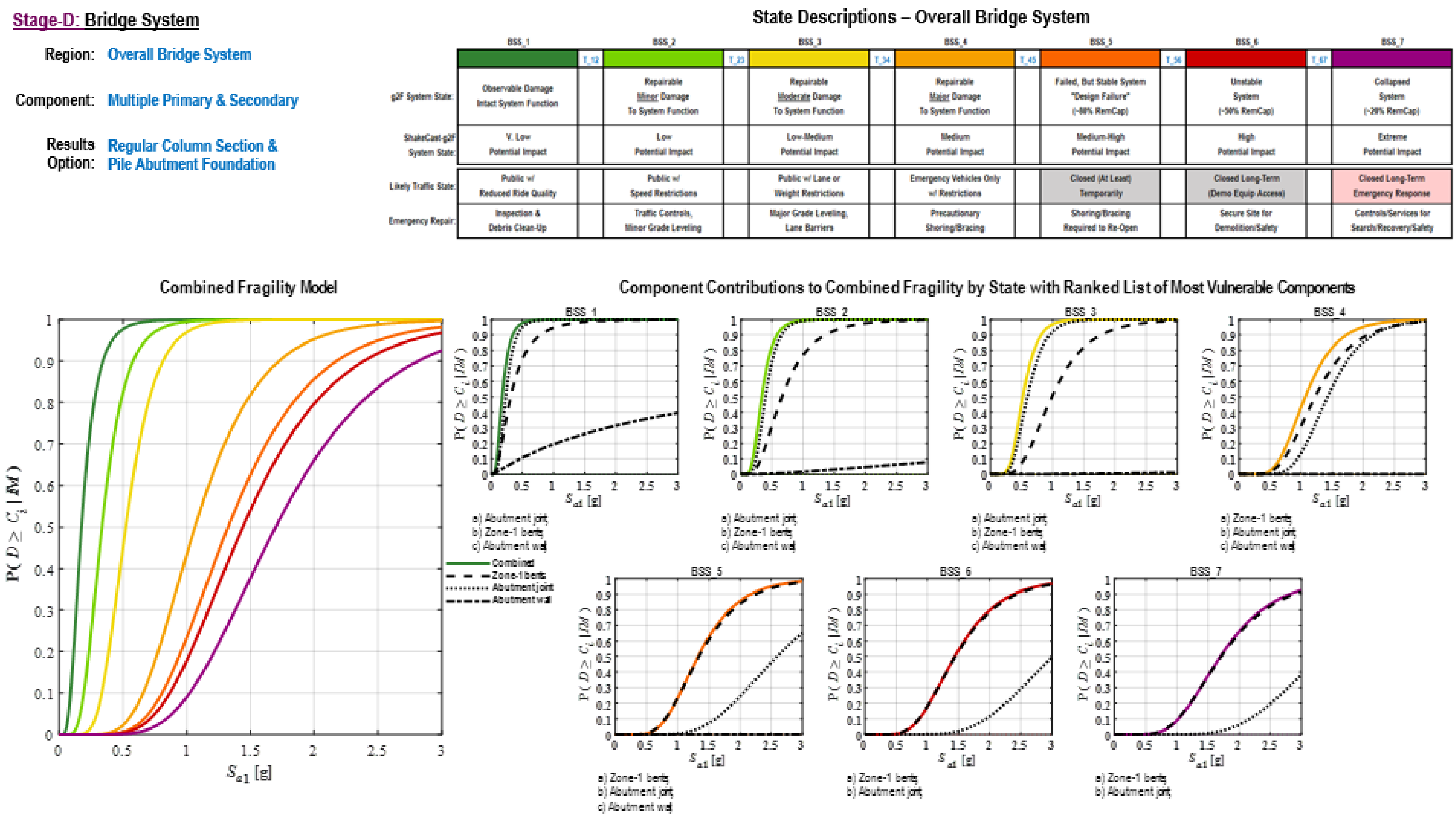

Figure G.15: Stage-D roll-up: system fragility curves with regular column sections and pile abutment foundations.

Stage-D: Bridge System

Region: Overall Bridge System

Component: Multiple Primary & Secondary

Results Option: Regular Column Section & Spread Footing Abutment Foundation

State Descriptions – Overall Bridge System

	BSS_1	T_12	BSS_2	T_23	BSS_3	T_34	BSS_4	T_45	BSS_5	T_56	BSS_6	T_67	BSS_7
g2F System State:	Observable Damage Intact System Function		Repairable Minor Damage To System Function		Repairable Moderate Damage To System Function		Repairable Major Damage To System Function		Failed, But Stable System "Design Failure" (~80% RemCap)		Unstable System (~50% RemCap)		Collapsed System (~20% RemCap)
ShakeCast-g2F System State:	V. Low Potential Impact		Low Potential Impact		Low-Medium Potential Impact		Medium Potential Impact		Medium-High Potential Impact		High Potential Impact		Extreme Potential Impact
Likely Traffic State:	Public w/ Reduced Ride Quality		Public w/ Speed Restrictions		Public w/ Lane or Weight Restrictions		Emergency Vehicles Only w/ Restrictions		Closed (At Least) Temporarily		Closed Long-Term (Demo Equip Access)		Closed Long-Term Emergency Response
Emergency Repair:	Inspection & Debris Clean-Up		Traffic Controls, Minor Grade Leveling		Major Grade Leveling, Lane Barriers		Precautionary Shoring/Bracing		Shoring/Bracing Required to Re-Open		Secure Site for Demolition/Safety		Controls/Services for Search/Recovery/Safety

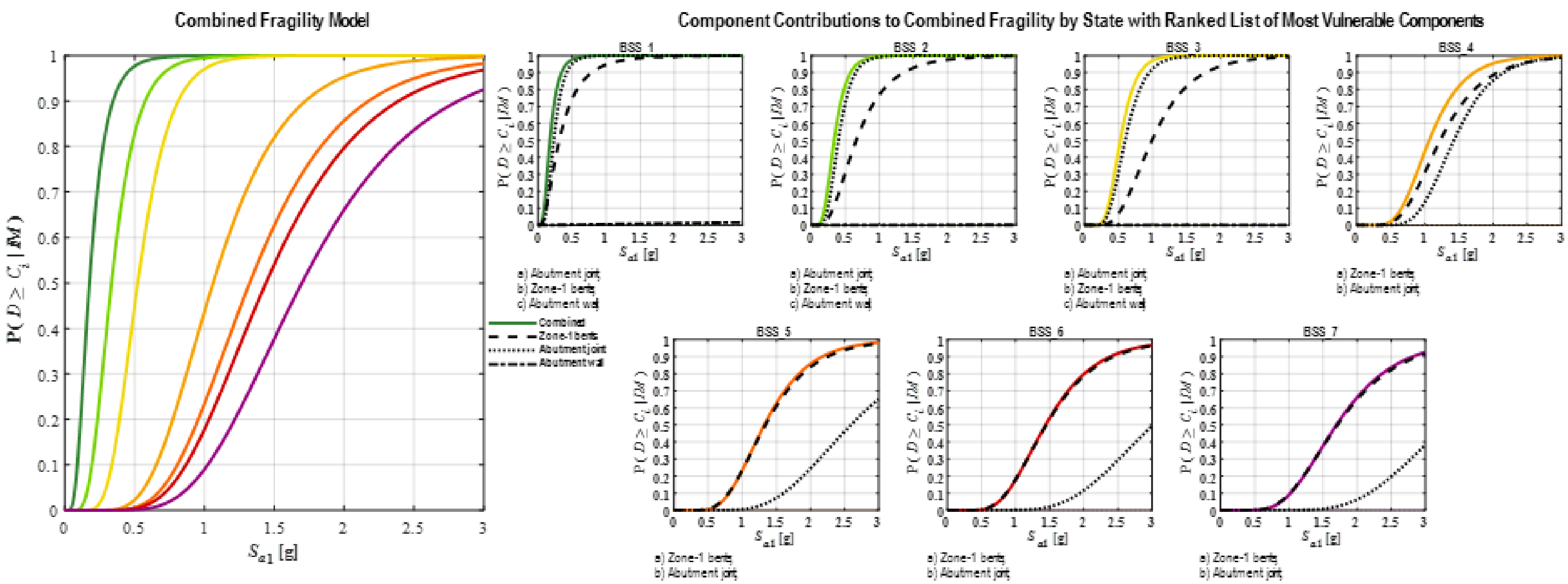

Figure G.16: Stage-D roll-up: system fragility curves with regular column sections and footing abutment foundations.

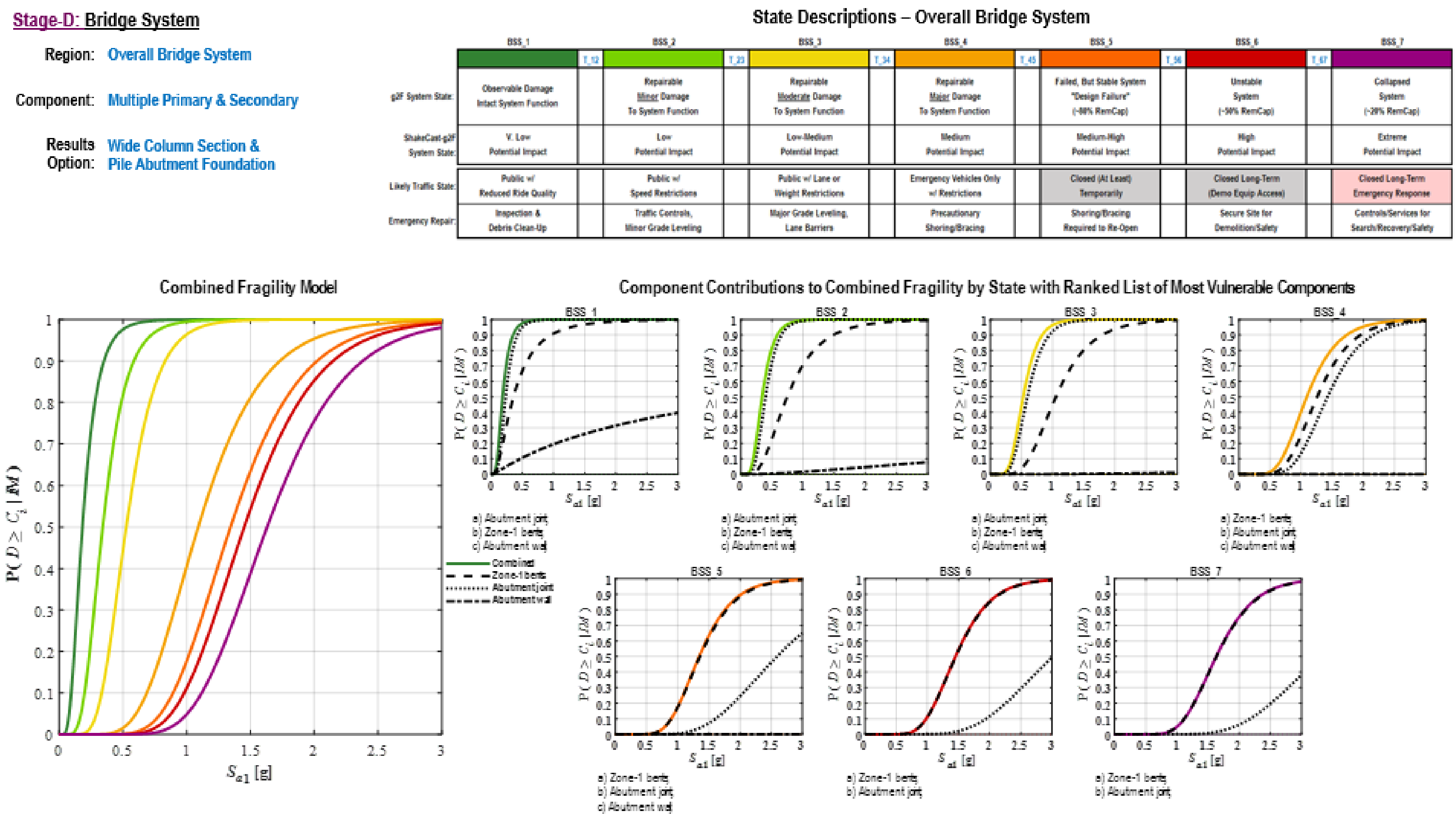

Figure G.17: Stage-D roll-up: system fragility curves with wide column sections and pile abutment foundations.

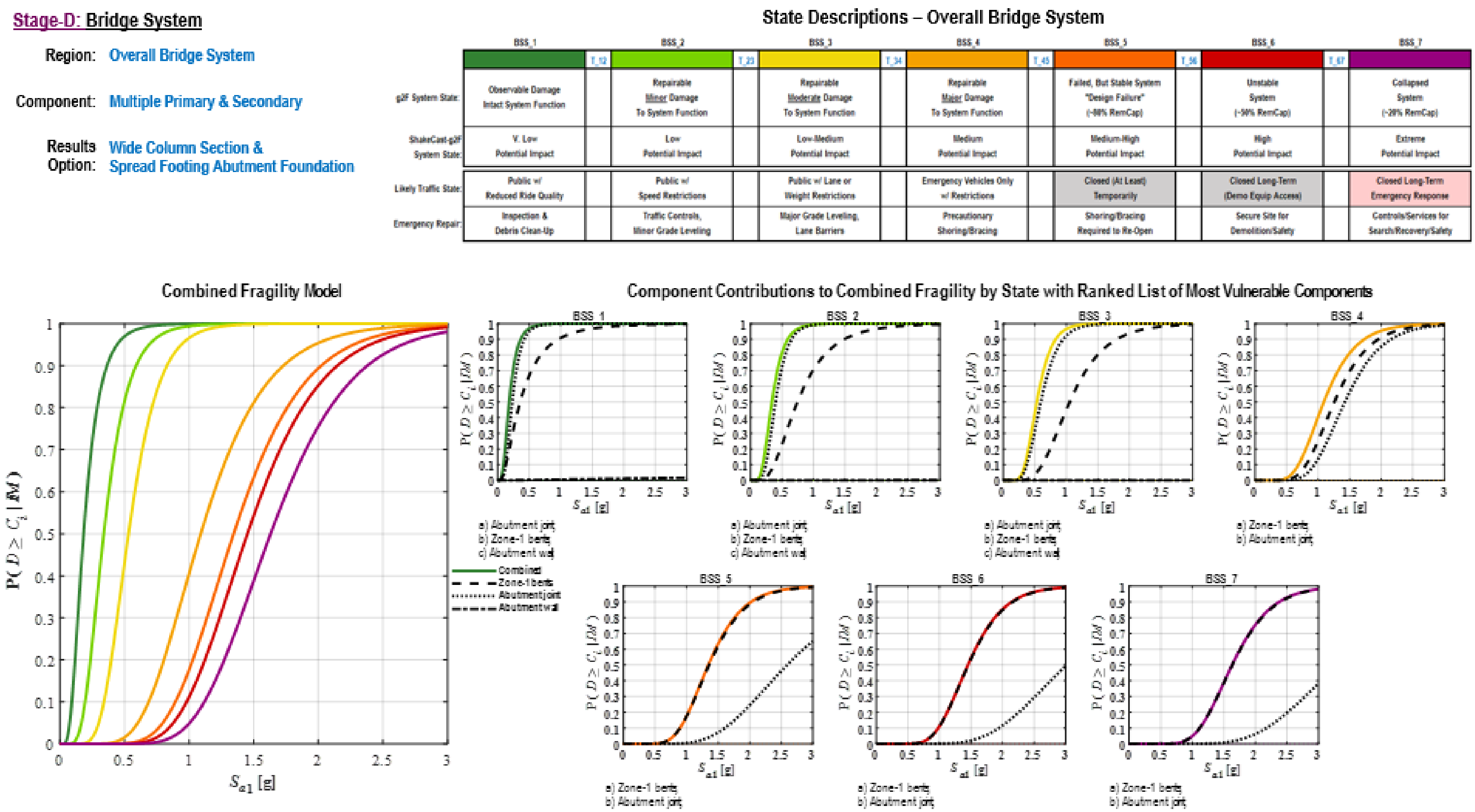

Figure G.18: Stage-D roll-up: system fragility curves with wide column sections and footing abutment foundations.

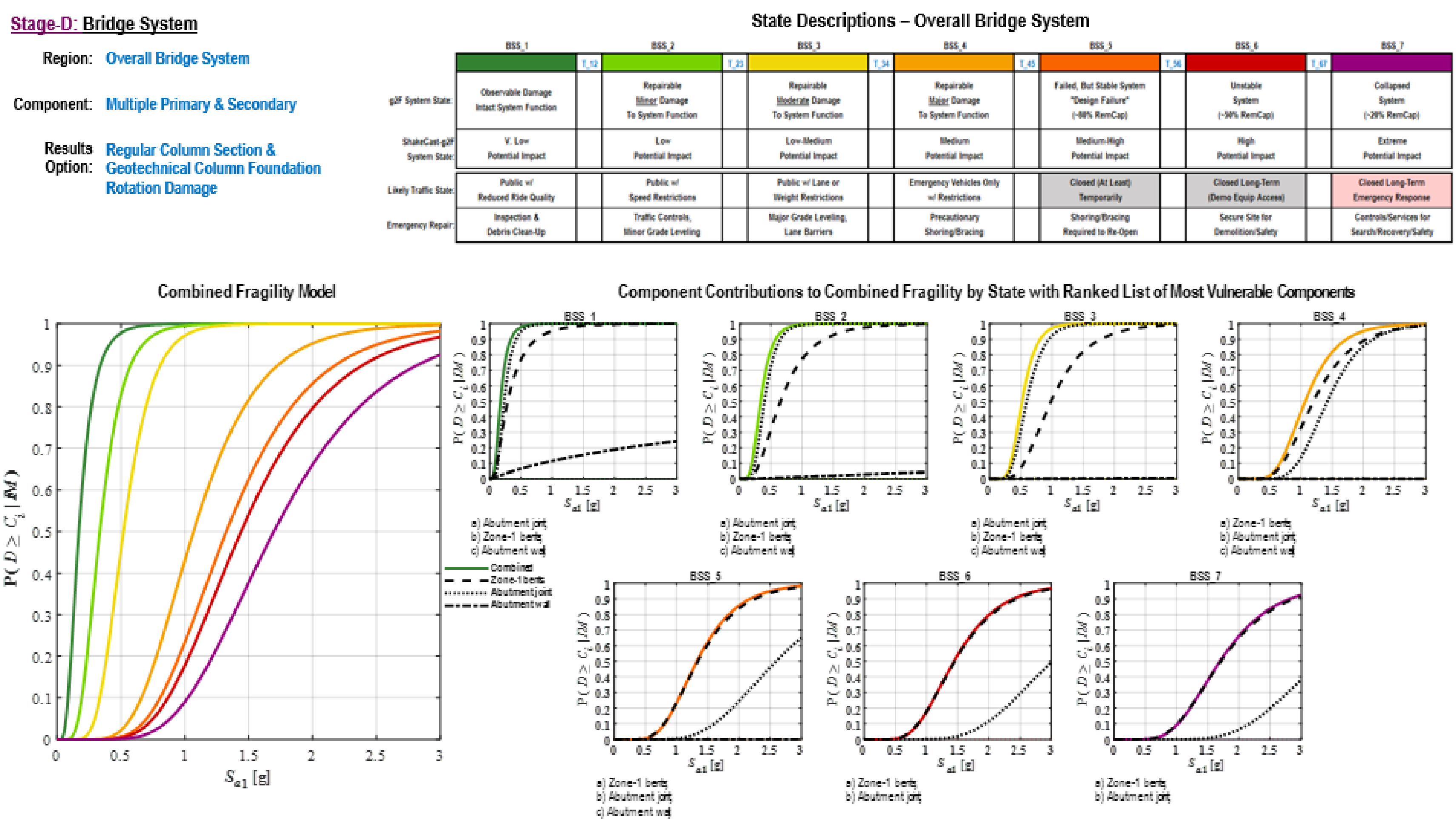

Figure G.19: Stage-D roll-up: system fragility curves with regular column sections and geotechnical foundation rotation damage.

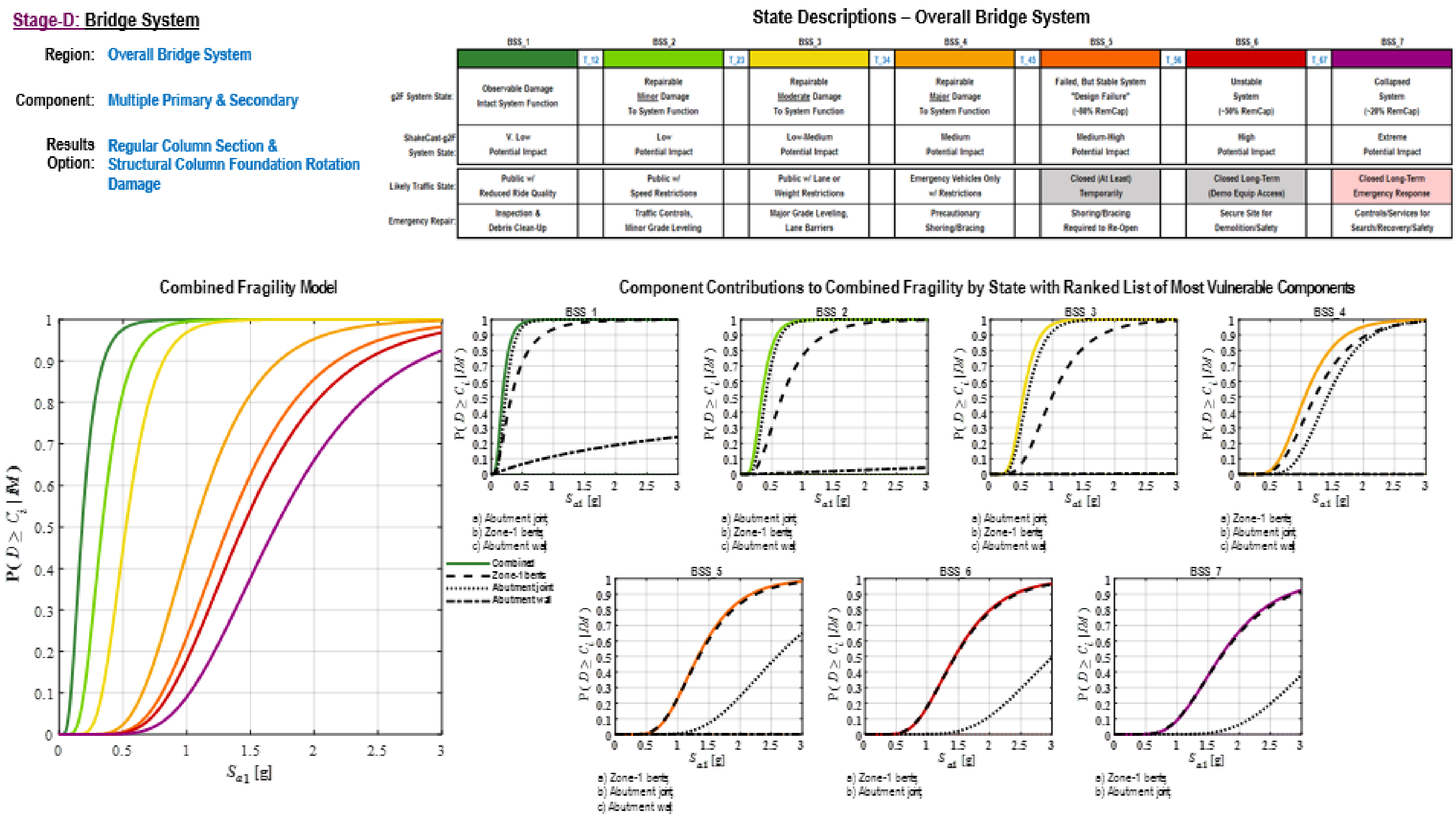

Figure G.20: Stage-D roll-up: system fragility curves with regular column sections and structural foundation rotation damage.

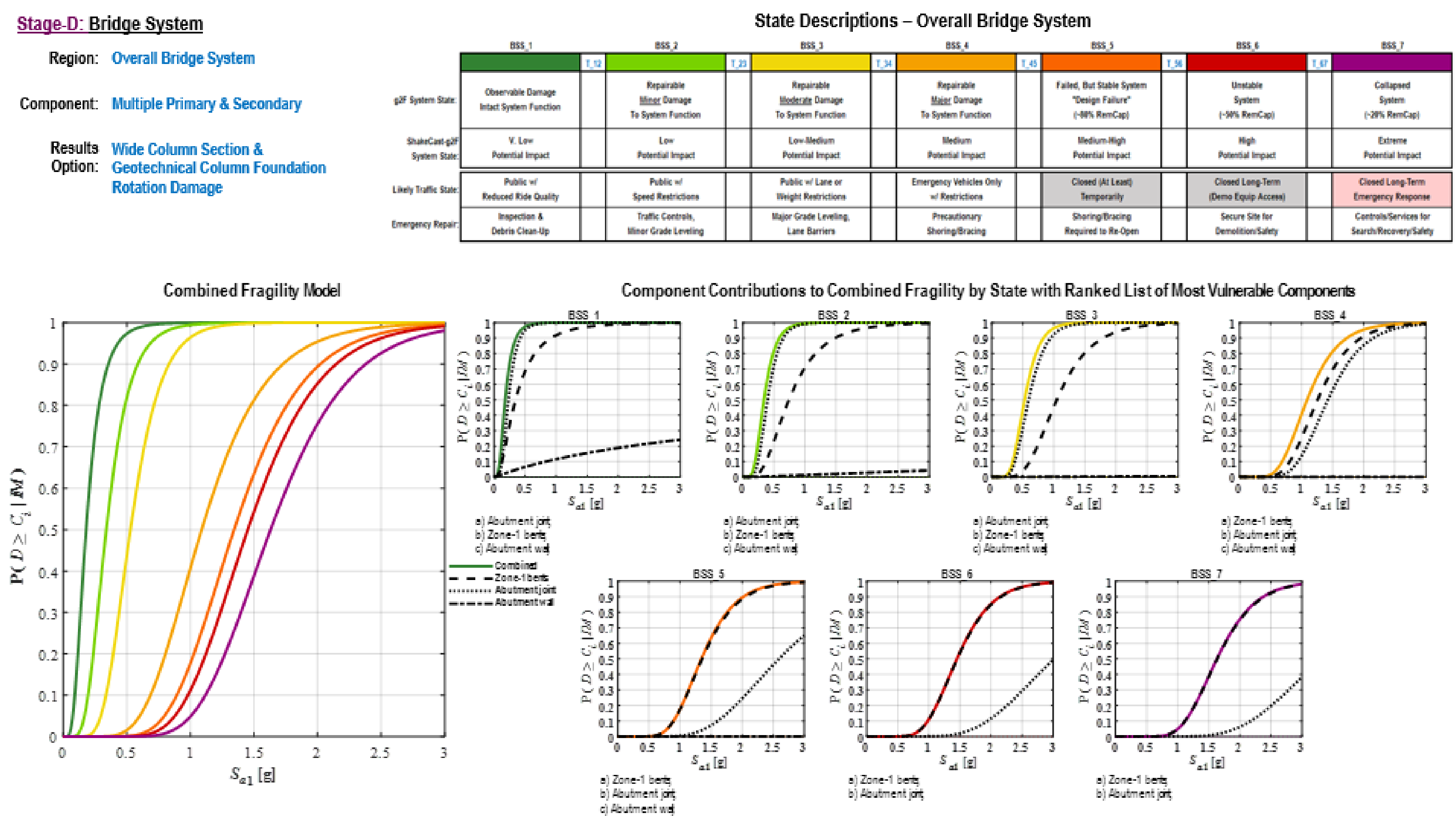

Figure G.21: Stage-D roll-up: system fragility curves with wide column sections and geotechnical foundation rotation damage.

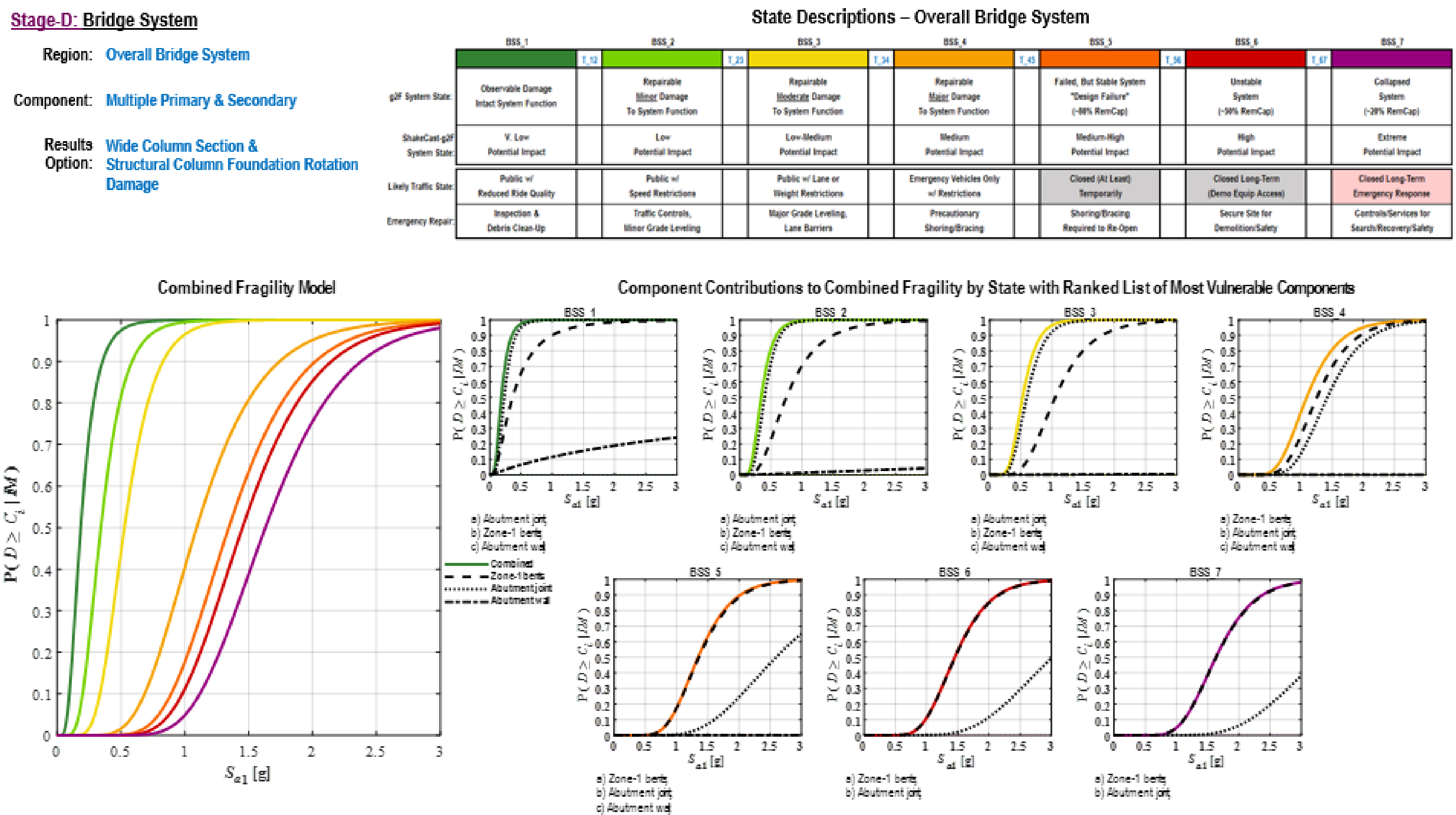

Figure G.22: Stage-D roll-up: system fragility curves with wide column sections and structural foundation rotation damage.

REFERENCE

AASHTO (2010), *Standard Specifications for Highway Bridges*, American Association of State Highway and Transportation Officials.

ACI (2014), Building Code Requirements for Structural Concrete (ACI 318-14): Commentary on Building Code Requirements for Structural Concrete (ACI 318R-14): An ACI Report, American Concrete Institute.

Ang, B. G. (1985), 'Seismic Shear Strength of Circular Bridge Piers.'.

ATC (1985), *Earthquake Damage Evaluation Data for California*, Applied Technology Council.

Baba, K., Shibata, R. and Sibuya, M. (2004), 'Partial Correlation and Conditional Correlation As Measures of Conditional Independence', *Australian & New Zealand Journal of Statistics* **46**(4), 657–664.

Baker, J. W. (2015), 'Efficient Analytical Fragility Function Fitting Using Dynamic Structural Analysis', *Earthquake Spectra* **31**(1), 579–599.

Baker, J. W., Lin, T., Shahi, S. K. and Jayaram, N. (2011), 'New Ground Motion Selection Procedures and Selected Motions for the PEER Transportation Research Program', *PEER report* **3**.

Banerjee, S. and Shinozuka, M. (2007), 'Nonlinear Static Procedure for Seismic Vulnerability Assessment of Bridges', *Computer-Aided Civil and Infrastructure Engineering* **22**(4), 293–305.

Bao, Y., Main, J. A., Lew, H. and Sadek, F. (2017), 'Performance of Precast Concrete Moment Frames Subjected To Column Removal: Part 2, Computational Analysis', *PCI Journal* **62**(5), 53–74.

Barkhordary, M., Farjadi, A. and Tariverdilo, S. (2009), 'Fragility Curves for Reinforced Concrete Frames with Lap-spliced Columns', *International Journal of Engineering* **22**(3), 213–224.

Basöz, N. I., Kiremidjian, A. S., King, S. A. and Law, K. H. (1999a), 'Statistical Analysis of Bridge Damage Data From the 1994 Northridge, CA, Earthquake', *Earthquake spectra* **15**(1), 25–54.

Basöz, N. and Kiremidjian, A. S. (1999b), Development of Empirical Fragility Curves for Bridges, *in* 'Optimizing post-earthquake lifeline system reliability', ASCE, pp. 693–702.

Bozorgnia, Y., Abrahamson, N. A., Atik, L. A., Ancheta, T. D., Atkinson, G. M., Baker, J. W., Baltay, A., Boore, D. M., Campbell, K. W., Chiou, B. S.-J. and Others (2014), 'NGA-West2 Research Project', *Earthquake Spectra* **30**(3), 973–987.

Bozorgzadeh, A., Megally, S., Restrepo, J. I. and Ashford, S. A. (2006), 'Capacity Evaluation of Exterior Sacrificial Shear Keys of Bridge Abutments', *Journal of Bridge Engineering* **11**(5), 555–565.

Bromenschenkle, R., Lee, D., Mahan, M. M., S. Yoon, Y. and Zokaie, T. (2015), Probabilistic Damage Control Approach for Seismic Design of Bridge Columns, Technical report, 14WCSI.

Buckle, I. E. and Friedland, I. M. (1995), 'Ll Seismic Retrofitting Manual for Highway Bridges'.

Calderone, A. J., Lehman, D. E. and Moehle, J. P. (2000), *Behavior of Reinforced Concrete Bridge Columns Having Varying Aspect Ratios and Varying Lengths of Confinement*, Pacific Earthquake Engineering Research Center, College of Engineering ....

Caltrans (1990), 'Bridge Design Specifications Manual'.

Caltrans (1994), 'The Northridge Earthquake', *Caltrans PEQIT Report* .

Caltrans (2014), 'Memo to Designers 3-1, Deep Foundations'.

Caltrans (2015*a*), '2015 Standard Plan B2-3, 16-Inch and 24-Inch Cast-In-Drilled-Hole Concrete Pile'.

Caltrans (2015*b*), '2015 Standard Plan B2-5, Pile Details Class 90 and Class 140'.

Caltrans (2015*c*), '2015 Standard Plan B2-8, Pile Details Class 200'.

Caltrans (2015*d*), 'Bridge Design Practice'.

Caltrans (2017), 'Bridge Memo To Designers. Section 5: General Type Selection of Abutment'.

Caltrans (2018), 'Bridge Design Specifications Manual'.

Caltrans (2019), 'Seismic Design Criteria'.

Chai, Y. H., Priestley, M. N. and Seible, F. (1991), 'Seismic Retrofit of Circular Bridge Columns for Enhanced Flexural Performance', *Structural Journal* **88**(5), 572–584.

Chang, G. and Mander, J. B. (1994), 'Seismic Energy Based Fatigue Damage Analysis of Bridge Columns: Part 1–evaluation of Seismic Capacity', *NCEER Technical Rep. No. NCEER-94* **6**.

Choi, E., DesRoches, R. and Nielson, B. (2004), 'Seismic Fragility of Typical Bridges in Moderate Seismic Zones', *Engineering structures* **26**(2), 187–199.

Choi, E. and Jeon, J.-C. (2003), 'Seismic Fragility of Typical Bridges in Moderate Seismic Zone', *KSCE Journal of Civil Engineering* **7**(1), 41–51.

Coleman, J. and Spacone, E. (2001), 'Localization Issues in Force-based Frame Elements', *Journal of Structural Engineering* **127**(11), 1257–1265.

Cornell, C. A., Jalayer, F., Hamburger, R. O. and Foutch, D. A. (2002), 'Probabilistic Basis for 2000 SAC Federal Emergency Management Agency Steel Moment Frame Guidelines', *Journal of structural engineering* **128**(4), 526–533.

DesRoches, R., Padgett, J., Ramanathan, K. and Dukes, J. (2012), Feasibility Studies for Improving Caltrans Bridge Fragility Relationships, Technical report, Caltrans Research Report CA12-1775, 540p.

Dukes, J. D. (2013), Application of Bridge Specific Fragility Analysis in the Seismic Design Process of Bridges in California, PhD thesis, Georgia Institute of Technology.

Duncan, J. M. and Mokwa, R. L. (2001), 'Passive Earth Pressures: Theories and Tests', *Journal of Geotechnical and Geoenvironmental Engineering* **127**(3), 248–257.

Dutta, A. and Mander, J. (1998), Seismic Fragility Analysis of Highway Bridges, *in* 'Proceedings of the INCEDE-MCEER center-to-center project workshop on earthquake engineering Frontiers in transportation systems', pp. 22–23.

Elwood, K. J. (2002), *Shake Table Tests and Analytical Studies on the Gravity Load Collapse of Reinforced Concrete Frames*, University of California, Berkeley.

Elwood, K. J., Matamoros, A. B., Wallace, J. W., Lehman, D. E., Heintz, J. A., Mitchell, A. D., Moore, M. A., Valley, M. T., Lowes, L. N., Comartin, C. D. et al. (2007), 'Update To ASCE/SEI 41 Concrete Provisions', *Earthquake Spectra* **23**(3), 493–523.

FEMA (1999), 'Earthquake Loss Estimation Methodology: User's Manual'.

FEMA (2003), *HAZUS-MH MR4 User Manual, Multi-hazard Loss Estimation Methodology Earthquake Model*, Federal Emergency Management Agency 366, Washington, DC.

Freedman, D., Pisani, R. and Purves, R. (2020), 'Statistics: Fourth International Student Edition'.

Friedman, J. H. (1991), 'Multivariate Adaptive Regression Splines', *The annals of statistics* pp. 1–67.

Gehl, P., Taalab, K., D'Ayala, D. and Cheng, T. (2014), Developing Fragility Functions for Roadway Bridges Using System Reliability and Support Vector Machines, *in* 'Proceedings of the 2nd European Conference on European Engineering and Seismology, Istanbul, Turkey'.

Ghannoum, W. M. and Moehle, J. P. (2012), 'Rotation-based Shear Failure Model for Lightly Confined RC Columns', *Journal of Structural Engineering* **138**(10), 1267–1278.

Giannini, R., Paolacci, F. and Sibilio, E. (2008), Experimental Study on the Cyclic Response of An Existing RC Bridge Pier, *in* 'Proceedings of the 14th world conference on earthquake engineering, China'.

Goel, R. K. and Chopra, A. K. (2008), 'Role of Shear Keys in Seismic Behavior of Bridges Crossing Fault-rupture Zones', *Journal of Bridge Engineering* **13**(4), 398–408.

Higham, N. J. (1988), 'Computing A Nearest Symmetric Positive Semidefinite Matrix', *Linear algebra and its applications* **103**, 103–118.

Hose, Y. D., Priestley, M. and Seible, F. (1997), Strategic Relocation of Plastic Hinges in Bridge Columns, Technical report.

Hwang, H., Jernigan, J. B. and Lin, Y.-W. (2000), 'Evaluation of Seismic Damage To Memphis Bridges and Highway Systems', *Journal of Bridge Engineering* **5**(4), 322–330.

Hwang, H., Liu, J. B. and Chiu, Y.-H. (2001), 'Seismic Fragility Analysis of Highway Bridges', *Mid-America Earthquake Center CD Release 01-06* .

Inel, M. (2002), 'Displacement-based Strategies for the Performance-based Seismic Design of Short Bridges Considering Embankment Flexibility.', *University of Illinois at Urbana-Champaign* .

Jalayer, F. (2003), *Direct Probabilistic Seismic Analysis: Implementing Non-linear Dynamic Assessments*, Stanford University.

Jeon, J.-S. (2013), Aftershock Vulnerability Assessment of Damaged Reinforced Concrete Buildings in California, PhD thesis, Georgia Institute of Technology.

Jeon, J.-S., Lowes, L. N., DesRoches, R. and Brilakis, I. (2015), 'Fragility Curves for Non-ductile Reinforced Concrete Frames That Exhibit Different Component Response Mechanisms', *Engineering Structures* **85**, 127–143.

Jeon, J.-S., Park, J.-H. and DesRoches, R. (2015a), 'Seismic Fragility of Lightly Reinforced Concrete Frames with Masonry Infills', *Earthquake Engineering & Structural Dynamics* **44**(11), 1783–1803.

Jeon, J.-S., Shafieezadeh, A., Lee, D., Choi, E. and DesRoches, R. (2015b), 'Damage Assessment of Older Highway Bridges Subjected To Three-dimensional Ground Motions: Characterization of Shear–axial Force Interaction on Seismic Fragilities', *Engineering Structures* **87**, 47–57.

Jibson, R. W. and Harp, E. L. (2011), *Field Reconnaissance Report of Landslides Triggered By the January 12, 2010, Haiti Earthquake*, US Department of the Interior, US Geological Survey.

Kato, D. and Ohnishi, K. (2002), Axial Load Carrying Capacity of RC Columns Under Lateral Load Reversals, *in* 'Proceedings of the Third US-Japan Workshop on Performance-Based Earthquake Engineering Methodology for Reinforced Concrete Building Structures'.

Kaviani, P., Zareian, F. and Taciroglu, E. (2012), ‘Seismic Behavior of Reinforced Concrete Bridges with Skew-angled Seat-Type Abutments’, *Engineering Structures* **45**, 137–150.

Kavianijopari, P. (2011), *Performance-based Seismic Assessment of Skewed Bridges*, University of California, Irvine.

Kenawy, M., Kunnath, S., Kolwankar, S. and Kanvinde, A. (2018), ‘Fiber-based Nonlocal Formulation for Simulating Softening in Reinforced Concrete Beam-columns’, *Journal of Structural Engineering* **144**(12), 04018217.

Kenawy, M., Kunnath, S., Kolwankar, S. and Kanvinde, A. (2020), ‘Concrete Uniaxial Nonlocal Damage-plasticity Model for Simulating Post-peak Response of Reinforced Concrete Beam-columns Under Cyclic Loading’, *Journal of Structural Engineering* **146**(5), 04020052.

Kent, D. C. and Park, R. (1971), ‘Flexural Members with Confined Concrete’, *Journal of the Structural Division* **97**(7), 1969–1990.

Kim, S.-H. and Shinozuka, M. (2004), ‘Development of Fragility Curves of Bridges Retrofitted By Column Jacketing’, *Probabilistic Engineering Mechanics* **19**(1-2), 105–112.

Kolmogorov, A. (1933), ‘Sulla Determinazione Empirica Di Una Lgge Di Distribuzione’, *Inst. Ital. Attuari, Giorn.* **4**, 83–91.

Kotsoglou, A. and Pantazopoulou, S. (2007), ‘Bridge–embankment Interaction Under Transverse Ground Excitation’, *Earthquake Engineering & Structural Dynamics* **36**(12), 1719–1740.

Kwon, O.-S. and Elnashai, A. S. (2010), ‘Fragility Analysis of a highway Over-crossing Bridge with Consideration of Soil–Structure Interactions’, *Structure and Infrastructure Engineering* **6**(1-2), 159–178.

Lehman, D. E. and Moehle, J. P. (2000), ‘Seismic Performance of Well-Confined Concrete Bridge Columns’, *University of California, Berkeley, CA, USA, PEER Research Report* .

Liang, X., Mosalam, K. M. and Günay, S. (2016), ‘Direct Integration Algorithms for Efficient Nonlinear Seismic Response of Reinforced Concrete Highway Bridges’, *Journal of Bridge Engineering* **21**(7), 04016041.

Lim, K. Y. and Mclean, D. I. (1991), ‘Scale Model Studies of Moment-reducing Hinge Details in Bridge Columns’, *Structural Journal* **88**(4), 465–474.

Lin, K.-W. and Wald, D. J. (2008), *ShakeCast Manual*, US Geological Survey.

Lloyd, S. (1982), ‘Least Squares Quantization in PCM’, *IEEE transactions on information theory* **28**(2), 129–137.

Lynn, A. C., Moehle, J. P., Mahin, S. A. and Holmes, W. T. (1996), ‘Seismic Evaluation of Existing Reinforced Concrete Building Columns’, *Earthquake Spectra* **12**(4), 715–739.

Mackie, K. R., Wong, J.-M. and Stojadinović, B. (2007), 'Integrated Probabilistic Performance-Based Evaluation of Benchmark Reinforced Concrete Bridges', *PEER report* .

Mander, J. B., Kim, D., Chen, S. and Premus, G. (1996), Response of Steel Bridge Bearings to Reversed Cyclic Loading, Technical report.

Mander, J. B., Priestley, M. J. and Park, R. (1988), 'Theoretical Stress-strain Model for Confined Concrete', *Journal of structural engineering* **114**(8), 1804–1826.

Mangalathu, S. (2017), Performance Based Grouping and Fragility Analysis of Box-girder Bridges in California, PhD thesis, Georgia Institute of Technology.

Mangalathu, S., Jeon, J.-S., Padgett, J. E. and DesRoches, R. (2016), 'ANCOVA-based Grouping of Bridge Classes for Seismic Fragility Assessment', *Engineering Structures* **123**, 379–394.

Maroney, B., Romstad, K. and Kutter, B. (1993), Experimental Testing of Laterally Loaded Large Scale Bridge Abutments, *in* 'Structural engineering in natural hazards mitigation', ASCE, pp. 1065–1070.

McKay, M. D., Beckman, R. J. and Conover, W. J. (2000), 'A Comparison of Three Methods for Selecting Values of Input Variables in the Analysis of Output From A Computer Code', *Technometrics* **42**(1), 55–61.

McKenna, F., Fenves, G. L., Scott, M. H. et al. (2000), 'Open System for Earthquake Engineering Simulation', *University of California, Berkeley, CA* .

Megally, S., Seible, F., Bozorgzadeh, A., Restrepo, J. and Silva, P. (2003), Response of Sacrificial Shear Keys in Bridge Abutments To Seismic Loading, *in* 'Proceedings of the FIB Symposium on Concrete Structures in Seismic Regions', pp. 6–9.

Megally, S., Silva, P. and Seible, F. (2001), 'Seismic Response of Sacrificial Shear Keys in Bridge Abutments', *STRUCTURAL SYSTEMS RESEARCH PROJECT* **23**.

Moehle, J. and Eberhard, M. (2003), 'Earthquake Damage to Bridges. in: Bridge Engineering: Seismic Design'.

Muthukumar, S. (2003), *A Contact Element Approach with Hysteresis Damping for the Analysis and Design of Pounding in Bridges*, Georgia Institute of Technology.

Muthukumar, S. and DesRoches, R. (2006), 'A Hertz Contact Model with Non-linear Damping for Pounding Simulation', *Earthquake engineering & structural dynamics* **35**(7), 811–828.

Nielson, B. G. (2005), Analytical Fragility Curves for Highway Bridges in Moderate Seismic Zones, PhD thesis, Georgia Institute of Technology.

Padgett, J. E. (2007), Seismic Vulnerability Assessment of Retrofitted Bridges Using Probabilistic Methods, PhD thesis, Georgia Institute of Technology.

Paik, J. K., Kim, K. J., Lee, J. H., Jung, B. G. and Kim, S. J. (2017), 'Test Database of the Mechanical Properties of Mild, High-tensile and Stainless Steel and Aluminium Alloy Associated with Cold Temperatures and Strain Rates', *Ships and Offshore Structures* **12**(sup1), S230–S256.

Pan, Y., Agrawal, A. K. and Ghosn, M. (2007), 'Seismic Fragility of Continuous Steel Highway Bridges in New York State', *Journal of Bridge Engineering* **12**(6), 689–699.

Park, R. (1989), 'Evaluation of Ductility of Structures and Structural Assemblages From Laboratory Testing', *Bulletin of the new Zealand society for earthquake engineering* **22**(3), 155–166.

Paulay, T. and Priestley, M. N. (1992), 'Seismic Design of Reinforced Concrete and Masonry Buildings'.

Powell, G. H. and Chen, P. F.-S. (1986), '3D Beam-column Element with Generalized Plastic Hinges', *Journal of engineering mechanics* **112**(7), 627–641.

Prakash, S. (2009), 'Seismic Behavior of Circular Reinforced Concrete Bridge Columns Under Combined Loading Including Torsion', *PhD Doctoral Dissertation* .

Priestley, M. N. and Benzoni, G. (1996), 'Seismic Performance of Circular Columns with Low Longitudinal Reinforcement Ratios', *Structural Journal* **93**(4), 474–485.

Priestley, M. N., Seible, F. and Calvi, G. M. (1996), *Seismic Design and Retrofit of Bridges*, John Wiley & Sons.

Priestley, M. N., Verma, R. and Xiao, Y. (1994), 'Seismic Shear Strength of Reinforced Concrete Columns', *Journal of structural engineering* **120**(8), 2310–2329.

Ramanathan, K. N. (2012), Next Generation Seismic Fragility Curves for California Bridges Incorporating the Evolution in Seismic Design Philosophy, PhD thesis, Georgia Institute of Technology.

Raychowdhury, P. and Hutchinson, T. C. (2008), 'ShallowFoundationGen OpenSees Documentation', *Open System for Earthquake Engineering Simulation (OpenSEES): University of California, San Diego* .

Rayleigh, J. W. S. B. (1896), *The Theory of Sound*, Vol. 2, Macmillan.

Roblee, C. (2015*a*), 'Caltrans P266-T1780 Project File '2015-03-17 Abutment Joint & ElastoPad Info.pdf' Summarizing Joint Bearing and Seal Hardware, Abutment Joint Gap Models, and Methods for Characterizing Bilinear Response Model for Elastomeric Bearings.'.

Roblee, C. (2015*b*), 'Caltrans P266-T1780 Project File "2015-07-30 V2 Process Overview.pdf" Outlining Methodology and Considerations for Selection and Scaling of the T1780 Ground Motion Set for Use in the Development of g2F Fragility Models.'.

Roblee, C. (2015*c*), 'Caltrans P266-T1780 Project File "CT1780 GM Sets Metadata – FINAL.xlsx" Listing Record Numbers and Metadata for the T1780 Ground Motion Set.'.

Roblee, C. (2016*a*), 'Caltrans P266-T1780 Project File '2016-08-21 Materials by PC-RC. Xlsx' Summarizing Data and Models for Nominal Structural Materials Strength Values, 4 tabs.'.

Roblee, C. (2016*b*), 'Caltrans P266-T1780 Project File '2016-08-22 Span_Depth Models.xlsx' Summarizing Data and Models for the Ratio of Deck Structural-Section Depth to Maximum Span Length, 7 tabs.'.

Roblee, C. (2016*c*), 'Caltrans P266-T1780 Project File '2016-10-25 ISF-BG Column-Size Constraints.xlsx' Summarizing Inventory Column Data and Used To Develop CDA Constraints, 11 tabs.'.

Roblee, C. (2016*d*), 'Caltrans P266-T1780 Project File "2016-04-12 Compare Ph 2 to Ph 1 Motions.pdf" Comparing Ground Motion Sets Used in Current Phase-2 g2F Production Development Work with Those Used in Prior Phase-1 Feasibility Study.'.

Roblee, C. (2016*e*), 'Caltrans P266-T1780 Project Technical Archives File '2016-05-28 MTF-BG Transverse Profiles.pdf' and Associated Workbooks '2016-05-28 MTF-BG Transverse Profiles-Part A (& B).xlsx' Summarizing Methods, Models and Data for Characterization of Box-Girder Bridge Transverse Profiles, 9 p & 36 tabs.'.

Roblee, C. (2016*f*), ''Pre-Analysis IBS-to-RBS Grouping Methods for the Box-Girder Bridge Inventory', 52 p.'.

Roblee, C. (2017*a*), 'Caltrans P266-T1780 Project File "2017-10-30 Sampled Starter Bar Lap-Splice.xlsx" Data on Starter Bar Lengths in a Sample of 141 Era-1 Box-Girder Bridge Column Designs.'.

Roblee, C. (2017*b*), 'Caltrans P266-T1780 Project Technical Archives File '2017-01-25 MTF-BG_ColHt Models.pdf' and Associated Workbooks '2017-01-25 BG_ColHt Models.xlsx' and '2016-07-23 MCG_dBG_syISF Data.xlsx' Summarizing Methods, Models and Data for Characterization of Box-Girder Bridge Column Heights and Unbalance Ratios, 22 p, 36 tabs.'.

Roblee, C. (2017*c*), 'Caltrans P266-T1780 Project Technical Archives File '2017-02-06 TO UPDATE MTF-BG_SpanLength Models.pdf' and Associated Workbooks '2017-02-06 BG SpanLength Models.xlsx', '2016-06-17 ISF-BG SpanLength Data.xlsx' and '2016-06-17 SSx-BG SpanLength Data.xlsx' Summarizing Methods, Models and Data for Characterization of Box-Girder Bridge Span Lengths, 17 p & 71 tabs.'.

Roblee, C. (2017*d*), ''Resource Packet #2a: Comparison of T1780v1 CCLS Models to Raw Data' Resource Materials Provided to Participants in 2017 Caltrans-PEER Workshop on Characterizing Uncertainty in Bridge-Column Capacity Limit States.'.

Roblee, C. (2017*e*), ‘’Resource Packet #4: Typical California Bridge-Column Details’ Resource Materials Provided to Participants in 2017 Caltrans-PEER Workshop on Characterizing Uncertainty in Bridge-Column Capacity Limit States.’.

Roblee, C. (2018*a*), ‘Caltrans P266-T1780 Project File ’2018-04-19 CJR Column Model Groups - Full Packet.pdf’ Summarizing Inventory Data and Models for Characterization of Box-Girder Bridge Column Sections and Reinforcement, 31 p.’.

Roblee, C. (2018*b*), ‘Caltrans P266-T1780 Project File ’2018-06-03 Inventory Abut Info.xlsx’ Summarizing Abutment Footing Width and Containing Sample Plans for 3 Eras of Abutment Shear Keys, 11 tabs.’.

Roblee, C. (2018*c*), ‘Caltrans P266-T1780 Project File ’2018-07-11 Abutment Joint Gap Models.xlsx’ Summarizing Abutment Joint Gap Size Models Based on Movement Rating Data From Bridge Inventory, 1 tab.’.

Roblee, C. (2018*d*), ‘Caltrans P266-T1780 Project File ’2018-08-02b Era_3 Fndn Geometry Summary.pdf’ Summarizing Inventory Dimensional Data for Era-3 Column-Foundation, 3 p.’.

Roblee, C. (2018*e*), ‘Caltrans P266-T1780 Project File ’2018-09-10 Cjr DRAFT Abutment Types for ET.pdf’ Summarizing Wide Range of California Bridge-Abutment Types for 3 Eras Including Inventory Proportions and Sample Plans, 21 p.’.

Roblee, C. (2018*f*), ‘Caltrans P266-T1780 Project File ’2018-09-19 DRAFT Std Pile Types & Usage.pdf’ Summarizing Standard Pile Types for All Eras and Pile-Type Mix Proportions for Use in Era-3 Column and Abutment Foundations, 5 p.’.

Roblee, C. (2018*g*), ‘Caltrans P266-T1780 Project File “2018-02-26 V3 Example AUS Abutment Backwalls.xlsx” Containing Abutment-backwall Design Details for A Random Selection of Box-girder Bridges in Caltrans Bridge Inventory.’.

Roblee, C. (2018*h*), ‘Caltrans P266-T1780 Project Files ’2018-04-02 e33-nr DBG SyISF Bridge Joint Info.xlsx’ (and E22 & E11 Equivalents) Summarizing Inventory Data and Models for Characterization of Elastomeric Bearing Dimensions and Stiffness, 12 tabs each.’.

Roblee, C. (2020*a*), ‘Caltrans P266-T1780 Project File ’2020-04-30 DRAFT Work-Plan Update.xlsx’ Outlining Set of Base RBS and Other Exploratory and Production Analyses Needs.’.

Roblee, C. (2020*b*), ‘Caltrans P266-T1780 Project File ’2020-05-18 Update of 2019_11_06 Era_3 Fndn Geometry Summary.xlsx’ Summarizing Inventory Data and Models for Characterization of Era-3 Column Foundations for Box-Girder Bridge Columns, 18 tabs.’.

Roblee, C. (2020*c*), ‘Caltrans P266-T1780 Project File ’2020-08-25 Archive E33 Inventory Details.xlsx’ (Incomplete) Summary File of Era-3 Bridge Inventory Information Pertaining to Column and Abutment Foundation Details, 14 tabs.’.

Roblee, C. (2020*d*), ‘Caltrans P266-T1780 Project File ’2020-08-27 g2F-Compatible 4-State CCLS Models for OSB1 Bridge Example.xlsx’ Outlining Mapping of G2F to HAZUS State Definitions and Development of Compatible CCLS Models for Selected OSB1 Components.’.

Roblee, C. (2020*e*), ‘’Seat-Type Abutment Sample From CA Multi-Span Box-Girder Bridge Inventory’. Example Seat-Type Abutment Plans Details for a Random Sample of 243 Box Girder Bridges (Bridge ID’s and Locations are Anonymized)’, *DesignSafe-CI. DOI: https://doi.org/10.17603/ds2-v6gk-8b47.* .

Roblee, C. (2021*a*), ‘Caltrans P266-T1780 Project File ’2021-03-20 Era-3 DBG Abutment Seat Widths’ Comparison of Specified Seat Width Models to Seat-Width Data From a Random Sample of 108 Era-3 Box-Girder Bridges.’.

Roblee, C. (2021*b*), ‘Caltrans P266-T1780 Project File ’2021-04-02 (v3) PSDM Y-Axis Scaling Idea (Column Foundation).xlsx’ Demonstrating Process to Establish Median Pile-Response Backbone Shapes for 3 Pile Groups From Weighted Average of Pile-Type and Embedment Depth Assignments Used in RBS.’.

Roblee, C. (2021*c*), ‘Caltrans P266-T1780 Project File ’2021-06-04 BSS-CDS Alignment Guidance’ Outlining Criteria Considered in the Alignment of Component Damage States With Bridge System States.’.

Roblee, C. (2021*d*), ‘Caltrans P266-T1780 Project File ’2021-06-04 T1780v2 Column CCLS Models - E3F.xlsx’ In-Depth Documentation of Methodology, Data and Models Used To Establish the Complete Set of 18 T1780v2 CCLS Models for Era-3 Flexural Columns and the Subset of 12 Models Used for G2F Applications.’.

Roblee, C. (2021*e*), ‘Caltrans P266-T1780 Project File ’2021-08-16 DRAFT Era-3 CCLS Models.xlsx’ Summary of Emerging Component Damage Models Needed for Era-3 Flexural-Column Bridges.’.

Roblee, C. (2021*f*), ‘Caltrans P266-T1780 Project File ’2021-08-17a Geotech Rotation Model.xlsx’ Outlining Methodology for Development of Geotechnically-Based Foundation Rotation Capacity Models for Fixed- and Pinned Base Column Foundations.’.

Roblee, C. and Zheng, Q. (2017), ‘Caltrans P266-T1780 Project File ’2017-08-02 Reinf Ratios - CJR Rev GT Update.xlsx’ Summarizing Inventory Data and Models for Characterization of Column Reinforcement Ratios for Box-Girder Bridge Columns, 14 tabs.’.

Rollins, K. M., Olsen, K. G., Jensen, D. H., Garrett, B. H., Olsen, R. J. and Egbert, J. J. (2006), ‘Pile Spacing Effects on 682 Lateral Pile Group Behavior: Analysis’, *Journal of geotechnical and geoenvironmental engineering* **132**(10), 1272–1283.

Saini, A. and Saiidi, M. (2014), Feasibility Studies for Improving Caltrans Bridge Fragility Relationships. final report no. ca14-2280, cceer 14-02, Technical report, Center for Civil Engineering Earthquake Research, 216 p.

Schoettler, M., Restrepo, J., Guerrini, G., Duck, D. E. et al. (2012), 'A Full-scale, Single-column Bridge Bent Tested By Shake-table Excitation'.

Scott, M. H. and Fenves, G. L. (2006), 'Plastic Hinge Integration Methods for Force-based Beam–column Elements', *Journal of Structural Engineering* **132**(2), 244–252.

Sezen, H. (2002), *Seismic Behavior and Modeling of Reinforced Concrete Building Columns*, University of California, Berkeley.

Shamsabadi, A., Dasmeh, A., Nojoumi, A., Rollins, K. and Taciroglu, E. (2020), 'Lateral Capacity Model for Backfills Reacting Against Skew-Angled Abutments Under Seismic Loading', *Journal of Geotechnical and Geoenvironmental Engineering* **146**(2), 04019129.

Shamsabadi, A. and Rollins, K. (2014), Three-dimensional Nonlinear Continuum Seismic Soilstructure Interaction Analysis of Skewed Bridge Abutments, *in* 'Procs., 8th European Conf. on Numerical Methods in Geotechnical Engineering, Delft, the Netherlands'.

Shamsabadi, A., Rollins, K. M. and Kapuskar, M. (2007), 'Nonlinear Soil–abutment–bridge Structure Interaction for Seismic Performance-based Design', *Journal of Geotechnical and Geoenvironmental Engineering* **133**(6), 707–720.

Shamsabadi, A. and Yan, L. (2008), Closed-form Force-displacement Backbone Curves for Bridge Abutment-backfill Systems, *in* 'Geotechnical Earthquake Engineering and Soil Dynamics IV', pp. 1–10.

Shinozuka, M., Feng, M. Q., Kim, H.-K. and Kim, S.-H. (2000b), 'Nonlinear Static Procedure for Fragility Curve Development', *Journal of engineering mechanics* **126**(12), 1287–1295.

Shinozuka, M., Feng, M. Q., Lee, J. and Naganuma, T. (2000a), 'Statistical Analysis of Fragility Curves', *Journal of engineering mechanics* **126**(12), 1224–1231.

Smirnov, N. et al. (1948), 'Table for Estimating the Goodness of Fit of Empirical Distributions', *Annals of mathematical statistics* **19**(2), 279–281.

Soleimani, F. (2017), Fragility of California Bridges-development of Modification Factors, PhD thesis, Georgia Institute of Technology.

Steelman, J., Filipov, E., Fahnestock, L., Revell, J., LaFave, J., Hajjar, J. and Foutch, D. (2014), 'Experimental Behavior of Steel Fixed Bearings and Implications for Seismic Bridge Response', *Journal of Bridge Engineering* **19**(8), A4014007.

Stefanidou, S. P., Sextos, A. G., Kotsoglou, A. N., Lesgidis, N. and Kappos, A. J. (2017), 'Soil-structure Interaction Effects in Analysis of Seismic Fragility of Bridges Using An Intensity-based Ground Motion Selection Procedure', *Engineering Structures* **151**, 366–380.

Sun, Z., Priestley, M. and Seible, F. (1993), *Diagnostics and Retrofit of Rectangular Bridge Columns for Seismic Loads*, Department of Applied Mechanics & Engineering Sciences, University of ....

Tanaka, H. (1990), 'Effect of Lateral Confining Reinforcement on the Ductile Behaviour of Reinforced Concrete Columns'.

Taskari, O. and Sextos, A. (2015), 'Probabilistic Assessment of Abutment-embankment Stiffness and Implications in the Predicted Performance of Short Bridges', *Journal of Earthquake Engineering* **19**(5), 822–846.

Umehara, H. (1983), 'Shear Strength and Deterioration of Short Reinforced Concrete Columns Under Cyclic Deformations.'.

Vamvatsikos, D. and Cornell, C. A. (2002), 'Incremental Dynamic Analysis', *Earthquake engineering & structural dynamics* **31**(3), 491–514.

Wilson, P. and Elgamal, A. (2006), Large Scale Measurement of Lateral Earth Pressure on Bridge Abutment Back-wall Subjected To Static and Dynamic Loading, *in* 'Proceedings of New Zealand Workshop on Geotechnical Earthquake Engineering', pp. 307–315.

Xie, Y. (2021), 'Caltrans P266-T1780 Project File '2021_06_15_Column_footing_added.pptx' Summary of the Development of Hyperbolic Response-Backbone Model Parameters for Spread Footings at Abutment-Wall and Column-Bent Locations.'.

Xie, Y., Zheng, Q., Roblee, C., Yang, C.-S., Padgett, J. and DesRoches, R. (2020), '"R5P Response Model", in Probabilistic Seismic Response and Capacity Models of Piles for Statewide Bridges in California.', *DesignSafe-CI. DOI: https://doi.org/10.17603/ds2-py7p-ec71.* .

Xie, Y., Zheng, Q., Roblee, C., Yang, C.-S. W., Padgett, J. E. and DesRoches, R. (2021), 'Probabilistic Seismic Response and Capacity Models of Piles for Statewide Bridges in California', *Journal of Structural Engineering* **147**(9), 04021127.

Xie, Y., Zheng, Q., Yang, C.-S. W., Zhang, W., DesRoches, R., Padgett, J. E. and Taciroglu, E. (2019), 'Probabilistic Models of Abutment Backfills for Regional Seismic Assessment of Highway Bridges in California', *Engineering Structures* **180**, 452–467.

Yamazaki, F., Hamada, T., Motoyama, H. and Yamauchi, H. (1999), Earthquake Damage Assessment of Expressway Bridges in Japan, *in* 'Optimizing Post-Earthquake Lifeline System Reliability', ASCE, pp. 361–370.

Yang, C.-S. (2020*a*), 'Caltrans P266-T1780 Project File '2020-08-28 e3_fFP Column-Fndn Rotational Spring Data.xlsx' Summary of the Development of Hyperbolic Response-Backbone Model Parameters for Rotational Failure of Era-3 Pinned-Base Foundation Designs.'.

Yang, C.-S. (2020*b*), 'Caltrans P266-T1780 Project File '2020-09-25 e3_fFF Column-Fndn Rotational Spring Data.xlsx' Summary of the Development of Hyperbolic Response-Backbone Model Parameters for Rotational Failure of Era-3 Fixed-Base Foundation Designs.'.

Yassin, M. H. M. (1994), Nonlinear Analysis of Prestressed Concrete Structures Under Monotonic and Cyclic Loads, PhD thesis, University of California, Berkeley.

Yen, W.-H. P., Chen, G., Buckle, I. G., Allen, T. M., Alzamora, D. E., Ger, J. and Arias, J. G. (2011), 'Post-earthquake Reconnaissance Report on Transportation Infrastructure Impact of the February 27, 2010, Offshore Maule Earthquake in Chile'.

Zareian, F., Kaviani, P. and Taciroglu, E. (2015), 'Multiphase Performance Assessment of Structural Response To Seismic Excitations', *Journal of Structural Engineering* **141**(11).

Zhang, J. and Makris, N. (2002), 'Kinematic Response Functions and Dynamic Stiffnesses of Bridge Embankments', *Earthquake Engineering & Structural Dynamics* **31**(11), 1933–1966.

Zhang, Y., Acero, G., Conte, J., Yang, Z. and Elgamal, A. (2004), Seismic Reliability Assessment of A Bridge Ground System, *in* '13th World Conference on Earthquake Engineering', Citeseer, pp. 1–6.

Zhao, J. and Sritharan, S. (2007), 'Modeling of Strain Penetration Effects in Fiber-based Analysis of Reinforced Concrete Structures', *ACI Materials Journal* **104**(2), 133.

Zheng, Q. (2019), 'Caltrans P266-T1780 Project File '2019-12-17 NIsoSK Model.xlsx' Documentation of Methodology, Data and Models Used To Establish the Four-Parameter External Non-Isolated Shear Key Model.'.

Zheng, Q. (2020*a*), 'Caltrans P266-T1780 Project File '2020-03-20 Sampling Reinforcement_DesignGM_AppliedGM.pdf' Outlining the Development of the Ground-Motion Pairing Constraint, 51 p.'.

Zheng, Q. (2020*b*), 'Caltrans P266-T1780 Project File '2020-05-28 Pin-Fix Section Model.xlsx' Outlining the Development of the Reduced Section (Pinned Hinge) Model for era-1 and era-3 Columns.'.

Zheng, Q. and Roblee, C. (2021), 'Caltrans P266-T1780 Project File '2021-05-12 Pushover Illustration of Bent-Redundancy Effect for Modern Flexural-Mode Bridge Columns.pdf'.'.

Zheng, Q., Yang, C.-S. W., Xie, Y., Padgett, J., DesRoches, R. and Roblee, C. (2021), 'Influence of abutment straight backwall fracture on the seismic response of bridges', *Earthquake Engineering & Structural Dynamics* **50**(7), 1824–1844.

Zheng, Q., Yang, C. W., Roblee, C., Kunnath, S., DesRoches, R., Padgett, J., Zhang, A. and Mangalathu, S. (2020), 'CT1780 — Experiment-Based Column Performance Database - RP1', *DesignSafe-CI. DOI: https://doi.org/10.17603/ds2-0nr1-8571* .

Zong, Z., Kunnath, S. and Monti, G. (2014), 'Material Model Incorporating Buckling of Reinforcing Bars in RC Columns', *Journal of Structural Engineering* **140**(1), 04013032.

VITA

Qiu was born in China in 1994. He received his Bachelor of Civil Engineering from Tongji University in Shanghai, China in 2016. He then entered the Georgia Institute of Technology to pursue his Ph.D. degree in Civil Engineering, focusing on Structural Engineering. During the Ph.D. program, he also earned two Master degrees: Master of Civil Engineering and Master of Statistics from Georgia Tech in 2020.